JOURNAL
OF
APPLIED PHYSICS

Vol. 31, No. 3 March, 1960

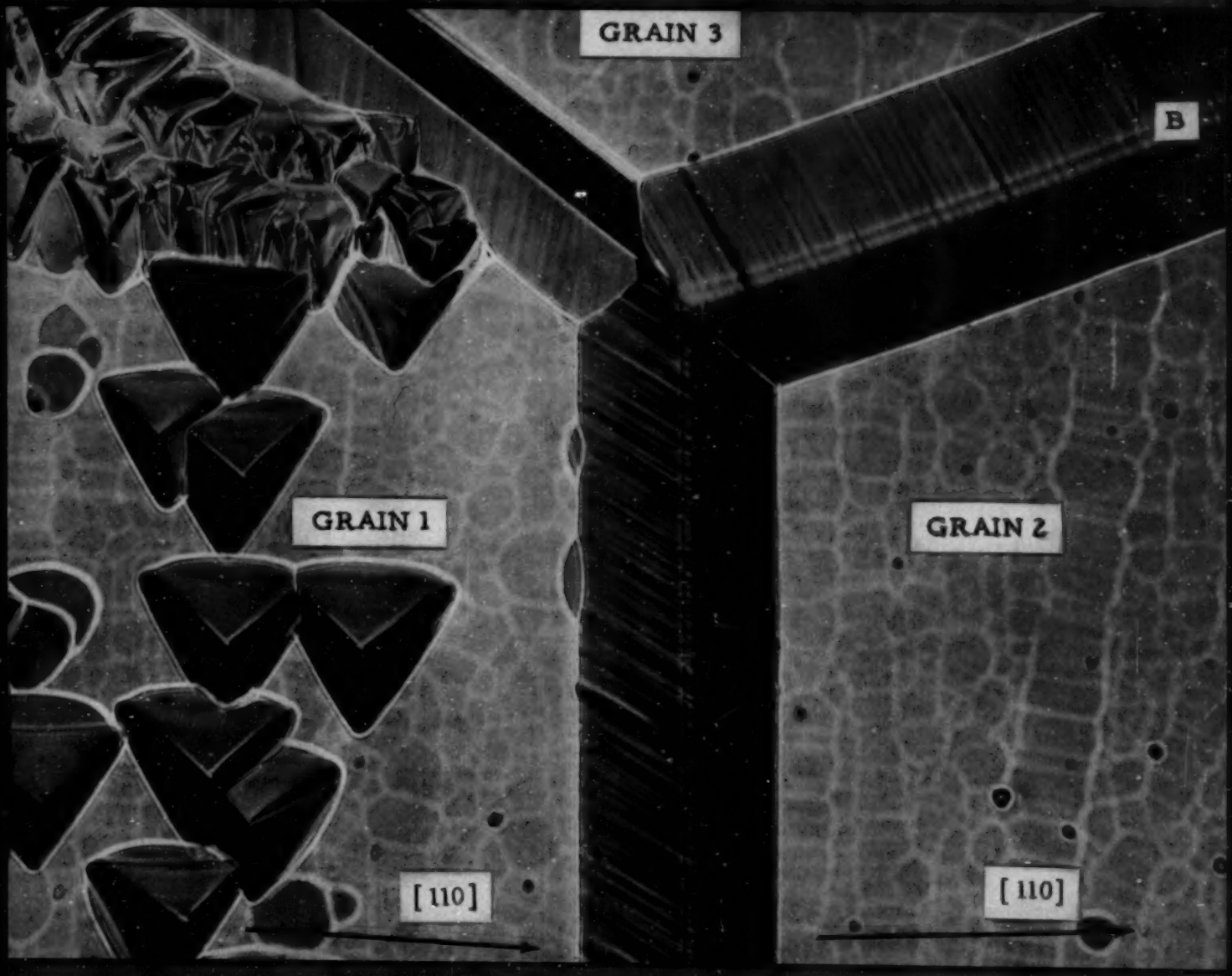

Grain Boundary Motion in Germanium. See Page 581.

Looking for an Electron Microscope with

"WORKHORSE" FEATURES?

then see the **NORELCO EM-75**

(this is not a delicate instrument)

The new EM-75B is a magnetic electron microscope designed to bridge the gap between light optics and high image resolution by providing enlargements ranging from 1,000 to 12,000 diameters under direct observation.

Its "workhorse" features are perhaps most outstanding. Reports from users indicate that upwards of 125 good quality micrographs are made daily . . . and all this with surprisingly low "down-time."

Exclusive operating features offer unusual dividends through broadening techniques and increasing applications. Its extreme flexibility provides a versatile tool for many newly conceived experimental techniques, requiring special manipulation and/or special physical treatment of the sample while being studied in the microscope.

The EM-75 is unmatched as a general service tool, an excellent educational instrument and a perfect control medium for laboratories. In addition, an electronics console and kit readily converts the EM-75 into an X-ray microscope – permitting exploitation and evaluation of opaque specimens.

Why don't you investigate the many other features of the EM-75? Write today for particulars.

Norelco

PHILIPS ELECTRONIC INSTRUMENTS

A Division of Philips Electronics and Pharmaceutical Industries Corp.

750 SOUTH FULTON AVENUE, MOUNT VERNON, N.Y.

In Canada: Research & Control Instruments • Philips Electronics Industries Ltd. • 116 Vanderhoof Ave. • Leaside, Toronto 17, Ont.

JOURNAL OF APPLIED PHYSICS

Vol. 31, No. 3 MARCH, 1960

In This Issue

High-Energy Sputtering . . . . . O. C. Yonts, C. E. Normand, and Don E. Harrison, Jr. 447

Influence of Irradiation with β Rays on the Electrification of KCl Crystals . . . . . Anna Szaynok 451

On the Nonconservation of Noise Parameters in Multivelocity Beams . . . J. Berghammer and S. Bloom 454

Focusing Molecular Beams of NH_3 . . . . . J. C. Helmer, F. B. Jacobus, and P. A. Sturrock 458

Molecular Beam Formation by Long Parallel Tubes . . . . . J. A. Giordmaine and T. C. Wang 463

Cratering and Shock Wave Phenomena in Steel Plates at High Impact Speeds . . . . . Earle B. Mayfield and James W. Rogers 472

Optical Studies of the Diffraction of Water Waves by Circular and Thin Elliptic Cylinders . . . . . Richard Barakat and Robert Barakat 474

Parametric Amplification along Nonlinear Transmission Lines . . . . . Rolf Landauer 479

Creep of Al_2O_3 Single Crystals . . . . . Roger Chang 484

Kinetics of Sintering of Sodium Chloride in the Presence of an Inert Gas . J. B. Moser and D. H. Whitmore 488

Effect of Pressure on Phosphor Decay . . . . . D. W. Gregg and H. G. Drickamer 494

Low-Temperature Transport Properties of Commercial Metals and Alloys. II. Aluminums . . . . . Robert L. Powell, William J. Hall, and Hans M. Roder 496

Low-Temperature Transport Properties of Commercial Metals and Alloys. III. Gold-Cobalt . . . . . Robert L. Powell, M. D. Bunch, and Edward F. Gibson 504

Noise and Signal Response in Lead Sulfide Photoconductive Films . . . . . H. E. Spencer 505

Ultimate and Secondary Electron Energies in the Negative Glow of a Cold-Cathode Discharge in Helium . . . . . J. M. Anderson 511

On the Behavior of Thermal Vacancies in Pure Aluminum . Doris Kuhlmann-Wilsdorf and H. G. F. Wilsdorf 516

Numerical Calculation of Absolute Bremsstrahlung Intensity for a Fully Ionized Fully Dissociated Hydrogenic Gas . . . . . G. Sargent Janes and H. Koritz 525

Effect of Fast Neutron Bombardment at Various Temperatures upon the Young's Modulus and Internal Friction of Copper . . . . . D. O. Thompson and V. K. Paré 528

Low Angle X-Ray Diffraction of Fibrous Polyethylene . . . . . A. S. Posner, L. Mandelkern, C. R. Worthington, and A. F. Diorio 536

Reflection of Sound from Randomly Rough Surfaces . J. M. Proud, Jr., R. T. Beyer, and Paul Tamarkin 543

Charged Sphere in Cylinder . . . . . W. R. Smythe 553

Flow of Polyethylene into a Capillary . . . . . E. B. Bagley and A. M. Birks 556

Alloying Behavior of Thin Bimetal Films, Simultaneously or Successively Deposited . . Richard B. Belser 562

Effect of Temperature on Photovoltaic Solar Energy Conversion . Joseph J. Wysocki and Paul Rappaport 571

Penetration of Rotating Shaped Charges . . . . . Sampooran Singh 578

Grain Boundaries in Germanium . . . . . Richard S. Wagner and Bruce Chalmers 581

Production of Very High Magnetic Fields by Implosion . . . C. M. Fowler, W. B. Garn, and R. S. Caird 588

Grain Boundary and Lattice Diffusion in Polycrystalline Bodies . . . . H. S. Levine and C. J. MacCallum 595

Growth of Gallium Arsenide by Horizontal Zone Melting . . . . . J. L. Richards 600

Evidence for Dislocation Reactions in Copper . . . . . F. W. Young, Jr., and T. S. Noggle 604

Letters to the Editor:

Comments on Article by Cook . . . . . M. H. Miller 607

Diffusion of Copper into AlSb . . . . . R. H. Wieber, H. C. Gorton, and C. S. Peet 608

Operation of a Chromium Doped Titania Maser . . . . . H. J. Gerritsen and H. R. Lewis 608

Manipulation of Cesium . . . . . P. Leliak 609

Print-Out Process in Photographic Emulsion Grains . . . . . J. F. Hamilton and L. E. Brady 609

Solution-Precipitation Deformation under an Applied Stress . . . . . W. D. Kingery and M. P. Lepie 610

Etch Pits in Gallium Arsenide . . . . . J. L. Richards and A. J. Crocker 611

Several New Methods to Measure the Thermal Diffusivity of Semiconductors . . . . . J. H. Becker 612

Esaki Diode in InSb . . . . . R. L. Batdorf, G. C. Dacey, R. L. Wallace, and D. J. Walsh 613

On the Possibility of Maser Action in Nuclear Quadrupole Systems . . . . . R. E. Donovan and A. A. Vuylsteke 614

Dislocation Etch Pits on P-Type Lead Telluride . . . . . B. B. Houston and Marriner K. Norr 615

Ductility of NaCl Crystals . . . . . Robert G. Greenler and William S. Rothwell 616

Radiation Limited Dislocation Motion in Crystals . . . . . Robb Thomson 617

Formation of Cavities on Dislocations in Crystals of NaCl and KCl . . . . . L. W. Barr and J. A. Morrison 617

Depth of Indentation on an Impacting Projectile . . . . . R. A. Graham 619

Announcements 620

JOURNAL OF APPLIED PHYSICS

A journal of general physics and its applications to other sciences and to industry

Published by the

American Institute of Physics

GOVERNING BOARD

Ralph A. Sawyer, *Chairman*

Walter S. Baird
J. G. Baker
Jesse W. Beams
R. H. Bolt
Harvey Brooks
J. W. Buchta
J. H. Dillon
Vernet E. Eaton
Herbert A. Erf
S. A. Goudsmit
W. W. Havens, Jr.
Winston E. Kock
R. Bruce Lindsay
Walter C. Michels
C. J. Overbeck
G. E. Pake
Joseph B. Platt
John Strong
George E. Uhlenbeck
V. F. Weisskopf

ADMINISTRATION

Elmer Hutchisson
Director

Henry A. Barton
Associate Director

Wallace Waterfall
Secretary and Treasurer

Ruth F. Bryans
Publication Manager

W. C. Kelly
Director of Education Projects

Eugene H. Kone
Director of Public Relations

Alice Mastropietro
Circulation Manager

Kathryn Setze
Assistant Treasurer

Edward Tober
Manager, Production and Distribution

Theodore Vorburger
Advertising Manager

Emily Wolf
Office Manager

Editor

James A. Krumhansl

Editorial Board

J. H. Crawford
Arthur Kantrowitz
A. F. Kip
J. E. Goldman
J. L. Tuck
C. A. Wert
Herman A. Haus
C. Lester Hogan
R. S. Rivlin

THE JOURNAL OF APPLIED PHYSICS is devoted to general physics and its applications to other sciences, to engineering, and to industry. Previous to 1937, this journal was called PHYSICS.

The JOURNAL OF APPLIED PHYSICS welcomes articles of two distinct kinds: (1) Descriptions of new results in experimental or theoretical physics which are of general interest to physicists. The author should explain his contribution in such a way that a physicist or engineer in another field of specialization can appreciate its objectives and essential features. (2) Critical reviews of particular areas of physics or surveys of extensive investigations at a single laboratory. Authors contemplating writing such should correspond with the Editor before they begin writing.

The JOURNAL OF APPLIED PHYSICS welcomes letters to the editor which describe in a few words the content of laboratory reports and theses and which tell readers how they may obtain copies of such reports.

Manuscripts should be submitted to the Editor, James A. Krumhansl, Rockefeller Hall, Cornell University, Ithaca, New York. Authors should read the "Information for Contributors," facing page 1 of the January issue, before writing articles or letters. The *Style Manual* of the American Institute of Physics is also helpful to writers preparing manuscripts for journals published by the American Institute of Physics. It can be obtained for $1.00 from the American Institute of Physics, 335 East 45 Street, New York 17, New York.

Corrected proofs and all correspondence concerning papers in the process of publication should be addressed to the Publication Manager, American Institute of Physics, 335 East 45 Street, New York 17, New York.

Subscriptions, renewals, and orders for back numbers should be addressed to the American Institute of Physics, 335 East 45 Street, New York 17, New York.

Subscription Price	U.S. and Canada	Elsewhere
To members of member organizations of the American Institute of Physics and Affiliated Societies ..	$12.00	$13.00
To all others	14.00	16.00

Back Number Prices

Yearly back number rate when complete year is available: $17.00.
Single copies: $1.75 each (exception: March, 1958—$3.00 each).

Changes of address should be sent to the American Institute of Physics.

Advertising rates supplied on request. Orders, advertising copy, and cuts should be sent to the American Institute of Physics.

Second-class postage paid at Lancaster, Pa.

ARNOLD:
YOUR H.Q.
FOR MAGNETIC MATERIALS
AT THE IRE SHOW

2nd Floor Facing the Escalators

★ **PERMANENT MAGNETS**

Cast Alnico • Sintered Alnico • Arnox • Vicalloy • Cunife

★ **MAGNETIC CORES**

Tape Wound Cores of Deltamax, Supermalloy, Permalloy, Supermendur, etc.

Type "C," "E" and "O" Cores of Silectron • Bobbin Cores

Mo-Permalloy Powder Cores • Iron Powder Cores • Sendust Cores

★ **SPECIAL MATERIALS**

Barium Titanates • Permendur • Vibralloy

AT THE ARNOLD EXHIBIT:

Booths 2509-11-13 and 15

ARNOLD

SPECIALISTS in MAGNETIC MATERIALS

THE ARNOLD ENGINEERING COMPANY, Main Office: MARENGO, ILL.
BRANCH OFFICES and REPRESENTATIVES in PRINCIPAL CITIES

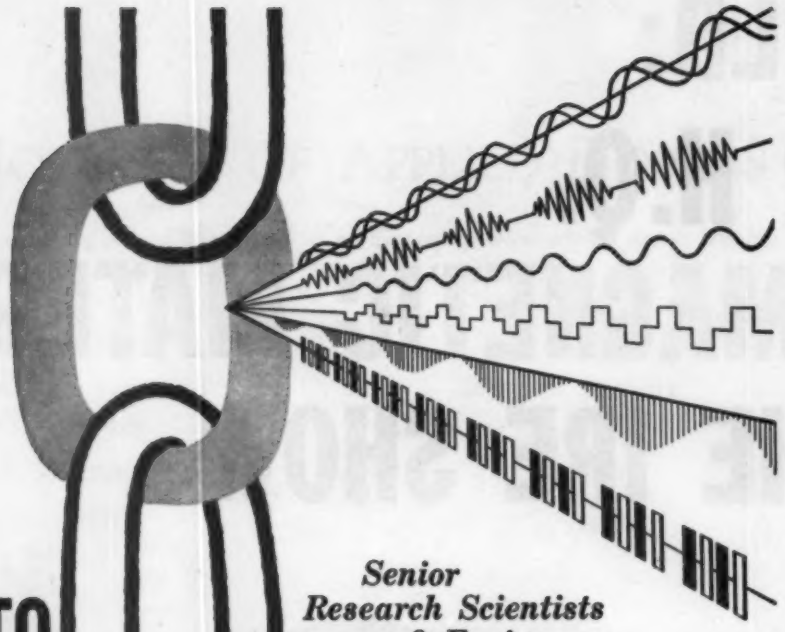

Senior Research Scientists & Engineers

TO CREATE A VITAL COMMUNI-CATIONS LINK

In large degree, the ultimate success of this country's defense mission may rest upon the effective operation of a long-range communications link now being studied at Sylvania's Amherst Laboratory. So exacting are the requirements of this system that techniques available to present-day technology would provide only marginal performance.

Considerations of the first magnitude involve supra-reliability and minimal degradation during single or multiple-path operation in a continually changing environment, despite electromagnetic disruption from natural or man-made sources.

Sylvania's Amherst Laboratory invites research scientists and engineers with advanced degrees to bring new concepts and techniques to the task of setting the parameters for, and demonstrating feasibility of, an operable system.

Send your confidential inquiry to
Dr. R. L. San Soucie
Amherst Laboratory / **SYLVANIA ELECTRONIC SYSTEMS**

A Division of

SYLVANIA GENERAL SYSTEM

Subsidiary of
GENERAL TELEPHONE & ELECTRONICS
1139 Wehrle Drive – Williamsville 21, New York

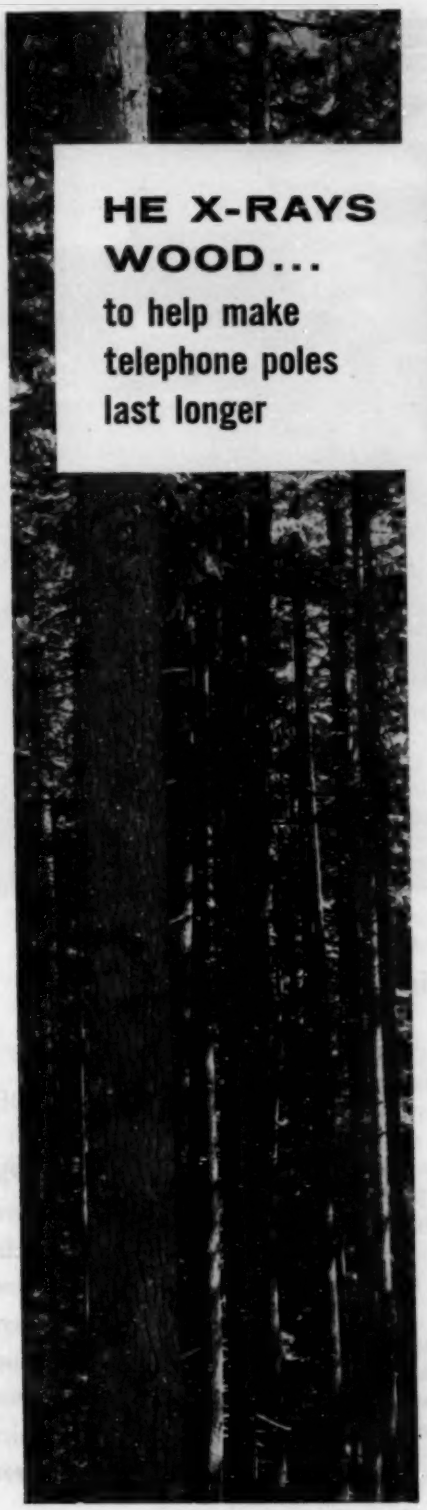

HE X-RAYS WOOD...

to help make telephone poles last longer

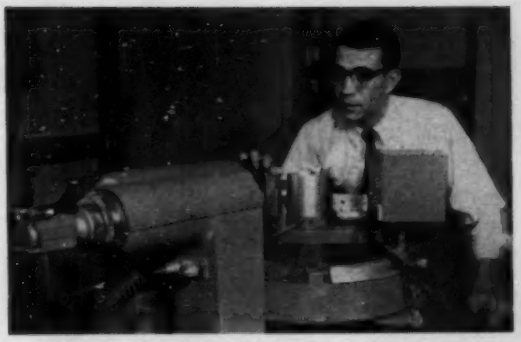

Chemist Jack Wright developed the use of this X-ray fluorescence machine for testing the concentration of preservatives in wood. Here he bombards a boring from a test telephone pole with X-rays.

This Bell Labs chemist is using a fast, new technique for measuring the concentration of fungus-killing preservative in telephone poles.

A boring from a test pole is bombarded with X-rays. The preservative—pentachlorophenol—converts some of the incoming X-rays to new ones of different and characteristic wave length. A radiation counter registers the intensity of these new rays. The intensity in turn reveals the concentration of preservative.

Bell Laboratories chemists must test thousands of wood specimens annually in their research to make telephone poles last longer. Seeking a faster test, they explored the possibility of X-ray fluorescence—a technique developed originally for metallurgy. For the first time, this technique was applied to wood. Result: A wood specimen check in just two minutes—at least 15 times faster than before possible with the microchemical analysis.

Bell Labs scientists must remain alert to *all* ways of improving telephone service. They must create radically new technology or improve what already exists. Here, they devised a way to speed research in one of telephony's oldest arts—that of wood preservation.

Nature still grows the best telephone poles. There are over 21 million wooden poles in the Bell System. They require no painting, scraping or cleaning; can be nailed, drilled, cut, sawed and climbed like no other material. Scientific wood preservation cuts telephone costs, conserves valuable timber acres.

BELL TELEPHONE LABORATORIES

World Center of Communications Research and Development

The nation's largest industrial computational facility

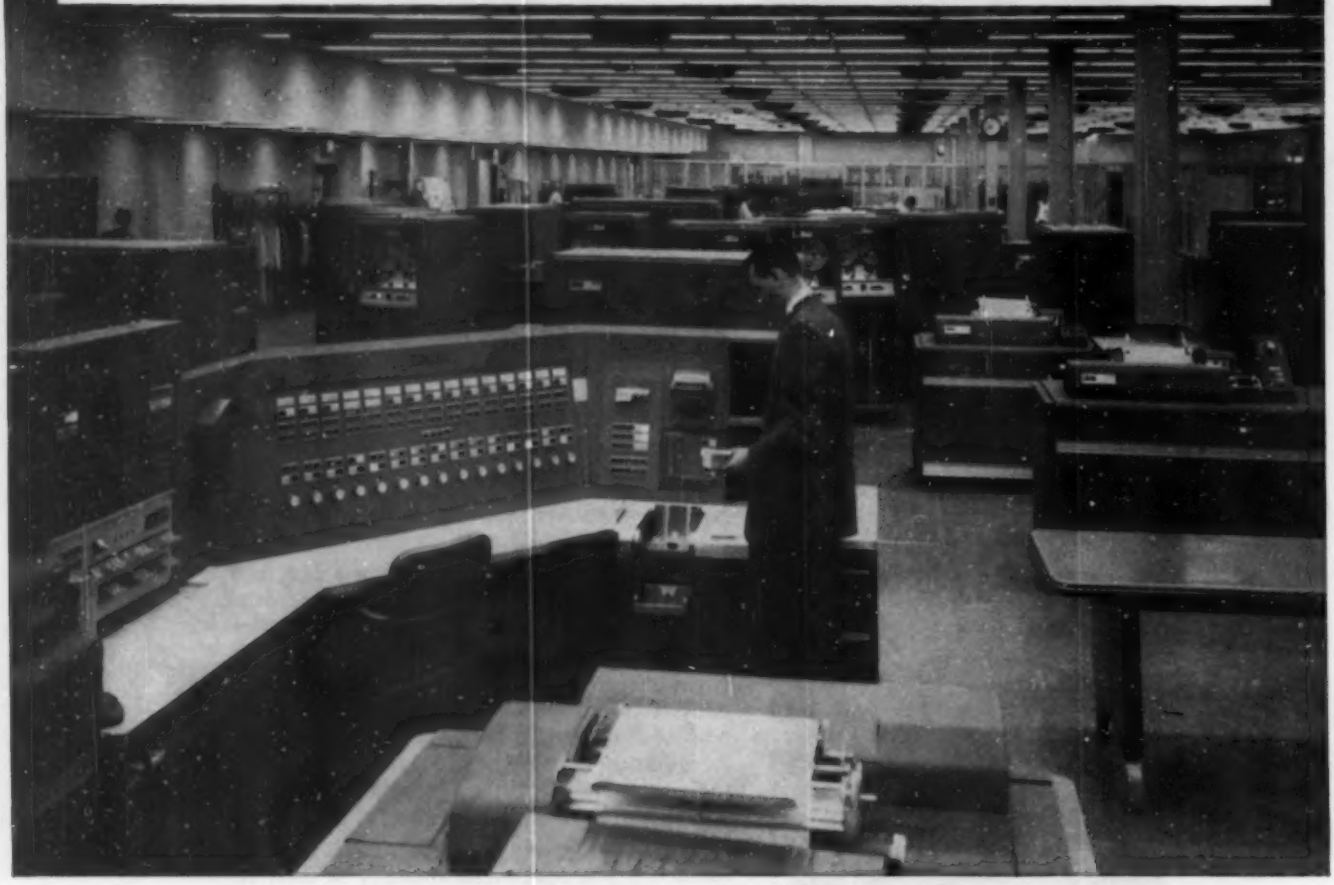

. . . important part of a unique research environment that can multiply your scientific accomplishments

Wherever you are carrying on scientific investigations, we doubt if you can call on advanced facilities and complementary scientific skills equal to those available at the Research Laboratories.

Here, leaders in a variety of scientific disciplines provide assistance in many areas that relate to your primary field of research. In addition, the nation's largest industrial computational facility can take over the routine of solving difficult calculations — routine that might otherwise burden you for months.

The Research Laboratories are organized to respect the time and abilities of men working in advanced scientific areas. If you appreciate an environment where a scientist can focus full mental power on scientific accomplishment, we would like to hear from you.

ATTRACTIVE OPENINGS
in many areas . . .

Solid State Physics
Plasma Physics
Gaseous Electronics
Chemical Kinetics
Particle Physics
Nuclear Engineering
Surface Chemistry
Cryogenics
Energy Conversion

Please write to Mr. W. M. Walsh, or phone Hartford, Conn., JAckson 8-4811, Ext. 7145

RESEARCH LABORATORIES
UNITED AIRCRAFT CORPORATION
400 Main Street, East Hartford 8, Conn.

UAC RESEARCH
. . . symbol of creative research

Kodak reports on:

the question of whether or not instrumentation people really need ultra-fast film . . . a simple-minded stunt with a little honest fudging . . . the profit viewpoint on nondestructive testing . . . organic chemistry and optical pumping

1600—no waiting

How come after all those promises we have made to innumerable instrumentation people over the years that some day there would be 16mm, 35mm, and 70mm film as fast as *Kodak Royal-X Pan Recording Film* now is—Index 1600—how come we now find ourselves in the ridiculous position of being able to make it at a greater rate than they're buying it? How come?

Don't they know that a note or phone call to Eastman Kodak Company, Photo Recording Methods Division, Rochester 4, N. Y., will set up the channel to supply it through a local dealer?

A tough window for the infrared

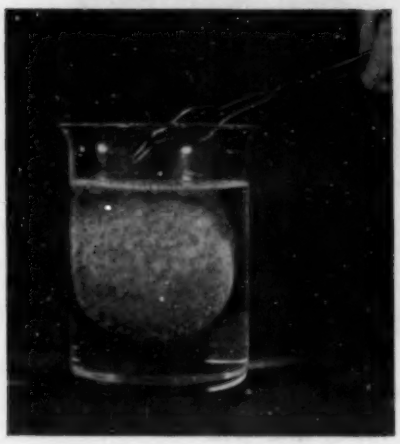

Our simple-minded stunt photo demonstrates that a 3-inch flat of the new *Kodak Irtran Optics, Type AB-1* can be fused so securely into a stainless steel mounting that plunging it at 200°C into tap water generates steam but does no harm.

We have developed this *Irtran* material for transmitting in structurally adequate thickness more than 90% of impinging energy from 3 to 6μ. Not only does it withstand thermal shock, weathering, humidity, and abrasion, but, defeating the emissivity of "hot windows," it retains its high transmittance at 800°C and, possessing a refractive index of less than 1.4, requires no coating to cut reflection losses.

The only fudging was a bit of detergent in the water. Actually we think it made the test more severe by increasing the cooling rate.

At present we can make Kodak Irtran *domes, flats, lenses, and interference filter substrates up to five inches in diameter. For details write Eastman Kodak Company, Special Products Division, Rochester 4, N. Y.*

Not too good, not too bad

One lady and 106 gentlemen, all materialists by profession whatever their private spiritual views, have labored long and brought forth two volumes of material philosophy that weigh in about average for newborn babes.

Title: *Nondestructive Testing Handbook*. Theme: better, safer, more *profitable* living through applied physics. Editor: Robert C. McMaster, The Ohio State University. Publisher: The Ronald Press Company, New York. Price: $24. No charge for the applause rendered the work here. What's good for nondestructive testing is good for Kodak.

Too much control of product characteristics squanders resources. Too little squanders reputation. Profit perfumes the happy valley in the middle.

The first section develops these thoughts in a manner to interest and please management, whether the product is bathtubs or Venus probes. The remaining 53 sections pursue the theme down every crevice of technical detail, not only in film radiography but in such others as liquid penetrants, magnetic particle tests, electrified particle tests, eddy currents, ultrasonics, brittle coatings, photoelastic coatings, strain gaging, radiation sources, fluoroscopy and x-ray image devices, x-ray diffraction and fluorescence, and even vision itself, properly aided.

Man passing out dotriacontane

We have a yarn that ties in the sperm whale with relativity. It has a moral but lacks a punchy climax.

On the theory that not only is the grass greener on the other fellow's lawn but he also leads a more interesting life, we would tell the organic chemists how the atomic physicists are looking for substances against which polarized free electrons can bounce without having their spins inverted. The physicists want to coat a substance like that on the walls of evacuated glass vessels. It should have no free or unpaired electrons, no crystal structure. To an electron scooting by, such a molecule should appear magnetically inert. The small residual pressure tolerable in the vessel should be mostly of rubidium vapor and not of the non-inverting substance. Also the coating must have good transmittance at around the 8000A wavelength of the radiation fed to excite the rubidium.

"Optical pumping," the theme these experiments share, has to do with the manipulation of quantum levels so that emission from the excited alkali metal atoms can be tuned with great elegance. People claim they need instrumentation to study the Van Allen radiation belts and satellite-borne atomic clocks to check out Einstein's old predictions about the meaning of time as told from a moving timepiece.

On the same greener grass theory, the yarn as spun for atomic physicists would focus on some little samples of non-inverting substance that were passed out at a recent optical pumping conference by a man who may well have bought the material from us as *Dotriacontane* (Eastman 3555). Now the sperm whale enters. Spermacetti wax once had a role in physics as the material of the standard candle which defined candlepower. When chemists attacked it, they found cetyl palmitate, $C_{16}H_{33}OCOC_{15}H_{31}$. We have to make a long, uniform, inert, homogeneous molecule out of that. First we snap off the $-OCOC_{15}H_{31}$ and replace it with bromine. Then, making use of a thought that occurred to Adolphe Wurtz around 1855, we react the cetyl bromide [which we call *1-Bromohexadecane* (Eastman 3375)] with sodium.

$$C_{16}H_{33}\boxed{Br + 2Na + Br}H_{33}C_{16} \rightarrow C_{32}H_{66} + 2NaBr$$

In effect, the two oxygens the whale put in the middle of the molecule have been replaced by hydrogens. That is *Dotriacontane*.

The climax, if any, will come when word filters through that *Dotriacontane* has done the job.

The moral is that with some 3800 organic compounds to milk, we need never be at a loss for words. They're all stocked by Distillation Products Industries, *Eastman Organic Chemicals Department, Rochester 3, N. Y. (Division of Eastman Kodak Company).*

Price quoted is subject to change without notice.

Kodak
TRADE MARK

This is another advertisement where Eastman Kodak Company probes at random for mutual interests and occasionally a little revenue from those whose work has something to do with science

zeus

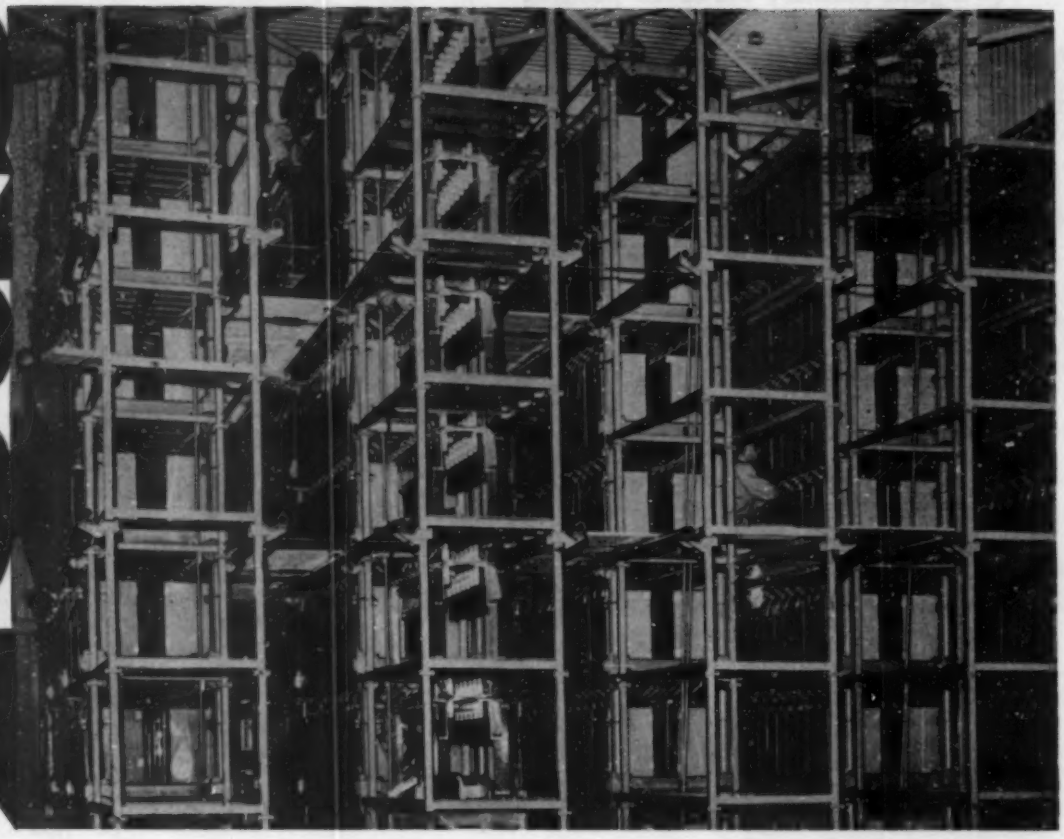

zeus...a giant **capacitor bank** at Los Alamos has a peak rating of 20 thousand volts, and will deliver 40 million amperes in 10 microseconds. It is a power supply for Project Sherwood investigations in controlled thermonuclear reactions. Los Alamos is one of the nation's leading centers for this and other aspects of plasma physics research.

For employment information write:
Director of Personnel Department 60 - 28

los alamos
scientific laboratory
OF THE UNIVERSITY OF CALIFORNIA
LOS ALAMOS, NEW MEXICO

HARSHAW MANUFACTURES A COMPLETE LINE OF SCINTILLATION AND OPTICAL CRYSTALS

SCINTILLATION *Mounted* NaI(T1) *Crystals*

Crystal detectors designed for the most sophisticated counting problems. Our physics and engineering group are available to assist you in your special detector problems.

More detailed information is contained in our 32-page book, "Harshaw Scintillation Phosphors." We invite you to write for your free copy!

STANDARD LINE
(Hermetically Sealed Crystal Assemblies)
- The accepted standard of the industry
- Proven through years of service in research, medical and industrial applications
- unparalleled performance
- dependability
- consistent good quality.

INTEGRAL LINE
(Crystal photo multiplier tube combination assembly)
- Improved resolution
- Ready to use plug-in unit
- Permanently light sealed
- Capsule design facilitates decontamination
- Close dimensional tolerances
- Harshaw guaranteed

Large Crystal **MATCHED WINDOW LINE**
(Designed primarily for crystals 4" dia. and larger)
- "Small crystal" performance achieved through improved optical design
- Low mass containers
- Available in standard aluminum or complete low background assemblies
- Convenient mounting flange
- Ready to use

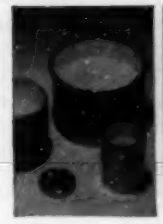

Every Harshaw crystal is a product of our experience in crystal growing technology since 1936

Other Phosphors Available from The Harshaw Chemical Company

ROUGH CUT THALLIUM ACITVATED SODIUM IODIDE CRYSTAL BLANKS • EUROPIUM ACTIVATED-LITHIUM IODIDE (NORMAL) • EUROPIUM ACTIVATED LITHIUM IODIDE (96% Li^6 ENRICHED) • THALLIUM ACTIVATED CESIUM IODIDE • THALLIUM ACTIVATED POTASSIUM IODIDE • ANTHRACENE • PLASTIC PHOSPHORS

OPTICAL *Crystals*

For Infrared and Ultra Violet Transmitting Optics

"HARSHAW QUALITY" INHERENT IN EACH HARSHAW-GROWN CRYSTAL GUARANTEES THE MOST EFFICIENT OPTICAL TRANSMISSION POSSIBLE THROUGH:

1) Negligible light scattering in crystals, permitting higher sensitivity and improved resolution
2) Freedom from absorptions caused by trace impurities in crystal optics
3) Minimum strain

"HARSHAW QUALITY" meets the demand for uniformity of optical properties such as dispersion and refractive index.

Prices, specifications, or other information will be sent in answer to your inquiry.

The following infrared and ultra violet transmitting crystals are available; others are in the process of development:

SODIUM CHLORIDE • SODIUM CHLORIDE MONOCHROMATOR PLATES POTASSIUM BROMIDE • POTASSIUM BROMIDE PELLET POWDER • (through 200 on 325 mesh) • POTASSIUM CHLORIDE • OPTICAL SILVER CHLORIDE • THALLIUM BROMIDE IODIDE • LITHIUM FLUORIDE • LITHIUM FLUORIDE MONOCHROMATOR PLATES • CALCIUM FLUORIDE • BARIUM FLUORIDE • CESIUM BROMIDE • CESIUM IODIDE

Additional information on the physical and optical properties of the above crystals is available in our 36-page booklet "Synthetic Optical Crystals". Send for your free copy.

HARSHAW

THE HARSHAW CHEMICAL CO.
Crystal Division • Cleveland 6, Ohio

MECHANICAL RADIATION

By R. B. LINDSAY, Brown University. *McGraw-Hill International Series in Pure and Applied Physics.* In Press.

The book provides an introduction to wave motion at the senior-graduate level, using mechanical radiation as the principal vehicle, but laying stress on these aspects common to all kinds of wave propagation. Mechanical relation is presented in the broad sense in integrated form by bringing together a unified treatment of the most significant radiation aspects of acoustics. Though the principal emphasis throughout is theoretical, the author has not allowed the mathematical analysis to dominate the physical meaning of the results.

RADIOISOTOPE TECHNIQUES

By RALPH T. OVERMAN, Oak Ridge Institute of Nuclear Studies; and HERBERT M. CLARK, Rennselaer Polytechnic Institute. 496 pages, $10.00.

A laboratory textbook designed to give the principles and typical procedures of working with radioactive materials. Discussions and techniques are included relative to the detection of radiation, errors in radioactivity measurements, the preparation of radioactive sources, the laboratory characterizations of radiation, the standardization of radioactive sources and the calibration of radiation detectors, the rates of radioactive processes, radiochemical separation methods, and applications of radioisotopes. Approximately 1,000 references to literature dealing with these techniques are included.

MISSILE AERODYNAMICS

By JACK N. NIELSEN, VIDYA, Inc. *McGraw-Hill Series in Missile and Space Technology.* Ready in April.

This volume presents a rational and connected account of principles of missile aerodynamics. It treats the subjects of bodies, wings, and tails and the interactions between them which are particularly important for missiles. Various methods are presented for determining the airflow about missiles, including the vortices which are frequently very prominent in the flow. The book is directed at the supersonic speed range, although most of the results are also applicable to subsonic speeds.

CONCEPTS OF THERMODYNAMICS

By EDWARD F. OBERT, University of Wisconsin. Ready in April.

In this book, emphasis on sound mathematical structure is a primary aim. It is a different book in that a new mathematical approach to thermodynamics is presented. Our reviewer comments: "Professor Obert is to be complimented on the comprehensive treatment and scholarly approach given to the various major topics. Extreme care is exhibited in the presentation of the material. This material will, without question, yield the most outstanding text on the subject of engineering thermodynamics."

Send for copies on approval

McGraw-Hill
BOOK COMPANY, INC.
330 West 42nd Street New York 36, N. Y.

superb new null detector and dc microvoltmeter

Model 151 offers non-linear and linear ranges, 10^{-17} watt sensitivity, 2 x 10^{-13} ampere current sensitivity.

The new Keithley 151, incorporating a unique photo-conductive modulator of Keithley design, is useful wherever a suspension galvanometer can be used and where a galvanometer is not sufficiently sensitive, fast or rugged.

As a null detector, has five non-linear ranges as well as linear ranges. Non-linear ranges each cover three decades, with full scale sensitivities of 0.001 to 10 volts. Center 10% of the log scale is linear, permitting extremely critical readings near null.

As a microvoltmeter or dc amplifier, has eleven linear ranges in 1x and 3x steps from 100 microvolts to 10 volts full scale. Input resistance on all ranges is ten megohms, yielding a maximum power sensitivity of better than 10^{-17} watt. Currents as low as 2 x 10^{-13} ampere can be detected. Output of 10 volts at 1 ma full scale permits use as a dc amplifier with gains to 100,000.

Other Features. Greater than 60 db rejection to 60 cps ac signals; zero drift below 10 microvolts per day; short-term noise within ± 2 microvolts.

MODEL 151 has 10^{-17} watt sensitivity, 2 x 10^{-13} ampere current sensitivity.

SPECIFICATIONS

Ranges: 11 linear ranges in 1x and 3x steps, from 100 μv to 10 v f.s.; 5 non-linear ranges of 0.001, 0.01, 0.1, 1.0 and 10 v f.s., each covering three decades.

Accuracy: Linear ranges, ± 3% of f.s. Non-linear ranges, ± 10% of input.

Input Resistance: 10 megohms on all ranges.

Response Speed: On 100 μv range, 2.5-sec.; 1-sec. on all others.

Noise: Less than 2% f.s. on all ranges.

Zero Drift: Less than 10 μv per day after warm-up.

Output: 10 volts at 1 ma f.s.; resistance, less than 50 ohms.

Price: Model 151, Cabinet Model $395.00
Model 151R, Rack Model $385.00

For complete details, write:

KEITHLEY INSTRUMENTS, INC.
12415 EUCLID AVENUE CLEVELAND 6, OHIO

WILEY BOOKS

Physics
for Students of Science and Engineering

Part I (*By* Robert Resnick, *Rensselaer Polytechnic Institute*, and David Halliday) of this book deals with the basic topics of mechanics, wave motion, and heat. Part II (*By* David Halliday, *University of Pittsburgh*, *and* Robert Resnick) is concerned with electromagnetism, optics, and quantum physics. Part I—*1960. 594 pages. $6.00.* Part II—*1960. Approx. 528 pages. $6.00.* Combined Edition—*1960. $10.75.*

Elementary Introduction to Nuclear Reactor Physics

By S. E. Liverhant, *New York State University. 1960. Approx. 424 pages. Prob. $9.50.*

Surface Effects on Spacecraft Materials

Edited by Francis J. Clauss, *Lockheed Aircraft Corporation. 1960. 404 pages. $11.50.*

Direct Conversion of Heat to Electricity

Edited by Joseph Kaye *and* John A. Welsh, *both of Massachusetts Institute of Technology. 1960. Approx. 384 pages. Prob. $8.75.*

Thermodynamics

By Herbert B. Callen, *University of Pennsylvania. 1960. 376 pages. $8.75.*

Optical Crystallography
Third Edition

By Ernest E. Wahlstrom, *University of Colorado. 1960. Approx. 352 pages. Prob. $7.00.*

Crystal-Structure Analysis

By Martin J. Buerger, *Massachusetts Institute of Technology. 1960. Approx. 664 pages. Prob. $16.00.*

Basic Data of Plasma Physics

By Sanborn C. Brown, *Massachusetts Institute of Technology. 1959. 336 pages. $6.50.*

Mechanics and Properties of Matter
Second Edition

By Reginald J. S. Stephenson, *College of Wooster, Ohio. 1960. Approx. 384 pages. Prob. $7.95.*

Modern Probability Theory and Its Applications

By Emanuel Parzen, *Stanford University. 1960. Approx. 440 pages. Prob. $9.75.*

Physics and Medicine of the Atmosphere and Space

Edited by Major General Otis O. Benson, Jr. *and* Hubertus Strughold, *both of the Aerospace Medical Center, Brooks Air Force Base. 1960. Approx. 672 pages. Prob. $12.50.*

Radiation Pyrometry and Its Underlying Principles of Radiant Heat Transfer

By Thomas R. Harrison, *Minneapolis-Honeywell Regulator Company, Brown Instruments Division. 1960. Approx. 240 pages. Prob. $12.00.*

Progress in Dielectrics
Volume I and II

Edited by J. B. Birks, *Manchester University, and* J. H. Schulman, *U. S. Naval Research Laboratory. 1960. In Press.*

Electromagnetic Energy Transmission and Radiation

By R. B. Adler, Lan Jen Chu, *and* R. M. Fano, *all of the Massachusetts Institute of Technology. 1960. Approx. 648 pages. Prob. $15.00.*

Electromagnetic Fields, Energy, and Forces

By R. M. Fano, Lan Jen Chu, *and* R. B. Adler, *all of the Massachusetts Institute of Technology. 1960. 520 pages. Prob. $10.00.*

Progress in Semiconductors
Volume 4

Edited by Alan F. Gibson, B.Sc., Ph.D. *1960. In Press.*

Theory of Mechanical Vibration

By KIN N. TONG, *Syracuse University. 1960. 348 pages. $9.75.*

Magnesium and Its Alloys

By C. Sheldon Roberts, *Fairchild Semiconductor Corporation. 1960. Approx. 248 pages. Prob. $8.50.*

Mathematical Methods for Digital Computers

Edited by Anthony Ralston, *Bell Telephone Laboratories, and* Herbert Wilf, *University of Illinois. 1960. Approx. 320 pages. Prob. $9.00.*

Theory of Thermal Stress

By Bruno A. Boley *and* Jerome H. Weiner, *both of Columbia University. 1960. Approx. 560 pages. Prob. $15.50.*

Send for examination copies.

JOHN WILEY & SONS, Inc., 440 Park Avenue South, New York 16

NEW NMR FLUXMETER

(Nuclear Magnetic Resonance)

FROM VARIAN

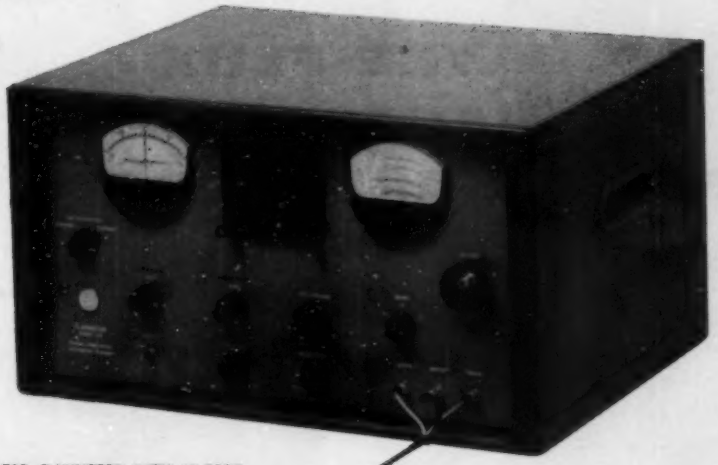

VARIAN MODEL F-8 NUCLEAR FLUXMETER WITH 50-FOOT EXTENSION CABLE REPRESENTED BETWEEN MAIN UNIT AND FIELD PROBE.
6-FOOT EXTENSION CABLE IS STANDARD EQUIPMENT.

The Varian Model F-8 Nuclear Fluxmeter provides precise *measurement* and/or *control* of magnets used in laboratory and industrial applications.

As a control device, the F-8 Fluxmeter holds fields stable against residual slow drift or external stray magnetic interferences not sensed by straight current regulation. Furthermore, the F-8 is capable of providing such control at extended distances from the magnet by mere addition of an accessory cable.

The frequency-determining (hence field-determining) circuitry of the F-8 Fluxmeter is buffered completely from the crossed-coil probe by several stages of amplification. Thus, for example, the varying probe position encountered during field plotting cannot inadvertently reduce accuracy.

CHARACTERISTICS AND ADDITIONAL FEATURES

- Wide frequency range and two probe samples (H^1 and H^2) permit field coverage from 1,000 gauss to an upper limit of 52,000 gauss.
- Accuracy—a function of signal-to-noise ratio, inherent sample line-width, and inhomogeneity of the field being measured — is as follows:

  ±0.05 gauss with 1 gauss external field gradient across ¼" diameter proton sample of 0.5 gauss natural line-width, using external frequency counter.

  ±0.2% with vernier and calibration curve (furnished).
  ±5% on convenient, direct-reading dial.

  Absolute accuracy is also limited by the accuracy of the NBS accepted determination for the gyromagnetic ratio of protons in water (approximately 1 part in 10^6).
- Standard probe cable is 6 feet long.
- F-8 may be used for NMR class-room experiments and demonstrations; absorption or dispersion signal may be chosen at will by one-knob balance adjustment on main unit.
- Plug-in jacks at rear of chassis permit external frequency measurement and crystal lock-in of transmitter.
- Control output suitable for direct use with Varian Regulated Magnet Power Supplies.
- Samples can be supplied in a choice of natural line widths for best match to available field homogeneity.
- Sweep amplitude and transmitter power are adjustable for optimum performance.

For full specifications, write the **Instrument Division,**

VARIAN associates
PALO ALTO 36, CALIFORNIA

NMR & EPR SPECTROMETERS, MAGNETS, FLUXMETERS, GRAPHIC RECORDERS, MAGNETOMETERS, MICROWAVE TUBES, MICROWAVE SYSTEM COMPONENTS, HIGH VACUUM EQUIPMENT, LINEAR ACCELERATORS, RESEARCH AND DEVELOPMENT SERVICES

PHYSICISTS
MATHEMATICIANS

By synthesizing three dimensional flux shapes from the results of one- and two-dimensional diffusion theory calculations, the physicists at Bettis Atomic Power Laboratory are able to compare these results to the shape and magnitude of the flux obtained under operating conditions in a light-water reflected, Zircaloy-uranium metal, light-water moderated reactor.

ANALYZE FLUX SHAPES IN CRITICAL ASSEMBLIES

If you are a physicist or mathematician interested in pursuing a career in reactor physics and you are a U. S. citizen, write to: Mr. M. J. Downey, Bettis Atomic Power Laboratory, Westinghouse Electric Corporation, Box 1526, Dept. B-41, Pittsburgh 30, Pennsylvania.

$$\overline{\alpha}_1 \nabla^2 Z - \overline{\alpha}_2 Z + \frac{\chi \ \overline{\alpha}_3 \ Z}{\lambda} = 0$$

$$\overline{\alpha}_i = \frac{\int \alpha_i \varphi (x, y) dA}{\int \varphi (x, y) dA}$$

$$\varphi (x, y, z) = \varphi (x, y) Z (z)$$

BETTIS ATOMIC POWER LABORATORY

Westinghouse

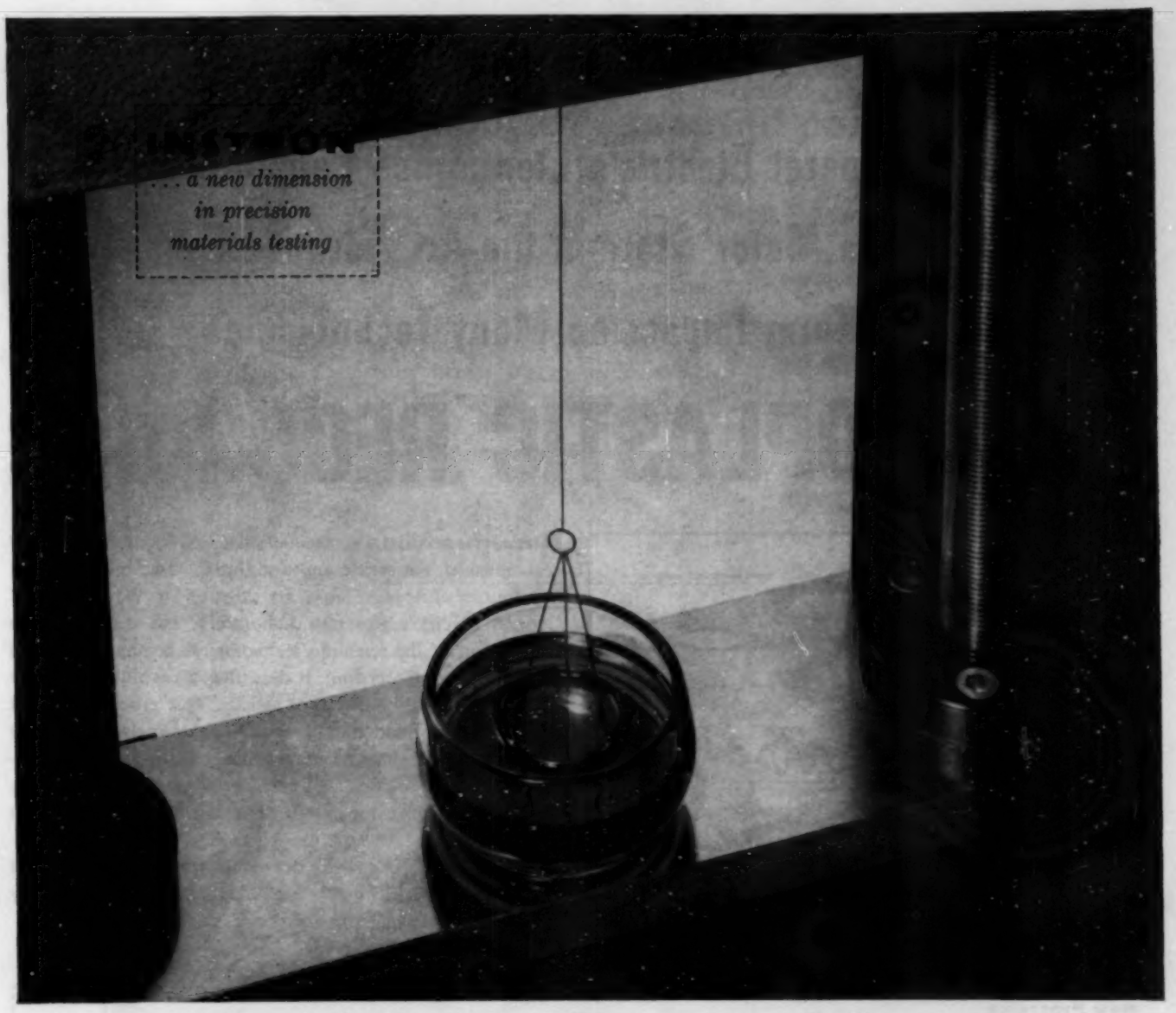

New twist for an old test

Instron — the same Instron that has the capacity to measure the strength of metal alloys and ceramics . . . or the rheological properties of plastics — here shows off its versatility anew.

The test: measuring surface tension of a liquid with a conventional du Nüoy tensiometer. The twist: Instron makes it possible to pull the ring from the liquid at various constant speeds, automatically plotting accurate force-displacement curves.

The complete laboratory report is available now — just ask for Bulletin X-2. It's one of a series of technical articles on advanced testing techniques that are yours for the asking. Among the subjects covered: testing tungsten at high temperature . . . the nature of twinning in metal single crystals . . . stress-strain properties of textile fibers . . . physical properties of plastics and elastomers. Let us know your field of interest.

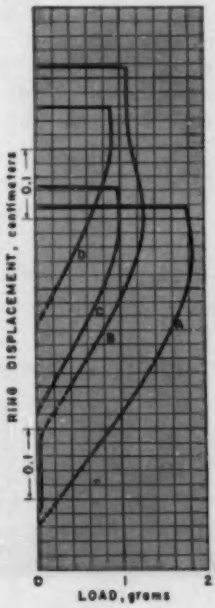

Load-ring displacement curves of various liquids at 23°C. A. Water. B. Epon 828. C Diallyl phthalate monomer. D. Dibutyl phthalate

YOU CAN DO MORE WITH INSTRON

The unusual versatility of this fine testing instrument is greatly extended by Instron's complete range of special accessories, which can be added as you need them. They include: digital equipment • conditioning cabinets • XY recorder for extensometers • quick-change crosshead-speed selector • capillary rheometer • high temperature equipment.

Write today for the complete Instron catalog.

INSTRON®

ENGINEERING CORPORATION

2512 WASHINGTON ST., CANTON, MASS.

EUROPEAN OFFICE: SEEFELDSTRASSE 45, ZURICH, SWITZERLAND

ENGINEERS • SCIENTISTS

Join General Electric's Electronics Laboratory In Exploiting a Major State-of-the-Art Advance Promising Long-Term Impact on Many Technologies

THERMOPLASTIC RECORDING

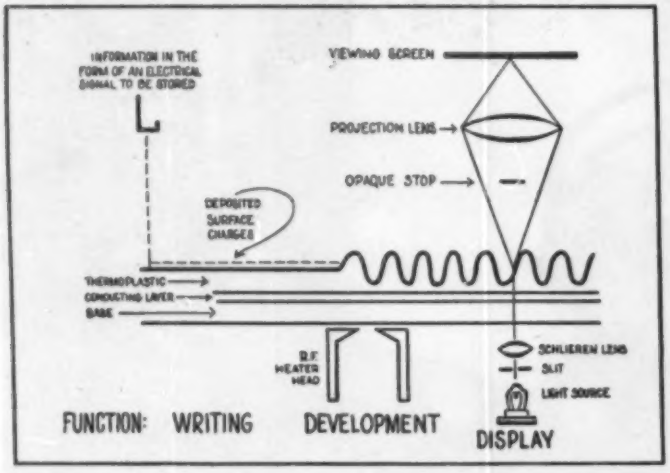

BREAKTHROUGHS are frequently talked about, infrequently accomplished. An article appearing in the December issue of *The Journal of Applied Physics*, written by Dr. W. E. Glenn of General Electric's Research Laboratory, has stimulated the imagination of the scientific/technological community. Titled *Thermoplastic Recording*, it describes a revolutionary new method of recording electrical signals. This process makes it possible for information to be written at extremely high density by means of an electron beam on a film consisting of a low melting thermoplastic material. Data can be projected as a black and white or full color image, or it can be converted to an electrical signal. The tape can be readily erased and reused. Summarizing, *Thermoplastic Recording* provides the equivalent of a high resolution, reusable "photographic" film developed by non-chemical means in the fraction of a second.

New Programs Utilizing invention and innovation, the Electronics Laboratory at Syracuse, New York is now engaged in a growing number of programs proving the feasibility of this new process for military and commercial applications which include direct image photography, projection displays, wideband analogue recording, sonar and radio signal correlation and processing.

Anti-Submarine Warfare Program Another program of current interest includes efforts devoted to submarine detection and classification by means other than sonar, secure underwater communications and submarine-to-aircraft communication.

Professional Opportunities Highly creative and experienced engineers and physicists are required to accomplish the objectives of these ambitious programs. Major areas of professional interest should include one or more of the following areas listed to the right.

A reprint of Dr. Glenn's article describing in detail the Thermoplastic Recording Process *is available upon request.*

- Geometrical, Physical and Electron Optics
- Circuit Design
- Mechanical Design
- Vacuum Technology
- Feedback Theory • Radar
- Oceanography • Television
- Sound Propagation
- Surface Physics • Sonar
- IR Phenomena

Additional openings in these areas:

- Materials • Circuits
- Devices • Systems
- Equipment

For further information on current openings
write in strict confidence to Mr. Robert Mason, Dept. 37-MC

ELECTRONICS LABORATORY

GENERAL ELECTRIC

Electronics Park, Syracuse, N. Y.

Announcing the new dd51—

computer readout at computer speed

Keeps pace with your computer and spells it out in plain English. Up to 4100 simultaneous characters without flicker. The presentation is so sharp and steady you can read it from across the room. Invaluable for debugging, maintenance, real time data monitoring, and rapid display of alphanumeric information. A variety of models in production.

More quick facts:

- 43 character repertoire
- simple to program
- solid state circuits
- precise registration
- low power consumption
- conventional cathode ray tubes
- character size may be programmed or manually controlled
- scopes are turntable mounted
- overall dimensions: 30"x22"x40"

For brochure, prices and delivery dates, phone MIdway 6-8673 or write to:

DATA DISPLAY
incorporated
1820 Como Avenue St. Paul 8, Minn.

We would be pleased to send you a copy of this unretouched photo. Actual size of scope is 7½".

plasma physics

new research programs at Hughes Research Laboratories

New means for generating and containing highly ionized dense plasmas—new processes to produce controlled fusion power—new concepts on the interaction of electro-magnetic waves with plasmas... these are some of the expanding projects pursued at the Hughes Research Laboratories in the field of plasma physics.

Openings currently exist in the field of plasma physics for SCIENTISTS and ENGINEERS—a variety of both junior and senior levels—at the Hughes Research Laboratories.

In Malibu, California... just above the Pacific in the foothills of the Santa Monica Mountains... this new facility has been specifically designed for effective research effort with private offices and complete research laboratories. In this uniquely creative atmosphere, Hughes scientists and engineers will continue their record of accomplishment in electronics and physics research.

Your inquiry regarding staff openings may be directed in confidence to Dr. Malcolm R. Currie, **HUGHES RESEARCH LABORATORIES,** *Malibu 1, California.*

Creating a new world with ELECTRONICS

HUGHES

© 1960, HUGHES AIRCRAFT COMPANY

RESEARCH LABORATORIES

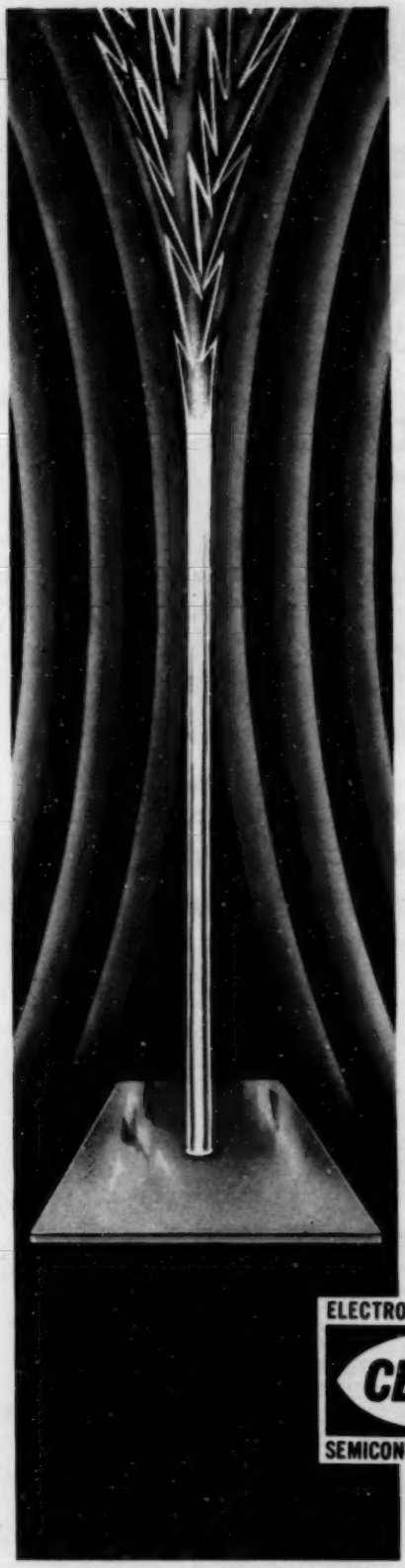

A SIGNIFICANT PROFESSIONAL CAREER ANNOUNCEMENT TO SEMICONDUCTOR ENGINEERS, CHEMISTS and PHYSICAL CHEMISTS...

CBS ELECTRONICS*

sets-up important

NEW MADT PROGRAM

THE PROGRAM... This is a major long range program in the mass production of Micro Alloy Diffused-base Transistors (FAST SWITCHES, HF AMPLIFIERS and HF POWER OSCILLATORS) through the use of electro-chemical jet etching and plating. These high-frequency transistors with extreme accuracy and uniformity for use in industrial and military computers are acknowledged to be the most challenging phase of *tomorrow's* data processing systems.

THE OPPORTUNITY... Engineers, Chemists and Physical Chemists with competence in semiconductors can now apply their full technical capabilities on CBS Electronics' new MADT program which offers exceptional ground-floor opportunities. Positions are available at all levels. Degree in one of the physical sciences required.

***THE COMPANY...** CBS ELECTRONICS is the engineering and manufacturing arm of COLUMBIA BROADCASTING SYSTEM, Inc. Supported by its full resources and under engineering-oriented management, we continue our sound expansion... with products characterized by ultra-high quality to meet the most exacting reliability standards.

As a member of the CBS professional family, you will work in our new $5,000,000 facility now nearing completion. You and your family will live in a pleasant New England community... with beaches, mountains, educational and cultural advantages nearby... and only 45 minutes from Metropolitan Boston.

Qualified applicants are invited to send resume to Mr. H. C. Laur. In replying, kindly designate Dept. 2929.

CBS ELECTRONICS
A Division of Columbia Broadcasting System, Inc.
900 Chelmsford Street, Lowell, Mass.

ARL
Applied Research Laboratory

RESEARCH POSITIONS
in Suburban Boston

Sylvania's new programs of expansion, enhanced by its merger last year with General Telephone & Electronics, offer increased opportunities for independent research at the Applied Research Laboratory. You will work with a distinguished organization of engineer-scientists whose achievements have already won them wide recognition in their fields. This laboratory is concerned with new approaches in:

• INFORMATION & COMMUNICATION THEORY • ELECTROMAGNETIC PROPAGATION • SOLID STATE PHYSICS • MICRO-ELECTRONICS • HYPERSONIC GASDYNAMICS • MATHEMATICAL ANALYSIS & OPERATIONS RESEARCH

If you hold a graduate degree or have equivalent experience in an applicable technical field, the advantages of a position with the Applied Research Laboratory merit your consideration—

• Problems of Major Magnitude in Advanced Areas • Ample Opportunity to Publish • Informal Professional Atmosphere & Extensive Opportunity for Creative Research

Write in confidence directly to Dr. L. S. Sheingold, Director, Applied Research Laboratory

Waltham Laboratories / **SYLVANIA ELECTRONIC SYSTEMS**
A Division of

SYLVANIA GENERAL SYSTEM
Subsidiary of
GENERAL TELEPHONE & ELECTRONICS

100 First Avenue—Waltham 54, Massachusetts

NEW

Jarrell-Ash

SPECTROGRAPHS

for problems beyond the scope of conventional instruments

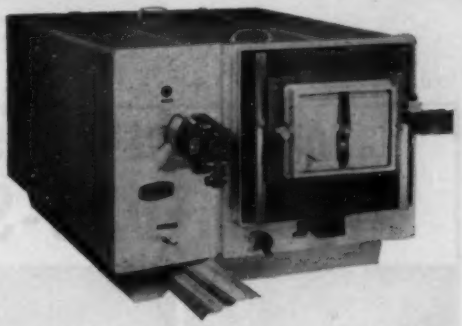

High Aperture Spectrographs

F /6.3 plane grating instruments for analysis of faint or short-duration light sources, as encountered in combustion studies, shock tube investigations, and temperature measurement. Excellent for chemical analysis of very small samples.

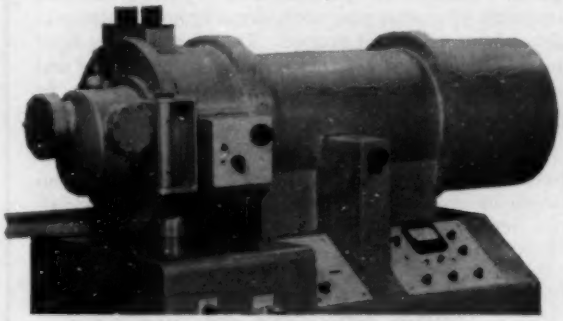

Vacuum Spectrographs and Spectrometers

Standard models in 1.0 to 6.8 meter focal lengths, grazing or normal incidence, photographic or photoelectric with automatic multispeed scanning.

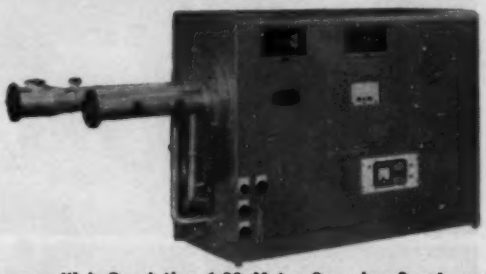

Vacuum High Resolution 1.83 Meter Scanning Spectrometer

Vacuum Ebert Scanning Spectrometer, 1.83 meter, high aperture (F /11.6) for use in ultraviolet, visible, and infrared regions. A high resolution instrument with precise multispeed scanning drive. Recommended for high-precision-wavelength determinations, and for isotopic, and infrared analysis. Resolving power (over 500,000) superior to other commercially available instruments. Also available as non-scanning spectrometer.

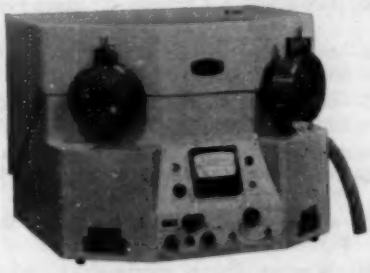

Vacuum Scanning Spectrometer Seya-Namioka Model

New, low cost Seya-Namioka Type Scanning Vacuum Spectrometer. Available in 1 and 0.5 Meter Models with optional camera. Virtually a universal monochromator, complete scanning range from 0 to 10,000A. Jarrell-Ash Company has a complete line of light sources and detectors for use in the 700A to 3400A region with these and other vacuum instruments.

Ebert Scanning Spectrometer

0.5 meter Ebert-type plane grating instruments, available with variety of photomultiplier receivers and electronics systems. Also available as a flame spectrometer with full accessories. Applications include combustion and reaction studies, flame temperature measurement.

May we assist you in solving unique analytical problems or pioneering a new approach to research. Write us full details and we'll be happy to suggest appropriate instruments and methods — even come up with an instrument modification tailored to your specific application, if necessary. Better yet, ask to have a Jarrell-Ash analytical methods engineer visit your laboratory for firsthand consultation. *No obligation, of course, in either case.*

Jarrell-Ash

JARRELL-ASH COMPANY

26 Farwell Street, Newtonville 60, Massachusetts

San Mateo, California Costa Mesa, California Dallas, Texas
New Brunswick, New Jersey Atlanta, Georgia Dearborn, Michigan
Arlington Heights, Illinois Pittsburgh, Pennsylvania
CANADA: Technical Service Laboratories, Toronto, Canada

FOR THE VERY BEST IN VACUUM PUMPS SELECT
WELCH DUO-SEAL® VACUUM PUMPS

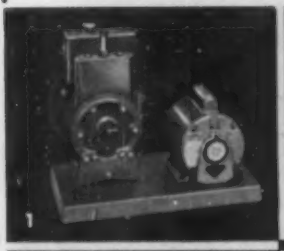
1

The complete line of Duo-Seal Vacuum Pumps is shown here. Descriptions and prices below.

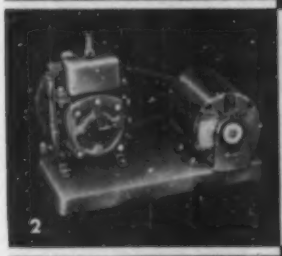
2

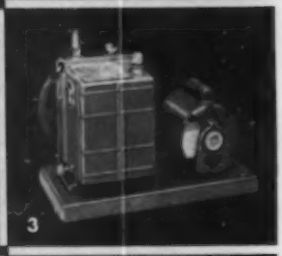
3

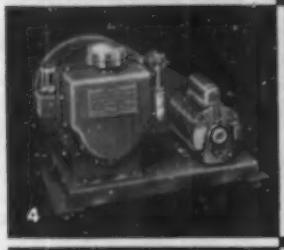
4

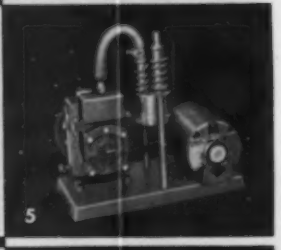
5

6

7

8

9

Whether it's in the laboratory, on a busy production line, in a classroom, reduced noise level means greater efficiency, higher quality work. Duo-Seal Vacuum Pumps are *quiet*. Welch engineers took noise and vibration out of the vacuum pump right on the drawing board. The result is a pump that runs as quietly as an electric motor.

Quiet operation means greater efficiency

Quiet, vibrationless operation means pumps that run smoothly year after year with virtually no maintenance beyond a periodic oil change. Duo-Seal pumps, built to close tolerances, actually improve with use, the seal and vanes become more highly polished and the fit more perfect.

There is a Duo-Seal pump available for almost every purpose, for every budget, from noncritical classroom problems to most exacting high-vacuum industrial-production and laboratory vacuum requirements.

Welch Pumps are best because:
Every pump is triple tested.
Specified performance guaranteed.
Lowest cost per year of use.
Highest vacuum of any mechanical pump.
Quietest mechanical pump made.

1. 1405 (2 speeds available) two-stage, No. 1405H. 0.05 micron, 33.4 liters per minute. $230.00. No. 1405B. 0.1 micron, 58 liters per minute. $255.00

2. 1400B—two-stage, 0.1 micron, 21 liters per minute. $133.00

3. 1402B—two-stage, vented exhaust, 0.1 micron, 140 liters per minute. $310.00

4. 1397B—two-stage, vented exhaust, 0.1 micron, 425 liters per minute. $645.00

5. 1392—mechanical and diffusion pump assembly, two-stage (each element) 0.001 micron, 600 liters per minute. (at 0.1 micron) $275.00

6. 1403B—single-stage, 5 microns, 100 liters per minute. $245.00

7. 1404H—Wegner Pump single-stage, 20 microns, 33.4 liters per minute. $150.00

8. 1406H—single-stage, 5 microns, 33.4 liters per minute. $150.00

9. 1410B—Wegner Pump single-stage, 20 microns, 21 liters per minute. $100.00

For complete specifications, request our pump catalog.

W. M. WELCH SCIENTIFIC COMPANY
DIVISION OF W. M. WELCH MANUFACTURING COMPANY
ESTABLISHED 1880
1515 Sedgwick Street, Dept. C-1 Chicago 10, Illinois U. S. A.
Manufacturers of Scientific Instruments and Laboratory Apparatus

Journal
of
Applied Physics

Volume 31, Number 3 March, 1960

High-Energy Sputtering

O. C. Yonts, C. E. Normand, and Don E. Harrison, Jr.*
Oak Ridge National Laboratory,† Oak Ridge, Tennessee
(Received August 28, 1959)

Sputtering ratios for copper have been determined in the energy ranges 5–40 kev for bombardment by Ar^+, He^+, and D^+. Argon values range from 6.48 at 5 kev to 9.25 at 27.5 kev, deuterium from 0.048 at 10 kev to 0.023 at 44 kev, and helium from 0.23 at 15 kev to 0.75 at 40 kev.

Preliminary data are included for 30-kev sputtering of copper by H^+(0.011), D^+(0.03), He^+(0.13), N^+(5.28), Ne^+(3.61), Ar^+(9.02), CU^+(9.60), Kr^+(15.15), and U^+(20.9). Also included are sputtering ratios at 30 kev for Ar^+ on Ta(2.7), Mo(3.31), and Al(2.38). Most of these data are the result of a single measurement, and require further verification.

A definite pressure dependence of the sputtering ratio for Ar^+ on Cu was found in the range of 0.04 to 0.08 μ.

INTRODUCTION

THE erosion of metallic surfaces by positive ion bombardment, i.e., "sputtering" has been observed since the earliest investigations of gaseous electric discharges. Rates of sputtering have been determined by a variety of methods for a variety of target metals, bombarding ions, ion energies, angles of incidence, etc.[1,2] The results of such measurements are generally reducible to a "sputtering ratio" which may be defined as the ratio of ejected target atoms to incident bombarding ions. Thus defined, the sputtering ratio is characteristic of target material and bombarding ion, but may vary with ion energy and angle of incidence.

Direct measurement of the sputtering ratio requires that the following conditions be fulfilled.

1. The total ion flux (integrated ion current) to the target must be accurately measurable.

2. The bombarding ions should have some sharply defined and measurable energy.

3. The weight loss of the target must be accurately measurable, either directly or by some indirect means such as the measured increase in electrical resistance of a fine wire.

4. Particles sputtered from the target must not return to it. Subsequent ionization, reflection from neighboring surfaces, and back diffusion due to high pressure near the target surface are possible causes of return. In practice, the pressure condition requires that the pressure near the target surface be less than about 10 μ of mercury to prevent back diffusion.

Early sputtering measurements were made using a glow discharge as the source of ions. As a consequence, experimental results are strongly dependent on gas pressure and on discharge tube geometry. Moreover, the ion energy spectrum was quite broad, and the small sputtering loss was usually determined by some indirect means.

DISCUSSION

Simple ion sources were first used by Guntherschultz and Meyer[3] working at the 100 to 1200 ev range and by Keywell[4] working at 1 to 6 kev. These workers were able to satisfy the conditions listed above with the possible exception of the uniform energy requirement.

The present experiments were initiated to provide what might be called "engineering" data on the rate

* Permanent address: Engineering Physics Department, University of Toledo, Ohio.
† Operated by Union Carbide Corporation for U. S. Atomic Energy Commission.
[1] G. K. Wehner, Adv. Electronics and Electron Phys. 8, 239 (1955).
[2] A. Guntherschultz, Vacuum 3, 360 (1953).
[3] A. Guntherschultz and K. Meyer, Z. Physik 62, 607 (1930).
[4] F. Keywell, Phys. Rev. 97, 1611 (1955).

Copyright © 1960 by the American Institute of Physics.

TABLE I. Calorimetric measurement of ion current.

Ion	Ion voltage (kev)	Target current (ma)	Power to target		% Difference
			Electric (watts)	Calorimetric (watts)	
H^+	40.2	27.5	1110	1230	9.8
	35.5	27.5	975	1031	10.1
	30.5	17.5	534	578	8.2
	18.2	46.2	841	880	4.4
	15.1	84.0	1261	1340	5.9
He^+	19.0	92.2	1765	1810	2.5
	13.2	94.1	1242	1227	−1.8

of sputtering by selected ions in the 10 to 40 kev range. They were planned to utilize one of the electromagnetic separators regularly used in the separation of stable isotopes. These separators (calutrons) are in effect large 180° focusing mass spectrometers having high ion current capacity. This equipment has a number of desirable characteristics for sputtering experimentation:

1. Ion currents up to several hundred milliamperes are readily produced for periods of several hours. The integrated target current can be determined with high precision, and the power delivered to the target is sufficient to permit accurate calorimetric current calibrations. Moreover, the target weight loss can be made large enough, in most cases, for accurate determination by direct weighing.

2. The equipment is designed to operate at highly regulated ion voltages (regulation to 1 part in 2500) over the 10 to 40 kev range; and the ion beam is focused in space and essentially mono-energetic.

3. The target can be well isolated in the large vacuum volume of the calutron, and the pressure in this volume is regularly maintained at 0.02 to 0.06 μ. There is, therefore, only slight probability that material sputtered from the surface will return to it; and target weight loss can be taken as a true measure of total sputtering.

In all of the experiments of this series, water-cooled targets of oxygen-free copper were used. Since the bombarding ions were Ar^+, He^+, D^+, and H^+, ion sources were of the gas-fed arc type. To compensate for this spread in ion mass, and to cover the proposed energy range without large variations of the applied magnetic field, the bombarding ion beam radius was varied from 24 in. for Ar^+ to 7 in. for He^+, D^+, and H^+. In all cases, the target was placed a few inches beyond the beam focal point and was oriented with its face normal to the central ray of the ion beam. This arrangement provided bombardment over a considerable area of the target and avoided intense local heating. No attempt was made to correlate sputtering rate with angle of incidence of the incident ions. It appears unlikely that an accurate correlation is possible in this type of experiment since the pitted appearance of the bombarded surface indicates that all angles of incidence are present.

If one accepts the weight loss of the target as a true measure of the amount of sputtering, and the integrated target current as a true measure of the bombarding ions, the sputtering ratio, mg/ma-sec, can be immediately expressed as

$$\text{sputtering ratio} = W/It,$$

where W is the target weight loss in milligrams and It is the integrated target current in (ma-hr)×3600. When weight loss is converted to an equivalent number of atoms N_i and integrated current to an equivalent number of bombarding ions N_j, the sputtering ratio S can be expressed as

$$S = N_i/N_j = 96500\, W/AIt.$$

Therefore, for a Cu target, $A = 63.5$, the sputtering ratio is

$$S_{Cu} = 1519W/It \text{ (atoms out/ions in)}.$$

Bombardments were carried out at currents ranging from 2 to 90 ma on target areas of approximately 20 cm².

TABLE II. Variation of sputtering ratio with total bombardment.

Sputtering ratio	Milliampere hours	Remarks
9.17	50	first 50 ma-hr
8.72	50	second 50 ma-hr
8.94 Av	100	average for 100 ma-hr
9.08	100	new location on same target
9.21	25	30 kev
8.81	25	30 kev
9.01	25	30 kev
8.85	25	30 kev
9.03	25	30 kev
mean = 8.99		
mean deviation = ±0.1 = 1.1%		
standard deviation = ±0.09 = ±1%		
probable error of mean = ±0.07 = 0.8%		

Since sputtering rates are higher for more massive ions, the following approximate schedule was followed:

Ar^+ 25 to 250 ma-hr, He^+ 500 ma-hr, D^+ and H^+ 1000 ma-hr.

The resulting target weight losses, determined by weighing the cleaned target before and after bombardment ranged from a high of about 8000 mg for Ar^+ to a low 13 mg for H^+.

Except for the case of H^+, the total weight of ions striking a target was a small fraction of the observed weight loss. Any possible penetration and absorption of ions into the target could, therefore, be neglected in determining sputtering loss. In the case of H^+, however, the weight of bombarding ions exceeded the observed weight loss and it was necessary to determine the extent of ion absorption by the target. Gas analysis of a target after 1152 ma-hr bombardment by 42-kev H^+ ions, (this corresponds to 42 mg of H^+ striking the target) showed less than 1 ppm of hydrogen in the bombard

ment area or a total weight of hydrogen in the target of approximately 0.4 mg.

The equivalence of sputtering loss to target weight loss appears to be well grounded in these measurements, and the magnitudes of the losses were such that weighing errors were less than 1% except in the case of sputtering by H^+ where the weighing error may have been as large as 10%. The equivalence of bombarding ion current to target current is not quite so clear.

Experience with the calutron as an isotope separator indicates an approximate equivalence between these quantities but cannot establish an exact equivalence. Obviously, these currents will not be equal if electrons in significant numbers are emitted from, or arrive at, the target. Secondary electron emission from the target appears unlikely, particularly because of the presence of a strong magnetic field (2–3 kilogauss), but some electrons are expected to arrive with the ion beam, as these intense ion beams must be approximately space-charged neutralized, and thus constitute a weak plasma.

To test over-all equivalence of target current to ion

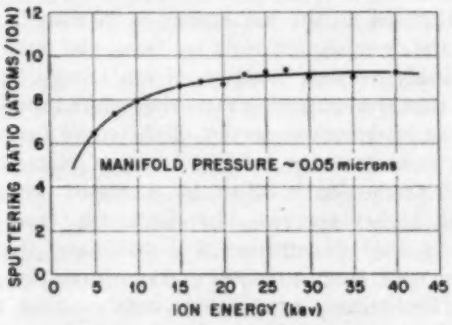

FIG. 1. Sputtering of copper by argon ions.

current, simultaneous measurements of the power delivered to the target were made electrically and calorimetrically for a range of ion currents and voltages. Typical measurements, shown in Table I, indicate that the power measured by the two methods usually varies by less than 10%. Except for one case, the difference is in such a direction as to indicate an ion current slightly greater than the measured target current. Such a discrepancy could result from a small net flow of plasma electrons to the target.

As normally run the target is positive with respect to ground by the few millivolts drop in the monitoring circuit. This will vary from 50–200 mv depending on the ion current and the dc meter used. To check directly on the flow of electrons from the beam plasma to the target, the target potential was varied from the normal few millivolts to −200 to +150 v, and the resulting current-voltage curves were determined at different beam currents. The extreme current variations are approximately 4% at 40 ma and 3% at 78 ma. It appears, therefore, that the error attributable to electron flow

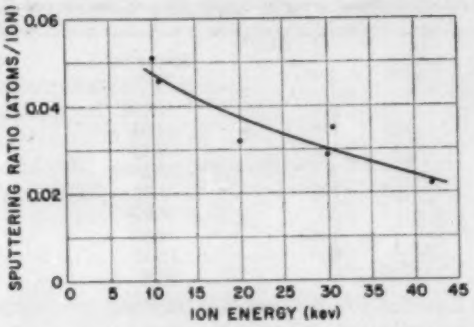

FIG. 2. Sputtering of copper by deuterium ions.

to the target is certainly less than the 10% error indicated by power measurements.

There is also a definite pressure effect upon the sputtering ratio. Three copper targets were bombarded with Ar^+ at 30 kev with the pressure higher by a factor of 2 than the normal calutron operating pressure of $2(10)^{-5}-4(10)^{-5}$. The mean of these measurements was 7.92 ± 0.01, which compares with 8.84 ± 0.02 for normal operation.

Apparently, the sputtering ratio is still sensitive to the background pressure in the $5(10^{-5})$ to 10^{-4} range.

The variation with pressure appears to be due to the formation of a surface layer which inhibits the emission of the sputtered copper from the surface. At 10^{-4} mm of Hg the number of neutral particles per square centimeter per second from the residual gas striking the target is an order of magnitude greater than the number of ions. Thus, the surface layers are self-renewing at higher pressures. Because pressure measurements are uncertain in a calutron the absolute values of these reported pressures are not meaningful, but the dependence on *pressure change* is significant.

Rol, Fluit, and Kistemaker[5] have reported A^+ on copper data which are some 20% lower than the present results, but this variation is perfectly possible between two essentially constant pressure systems in which the operating pressure is not accurately known.

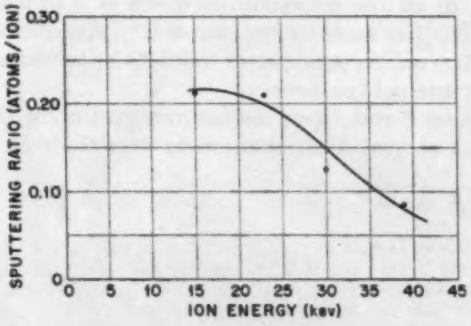

FIG. 3. Sputtering of copper by helium ions.

[5] Rol, Fluit, and Kistemaker, *Proceedings International Symposium on Isotope Separation Amsterdam. 1957* (North-Holland Publishing Company, Amsterdam, 1958), p. 637.

TABLE III. Sputtering of copper by various ions at 30 kev.

Ion	Sputtering ratio
H^+	0.011
D^+	0.03
He^+	0.13
N^+	5.28
Ne^+	3.61
A^+	9.02
Cu^+	9.60
Kr^+	15.15
U^+	20.9[a]

[a] Not corrected for uranium left on the target.

A series of determinations at 30 kev with A^+ on copper were made to find the actual difference in values and the effect of various operating parameters. The results of this series is given in Table II.

One helium-annealed target was used to check the effect of surface deterioration during a run. It was first run for 50 ma-hr and the sputtering ratio determined to be 9.17. The same target area was then bombarded for an additional 50 ma-hr, giving 8.72, and an average of 8.94 for 100 ma-hr. The target was then relocated and another target area was bombarded for 100 ma-hr, producing a sputtering ratio of 9.08.

Additional studies along these lines are clearly required, but this preliminary trial indicates that even under conditions of intense bombardment there is some dependence of the sputtering ratio upon the history and present conditions of the target surface.

To compensate these surface effects, two procedural changes were made. First, Ar^+ bombardment was reduced to 25 ma-hr, which significantly reduced the visible target erosion, and second, more attention was given to the initial state of the target surface. In addition to the usual cleaning and machining procedure, all targets were annealed in a helium atmosphere for one hour at 400°C.

The limit of error on the curves of Fig. 1 should approach the probable error of the mean which is ± 0.07 although the probable error of any point is more nearly ± 0.09. At constant pressure, the net effect of all the uncertainties noted is approximately 10% (20% or more for the case of H^+). Experimentally, the Ar^+ on copper system exhibits approximately a $\pm 3\%$ internal consistency.

Figures 2 and 3 give similar information for D^+ and He^+ on copper. Most of the runs were made on unannealed targets, but they are included because the indicated later runs made on annealed targets appear to be consistent with the earlier data.

Table III exhibits sputtering ratios for various ions incident on copper at 30 kev, taken on unannealed targets. These results are probably not very reliable.

Table IV gives some preliminary results for the sputtering of materials other than copper.

TABLE IV. Sputtering by A^+ at 30 kev.

Target	Sputtering ratio
Ta	2.7
Mo	3.31
Cu	9.02
Al	2.38[a]

[a] Mean of 2 determinations.

ANALYSIS AND CONCLUSIONS

Figure 1 can be analyzed from our present understanding of the sputtering mechanism. The initial rise of the curve occurs with increased production of moving lattice atoms as the ion energy is increased. In this range the cross-section ratio for beam and lattice atom is a slowly varying function of ion energy, with the result that the sputtering ratio rises quite rapidly.

In the intermediate section of the curve the sputtering ratio remains on a fairly constant plateau as increased production is off-set by increased penetration. At still higher energies, the decreasing cross-section indicates that penetration will dominate production and the sputtering ratio will decrease from the plateau value. Preliminary experiments indicate that the decrease begins around 50 kev for the Ar^+-Cu system. In the light incident ion systems this high energy break comes at lower energies, however much more work must be done to obtain definite results in this energy range.

ACKNOWLEDGMENTS

The authors wish to thank L. O. Love, K. A. Spainhour, and other members of the Calutron Separation Department for their cooperation and assistance during the early stages of the program. We are especially appreciative of the assistance of J. P. Wood, H. L. Huff, and D. F. Leach for operation, design, and construction of equipment used in the program.

Influence of Irradiation with β Rays on the Electrification of KCl Crystals

ANNA SZAYNOK
Department of Physics, Institute of Technology, Wroclaw, Poland
(Received September 4, 1958)

The measurements of electrical charges on dust clouds of crushed KCl monocrystals previously irradiated with β rays shows that the value of the mean charge depends on irradiation time. In the case of KCl irradiated with β rays, a photoelectric effect is not observed, despite the presence of F centers.

INTRODUCTION

THE phenomenon of electrification of pulverized and dispersed solid bodies or fluids is well known. This phenomenon often occurs in technological processes where dangerous explosions of easily combustible materials can occur. In spite of its common occurrence, the mechanism of formation of the electric charges is not precisely known. The present state of this problem was given in Harper's review article.[1] The measurement of the charges on single particles is based chiefly on Millikan's method of elementary charge measurement modified by Hopper and Laby.[2] Measurements of solid particles were carried out by Kunkel and Hansen,[3] and on liquids by Natanson.[4] The results obtained by Kunkel[5] on the electrification of dust particles can be explained by assuming the existence of lattice defects in the pulverized crystals. The measurements of electrical charges created during the pulverization of NaCl crystals previously irradiated by x-rays showed the influence of lattice defects on the mean charge.[6] The concentration of F centers produced in NaCl crystals by x-ray irradiation was of the order of 10^{15} cm^{-3}. This paper presents the results of measurements for KCl crystals irradiated with β rays.

FIG. 1. The photograph of tracks of falling charged particles in the electric field.

EXPERIMENTAL DETAILS

The KCl monocrystals used in these measurements were grown from the melt according to the Kyropoulos method. The spectrographic analysis showed only small contamination of sodium (around 0.01%) and traces of calcium and strontium (below 0.001%). The crystals were irradiated using β rays from a Sr-90 source. The half-life of the β rays is 19.9 0.3 years and disintegration energy is 0.54 Mev; there are no gamma rays in this case. The radiation intensity of the source amounted to 10 mc. The irradiated samples were cut out of larger crystals and their dimensions were about 10×10×1.5 mm. The concentration of the F centers produced by the irradiation was determined spectrophotometrically. The crystals were stored in darkness from the time they were irradiated until they were measured. The electrical charge measurement of the pulverized crystals was carried out by the apparatus described by Kunkel and Hansen.[3] This method was described more exactly in an earlier publication[7] and only the principles of the measurement will be given. It differs from Millikan's method in only one detail. The condenser is set vertically. The pulverized salt is introduced at the top of a thermally isolated column. The particles of salt fall through the electric field set

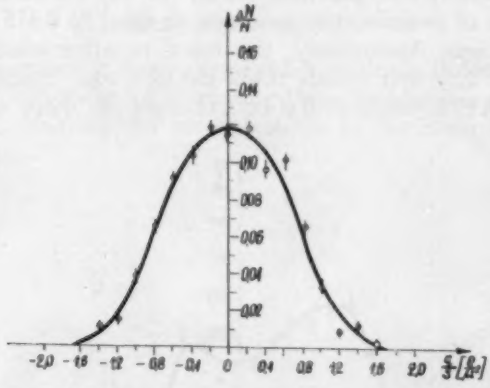

FIG. 2. The charge distribution in dust cloud produced from KCl monocrystal un-irradiated with β rays. (q/s), the ratio of dust particle charge to its surface in units electrons per square micron; $(\Delta N/N)$, the ratio of particles number ΔN with value (q/s) between (q/s) and $(q/s)+\Delta(q/s)$ to total number of particles N.

[1] W. R. Harper, *Advances in Physics* (Taylor and Francis, Ltd., London, 1957), Vol. 6, p. 365.
[2] V. D. Hopper and T. H. Laby, Proc. Roy. Soc. (London) A178, 234 (1941).
[3] W. B. Kunkel and J. W. Hansen, Rev. Sci. Instr. 21, 308 (1950).
[4] G. L. Natanson, Compt. rend. acad. sci. U.R.S.S. 53, 115 (1946).
[5] W. B. Kunkel, J. Appl. Phys. 21, 820 (1950).
[6] A. Szaynok, Zeszyty Nauk. Politech. Wrocław. Chem. (to be published).
[7] A. Szaynok, Zeszyty Nauk. Politech. Wrocław. Chem. 4, 43 (1954).

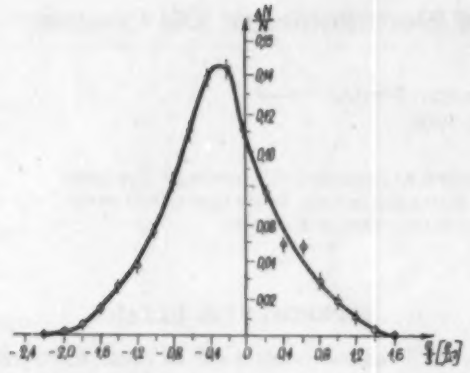

FIG. 3. The charge distribution in dust cloud produced from KCl monocrystal irradiated with β rays during 30 hr by Sr-90 source with intensity of 10 Mc.

up between the plates of the condenser whose plates are plane parallel and vertical. Periodic illumination was provided by means of a rotating disk, making it possible to photograph the tracks of falling dust particles as bright points on a dark background (Fig. 1). The duration of one flash of light is in the order of 1/50th of a second and depends on the speed of rotation of the disk. The light source was an electric arc. The measurements of the electrical charges on the small particles of KCl were carried out for both irradiated and un-irradiated samples.

RESULTS

On Fig. 2 is plotted the charge distribution in the cloud of un-irradiated KCl dust. The curve is symmetric about the axis showing the equilibrium number of positive and negative charges. The whole dust cloud is electrically neutral. The average charge per unit surface, namely (Σ_q^+/Σ_s^+), where Σ_q^+ is the sum of charges of positive dust particles and Σ_s^+ is the sum of surface areas of positive dust particles, is equal to 0.475 electron/sqμ. Analogously, the mean negative charge is (Σ_q^-/Σ_s^-) and equals 0.482 electron/sqμ. Irradiating the KCl crystals with β rays changes the shape of the curve, translating the curve in the direction of negative charge, and increasing the mean positive and negative charge. Since the crystal is bombarded by electrons, the increase of the mean positive charge is distinctly slower than the increase of negative charge. This results in a partial neutralization of positive charges. In spite of this, however, the magnitude of the charges per unit surface area increases with irradiation. On Figs. 3 and 4 are plotted the charge distributions for KCl monocrystals irradiated with β rays for 30 hr and 133 hr, respectively. The shape of the curve clearly indicates the influence of irradiation on the phenomenon of dust electrification. Table I shows the dependence of the mean positive and negative charge on the time of irradiation. The dependence of F-center concentration produced by β irradiation is shown in Fig. 5. The shape of this curve is in agreement with the previous results published.[8] From these curves, one can plot the relation between the concentration of F centers in the crystal and the mean positive and negative charges of the dust clouds. This is shown in Fig. 6.

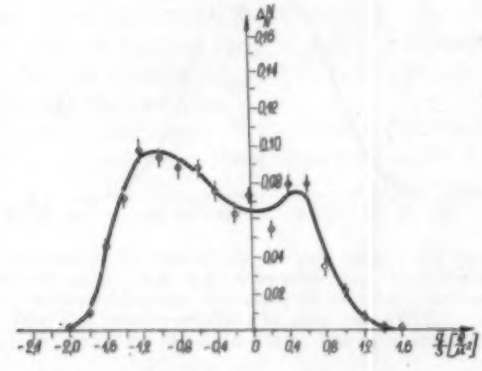

FIG. 4. The charge distribution in dust cloud produced from KCl monocrystal irradiated with β rays during 133 hr by Sr-90 source with intensity of 10 Mc.

TABLE I. The dependence of the mean positive and negative charge from the irradiation time.

Irradiation time (hr)	0	30	100	133
Mean positive charge (electrons/μ^2)	0.457	0.447	0.536	0.523
Mean negative charge (electrons/μ^2)	0.482	0.652	0.821	0.907

DISCUSSION

The magnitude of the electric charge on the dust cloud of irradiated KCl crystals is influenced by two factors, absorption of electrons by the crystal and increase of F-center concentration. The absorption of electrons by the crystal causes a predominance of the negative charge. Since the conductivity of KCl crystals is small, most of the negative charge is maintained for a long time. However, measurements of electrification performed ten days after the irradiation was finished did not exhibit any excess of negative charge in the dust cloud. An increase in F-center concentration induces an increase in both positive and negative charges. KCl not irradiated with β rays showed smaller mean charges than the irradiated dust. If the increase in charge was caused only by the absorption of electrons, a distinct decrease in the mean positive charge should have taken place. The fact that the positive charge was observed to increase can only be explained by the influence of F centers on charge concentration.

This is in agreement with Mott's theory.[9] The existence of lattice defects causes an irregular and acci-

[8] K. Przibram, Verfarbung und Lumineszenz (Vienna) 24 (1953).

[9] N. F. Mott, Proc. Cambridge Phil. Soc. 34, 568 (1938).

dental distribution of electrical charges in the crystal. The breaking of crystal bonds can lead to an unequal distribution of charges. This is the reason for the existence of separate particles positively or negatively charged. By using the differences between mean positive and negative charges on the dust particles, the magnitude of the absorption and F-center effects can be estimated. It can be shown that the mean charge induced by F centers is proportional to the concentration of F centers. The lack of a photoelectric effect is characteristic for crystals irradiated with β rays. For crystals irradiated with x-rays or containing an excess of the alkaline metal, a photoelectric effect is observed when these crystals are illuminated with light in the F band. This phenomenon is well known.[10] It has been observed during the measurement of charges on dust clouds of NaCl previously irradiated with x-rays. The photoelectric effect takes place when the falling particles pass through the stream of light with about 37%

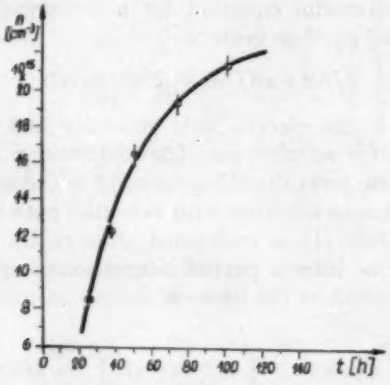

FIG. 5. The dependence of F-center concentration in KCl monocrystal on the time of irradiation by Sr-90 source with intensity of 10 Mc.

of the dust particles showing track discontinuities due to loss of electrons. In the case of KCl dust, in which the F centers were created by irradiation with β rays, a photoelectric effect does not take place. Tests carried

[10] N. Gudris and L. Kulikowa, Z. Physik 45, 801 (1927).

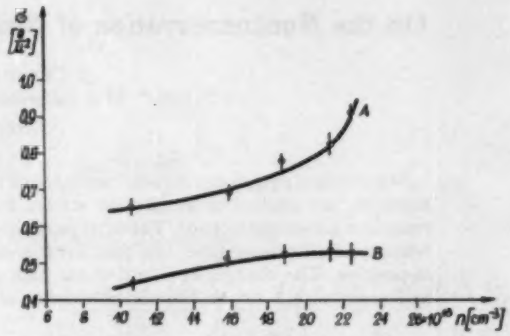

FIG. 6. The dependence of mean dust cloud charge on F-center concentration in KCl monocrystal irradiated with β rays by Sr-90 source with intensity of 10 Mc. (a). The curve representing the dependence of the mean negative charge $\sigma^- = (\Sigma_q^-/\Sigma_s^-)$ on F-center concentration. (b) The curve representing the dependence of the mean positive charge $\sigma^+ = (\Sigma_q^+/\Sigma_s^+)$ on F-center concentration.

out for KCl crystals irradiated with x-rays and additively colored with an excess of potassium showed a photoelectric effect. It is possible that a lack of photoemission during the charge measurement is caused by a very strong triboluminescence observed when the crystals irradiated with β rays are crushed. In this case, the electrons might have been ejected before the charge measurements were made. Even so, a small number of photoemissions would be expected. However, in the case of KCl dust, no photoeffect was observed. It is possible that irradiation by β rays might produce other lattice defects from which photoemission might take place. Data in the literature do not show any differences in the absorption spectra of crystals irradiated with various kinds of radiation. On the basis of the experimental material obtained up to now it is impossible to explain the lack of photoelectric effects from the KCl crystals irradiated with β rays.

ACKNOWLEDGMENTS

The author wishes to express her gratitude to Professor J. Nikliborc for discussing these problems and to Dr. J. Rohleder for measurements of the absorption spectra.

On the Nonconservation of Noise Parameters in Multivelocity Beams*

J. Berghammer and S. Bloom
RCA Laboratories, Princeton, New Jersey
(Received July 24, 1959)

Macroscopic equations for conservation of charge, momentum, and energy, as derived from the Boltzmann equation, are applied to an electron stream having a velocity spread. For small velocity spreads, these equations are simple to treat. The noise parameters, S and Π, which determine the minimum noise figure of a beam-type microwave tube, lose their invariance in the presence of velocity spread; they become functions of position. The changes of S and Π are such as to lower the minimum noise figure. These results are in agreement with a detailed numerical solution of the Boltzmann equation as previously reported by others.

I. INTRODUCTION

THE very low noise factors of traveling-wave tubes that have recently been observed[1] have led to a re-examination of noise processes in the vicinity of the potential minimum. In particular, it has been shown[2] that in this low-velocity region the single-velocity approximation is invalid and that the velocity spread of the beam introduces large and, somewhat paradoxically, beneficial effects on the noise. By means of a detailed machine integration of the fundamental Boltzmann equation, Siegman, Watkins, and Hsieh have shown that in the low-velocity region the beam "noiseness," S, rapidly decreases and the real noise "power," Π, rapidly increases with distance from the potential minimum. Sufficiently far from the potential minimum the relative velocity spread is nil and S and Π settle down to constant values. From this point on the single-velocity noise analyses are valid.[3,4] The noise factor of the tube, being proportional to S-Π, is thus reduced by these velocity-spread effects.

Although the microscopic analysis of Siegman *et al.* is rigorous, it is also intricate. One wonders whether a simpler macroscopic model might also describe the effects uncovered by these authors. Such a model does exist and does describe at least the *first-order* effects of velocity spread. This is the "hydrodynamical" model of an electron beam introduced by Hahn[5] and later used by Parzen and Goldstein[6] in a discussion of traveling-wave tube gain.

In the present paper the hydrodynamic method is applied to the noise problem. In this method the microscopic Boltzmann equation is used to derive three macroscopic transport equations of charge, momentum and energy. When the velocity spread is sufficiently small, but nonzero, these transport equations become tractable yet remain accurate enough to describe the nonconservation of S and Π. Of course, the macroscopic method can in principle be applied for arbitrary velocity spread; however the analysis then becomes as intricate as that of the microscopic method.

II. DERIVATION OF SPACE-CHARGE-WAVE EQUATIONS FOR A MULTIVELOCITY BEAM

The Boltzmann equation for a collision-free, one-dimensional electron beam is

$$\partial f/\partial t+u\partial f/\partial x+\eta E\partial f/\partial u=0, \tag{1}$$

where E is the electric field intensity and η is the e/m ratio for an electron. The distribution function, $f(x,u,t)dxdu$, gives the charge density in the interval dx at time t due to electrons with velocities between u and $u+du$. When (1) is multiplied through by $Q=Q(u)$ there results, after a partial integration in which f is taken to vanish at the limits of u,

$$\frac{\partial}{\partial t}\int Qfdu+\frac{\partial}{\partial x}\int uQfdu-\eta E\int\frac{dQ}{du}fdu=0. \tag{2}$$

The charge-average macroscopic charge density, velocity and convection current density are

$$\rho(x,t)=\int fdu$$

$$v(x,t)=\frac{1}{\rho}\int ufdu \tag{3}$$

$$i(x,t)=\int ufdu=\rho v.$$

Thus, with $Q=1$, u, u^2, $\cdots$, (2) gives the following transport equations:

$$\frac{\partial}{\partial t}\rho+\frac{\partial}{\partial x}\rho v=0$$

$$\frac{\partial}{\partial t}\rho v+\frac{\partial}{\partial x}(\rho\langle u^2\rangle)-\eta\rho E=0 \tag{4}$$

$$\frac{\partial}{\partial t}\rho\langle u^2\rangle+\frac{\partial}{\partial x}(\rho\langle u^3\rangle)-2\eta\rho vE=0$$

$$\vdots$$

* Portions of this material were presented by J.B. at the Sixteenth Annual Conference on Electron Tube Research, Quebec, June, 1958.

[1] M. R. Currie and D. C. Foster, J. Appl. Phys. **30**, 94 (1959).
[2] Siegman, Watkins, and Hsieh, J. Appl. Phys. **28**, 1138 (1957).
[3] H. A. Haus and F. N. Robinson, Proc. Inst. Radio Engrs. **43**, 981 (1955).
[4] S. Bloom and R. W. Peter, RCA Rev. **15**, 252 (1954).
[5] W. C. Hahn, Proc. Inst. Radio Engrs. **36**, 1115 (1948).
[6] (a) P. Parzen and L. Goldstein, J. Appl. Phys. **22**, 398 (1951); (b) P. Parzen, *ibid.* **23**, 394 (1952).

where the mean value of u^n is defined by

$$\langle u^n\rangle=\frac{1}{\rho}\int u^n f\,du. \tag{5}$$

Next, the velocity u is written as the sum of the macroscopic velocity, v, and a random component, w, due to velocity spread:

$$u=v+w$$
$$\langle u\rangle=v,\quad \langle w\rangle=0.$$

Then, since

$$\langle u^2\rangle=v^2+\langle w^2\rangle$$
$$\langle u^3\rangle=v^3+3v\langle w^2\rangle+\langle w^3\rangle, \tag{6}$$

(4) becomes

$$\frac{\partial\rho}{\partial t}+\frac{\partial}{\partial x}\rho v=0$$

$$\frac{\partial v}{\partial t}+v\frac{\partial v}{\partial x}=\eta E-\frac{1}{\rho}\frac{\partial}{\partial x}\left(\rho\frac{kT}{m}\right) \tag{7}$$

$$\frac{\partial}{\partial t}\left(\rho\frac{kT}{m}\right)+v\frac{\partial}{\partial x}\left(\rho\frac{kT}{m}\right)=-3\rho\frac{kT}{m}\frac{\partial v}{\partial x}-\frac{\partial}{\partial x}(\rho\langle w^3\rangle),$$
$$\vdots$$

where the beam temperature is related to the second-order moment-about-the-mean by

$$\frac{kT(x,t)}{m}=\langle w^2\rangle=\frac{1}{\rho}\int(u-v)^2 f\,du. \tag{8}$$

At this point the fundamental approximation is made of taking the velocity spread to be sufficiently small that the third order moment may be neglected. With $\langle w^3\rangle=0$, the first and third equations of (7) give

$$\frac{d}{dt}(T/\rho^2)=0. \tag{9}$$

With all quantities written in the form

$$\rho(x,t)=\rho_0(x)+\rho_1'(x)\exp(j\omega t),$$

(7) and (9) lead to the following dc equations

$$\rho_0 v_0=i_0=\text{const}$$

$$v_0\frac{d}{dx}v_0=\eta E_0-\frac{k}{m\rho_0}\frac{d}{dx}(\rho_0 T_0) \tag{10}$$

$$T_0 v_0^2=\text{const},$$

and to the following small-signal ac equations:

$$j\omega\rho_1'+\frac{d}{dx}i_1'=0$$

$$i_1'=\rho_0 v_1'+\rho_1' v_0 \tag{11}$$

$$j\omega v_1'+\frac{d}{dx}(v_0 v_1')=\eta E_1'-\frac{k}{m\rho_0}\frac{d}{dx}(\rho_0 T_1')-\frac{kT_0}{m}\frac{d}{dx}(\rho_1'/\rho_0).$$

In addition, the ac part of (9) is

$$j\omega\left(\frac{T_1'\rho_0-2T_0\rho_1'}{\rho_0^3}\right)+v_0\frac{d}{dx}\left(\frac{T_1'\rho_0-2T_0\rho_1'}{\rho_0^3}\right)=0,$$

which yields

$$\frac{T_1'}{T_0}=2\frac{\rho_1'}{\rho_0}+\left(\frac{T_1'}{T_0}-2\frac{\rho_1'}{\rho_0}\right)_{x=0}\exp\left(-j\omega\int_0^x dx/v_0\right). \tag{12}$$

The ac temperature, T_1', is seen to consist of a term proportional to the ac charge density and of a "kinematic" term propagating with the mean dc velocity. As has been shown by Pierce[7] and others, in the microscopic method of noise analysis the injected noise test charge sets up not only the two space-charge waves but also a kinematic wave propagating at the velocity of the injected charge. These authors have furthermore shown that space-charge very effectively suppresses the kinematic portion of the total noise current. The main portion of the noise is carried by the space charge waves, the normal modes of the system. For this reason we neglect the second term of (12) which represents a kinematic wave. Under this restriction, (12) can be approximated for sufficiently small velocity spread, by

$$T_1'=2T_0\rho_1'/\rho_0. \tag{13}$$

In terms of v_1' and i_1', (11) then reads

$$\frac{d}{dx}i_1'+\frac{j\omega}{v_0}i_1'=\left(\frac{j\omega i_0}{v_0^2}\right)v_1'$$
$$j\omega v_1'+\frac{d}{dx}(v_0 v_1')=\eta E_1'-\frac{3kT_0 i_0}{m\rho_0^2}\frac{d}{dx}[(i_1'-\rho_0 v_1')/v_0^2], \tag{14}$$

in which the ac field and ac convection current density for a one-dimensional beam are related by the open-circuit relation

$$E_1'=j\frac{i_1'}{\omega\epsilon_0}. \tag{15}$$

The transformation of ac quantities by

$$\rho_1'(x)=\rho_1(x)\exp\left(-j\omega\int_0^x dx/v_0\right), \tag{16}$$

[7] J. R. Pierce, Proc. Inst. Radio Engrs. **40**, 1675 (1952).

simplifies the equations. Finally, the introduction of the Chu kinetic potential,

$$V_1 = v_0 v_1/\eta, \tag{17}$$

leads to the following "transmission-line" equations for the case of small velocity spread:

$$\begin{aligned} \frac{dV_1}{dx} &= (R+jX)i_1-(M+jN)V_1 \\ \frac{di_1}{dx} &= jBV_1, \end{aligned} \tag{18}$$

where

$$\begin{aligned} R(x) &= \frac{2\sigma^2}{1-\sigma^2}\frac{v_0}{\eta i_0}\frac{dv_0}{dx} \\ X(x) &= \frac{1}{\omega\epsilon_0}(1+\sigma^2\omega^2/\omega_p^2)\frac{1}{1-\sigma^2} \\ M(x) &= \frac{4\sigma^2}{1-\sigma^2}\frac{1}{v_0}\frac{dv_0}{dx} \\ N(x) &= \frac{2\sigma^2}{1-\sigma^2}\frac{\omega}{v_0} \\ B(x) &= \eta\omega i_0/v_0^3, \end{aligned} \tag{19}$$

in which the relative velocity spread is measured by

$$\sigma^2(x) \equiv 3kT_0/mv_0^2, \tag{20}$$

and the plasma frequency is $\omega_p^2 = \eta\rho_0/\epsilon_0$. The extended transmission line equations (18) are a convenient form to use in deriving equations for the spectral density functions of the fluctuations.

The spectral density functions are defined as[3]

$$\begin{aligned} 4\pi\Delta f\Psi &= |i_1|^2 \\ 4\pi\Delta f\Phi &= |V_1|^2 \\ 4\pi\Delta f\Pi &= \tfrac{1}{2}(i_1V_1^* + i_1^*V_1) \\ 4\pi\Delta f\Lambda &= (j/2)(i_1V_1^* - i_1^*V_1) \\ S^2 &= \Psi\Phi - \Lambda^2 \\ C^2 &= S^2 - \Pi^2. \end{aligned} \tag{21}$$

Thus, by (18), one finds

$$\begin{aligned} d\Psi/dx &= -2B\Lambda \\ d\Phi/dx &= 2R\Pi + 2X\Lambda - 2M\Phi \\ d\Pi/dx &= R\Psi - M\Pi + N\Lambda \\ d\Lambda/dx &= -B\Phi + X\Psi - M\Lambda - N\Pi \\ dS^2/dx &= -2MS^2 + 2N\Pi\Lambda + 2R\Pi\Psi \\ dC^2/dx &= -2MC^2, \end{aligned} \tag{22}$$

from which the following two conservation laws are obtainable:

$$C^2(x)[1-\sigma^2(x)]^2 = \text{const} \tag{23}$$

$$(1-\sigma^2)\Pi + \left(\frac{v_0^2\sigma^2}{\eta i_0}\right)\Psi = \text{const}. \tag{24}$$

The first four equations of (22) describe the x-dependence of the spectral density functions, if proper initial conditions are specified. Consider an electron beam having an increasing mean velocity $(dv_0/dx) > 0$ at some initial position $x=0$. Assume the initial current and velocity fluctuations to be uncorrelated:

$$\Pi(0) = 0 = \Lambda(0).$$

It is seen from (22) that Π will initially increase and S will initially decrease. The "correlation determinant" C is a measure of the randomness of the noise fluctuations. Fully correlated fluctuations are characterized by $C=0$. The relative velocity spread, σ^2, decreases as the mean velocity of the beam is increased. From conservation law (23) it is seen that C^2 decreases due to a reduction in σ^2 when the beam is accelerated.

III. DRIFTING BEAM

For a drifting beam all dc quantities are constant along the beam. With $R=0=M$, the solutions of (22) are found to be

$$\begin{aligned} \frac{\Psi-\Psi(0)}{-B} = \frac{\Phi-\Phi(0)}{X} = \frac{\Pi-\Pi(0)}{N/2} = \frac{1}{\beta_p'}\Big\{ & \Lambda(0)\sin 2\beta_p' x \\ & + \frac{1}{2\beta_p'}[X\Psi(0) - B\Phi(0) - N\Pi(0)] \\ & \cdot (1-\cos 2\beta_p' x)\Big\}, \end{aligned} \tag{25}$$

$$\begin{aligned} \Lambda = \Lambda(0)\cos 2\beta_p' x \\ + \frac{1}{2\beta_p'}[X\Psi(0) - B\Phi(0) - N\Pi(0)]\sin 2\beta_p' x, \end{aligned}$$

where the plasma wave number is

$$\beta_p' = \beta_p\frac{1}{1-\sigma^2}\{1+\sigma^2[(\omega^2/\omega_p^2)-1]\}^{\frac{1}{2}}, \tag{26}$$

$$\beta_p \equiv \omega_p/v_0.$$

As an example consider the case of a beam drawn from a temperature-limited diode. The noise power density spectra at plane $x=0$, the start of the drift region, have the same values as at the cathode, e.g., uncorrelated full shot noise:

$$\begin{aligned} &\Psi(0) = ei_0/2\pi, \qquad \Phi(0) = (kT_c)^2/2\pi ei_0 \\ &\Pi(0) = 0 = \Lambda(0), \quad S^2(0) = \Psi(0)\Phi(0) = (kT_c/2\pi)^2. \end{aligned} \tag{27}$$

By (25) and (19) the normalized kinetic power is

$$\frac{\Pi(x)}{S(0)}=\frac{2N}{(2\beta_p')^2}\left[X\frac{\Psi(0)}{S(0)}-\frac{B\Phi(0)}{S(0)}\right]\sin^2\beta_p'x$$

$$=2\sigma^2\left(\frac{eV_0}{kT_0}\right)\left[\frac{1+\sigma^2(\omega/\omega_p)^2-(1-\sigma^2)(\omega/\omega)_p{}^2(kT_c/2eV_0)^2}{1+\sigma^2(\omega/\omega_p)^2-\sigma^2}\right]\sin^2\beta_p'x \tag{28}$$

where $v_0^2\doteq 2\eta V_0$. For a Maxwellian distribution of electrons, all of which have been accelerated by a voltage V_0 from a cathode at temperature T_c, the dc temperature and velocity are related by†

$$\frac{kT_0}{m}v_0^2=\left(\frac{kT_c}{m}\right)^2 \tag{29}$$

and therefore

$$\sigma^2\equiv\frac{3kT_0}{mv_0^2}=\tfrac{3}{4}(kT_c/eV_0)^2. \tag{30}$$

Equation (28) then becomes

$$\frac{\Pi(x)}{S(0)}=(3\sigma^2)^{\frac{1}{2}}\left[\frac{1+\frac{3}{4}\sigma^2(\omega/\omega_p)^2-(\sigma^4/3)(\omega/\omega_p)^2}{1-\sigma^2+\sigma^2(\omega/\omega_p)^2}\right]\sin^2\beta_p'x.$$

$$\equiv y\sin^2\beta_p'x. \tag{31}$$

Furthermore, for a drifting beam (23) gives

$$S(x)=S(0)[1+\pi^2(x)/S^2(0)]^{\frac{1}{2}}$$

and so the minimum noise factor expression of a traveling-wave tube employing such a temperature-limited diode is[3,4]

$$F_{\min}=1+\frac{T_e}{T_r}\frac{S-\Pi}{S(0)}, \tag{32}$$

where

$$\frac{S(x)-\Pi(x)}{S(0)}=(1+y^2\sin^4\beta_p'x)^{\frac{1}{2}}-y\sin^2\beta_p'x. \tag{33}$$

This gives an optimum noise factor of

$$(F_{\min})_{\text{opt}}=1+\frac{T_e}{T_r}[(1+y^2)^{\frac{1}{2}}-y] \tag{34}$$

if the length of the drift space is such that

$$\beta_p'x=(2n+1)(\pi/2).$$

A result similar to Eq. (34) has been obtained by Feinstein[5] using a model consisting of quasi-discrete beamlets.

Equation (34) for the optimized minimum noise factor indicates that velocity spread effects tend to *lower* the noise factor. The decrease is determined by the quantity y as defined by (31). The application of (34) is restricted to small values of y because of the assumption of small velocity spread. It is however interesting to note that this effect due to velocity spread is almost independent of ω/ω_p since y is a very slowly varying function of ω/ω_p.

ACKNOWLEDGMENT

The authors are indebted to F. E. Paschke for several interesting discussions.

APPENDIX. DERIVATION OF EQ. (29)

By definition of dc temperature

$$\frac{kT_0}{m}v_0^2=(\langle u^2\rangle-v_0^2)v_0^2, \tag{A-1}$$

where

$$\langle u^2\rangle=\frac{1}{\rho_0}\int u^2f_0du,\quad v_0=\frac{1}{\rho_0}\int uf_0du=i_0/\rho_0. \tag{A-2}$$

For a half-Maxwellian distribution of velocities in which the slowest electrons have velocity $u_s=(2\eta V_0)^{\frac{1}{2}}$, the distribution function is

$$f_0(u,x)=2\alpha i_0\exp[-\alpha(u^2-u_s^2)]S(u-u_s), \tag{A-3}$$

where $\alpha\equiv m/2kT_c$. Thus

$$\langle u^2\rangle=-\frac{1}{I}\frac{dI}{d\alpha},\quad v_0=\exp(-\alpha u_s^2)/2\alpha I \tag{A-4}$$

where

$$I\equiv\int_{u_s}^{\infty}\exp(-\alpha u^2)du$$

$$=\tfrac{1}{2}(\pi/2)^{\frac{1}{2}}\operatorname{erfc}[u_s(\alpha)^{\frac{1}{2}}]. \tag{A-5}$$

† See Appendix, Eq. (A-8).

[5] J. Feinstein, paper presented at Electron Tube Research Conference, Quebec, June, 1958.

Thus

$$dI/d\alpha=-\frac{1}{4\alpha}(\pi/\alpha)^{\frac{1}{2}}\operatorname{erfc}[u_s(\alpha)^{\frac{1}{2}}]-\frac{u_s}{2\alpha}\exp(-\alpha u_s^2),$$

and therefore

$$\langle u^2\rangle=(1/2\alpha)+u_sv_0. \tag{A-6}$$

Returning to (A-4) and differentiating, one obtains

$$\frac{dv_0}{du_s}=2\alpha v_0(v_0-u_s),$$

which, for large u_s, i.e., large V_0, has the series solution

$$v_0=u_s\left(1+\frac{1}{2\alpha u_s^2}-\frac{2}{(2\alpha u_s^2)^2}+\cdots\right). \tag{A-7}$$

Combination of (A-1, 6, 7) therefore gives

$$\frac{kT_0}{m}v_0^2=\left[\frac{1}{2\alpha}+u_s^2+\frac{1}{2\alpha}-\frac{2}{4\alpha^2u_s^2}+\cdots-u_s^2\left(1+\frac{1}{4\alpha^2u_s^4}+\frac{1}{\alpha u_s^2}-\frac{1}{\alpha^2u_s^4}+\cdots\right)\right]u_s^2(1+\cdots)$$

$$\doteq\tfrac{1}{4}\alpha^2=(kT_e/m)^2 \tag{A-8}$$

as u_s becomes large.

Equations (A-1, 6) give

$$(m/2)v_0^2=(m/2)v_0u_s+(k/2)(T_e-T_0) \tag{A-9}$$

which is the dc energy equation for a beam with arbitrary velocity spread. This equation has also been derived by Pötzl.[9]

[9] H. Pötzl (private communication).

JOURNAL OF APPLIED PHYSICS VOLUME 31, NUMBER 3 MARCH, 1960

Focusing Molecular Beams of NH_3*

J. C. Helmer and F. B. Jacobus, *Varian Associates, Palo Alto, California*

and

P. A. Sturrock, *W. W. Hansen Laboratories of Physics, Stanford, California*

(Received August 28, 1959;

The problem of forming molecular beams for use in ammonia masers is examined. It is shown theoretically and experimentally that through the use of a new type of parabolic focuser with a "point source" effuser, the molecular flow may either be reduced by a factor of 8, for the same power output, or the power output may be increased by a factor of 2 for the same molecular flow. A theory of beam formation in a multitube effuser is described. This shows that the most intense molecular beam is formed by an effuser of small overall diameter. Design considerations are discussed for parabolic, upper-state focusers, and for coaxial, lower-state focusers. The operation of a system is described, using a lower-state focuser and an ionization detector, in which lower-state molecules produced by maser oscillation may be detected.

I. INTRODUCTION

An investigation of the properties of the ammonia beam maser[1] leads directly to a study of the formation and focusing of the molecular beam. In addition, it is desirable to know how to obtain the most intense molecular beam, and how to make the most efficient use of the molecules leaving the effuser. The following discussion summarizes some of the results of a three year study of NH_3 beams as used in the ammonia maser.

II. NONUNIFORM FOCUSERS

Focusers used in the past have been uniform in cross section from effuser to cavity. These produce beams of uniform cross section. Consider now a beam whose cross-sectional area varies in a more or less arbitrary way from the molecular source to the cavity, as shown in Fig. 1. The number of molecules N leaving the source and entering the cavity is given by

$$N=I_1A_1\Omega_1=I_2A_2\Omega_2,$$

where A_1, A_2 are the areas of the source and cavity apertures; Ω_1, Ω_2 are the solid capture angles occupied by the molecular trajectories, averaged over A_1 and A_2; and I_1, I_2 are the beam intensities at the source and the cavity apertures. Since the volume of phase space occupied by the beam is constant, we have

$$A_1\Omega_1=A_2\Omega_2, \tag{1}$$

and hence

$$I_2=I_1.$$

In maser application the minimum molecular bandwidth, $\Delta f_{\min}$, is determined by Ω_2, so that

$$\Delta f_{\min}\simeq 2v/\lambda(\Omega_2/\pi)^{\frac{1}{2}}, \tag{2}$$

* Supported by the U. S. Army Signal Corps under Contract No. DA-36-039 sc-73266.

[1] Gordon, Zeiger, and Townes, Phys. Rev. 99, 1264 (1955).

where v is the axial molecular velocity and λ is the wavelength of the molecular line. If Δf_{min} and therefore Ω_2 are to be held constant, the only way that the molecular flux may be increased is to increase I_1, the source intensity. We will consider this problem in Sec. III. The value of Ω_2 is determined by the strength of the focusing fields. Increasing the strength of the focusing fields increases the molecular flux and the minimum molecular bandwidth at the same time. For sufficiently short cavities, the change in Δf_{min} may be ignored, but in long cavities where Δf_{min} is greater than the "transit time" bandwidth, the change in Δf_{min} is an important, complicating factor.[2]

In practice, the capture solid angle at source, Ω_1, is much smaller than the solid angle, Ω_e, occupied by the molecules leaving the effuser. The total gas input to the device is therefore $I_1 A_1 \Omega_e$, independent of Ω_1. It follows that if a focuser can be designed such that A_1 is reduced while maintaining the same value of Ω_2, a substantial reduction in the gas input may be achieved. This problem has been solved by P. A. Sturrock.[3] A solution exists for the molecular trajectories in a harmonic potential well, such that the envelope of the beam defines a paraboloid of revolution. Sturrock shows that the focusing fields which form this beam are provided by quadrupole electrodes which lie on the surface of the paraboloid. The paraboloid may be cut at any two planes, normal to the axis, and these define the entrance and exit apertures. It is assumed that the area of the molecular source is equal to the area A_1 of the entrance aperture. The design of such a focuser is particularly simple, since the entrance and exit apertures uniquely define the parabola. If R_1 is the radius of the input aperture and R_2 the radius of the output aperture, then the beam radius R is given by

$$R=\left(\frac{Z}{L}(R_2^2-R_1^2)+R_1^2\right)^{\frac{1}{2}}, \tag{3}$$

where L is the length of the focuser and Z is the distance along the beam axis. In practice, the focusing electrodes have circular cross sections which match the radius of curvature of the theoretical hyperbolic equipotentials, at the closest approach to the beam axis. This condition is obtained when the diameter of the focusing electrode is equal to the beam diameter, where the beam diameter is defined by the inscribed circle which grazes the electrodes.

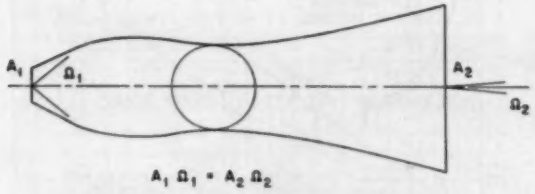

FIG. 1. Arbitrary beam envelope.

To obtain the maximum beam transmission, the period in space of the molecular trajectories must change sufficiently slowly along the length of the beam. In a given focuser this condition can be obtained by applying a sufficiently high potential. This condition will hold if the applied potential is of a value such that a uniform focuser of length L and radius R_2 is one-quarter of a focusing period long or more. Therefore, the length of the parabolic, quadrupole focuser will be the same as the length of a uniform quadrupole focuser with the same applied potential and exit aperture R_2. If the molecular sources have the same intensities I_1, then the beams emerging from the two focusers will be identical. But, under the condition $\Omega_e \gg \Omega_1$, which is true in practice, the total gas input is reduced, using the parabolic focuser, by the factor A_1/A_2. The limit to which this situation may be carried is reached when R_1 becomes so small that breakdown occurs due to the applied potential. However, this type of focuser is favored by the experience that breakdown usually occurs across insulators, and if not, then it is always possible to obtain higher electric fields, before breakdown, with conductors of small diameter than with conductors of large diameter. Secondly, this geometry favors the production of molecular beams of greater intensity than has been obtained in uniform focusers. This is discussed in Sec. III.

The parabolic shape is not the only possible shape for a nonuniform focuser. The shape is primarily determined by an upper limit on the allowed rate of variation. This upper limit is given by a solution of the harmonic oscillator equation with time varying force constant,

$$(d^2r/dt^2)+\omega^2(t)r=0. \tag{4}$$

Subject to the condition that

$$d\omega/\omega^2 dt \ll 1, \tag{5}$$

a solution of (4) is[4]

$$r=A\left(\frac{\omega(0)}{\omega(t)}\right)^{\frac{1}{2}} \exp \pm j\int_0^t \omega dt, \tag{6}$$

where A is a constant. A feature of Eq. (6) is that

$$|dr/dt|_{max} \times |r|_{max} = \text{const.} \tag{7}$$

This is a specific example of the law expressed in Eq. (1). For maximum beam transmission, the condition (5) is a little too strong and it is sufficient that

$$d\omega/\omega^2 dt \leq 1 \tag{8}$$

or, if $T=2\pi/\omega$ is the period of oscillation, then

$$dT/2\pi dt \leq 1. \tag{9}$$

[2] J. C. Helmer, J. Appl. Phys. **30**, 118 (1959).

[3] P. A. Sturrock, "Research on atomic and molecular resonance devices," Varian Associates Engineering Report No. 218-3Q, January, 1958 (to be published).

[4] For example, see the WKB approximation.

In a quadrupole focuser, the Stark energy is

$$W=C|E|^2, \quad |E|=V_0r/R^2, \tag{10}$$

where C is a molecular constant, E is the electric field strength, R is the inscribed radius of the focuser, and V_0 is the applied voltage. It follows that

$$T=\frac{2\pi}{\omega}=2\pi\left(\frac{mr}{dW/dr}\right)^{\frac{1}{2}}=\frac{2\pi R^2}{V_0(2C/m)^{\frac{1}{2}}}, \tag{11}$$

where m is the molecular mass. For a nonuniform focuser, we therefore require that

$$\frac{1}{2\pi}\frac{dT}{dt}=\frac{d}{dt}\left(\frac{R^2}{V_0(2C/m)^{\frac{1}{2}}}\right)\leq 1. \tag{12}$$

If V_0 and C are constant with length $z(z=vt$, where v is the axial velocity), then the shape of a focuser in which $dT/dt=$const is given by

$$R^2=At+B. \tag{13}$$

This is the equation of the parabolic focuser. The parabolic focuser is the shortest nonuniform focuser, however, it is only necessary in general to satisfy Eq. (9). This relation may be satisfied by a *linear* taper in which at $R=R_2$, $dT/2\pi dt=1$. Then it follows that, for $R<R_2$, $dT/2\pi dt<1$.

In NH_3 and in other molecules as well, a complicating effect is the change in molecular constants at high field strength. In ammonia, the Stark energy undergoes a transition from second order to first order for field strengths above 30 000 v/cm. At the small end of a nonuniform focuser, field strengths in excess of 200 000 v/cm are easily obtained. In this region, $W\sim|E|$ and a linear taper is more nearly the optimum electrode shape. These remarks also hold for the focusing of linear molecules which have rotational constants above 30 kmc. Molecules with small rotational constants will not focus properly in high fields due to a sign reversal in the slope of the Stark energy.

III. MOLECULAR EFFUSERS

The limiting intensity I of a molecular effuser is determined by mean-free-path considerations in much the same way that molecular flow is limited in a thin hole. Due to the frequent crossings of the molecular paths on the exit side of a thin hole, the molecular density remains roughly constant for a distance along the axis about equal to the diameter of the hole. If a molecule can get through this region, it enters the inverse-square-law region of molecular density where the collision probability rapidly vanishes. Thus, the maximum intensity of molecular effusion is reached when the pressure at the entrance side of the hole is such that the molecular mean-free-path is equal to the diameter of the hole.

For long single tubes, we have instead the requirement that the mean-free-path be greater than the length of the tube. Effusers for intense molecular beams usually consist of bundles of such tubes. In addition, the effuser is operated at a sufficiently high entrance pressure so that the gas enters a tube in viscous flow. We may imagine a condition such that as we travel along the tube the pressure drops until the mean-free-path is equal to the remaining tube length. From this transition region the gas streams out in molecular flow. If this picture is correct then the angle between half intensity points in the molecular beam thus formed is given by

$$\theta=2d/(\lambda), \tag{14}$$

where d is the tube diameter and λ is the mean-free-path at the transition region. Since λ is inversely proportional to the pressure at the transition region, it follows that the central beam intensity will be proportional to the angular beam width.

If the effuser consists of a bundle of diameter D of such tubes then, as we have described for the case of a thin hole, a region of constant beam density will exist in front of the effuser, and the length ℓ of this region along the axis will be

$$\ell\sim D/\theta \tag{15}$$

The maximum beam intensity is determined by the condition that a molecule be able to pass through this region of constant density without collision. Our calculations suggest that

$$I_{\max}\sim(t/Dd)^{\frac{1}{2}}, \tag{16}$$

where t is the transparency of the effuser. Thus, greater intensity is obtainable from effusers of high transparency t and small diameter D. In our opinion, it is this relation which explains the confusing results obtained by various workers in the field in comparing large, multi-tube effusers, with smaller ones.

According to the above remarks, it is a fortunate circumstance that the parabolic focuser uses a small diameter source, for with this combination we have the choice of either reducing the total gas flow for the same beam intensity, or achieving a higher beam intensity with the same gas flow.

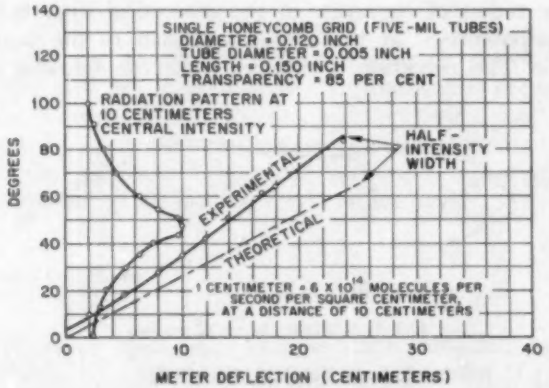

FIG. 2. Beam pattern and beam width (single honeycomb grid, five-mil tubes).

IV. LOWER-STATE FOCUSING

It will be described in Sec. V how interesting experiments can be carried out with lower-state focusers.[5] A lower-state focuser must have strong electric fields along the axis, and the obvious configuration which achieves this is a coaxial line with voltage applied between the center conductor and the outside conductor. The catastrophic increase in field strength as the center conductor is approached prevents this focuser from being a true focuser in the sense of imparting periodic motion to the lower-state molecules. Molecules which enter this focuser must ultimately strike either the inner or the outer conductor if the focuser is infinitely long. However, molecules of certain classes are strongly deflected and their radial velocities are reversed. These consist of molecules with large angular momentum and inward directed radial velocities, and molecules of small angular momentum with outward directed radial velocities. The latter class could have periodic motion if the center conductor were cut away at intervals. Calculations show that the beam transmission is optimized when the diameter ratio between the outer and inner conductor is between 3 and 4. In addition, at the operating potential the coaxial focuser should have about the same length as a quadrupole focuser of the same diameter (inscribed circle diameter) and potential.

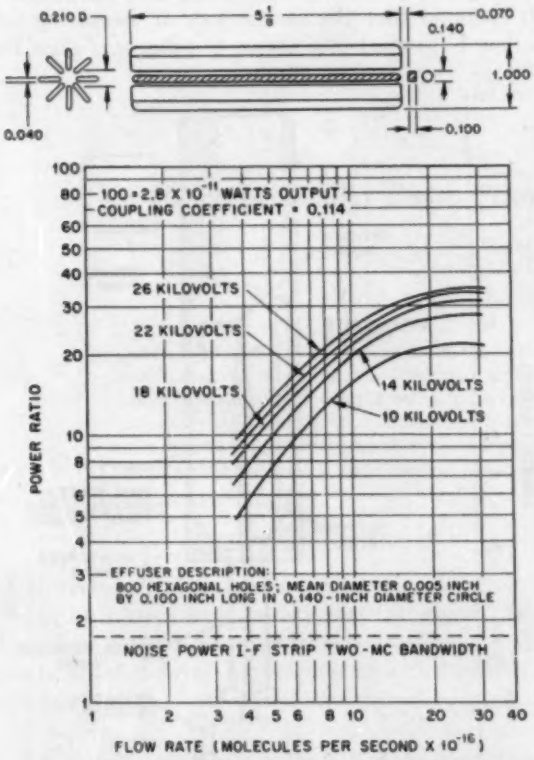

FIG. 3. Power ratio *vs* flow rate for eight-pole focuser (all dimensions in inches).

[5] See also W. H. Higa, Proceedings of the 11th Annual Symposium on Frequency Control (May, 1957), p. 352.

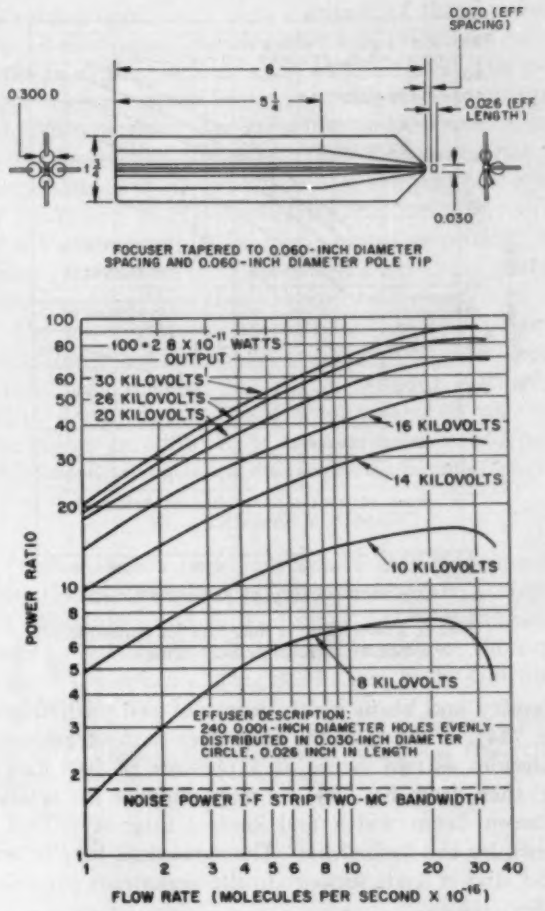

FIG. 4. Power ratio *vs* flow rate for parabolic focuser with 240-hole effuser (all dimensions in inches).

V. EXPERIMENTAL RESULTS

A. Effusers

It was suggested by Jepsen[6] that short lengths of klystron grid stock could be promising as molecular effusers. These grids are made by plating fine aluminum wire, of diameter equal to the tube diameter in the effuser, with a thin layer of copper. The plated wire is cut in six inch lengths and stacked in a copper pipe until the pipe is full. The pipe is then swaged so that the wire cross sections deform and fill the empty spaces. A molecular effuser is made by cutting off a desired length and etching out the aluminum, leaving a thin wall, copper honeycomb structure. The technique may be used with wire diam of 0.001 in. and above. A transparency of 85% is obtained with 0.005-in. wire.

The beam pattern for a 0.140-in. diam grid with 0.005-in. diam tubes was measured with a Pirani gauge and a rotating grid mount. The Pirani gauge was calibrated by the beam formed by a small, thin hole, with a known pressure behind it. The results are shown in Fig. 2. The nearly linear relation between central

[6] R. L. Jepsen (private communication).

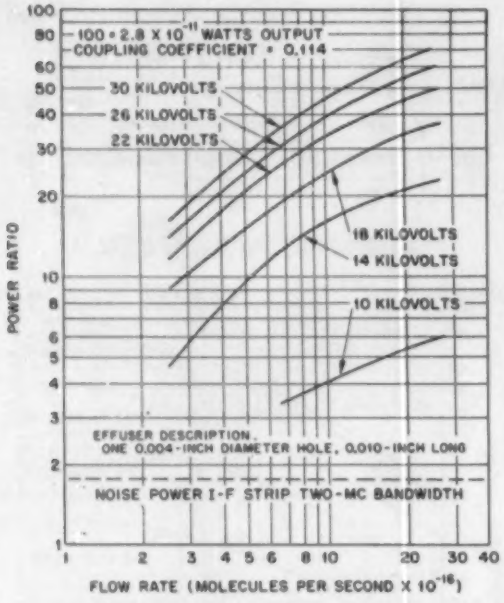

FIG. 5. Power ratio *vs* flow rate for parabolic focuser with single-hole effuser.

intensity and beam width bears out the prediction of Eq. (14). If we take the mean-free-path of ammonia molecules as two inches at a pressure of 10^{-3} mm of Hg, then, from Eq. (14) we may compute the relation between beam width and central intensity. This is shown by the dashed line. The agreement here is very good, and it lends support to the arguments presented in Sec. III.

Grids of the type described above have been used extensively in this laboratory for molecular effusers with uniform focusers, in which the beam diameter is about 0.375 in. The rather small diameter of the effuser has not been a disadvantage as at first we thought it might be. In fact, the performance of larger diameter effusers, made up from 3 or 7 of these grids mounted in parallel, as measured by the microwave power output of the maser, has been noticeably poorer. And the 7 grid effuser produced much less power output than the 3 grid effuser. These results support the general idea that the most intense molecular beams are produced by effusers of small diameter and high transparency.

B. Parabolic Focusers

For reference, Fig. 3 shows the maser power output when the beam is formed by an eight-pole focuser using the klystron grid effuser described in part A. In Fig. 4 is shown the same measurement for a parabolic quadrupole focuser, using a 0.030-in. diam effuser containing 240, 0.001-in. diam tubes. In comparison with Fig. 3, we see that at a relative power of 20 the parabolic focuser uses a factor of 8 less gas flow, while the maximum output, at constant flow rate, is greater by a factor of 2. This again agrees qualitatively with the predicted results. The amount of gas saved should be given by the area ratio of the exit and entrance apertures, about 25. At least part of the reason that only a factor of 8 is obtained is that at the very high fields produced in the entrance aperture, about 200 kv per centimeter, the Stark effect is well into the linear region. The design of the focuser is based on the second order Stark effect which, if it were to hold at the input aperture, would produce considerably higher deflections than are actually obtained.

Of additional interest is the performance of the parabolic focuser with a single 0.004-in. diam tube for the effuser; shown in Fig. 5. It does not perform quite as well as the multitube effuser with the parabolic focuser, but it is quite superior to the uniform, eight-pole focuser with the klystron grid effuser.

All of these measurements were made with a six-inch long cavity. We suggest that the quadrupole, parabolic focuser performs best with such a long cavity. This is due to the better defocusing of lower-state molecules which travel close to the beam axis. In the case of uniform focusers which have more than four poles, there is a definite tendency for the production of beams which, within a small axially directed solid angle, are deficient in upper state population excess.[7] However, it is just these molecules which are put to the best use in very long cavities.

It is found that the easiest way of measuring total gas flow is to allow the maser to exhaust a glass bulb

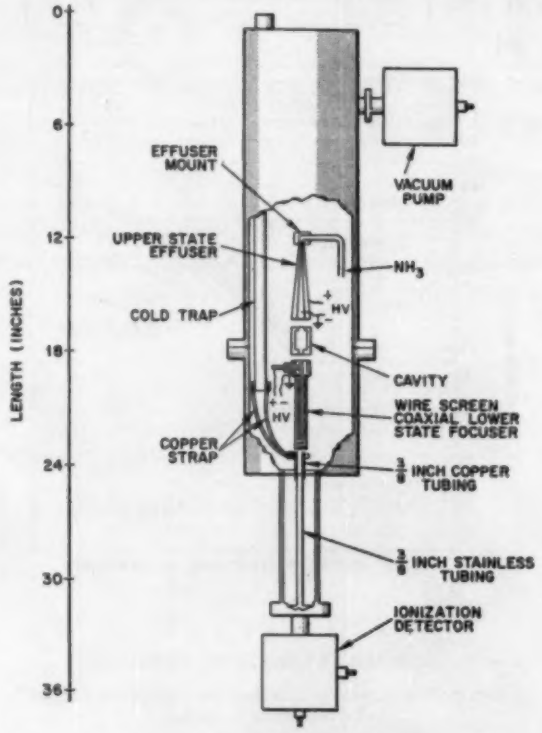

FIG. 6. Lower state beam detector.

[7] M. Hirono, J. Radio Research Laboratories **6**, 515 (1959).

of known volume, containing NH_3. The pressure in the bulb is monitored by an oil monometer whose reference end is connected to vacuum. If the flow conditions in the effuser are molecular, then the pressure in the bulb is a simple exponential function of time, from which the initial flow rate is easily deduced. There is no reason to suppose that the flow conditions are molecular, however, in all cases, a perfect exponential decay of pressure with time is observed.

C. Lower State Focusing

Through the use of a lower-state focuser it is possible to detect oscillation in the cavity by detecting the lower state molecules which are produced by the oscillation. The experimental setup for such a system is shown in Fig. 6. If there is no oscillation, upper state molecules passing into the lower state focuser are defocused and do not reach the ionization detector. Oscillation produces lower state molecules which are focused by the lower state focuser into the ionization detector, resulting in an increase in detector current. By using an all metal vacuum system, pumped by a small VacIon† high vacuum pump and a liquid nitrogen cold trap, we obtain an increase in detector current of five per cent due to oscillation, with a voltage signal to noise ratio of 15. The ionization gauge, a modified VacIon high vacuum pump, has a time constant of three minutes due to adsorption and desorption of molecules on the surfaces of the entrance tube and chamber. The principle of operation of this gauge, with its long entrance tube, is the same as the more conventionally used Pirani gauge.[5] In addition, it may be shown that the gauge sensitivity is independent of the pumping speed of the gauge. In this application, the main advantage of a VacIon pump is its high current sensitivity, 800 times greater than the filament type ion gauge, and the very important fact that it keeps itself clean.

The lower state beam detector has two potential uses. Due to the fact that it counts only those molecules which pass through the cavity without hitting the walls, it may be used as a spectrometer of very high resolution. In addition, it may be used as a detector of infrared oscillation in the ammonia beam.

VI. ACKNOWLEDGMENT

This work has benefited considerably from the contributions, advice, and encouragement of R. L. Jepsen, M. W. Muller, and W. L. Beaver. Many of the experiments would have been impossible without the expert technical assistance of E. B. Hodges, R. E. Uhlenberg, and W. W. Wood.

† Registered U. S. Patent Office.

[5] N. F. Ramsey, *Molecular Beams* (Clarendon Press, Oxford England, 1956).

JOURNAL OF APPLIED PHYSICS VOLUME 31, NUMBER 3 MARCH, 1960

Molecular Beam Formation by Long Parallel Tubes*

J. A. GIORDMAINE AND T. C. WANG†
Columbia University, New York, New York
(Received August 13, 1959)

The characteristics of molecular beams formed by sources consisting of long tube arrays are measured for several sources. The peak beam intensity and the beam width are calculated when collisions in the source are taken into account under the assumption that a limited region of Knudsen type flow occurs near the low-pressure end of the source. The peak beam intensity and the beam width are calculated to vary as the square root of the total flow rate for source pressures giving useful directivity, in good agreement with the observations. Considerations in the design of sources are discussed.

I. INTRODUCTION

IN recent years, several types of molecular beam devices have been constructed in which beams of high intensity are required from sources having an area of the order of 1 cm^2. An example of such a system is the ammonia maser,[1] in which the necessary peak beam intensity is approximately 10^{19} molecules per second per steradian. In order to reduce pumping requirements in such systems, arrays of long parallel tubes[2] have been used as beam sources. In this way the peak intensity has been increased in some systems by a factor of about 20 compared to a cosine law source for the same total flow. In this paper we discuss the properties of molecular flow in such sources and report on the characteristics of several different types of sources.

* Work supported jointly by the U. S. Army Signal Corps, the Office of Naval Research, and the Air Force Office of Scientific Research.

† Present address: Arthur D. Little, Inc., Cambridge, Massachusetts.

[1] Gordon, Zeiger, and Townes, Phys. Rev. 99, 1264 (1955).

[2] This technique was first used by J. R. Zacharias; see N. F. Ramsey, *Molecular Beams* (Clarendon Press, Oxford, 1956), p. 363.

We shall make use of the following symbols:

a tube radius, cm
L tube length, cm
n molecular density, molecules cm^{-3}
n_0 density at the high-pressure end of the tube
A cross-sectional area of tube, cm^2
$d\omega$ element of solid angle, steradians
θ angle between a given direction and the tube axis
$\bar{c}$ average molecular velocity, cm sec^{-1}
λ mean free path, cm
σ molecular diameter, cm
$I(\theta)$ beam intensity in the direction θ, molecules $(steradian)^{-1}$ sec^{-1}
z distance into tube, measured from low-pressure end, cm
N rate of flow through the tube, molecules sec^{-1}
$\bar{\lambda}$ average mean free path over the length of the tube, where

$$\bar{\lambda} \equiv L\left(\int_0^L dz/\lambda(z)\right)^{-1}. \tag{1}$$

Depending on the ratio of the molecular mean free path to the radius and length of the tube, several modes of molecular flow can be defined for the purposes of the present work. It will be assumed through that $L \gg a$.

Mode I. $\bar{\lambda} \gg L$. In this mode of flow the tube is "transparent," i.e., a molecule at the high pressure end of the tube traveling in the direction of the tube axis passes through the tube without a collision. The peak intensity and the flow rate are proportional to the pressure behind the source.

The peak intensity is

$$I(0)d\omega = \frac{n_0 \bar{c} a^2}{4} d\omega \tag{2}$$

and the flow rate is given[3] by

$$N = \frac{2\pi}{3} \frac{n_0 \bar{c} a^3}{L}. \tag{3}$$

The beam shape, that is, $I(\theta)/I(0)$ is determined almost completely by the tube geometry and is independent of n_0 and N. The beam shape under these conditions is calculated below on the basis of certain reasonable assumptions.

Mode II. $\bar{\lambda} \gtrsim L$; $\lambda \gg a$ throughout the tube. In this mode the tube is no longer transparent, and the peak intensity no longer proportional to the pressure behind the source. Equation (3) remains valid for the flow rate. The beam shape for Mode II is a function of flow rate as well as the tube geometry. If $\bar{\lambda} \gg L$ the beam shape is determined almost completely by a and N, with no direct dependence on L. Under this condition the tube is referred to as "opaque."

Mode III. $\bar{\lambda} \ll L$; $\lambda \gg a$ for $z < L_0$; $\lambda \gtrsim a$ for $L > z > L_0$, where $L_0 \gg a$. In this mode, Knudsen type flow ($\lambda \gg a$) is a valid approximation only over a limited region L_0 near the discharge end of the tube. Neither peak intensity nor flow rate is any longer proportional to the pressure behind the source.

As the pressure behind the source is further increased, the molecular beam becomes less well defined. It will become clear that useful collimation is usually provided only for flow described by one of these three modes.

Clearly the optimum collimation for a given tube is obtained in collision-free flow (Mode I). However, to obtain peak intensities of the order of $I(0) = 10^{19}$ sec^{-1} cm^{-2} $sterad^{-1}$ according to Eq. (2), source pressures of the order of several tenths of mm are indicated. At such pressures the mean free path is of the order of 10^{-2} cm, so that long-tube collision-free flow could occur only in tubes of radius considerably less than 10^{-3} cm. At present, densely packed arrays of such narrow bore tubes are not available. For this reason, sources giving high beam intensities are operated under Mode II or III conditions, in which the peak intensities and collimation are essentially determined by intermolecular collisions in the tubes.

All of the experimental work reported below was carried out under Mode II and III conditions.

II. EXPERIMENTAL TECHNIQUE

The angular distribution of intensity from the tube arrays was studied by use of the apparatus shown in Fig. 1. The sources were mounted so as to allow rotation about an axis through the center of the source face and perpendicular to the tube axes.

The detector was a Pirani gauge in which the chambers and slits were milled in a pair of lapped stainless steel blocks.[4] The four platinum ribbon elements were soldered to springs which kept the ribbons taut in the channels. The characteristics of the gauge are shown in Table I. The gauge was used in a conventional

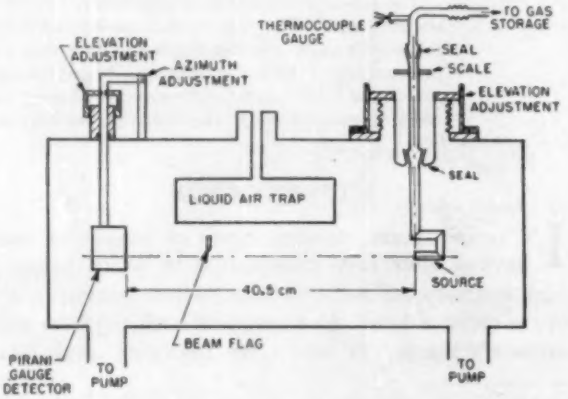

FIG. 1. Experimental apparatus, showing the mounting and relative positions of the source and detector.

[3] L. B. Loeb, *The Kinetic Theory of Gases* (McGraw-Hill Book Company, Inc., New York, 1934), 2nd edition, p. 294.

[4] R. S. Julian, Ph.D. Thesis, Massachusetts Institute of Technology, Cambridge, Massachusetts (1947). This gauge is described by N. F. Ramsey, reference 2, p. 392.

Wheatstone bridge circuit with a mirror galvanometer. The gauge mounting allowed for adjustment of height and azimuth, and the final alignment of the gauge was carried out by adjustment of the gauge for maximum response with the beam from the source being studied.

The sources and detectors were mounted in a molecular beam can which was already available.[5] Two MCF 300 pumps and one MCF 700 pump were used, as well as a liquid nitrogen trap. Nevertheless, can pressures with the sources operating were in the range 1 to 6×10^{-5} mm.

The source-detector spacing was 40.5 cm. As a result of the high can pressure, the measured beam intensities had to be corrected for attenuations of between 10% and 55% between the source and the detector.

Flow rates through the sources could be measured by observing the rate of change of pressure in a bulb of approximately 5 liter volume connected to the source. The bulb pressures were measured by a thermocouple gauge (Hastings Model AP-1) mounted at the neck of the bulb. Pressures at the source were measured by a second thermocouple gauge mounted near the source. The thermocouple gauges were calibrated for CO_2 at

TABLE I. Design of Pirani gauge.

Chamber dimension:	$0.100\times0.020\times1.75$ in.
Slit cross section:	0.006×0.188 in.
Slit length:	0.247 in.
Ribbon dimensions:	$0.00005\times0.015\times1.59$ in.
Gauge sensitivity (CO_2):	1 cm deflection $\sim1.6\times10^{13}$ molecules cm^{-2} sec^{-1}

pressures of a few tenths of a mm and higher against a mechanical pressure gauge (Wallace-Tiernan FA-160).

The Pirani gauge was calibrated by observing the flow rate through one of the sources (A) and the integrated beam intensity as indicated by the gauge, taking into account the beam attenuation in the can. The flow rates quoted below were obtained from the integrated angular distribution patterns and the Pirani gauge calibration factor.

Beam attenuation in the can was calculated using a mean free path derived from the quoted[6] values for CO_2.

$$\lambda=2.95\times10^{-3}\text{ cm} \quad 0°\text{C, 1 mm pressure}$$
$$\lambda=3.34\times10^{-3}\text{ cm} \quad 26°\text{C, 1 mm pressure.}$$

Because of the small angular aperture of the Pirani gauge, it was necessary to apply a correction for decreased effective detection sensitivity with sources B and C, which had larger diameters than source A. The sensitivity was calculated to be less than that with source A by 19% and 15%, respectively.

All of the results quoted are for CO_2. Attempts were made to observe source behavior using NH_3. However, the Pirani gauge detected NH_3 very sluggishly, with low sensitivity and little reproducibility. This behavior may have been caused by adsorption of the gas in the detector.

TABLE II. Characteristics of long tube sources.

Source	Tube length cm	Effective radius of single tube cm	No. of tubes	Over-all source diameter cm	Approximate shape of tube cross section
A	0.66	1.65×10^{-2}	224	0.51	Hexagonal
B	0.31	2.35×10^{-2}	1.28×10^{4}	1.3	Circular
C	0.95	2.69×10^{-2}	1.80×10^{4}	1.1	Triangular

The over-all accuracy of the flow rate measurements is estimated as about $\pm20\%$. The peak intensities are known to the same absolute accuracy. Ratios of peak intensity to flow rate are known to about $\pm5\%$.

The three sources studied in this investigation are described in Table II.

Source A, an extended klystron grid structure, had a honeycomb cross section, with the individual tubes separated by walls of approximately 0.001-in. thickness. Source B consisted of an aligned stack of photographically etched metal foils,[7] with the holes of circular cross-section arranged in hexagonal format. The alignment accuracy was such that the optical transparency of the stack was about 85% that of a single foil. Source C was prepared by rolling together two strips of nickel foil, one finely corrugated, the other flat, onto a thin spindle.[8] Source A was surrounded by a sleeve whose front edge was flush with the front of the source. The sleeves for sources B and C protruded about 3 and 2 mm respectively in front of the source face.

The effective radius quoted in Table II is defined as the perimeter of the tube cross section divided by 2π. The effective radius is equal to the actual radius for source B. The tube radii were measured with a magnifying optical projector and are minimum radii for the entire tube length. As a result of nonuniformity in the source construction, they may be up to 10% smaller than the average cross section for source B and 20% for C.

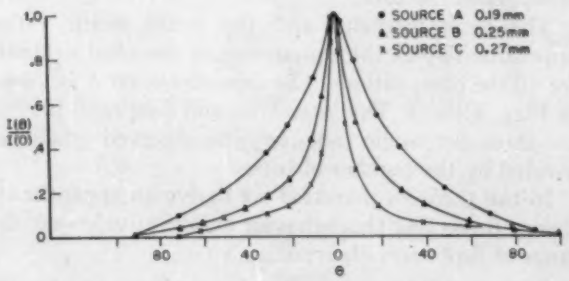

FIG. 2. Some representative measurements of $I(\theta)/I(0)$ as a function of θ for various sources and source pressures, showing the characteristic dependence of beam shape on half-width.

[5] Heberle, Reich, and Kusch, Phys. Rev. **101**, 612 (1956).
[6] *Smithsonian Physical Tables* (1954), ninth edition.
[7] This source was kindly loaned by Mr. J. P. Cedarholm.
[8] J. R. Zacharias and R. D. Haun, Jr., Quarterly Progress Report, M.I.T. Research Laboratory of Electronics, 34, October, 1954 (unpublished).

TABLE III. Beam formation by long tube sources.

Source	Pressure behind source mm	Peak intensity molecules sec^{-1} $sterad^{-1}$	Total flow molecules sec^{-1}	Half-width of beam at half-intensity degrees
A	0.024	1.42×10^{17}	8.91×10^{18}	5.0
	0.060	3.19	1.87×10^{19}	8.3
	0.110	5.70	5.26	15.0
	0.190	9.66	1.21×10^{19}	21.1
B	0.03	9.16×10^{17}	2.69×10^{19}	3.5
	0.075	1.49×10^{18}	4.56	4.3
	0.15	2.80	1.25×10^{19}	6.0
	0.25	3.73	2.28	9.1
	0.44	5.01	4.61	15.7
C	0.035	3.05×10^{17}	5.42×10^{18}	2.5
	0.13	7.87	1.81×10^{19}	3.3
	0.265	1.30×10^{18}	3.88	4.5
	0.61	2.29	1.03×10^{19}	5.7
	1.28	3.74	2.18	7.8
	1.90	4.79	3.58	11.3

III. EXPERIMENTAL RESULTS

Typical beam shapes produced by the sources are shown in Fig. 2. The beam shapes are shown normalized to the same peak intensity. These illustrations are reproduced to indicate the changing character of the beam shape with source pressure that was observed for all three sources, rather than to compare the effectiveness of the various sources. For a given beam width of half-intensity, the beam shapes were approximately the same for each source.

The experimental data are collected in Table III. The values quoted are corrected for beam attenuation in the can and for the limited angular aperture of the detector.

The source pressures shown in Table III are accurate to about ±0.03 mm. As a result of this low relative accuracy, the flow rates at the lowest pressures, where Knudsen flow would be expected throughout the tube, could not be compared quantitatively with the prediction of Eq. (2). In what follows, we shall be concerned with the flow rates themselves as the variable, irrespective of whether Knudsen flow is a valid approximation throughout the tube.

The peak intensity and the beam width varied approximately as the square root of the total flow rate for all the observations. The dependence on N is shown in Figs. 3 and 4. The intensities and flow rates plotted are those per single tube, i.e., the observed quantities divided by the number of tubes.

In the theoretical section we derive an approximate theory predicting this behavior quantitatively over the range of flow rates observed.

IV. THEORY

A. Peak Intensity

In this section the peak intensity is calculated as a function of the flow rate for a single tube of circular cross section. The approximate generalization to tubes of arbitrary cross section is discussed briefly at the end of this section.

We assume that, at least near the low-pressure end of the tube, the mean free path λ is much larger than the tube radius a, and that this condition obtains for a distance L_0 into the tube, where $L_0 \gg a$. This assumption of Knudsen type flow over at least a limited region will be seen to be valid for cases in which a beam of useful directivity is formed. We are thus considering flow in Modes I, II, and III.

The second assumption is that in the limited region of Knudsen flow the density of molecules in the tube n is related to the distance into the tube z by the relation:

$$n = rz \tag{4}$$

where r is a constant determined by the flow rate, the mean molecular velocity $\bar{c}$, and the tube radius. This assumption is strictly valid for $z \gg a$ only, since end corrections for $z \lesssim a$ are neglected. However, it will be

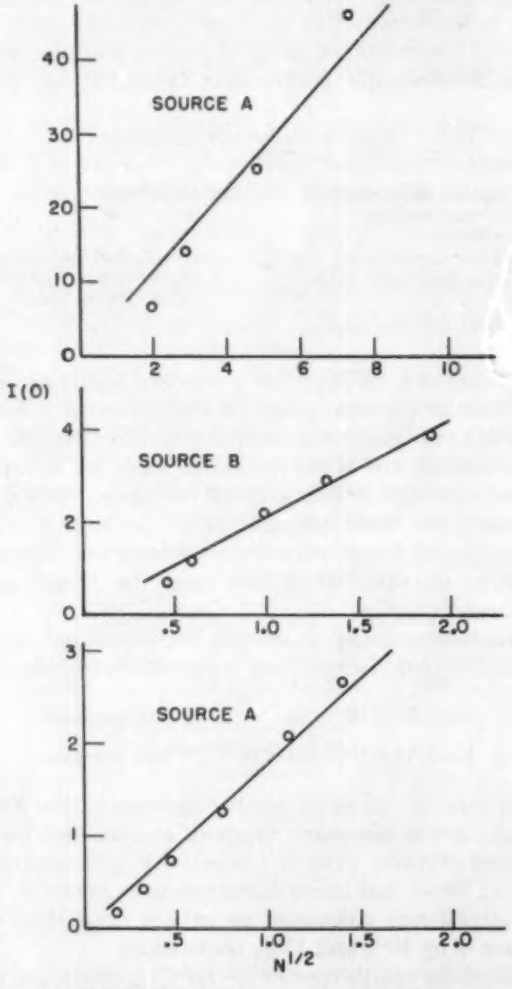

FIG. 3. Peak intensity per tube as a function of the square root of the total flow rate per tube. The units of $N^{\frac{1}{2}}$ are (molecules per second)$^{\frac{1}{2}}\times10^{7}$, and of $I(0)$ (molecules per steradian per second)$\times10^{14}$. *Note added in proof.* The bottom graph, incorrectly labeled Source *A*, refers to Source *C*.

seen that the peak intensity in cases of high collimation is determined mainly by the behavior of n for $z \gg a$, where this assumption is valid.

Consider an element of tube volume $\pi a^2 dz$ at a distance z from the low-pressure end of the source. The number of collisions per second in this volume element is $(\pi a^2 dz n\bar{c})/2\lambda$.

Let σ be the equivalent molecular diameter for collisions, as defined by

$$\lambda = 1/(\sqrt{2}\pi\sigma^2 n). \tag{5}$$

The number of collisions in $\pi a^2 dz$ is $(\pi^2 n^2 \sigma^2 \bar{c} a^2 dz)/\sqrt{2}$ from which arise $(\pi n^2 \sigma^2 \bar{c} a^2 dz d\omega)/2\sqrt{2}$ molecules traveling within the solid angle $d\omega$ in the direction of the tube axis toward the detector.

The fraction of these molecules undergoing collision in the distance dz' is dz'/λ or $\sqrt{2}\pi\sigma^2 n dz'$. The fraction of molecules leaving the element $\pi a^2 dz$ in the direction $d\omega$ which leave the source without a further collision is $\exp[-\pi\sigma^2 r z^2/\sqrt{2}]$.

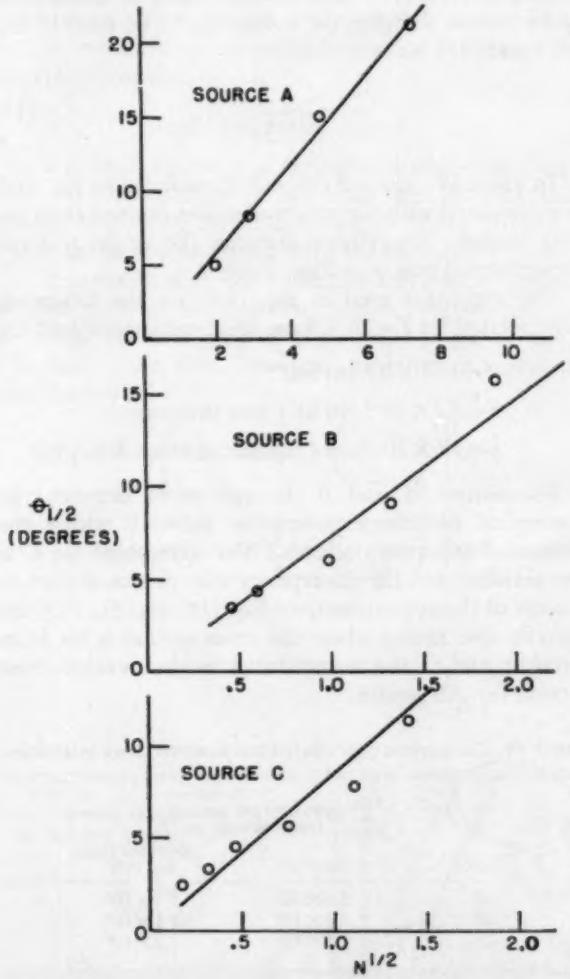

FIG. 4. Half-width of beam at half-intensity as a function of the square root of the total flow rate per tube. The units of $\theta_{\frac{1}{2}}$ are degrees, and of $N^{\frac{1}{2}}$ (molecules per second)$^{\frac{1}{2}} \times 10^7$.

Thus the total contribution to the peak intensity $I(0)d\omega$ from the collisions in the volume element $\pi a^2 dz$ is

$$I(0,z)d\omega dz = \frac{\pi\sigma^2\bar{c}a^2n^2}{2\sqrt{2}} \exp\left(\frac{-\pi\sigma^2 r z^2}{\sqrt{2}}\right) d\omega dz$$
$$= \frac{\pi\sigma^2\bar{c}a^2r^2z^2}{2\sqrt{2}} \exp\left(\frac{-\pi\sigma^2 r z^2}{\sqrt{2}}\right) d\omega dz. \tag{6}$$

The total contribution to $I(0)$ from collisions throughout the tube is

$$I_i(0)d\omega$$
$$= \int_0^L I(0,z)d\omega dz = \frac{\pi\sigma^2\bar{c}a^2r^2 d\omega}{2\sqrt{2}} \int_0^L \exp\left(\frac{-\pi\sigma^2 r z^2}{\sqrt{2}}\right) z^2 dz$$
$$= \frac{a^2 r^{\frac{1}{2}}\bar{c}d\omega}{2^{7/4}\pi^{\frac{1}{2}}\sigma}\left[\int_0^{L'} \exp(-y^2)dy - L' \exp(-L'^2)\right]$$
$$= \frac{a^2 r^{\frac{1}{2}}\bar{c}d\omega}{2^{7/4}\pi^{\frac{1}{2}}\sigma} \int_0^{L'} \exp(-y^2)dy - \frac{a^2 r\bar{c}Ld\omega}{4} \exp(-L'^2), \tag{7}$$

where L is the tube length and

$$L' = \frac{\pi^{\frac{1}{2}}\sigma r^{\frac{1}{2}} L}{2^{\frac{1}{2}}}.$$

An additional contribution to $I(0)$ arises from molecules which pass through the entire tube length without a collision. It can be shown by a development similar to that of Eq. (7) that this contribution is

$$I_s(0)d\omega = \frac{a^2 r\bar{c}Ld\omega}{4} \exp(-L'^2). \tag{8}$$

The total intensity in the peak direction is

$$I(0)d\omega = I_i(0)d\omega + I_s(0)d\omega$$
$$= \frac{a^2 r^{\frac{1}{2}}\bar{c}d\omega}{2^{7/4}\pi^{\frac{1}{2}}\sigma} \int_0^{L'} \exp(-y^2)dy. \tag{9}$$

The peak intensity is given explicitly in terms of the total flow rate by using Eq. (3) for Knudsen flow, or

$$r = \frac{3N}{2\pi\bar{c}a^3}. \tag{9a}$$

Substituting Eq. (9a) into Eq. (9), we obtain

$$I(0) = \frac{3^{\frac{1}{2}}\bar{c}^{\frac{1}{2}}a^{\frac{1}{2}}(N)^{\frac{1}{2}}}{4\,2^{\frac{1}{2}}\pi\sigma} \int_0^{L'} \exp(-y^2)dy, \tag{10}$$

where

$$L' = \frac{3^{\frac{1}{2}}\sigma L(N)^{\frac{1}{2}}}{2^{\frac{1}{2}}\bar{c}^{\frac{1}{2}}a^{\frac{1}{2}}}.$$

Formula (10) gives the peak intensity as a function of flow rate at all flow rates at which the source has appreciable directivity.

Simplified forms of Eq. (10) are useful in special limiting cases.

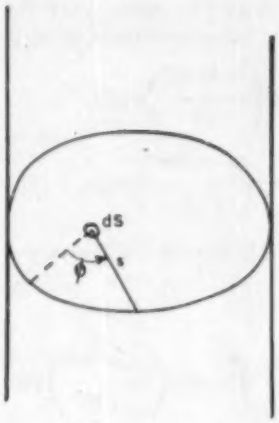

FIG. 5. Element of tube cross section, illustrating Eq. (13).

Case 1: Source Transparent: $L' \ll 1$

In this limit, the collisions in the source play a completely negligible role. In the limit of very low pressures and flow rates,

$$I(0)=\frac{(\pi a^2)n_0\bar{c}}{4\pi} \tag{11}$$

where n_0 is the molecular density at the high pressure end of the source. Equation (11) is just the expression for the peak intensity of molecules effusing from a hole of area πa^2 in a container of molecules of density n_0, where $\lambda \gg a$.

Case 2: Source Opaque: $L' \gg 1$

In this limit, the density in the source is so large that the probability of a molecule passing through the source without a collision is negligible. In the limit of L' large compared to unity,

$$I(0)=\frac{3^{\frac{1}{2}}\bar{c}^{\frac{1}{2}}a^{\frac{1}{2}}}{8\,2^{\frac{1}{2}}\pi^{\frac{1}{2}}\sigma}(N)^{\frac{1}{2}}. \tag{12}$$

The criterion for the validity of Eq. (12) to an accuracy of 1% is

$$L' \geqslant 2.5$$

or

$$L \geqslant \frac{2.5\ 2^{\frac{1}{2}}\bar{c}^{\frac{1}{2}}a^{\frac{1}{2}}}{3^{\frac{1}{2}}\sigma(N)^{\frac{1}{2}}}=\Lambda. \tag{12a}$$

This criterion is satisfied for all the measurements reported above and will generally be satisfied in application of long tube sources to molecular beam devices. From Eq. (12a) it follows that for a source tube of radius a carrying N molecules per second, increasing the length of the tube beyond Λ has a negligible effect on the source characteristics.

A special case of Eq. (12) arises when $\lambda \gg a$ throughout the tube. From Eqs. (3) and (12)

$$I(0)=\frac{2^{\frac{1}{2}}(\pi a^2)\bar{c}n_0^{\frac{1}{2}}}{8\pi\sigma L^{\frac{1}{2}}}. \tag{12b}$$

Equation (12b) expresses the peak intensity explicitly in terms of the pressure behind the source.

For tubes of uniform but noncircular cross section, Eq. (3) becomes[9]

$$N=\frac{1}{8}\frac{n_0}{L}\bar{c}\int dS\int_0^{2\pi} s\,d\phi, \tag{13}$$

where dS is an element of cross-sectional area and s is the distance measured at an angle ϕ with a fixed direction in the plane of the cross section, from the element dS to the boundary. The cross section is shown in Fig. 5.

An approximate expression for N for tubes of uniform and almost circular cross section is[10]

$$N=\frac{4}{3}\frac{n_0}{L}\bar{c}\frac{A^2}{P}, \tag{14}$$

where A is the cross-sectional area of the tube and P is the perimeter. From the derivation of Eq. (10) and from Eq. (14), it follows that for tubes of noncircular cross section the effective radius a_{eff} to be used in Eq. (10) and (12) is

$$a_{eff}=\frac{P}{2\pi}. \tag{15}$$

In Table IV values of $I(0)/(N)^{\frac{1}{2}}$ predicted by Eq. (12) are compared with the observed values derived from the best straight lines drawn through the origin and the experimental points in Figs. 3 and 4.

The constants used in Eq. (12) are the following, interpolated for $T=20°C$ from observed values[6] for CO_2.

$\bar{c}=3.74\times10^4$ cm sec^{-1}

$\lambda=3.2\times10^{-3}$ cm at 1 mm pressure

$\sigma=4.6\times10^{-8}$ cm [calculated from Eq. (5)].

For sources A and B the agreement between the theoretical and the experimental values is within the estimated experimental error. The agreement for C is less satisfactory; the discrepancy may be due in part to the use of the approximations Eq. (14) and Eq. (15) for the effective radius where the cross section is far from circular, and to the uncertainties in the average cross section for this source.

TABLE IV. Comparison of predicted and observed peak intensities.

Source	$\frac{I(0)}{(N)^{\frac{1}{2}}}$ molecules per steradian per second (molecules per sec)$^{-\frac{1}{2}}$	
	Observed	Calculated from Eq. (12)
A	5.6×10^7	5.5×10^7
B	2.1×10^7	2.1×10^7
C	1.8×10^7	2.2×10^7

[9] E. H. Kennard, *Kinetic Theory of Gases* (McGraw-Hill Book Company, Inc., New York, 1938), p. 304.
[10] L. B. Loeb, reference 3, p. 292.

The agreement observed indicates that Eq. (12) is a useful approximation in predicting peak intensity in terms of the flow rate and the constants of the tube and gas. The peak intensity appears to be determined essentially by the density gradient r and to be insensitive to end effects.

B. Beam Width

In this section the beam width is calculated for tubes of circular cross section for two of the limiting cases described in Part A, (a) "transparent source," (b) "opaque source." In both cases we make the assumption of uniform pressure gradient, in (a) over the entire tube, and in (b) over a limited region near the end of the tube. In applying Eq. (4) we again make the assumption of zero pressure at the end of the tube. It would be expected that the beam shape would be considerably more sensitive to the neglect of end corrections than the peak intensity. However in cases of high collimation, the beam intensity for angles up to the angle of half-maximum intensity is still determined largely by the pressures at points distant from the end of the tube. For this reason it seems useful to present the theory in this approximation.

(a) *Transparent Source*

In this limit the effect of collisions is neglected. Consider the contribution of the molecules leaving the exposed portion of the surface strip dz to the intensity in the direction θ measured from the tube axis (Fig. 6). If it is assumed that the molecules leave each surface element with an angular distribution proportional to the cosine of the angle with the normal to the surface, it is easily seen that the strip of width dz makes a contribution

$$I(\theta,z)dzd\omega=\frac{a\bar{c}}{2\pi}n(z)\sin\theta\left[1-\left(\frac{z\tan\theta}{2a}\right)^2\right]^{\frac{1}{2}}dzd\omega$$

$$=\frac{a\bar{c}r}{2\pi}\sin\theta z\left[1-\left(\frac{z\tan\theta}{2a}\right)^2\right]^{\frac{1}{2}}dzd\omega. \quad (16)$$

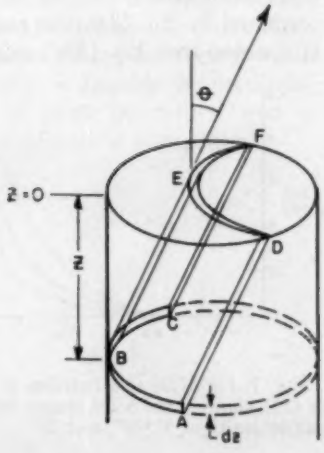

FIG. 6. Tube geometry, showing division of the exposed tube surface into strips ABC of width dz.

(*i*) $\pi/2>\theta\geqslant tan^{-1}(2a/L)$.—Integrating over the wall area contributing to $I(\theta)d\omega$,

$$I(\theta)d\omega=\frac{a\bar{c}r\sin\theta d\omega}{2\pi}\int_0^{2a/\tan\theta}z\left[1-\left(\frac{z\tan\theta}{2a}\right)^2\right]^{\frac{1}{2}}dz \quad (16a)$$

$$=\frac{2a^3\bar{c}r}{3\pi}\frac{\cos^2\theta}{\sin\theta}d\omega. \quad (17)$$

(*ii*) $tan^{-1}(2a/L)>\theta\geqslant 0$.—For θ in this range, the exposed area of the cross section at $z=L$ is

$$A=2a^2[\cos^{-1}y-y(1-y^2)^{\frac{1}{2}}].$$

where $y=(L\tan\theta/2a)$. The contribution from molecules passing through the source without colliding with the walls is then

$$I_1(\theta)d\omega=A\cos\theta\frac{n_0\bar{c}}{4\pi}d\omega.$$

The contribution from the walls, by analogy with Eq. (16a) is

$$I_2(\theta)d\omega=\frac{a\bar{c}r\sin\theta d\omega}{2\pi}\int_0^L z\left[1-\left(\frac{z\tan\theta}{2a}\right)^2\right]^{\frac{1}{2}}dz.$$

The total intensity is then

$$I(\theta)d\omega=\frac{a^2n_0\bar{c}\cos\theta d\omega}{2\pi}$$

$$\times\{\cos^{-1}y-y(1-y^2)^{\frac{1}{2}}+\tfrac{2}{3}y[1-(1-y^2)^{\frac{1}{2}}]\}. \quad (18)$$

Formulas (17) and (18) give the intensity distribution for all θ. From Eq. (17) and (18) the value of at which $I(\theta)=[I(0)/2]$ is

$$\theta_{\frac{1}{2}}=\frac{1.68a}{L} \quad (19)$$

for $a\ll L$. As expected the half-width at half-intensity in this limit is of the order of a/L. Since this mode of source operation is not of great use we do not discuss it further.

(b) *Opaque Source*

We again make the assumption of a cosine distribution for molecules, leaving the walls of the source. We shall be concerned only with tubes which are opaque according to the criterion of Eq. (12a).

The contribution to $I(\theta)d\omega$ of molecules leaving the wall element dz and undergoing no further collisions will be given by Eq. (16) modified by a suitable attenuation factor. Molecules in this category travel a distance $z/\cos\theta$ within the tube and suffer an attenuation

$$\exp\left(\frac{-\pi\sigma^2rz^2}{\sqrt{2}\cos\theta}\right).$$

The contribution to $I(\theta)d\omega$ from dz is then

$$I_1(\theta,z)dzd\omega=\frac{a\bar{c}r\sin\theta}{2\pi}z\left[1-\left(\frac{z\tan\theta}{2a}\right)^2\right]^{\frac{1}{2}}\times\exp\left(\frac{-\pi\sigma^2rz^2}{\sqrt{2}\cos\theta}\right)dzd\omega$$

or

$$I_1(\theta,z')dz'd\omega=\frac{2^{\frac{1}{2}}a^2\cos^{\frac{1}{2}}\theta r^{\frac{1}{2}}\bar{c}}{\pi^{\frac{1}{2}}\sigma}kz'(1-z'^2)^{\frac{1}{2}}\times\exp(-k^2z'^2)d\omega dz', \tag{20}$$

where the substitutions of Eq. (21) have been made.

$$z'=\frac{z\tan\theta}{2a}$$
$$k=\frac{2a}{\tan\theta}\left(\frac{\pi\sigma^2r}{\sqrt{2}\cos\theta}\right)^{\frac{1}{2}}. \tag{21}$$

In addition to the molecules whose final collision before leaving the source is made with the tube wall, we must consider those diverted into $d\omega$ by collisions with other molecules. We divide the tube volume contributing to the intensity in the direction of $d\omega$ into elementary volumes as follows (Fig. 6). The volume element dV associated with dz is defined as that bounded by the exposed portion ABC of the curved strip dz, by the envelope of lines in the direction of θ passing through the boundary of the strip dz, and by the projection DEF in the direction of θ of the strip dz onto the tube cross section at $z=0$. The length of this element is $z/\cos\theta$ and the cross sectional area is

$$2a\sin\theta\left[1-\left(\frac{z\tan\theta}{2a}\right)^2\right]^{\frac{1}{2}}dz.$$

Using reasoning analogous to that used in deriving Eq. (7), the contribution to $I(\theta)d\omega$ from collisions in an elementary volume element is

$$I_2(\theta,z')dz'd\omega=\frac{2^{5/4}a^2r^{\frac{1}{2}}\bar{c}\cos^{\frac{1}{2}}\theta(1-z'^2)^{\frac{1}{2}}dz'}{\sigma\pi^{\frac{1}{2}}}\times\int_0^{kz'}y^2\exp(-y^2)dy. \tag{22}$$

Combining Eqs. (20) and (22), the total contribution of the wall element dz' and the associated volume element is

$$I(\theta,z')dz'd\omega=\frac{2^{\frac{1}{2}}a^2r^{\frac{1}{2}}\bar{c}\cos^{\frac{1}{2}}\theta d\omega dz'}{\sigma\pi^{\frac{1}{2}}}(1-z'^2)^{\frac{1}{2}}\times\int_0^{kz'}\exp(-y^2)dy.$$

The integrated intensity arising from all the contributing elements is

$$I(\theta)d\omega=\frac{2^{\frac{1}{2}}a^2r^{\frac{1}{2}}\bar{c}\cos^{\frac{1}{2}}\theta d\omega}{\sigma\pi^{\frac{1}{2}}}\times\int_0^1(1-z'^2)^{\frac{1}{2}}\int_0^{kz'}\exp(-y^2)dydz'. \tag{23}$$

Substituting for r from Eq. (9a), Eq. (23) becomes

$$I(\theta)d\omega=\frac{3^{\frac{1}{2}}a^{\frac{1}{2}}\bar{c}^{\frac{1}{2}}\cos^{\frac{1}{2}}\theta(N)^{\frac{1}{2}}d\omega}{2^{\frac{1}{2}}\pi^2\sigma}\times\int_0^1(1-z'^2)^{\frac{1}{2}}\int_0^{kz'}\exp(-y^2)dydz'. \tag{23a}$$

Typical beam shapes calculated from Eq. (23a) are shown in Fig. 7. It is noted that these curves are qualitatively similar in shape to those observed (Fig. 2). In cases of high collimation, the angle $\theta_{\frac{1}{2}}$ at which $I(\theta)=[I(0)/2]$ is given approximately by

$$\theta_{\frac{1}{2}}\approx\frac{2^{\frac{1}{2}}3^{\frac{1}{2}}\sigma}{1.78a^{\frac{1}{2}}\bar{c}^{\frac{1}{2}}}(N)^{\frac{1}{2}}. \tag{24}$$

Expression (24) follows from Eq. (23a) in the approximation $\cos\theta\sim1$.

The predictions of Eq. (24) are compared with the measured half-widths (Fig. 4) in Table V. $\theta_{\frac{1}{2}}$ is the half-width of the beam at half-maximum intensity. Although the theory is relevant only for sources of circular cross section, the predictions for all the sources are included in Table V, by making use of the effective radius Eq. (15). The observed half-widths are larger than the theoretical values by about 60% in the case of A and B which have cross sections close to circular. The deviation is about 100% in the case of C.

A major source of the discrepancy in Table V is the inadequacy of the relation $n=rz$ near $z=0$. Since $n\neq0$ at the end of the tube, it would be expected that the observed intensity would be less than the intensity predicted by Eq. (23a) for angles away from the peak. It is noted that Eq. (23a) reduces to Eq. (12) at $\theta=0$.

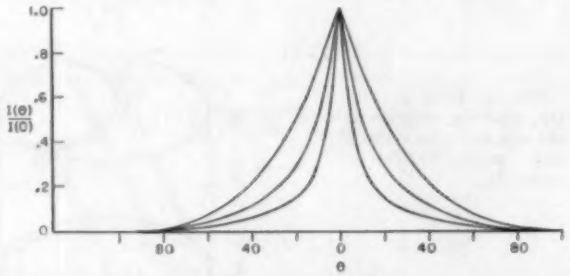

FIG. 7. $I(\theta)/I(0)$ as a function of θ, calculated from Eq. (23a) or (26), showing the beam shapes corresponding to half-widths at half-intensity of 5°, 10°, and 20°.

TABLE V. Comparison of predicted and observed beam widths.

Source	$\theta_{\frac{1}{2}}/(N)^{\frac{1}{2}}$ degrees (molecules sec^{-1})$^{-\frac{1}{2}}$ Observed	Calculated from Eq. (24)
A	2.9×10^{-7}	1.8×10^{-7}
B	7.3×10^{-7}	4.6×10^{-7}
C	8.4×10^{-7}	4.3×10^{-7}

In the limit of $N/a \to 0$ it can be shown that

$$\int_0^{\pi/2} I(\theta)2\pi \sin\theta d\theta \to N/2 \tag{25}$$

where $I(\theta)$ is given by Eq. (23). At values of N/a reported on in the present work, the integral in Eq. (25) is somewhat less than $N/2$. It would be expected from Eq. (25) that the half-widths predicted by Eq. (24) would be small by a factor of the order of 2.

A formula predicting the proper peak intensity, and with integrated intensity normalized to N rather than $N/2$, can be obtained by substituting $2k$ for k in the integration limit in Eq. (23a). This somewhat *ad hoc* procedure leads to Eq. (26)

$$I'(\theta)d\omega = \frac{3^{\frac{1}{2}}a^{\frac{1}{2}}c^{\frac{1}{2}}\cos^{\frac{1}{2}}\theta(N)^{\frac{1}{2}}d\omega}{2^{\frac{1}{2}}\pi^2\sigma} \times \int_0^1 (1-z'^2)^{\frac{1}{2}}\int_0^{2kz'} \exp(-y^2)dydz'. \tag{26}$$

The half-width predicted by Eq. (26) is

$$\theta_{\frac{1}{2}}' \approx \frac{2^{7/4}3^{\frac{1}{2}}\sigma(N)^{\frac{1}{2}}}{1.78a^{\frac{1}{2}}c^{\frac{1}{2}}} \tag{27}$$

which is twice the value of Eq. (24) and in better accord with the observations. The beam shape $I'(\theta)/I(0)$ predicted by Eq. (26) for a given half-width at half-intensity is identical with that of Eq. (23a), illustrated in Fig. 7.

Further sources of the discrepancy are the protruding sleeves discussed earlier, and molecular collisions outside the source. Thus it appears that the theory in its present state of refinement is capable of predicting rather accurate values of peak intensities, and of providing at least useful estimates of half-widths.

V. SOURCE DESIGN CONSIDERATIONS

Under the assumptions and restrictions described in Sec. IV, the peak intensity and half-width of the beam are given approximately by

$$I(0) = \frac{3^{\frac{1}{2}}c^{\frac{1}{2}}a^{\frac{1}{2}}(N)^{\frac{1}{2}}}{8\,2^{\frac{1}{2}}\pi^{\frac{1}{2}}\sigma} \tag{12}$$

$$\theta_{\frac{1}{2}} = \frac{2^{7/4}3^{\frac{1}{2}}\sigma(N)^{\frac{1}{2}}}{1.78a^{\frac{1}{2}}c^{\frac{1}{2}}}. \tag{27}$$

Expressions (12) and (27) refer to flow per single tube.

For an array of tubes in a fixed total area, it follows from (12) that the available peak intensity for a fixed total flow rate varies as $a^{-\frac{1}{2}}$, while the half-width varies as $a^{+\frac{1}{2}}$, as long as the tube walls do not occupy an appreciable fraction of the available total area. As sources are made with increasingly fine tubes, the fractional area of the source taken up by the tube walls necessarily becomes greater, and tube alignment usually becomes increasingly difficult. As a result an optimum tube radius exists which depends on the details of the source construction, but which is probably of the order of 1 to 2×10^{-3} in.

The critical source length is that length at which the source becomes opaque. Increasing the source length beyond this point does not change the available collimation of the source. For a given peak intensity the critical source length Λ can be obtained from the opacity criterion Eq. (12a) and from Eq. (12).

$$\Lambda \approx \frac{2.5\,2^{\frac{1}{2}}c^{\frac{1}{2}}a^2}{8\pi^{\frac{1}{2}}\sigma^2 I(0)} \tag{25}$$

where $I(0)$ refers to the peak intensity per single tube.

VI. CONCLUSION

The characteristics of long tube sources can be predicted theoretically to a useful approximation on the basis of a simplified model of the pressure distribution in the source.

ACKNOWLEDGMENTS

This work was proposed by Professor P. Kusch. The authors wish to thank him and Professor C. H. Townes for valuable discussions and advice.

Cratering and Shock Wave Phenomena in Steel Plates at High Impact Speeds

EARLE B. MAYFIELD* AND JAMES W. ROGERS
Michelson Laboratory, U. S. Naval Ordnance Test Station, China Lake, California
(Received September 22, 1959)

The impact of aluminum projectiles on steel plates for impact velocities of 2500 m/sec to 3000 m/sec and about 1100 m/sec was studied. Crater volume and penetration were measured. Shock wave velocity from the free surface was determined and the particle velocity calculated. For annealed 4130 steel plates impacted at 2750 m/sec average velocity, the average free surface particle velocity was 0.205 mm/μsec. Existing theory on cratering and penetration gave excellent agreement with the observed values.

INTRODUCTION

A NUMBER of publications[1–4] in recent years have dealt with the craters produced in thick plates by the impact of projectiles of various shapes at velocities as high as 5000 m/sec. Results of these studies indicate that for impact velocity greater than about 1000 m/sec the crater produced is approximately a spherical section of radius, R, and depth or penetration, P, for which R is greater than P. The crater volume, V, per unit kinetic energy, E, for a given plate and projectile material has been reported as constant[5] and as a function of the impact velocity.[6,7] In a recent paper by Van Valkenburg, Clay, and Huth,[5] results of the impact of similar plate and target metals in the velocity region 1000 m/sec to 5000 m/sec are reported and equations for predicting both the crater volume and penetration are presented. This paper discusses results obtained on both impact and shock wave phenomena in the target plate using a light gas gun developed by Crozier and Hume[8] and modified and built at the U. S. Naval Ordnance Test Station. With this gun, aluminum projectiles of 4.5 gm mass and controlled shape can be impacted on plates at about 3000 m/sec and data on shock wave phenomena as well as cratering and penetration obtained.

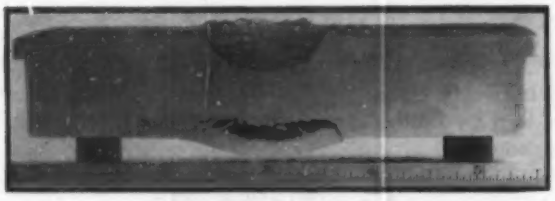

FIG. 1. Cross section of plate impacted at 2540 m/sec showing crater and spall.

EXPERIMENTAL

Impact of 4.5 gm 75 ST aluminum right circular cylinders of diameter and length 1.27 cm on annealed 4130 steel plates was studied. The plates were supported in a spark shadowgraph range by an enclosed support so that shadowgraphs of the shock waves from the free surface could be made. This device has been previously described by Allen, *et al.*[9] The target plates were 12.7 cm diam and varied in thickness from 1.90 cm to 2.38 cm.

Two velocity regions were studied, ordnance velocity near 1100 m/sec obtained with an M2 Browning machine gun using a standard propelling charge and hypervelocity between 2500 and 3000 m/sec obtained with the light gas gun. Velocities were determined by measuring the time of flight over a range of known length by means of a Berkeley model 5510 counter. Conducting grids printed on paper which were broken by the projectile started and stopped the counter.

The character of the impact differed markedly in the two cases. At ordnance velocity the projectiles rebounded after impact and were recovered. The crater formed was not spherical in section. There was no evidence of spalling or fracture in the target plate. Target penetration and crater volume were 2 mm and 0.23 cm³, respectively. The ratio of crater volume per unit energy, V/E, was 0.82×10^{-4} cm³/joule. At hypervelocity, however, the projectile disintegrated on im-

TABLE I. Data for impact of 75 ST aluminum cylinders on 4130 annealed steel plates.

Impact velocity m/sec ×10⁻³	Kinetic energy joules ×10⁻⁴	Crater volume cm³	Average crater diameter cm	Crater depth mm	Target thickness cm	V/E cm³/joule ×10⁴
1.11	0.28	0.24	1.77	2.0	1.90	0.86
1.12	0.28	0.22	1.70	1.9	2.38	0.78
2.44	1.34	3.12	2.83	10.2	2.22	2.33
2.54	1.45	3.17	2.83	10.0	2.38	2.19
2.76	1.71	3.38	2.78	11.3	2.22	1.98
3.00	2.02	3.35	2.83	11.1	2.38	1.66
3.00	2.02	2.90	2.79	8.4	2.38	1.44

* Now at Physical Research Laboratory, Space Technology Laboratories, Inc., Los Angeles, California.

[1] W. S. Partridge and H. B. Vanfleet, Astrophys. J. **128**, 416 (1958).

[2] Partridge, Vanfleet, and Whited, J. Appl. Phys. **29**, 1332 (1958).

[3] J. S. Rinehart and W. C. White, Am. J. Phys. **20**, 14 (1952).

[4] O. G. Engel, J. Research Natl. Bur. Standards **61**, 47 (1958).

[5] Van Valkenburg, Clay, and Huth, J. Appl. Phys. **27**, 1123 (1956).

[6] Norman Rostoker, Meteoritics **1**, 11 (1953).

[7] Proc. Third Symposium on Hypervelocity Impact, Vol. *1*, (February, 1959), Vol. 1, Armour Research Foundation of Illinois Institute of Technology, Chicago, Ill.

[8] W. D. Crozier and William Hume, J. Appl. Phys. **28**, 892 (1957).

[9] Allen, Mapes, and Mayfield, J. Appl. Phys. **26**, 1173 (1955).

pact and was not recovered. A crater of roughly spherical section was formed in the target plate with radius greater than the penetration. Penetration and crater volume averaged 10.2 mm and 3.18 cm³, respectively. A spall occurred on the free surface and fracturing was present along the axis. Figure 1 shows a cross section of one of the plates impacted at 2540 m/sec. V/E, the volume to projectile energy ratio was 1.92×10^{-4} cm³/joule an increase of 2.34 times over the ordnance velocity case. Complete data for all cases are given in Table I.

SHOCK WAVES

Previous studies by Allen *et al.*[10] of shock waves at the free surface due to ordnance velocity impact have shown the existence of two possible wave velocities. These were related to an elastic and a plastic wave

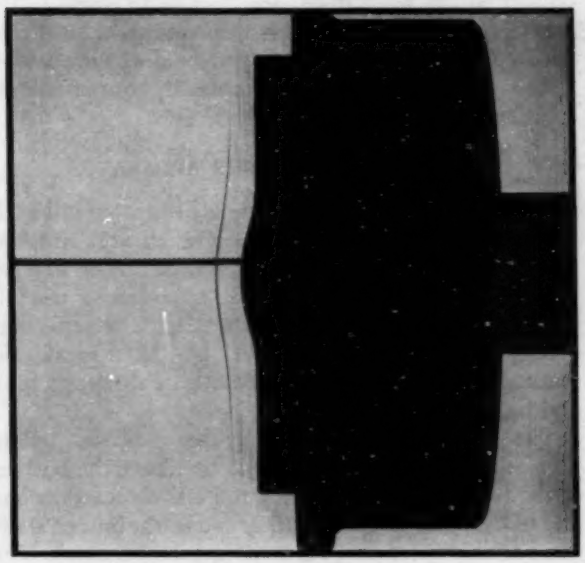

FIG. 2. Spark shadowgraph of plate under impact at 2540 m/sec showing single shock wave.

propagated in the plate. For 4130 steel plates impacted at ordnance velocities both waves existed. In the present case for impact at hypervelocities, only one such wave is observed. Figure 2 is a shadowgraph of the front surface of the plate under impact at 2540 m/sec. It was taken in air at 710 mm Hg pressure and 32°C temperature.

The Mach number of the shock wave on axis was determined from measurements of path difference between the on axis shock wave and the outer rim shock wave assuming a value of Mach one for the latter. A sound velocity in the target plate of 6.36 mm/μsec was used. The particle velocity was then computed using

[10] Allen, Mapes, and Mayfield, J. Appl. Phys. **26**, 125 (1955).

TABLE II. Free surface particle velocities of 4130 annealed steel plates computed from shock wave velocities in air.

Impact velocity mm/μsec	Shock wave velocity mm/μsec	Particle velocity mm/μsec
2.44	0.496	0.190
2.54	0.518	0.217
3.00	0.503	0.199
3.00	0.514	0.213

TABLE III. Comparison of observed and calculated values of penetration and crater volume.

Impact velocity m/sec $\times10^{-5}$	k_1	k_2	Observed p mm	Observed V cm³	Calculated p mm	Calculated V cm³
1.11	17.0	0.46	2.0	0.24	2.0	0.23
1.12	15.3	0.42	1.9	0.22	1.6	0.13
2.44	45.7	1.62	10.2	3.12	10.1	3.04
2.54	42.8	1.47	10.0	3.17	9.9	3.11
2.76	38.7	1.68	11.3	3.38	11.3	3.39
3.00	32.4	1.49	11.1	3.35	11.0	3.28
3.00	28.1	0.88	8.4	2.90	8.4	2.85

the values of the NACA Rept 1135[11] for compressible flow. Results of this calculation for the hypervelocity case are given in Table II. It is of interest to compare the results of this study with those reported in reference 8 for ordnance velocity impact and explosive charges. For similar target plate thickness, the particle velocity reported for impact by projectiles at about 850 m/sec was 0.04 mm/μsec, for high explosives the particle velocity was 0.06 mm/μsec. The average value of particle velocity in the case of hypervelocity impact was 0.20 mm/μsec.

DISCUSSION

The application of the equations of reference 5 to the data of this study yields the results given in Table III. It is seen that the agreement between observed and calculated penetration and crater volume is excellent in all but one instance despite the large variation in the experimental constants k_1 and k_2.

The results of this study indicate that the equations of Van Valkenburg, Clay, and Huth are able to predict both penetration and crater volume for dissimilar projectile and target materials of large density difference, and for an impact velocity range sufficient to include the two cases of projectile rebound with small mass loss and projectile disintegration. However, the values of the experimentally determined constants k_1 and k_2 were different for these cases. For ordnance velocity impact, the average values of k_1 and k_2 are 16.1 and 0.44, respectively, while for hypervelocity impact they are 37.5 and 1.43, respectively. The values given in reference 5 are 25.4 for k_1 and 1.66 for k_2 for all impact velocities.

[11] Ames Research Staff, NACA Rept. No. 1135 (1953).

JOURNAL OF APPLIED PHYSICS VOLUME 31, NUMBER 3 MARCH, 1960

Optical Studies of the Diffraction of Water Waves by Circular and Thin Elliptic Cylinders*

RICHARD BARAKAT, *Research Laboratory, Itek Corporation, Boston, Massachusetts*

AND

ROBERT BARAKAT, *Suffolk University, Boston, Massachusetts*

(Received June 5, 1959)

By using the optical grid method the diffraction of water waves from circular and elliptic cylinders were measured and compared with theory. The scattered wave intensity S and the total energy scattered per sec per unit intensity Q were measured and the results bear out the well-known fact that for angles less than 30 deg or in the vicinity of 180 deg, one cannot separate out the scattered wave and the incident plane wave. The optical grid method is described in detail and the advantage of its being able to measure the instantaneous field emphasized.

I. INTRODUCTION

THE diffraction of water waves by rigid obstacles has been a subject of some interest recently from both an experimental[1] and a theoretical[2] point of view. The authors have used a variant of the optical grid method to study the diffraction of water waves by a variety of bodies. Both two-dimensional (circular and elliptic cylinders, wedge-shaped bodies) and three-dimensional (sphere, prolate spheroid) objects were investigated with the intention of comparing with theory wherever possible. One of the advantages of the optical grid method lies in the fact that the instantaneous diffracted field can be measured whereas the probe techniques used in acoustics or microwave optics must necessarily deal with average fields.

Mogi[3] has already made an experimental study of water wave diffraction by a semi-infinite screen (Sommerfeld's problem), slits, and circular cylinders. However, his results are somewhat questionable as the waves generated in his tank were short enough to have appreciable viscous damping for which the present diffraction theory makes no provision.

The purpose of the present paper is to restudy the case of the circular cylinder and examine the diffraction from elliptic cylinders whose minor axes are perpendicular to the wave front, and also at an angle to the major axis. A further paper, in preparation, will deal with diffraction from ship-shaped bodies, with a view toward comparing the experiments and the approximate solutions by the source technique.[4]

FIG. 1. Photograph of experimental setup.

II. DESCRIPTION OF THE APPARATUS

The experimental arrangement is illustrated in Fig. 1. The far end of the wave tank has a beach of 15° inclination made of layers of black felt tacked on the wooden incline. Sufficient percolation was provided by the felt layers to insure practically no reflection. The water was blackened by ink as demanded by the optical grid method. Figure 2 shows a schematic of the wave tank and lighting setup.

The waves are generated by an oscillating plate pivoted about an axis located 0.5 cm above the bottom of the tank. A long connecting rod was attached at one end to the plate and at the other end to the output shaft of a variable speed unit via an adjustable eccentric. The amplitude of the incident wave was controlled by adjusting the eccentric; the wavelength could be varied by changes in the variable speed unit. In this manner a wide variety of reproducible waves could easily be obtained. The variable speed unit was a Graham variable speed transmission unit, Model 20BE, capable of an output rpm range of 0–325 (gear setting on unit, 0–20). The motor was a 0.25 hp electric motor. Figure 3 illustrates the change in wavelength as a function of gear setting. The wave generating apparatus is not capable of producing exactly the desired wave motion because the method of wave generation cannot reproduce the exponential decrease of wave height with depth, although motion imparted to the water is zero near the bottom. Nevertheless this method gives reasonably good results provided the water is deep.

The chief effect of viscosity is to diminish wave height and this in turn effects the form of the wave.

* Research performed while the authors were on the staff of the Woods Hole Oceanographic Institution and is Contribution No. 1074 from the Woods Hole Oceanographic Institution.

[1] "Gravity waves," Natl. Bur. Standards Circ. No. 521 (1952).

[2] J. J. Stoker, *Water Waves* (Interscience Publishers, Inc., New York, 1958).

[3] K. Mogi, Bull. Earthquake Research Inst. **34**, 267 (1956).

[4] F. Ursell, Quart. J. Mech. Appl. Math. **7**, 427 (1954).

Mogi was faced with viscous damping of his waves as they progressed down his tank; however, his waves were only 5 cm long and one expects large damping in this range. In order to avoid this complication, waves of 9.5 cm were used as a standard; now these waves are capillary-gravity waves, but to within an error of less than 4% they can be considered as pure gravity waves. It is known that the modulus of decay T (time for the wave amplitude to decay to $1/e$ of its original value) for a clean surface of water is $0.712\ \lambda^2$ where λ is the wavelength expressed in centimeters.[5] Waves take about 4 sec to travel down the tank and it is easy to show there is only a 6% diminution in wave amplitude down the tank. Our optical measurements are good to about 5% so that any change in wave amplitude arising from viscosity is within the limits of error of our own measurements. In order to test this neglect of wave height attenuation, a series of wave height measurements down

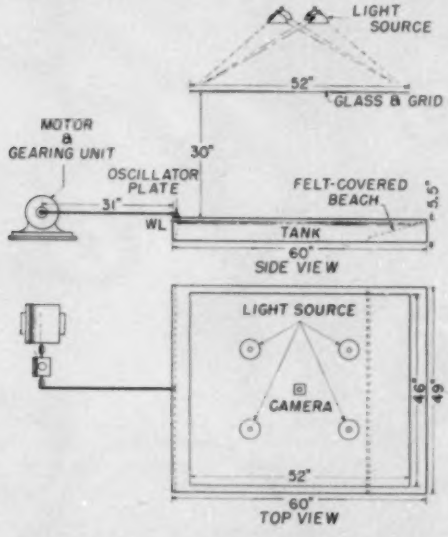

FIG. 2. Diagramatic sketch of wave tank.

the tank were made and the results averaged at various points along the tank. When the averaged results were plotted as a function of distances from the face of the wave generator, an almost straight line of zero slope was obtained except very near the generator where complications due to higher harmonics, standing waves, etc., manifested themselves.

The test objects were made of laminated wood and sanded down to the correct dimensions. They were then attached by screws to a thin brass plate which could be laid on the floor of the tank.

III. OPTICAL GRID METHOD

The principle underlying the optical grid method is quite simple. A grid of lines is placed above the tank, the image of which photographed in the mirror formed

[5] H. Lamb, *Hydrodynamics* (Dover Publications, New York, 1945), p. 624.

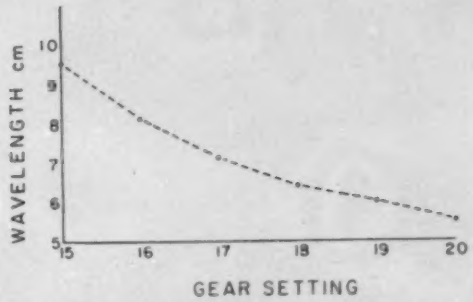

FIG. 3. Change in wavelength of incident waves as a function of gear setting on wave generator.

by the water surface. When the surface is calm there is no distortion of the grid lines; however, when the surface is disturbed by waves there is a distortion of the image of the grid. The wave height can then be calculated by an analysis of the distorted grid.

It is probably of interest to describe in detail the working formulae used in the method since we cannot find any accounts in the literature. We are indebted to Professor Mogi of the University of Tokyo for informative correspondence concerning the method, especially in its two-dimensional form. If we knew the slope $\Delta\alpha$ at every point we could reconstruct the wave and from this find the wave height. The slope $\Delta\alpha$ can be obtained from the simple relation $\Delta\alpha = d/2L$ [see Fig. 4(a)] provided that $\Delta\alpha \ll 1$ and the angle β in the figure is not too large. The symbol d represents the change of scale due to the distortion of the water surface. The grid of Fig. 4(b) represents the photograph of the undisturbed grid. Locate at position R the grid point (a,b). When the surface is covered with waves, the image of the grid will deform and another point of the grid, say (a', b'), will appear at position R. The slope can be obtained from

$$\Delta\alpha = \frac{d}{2L} = \frac{1}{2L}[(a-a')^2+(b-b')^2]^{\frac{1}{2}}. \qquad (1)$$

The difference in the height between any two positions can be evaluated numerically as follows. Let $\eta(x,y)$ represent the surface profile; then η is expressed in

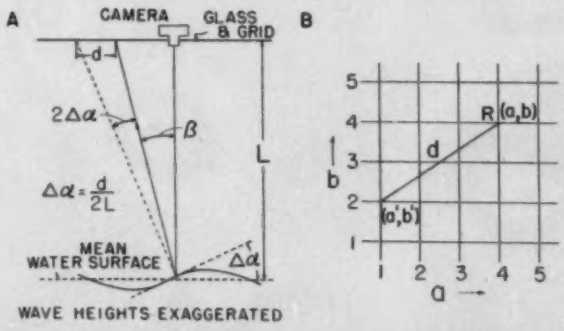

FIG. 4. Diagram showing the principles of the optical grid method; (a) relation between the wave slope and change in scale of grid; (b) relation between undistorted and distorted grid.

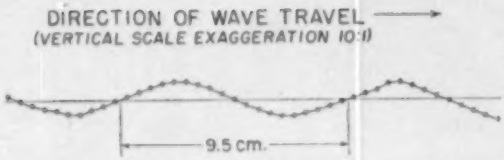

FIG. 5. Reconstruction of wave profile using one-dimension numerical integration of Eq. 3.

terms of the gradient $g(x,y)$ via the expression

$$\eta(x,y)=\int_{S_1}^{S_2} g(x,y)dS, \tag{2}$$

where S is the arc length. Therefore, the difference in wave height is simply

$$\eta(x_2,y_2)-\eta(x_1,y_1)=\int_{S_1}^{S_2} g(x,y)dS$$
$$=\sum_i g(x_i,y_i)\Delta S_i. \tag{3}$$

From this expression we can calculate $\eta(x,y)$ by numerical integration if necessary. Provided that we have a one-dimensional sine wave, the formulas simplified considerably and, in fact, the foregoing integration can be carried out analytically. If $\eta(x,y,t)=A\sin(kx-\omega t)$ where A is the amplitude and k the wave number, then the amplitude A is given by

$$A=\frac{1}{k}(d\eta/dx)_{x=\lambda/2}=\frac{\lambda}{4\pi L}(d)_{x=\lambda/2}. \tag{4}$$

since $(d\eta/dx)=d/2L$. Thus the wave height H is given by

$$H=2A=\frac{\lambda}{2\pi L}(d)_{x=\lambda/2}. \tag{5}$$

This is the basic equation. Therefore, we can obtain the wave height by simply measuring d (at the position $x=\lambda/2$) directly from the photograph. Or looking at it another way, the change of gradation of the grid image at the position $x=\lambda/2$ is sufficient to allow us to measure wave height. This method fails if the wave height is such as to violate the condition $(H\sim\lambda)$.

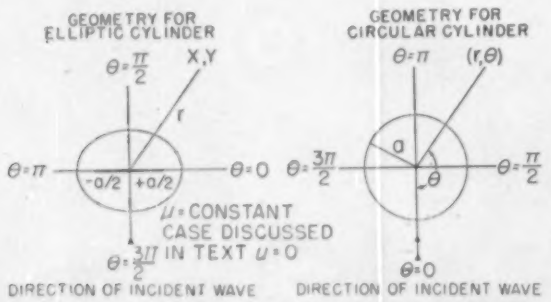

FIG. 6. Geometry of the scattering for both types of cylinders.

The assumption that the waves are essentially sine waves was tested by actually carrying out the one-dimensional numerical integration and reconstructing the wave profile. Figure 5 shows a section of the wave profile located about 2 ft from the face of the wave generator. We concluded that for most of the work the sine wave analysis was sufficient.

The grid was a translucent black-line print ruled with black lines drawn at 1 cm intervals in both directions. The use of this material greatly facilitated our work since we could easily make copies of the master grid and mark on the copies as desired.

IV. CIRCULAR CYLINDERS

All measurements are normalized by division of the incident wave height H_0 so that our measure of the diffraction effect H/H_0 will be a pure number.

An examination of Mogi's experimental data on circular cylinders reveals that the theoretical solution is always larger than the experimental answer. The reason for this is simple enough; the waves are being damped for which the theory makes no provision. Mogi's attempt to correct for this via normalizing by the incident wave height at the point in question is partially successful, but nevertheless agreement is to some extent circumspect. In view of this, we decided to repeat as closely as possible Mogi's experiment for a circular cylinder of radius $a=1.6\lambda$ $(ka=10)$. See Fig. 6 for geometry of circular cylinder.

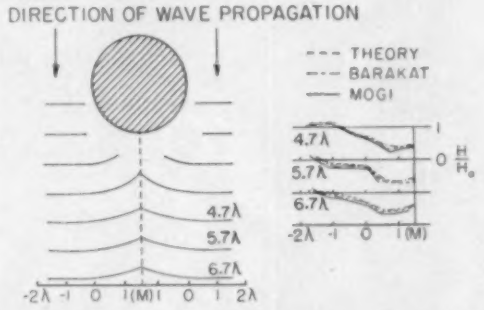

FIG. 7. Comparison of experimental data of Mogi and Barakat with theoretical values for $ka=10$. The left-hand side of the figure shows the position of the wave fronts, while the graph illustrates the computed and experimental normalized wave heights along the wave fronts at 4.7λ, 5.7λ, and 6.7λ.

Figure 7 shows the positions of the wave fronts according to Mogi; a considerable amount of trial and error was necessary before we could obtain comparable geometric relationships implied in the figure. The right-hand side of the figure summarizes the theory and observation. The theoretical result was obtained by summing the Hankel function series for $ka=10$ using eleven terms in the series. Our measurements seem to overestimate the wave heights along the horizontal scale 0 to (M) while Mogi's data underestimate the heights. The results seem to agree quite well with

theory along the rest of the horizontal scale, although slightly under the theoretically predicted heights.

When kr is large, we can obtain a measure of the scattered intensity at a point (r,θ) from the well-known formula[6]

$$S(\theta)=\frac{2}{\pi kr}\sum_{m,n=0}^{\infty}\epsilon_m\epsilon_n\sin\delta_n'\sin\delta_m'\times\cos(\delta_m'-\delta_n')\cos m\theta\cos n\theta, \quad (6)$$

expressing the ratio of the scattered intensity at (r,θ) to the intensity of the incident wave. The measure of intensity is the height of the wave squared at the point in question. By fixing the angle θ we measured the wave heights at a series of fixed distances (kr) from the center of the cylinder and repeated the procedure every 10 deg from 30 to 150 deg. Any attempt to measure $S(\theta)$ at smaller angles than 30 deg or much larger than 150 deg is illusory since we can only measure the total of plane and scattered wave in these angular regions. We refer the reader to Morse and Feshbach[7] for a full discussion

TABLE I. Comparison of theoretical and experimental values of $S(\theta)$ for $ka=3$ and $kr=18$.

	Theoret.	Exptl.
30°	0.0978	0.110
40	0.1181	0.135
50	0.1351	0.139
60	0.1321	0.128
70	0.1031	0.095
80	0.0596	0.050
90	0.0222	0.020
100	0.0059	0.007
110	0.0102	0.010
120	0.0384	0.040
130	0.0535	0.053
140	0.1331	0.130
150	0.1446	0.145

of the condition under which we can separate the scattered wave and plane wave.

Table I gives the results of theory and experiment for a cylinder of $ka=3$ and a field point $kr=18$; the field point condition does not represent exactly the far field constraint $(kr\gg1)$ upon $S(\theta)$, yet is sufficient to permit comparison. Since we have to square the experimental wave heights and thereby introduce an even larger error into the problem, we should not expect to get close quantitative agreement with theory. Nevertheless the comparison was excellent. The experimental results are the average of 5 different measurements.

The relative intensity $S(\theta)$ was also measured for $ka=1.5$ and $ka=2$ at $kr=18$ essentially the same agreement with theory was obtained. We have not thought it necessary to reproduce this data.

The long wavelength or Rayleigh scattering limit

[6] P. M. Morse and H. Feshbach, *Methods of Mathematical Physics* (McGraw-Hill Book Company, Inc., New York, 1953), Part II, p. 1378

[7] See reference 6, p. 1378–1382.

TABLE II. Comparison of theoretical and experimental values of $S(\theta)$ using Rayleigh scattering approximation with $ka=0.5$ and $kr=10$.

θ	Theoret.	Exptl.	θ	Theoret.	Exptl.
0°	2.39	2.95	100°	4.34	4.45
10	2.26	2.55	110	6.78	6.85
20	1.86	2.10	120	9.55	10.00
30	1.29	1.40	130	12.50	12.25
40	0.68	0.70	140	15.35	15.40
50	0.20	0.18	150	17.85	18.00
60	0.00	0.10	160	19.80	20.00
70	0.24	0.30	170	21.10	21.50
80	1.00	1.00	180	21.50	22.00
90	2.39	2.45			

$(ka\ll1)$ for $S(\theta)$ can be shown to be given by[8]

$$S(\theta)\underset{ka\to0}{\sim}(\pi a/8r)(ka)^3(1-2\cos\theta)^2. \quad (7)$$

Note here that there is a linear dependence of $S(\theta)$ upon the ratio (a/r) entirely independent of the incident wave number k. It is important to study this limiting case as most circular piles in practical problems would be subsumed under this category.

Table II gives a summary of the results using the Rayleigh scattering approximation. The table represents the average results of 10 measurements; the individual measurements fluctuated considerably but the average experimental values tend to confirm the theoretical values. Note the wide departure of theory and experiment for angles close to 0° to 180°. This confirms the well-known result that for angles close to 0° and 180°, we cannot separate out the scattered and plane waves but only measure the combination.

Finally there is one other quantity of interest which we can measure via the optical grid method; this is the total energy scattered, per second, per unit intensity which in the Rayleigh scattering range assumes the simple form[9]

$$Q\sim\tfrac{3}{4}\pi a(ka)^3. \quad (8)$$

We note that Q has dimensions of a length. We chose to

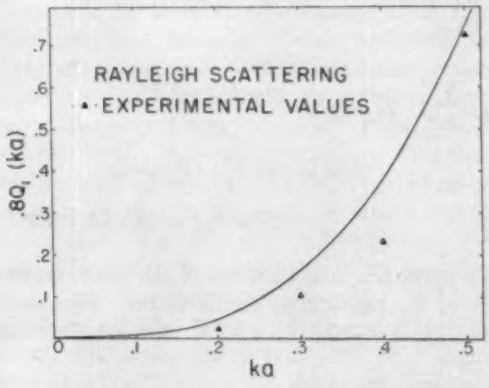

FIG. 8. Normalized measure of energy scattered in the Rayleigh scattering range for circular cylinder.

[8] See reference 6, p. 1382.

[9] See reference 6, p. 1379.

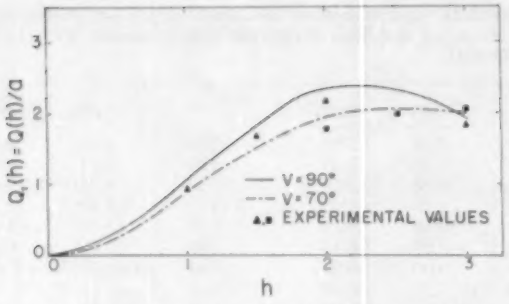

FIG. 9. Normalized measure of energy scattered for thin elliptic cylinder.

measure the dimensionless quantity $Q_1(ka)=Q/a$ which is simply the total area under $S(\theta)$. Figure 8 illustrates the dependence of Q_1 on (ka) in the longwave approximation. The experimental points again represent the average of 10 measurements. The experimental values all lie considerably below the predicted values as we would expect. As (ka) becomes very small, the scattered intensity $S(\theta)$ develops a very narrow peak in the forward direction, where we cannot separate out scattered and plane waves. When (ka) is sufficiently small we will not be able to measure any part of the forward peak at all; consequently our measured values are less than theory.

V. THIN ELLIPTIC CYLINDERS

We have a situation equivalent to diffraction by a finite lamina when an elliptic cylinder has an eccentricity near unity and is placed such that the major axis is parallel to the wave crests (see Fig. 6 for the geometry).

The dimensionless parameter governing the scattering is $h=ka/2$ where a is the interfocal distance. Reference is made to Morse and Feshbach[10] for the appropriate notation for the various Mathieu functions used. The boundary condition on the cylinder is that the gradient of the total velocity potential is zero. The relative intensity scattered at large distances from the strip is given by

$$S \to \frac{8\pi}{kr} \sum_{m,n} \frac{\sin\delta_m^0 \sin\delta_n^0}{M_m^0 M_n^0} \cos(\delta_m^0 - \delta_n^0) \cdot So_m(h, \cos v) So_n(h, \cos v) \times So_m(h, \cos\theta) So_n(h, \cos\theta) \quad (14)$$

where v is the angle of incident of the plane wave with respect to the major axis of the ellipse. Two cases are studied: (1) $v=90°$, (2) $v=70°$. Case 1 (normal incidence) simplifies since $So_{2n}(h,0)=0$. Table III shows contrasts for the theoretical results for a cylinder of eccentricity unit with the experimental results of a cylinder having an eccentricity of 0.9. The experimental values represent the average of 5 observations. Table IV summarizes the results for case 2. Again the experimental values represent averages of 5 measurements. Note that the curve decreases in magnitude as the angle v decreases; in fact as v approaches zero, Q_1 also goes to zero.

[10] See reference 6, p. 1407.

TABLE III. Comparison of theoretical and experimental values of S for $h=3$ and $h=2$ at $kr=20$ for normal wave incidence.

θ	$h=3$ Theoret.	$h=3$ Exptl.	$h=2$ Theoret.	$h=2$ Exptl.
30°	0.016	0.020	0.023	0.025
40	0.036	0.040	0.044	0.050
50	0.073	0.075	0.074	0.075
60	0.128	0.130	0.110	0.110
70	0.193	0.195	0.147	0.150
80	0.247	0.255	0.175	0.180
90	0.269	0.265	0.185	0.195

TABLE IV. Comparison of theoretical and experimental values of S for $h=3$ and $h=2$ at $kr=20$ for wave incident at 70°.

θ	$h=3$ Theoret.	$h=3$ Exptl.	$h=2$ Theoret.	$h=2$ Exptl.
30°	0.068	0.075	0.032	0.040
40	0.126	0.130	0.058	0.065
50	0.193	0.195	0.089	0.090
60	0.250	0.250	0.121	0.120
70	0.271	0.275	0.146	0.145
80	0.245	0.255	0.155	0.160
90	0.188	0.195	0.146	0.150

VI. CONCLUSION

The optical grid method is described in detail and the importance of its being able to measure the instantaneous diffracted field emphasized. The scattered wave intensity and the scattering cross section were determined experimentally and compared with theory. The experimental values agreed very well with theory for large distances from the object.

Much work remains to be done on bodies that are not simple and here the combination of optical grid method and source technique should provide adequate tools for future work.

ACKNOWLEDGMENTS

The research reported in this paper was supported by the Office of Naval Research. We wish to thank Dr. Paul Fye for making available to us all necessary facilities. We also wish to thank Mr. John Stimpson who made the translucent grid as well as helping us with a number of photographic problems that occurred.

Parametric Amplification along Nonlinear Transmission Lines

ROLF LANDAUER
Research Laboratory, International Business Machines Corporation, Poughkeepsie, New York
(Received July 14, 1959)

A pump signal propagating along a dispersionless transmission line with a distributed nonlinear capacitance is subject to deformation, since different parts of the signal move with different velocities. This process of deformation will eventually result in the formation of an electromagnetic shock wave. The deformation will affect the parametric amplification process. If a small signal consisting of a positive pulse, short compared to the pump cycle, is added to the pump signal at the input end, then it is shown that the small signal at the output must be non-negative. All other small signals, including in particular those with sinusoidal time variation, can be regarded as superpositions of these short pulses. As a consequence it is shown that, in general, a sinusoidal signal will not be increased in its fundamental frequency component, by traveling down the line together with the pump signal. There are certain exceptional frequencies, multiples of one half the pump frequency, where a suitably phased small signal may be increased at its fundamental frequency, but not by a sufficient amount to be of practical interest.

1. INTRODUCTION

THE fact that parametric amplification may be obtained on propagating structures has been discussed by Tien and Suhl,[1] Tien,[2] and A. L. Cullen.[3] The word "parametric" is used here in the sense currently common in electronic applications and denotes the fact that a small signal sees a time varying reactance produced by the simultaneous application of a large signal, and the existence of a nonlinear reactance. This is in contrast to its use in the older literature on nonlinear oscillations, where "parametric" refers to a strictly linear reactance which is varied in time. It has been experimentally observed by Engelbrecht, and later by Lombardo and Sard,[4] that a low-pass filter whose capacitances are the non-linear capacitances of junction diodes can provide parametric amplification. It then becomes natural to ask whether a simple transmission line with distributed nonlinear reactances, rather than the lumped reactances used by Engelbrecht, can actually provide parametric amplification. The most obvious embodiment we have in mind would be a ferroelectric crystal with thin metallic strips evaporated on its surfaces, serving as electrodes. Ferroelectric crystals, at temperatures just above the transition at which the spontaneous polarization disappears, are strongly nonlinear capacitances.[5,6] The possibility for parametric amplification in such a structure has, in principle, already been pointed out by Tien and Suhl[1] as well as by Cullen.[3] Their method of analysis, however, involves approximations which are somewhat questionable when applied to a relatively dispersionless structure. First of all in these analyses there is a small signal capacitance, seen by the signal which is to be amplified, which consists of a steady term plus an undistorted traveling sinusoidal term. This could be correct if the pump signal itself consisted of a traveling wave which moves without changing its wave shape. For the case that we have in mind, however, where there is one line which carries both the small signal and the pump power, the same nonlinearity which provides amplification in the theories of Tien, Suhl, and Cullen,[1,3] will also cause a progressively increasing distortion in the pump signal, as the latter moves down the line. The second approximation that has been made in the earlier analyses is to neglect, in the behavior of the small signal, all frequencies except the original frequency, ω, and the difference frequency, or idling frequency, $\omega_p-\omega$ (ω_p is the angular frequency of the pump signal) In the conventional parametric amplifier, involving tuned circuits, this neglect of other frequencies is justified by the fact that the resonances of the circuit permit appreciable power flow, in and out of the nonlinear reactance, only at these special frequencies. A dispersionless transmission line, however, permits power flow at all frequencies.

We shall in this note, attempt to give a more rigorous analysis of the dispersionless line. In contrast to the earlier work,[1,3] we will find that there is no exponential gain available on these structures, and in fact, for all practical purposes, no gain. These pessimistic conclusions are, of course, only applicable to the "relatively" dispersionless line. (The exact meaning of the word "relative" in the preceding sentence is best specified in the course of the detailed discussion.) Our negative conclusions are, to some extent, anticipated elsewhere. The undesirability, for instance, of power flow at the frequency $\omega_p+\omega$ is a basic part of Engelbrecht's[4] design criterion. This fact, in connection with Engelbrecht's structure, has also been stressed by L. S. Nergaard.[7] Furthermore, analyses have been given by N. M. Kroll[8] and also by G. M. Roe and M. R. Boyd which

[1] P. K. Tien and H. Suhl, Proc. Inst. Radio Engrs. **46**, 700 (1958).
[2] P. K. Tien, J. Appl. Phys. **29**, 1347 (1958).
[3] A. L. Cullen, Nature **181**, (1958).
[4] R. S. Engelbrecht, Proc. Inst. Radio Engrs. **46**, 1655 (1958). P. P. Lombardo and E. W. Sard, *ibid.* **47**, 995 (1959).
[5] Drougard, Landauer, and Young, Phys. Rev. **98**, 1010 (1955).
[6] S. Triebwasser, IBM Journal **2**, 212 (1958).
[7] L. S. Nergaard, RCA Rev. **20**, 3 (1959).
[8] N. M. Kroll, ONR Symposium on Microwave Techniques for Computer Systems, Washington, D. C. (March 12, 1959). G. M. Roe and M. R. Boyd, Proc. Inst. Radio Engrs. **47**, 1213 (1959).

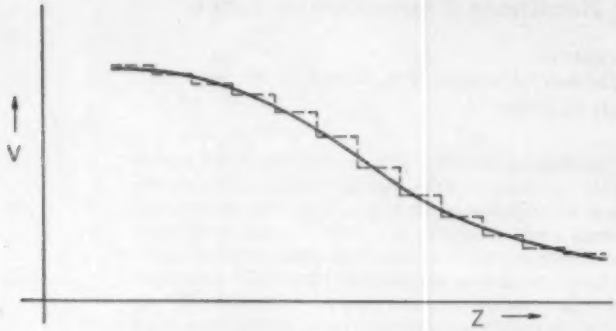

FIG. 1. The solid line indicates a voltage wave moving to the right. The dotted line approximates this by a function which is constant over small intervals, and discontinuous between them.

neglect the distortion of the pump signal, but do allow for small signal power flow at frequencies other than the most important ones. Their analyses indicate gain possibilities in this case, but much below those of the first treatments of this problem.[1,3]

Despite these negative conclusions, we believe that the original treatments,[1,3] are of interest, if one regards the conditions involved not as assumptions made for ease of mathematical treatment, but as actual physical requirements on the nonlinear transmission system. Since these original treatments permit power flow only at the most relevant frequencies and do not consider power which may be "wasted" at other frequencies, it is likely that the original results of Tien, Suhl, and Cullen give maxima for the gain per wavelength available, among the whole class of nonlinear transmission systems.

2. TRANSMISSION LINE EQUATIONS

We shall, in the subsequent discussion, be concerned with transmission line whose capacitances are nonlinear. There is no essential difference between this case, and the one discussed by Tien and Suhl,[1] where it is the inductances that are nonlinear. The equations governing such a transmission line are

$$\frac{\partial V}{\partial z}=-l\frac{\partial I}{\partial t}, \tag{1}$$

$$\frac{\partial I}{\partial z}=-\frac{\partial Q}{\partial t}=-c(V)\frac{\partial V}{\partial t}. \tag{2}$$

Equation (1) is linear, $V(z,t)$ is the voltage existing across the line, and $I(z,t)$ is the current flow in one of the electrodes. l is the inductance per unit length. Equation (2) is the nonlinear one. Q is the capacitive charge, per unit length. $c(V)$ is the differential capacitance, dQ/dV, per unit length of line. Equations (1) and (2) constitute a set of nonlinear hyperbolic differential equations, whose general properties are discussed, for example, in Courant-Hilbert.[9] The properties which are of particular interest to us are also the ones which are relevant in the treatment of fluid flow, and these are described in detail in the literature on supersonic flow and shock waves.[10] We shall, however, in the present note only require some very simple facts concerning Eqs. (1) and (2), and leave to a subsequent paper the detailed description of their solution. In order to arrive at our conclusions, without introducing the full complexity of the more conventional treatments of Eq. (1), we shall have to use somewhat intuitive arguments in this Section, and in Sec. 3. All of our arguments can, however, be given in a more formal manner.

Consider a forward moving voltage wave, on this line, as shown in Fig. 1, by the solid line. This can be approximated arbitrarily closely by the type of function illustrated with a dotted line. This function is constant over short intervals, and is discontinuous at the end of each interval. Each of the steps in this function sees a line ahead of it which has been charged up to a certain voltage V, and is therefore associated with a well-defined differential capacitance $c(V)$. Therefore each step will move with a velocity $u(V)=1/[lc(V)]^{\frac{1}{2}}$, characteristic of the voltage in the vicinity of the step. Furthermore the current change through each step is related to the voltage change by a well-defined characteristic impedance, $[l/c(V)]^{\frac{1}{2}}$. In the limit, therefore, as each step becomes smaller and smaller, the velocity becomes a continuous function of the voltage height. Equations (1) and (2) therefore have solutions which have constant values of V along the trajectories

$$z=z_0+u(V)(t-t_0), \tag{3}$$

where (z_0,t_0) is one particular point in space and time at which the voltage V occurred. This fact is basic in the treatment of non-linear hyperbolic differential equations[10] and can be proven by more respectable means than the method we have employed. Since the speed of a given part of the wave depends upon the voltage, the general nature of the resulting distortion is obvious. The portion of each wave which is associated

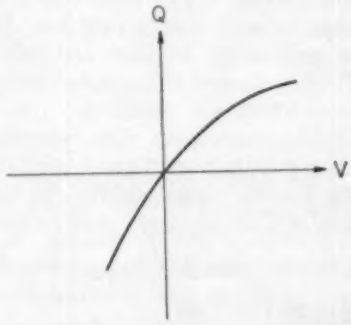

FIG. 2. Nonlinear capacitance characteristic with $d^2Q/dV^2<0$.

[9] R. Courant and D. Hilbert, *Methoden der Mathematischen Physik* (Julius Springer, Berlin, 1937), Chapter 5.
[10] R. Courant and K. O. Friedrichs, *Supersonic Flow and Shock Waves* (Interscience Publishers, Inc., New York, 1948).

with the smallest values of differential capacitance will be fastest, and will tend to catch up with the preceding slower portions, and will simultaneously move away from the slower portions that follow it. For a Q-V characteristic as shown in Fig. 2 where dQ/dV is a monotonically decreasing function of voltage, a pulse as shown in Fig. 3(a) will eventually deform to the shape shown in Fig. 3(b). Eventually portions of the voltage wave which were launched at different instants of time will catch up with each other, and the wave will have a front with infinite slope. At this point Eqs. (1) and (2) become inapplicable, and the discontinuity which starts forming at this point, and which will subsequently grow, must be treated by the methods used for the handling of shock waves.[10]

Physically, the deformation process consists in the continual growth of the relative harmonic content of the wave form. Equations (1) and (2) assume that the same capacitive relationship, $Q=Q(V)$, holds regardless of the rate at which V changes. Actually, however, the nonlinear capacitance must depend upon the physical motion of charges within a polarizable medium. At sufficiently high frequencies the damping or the inertial effects associated with this motion will become important, and will lead to a dispersion. If this dispersion had been included correctly in Eqs. (1) and (2) no shock would ever form. The formation of shock waves corresponds to an idealization in which the dispersion is assumed to occur at frequencies which are very high compared to those which are otherwise of interest in the problem.

3. PROPAGATION OF LOCALIZED SMALL SIGNAL

In this section we shall be concerned with lines which are short enough so that shock waves do not have a chance to develop. We shall assume that the line is terminated so that no reflections are generated, and that the pump signal, therefore, has the form of a simple forward moving wave, characterized by Eq. (3). While a nonreflecting termination for a nonlinear line can only be approximated by a linear lumped element, a second section of line with the same nonlinear capacitance as the original line, but with heavier losses, should be a reasonably nonreflecting termination. With such a nonreflecting termination the addition of a small signal to the original pump signal will modify the signal sent onto the line, but will not cause reflections to be produced; the propagation of the new combination signal is still characterized by Eq. (3).

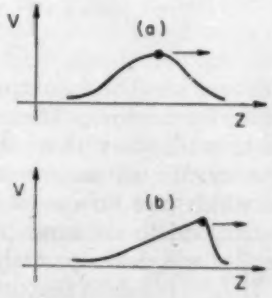

FIG. 3. (a) Original wave shape, with dot labeling fastest portion of wave form. (b) Subsequent deformation of wave shape.

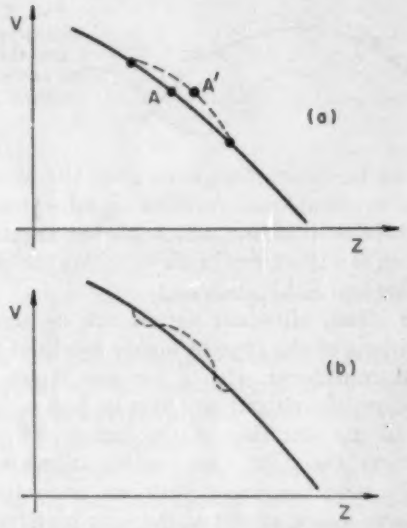

FIG. 4. Pump signal is solid line; combination of pump and small signal is represented by dotted line, where it deviates from original pump signal. For initial situation shown in 4(a) to develop into Fig. 4(b), waves must cross each other.

Consider now, a small signal which is highly localized in time, when compared to the duration of a pump frequency cycle. Furthermore let the small signal be one which does not change sign in the short interval in which it is nonvanishing. Figure 4(a) represents the pump signal by the solid line, and the combination of pump and small signal by the dotted line. The diagram is drawn so as to stress the fact that the combination signal has a derivative which is close to that of the original pure pump signal. Now the voltages at point A on the original signal equals the voltage of the combination signal at A'. Hence these two voltages, according to Eq. (3), travel down the line at the same velocity, and therefore will always remain apart by the same distance. An initial situation as shown in Fig. 4(a) can therefore never lead to the situation shown in Fig. 4(b), where the two waves under consideration, have crossed.

The situation near a maximum of the original pump signal can be slightly more complicated, as shown in Fig. 5. The conclusions, however, are the same, B cannot catch up with B' and C' cannot catch up with C. Hence for both Figs. 4(a) and 5, the localized small signal, which at the initial end of the line was nonnegative, will remain so along the entire line.

We have extended these considerations to the case where the line is long enough to cause the formation of shock waves, and we expect to publish this analysis separately in a forthcoming issue of the IBM Journal of Research Development. If the shocks are "weak," i.e., if the capacitance variation introduced by the pumping signal is small compared to the average capacitance,

FIG. 5. C' moves with same velocity as C and therefore cannot catch up with it. Similarly for B and B'.

then it can be shown that even after the formation of shocks, a localized small positive signal will result in a small signal down the line, which is never negative. (The assumption of a small reactance variation was also made in the Tien and Suhl[1] analysis.)

At the input, all small signals can be regarded as superpositions of the type of highly localized signal we have just considered. Hence for any input which is non-negative, the output will also be non-negative, regardless of the duration of the input signal and its detailed time variation. Our considerations up to this point have been concerned with the transmission line which has no losses, except at the very high frequencies inevitably involved in the shock waves. It seems reasonable, intuitively, that adding losses to such a line would cause the output wave, for a localized input, to be spread out more in time, but it seems unlikely that adding losses (in particular a finite relaxation time for the dielectric) would cause oscillations to appear in the output, where they were not present originally. The reader should note that this particular intuitive argument, unlike others used in this note, is not backed up by the existence of a more formal version. In Sec. 1 we referred to a relatively dispersionless line. This was meant to designate a line, which in the presence of a pump signal, has the property we have just invoked: A nonoscillatory small signal input results in a nonoscillatory output.

4. GENERAL CONSIDERATIONS

Our remaining considerations will proceed from the fact that we have a transmission system, whose properties are varied in a periodic manner, with the frequency $\omega_p/2\pi$.

This transmission system is linear as far as any small signals go, superimposed on whatever provides the variation at $\omega_p/2\pi$. Furthermore a small extra localized charge q, added at the input end, will all emerge at the output, without any reflected charge returning to the input. The exact delay this charge suffers, and the extent to which it is spread out in time will depend on the relation of the input time, t_i, to the pumping cycle. Let this output charge, as a function of the output time t be given by $qf(t-t_i, t_i)$, which designates that it is not only the delay time $t-t_i$, that matters, but also the input time t_i. The function f is periodic in its second argument, with the period $2\pi/\omega_p$. Furthermore

$$\int f(\tau,t_i)d\tau=1, \tag{4}$$

since charge is conserved. Furthermore we have assumed that f is never negative, so that the line provides variable delays and also, perhaps, a smearing out of the charge.

Now consider an input of the form $q=e^{i\omega t_i}$. The output will then be

$$q_{\text{out}}(t)=\int_{-\infty}^{t_i} e^{i\omega t_i} f(t-t_i, t_i)dt_i. \tag{5}$$

If we take f to be zero for $t_i>t$, then this can equally well be written

$$q_{\text{out}}(t)=\int_{-\infty}^{\infty} e^{i\omega t_i} f(t-t_i, t_i)dt_i. \tag{6}$$

Since f is periodic in its second argument we can expand it in a Fourier series

$$f=\sum_{n=-\infty}^{\infty} f_n(t-t_i)e^{in\omega_p t_i}, \tag{7}$$

substituting this in Eq. (4) gives

$$\sum_{n=-\infty}^{\infty} e^{in\omega_p t_i}\int f_n(\tau)d\tau=1. \tag{8}$$

Equation (8) must hold for all t_i and therefore implies

$$\int f_0(\tau)d\tau=1$$
$$\int f_n(\tau)d\tau=0 \quad \text{for} \quad n\neq 0. \tag{9}$$

We can now use the expansion of Eq. (7) in Eq. (6) and obtain

$$q_{\text{out}}(t)=\sum_n \int_{-\infty}^{\infty} e^{i(\omega+n\omega_p)t_i} f_n(t-t_i)dt_i$$
$$=\sum_n e^{i(\omega+n\omega_p)t}\int_{-\infty}^{\infty} e^{i(\omega+n\omega_p)(t_i-t)} f_n(t-t_i)dt_i. \tag{10}$$

Letting, as in (4), $\tau=t-t_i$, Eq. (7) becomes

$$\sum_n e^{i(\omega+n\omega_p)t}\int_{-\infty}^{\infty} e^{-i(\omega+n\omega_p)\tau} f_n(\tau)d\tau. \tag{11}$$

We thus see that the output signal contains frequencies of the form $\omega+n\omega_p$. The component of greatest interest to us is the one with $n=0$, which is at the original frequency. We will assume in this section that $\omega\neq n\omega_p/2$, in which case no two of the terms in the expansion correspond to the same physical frequency. The next section will deal separately with this exceptional case.

If $f_0(\tau)$ is a delta function, $\delta(\tau-\tau_0)$, then the output,

at the original frequency would be, according to (11),

$$e^{i\omega(t-\tau_0)}, \tag{12}$$

so that the line serves only as a delay element. In general, however, $f_0(\tau)$ will be a more complicated function. $f_0(\tau)$ is the function obtained by averaging $f(\tau,t_i)$ over all t_i. Hence if $f(\tau,t_i)$ is never negative, $f_0(\tau)$ has this same property. For such a function $f_0(\tau)$, whose integral is unity, as given in (7), we have, as is argued in the Appendix,

$$\left|\int_{-\infty}^{\infty} e^{-i\omega\tau} f_0(\tau)d\tau\right| \leq 1. \tag{13}$$

Hence the amplitude of the term $e^{i\omega t}$ in (11) can never exceed unity, and the simple transmission given in Eq. (12) represents a maximum output.

To violate (13) we must have a function f_0, and consequently also functions f, which have oscillations. This means that a charge added to the line, is not only spread out, but gives rise to oscillations. Oscillations in f presumably reflect some characteristic frequency associated with the propagating system, such as the resonance frequency of the filter sections in Engelbrecht's[4] low-pass filter.

5. SIGNAL IS A MULTIPLE OF ONE HALF THE PUMP FREQUENCY

Equation (11) of the preceding section assumed that only the term $n=0$ represented an output at the original signal frequency. The terms $\omega+n\omega_p$ include negative as well as positive values, and it is possible that one of the negative values is equal in magnitude to ω. We then have for some positive integer m:

$$\omega - m\omega_p = -\omega,$$

or

$$\omega = m\omega_p/2, \tag{14}$$

and in this case the reasoning of the preceding section becomes inapplicable.

The signal frequencies specified by Eq. (14) are of particular interest since they are the frequencies at which the phase sensitive computing scheme of von Neumann operates.[11] At these frequencies we can expect the gain of the line to depend on the relative phase of the signal and the pump.

Equation (14) states that the pump period is an integral multiple of the time taken by one half signal cycle. Consider first, in detail, the special case of greatest interest, namely $m=1$. If the small signal is divided into a succession of positive and negative half-cycles, each of these half-cycles will be distorted and/or amplified in the same way, in passing down the line. The charge in each half-cycle may be compressed, or may spread out, but we will assume, in accordance with the treatment of the preceding section, that a positive charge put on the line at the initial end gives rise to a nonoscillatory charge pattern at the output end. Any charge which moves away from its original cycle and catches up (similar reasoning applies to the case where it slows down) with another half-cycle of the same sign, will be replaced in its original half-cycle by the same effect bringing up charge from an even later half-cycle. Charges, however, which move away from their original cycle and merge with a cycle of opposite sign will cause the magnitude of the charge per half-cycle to decrease. We see therefore that the total charge in each half-cycle at the output must be equal to or smaller than the input charge per half-cycle.

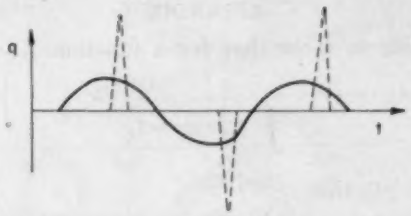

FIG. 6. Input small signal charge variation is shown by solid sinusoidal curve. Output charge must have same charge per half-cycle. The maximum Fourier component at the input frequency is obtained by bunching charge as shown in the dotted curve.

We can now ask what this implies about the relative magnitudes of the components at the original signal frequency. The output is a signal of the same frequency as the input, and with no more charge per half-cycle than at the input. The maximum increase in the component at the fundamental frequency available this way is demonstrated in Fig. 6, where all of the original charge per half-cycle is concentrated in one short period of time. Even in that extreme case the output charge wave form has a fundamental component which is at most $4/\pi(=1.27)$ times the amplitude of the input charge.[12] Gain, therefore, even if possible, cannot be sufficient to be of practical interest. The consideration up to now has been limited to the case in which the signal is one-half the pump frequency. The other special cases of Eq. (14) require a slightly more elaborate argument, since successive half-signal cycles are not treated identically. If, however, we consider the behavior of the small signal averaged over all the possible pump phases which give rise to the same amplification at the frequency of interest, then we can again apply the above argument leading to a maximum signal multiplication by $4/\pi$.

ACKNOWLEDGMENT

R. Van Blerkom, an IBM summer employee in 1955, assisted in some early attempts to deal with the nonlinear transmission line problem.

[11] R. L. Wigington, Proc. Inst. Radio Engrs. **47**, 516 (1959).

[12] The number $4/\pi$ in this connection was first derived by an approximate method by N. M. Kroll, and is also found by G. M. Roe and M. R. Boyd.

APPENDIX

We wish to show that for a function $f_0(\tau)$ which satisfies

$$\int f_0(\tau)d\tau=1, \tag{A.1}$$

and $f_0(\tau)\geq 0$, that

$$\left|\int_{-\infty}^{\infty} e^{-i\omega\tau}f_0(\tau)d\tau\right|\leqq 1. \tag{A.2}$$

To demonstrate (A.2), it will be adequate to show

$$\left|\int_{-\infty}^{\infty} e^{-i\omega\tau}f_0(\tau)d\tau\right|\leqq\int_{-\infty}^{\infty} f_0(\tau)d\tau. \tag{A.3}$$

The magnitudes of the two integrands shown in (A.3) are the same, for each value of τ. The integrand on the right-hand side, however, has the same phase for all values of τ, whereas the phase of the left-hand integrand is variable. Hence the inequality follows.

JOURNAL OF APPLIED PHYSICS VOLUME 31, NUMBER 3 MARCH, 1960

Creep of Al_2O_3 Single Crystals*

ROGER CHANG
Atomics International, A Division of North American Aviation, Canoga Park, California
(Received August 28, 1959)

The "steady-state" creep of Al_2O_3 single crystals was investigated. The experimental data are analyzed according to three mechanisms: the dislocation climb mechanism, the micro-creep mechanism, and the Peierls stress mechanism. It is shown that the dislocation climb mechanism fits experimental data best. The expectation that Peierls stress mechanism is rate controlling in the "steady-state" creep of Al_2O_3 is ungrounded.

I. INTRODUCTION

PLASTIC deformation of crystalline solids at high temperatures is accompanied by recovery. If the rate of recovery is sufficiently fast, it will balance the work-hardening rate. When this condition is satisfied, the crystal will under a given stress deform at a constant rate, hence "steady-state" creep. The modern concept of flow in crystalline solids is the generation and motion of dislocations. There are several major mechanisms of "steady-state" creep based on the concept of dislocation motion. The first mechanism, originally proposed by Mott,[1] implies that "steady-state" creep is controlled by the rate of dislocation climb. Since dislocation climb requires material transport, the activation energy for "steady-state" creep is approximately equal to that for lattice diffusion.†

When dislocation climb becomes so rapid that it is no longer rate controlling. Two other important mechanisms of "steady-state" creep have been proposed[2]:

1. The dislocations are considered to move in a viscous manner, impeded by an atmosphere of imperfections or impurities, their velocity of motion being proportional to the force exerted on them. This is the so-called micro-creep mechanism. The activation energy for "steady-state" creep according to this mechanism is usually that for diffusion of the impurities or imperfections concerned.

2. The motion of dislocation lines over Peierls stress hills is considered as the rate-controlling process. When the Peierls stress is large, dislocation lines, forced to run along definite crystallographic directions, must overcome the Peierls barrier in order to move one interatomic distance. The activation energy for "steady-state" creep is determined by, among other things, the Peierls force of the material.

Since Peierls stress is usually high in nonmetallic crystals, it would be natural to expect the Peierls stress mechanism to be rate controlling in the "steady-state" creep of oxide crystals, such as Al_2O_3. It is the purpose of this report to describe experiments on the "steady-state" creep of Al_2O_3 single crystals. The data are analyzed and interpreted in terms of the three mechanisms outlined above.

II. EXPERIMENTAL METHODS AND RESULTS

The tensile creep apparatus used in this work has been described elsewhere.[3] Centerless ground Linde sapphire and ruby rods were used. Both the sapphire and ruby specimens had an average dislocation density of approximately 10^6 per sq cm from etch pit counts. The sapphire rods contained, according to Linde estimates, 10–100 ppm Fe and 1–10 ppm Mg and Si,

* This work was supported by the U. S. Atomic Energy Commission.
[1] N. F. Mott, Nature **175**, 365 (1955).
† Further considerations of the dislocation climb mechanism yield a power law dependence of the "steady-state" creep rate on applied stress.
[2] J. Weertman, J. Appl. Phys. **28**, 1185 (1957).
[3] R. Chang, J. Nuclear Materials **1**, 174 (1959).

while the ruby rods analyzed approximately 2 weight % Cr_2O_3. Figure 1 shows the photograph of an actual specimen.‡

A typical creep curve for sapphire is shown in Fig. 2. Data describing the dependence of "steady-state" creep rate on stress at constant temperature, and on temperature at a given stress, are shown respectively in Fig. 3 and Fig. 4 for both sapphire and ruby.

III. DISCUSSION

A. The Dislocation Climb Mechanism

Weertman has treated extensively the dislocation climb mechanism,[4] assuming that at high temperatures a dislocation can climb perpendicular to the slip plane by diffusion of lattice vacancies. By assuming further that vacancy equilibrium is established along the dislocation lines during climb, he obtained the following equation for "steady-state" creep rate,

$$\dot{\epsilon}=(6\pi^2\nu\tau^2/\mu^2)\sinh[3\tau^5b^3/2k^2T^2\mu^3M]^{\frac{1}{2}} \times\exp\left(\frac{\Delta S}{k}\right)\exp\left(\frac{-\Delta H}{kT}\right), \quad (1)$$

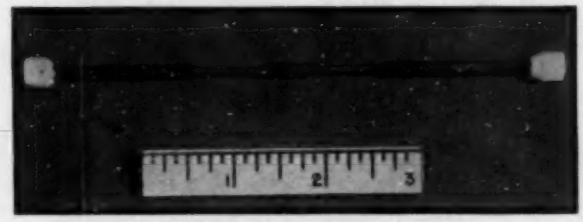

FIG. 1. Creep specimen.

where ν is the vibrational frequency of a vacancy; τ is resolved shear stress; μ is rigidity modulus; b is the length of the Burgers vector of a dislocation; k is Boltzman's constant; T is the absolute temperature; ΔS and ΔH are, respectively, the entropy and the activation energy for self-diffusion; M is the average density of Frank-Read sources.

When the energy of jog formation is high, such that equilibrium concentration of vacancies cannot be maintained along the dislocation lines because too few jogs are present, the "steady-state" creep rate is given by:

$$\dot{\epsilon}\cong\left(\frac{L}{b}\right)(6\pi^2\nu\tau^2/\mu^2)\sinh[3\tau^5b^3/2k^2T^2\mu^3M]^{\frac{1}{2}} \times\exp\left(\frac{\Delta S^*}{k}\right)\exp\left(\frac{-\Delta H^*}{kT}\right) \quad (2)$$

where L is half the average distance between Frank-Read sources; ΔS^* and ΔH^* are, respectively, the sum of entropies and activation energies for self-diffusion and jog formation. Equation (2) breaks down and Eq. (1) is applicable when the probability that a jog exists in a dislocation segment of length L is greater than unity.

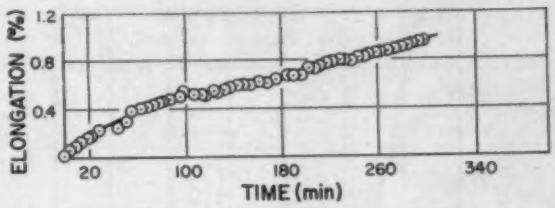

FIG. 2. Typical creep curve, sapphire (1.4×10^8 d/cm², 1823°K).

It is readily shown that for applied stresses of the order of 10^8 d/cm² or less, the hyperbolic sine term is such that the condition $\sinh x\cong x$ ($x\ll1$) is satisfied. Equation (1) is then simplified to:

$$\dot{\epsilon}=72.4\left(\frac{\nu^2b^3\tau^9}{k^2T^2\mu^7M}\right)^{\frac{1}{2}}\exp\left(\frac{\Delta S}{k}\right)\exp\left(\frac{-\Delta H}{kT}\right). \quad (1a)$$

According to Eq. (1a):

$$\dot{\epsilon}=(\text{constant})\ (\tau)^{9/2}, \quad \text{at constant temperature,} \quad (1b)$$

while

$$\epsilon=(\text{constant})\frac{1}{T\mu^{7/2}}\exp\left(\frac{-\Delta H}{kT}\right),$$

at constant stress. (1c)

The plot of $\log\dot{\epsilon}$ *vs* $\log\tau$ from experimental data is shown in Fig. 3 for sapphire and ruby. The slope yields an exponent 4.5 for sapphire and 5.0 for ruby, comparing favorably with the expected value of 9/2.

In the temperature range studied, the variation of both T and μ is negligibly small, hence Eq. (1c)

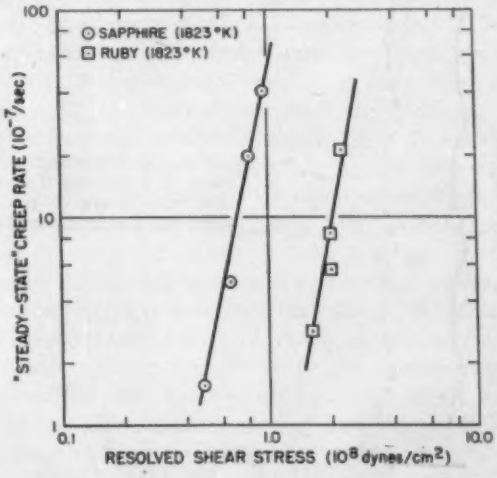

FIG. 3. "Steady-state" creep rate *vs* applied resolved shear stress, sapphire and ruby (1823°K).

‡ To avoid complications due to variations in imperfections and impurities from rod to rod, direct comparison was made of data from specimens cut from a single rod.

[4] J. Weertman, J. Appl. Phys. **26**, 1213 (1955); **28**, 362 (1957).

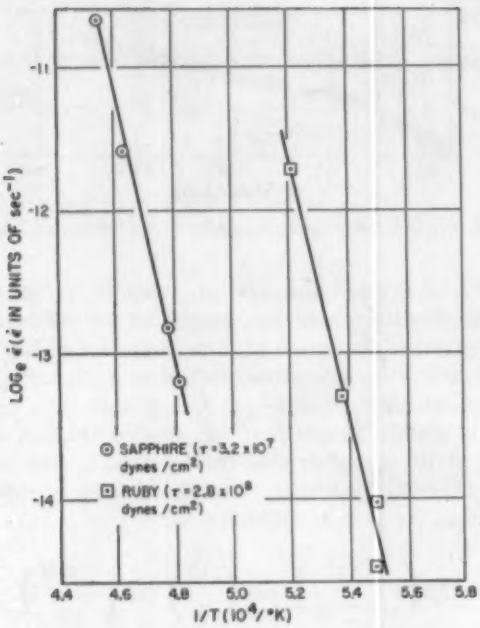
-11
-12
-13
-14
LOG$_e$ $\dot{\epsilon}$($\dot{\epsilon}$ IN UNITS OF sec^{-1})
⊙ SAPPHIRE (τ = 3.2 x 10^7 dynes / cm^2)
⊡ RUBY (τ = 2.8 x 10^8 dynes / cm^2)
4.4 4.6 4.8 5.0 5.2 5.4 5.6 5.8
1/T (10^4/°K)

FIG. 4. "Steady-state" creep rate *vs* temperature, sapphire and ruby.

becomes:

$$\dot{\epsilon} \cong (\text{constant}) \exp\left(\frac{-\Delta H}{kT}\right). \qquad (1d)$$

The plot of log$\dot{\epsilon}$ *vs* $1/T$ (stress constant) is shown in Fig. 4 for sapphire and ruby, giving $\Delta H \cong 7.8$ ev for both materials.

The activation energy for self-diffusion evaluated indirectly from sintering data[5] is from 7.0 to 7.8 ev. The activation energy for diffusion of oxygen in Al_2O_3 is about 7.5 ev.[6] It appears that the activation energy for "steady-state" creep in Al_2O_3 single crystals is almost equal to that for self-diffusion. These observations suggest that "steady-state" creep in Al_2O_3 single crystals goes most probably by the dislocation climb mechanism.

It is at present not possible to calculate the "steady-state" creep rate from Eq. (1a) without knowing the density of Frank-Read sources M and the entropy term $\Delta S/k$. The agreement between theory and experiment is fair if one assumes $M \sim 10^{11}$/cc and $\Delta S/k \sim 20$.

B. The Viscose Drag Mechanism

Since the observed activation energy for "steady-state" creep is high, a viscous drag mechanism of dislocations against impurities appears unlikely. It is more probable that lattice imperfections or clusters of lattice imperfections are acting as dragging points. Figure 5 shows schematically the form of a moving dislocation under resolved shear stress τ with dragging points spaced at a mean distance ℓ. The "steady-state" creep rate is given by:[7]

FIG. 5. Schematic diagram of a moving dislocation with dragging points spaced at a mean distance ℓ.

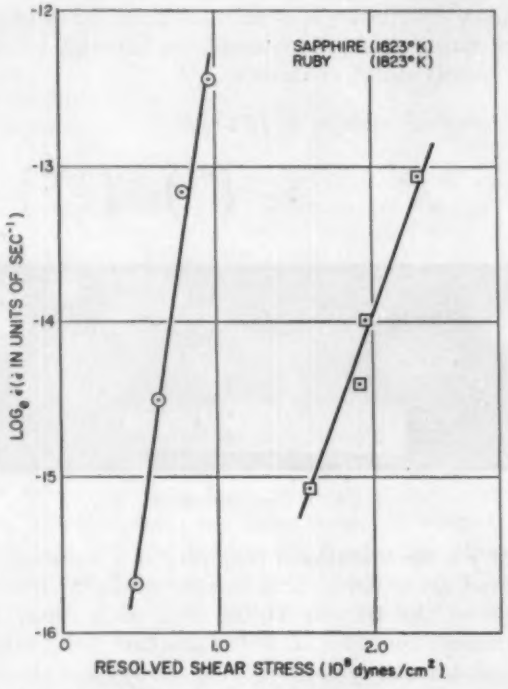

FIG. 6. Semi-logarithmic plot "steady-state" creep rate *vs* resolved shear stress, sapphire and ruby.

$$\dot{\epsilon} \cong 2\lambda\Lambda b^2 \nu_0 \exp\left(\frac{-\Delta F}{kT}\right) \sinh\left(\frac{\ell b^2 \tau}{kT}\right), \qquad (3)$$

where Λ is the total free length of dislocation per unit volume ($\sim 10^6$ cm per cc); b is the Burgers vector (8.22×10^{-8} cm); ΔF is the free energy of activation; ν_0

[5] R. L. Coble, J. Am. Ceram. Soc. 41, 55 (1958).
[6] D. W. Kingery (private communication).
[7] H. G. van Bueren, Physica 24, 831 (1958).

is the vibrational frequency of an atom ($\sim 10^{13}$ per sec); k is Boltzmann's constant (1.38×10^{-16} ergs per deg); T is the absolute temperature; and λ is a correction factor converting shear strain to tensile strain ($(\frac{3}{2})^{\frac{1}{2}}$ for rods having basal plane inclined at 30 deg from rod axis). In expressing ΔF as $\Delta H - T\Delta S$ (ΔH and ΔS being, respectively, the heat of activation and entropy of activation) and writing $\sinh(\ell b^2\tau/kT) \cong \frac{1}{2}\exp(\ell b^2\tau/kT)$ for $\ell b^2\tau \geqq kT$, one obtains from Eq. (3) the following,

$$\dot{\epsilon} \cong \lambda A b^2 \nu_0 \exp\left(\frac{\Delta S}{k}\right)\exp\left(\frac{-\Delta H + \ell b^2\tau}{kT}\right). \quad (4)$$

According to Eq. (4), the plot of $\log\dot{\epsilon}$ *versus* τ at constant temperature (Fig. 6) should be a straight line with slope

$$\ell b^2/kT \quad (5)$$

and intercept extrapolated to zero stress

$$\log(\lambda A b^2 \nu_0) + (\Delta S/k) - (\Delta H/kT), \quad (6)$$

TABLE I. Slopes and intercepts from "steady-state" creep data (Fig. 4 and Fig. 6).

	Item	Sapphire	Ruby
(5)	$\frac{\ell b^2}{kT}$ (d^{-1} cm^2)	6.7×10^{-8}	2.8×10^{-8}
(6)	$\log(\lambda A b^2\nu_0)+\frac{\Delta S}{k}-\frac{\Delta H}{kT}$	−18.7	−19.6
(7)	$\frac{-\Delta H+\ell b^2\tau}{k}$ (°K)	9.4×10^4	9.1×10^4
(8)	$\log(\lambda A b^2\nu_0)+\frac{\Delta S}{k}$	33	36

while the plot of $\log\dot{\epsilon}$ *vs* $1/T$ at a given stress (Fig. 4) should be a straight line with slope,

$$\frac{-\Delta H + \ell b^2\tau}{k} \quad (7)$$

and intercept extrapolated to $1/T=0$

$$\log(\lambda A b^2\nu_0) + \Delta S/k. \quad (8)$$

These quantities obtained from data shown in Fig. 4 and Fig. 6 are summarized in Table I.

The mean dragging distance ℓ can be obtained from (5). The quantity ΔH can be evaluated from (5) and (7), and independently from the difference between (6) and (8). If we know ΔH, the entropy term $\Delta S/k$ can be determined from either (6) or (8). These parameters are summarized in Table II.

The ΔH parameters evaluated from the stress-varying-temperature-constant experiments and from the temperature-varying stress-constant experiments agree among themselves within the limits of experimental error. The average distance ℓ between local dragging points along a dislocation line is of the order of a few hundred angstroms. It is also interesting to find that the ΔH and $\Delta S/k$ parameters are almost equal to those obtained according to the dislocation climb mechanism. It is at present difficult to reason why the average distance between dragging points should be of the order of a few hundred angstroms, and why the activation energy should be same as that for self-diffusion. The validity of this mechanism is doubtful, unless future studies justify the above findings.

TABLE II. Determination of ℓ, ΔH and $\Delta S/k$ from "steady-state" creep data.

Evaluation from	Sapphire ℓ, 10^{-8} cm	Sapphire ΔH, ev/atmos	Sapphire $\frac{\Delta S}{k}$	Ruby ℓ, 10^{-8} cm	Ruby ΔH, ev/atmos	Ruby $\frac{\Delta S}{k}$
(5)	240	...	...	100	...	...
(5,7)	...	7.8	...	...	9.1	...
(6,8)	...	8.1	...	...	8.7	...
(6,8)	...	...	22	...	...	25

C. Peierls Stress Mechanism

Weertman has proposed the following equation for the "steady-state" creep of crystalline solids where the the Peierls stress mechanism is rate controlling:[4]

$$\dot{\epsilon} \cong (12\tau^5\gamma^2 a^2/\mu^5 b^5 M)^{\frac{1}{2}} \exp(-Q/kT) \times \exp(\pi\tau Q/2\tau_0 kT), \quad (9)$$

where a is the distance between Peierls hills; Q is the activation barrier for dislocations to climb over the Peierls hills; τ_0 is the Peierls force. According to Seeger,[8] Q is related to τ_0 according to

$$Q \sim (4ab/\pi)(2\mu\tau_0 ab/5\pi)^{\frac{1}{2}}. \quad (10)$$

The Peierls force τ_0 is very difficult to evaluate accurately. On assuming that Q is equal to ΔH (7.8 ev) from experimental data, Eq. (10) yields a Peierls force of approximately 2×10^9 d/cm² for Al_2O_3. The calculated "steady-state" creep rates according to Eq. (9) are about a factor of 10^7–10^8 too low, suggesting that the Peierls stress mechanism is not rate controlling in the "steady-state" creep of Al_2O_3 single crystals.

The above analysis shows that the "steady-state" creep rate of Al_2O_3 single crystals is controlled most probably by a dislocation climb mechanism. For hexagonal crystals where immobile dislocations could not be formed to block dislocation motion, Weertman[4] has suggested that pile-up of dislocations may take place on neighboring slip planes. Further studies are needed to reveal the nature of defects which block the motion of mobile dislocations generated during creep.

It is interesting to note that the entropy of activation for "steady-state" creep of Al_2O_3 single crystals is comparatively large ($\Delta S/k = 20$ to 25). A large entropy of activation for volume diffusion in Al_2O_3 single crystals has been similarly observed by Kuczynski[9] and his colleagues from their sintering studies.

[8] A. Seeger, Phil. Mag. 1, 651 (1956).
[9] G. C. Kuczynski (private communication).

JOURNAL OF APPLIED PHYSICS VOLUME 31, NUMBER 3 MARCH, 1960

Kinetics of Sintering of Sodium Chloride in the Presence of an Inert Gas*

J. B. Moser and D. H. Whitmore
Department of Metallurgy and Materials Science, Northwestern University, Evanston, Illinois
(Received August 28, 1959)

Direct observations of interfacial growth and the approach of centers between spheres of sodium chloride were made in an argon atmosphere and over a temperature range of 700 to 800°C. The rate law governing the increase of the contact area between spheres, the effect of changing size scale on this rate and the absence of a change in the center-to-center distance during sintering all indicate that the rate-determining mechanism of material transport in this sintering process is evaporation-condensation. A model is presented which considers Stefan flow to occur within a thin boundary layer in the gaseous phase adjacent to the condensing surface, the sintering rate being predominantly governed by the rate at which sodium chloride vapor diffuses through this boundary layer. The marked pressure-dependence of the empirical relationship between contact area and sintering time for fixed temperature and sphere size is consistent with the proposed model.

I. INTRODUCTION

It is now widely accepted that detailed and unambiguous information about sintering mechanisms can be derived from studies of sintering in geometrically simple, particulate systems involving sphere-to-sphere, cylinder-to-plate, or sphere-to-plate bonding. Moreover, it has been firmly established that surface tension provides the motivation for sintering; and, as Herring[1,2] and Kuczynski[3] have shown using classical macroscopic concepts, rates of sintering can be predicted for various mechanisms of material transport when certain, very general conditions are fulfilled.

The present investigation is concerned only with the initial or bonding stage of sintering, wherein a common interface or "neck" forms between two neighboring particles when they are held at some elevated temperature below the melting point of the particles. Those transport processes which might produce this interface growth are: surface and volume diffusion, plastic and viscous flow, and evaporation from convex regions of the system and condensation on the concave surface of the neck.

Evidence on the sintering kinetics of sodium chloride presented by Kingery and Berg[4] suggests that an evaporation-condensation mechanism is responsible for initial-stage sintering of this material. However, insufficient data (three experimental runs in the range 700 to 750°C) were included for a critical analysis of their results. Furthermore, even though their paper was devoid of any direct reference to the specific sintering atmosphere used, it must be assumed that Kingery and Berg carried out their sodium chloride experiments in vacuum because they invoked the Langmuir expression[5] for evaporation from a solid into a vacuum to determine the rate of transport of sodium chloride to the neck region. Of course, in vacuum the mean free path of the sodium chloride molecules evaporating from the surface of the solid is large compared with the distance over which appreciable transport occurs.

In this paper, the results of extensive measurements of the rate of sintering of sodium chloride in a purified argon atmosphere are reported and an analytic description of sintering is presented under conditions such that the mean free path of the evaporating molecules is small by comparison with the transport distance; in this instance, the rate of sintering is determined by diffusion of the condensing vapor across a hydrodynamic boundary layer in the gaseous phase in the immediate vicinity of the neck. The natural advantages accruing from the use of an inert gas atmosphere (rather than vacuum) for sintering experiments involving materials of high vapor pressure are: (a) minimization of evaporation losses; and (b) diminution of the rate of sintering so that the time interval and precision of the observations are increased.

II. EXPERIMENTAL

1. Preparation of Spherical Specimens

The material used in the present study for the preparation of spheres was A.C.S. reagent grade sodium chloride in the approximate form of cubic grains. The original material was crushed in an agate mortar, sized with the aid of a set of standard sieves and fused into spheres 98 to 227 microns in diameter by feeding the separate size fractions into the three-phase carbon arc of an electric fusion furnace similar to that described by Kingery and co-workers.[4] A slow stream of purified argon gas was continuously passed through the furnace chamber during the spheroidizing operation. Following this, the spheres were hand-checked for sphericity and sized by means of sieves. A number of careful density

* This paper is a version of a thesis submitted by J. B. Moser to the graduate school to fulfill one of the requirements for the M.S. degree in Metallurgy. The research was supported in part by the Air Force Office of Scientific Research under contract with Northwestern University.

[1] C. Herring, Chapter in *Structure and Properties of Solid Surfaces*, edited by R. Gomer and C. S. Smith (The University of Chicago Press, Chicago, Illinois, 1952).

[2] C. Herring, Chapter in *Physics of Powder Metallurgy*, edited by W. E. Kingston (McGraw-Hill Book Company, Inc., New York, 1951).

[3] G. C. Kuczynski, Trans. Am. Inst. Mining Met. Engrs. **185**, 169 (1949).

[4] W. D. Kingery and M. Berg, J. Appl. Phys. **26**, 1205 (1955).

[5] I. Langmuir, Phys. Rev. **2**, 329 (1913).

measurements on fused spheres revealed that the extent of internal porosity in the spheres was negligibly small.

2. Sintering Rate Measurements

A high-temperature microstage furnace was constructed to facilitate observation of the growth of the contact area between the spheres of sodium chloride. The electrical heating element was fabricated from molybdenum sheet by means of a deep-drawing die so as to have a central depression or trough in which the spheres could be positioned during heating. This heater was supported by two heavy copper electrode posts and chromel-alumel thermocouple wires were spot-welded to the outside of the trough section at its bottom, thereby allowing an average temperature measurement to be made over the central region of the heater. Power to the heater was supplied from a voltage stabilizer, an autotransformer and an induction regulator, with the voltage drop and the amperage applied to the heater being constantly monitored. Manual adjustment of the induction regulator kept the temperature within ± 5°C of the control temperature during the course of a sintering run.

The furnace chamber was connected directly to a pumping system, capable of maintaining pressures of about 10^{-5} mm Hg, which consisted of a two-inch metal oil diffusion pump backed by a mechanical vacuum pump. Moreover, purified argon gas could be introduced into the heating chamber, at any desired pressure up to two atmospheres, to serve as a static sintering atmosphere. Pressure readings were taken to the nearest millimeter with the aid of an open-tube, mercury manometer. The sintering temperature was measured by means of a potentiometer and the aforementioned thermocouple welded to the heater; this thermocouple was initially calibrated by noting the emf corresponding to the observed melting point of several pure materials on the hot-stage heater and was likewise calibrated against the melting point of sodium chloride at the completion of each sintering run.

Radii of the contact area between spheres were measured with a vertically mounted metallurgical microscope, equipped with a Filar-Ramsden eyepiece which was focused on the heater through a quartz window of the hot stage. The usual magnification employed was 160 X and this was periodically calibrated with the aid of a stage micrometer. It was estimated that the theoretical resolution of this optical system is somewhat less than one micron.

Measurements of the times of observation of the neck radii were recorded on a high speed, strip chart recorder, and these were later correlated with the microscopic readings. This scheme of measuring the sintering time was checked repeatedly during the course of the investigation and the error never exceeded two percent.

Following careful alignment of the sodium chloride spheres on the heater, the stage was closed, evacuated and filled with purified argon to some desired pressure; then the spheres were heated, in a matter of seconds, to the sintering temperature. Microscopic measurements of the interfacial radii were made at the sintering temperature, starting with the spheres at one end of the heater trough and progressing to those at the other as rapidly as possible in order to permit a maximum amount of data to be taken during the comparatively short duration of the sintering experiment. Any possible shrinkage was checked by periodic observations of the distance between a fixed number of interfaces.

III. THE RATE EQUATION AND SCALING LAW FOR EVAPORATION-CONDENSATION SINTERING IN THE PRESENCE OF AN INERT GAS

In this sintering model it will be assumed that sintering occurs by an evaporation-condensation mechanism and that diffusion of sodium chloride vapor in the gas phase is rate-controlling; and, more particularly, the general case will be discussed in which the components of the gas mixture (argon and sodium chloride vapor) diffuse at different rates thereby giving rise to pressure differences and a mass flow perpendicular to the surface of condensation. Such flow is known as Stefan flow[6] and, in some instances, plays a prominent role in material transport in gaseous mixtures.

As a first approximation, the details of the geometric shape and roughness of the condensation surface are ignored; rather, Stefan flow is considered to be localized within a thin, diffusion boundary-layer adjacent to the surface of the neck.[7]

It is further postulated that all viscous effects are confined to the boundary layer near the surface and that the flow outside this layer is inviscid. Furthermore, it is assumed that the thickness of this layer, δ, is small compared to the characteristic dimension of the surface, thus, except in the initial stage of the neck growth, the ratio of the boundary-layer thickness to the radius of neck, δ/x, will be extremely small and the curvature of the neck can be disregarded insofar as the diffusion process is concerned. Moreover, it will be assumed that the total flux of material, as well as the flow velocity, v_r, normal to the surface of the neck† is independent of r in the range $x \leqslant r \leqslant x+\delta$ and that the concentration of sodium chloride vapor is essentially uniform for $r > x+\delta$. Thus, all the changes occur within this thin diffusion boundary-layer and purely molecular processes are responsible for the mass transfer taking place therein.

Taking account of Stefan flow and considering the sodium chloride vapor to be largely diluted by argon, the flux of sodium chloride vapor, J, through the dif-

[6] J. Stefan, Ann. Physik **17**, 551 (1882); **41**, 725 (1890); Wien. Ber. **68**, II, 385 (1874); **83**, II, 545, 943 (1881); **98**, II, 1418 (1889); J. phys. **1**, 202 (1882).

[7] D. A. Frank-Kamenetskii, *Diffusion and Heat Exchange in Chemical Kinetics*, translated by N. Thon (Princeton University Press, Princeton, New Jersey, 1955), pp. 128–145.

† Along with Kuczynski,[5] we shall assume the neck to have cylindrical symmetry.

fusion boundary layer above the neck may be written as

$$J=\frac{-D_{21}PM_2}{\delta RT}\ln\left[\frac{P-p_1}{P-p_n}\right] \tag{1}$$

where D_{21} is the diffusion coefficient for sodium chloride vapor in argon, P is the total gas pressure, M_2 is the gram molecular weight of sodium chloride, R the gas constant, T the absolute temperature, p_1 the partial pressure of sodium chloride in the bulk gas, and p_n is the equilibrium partial pressure of sodium chloride above the surface of the neck. Expanding the logarithm, Eq. (1) can be rewritten as

$$J=\frac{D_{21}M_2}{\delta RT}(p_1-p_n)+\frac{D_{21}M_2}{\delta RT}\sum_{m=2}^{\infty}\frac{1}{mP^{m-1}}(p_1^m-p_n^m). \tag{2}$$

Since, in the present case, p_1 and p_n are small compared with P, the higher powers of p in the summed terms may be neglected. Thus, the flux of sodium chloride vapor to the surface of the neck is approximated by

$$J\cong\frac{D_{21}M_2}{\delta RT}(p_1-p_n). \tag{3}$$

Employing the Fuchs model for evaporation and condensation,[8] it may be shown that, if the diffusion boundary-layer adjacent to the surface of the sphere is small in comparison with the radius of the sphere, the partial pressure p_1 in the bulk gas stream is approximately the equilibrium partial pressure of sodium chloride p_s above the sphere. Consequently Eq. (3) becomes‡

$$J\cong\frac{D_{21}M_2}{\delta RT}(p_s-p_n). \tag{4}$$

It is of interest to note that Eq. (4) is a modification of the Noyes-Nernst relationship[9–11] frequently employed in interpreting the kinetics of dissolution of solids in liquids.

Now, it is assumed, along with Kingery and Berg,[4] that the neck formed between two sintering spheres has a circular cross section of radius x and an external radius of curvature $\epsilon(\epsilon\cong x^2/2a$ for $x/a<0.3$ where a is the sphere radius); then the volume of sodium chloride, V, filling in between the spheres is approximately $\pi x^4/2a$ while its area A is about π^2x^3/a. The vapor pressure p_s of sodium chloride above the surface of the sphere (evaporation surface) and p_n above the surface of the neck (condensation surface) are related to their respective radii of curvature by the Thomson-Gibbs equation. Thus,

$$\ln\frac{p_n}{p_s}=\frac{-2M_2\gamma}{RT\rho}\left(\frac{1}{\epsilon}+\frac{1}{a}\right) \tag{5}$$

where γ is the surface tension of solid sodium chloride and ρ is its density. Since $a\gg\epsilon$, Eq. (5) reduces to

$$p_s-p_n=\frac{2M_2\gamma p_s}{RT\rho\epsilon} \tag{6}$$

where all symbols have their usual significance. Substituting for the pressure difference from Eq. (6) into Eq. (4), the steady-state flux of sodium chloride vapor to the surface of the neck is obtained; this latter quantity, multiplied by A/ρ, is equated to the rate of volume increase of the neck with appropriate substitution for ϵ. Integration of the resulting expression yields the sintering rate expression appropriate to the proposed model:

$$\frac{x^3}{a}=\frac{6\pi D_{21}}{\delta}\left(\frac{M_2}{\rho RT}\right)^2\gamma p_s t. \tag{7}$$

Since the diffusion coefficient for sodium chloride vapor appears in the proportionality factor in the relation between x^3/a and t given in Eq. (7), this factor should depend upon the total gas pressure because of a well-known inverse relation between the diffusion coefficient of a gaseous species and the total pressure.[12] Thus, Eq. (7) may be written as

$$\frac{x^3}{a}=K(T,P)t \tag{8}$$

where $K(T,P)$ is a function of both temperature and pressure and not just temperature alone as has been the case in the proportionality factors appearing in previously derived[3,4] rate equations for this mechanism. Herring,[13] using similitude considerations, analyzed the effect of a change of scale on the rate for particles sintered by an evaporation-condensation process. However, in deriving the scaling law appropriate to this mechanism, he assumed that the mean-free-path in the gas phase was large compared with the transport distance. Since this condition was never realized in the

[8] N. Fuchs, Physik. Z. Sowjetunion **6**, 224 (1934).

‡ Equation (4) can be derived equally well on the basis that diffusion and natural convection (due to a density difference existing between the condensing vapor adjacent to the surface of the neck and that in the bulk gas stream) are rate-determining factors. However, there is some uncertainty regarding the form of the Nusselt criterion, i.e., the particular function of the Schmidt and Grashof numbers, applicable to the present experimental conditions. Hence, the alternative model involving Stefan flow is thought to be more generally useful, not being dependent upon a detailed knowledge of convective conditions. Either approach will lead to the same sintering rate law, Eq. (7), developed in the text provided that $\delta\ll x$.

[9] A. A. Noyes and W. R. Whitney, Z. physik. Chem. **23**, 689 (1897).

[10] W. Nernst, Z. physik. Chem. **47**, 52 (1904).

[11] E. Brunner, Z. physik. Chem. **47**, 56 (1904).

[12] See, for example, Hirschfelder, Curtiss, and Bird, *Molecular Theory of Gases and Liquids* (John Wiley & Sons, Inc., New York, 1954).

[13] C. Herring, J. Appl. Phys. **21**, 301 (1950).

present experiments, the original form of Herring's scale law is not applicable here; rather, it was necessary to develop a scaling law for an evaporation-condensation mechanism with diffusion through a gaseous boundary layer being rate-controlling.

Considering the gas mixture to be ideal and employing the well-known Thomson-Gibbs relation, the difference between the chemical potential of sodium chloride in the bulk stream, μ', and that above the surface of the neck, μ_n, is given by

$$\mu'-\mu_n=\frac{-2\Omega_0\gamma}{\epsilon} \tag{9}$$

where Ω_0 is the molecular volume and the product $2\Omega_0\gamma$ is the same at corresponding points of the surfaces of geometrically similar clusters.[13]

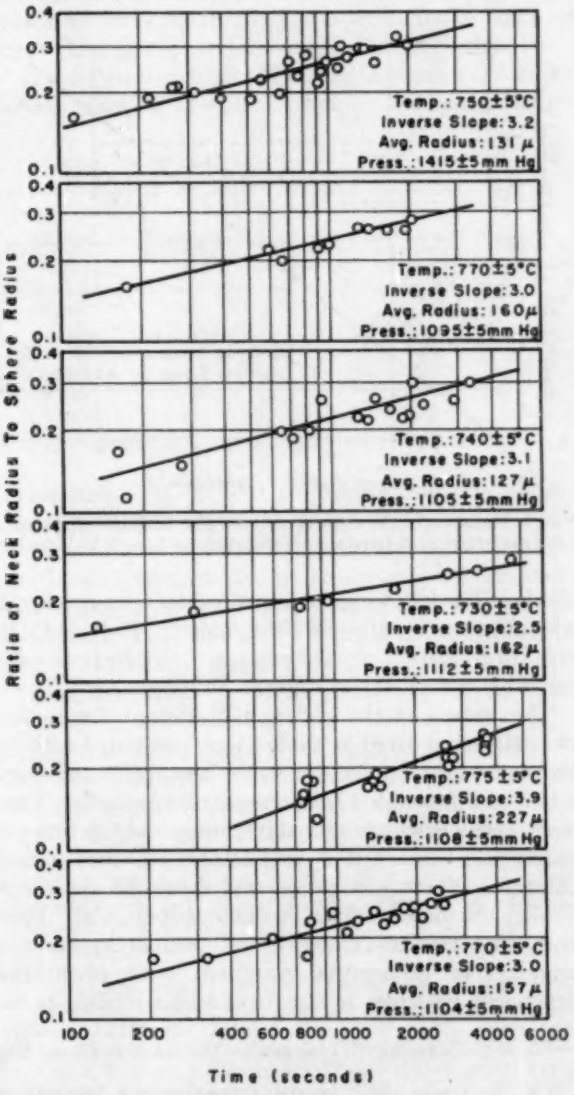

FIG. 1. Ratio of neck radius to sphere radius (log scale) as a function of sintering time (log scale).

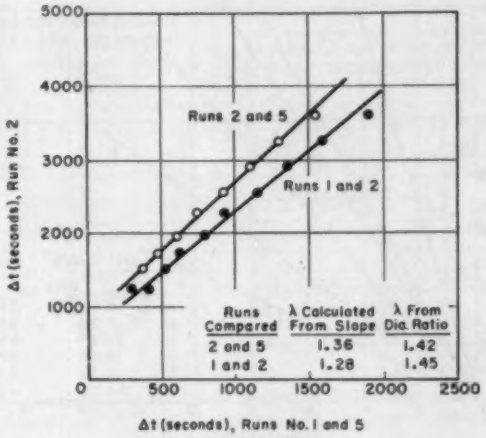

FIG. 2. Effect of change of scale of particles on sintering time.

Consider two sets of different diameter spheres being sintered at the same temperature and pressure, all spheres within the first set having radius a_1 and those in the second set having a radius a_2. Now, according to the foregoing considerations of the neck geometry, $x^2/2a=\epsilon$. So that, if the two geometrically similar clusters are sintered for different times but to the same degree, i.e., x/a ratio, it follows that

$$\epsilon_1=\lambda\epsilon_2 \tag{10}$$

and hence, that

$$\frac{(\mu'-\mu_n)_1}{(\mu'-\mu_n)_2}=\frac{\epsilon_2}{\epsilon_1}=\frac{1}{\lambda} \tag{11}$$

where the subscripts refer to the corresponding clusters and $\lambda=a_1/a_2$. Since the boundary layer thickness is generally not a function of any linear dimension of the solid particles, the fluxes of sodium chloride vapor to the necks in the two clusters are related as follows:

$$J_1=(J_2/\lambda). \tag{12}$$

Because corresponding areas in the two clusters bear the ratio λ^2 and the amount of material which must be transported in cluster 1 is λ^3 times that for cluster 2, it follows that, when steady-state diffusion prevails, the times required to produce corresponding degrees of sintering satisfy

$$\frac{\Delta t_1}{\Delta t_2}=\frac{J_2A_2\Delta V_1}{J_1A_1\Delta V_2}$$

$$=\lambda\cdot\lambda^{-2}\cdot\lambda^3=\lambda^2. \tag{13}$$

IV. RESULTS AND DISCUSSION

Referring to the sintering rate equation in the previous section, it is apparent that by plotting x/a against t, on logarithmic scales, a straight line should obtain whose inverse slope is 3.0. In Fig. 1 the data from several typical runs in the temperature range 730° to 795°C are

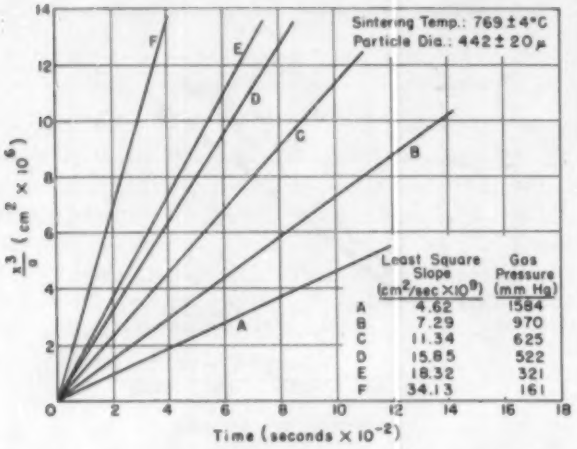

FIG. 3. Influence of total gas pressure on the slope of x^3/a *vs* t plots at constant temperature and particle size (curves normalized to pass through origin).

plotted in this manner; the inverse slopes of these curves were indeed found to lie close to 3.0, ranging from 2.5 to 3.9. More than twenty sintering runs were made during the course of the present investigation and only rarely did the individual inverse slope values deviate by more than ± 0.5 from the value predicted by the rate equation (7) for the evaporation-condensation mechanism.

A comparison is made in Fig. 2 of the sintering times necessary to produce the same degree of sintering (same x/a value) for spheres of different sizes. Equation (13) indicates that the slope of such a plot should equal λ^3; accordingly, the square root of the slope should be λ and these values are compared in the figure with those determined directly from the diameter ratio.

It was not practicable in the present work to use spheres of widely different diameters; however, to employ the scaling-law criterion for a sintering mechanism this is essential. Due to the scatter of the present experimental data, only a forty percent size difference makes it very difficult to decide unambiguously between a volume diffusion and an evaporation-condensation mechanism. On the other hand, with an order-of-magnitude size difference and comparable experimental errors, the scaling-law criterion would be much more effective in selecting the mass-transfer mechanism operating in a particular situation.

As has been indicated by Kingery and Berg,[4] if either evaporation-condensation or surface diffusion occurs, there can be no change in the distance between centers; whereas the occurrence of a viscous or plastic flow or any volume diffusion mechanism, except for the case of a vacancy surface sink, would result in a decrease in the center-to-center distance of the spheres. In the present investigation, the observed absence of a change in the center-to-center distance further strengthens the case for an evaporation-condensation mechanism.

Figure 3 illustrates graphically the effect of total gas pressure on the slope of typical isothermal sintering plots for spheres of constant diameter, while Fig. 4 shows the inverse relation predicted in the previous section between the slope of these plots and the total gas pressure. Within the range of pressure investigated (0.2 to 2.0 atmospheres), a thirty-five-fold alteration in the slope occurs and this change follows accurately the inverse relationship. It should be remarked that, when a sufficiently low gas pressure is achieved so that evaporation from the surface of the sphere rather than diffusion across a boundary layer is rate-controlling, the foregoing relationship between slope and pressure should be invalid. In this instance, the Langmuir equation for evaporation into vacuum[14,15] may be invoked to obtain the steady-state rate of mass transported to the neck as was done by Kingery and Berg.[4]

Utilizing the sintering rate expression [Eq. (7)] and the experimental values of the slopes of x^3/a *versus* t plots, D/δ ratios were calculated and are compiled in

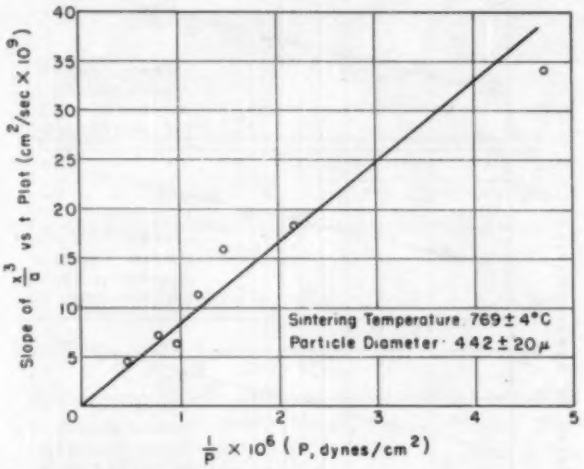

FIG. 4. Variation of the slope of x^3/a *vs* t plot with the reciprocal of the gas pressure at constant temperature and particle diameter.

Table I. The following numerical values were employed: $\rho = 1.97$ g cm^{-3}; $M_2 = 58.454$ g mole^{-1}; $R = 8.314 \times 10^7$ ergs (deg-mole)$^{-1}$; $\gamma = 189$ ergs cm^{-2} (theoretical value for (110) planes of NaCl due to Shuttleworth[16]).

The values of the diffusion coefficient for sodium chloride vapor listed in Table I were computed with the simple assumption that the vapor is nonpolar and obeys a Lennard-Jones (6–12) intermolecular potential. Thus, these coefficients are probably correct only in order of magnitude because it is well established that sodium chloride vapor is a polar gas and should be considered to obey the more complex Stockmayer potential.[13] However, due to the complexity of evaluating multiple integrals of exponential functions with orientation dependent variables in the Stockmayer model, its use

[14] G. A. Sofer and H. C. Weingartner, Advances in Chem. Eng. **2**, 117 (1958).
[15] N. E. Cooke, Sc.D. thesis (Massachusetts Institute of Technology, Cambridge, Massachusetts, 1955).
[16] R. Shuttleworth, Proc. Phys. Soc. (London) **A62**, 167 (1949).

was not attempted here. Actually no calculations of transport properties using this model have appeared in the literature to date.[17] A further complication in any rigorous calculation of the diffusion coefficient of sodium chloride vapor in argon gas arises from the presence of polymeric species (36% dimers) in the sodium chloride vapor in equilibrium with the solid phase.[18,19]

The magnitude of the boundary layer thickness can be estimated from the data of Table I with the result that $\delta \sim 10^{-5}$ cm. In the theoretical model for evaporation and condensation due to Fuchs[8] and used by several investigators,[20–22] this boundary layer thickness should be of the same order of magnitude as the mean-free-path in the gas phase which, for the conditions of the experimental data of Table I, is indeed of the order of 10^{-5} cm. Thus, despite the shortcomings of the aforementioned method of calculating the diffusion coefficients, the proposed sintering model allows the prediction of boundary layer thicknesses consistent with Fuchs' theory.

It is noteworthy that the ratio x/δ which was assumed to be large in the derivation of the sintering rate expression [Eq. (7)] is estimated from the data of Table I to be in the range 50 to 500.

TABLE I. Values of D/δ computed from experimental data. (Total gas pressure = 1.46 atmospheres.)

Diffusion coeff. D_{21}, cm²/sec	Sintering temperature, °K	Expt. slope cm²/sec ×10⁹	Equil. vapor pressure p_s, dynes/cm²	D/δ cm/sec ×10⁻⁴
0.148	1003	0.93	0.74	1.85
0.149	1013	1.18	0.96	1.58
0.152	1023	1.04	1.25	1.38
0.159	1043	2.24	2.05	1.74
0.162	1056	2.05	2.80	1.34
0.165	1068	2.43	3.35	1.22

Examination of Table I also reveals that, at least over the limited temperature range covered by the present investigation, the D/δ ratio does not demonstrate any systematic variation with temperature and, indeed, is nearly of constant magnitude.

Assuming that the surface tension of solid sodium chloride is also invariant with temperature over the range of interest, the product of all terms in $K(T,P)$ of Eq. (8), exclusive of the vapor pressure of sodium chloride, is largely independent of temperature. That is, any observed variation in K with temperature in the present work should be a reflection of changes in the equilibrium vapor pressure of sodium chloride with temperature. The equilibrium vapor pressure of a condensed phase usually exhibits an Arrhenius behavior with temperature so that a straight line plot results when the vapor pressure, on a logarithm basis, is plotted against the reciprocal of the absolute temperature. Such a plot is presented in Fig. 5 for the present data, the plotted ordinate being the logarithm of the experimental K values instead of the equilibrium vapor pressure values. The heat of sublimation, estimated from this figure, is 51.2 kcal/mole which is in satisfactory agreement with a value of 52.5 kcal/mole obtained by direct experimental observation.[23]

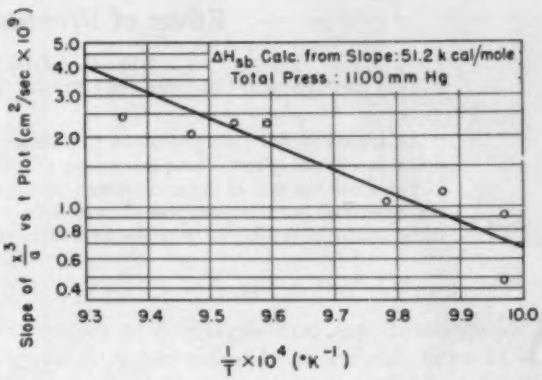

FIG. 5. Variation of the slope of x^3/a *vs* t plot (log scale) with the reciprocal of the temperature at a fixed total pressure.

V. SUMMARY

Sintering of sodium chloride at 700 to 800°C in an inert gas atmosphere occurs by an evaporation-condensation mechanism with the rate-controlling step in the material transport process assumed to be diffusion of sodium chloride vapor through a thin boundary layer adjacent to the condensing surface. Solutions for the rate law governing the sintering process and a scaling law, both calculated under the foregoing assumption, are in good agreement with the experimental observations of interface growth. The marked pressure-dependence of the empirical relationship between contact area and sintering time at a fixed temperature and particle size is also consistent with the assumption that the rate is governed by diffusion of the condensing species through a boundary layer.

The heat of sublimation for sodium chloride calculated from sintering rate data agrees favorably with direct measurements of this quantity. Using the derived rate expression, values of the boundary layer thickness are predicted to be of the order of one mean-free-path distance in the gaseous phase.

[17] P. E. Liley, *Thermodynamics and Transport Properties of Gases, Liquids and Solids* (American Society of Mechanical Engineers, New York, 1959), p. 43.
[18] J. Berkowitz and W. A. Chupka, J. Chem. Phys. **29**, 653 (1958).
[19] R. C. Miller and P. Kusch, J. Chem. Phys. **25**, 860 (1956).
[20] Bradley, Evans, and Whytlaw-Gray, Proc. Roy. Soc. (London) **A186**, 368 (1946).
[21] L. Monchick and H. Reiss, J. Chem. Phys. **22**, 831 (1954).
[22] R. S. Bradley, J. Colloid Sci. **10**, 571 (1955).
[23] O. Kubashewski and E. L. Evans, *Metallurgical Thermochemistry* (Butterworth-Springer Ltd., London, 1958).

Effect of Pressure on Phosphor Decay*

D. W. Gregg and H. G. Drickamer
Department of Chemistry and Chemical Engineering, University of Illinois, Urbana, Illinois

An apparatus has been developed to measure the effect of pressure to over 50 000 atmospheres on the decay rate of phosphors. Three manganese activated phosphors with exponential decay curves were studied. In two cases the rate of decay decreased, in the third case it increased. A tentative explanation is offered. An hexagonal ZnS:Cu phosphor showed little pressure effect to 40 000 atmospheres at which pressure it transformed irreversibly to the cubic form with a sharp increase in decay rate and a large decrease in intensity.

AN apparatus has been developed to measure the effect of pressure on phosphor decay. It has been operated to 52 000 atmospheres, and, under favorable conditions, is capable of considerable extension of the pressure range. The high-pressure bomb and press is the same as that used for spectroscopic studies.[1,2] The press is incorporated with a shutter system as shown in Fig. 1. The shutters are aluminum disks 13 in. in diameter cut as indicated in the figure, and rotated on a common shaft. A rubber wheel on the shaft makes a friction contact with a fly wheel turned by a 1/12 *hp* motor. The rpm can be adjusted by sliding the rubber wheel to different points on the radius of the fly wheel. The entire setup is enclosed to prevent light leak.

The light source is a BH-6 Mercury lamp which is focused on the bomb window with appropriate lenses. The phosphor output is focused on a 1*P*21 photomultiplier tube. The tube output goes to a Tektronix 122 Preamplifier, then to a Tektronix 545 Oscilloscope. The decay curves were photographed with a Polaroid type 2620 camera. The transparencies were projected on a screen to permit more accurate measurement of the decay. Six to eight pictures were taken at each pressure, and each material was run with at least 2–3 separate loadings. In order to minimize shear effects, which are particularly serious with ZnS phosphors, the samples were suspended in Canada Balsam which was inserted in a hole drilled in the NaCl pressure transmitting "fluid."

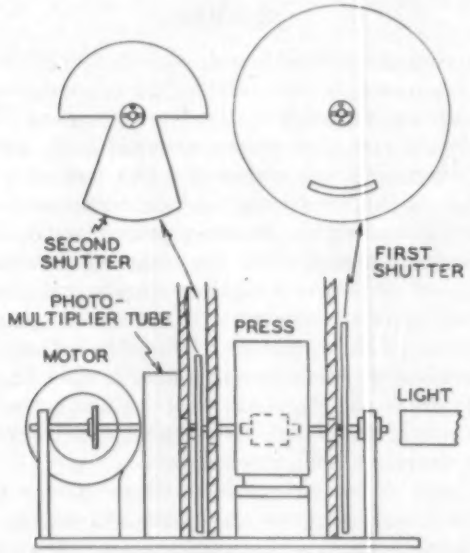

FIG. 1. Schematic diagram of high-pressure apparatus for decay studies.

RESULTS

Data were obtained on three manganese activated phosphors with substantially time independent exponential decays. These were Bureau of Standards numbers 1030, 1028, and 1025, which had compositions $(MgO)_x(As_2O_5)_y$:Mn, $ZnSiO_4$:Mn, and $Zn_3(PO_4)_2$:Mn. Plots of decay time *versus* pressure are shown in Fig. 2–4. In all cases the decays were reversible with pressure within the accuracy of the measurements. For phosphors 1030 and 1028 the decay constant increased by

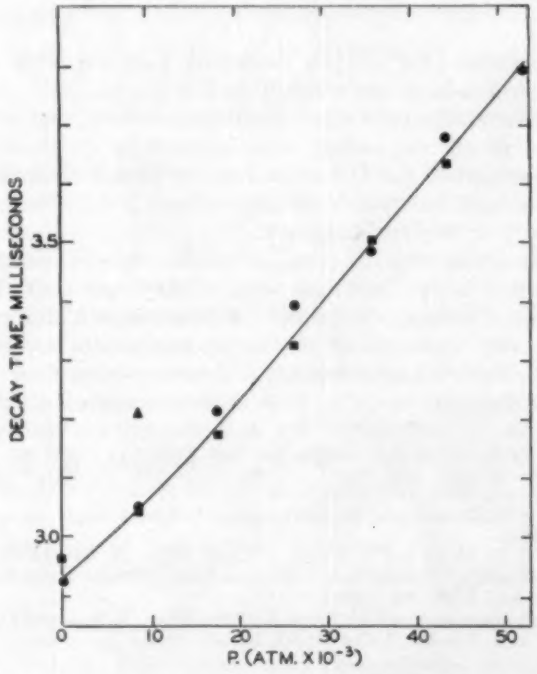

FIG. 2. Decay time *vs* pressure for $(MgO)_x(As_2O_5)_y$: Mn (1030).

* This work was supported in part by U. S. Atomic Energy Commission Contract, Chemical Engineering Project 5.

[1] Fitch, Slykhouse, and Drickamer, J. Opt. Soc. Am. 47, 1015 (1957).

[2] T. E. Slykhouse and H. G. Drickamer, J. Phys. Chem. Solids 7, 210 (1958).

40–50% in 50 000 atmospheres (i.e., the rate of decay decreased). For 1025 (the $Zn_3(PO_4)_2$ phosphor) the decay constant decreased with pressure (i.e., the rate of decay increased).

A tentative possible explanation can be offered as is illustrated in Fig. 5. These constitute plots of energy *versus* a configuration coordinate for the ground and excited states similar to those of Leverenz.[3] The configuration coordinate presumably is related to some characteristic dimension of the system. There are two factors which affect the location of the minimum in the excited state relative to that in the ground state. The higher energy tends to move the minimum to larger values of X (configuration coordinate). On the other hand, the fact that the manganese ion has at least partially lost an electron tends to bind the neighboring anions more tightly and move the minimum to smaller X. The minimum in the excited state may thus occur on either side of the ground-state minimum [Fig. 5(a) or 5(b)]. Let us assume (perhaps rashly) that the excited state always compresses more than the ground state. The rate of decay depends on the overlap between ψ_1 and ψ_2. The decays are presumed to be vertical (Franck-Condon) processes. In case 5(a) where the excited state minimum occurs outside the ground state minimum, the effect of pressure in our picture will be to increase the overlap and decrease the decay constant, i.e., to cause the phosphor to decay faster. This is so because the ground-state level ψ_1 to which the phosphor decays is more concentrated at high pressure. In case 5(b) where the excited state minimum occurs inside the ground-state minimum, the opposite effect would obtain. This explanation is purely speculative, but worthy of consideration.

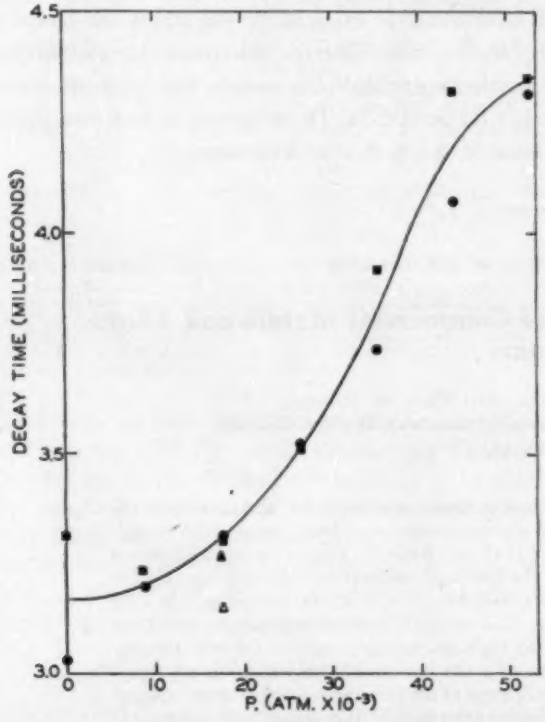

Fig. 3. Decay time *vs* pressure for Zn_2SiO_4:Mn (1028).

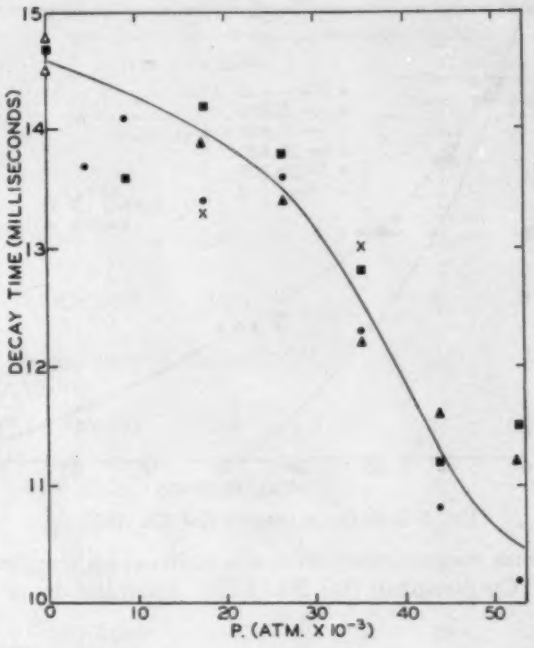

FIG. 4. Decay time *vs* pressure for $Zn_3(PO_4)_2$:Mn(1025).

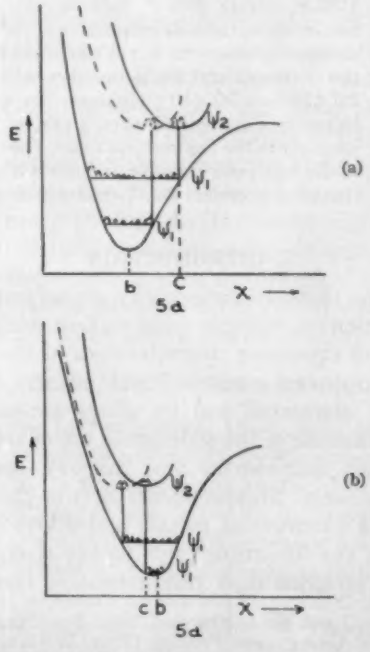

FIG. 5. Energy *vs* interionic distance: Mn^{++} in solid phosphor.

[3] H. W. Leverenz, *Luminescence of Solids* (John Wiley & Sons, Inc. New York, 1950).

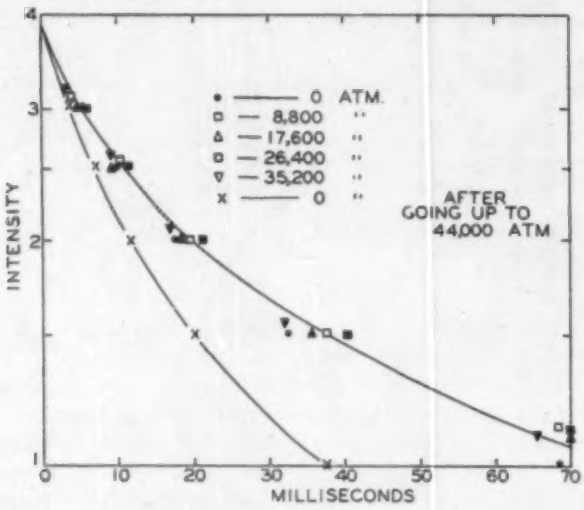

FIG. 6. Intensity *vs* pressure ZnS:Cu (1020).

Some measurements were also made on an hexagonal ZnS:Cu phosphor (BS No. 1022). Since the decay is not a simple exponential, no characteristic time can be given, but decay curves are shown in Fig. 6. The rate of decay was substantially independent of pressure to 35 000 atmospheres. In the neighborhood of 40 000 atmospheres there was an apparent abrupt increase in the decay rate accompanied by a large decrease in intensity. The rate at high pressure was difficult to reproduce because of low intensity. This change of decay rate was irreversible, as the rate changed only slightly upon returning to one atmosphere pressure. X-ray powder patterns of the material before and after pressurizing showed that the hexagonal crystal had been converted substantially completely to the cubic (zincblende form). A pressure induced transition of this kind would be expected as the stable low-temperature form is cubic. Some measurements were attempted on another cubic ZnS:Cu sample, but intensities were too low for good data. There seemed to be a measurable increase in decay rate with pressure.

JOURNAL OF APPLIED PHYSICS VOLUME 31, NUMBER 3 MARCH, 1960

Low-Temperature Transport Properties of Commercial Metals and Alloys. II. Aluminums

ROBERT L. POWELL, WILLIAM J. HALL, AND HANS M. RODER
Cryogenic Engineering Laboratory, National Bureau of Standards, Boulder, Colorado

(Received October 19, 1959)

The thermal conductivity, electrical resistivity, Lorenz number, thermoelectric force, and thermoelectric power are given in the temperature range 4–120°K for ten aluminums and aluminum alloys: high-purity, 1100-F, 1100-O, 3003-F, 2024-T4, 5052-O, 5083-O, 5086-F, 5154-O, and 6063-T5. Four of the samples show a maximum in thermal conductivity, the others do not. For the four high-thermal conductivity samples the separate components in the electronic thermal resistivity are resolved; for the others, components in both the electronic and the lattice thermal resistivities are given. The residual electrical resistivities vary from 2.5×10^{-9} to 3.2×10^{-8} ohm cm. The Lorenz numbers for the high-conductivity samples fall considerably below the Sommerfeld value 2.44×10^{-8} watt-ohm/°K²; those for the low-conductivity samples are somewhat above the Sommerfeld value. The thermoelectric power of some of the the alloys is positive with respect to the high-purity sample, for others it is negative. The various properties, methods of analysis, and separation of components are discussed in detail.

I. INTRODUCTION

DATA on thermal conductivity are necessary for the selection of suitable construction materials and prediction of operating characteristics of low-temperature apparatus used in research and industry. Values for commercial aluminum and its alloys are particularly important because of the widespread use of those metals in large-scale commercial and military storage and transport vessels. Measurements of the thermal conductivity of commercial metals and alloys that were reported in the literature prior to the spring of 1954 have been included in a comprehensive compilation.[1] Previous reports on aluminum or its alloys include the work of de Nobel,[2] Andrews *et al.*,[3] Powers *et al.*,[4] and Rosenberg[5] on pure aluminum; and the work of Mannchen,[6] de Nobel,[2] and Powers *et al.*[7] on aluminum alloys.

Some of the experimental results presented in this paper were reported in the Fifth (1957) International

[1] R. L. Powell and W. A. Blanpied, Natl. Bur. Standards Circ. No. 556 (U. S. Government Printing Office, Washington, D. C., 1954).

[2] J. de Nobel, Physica **17**, 551 (1951).

[3] Andrews, Webber, and Spohr, Phys. Rev. **84**, 994 (1951).

[4] Powers, Schwartz, and Johnston, Technical Report 264-5, Cryogenics Laboratory, Ohio State University, 1951 (unpublished).

[5] H. M. Rosenberg, Phil. Trans. Roy. Soc. (London) **A247**, 441 (1955).

[6] W. Mannchen, Z. Metallkunde **23**, 193 (1931).

[7] Powers, Ziegler, and Johnston, Technical Report 264-7, Cryogenics Laboratory, Ohio State University, 1951 (unpublished).

TABLE I. Physical and chemical specifications for aluminums and aluminum alloys.

Sample	Composition[a] (weight percent)	Average grain size[b,c] mm		Hardness[b] Diamond point	
		Long.	Trans.	Long.	Trans.
Single crystal	Johnson-Matthey JM 340 99.995% pure (originally).	single crystal		...	...
1100-F	Si, 0.13; Cu, Ga, Fe, Mg, V 0.1; Cr 0.02; Pb, Mn, Sn, Ti 0.01; Ca, Zr 0.001.	0.024×0.008	0.012	24	21
1100-O	Fe 0.41; Si 0.22; Cu, Ga, Mg, Mn 0.1; Cr; Pb, Ti, V, Zn 0.01; Ca, Zr 0.001; Bi 0.0001.	0.040×0.032	0.036	11	13
3003-F	Mn* 1.23; Fe 0.48; Si 0.15; Cu, Ga, Mg 0.1; Cr 0.02; Ga, Ti, V, Zn 0.01; Bi, Pb, Zr 0.001.	0.016×0.008	0.012	25	27
2024-T4	Cu* 4.58, Mg* 1.70; Ga, Fe, Mn*, Si, V, Zn 0.1; Cr 0.05; Sn, Ti 0.01; Ca, Ag, Zr 0.001.	0.080×0.052	0.048	66	66
5052-O	Mg* 2.46; Cr* 0.22; Cu, Ga, Fe, Mn, Si, Zn 0.1, Ti, V 0.01; Ca, Zr 0.001.	0.056×0.032	0.04	31	24
5083	Mg* 4.44; Mn* 0.7, Cr, Fe, Si 0.1; Cu 0.04.	0.74 ×0.21	0.54 ×0.14	21	20
5086	Mg* 4.10; Mn* 0.51; Fe 0.28, Cr, Si, Zn 0.1; Cu 0.07, Ti 0.02.	0.061×0.022	0.086×0.020	25	18
5154-O	Mg* 3.32; Cr* 0.21; Cu, Fe, Mn, Si 0.1; Ti, V, Zn, Zr 0.01; Ca, Pb 0.001.	0.036×0.028	0.032	40	33
6063-T5	Mg* 0.65, Si* 0.38; Ga, Fe, Mn 0.1; Cr, Cu, Ti, V, Zn 0.01; Ca, Pb, 0.001.	0.052×0.048	0.052	29	30

[a] The analyses on 1100-F, 1100-O, 3003-F, 2024-T4, 5052-O, 5154-O, and 6063-T5 were performed by Herbert M. Ochs of Denver, Colorado. The analyses on 5083 and 5086 were supplied by R. D. Olleman of Kaiser Aluminum and Chemical Corporation. The elements marked with an asterisk* were deliberately added for alloying purposes, the other elements were incidental impurities.
[b] The photomicrographs, grain size determinations, and hardness tests were performed by R. P. Reed and R. L. Greeson of this laboratory.
[c] The 5083 and 5086 alloys were etched with a 49% CH_3OH, 49% H_2O, 2% HF solution; the 2024-T4 alloy, with Keller's dilute etch, HNO_3, HF, and HCl; and the rest, with a ½% HF solution.

Conference on Low Temperature Physics and Chemistry[8] and the 1957 Cryogenic Engineering Conference.[9] In addition to the thermal conductivity data obtained for practical applications, concurrent measurements were made on the electrical conductivity and thermoelectric force. Detailed analyses of the three properties help to clarify the general phenomena of electronic transport processes in aluminum and its alloys.

II. APPARATUS

A detailed description of the apparatus and measurement techniques has been previously published,[10] and a summary description of the apparatus was included in the first article in this series.[11] The method of determining thermal conductivity by axial heat flow through a long cylindrical sample is used.

Since the previous publications, the apparatus has been modified to allow simultaneous measurements of electrical resistance and thermoelectric force. Wires of commercial purity copper magnet wire are connected electrically to the top and bottom thermocouple holders, approximately seven inches apart. Electrical current leads are connected to the ends of the sample. The thermoelectric force of the sample rod relative to the commercial purity copper is determined by measuring the potential difference between the two copper wires when no electrical current is flowing through the sample. The temperatures of the two contact points are determined by the gold-cobalt *vs* copper thermocouples that are connected thermally, but not electrically, to the thermocouple holders. The electrical resistance of the sample is determined by measuring the potential drop across the same two wires when a measured current is flowing through the sample. The thermoelectric force is subtracted from the total potential drop to obtain the potential drop resulting from the electrical current. The calculated values for both the electrical resistance and thermoelectric force have a scatter of about 2%.

III. SAMPLE SPECIFICATIONS

Aluminums and aluminum alloys were selected that are most commonly utilized in the construction of low-temperature engineering equipment. For the same reason each sample was tested in the usual fabricated condition or with the standard anneal or heat treatment indicated. However, to help specify each sample more concretely, auxiliary measurements included the chemical analysis, grain size, and hardness. The specifications for each sample are included in Table I. The primary

[8] *Low Temperature Physics and Chemistry*, edited by Joseph R. Dillinger (University of Wisconsin Press, Madison, Wisconsin, 1958), Paper XVI-1, p. 389.
[9] *Proceedings of the 1957 Cryogenic Engineering Conference*, edited by K. D. Timmerhaus (University of Colorado, Boulder, Colorado, 1958), Paper G-6, p. 408.
[10] Powell, Rogers, and Coffin, J. Research Natl. Bur. Standards **59**, 349 (1957).
[11] Powell, Roder, and Rogers, J. Appl. Phys. **28**, 1282 (1957).

additives to the aluminum were determined by chemical quantitative analysis; the minor impurities were determined by spectrographic analysis. The grain sizes in the longitudinal and transverse directions were obtained from 250× photomicrographs. Hardness measurements were made on plastic mounted specimens with a pyramid hardness testing machine using a one kilogram load for all samples, except the 2024-T4, 5052-O, and 6063-T5, where a five kilogram load was used. All of the commercial samples are wrought alloys.

A. Single Crystal, High-Purity

The rod was made from Johnson-Matthey stock by Horizons, Inc., Cleveland, Ohio. Apparently the crystal absorbed impurities during the crystallization or later during the fabrication at this laboratory because the residual electrical resistivity was not as low as one would expect from a crystal of 99.995% purity. The rod was supplied with about 3.68 mm diameter and was ground down to 3.66 mm at this laboratory. Chemical etching after the reduction in diameter indicated that the material was still a single crystal. After the last fabrication the rod was annealed in vacuum at about 400°C for two hours. The orientation of the single crystal was determined by Horizons, Inc. The [001] line was inclined 6° to the axis of the rod; the [011] line, 40°; and the [111] line, 50°.

B. Commercially-Pure Aluminum, 1100-F

This sample and all of the remaining alloys, except the 5083 and 5086, were supplied by R. L. Horst, Chemical Section, Sales Development Division, Aluminum Company of America. The rods of this and the following item, 1100-O, were turned down and drawn to the final diameter, 3.66 mm, from a flat sheet of about $\frac{1}{2}$-in. thickness. Photomicrographs showed inclusions of Si primary crystals.[12] The sample was in the commercial "as fabricated" condition. The 1100 aluminums have good formability and corrosion resistance and are therefore used in tubing for liquid lines, machine fittings that are to be welded, and in shells for dewars.[13]

C. Commercially-Pure Aluminum, 1100-0

This sample had significantly more impurities than the 1100-F one. In addition to Si primary crystals, $FeAl_3$ inclusions were also observed. After fabrication the rod was annealed in vacuum for one hour at 350°C.

D. Alloy 3003-F

The sample rods of this alloy and all of the following items, except 6063-T5, were turned and then drawn down to 3.66-mm diameter from oversized commercial rods supplied by the manufacturers. Photomicrographs showed inclusions of Si, $MnAl_6$, $FeAl_3$, and $(MnFe)Al_6$ peritectic. The measured sample was in the commercial "as fabricated" condition. The characteristics and uses of this alloy are quite similar to the ones for the 1100 alloys, except that the 3003 alloy has slightly greater structural strength.

E. Alloy 2024-T4

Inclusions of $CuAl_2$ and $MnAl_6$ were observed in this alloy. The added magnesium was in solid solution since up to 1.9 weight percent of magnesium is soluble in the alpha phase of aluminum.[14] The commercial rod was supplied in the "T-4" condition, solution heat-treated. This alloy is noted for its high strength and is therefore used in structural members and in baffle plates within Dewars.

F. Alloy 5052-0

Inclusions of $CrAl_7$, Si, and possibly $MnAl_6$ were observed in this alloy. The main inclusion, however, was the extremely complex β phase of (MgAl) with an approximate composition of Mg_5Al_8.[15] The sample was annealed in vacuum for one hour at 350°C after the last fabrication. The 5052 alloys have good corrosion resistance, high fatigue strength, and a moderate static strength. They are used in the inner and outer cylinders for fluid tanks and in tubing.

G. Alloy 5083-0

This sample and the 5086 alloy were supplied by R. D. Olleman, Kaiser Aluminum and Chemical Corporation. Photomicrographs showed inclusions of β phase (Mg_5Al_8), $MnAl_6$, and possibly Si, Mg_2Si, $CrAl_7$, and $(FeMn)Al_6$. The crystal grains were very large and also showed marked elongation even in the transverse direction. After fabrication the rod was annealed in vacuum for one hour at 350°C. Both 5083 and 5086 alloys are high-strength weldable magnesium-aluminums that are used for shells and structural members in Dewars.

H. Alloy 5086-F

Inclusions were observed of β phase (Mg_5Al_8), $FeAl_3$, $MnAl_6$, $(MnFe)Al_6$ and either Si or Mg_2Si. The crystal grains showed marked elongation even in the transverse direction. The sample was tested in the commercial "as fabricated" condition.

[12] Photomicrographs and discussions of inclusions in aluminum alloys are given by L. F. Mondolfo, *Metallography of Aluminum Alloys* (John Wiley & Sons, Inc., New York, 1943).

[13] More lengthy and detailed discussions of the uses, fabrication techniques, heat treatments, phase diagrams and general properties of most aluminum alloys are included in the *Metals Handbook* (American Society for Metals, Cleveland, Ohio), 1948 edition, and in company product information books such as those published by Aluminum Company of America and Kaiser Aluminum and Chemical Sales, Inc.

[14] Phase diagrams for many aluminum binary alloys are given in the extensive compilation and review by Max Hansen, *Constitution of Binary Alloys* (McGraw-Hill Book Company, Inc., New York, 1958), second edition. Diagrams for ternary alloys are given in references 12 and 13.

[15] H. Perlitz, Chalmers Tekniska Högskolas Handlingar **50** (1946) reported the structure to be a complex face-centered cube with 1166 atoms to a unit cube. See also W. B. Pearson, *A Handbook of Lattice Spacings and Structures of Metals and Alloys* (Pergamon Press, New York, 1958).

I. Alloy 5154-0

This sample contained inclusions of β phase (Mg_5Al_8), $CrAl_7$, and a small amount of $FeAl_3$ and $MnAl_6$. After fabrication the rod was annealed in vacuum for one hour at 350°C. This alloy is quite similar in physical properties and uses to the 5083 and 5086 alloys except that it has somewhat less strength.

J. Alloy 6063 T-5

This alloy containing deliberate small additions of magnesium and silicon was quite similar to the "J-51" alloy studied by Powers *et al.*[4] The sample rod was turned down and drawn to the final diameter, 3.66 mm, from a flat sheet of about ½-in. thickness. Photomicrographs showed inclusions of Si primary crystals and small amounts of $FeAl_3$ and $MnAl_6$. The magnesium was in solid solution. The plate was supplied in the "T-5" condition, precipitation heat-treated.[13] This material is used for extrusions, tubing, and structural reinforcement on Dewar walls.

IV. EXPERIMENTAL RESULTS AND DISCUSSION

A. Thermal Conductivity

Several articles have been published recently that give summaries of the experimental and theoretical developments of the thermal conductivity of metals.[16–18] Therefore, only a brief review is given here, enough to allow a discussion of the methods of analysis and separation of conductivity components.

Two principal mechanisms are responsible for the low-temperature transport of heat in a metal. The first and most important is the electronic thermal conduction, the transport of thermal energy by the motion of conduction electrons. The second is the lattice thermal conduction, the transport by directional cooperative quantized vibrations (phonons) of the interacting lattice ions. For the pure aluminums and the dilute alloys, the lattice thermal conductivity is insignificant compared to the electronic thermal conductivity. However, for the alloys with several percent of additives the decrease of electronic thermal conductivity makes the lattice contribution significant, though still small compared to the electronic contribution. The total conductivity λ is approximately the sum of the electronic conductivity λ_e and the lattice conductivity λ_g, that is,

$$\lambda=\lambda_e+\lambda_g. \tag{1}$$

The electronic thermal conductivity λ_e is predominant in all of the samples measured. There are two main scattering processes that limit this electronic conductivity. The first is the scattering of conduction electrons by thermal vibrations of the lattice, as represented by the electron-phonon resistivity W_L a characteristic property for a given metal. This scattering is most important at intermediate and higher temperatures. The second process is the scattering of conduction electrons by imperfections (both impurity atoms and lattice defects), as represented by the electron-defect resistivity W_0. This scattering is most important at the lower temperatures. The total electronic thermal resistivity W_e, defined as the reciprocal of the total electronic thermal conductivity λ_e is assumed to be the sum of the two resistivities W_L and W_0 plus a deviation term W_{L0}; that is,

$$1/\lambda_e \equiv W_e = W_L+W_0+W_{L0}. \tag{2}$$

The deviation term is given by an expression of the form[19]

$$W_{L0}=(\alpha W_L W_0/\beta W_L+\gamma W_0), \tag{3}$$

where α, β, and γ are constants of order 1 and can be determined experimentally.

Both theoretical and experimental research have led to expressions for the magnitudes and temperature dependences of the electron-phonon and electron-defect resistivities:

$$\begin{aligned} &W_L=AT^n, && (n\approx 2 \text{ to } 3,\ T<40^\circ\text{K});\\ &W_L\approx \text{a constant}, && (\text{near room temperatures});\\ &W_0=B/T, && (\text{at all temperatures}). \end{aligned} \tag{4}$$

The constant A in the electron-phonon resistivity term is related to characteristic properties of the given metal; B in the electron-defect resistivity term is related to the amount of imperfections and residual electrical resistivity of the specific sample. Above 40°K the electron-phonon resistivity approaches a constant value, often labeled W_∞. The methods of analysis and techniques for separation of electronic components are outlined in a previous paper.[19]

In several of the aluminum alloys the lattice thermal conductivity λ_g is also measurable and the separate scattering components may be resolved. Klemens[20] has recently given a survey of lattice thermal conductivity in dielectrics and metals. For the samples of aluminum alloys reported in this paper there are three main processes that limit the lattice conductivity. The first process is scattering of the lattice waves by conduction electrons, as represented by phonon-electron resistivity W_E; the second is scattering by dislocations, the phonon-dislocation resistivity W_D, and the third is scattering by point imperfections, the phonon-point imperfection resistivity W_P. The first two processes will limit the lattice conductivity at the lower temperatures; the third, at higher temperatures.

The phonon-electron resistivity has approximately the same temperature dependence as the phonon-

[16] P. G. Klemens, *Handbuch der Physik* (Springer-Verlag, Berlin, 1956), Vol. 14, pp. 198–281.
[17] J. M. Ziman, Nuovo cimento Suppl. 7, 353 (1958).
[18] H. Jones, *Handbuch der Physik* (Springer-Verlag, Berlin, 1956), Vol. 19, pp. 227–315.
[19] Powell, Roder, and Hall, Phys. Rev. 115, 314 (1959).
[20] P. G. Klemens, *Solid State Physics*, edited by F. Seitz and D. Turnbull (Academic Press, Inc., New York, 1958), Vol. 7, pp. 1–98.

TABLE II. Thermal conductivity of several aluminums and aluminum alloys.[a]

Sample	Single crystal						1100-F					1100-O	6063-T5
Temp. (°K)	λ_e[b] watts cm °K	W_e[c] (exptl.)	W_L[c]	W_0[c]	W_{L0}[c]	W_e[c] (calc.)	λ_e[b] watts cm °K	W_e[c] (exptl.)	W_0[c]	W_{L0}[c]	W_e[c] (calc.)	λ_e watts cm °K	λ_e watts cm °K
4	3.58	0.279	0.0001	0.272	0.0001	0.272	0.554	1.80	1.75		1.75	0.459	0.351
6	5.42	0.184	0.0003	0.182	0.0002	0.183	0.823	1.21	1.17		1.17	0.688	0.522
8	7.22	0.138	0.0006	0.136	0.0004	0.137	1.107	0.903	0.875		0.876	0.918	0.697
10	8.95	0.112	0.0011	0.109	0.0008	0.111	1.395	0.717	0.700	0.001	0.702	1.145	0.868
14	11.8	0.0847	0.0027	0.0778	0.0019	0.0824	1.96	0.510	0.500	0.002	0.505	1.61	1.215
20	14.8	0.0676	0.0073	0.0545	0.0048	0.0666	2.70	0.370	0.350	0.005	0.362	2.28	1.70
24	15.8	0.0633	0.0120	0.0454	0.0059	0.0633	3.12	0.320	0.292	0.008	0.312	2.62	2.00
30	15.3	0.0654	0.0221	0.0363	0.0074	0.0658	3.58	0.279	0.233	0.014	0.269	3.04	2.35
40	12.0	0.0833	0.0482	0.0272	0.0079	0.0833	3.89	0.257	0.175	0.023	0.246	3.32	2.68
50	8.40*	0.119	0.090	0.0218	0.0073	0.119	3.78	0.264	0.140	0.030	0.260	3.31	2.76
60	6.02*	0.166	0.142	0.0182	0.0064	0.167	3.40	0.294	0.117	0.031	0.290	3.12	2.67
70	4.51	0.222	0.200	0.0156	0.0056	0.221	3.04*	0.329	0.100	0.030	0.330	2.83	2.52
80	3.70	0.270	0.251	0.0136	0.0050	0.270	2.74	0.365	0.087	0.028	0.366	2.57	2.34
100	2.88	0.347	0.332	0.0109	0.0040	0.347	2.38	0.420	0.070	0.024	0.426	2.27	2.13
120	2.57	0.389	0.377	0.0091	0.0034	0.389	2.23	0.448	0.058	0.020	0.455	2.12	2.06

[a] The equations for the separate terms are given in Eqs. (2), (3), and (4) in the text.
[b] The asterisks indicate interpolated values.
[c] W_e (exptl.) $=\lambda_e^{-1}$; W_L and W_0 are given by Eq. (4) in the text; W_{L0}, by Eq. (3); and W_e (calc.) by Eq. (2). The constants used in the equations are: (a) For W_L at and below 60°K, $A=2.03\times10^{-6}$, $s=2.72$. (b) For W_0: $B=1.09\pm0.01$ for single crystal; $B=7.00\pm0.05$ for 1100-F; $B=8.38\pm0.05$ for 1100-O; $B=11.23\pm0.12$ for 6063-T5. (c) For W_{L0}: $\alpha=\frac{1}{2}$, $\beta=1$, $\gamma=2$. All W are in units of cm °K/watt.

dislocation resistivity. Therefore, for one sample, the two scattering mechanisms may not be unambiguously separated. For annealed samples the two resistivities will be of about the same magnitude; for unannealed samples the dislocation resistivity will greatly outweigh the other. Below about 40°K the lattice conductivity can be represented by

$$1/\lambda_g \equiv W_g = W_D + W_E + W_P = (D+E)T^{-2} + P\,T; \quad (5)$$

above about 40°K the lattice conduction in these alloys can not be separated experimentally from the electronic conduction because the latter has a much greater magnitude.

The thermal conductivities of samples *a*, *b*, *c*, and *j* (Single crystal, 1100-F, 1100-O, and 6063-T5) are given in Fig. 1 and Table II. The thermal conductivity of sample *d*(3003-F) is also given in Fig. 1 for comparison. The calculated values of the electron-defect resistivity, W_0, and the deviation term, W_{L0}, are given in Table II for the single crystal and 1100-F samples. Curves for the calculated deviation term, W_{L0}, and the equivalent experimental term, $(W_e - W_L - W_0)$, are given in Fig. 2 for the same two samples. The values and graphs for the interaction terms for the other two samples are not given because the technique of separation of electric components is not applicable to alloys with more than about 1% additives or impurities.

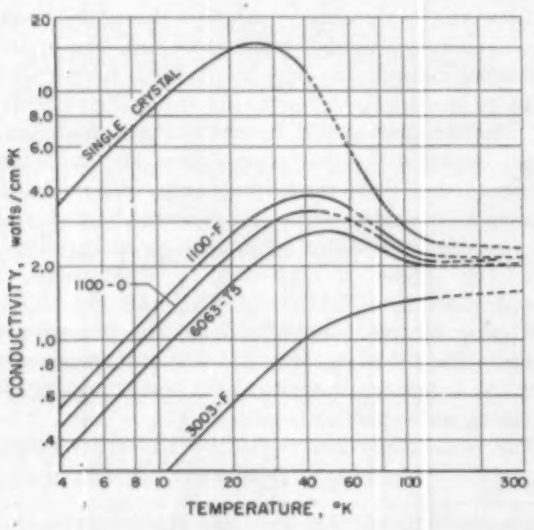

FIG. 1. Thermal conductivity of several aluminums and aluminum alloys. (The dashed parts of the curves indicate interpolated values.)

Several comments on the results can be given. The single crystal did not have a conductivity as expected,[3] probably because of impurities absorbed during the melting and annealing. The 1100-O sample had a lower conductivity than the 1100-F sample, in spite of the annealing, because of the greater amount of chemical impurities in the original stock. The values for the 6063-T5 alloy are almost identical (in the overlapping temperature ranges) with the values obtained by Powers *et al.*[4] for a J-51 alloy of similar composition. It should be specially noted that the temperature exponent in the electron-phonon term W_L is about 2.72 and not 2 as is often assumed. A similar exponent, 2.76, was obtained in our previous work on copper.[19]

The thermal conductivities of the alloy samples *d*, *e*, *f*, *g*, *h*, and *i* (3003-F, 2024-T4, 5052-O, 5083-O, 5086-F and 5154-O) are given in Fig. 3 and Table III. Below about 10°K the electron-imperfection resistivity is predominant in the electronic conductivity and the phonon-electron and -dislocation resistivities are predominant in the lattice conductivity. The separation of components for these low conductivity alloys can then be carried out in the following manner. A value for the electronic constant B, and a first approximation to the lattice constant $(D+E)$ may be obtained graphically

from a plot of (λ/T) *vs* T below 10°K. The resultant value for B is given in Table III and is used to estimate the electronic conductivities at all measured temperatures. However a small electron-phonon term must also be accounted for at the higher temperatures. The electronic conductivity is subtracted from the total conductivity to obtain the lattice conductivity contribution, λ_g, the values for which are given in Fig. 4.

It is seen that the lattice conductivity is about 10% or less of the total thermal conductivity. The values for the lattice constants, $(D+E)$ and P, obtained graphically from a plot of (λ_g/T) *vs* T^{-3} between 10 and 30°K, are given in Table III. The variation between this value of $(D+E)$ and the one obtained from the total conductivity by the method mentioned in the previous paragraph is about 5%. Theoretical values for the phonon-electron interaction resistivity W_E are not sufficiently accurate to allow a separation of the latter from the phonon-dislocation interaction resistivity W_D and thus obtain specific values for D and E. It is expected, however, that the phonon-dislocation term is the larger of the two in all of the alloys reported here.

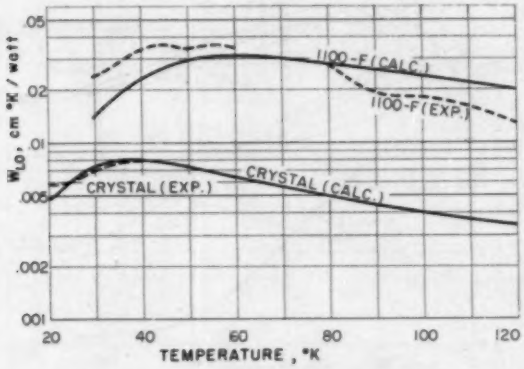

FIG. 2. Thermal resistivity deviation term W_{L0}. The term calculated from the theoretical Eq. (3) is given as a solid line; the equivalent experimental term is dashed.

B. Electrical Conductivity

Several lengthy review articles or books on the subject have been published in recent years,[17,18,21,22] so only very brief comments are given here. A discussion of the separation of components and scattering mechanisms for electrical conductivity would follow almost exactly the discussion given in Sec. A on the *electronic* thermal conductivity. The total electrical resistivity ρ is assumed to be the approximate sum of two separate resistivities, the intrinsic or electron-phonon resistivity ρ_L, and the residual or electron-imperfection resistivity ρ_0. In other words, Matthiessen's rule for electrical resistivity is

[21] D. K. C. MacDonald, *Handbuch der Physik* (Springer-Verlag, Berlin, 1956), Vol. 14, pp. 137–197.

[22] A. N. Gerritsen Handbuch der Physik (Springer-Verlag, Berlin, 1956), Vol. 19, pp. 137–226.

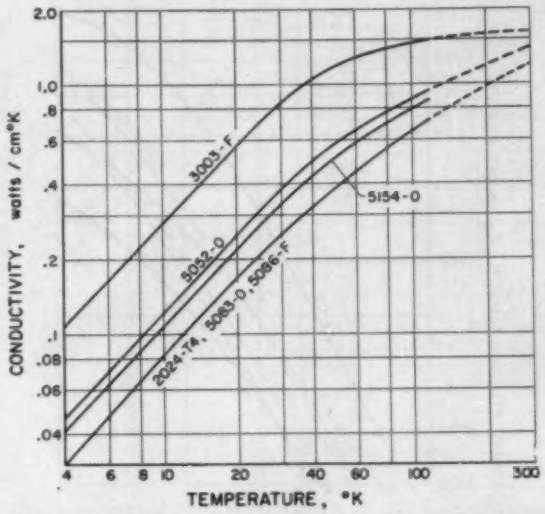

FIG. 3. Thermal conductivity of several aluminum alloys. (The dashed parts of the curves indicate interpolated values.) The values for the 2024-T4, 5083, and 5086 alloys are close enough together to be represented by one curve.

assumed to be approximately correct:

$$\rho \approx \rho_L + \rho_0. \tag{6}$$

The expressions for the temperature dependences of the intrinsic and residual terms have been found to be given approximately by

$$\begin{aligned} &\rho_L = \alpha T^n; \quad (n \approx 4 \text{ to } 5)\ T < 40°\text{K} \\ &\rho_0 = \beta \qquad \text{(constant)}. \end{aligned} \tag{7}$$

The electrical resistivities for seven of the samples are given in Fig. 5. Because of apparatus difficulties, values

TABLE III. Thermal conductivity of several aluminum alloys.[a]

Temp. (°K)	3003-F	2024-T4	5052-O	5083-O	5086-F	5154-O
4	0.107	0.0315	0.0452	...	0.0302	0.0412
6	0.163	0.0489	0.0698	0.0486	0.0469	0.0630
8	0.222	0.0661	0.0952	0.0669	0.0644	0.0857
10	0.282	0.0832	0.121	0.0852	0.0820	0.109
14	0.402	0.117	0.174	0.122	0.118	0.156
20	0.575	0.170	0.250	0.173	0.172	0.228
24	0.682	0.203	0.304	0.206	0.208	0.272
30	0.833	0.249	0.379	0.254	0.261	0.337
40	1.06	0.322	0.487	0.332	0.337	0.436
50	1.20	0.390	0.578	0.395	0.407	0.521
60	1.28	0.452	0.655	0.451	0.462	0.591
70	1.33	0.508	0.719	0.501	0.513	0.649
80	1.38	0.557	0.768	0.546	0.559	0.699
100	1.44	0.645	0.859	0.627	0.635	0.790
120	1.47	0.727	0.939	0.683	0.698	0.872
electronic constant B	39	135	94	141	141	101
lattice constants $(D+E)\times10^{-3}$	3.5	8.3	6.7	6.0	8.7	10.0
lattice constant P	0.4	1.5	0.5	1.0	0.6	0.6

[a] The equations for the separate terms are given in Eqs. (1), (2), (4), and (5) in the text. The units for thermal conductivity are watts/cm-°K.

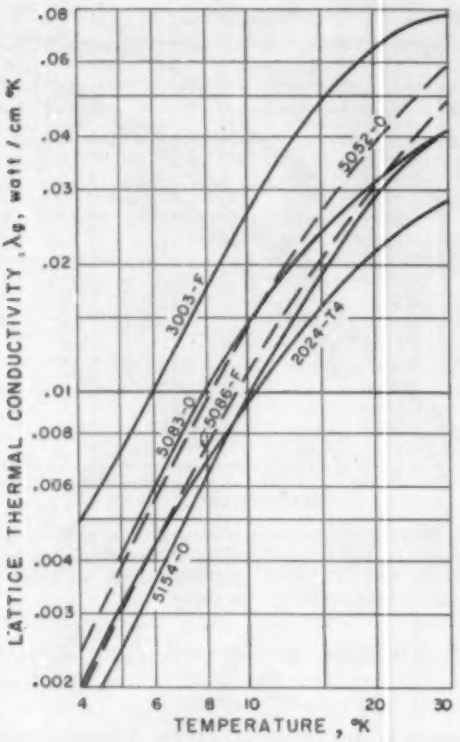

FIG. 4. Lattice thermal conductivity of several aluminum alloys. The values are obtained by subtracting the electronic term from the total thermal conductivity.

were not obtained for 1100-F, 3003-F, or 5083-O alloys. The intrinsic resistivity term ρ_L was found to vary approximately as $T^{4.2}$ rather than T^5 below 40°K. However, the exact temperature dependence of the

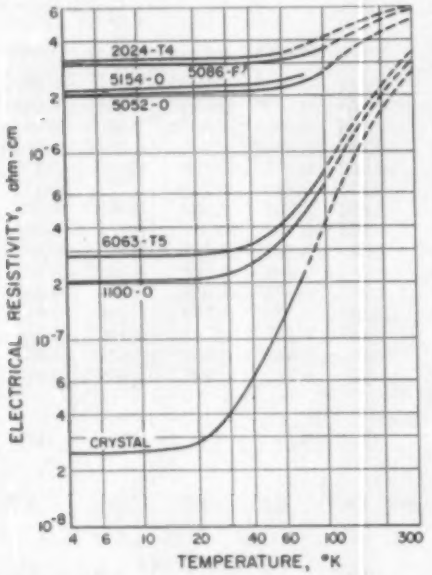

FIG. 5. Electrical resistivity of several aluminums and aluminum alloys. (The dashed parts of the curves indicate interpolated values.)

term will have to be determined in another more specialized and accurate apparatus.

C. Lorenz Ratio

The electrical resistivity may be compared to the *electronic* thermal resistivity by means of the Wiedemann-Franz-Lorenz law

$$\rho = LW_eT, \tag{8}$$

where L is the Lorenz number, assumed to be a fundamental constant given by the Sommerfeld value

$$L = (\pi^2/3)(k/e)^2 = 2.44\times10^{-8}(\text{watt-ohm/°K}^2).$$

The Lorenz numbers given in Fig. 6 are slightly different in that they express the ratios of the electrical resistivities to the *total* thermal resistivities. However, the extrapolated values L_0 should represent ratios of electronic terms only because the lattice contribution to

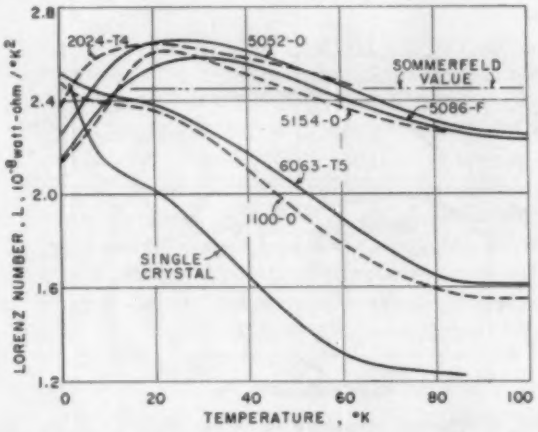

FIG. 6. Lorenz number of several aluminums and aluminum alloys. The Sommerfeld theoretical value is 2.44×10^{-8} watt-ohm/°K².

the total thermal conductivity is greatly reduced at the lowest temperatures. Most of the variations and errors are caused by the uncertainties in the electrical resistivity values.

It is seen that the Lorenz numbers for the high-conductivity samples extrapolate to approximately the Sommerfeld value at 0°K, but fall considerably below it at higher temperatures. The behavior of the low conductivity alloys is different: the extrapolated 0°K value is appreciably lower than the Sommerfeld value, the values between about 10 and 60°K are higher, but above 60°K the values are again lower.

Kohler[23] showed that the Lorenz number should be constant if the conduction electrons were scattered elastically. That condition is approximately true at high temperatures and at very low temperatures where the residual term is predominant in the electrical resistivity. At intermediate temperatures the condition

[23] M. Kohler, Ann. Physik **40**, 601 (1941).

of elasticity no longer holds and the Lorenz number decreases considerably from the Sommerfeld value (if the lattice thermal conductivity is negligible). Any significant amount of lattice thermal conductivity will raise the Lorenz number above the value it would have had if only the electronic term in the thermal conductivity were considered.

Nearly all of the variations observed in the Lorenz numbers plotted in Fig. 6 can be explained, at least qualitatively, by the foregoing arguments. However, we do not have any reasonable explanation for the decrease of the Lorenz number below the Sommerfeld value for the low conductivity alloys in the temperature range below 10°K.

D. Thermoelectric Force and Power

There is comparatively very little literature on the thermoelectric forces for pure metals or for alloys not suitable as thermocouple elements. Both the quantitative and qualitative predictions of the standard theory for simple metals as outlined by Wilson[24] are in serious error. More recent general theoretical discussions of thermoelectric power have been given by Domenicali,[25] Domenicali and Otter,[26] ter Haar and Neaves,[27] Sondheimer,[28] and MacDonald.[29] Considerable improvement in the agreement between theoretical predictions and experimental measurements will probably be brought about by advances along two separate lines: (1) refinements in the "phonon-drag" concepts introduced by Gurevich[30] and recently calculated in detail by Bailyn,[31] and (2) progress in two-band model calculations as they pertain to aluminum and similar metals.[24,32]

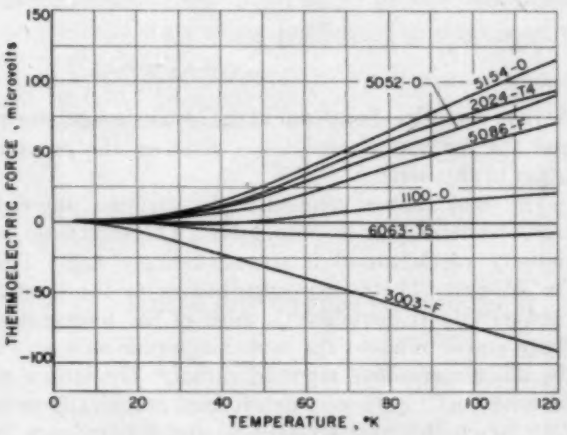

FIG. 7. Thermoelectric force of the aluminum alloys with respect to the high-purity sample. The low-temperature reference junction is 4°K.

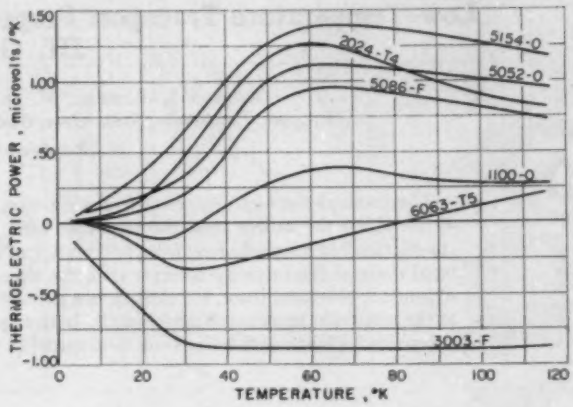

FIG. 8. Thermoelectric power of the aluminum alloys with respect to the high-purity sample.

For seven of the alloys the thermoelectric forces and powers with respect to the pure sample are given in Figs. 7 and 8, respectively. Crussard[33] has made measurements *at high temperatures* on several controlled alloys of aluminum and his work was discussed theoretically by Galt[34] and Friedel.[35] Our results are difficult to interpret because of the simultaneous presence in the samples of physical imperfections and several types of chemical impurities. However, they are in rough qualitative agreement with Crussard's results: the alloy with an appreciable amount of Mn(3003-F) shows the largest negative thermoelectric power and the alloys with Mg have a positive thermoelectric power.

V. ACKNOWLEDGMENTS

We would like to thank R. L. Horst of Aluminum Company of America and R. D. Olleman of Kaiser Aluminum and Chemical Corporation for supplying the samples and their commercial specifications; M. D. Bunch for assistance on some of the experimental runs; and J. L. Harden and E. F. Gibson for many of the calculations and preliminary graphs.

[24] A. H. Wilson, *Theory of Metals* (Cambridge University Press, Cambridge, 1953), second edition.
[25] C. A. Domenicali, Revs. Modern Phys. **26**, 237 (1954).
[26] C. A. Domenicali and F. A. Otter, Phys. Rev. **95**, 1134 (1954).
[27] D. ter Haar and A. Neaves, Proc. Roy. Soc. (London) **A228**, 568 (1955).
[28] E. H. Sondheimer, Proc. Roy. Soc. (London) **A234**, 391 (1956).
[29] D. K. C. MacDonald, Z. Phys. Chem. **16**, 310 (1958).
[30] L. Gurevich, J. Physics (Moscow) **9**, 477 (1945).
[31] M. Bailyn, Phys. Rev. **112**, 1587 (1958).
[32] E. J. Moore, Australian J. Phys. **11**, 235 (1958).
[33] C. Crussard, *Report on a Conference on Strength of Solids* held at H. H. Wills Physical Laboratory, July 7–9, 1947 (London, Physical Society, 1948), p. 119.
[34] J. K. Galt, Phil. Mag. **40**, 309 (1949).
[35] J. Friedel, J. Phys. Rad. **14**, 561 (1953).

Low-Temperature Transport Properties of Commercial Metals and Alloys. III. Gold-Cobalt

ROBERT L. POWELL, M. D. BUNCH, AND EDWARD F. GIBSON
Cryogenic Engineering Laboratory, National Bureau of Standards, Boulder, Colorado

(Received October 19, 1959)

The thermal conductivity, electrical resistivity, and Lorenz number are given in the temperature range 4–100°K for the widely used thermocouple wire, gold-2.1 atomic percent cobalt alloy. The total thermal conductivity is relatively low: from 0.01 watt/cm°K at 4°K to 0.23 at 100°K. The lattice contribution to the total thermal conductivity is larger than the electronic contribution. The electrical resistivity is nearly independent of temperature, but does have a definite minimum of about 1.20×10^{-5} ohm-cm at 30°K. Because of the relatively large contribution of the lattice term to the total thermal conductivity, the Lorenz number is considerably above the electronic Sommerfeld value, 2.44×10^{-8} watt-ohm/°K².

I. INTRODUCTION

DATA on the thermal conductivity and electrical resistivity of thermocouple wires used at low temperatures are important for the proper design of cryogenic apparatus. These properties have been measured for many thermocouple metals, e.g., copper,[1,2] constantan,[3,4] silver −0.37 atomic percent gold,[5] but not for the important thermocouple alloy, gold−2.1 atomic percent cobalt. This report presents results on the thermal and electrical conductivity of the latter alloy. A detailed calibration of thermoelectric power and force of the same material will be published elsewhere.[6] A discussion of the conduction apparatus and techniques has been published previously[7] and will not be given here.

The prepared sample was obtained from Sigmund Cohn Corporation, Mt. Vernon, New York. It was in the hard-drawn condition (the same as the thermocouple wire) because the cobalt is in unstable solution and will precipitate out if annealed or even heated above 100°C.

II. EXPERIMENTAL RESULTS AND DISCUSSION

A. Thermal Conductivity

The total thermal conductivity of the sample, given in Fig. 1, consists of two additive conductivity terms, the electronic λ_e, and the lattice λ_g. For this alloy the predominant term in the electronic thermal resistivity W_e is the electron-imperfection interaction W_0, given by the relation

$$(1/\lambda_e)\equiv W_e\approx W_0=(B/T). \quad (1)$$

Similarly the predominant terms in the lattice thermal resistivity W_g are the phonon-dislocation interaction W_D, the phonon-conduction electron interaction W_E, and the phonon-point imperfection interaction W_P, given by

$$(1/\lambda_g)\equiv W_g\approx W_D+W_E+W_P = DT^{-2}+ET^{-2}+PT. \quad (2)$$

A more complete discussion of the separate components and the method of analysis is given in the previous paper of this series.[8]

The total thermal conductivity is very low, the electronic contribution is even lower. The electronic resistivity coefficient B is correspondingly high: 1100 cm°K²/watt. The lattice contribution to the thermal conductivity is dominant in most of the temperature range and is of about the same magnitude as it was in the aluminum alloys reported earlier.[8] The lattice resistivity coefficients were determined graphically to be 2.8×10^3 cm°K²/watt for $(D+E)$ and 0.4 cm/watt for

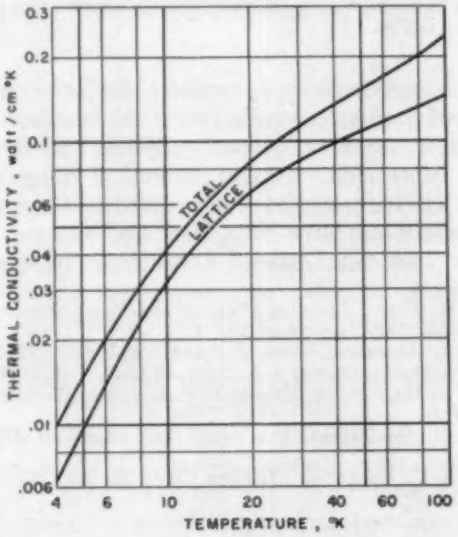

FIG. 1.

[1] Powell, Roder, and Rogers, J. Appl. Phys. **28**, 1282 (1957).
[2] T. M. Dauphinee and H. Preston-Thomas, Rev. Sci. Instr. **25**, 884 (1954).
[3] R. Berman, Phil. Mag. **42**, 642 (1951).
[4] For a review of thermal conductivities of metals and alloys see R. L. Powell and W. A. Blanpied, National Bureau of Standards Circular No. 556 (U. S. Government Printing Office, Washington, D. C., 1954).
[5] E. Grüneisen and H. Reddemann, Ann. Physik **20**, 843 (1934).
[6] Bunch, Powell, and Corruccini, J. Research Natl. Bur. Standards **63A**, (to be published).
[7] Powell, Rogers, and Coffin, J. Research Natl. Bur. Standards **59**, 349 (1957).
[8] Powell, Hall, and Roder, J. Appl. Phys. **31**, 496 (1960).

P. It is unusual for a noble-metal alloy to have such a large fraction of the thermal conductivity be due to the lattice term. The low electronic conductivity is undoubtedly caused by the large inter-band scattering of conduction electrons by the cobalt ions.

B. Electrical Resistivity and Lorenz Number

The electrical resistivity and Lorenz number for this sample are given in Fig. 2. Although the electrical resistivity does not vary appreciably with temperature, it does have a definite minimum at about 30°K. Similar results have been observed many times in more dilute noble metal-iron group alloys.[9,10]

The Lorenz number L, defined by

$$\rho = LWT, \tag{3}$$

is considerably above the electronic Sommerfeld value, 2.44×10^{-8} watt-ohm/°K². This is another indication that the total thermal conductivity consists primarily of the lattice contribution. The maximum of about 5.2 at 15°K occurs where the lattice contribution is the largest fraction of the total; the approach to the Sommerfeld value at the highest and lowest temperatures indicates the increasing importance of the electronic contribution at the extremes of temperature investigated during this work.

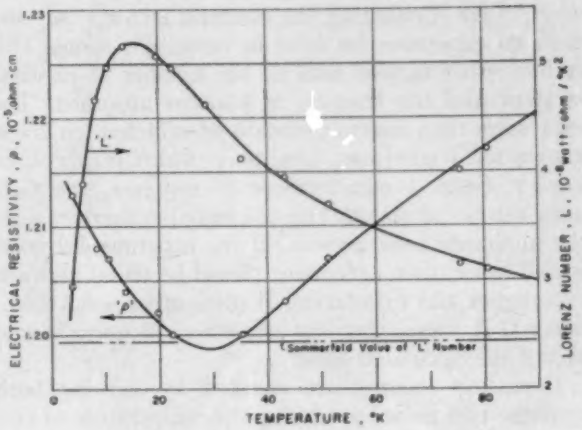

FIG. 2.

[9] D. K. C. MacDonald, *Handbuch der Physik* (Springer-Verlag, Berlin, 1956), Vol. 14, pp. 137-197.
[10] A. N. Gerritsen, Physica **25**, 489 (1959).

JOURNAL OF APPLIED PHYSICS VOLUME 31, NUMBER 3 MARCH, 1960

Noise and Signal Response in Lead Sulfide Photoconductive Films*

H. E. SPENCER†
Eastman Kodak Company, Navy Ordnance Division, Rochester, New York
(Received July 15, 1959)

Experimental noise and signal response data of two lead sulfide photoconductive films have been obtained as a function of frequency and radiation wavelength at temperatures ranging from about 25°C to −173°C. Good agreement between experiment and a theory proposed by Petritz is found. The theory is used in such a way that correlations between noise and response may be made independent of the temperature. The measured time constants enter into the correlations only indirectly; they are necessary only to extrapolate data measured at a given frequency to some lower frequency. Generation-recombination (G-R) noise predominates at all temperatures. Time constants measured by noise and by response agree. The role of absorbed ambient photons is described. These photons are important at the lower temperatures. The concentrations of the majority carriers (holes) and their mobility as derived from signal data are listed.

INTRODUCTION

NOISE in lead sulfide films caused by fluctuations in carrier concentration has been studied in considerable detail.[1-5] This noise is called generation-recombination (G-R) noise and is necessarily present because of its fundamental nature. At times, it is masked because the excess $(1/f)$ noise or the Johnson noise exceeds the G-R noise. However, the G-R noise is always the lower limit of noise possible. The measured noise of a film may exceed G-R noise, but it can never be less than the G-R noise.

Petritz[1] has given a theory of G-R noise in thin films and also a theory of photoconductive response to incident photons. According to these theories, both the noise and response are related to the same factor τ/pd, where τ is the lifetime of majority carriers, p is the hole (majority carrier) concentration, and d is the film thickness. The theories can be derived in other

* This work was performed under contract with the Navy Bureau of Ordnance.
† Present address: Research Laboratories, Eastman Kodak Company, Rochester, New York.
[1] R. L. Petritz, Phys. Rev. **104**, 1508 (1956).
[2] F. L. Lumis and R. L. Petritz, Phys. Rev. **105**, 502 (1957).
[3] B. Wolfe, Rev. Sci. Instr. **27**, 60 (1956).
[4] R. L. Williams, Abstract Number 49, The Electrochemical Society New York Meeting (April 27, 1958); Can. J. Phys. **37**, 841 (1959).
[5] H. E. Spencer, Phys. Rev. **109**, 1074 (1958).

ways.[5,6] By eliminating the common factor τ/pd, one finds an expression for noise in terms of response and certain other factors such as the number of photons incident and the fraction of photons absorbed. The expression then does not contain pd, which often is not known for a particular film, or τ, which may not be known. From a measurement of response, the G-R noise can be calculated. This calculated value represents the minimum noise present. If the experimental noise is G-R noise, then agreement should be found between experiment and calculation. If some other noise dominates G-R noise, then the experimental noise should exceed the calculated noise.

Here, the theories are checked by varying both response and noise by varying the temperature of two films of lead sulfide of different characteristics. Noise calculated from response data is compared with experimentally measured noise.

The theory of the relationship between noise and photoconductive response will now be given and the terminology used will be explained.

The usual circuit used for measuring photoconductivity in films of lead sulfide is a series combination of a dc voltage E, the photoconductor of conductance G, and a load resistor of conductance G_r. When radiation is absorbed by the photoconductor, G changes by a small amount ΔG causing a small change in current in the circuit. A voltage change ΔV_s is developed across the load resistor. The radiation is usually chopped so that ΔV_s is an ac voltage that may be easily amplified to give a measurable signal. Under dark conditions a noise voltage ΔV_n is developed across the load resistor.

It can be shown that the photoconductive response ΔV_s is related to the fractional change in conductance $\Delta G/G$ by,

$$\Delta V_s = EGG_r\Delta G/G(G+G_r)^2. \tag{1}$$

Petritz[1] defines a specific responsivity R_s as

$$R_s = \tfrac{1}{4}\Delta G/GJ, \tag{2}$$

where J is the number of w/cm² incident upon the cell.

Since the factor $\frac{1}{4}$ in Eq. (2) is due to the circuit, we will define another specific responsivity $\mathfrak{R}_s$ as

$$\mathfrak{R}_s = 4R_s.$$

The quantity $\mathfrak{R}_s$ is thus characteristic of the photoconductor and not of the circuit and is the fractional change in conductance caused by the incidence of one w/cm² of radiation.

It should be noted that $\mathfrak{R}_s$ as defined has the dimensions cm²/w. The fraction $\Delta G/G$ in Eq. (1), however, is dimensionless.

The dependence of $\mathfrak{R}_s$ on the angular frequency ω at which the incident radiation is chopped is given[7] by

$$\mathfrak{R}_s = \mathfrak{R}_s^0(1+\omega^2\tau^2)^{-\frac{1}{2}}, \tag{4}$$

where $\mathfrak{R}_s^0$ is the value of $\mathfrak{R}_s$ at some low frequency such that $\omega^2\tau^2 \ll 1$.

By following Petritz,[1] it can be shown that

$$\mathfrak{R}_s^0 = \eta_s F(\tau/pd), \tag{5}$$

where F is the number of photons/sec in one w/cm² incident on the cell and η_s is the fraction of photons that is absorbed. A term designated B by Petritz[1] is omitted as it has been shown[2] to be almost zero and thus is negligible. $\eta_s F$ is really the rate of excitation of electron-hole pairs. Spencer[6] has shown that the rate of excitation and the rate of absorption of photons may be considered identical. That is, one absorbed photon creates one electron-hole pair. Thus, F can be defined in terms of rate of incidence of photons.

Petritz[1] also defines a specific noise N_s as

$$N_s = \Delta V_n(A/\Delta f)^{\frac{1}{2}}(G+G_r)^2/4GG_rE, \tag{6}$$

where Δf is the band width of the amplifier, and A is the area of the cell. This specific noise is proportional to one quarter of the rms fractional change in conductance caused by fluctuations in that conductance. Again, the $\frac{1}{4}$ is a function of the circuit, and we define another specific noise $\mathfrak{N}_s$ as

$$\mathfrak{N}_s = 4N_s. \tag{7}$$

This specific noise is effectively the rms fractional change in conductance of a cell whose area is 1 cm² measured with a 1 c/sec band width. Note that $\mathfrak{N}_s$ has dimensions of centimeters.

The Petritz theory[1] gives

$$\mathfrak{N}_s = 2(\tau/pd)^{\frac{1}{2}}/(1+\omega^2\tau^2)^{\frac{1}{2}}, \tag{8}$$

which may be written as

$$\mathfrak{N}_s = \mathfrak{N}_s^0/(1+\omega^2\tau^2)^{\frac{1}{2}}. \tag{9}$$

On dividing Eq. (4) by Eq. (8) and substituting Eq. (5) we find

$$\begin{aligned}\mathfrak{R}_s/\mathfrak{N}_s &= \mathfrak{R}_s^0/\mathfrak{N}_s^0 \\ &= \tfrac{1}{2}\eta_s F(\tau/pd)^{\frac{1}{2}} \\ &= \tfrac{1}{2}[\eta_s F\mathfrak{R}_s^0]^{\frac{1}{2}}.\end{aligned} \tag{10}$$

This is the signal/noise ratio of a cell of unit area, measured with unit band width, with one w/cm² incident upon the cell.

By rearranging Eq. (10), we find $\mathfrak{R}_s^0$ as a function of $\mathfrak{N}_s^0$

$$\mathfrak{R}_s^0 = \tfrac{1}{4}\eta_s F[\mathfrak{N}_s^0]^2. \tag{11}$$

If the incident radiation is monochromatic and the wavelength λ is in units of microns, F is found to be

$$F = \tfrac{1}{2}\lambda \times 10^{19}.$$

EXPERIMENTAL

The cells used were two experimental ones manufactured in this laboratory. At room temperature, one was more sensitive than the other and had a time con-

[6] B. Davydov and B. Gurevich, J. Phys. U. S. S. R. **7**, 137 (1943); A. Van der Zeil, *Noise* (Prentice-Hall, Inc., Englewood Cliffs, New Jersey, 1954) p. 310.

[7] R. C. Jones, Advances in Electronics **5**, 2 (1953).

stant about eight times longer than the other one. The large difference in room temperature properties was chosen so that a stringent test of the theory was possible. The cells were fastened to a copper block suitably mounted in a glass Dewar vessel with a sapphire window for photoconductive measurements. Cooling was accomplished by using ice and water, solid carbon dioxide and acetone, and liquid nitrogen in the Dewar flask. The flask was evacuated to prevent frosting. Thermocouples were used to monitor the temperature of the cells.

The resistances of the cells were measured with a calibrated ohmmeter. The relative spectral responses were measured on a Perkin-Elmer Model 12-C infrared spectrometer adapted for photoconductivity measurements. The absolute value of responsivity was measured at a wavelength of 2 μ. This equipment consisted of a tungsten light source with a combination of two filters, a germanium blocking filter and a spike interference filter transmitting at 2 μ. The intensity of radiation emitted by this source filter combination was calibrated against a Bureau of Standards lamp.

Time constants were measured in two ways. Both used a variable-frequency square pulse of light from a neon bulb. In the first method, the response of the cell was presented on an oscilloscope and the time constant was taken to be the time for the response to rise to 63% of the steady-state value. The second method consisted of varying the frequency of the exciting light and measuring the magnitude of the response of the cell with a General Radio Wave Analyzer. Since the band pass of that instrument was 5 cps, the response to the fundamental frequency could be measured without interference from the harmonics. The time constant was calculated from the frequency at which the response was 70% of the value at a low frequency where the response was independent of frequency. Both methods gave time constants which agreed with each other.

The noise-frequency spectra were measured using the same wave analyzer as was used for the time-constant measurements. Since it was found that the noise-frequency spectra paralleled the signal-frequency spectra, no attempt was made to measure noise at frequencies higher than those necessary to calculate time constants from the noise data. Precautions were taken to insure that the noise with the dc voltage E in the circuit was considerably higher than noise with the dc voltage out of the circuit. In other words, care was taken to insure that the measured noise voltage was a linear function of the magnitude of the dc voltage.

RESULTS AND DISCUSSION

From the measured value of response at a given frequency (87 cps in many of the experiments reported here) $\mathcal{R}_s$ may be calculated. By multiplying $\mathcal{R}_s$ by $(1+\omega^2\tau^2)^{\frac{1}{2}}$ one obtains $\mathcal{R}_s^0$. A similar procedure is used to obtain $\mathfrak{N}_s^0$.

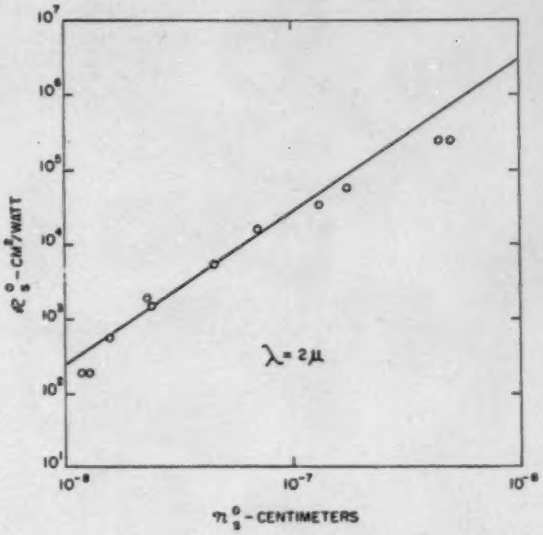

FIG. 1. Variation of signal with noise.

In Fig. 1, experimental values of $\mathcal{R}_s^0$ *vs* $\mathfrak{N}_s^0$ are plotted for a wavelength of two microns. The parameter in Fig. 1 is temperature. The value of F at that wavelength is 10^{19} $\text{sec}^{-1}\text{cm}^{-2}$. The line drawn in the figure is calculated from Eq. (11) assuming η_s equal to unity. The actual value of η_s is certainly less than unity because of reflection and transmission losses. An estimate of about 0.7 for its value would probably be not too far from the actual value. However, since the actual value is not known and since the difference between 0.7 and 1.0 will not change the interpretation, the latter value is assumed. The fit of the data to the line is excellent considering that $\mathcal{R}_s^0$ ranges over almost four decades and $\mathfrak{N}_s^0$ ranges over almost two decades.

The data should lie below the line for two reasons. The first is that η_s equal to unity is larger than the actual value. The effect of a lower value of η_s would be to move the data vertically downward below the line. The second reason is that the G-R noise assumed in the derivation of Eq. (11) is the lower limit of noise actually present in a cell. Any other noise present in the cell ($1/f$ noise) would increase the total noise above G-R noise. The presence of such noise would have the effect of moving the experimental points horizontally to the right of the line. The fact that some of the points lie above the line is attributed to experimental error in measuring signal and noise, and errors in extrapolating the measured values to lower frequencies to obtain $\mathcal{R}_s^0$ and $\mathfrak{N}_s^0$.

Figure 2 shows the variation of $\mathcal{R}_s^0$ with wavelength for the two cells at four different temperatures. The wide variations in characteristics between the two cells and the four temperatures are evident. Yet Fig. 1 shows that the theory describes the experimental data well.

Several points can be noticed about Fig. 2. One is that the increase in long wavelength limit of response

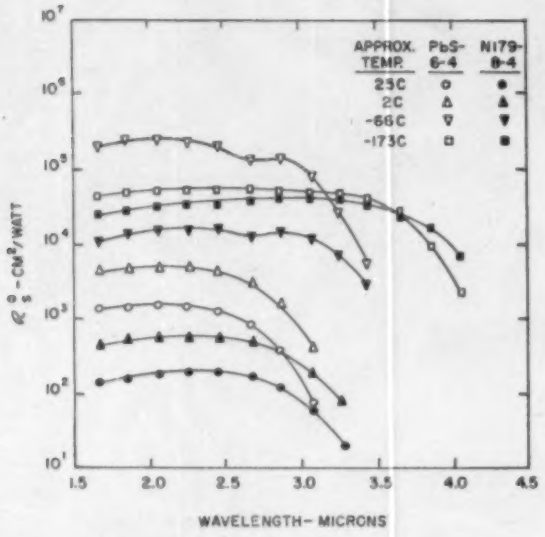

FIG. 2. Variation of $\mathcal{R}_s^0$ with wavelength and temperature.

increases as the temperature decreases. From the temperature coefficient of the band-gap energy of lead sulfide[8] (4×10^{-4} ev/°K) and approximately a 200°K temperature difference between room temperature and liquid-nitrogen temperature one calculates a shift in long wavelength limit of approximately 0.8 μ. It can be seen that this value is approximately the wavelength shift exhibited by the spectra of the two cells shown in Fig. 2.

The dip in response at about 2.7 μ shown by the two spectra of cells cooled with solid carbon dioxide and acetone is due to absorption of radiation by the carbon dioxide gas surrounding the Dewar vessel containing the coolant. The sublimation of the carbon dioxide caused a high concentration of gaseous carbon dioxide in the pathway of the incident radiation and consequently high absorption at this wavelength.

Another feature shown in Fig. 2 is the higher response at short wavelengths of cell PbS-6-4 when it is cooled with dry ice and acetone than when it is cooled with liquid nitrogen. This is due to the absorption of ambient photons and will be discussed in more detail later.

Figure 3 shows the signal/noise ratio as a function of wavelength and temperature. The frequency at which these measurements were taken was 87 cps.

Figure 4 shows the noise-frequency spectra of one cell (PbS-6-4) at four temperatures. The solid curves are those calculated from signal measurements alone, whereas the points on the figure are the experimental points. The signal measurements yield $\mathcal{R}_s$ and τ. From these, $\mathcal{R}_s^0$ is calculated as has already been outlined.

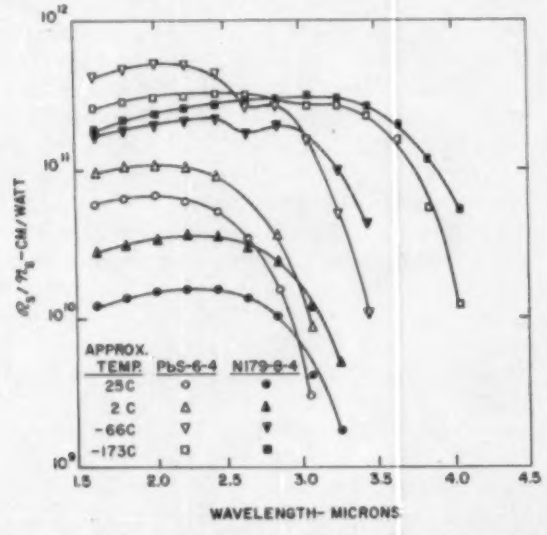

FIG. 3. Variation of $\mathcal{R}_s/\mathfrak{N}_s$ with wavelength and temperature.

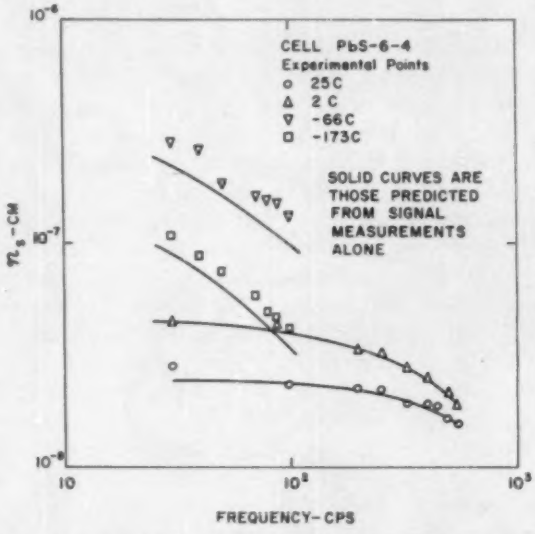

FIG. 4. Noise of PbS-6-4 at various frequencies and temperatures.

Equations (11) and (9) are then used to solve for $\mathfrak{N}_s$ at the various frequencies.

There is good agreement in Fig. 4 between calculated noise and experimental noise both in magnitude and shape of the curves.

Good agreement can also be seen in Fig. 5 where signal/noise ratio is shown as a function of frequency and temperature. The horizontal lines are again the lines calculated from signal measurements alone. The fact that the lines are horizontal is dramatic evidence that the time constants derived from signal-frequency and noise-frequency curves are identical.

The agreement between calculated and experimental points in Figs. 4 and 5 is not perfect. The difference again is believed to be due to experimental error. Some of the same arguments used to explain the experimental errors shown by points in Fig. 1 can be applied here.

There are three assumptions[1] used in deriving the

[8] R. P. Chasmar in *Photoconductivity Conference*, edited by Breckenridge, Russel, and Hahn (John Wiley & Sons, Inc., New York, 1956), p. 463.

theory outlined in the *Introduction* about which comment is merited. One is that the measured time constant is the lifetime of the majority carriers. Another is that each absorbed photon produced one electron hole pair. Both assumptions are commonly made and the good agreement between experiment and theory at all temperatures studied here is vindication for making the assumptions. In particular, there has been some controversy about the quantum efficiency[2,3,5] (the number of electron-hole pairs produced per absorbed photon) which Jones calls responsive quantum efficiency.[9] The agreement between experiment and theory here indicates that the responsive quantum efficiency at all temperatures is almost unity in agreement with Lumis and Petritz[2] and Spencer[5] who calculated the responsive efficiency at room temperature.

It should be also pointed out that another assumption used to derive the theory is that the conductivity

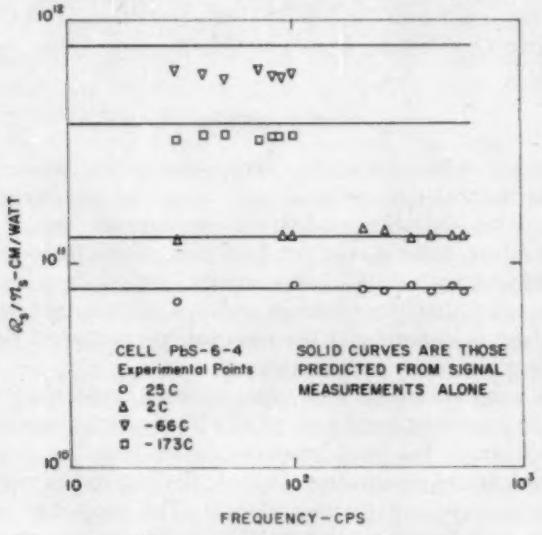

FIG. 5. Signal/noise of PbS-6-4 at various frequencies and temperatures.

is predominantly due to holes. Again, this would seem to hold for all temperatures studied here.

It has been shown by Spencer[5,10] that signal, resistance, and time constant measurements may be used to calculate mobilities and concentrations of majority carriers. The mobility μ_s so calculated is called signal mobility. The equation for μ_s in terms used here

$$\mu = \mathcal{R}_s^0/eFR_{sq}\tau, \tag{13}$$

where e is the electronic charge and R_{sq} is the resistance of a 1 cm×1 cm in area.

The equation for the product of concentration of holes times the thickness of the film is

$$pd = 1/\mu_s eR_{sq}. \tag{14}$$

[9] R. C. Jones, Advances in Electronics and Electron Physics **11**, 87 (1959).

[10] H. E. Spencer, J. Appl. Phys. **30**, 927 (1959).

TABLE I. Properties of cells at various temperatures.

Cell PbS-6-4				
Cell coolant	(Room temperature)	Ice water	Dry ice-acetone	Liquid nitrogen
Approximate temperature (°C)	25	2	−66	−173
R_{sq} (megohms)	0.49	1.06	31	11
τ (millisec)	0.38	0.58	4.7	6.2
μ_s (cm²/v-sec)	5.2	4.9	1.0	0.46
pd (cm^{-2})	2.4×10^{12}	1.2×10^{12}	2.0×10^{11}	1.2×10^{12}
Cell N179-8-4				
Cell coolant	(Room temperature)	Ice water	Dry ice-acetone	Liquid nitrogen
Approximate temperature (°C)	25	2	−66	−173
R_{sq} (megohms)	0.56	1.1	19	83
τ (millisec)	0.045	0.095	0.86	3.7
μ_s (cm²/v-sec)	4.6	3.3	0.55	0.062
pd (cm^{-2})	2.4×10^{12}	1.8×10^{12}	6.0×10^{11}	1.2×10^{12}

The thickness of the films studied here are not known but experience in measuring thicknesses of similar films indicates that 0.6μ is a fair approximation to the thickness.

Table I contains the calculated mobilities and concentrations for the films at the various temperatures.

To check the role played by the absorption of ambient photons, the resistances of the two cells were measured at the four temperatures with a brass cover over the cells. The cover was in contact with the cooled copper block, but not in contact with the cells. It was found that the resistances at the two lower temperatures were appreciably higher with the cover than without the cover over the cells. This fact indicates that the absorption of ambient photons appreciably affects the concentration of carriers present at the lower temperatures.

A method of estimating the role of absorption of ambient photons makes use of the equation,

$$F_a = pd/\tau, \tag{15}$$

where F_a is the rate of absorption of the effective ambient photons. This equation states that the rate of generation of holes (hole-electron pairs) is equal to the steady-state concentration of holes divided by the lifetime of the holes. The rate of absorption of ambient photons (ambient temperature is assumed to be 300°K) was calculated by graphically integrating over all wavelengths the product of the relative quantum response of a cell at the particular temperature and the rate of incidence of ambient photons.[1,2,11] Table I contains both pd and τ. If F_a calculated from Eq. (15) equals F_a calculated from the relative response curve and the photons incident from the surroundings (300°K blackbody radiation is assumed) it is reasonable to conclude that the major mode of generation of holes is by the absorption of ambient photons. Table II contains the comparison of F_a calculated by these two methods.

[11] T. S. Moss, J. Opt. Soc. Am. **40**, 602 (1950).

TABLE II. The rate of absorption of ambient photons.

Cell	Temperature °C	F_a calculated from relative quantum response	pd/τ
PbS-6-4	25	1.6×10^{13}	6.3×10^{15}
	2	2.0×10^{13}	2.1×10^{15}
	−66	4.9×10^{13}	4.3×10^{13}
	−173	4.6×10^{14}	1.9×10^{14}
N179-8-4	25	6×10^{13}	5.3×10^{16}
	2	8×10^{13}	1.9×10^{16}
	−66	1.7×10^{14}	7.0×10^{14}
	−173	9.4×10^{14}	3.2×10^{14}

There is fair agreement between the two methods for cell PbS-6-4 at −66°C and −173°C and for cell N179-8-4 at −173°C. Table II indicates that the F_a calculated from relative quantum response and 300°K blackbody radiation is too high. This could be due to experimental error in the various measurements used in calculating, or to assuming that the cells surrounding on one side may be adequately represented by a 300°K blackbody. The latter assumption is certainly not rigorously true. The estimate of the solid angle subtended by the cell is, undoubtedly, too large.

It seems clear, however, that at the lowest temperature the absorption of ambient photons determines the concentration of carriers in the films. Thus, the noise of the films at that temperature could be termed radiation noise.[12] Similarly, the noise at room temperature could be termed thermal or lattice noise. As has been shown earlier in this paper, the noise in both cases is G-R noise and is due to the fluctuations in the carrier concentrations. The terms thermal and radiation then merely indicate the origins of the carriers, i.e., the carriers are generated thermally by the absorption of lattice energy in one case, and by the absorption of radiation in the other case.

Going back to Fig. 2, we now can see the explanation of the decrease in responsivity of cell PbS-6-4 cooled with liquid nitrogen compared with the same cell cooled with dry ice and acetone. The increased absorption of ambient photons causes the carrier concentration to be appreciably higher at the lower temperature. At the same time, the time constant is not greatly different. Thus, τ/pd has a lower value and the responsivity is lower at the lower temperature. The same is not true of cell N179-8-4 because the time constant increases greatly between the two temperatures.

F_a must increase with cooling because the spectral response goes to longer wavelengths with cooling. By substituting Eq. (15) into Eq. (5) we have

$$\mathcal{R}_s^0=\eta_s F/F_a. \tag{16}$$

This equation is valid only at the temperatures where the absorption of ambient radiation determines the concentration of holes. For monochromatic radiation, $\eta_s F$ is a constant. Thus, the effect of further cooling and consequently increasing F_a is to decrease $\mathcal{R}_s^0$. It can now be seen that if cooling initially increases signal, further cooling causes the signal to reach a maximum and then decrease beyond a certain temperature. The maximum occurs at the point where absorption of ambient photons becomes the major mode of generation of holes. The temperature at which this occurs is different for different cells and depends on the degree of shielding from ambient photons given this cell.

CONCLUSIONS

It is concluded that the Petritz[1] theory describes the experimental data over a wide range of conditions. Consequently, the underlying assumptions of the theory are probably correct. G-R noise seems to be the dominant noise at all temperatures studied. It is also concluded that the absorbed ambient photons are important in determining the electrical properties of the cells at the lower temperatures.

A word of caution is in order as to the applicability of the results reported here to all PbS photoconductors. No attempt has been made to insure that the cells chosen are representative. In fact, they should be considered only as experimental cells. The properties of films such as those used in this study are structure sensitive (for example, the low values of mobility are typical of films rather than single crystals) and it is to be expected that wide variation in properties could be found for films of different manufacture.

ACKNOWLEDGMENTS

Much of the apparatus utilized was constructed by D. E. Carter. His assistance in conducting the experiments was appreciated. Several discussions with J. V. Morgan and G. J. Koch were helpful. The encouragement of G. J. Koch was greatly appreciated.

[12] K. M. Van Vliet, Proc. Inst. Radio Engrs. 46, 1004 (1958), has pointed out that the actual noise in the semiconductor can never be less than twice the noise in the photon stream incident upon the semiconductor.

Ultimate and Secondary Electron Energies in the Negative Glow of a Cold-Cathode Discharge in Helium

J. M. ANDERSON
General Electric Research Laboratory, Schenectady, New York
(Received September 10, 1959)

The "ultimate" electron density in the negative glow plasma of a cold-cathode discharge in helium at gas pressures 3–12 mm Hg has been determined by simultaneous Langmuir probe and microwave transmission methods. A correlation is obtained at densities above $\sim 4\times 10^{11}/cm^3$ when the influence of positive ion scattering of the electrons diffusing to the probe is considered. The ultimate electron temperature in the helium negative glow was measured by the metallic probe to be quite low, $\sim 400°K$, and the "secondary" electron temperature was found to be $\sim 50\,000°K$. These probe indications are substantiated by measurement of the microwave noise power radiated from the plasma which is found to correspond to an effective temperature varying from 300 to $\sim 1000°K$.

INTRODUCTION

PROPERTIES of the free electrons in the negative glow region of a cold-cathode gaseous discharge have been determined, in most past studies, with the Langmuir metallic probe. A survey by Francis[1] discusses the results and gives a current view of the general features of a glow discharge.

In this work a dc cold-cathode discharge established in helium was examined to determine the number density and mean energy of the "ultimate" and "secondary" electron groups. The secondary electrons, studied here, were presumed to be the immediate products of ionization of gas atoms. The ultimate electrons were further presumed to be secondary electrons which have lost energy in numerous collisions with gas atoms and ions (see reference 1, page 111). The Langmuir probe with swept potential and instantaneous probe curve display was interpreted for use at gas pressures of 3–12 mm Hg. In addition, the number density of the ultimate electrons was determined from the microwave conductivity of the plasma medium, and microwave noise power radiated from the negative glow was measured to infer the effective temperature of the ultimate and secondary electrons. Results of the above procedures may be compared to establish more firmly the properties of the free electrons of the negative glow plasma.

PROCEDURE

The Langmuir metallic probes used for these experiments were in the form of 0.5 cm lengths of tungsten wire with diameters of one or one-half mil. It was quickly discovered that with the probe collecting appreciable electron current from the plasma the compensating effect of the discharge tube anode in relaxing its collection of electron current in favor of the probe was not complete, and the plasma space potential moved positively as detected by an auxiliary floating probe. This has the major effect of falsifying the probe-measured temperature. An electronic correcting network was devised external to the discharge tube which altered the tube anode potential sufficiently to establish a constant plasma space potential for all probe currents.

The manner of presentation of the probe voltage-current characteristics was essentially instantaneous. The appropriate voltages were amplified with retention of dc response and appeared on the cathode-ray oscilloscope with a vertical axis proportional to logarithm probe current and horizontal axis proportional to probe potential. The tungsten probes were heated to incandescence by electron bombardment and data were taken from the oscilloscope presentation before accumulated surface impurities distorted the probe curves. The probe potential was swept at a low audio rate of ~ 20 cps in a compromise to minimize impurity effects and to allow formation of a positive ion sheath in equilibrium with the probe potential.

The interpretation of the probe curves followed the straightforward procedure outlined by Langmuir except where noted later. Information concerning the ultimate electrons was thus obtained. Knowledge of the secondary electron group was gained from point by point probe current measurements with one-half of one percent electrical meters and necessary correction for positive ion current where important. No well-defined measurement of the primary electron group was possible with this simple probe type.

The known limitations to metallic probe procedure, as pointed out by Francis[1] and Loeb,[2] were considered. It was concluded that for the conditions described here there is not likely to be more than a few percent error introduced by neglect of any stated error source not otherwise accounted for in this work.

The average microwave conductivity of the plasma was measured by a transmission microwave method[3] with a wave frequency of 9375 Mc/sec (X-band). For

[1] G. Francis, *Handbuch der Physik* (Springer-Verlag, Berlin, 1956), Vol. 22, p. 53.

[2] L. Loeb, *Basic Processes of Gaseous Electronics* (University of California Press, Berkeley, California, 1955). See also an excellent article by G. Wehner and G. Medicus, J. Appl. Phys., **23**, 1035 (1952).

[3] J. M. Anderson and L. Goldstein, Phys. Rev. **100**, 1037 (1955).

this purpose the negative glow plasma was established within a section of copper wave guide (RG 52/u) sealed with mica windows to allow helium gas fillings at pressures of 3–12 mm Hg. The aluminum cathode of this wave-guide discharge tube formed an insulated portion of a broad inner wall along the axis of the wave guide, and the anode was composed of the remaining three walls of the guide. The effective length of the tube was 16 cm. The microwave conductivity was calculated from measurements, with a phase bridge, of the extent to which the velocity of propagation of the microwave was altered by the presence of the plasma medium. The negative glow incompletely filled the guide cross section, due to the necessary cathode fall region of the discharge, and metallic probes were used to determine the electron density spatial variations of the plasma. Plasma inhomogeneities were accounted for in the approximate microwave conductivity calculation, as well as an electric polarization[4] of the plasma at the highest electron densities measured. Coupling of microwave propagation modes by the inhomogeneous plasma was considered with the method of Chambers and of Bradshaw[5] for TE_{01} and TE_{03} modes (excited by symmetry). A relatively small error of $\sim 2\%$ is introduced and consequently coupling to other modes was neglected.

The noise power at microwave frequencies radiated from the plasma filled portion of wave guide was measured with a radiometer similar to that used by Dicke.[6] Microwave noise was accepted at a center frequency of 9375 Mc/sec and with an effective band pass of $\cong 6$ Mc/sec. The receiver noise figure of 8.6 db and integration time of about one second predicts[7] a sensitivity $\sim \pm 10°$K at 300°K and this was essentially attained. Determination of the effective noise temperature of the plasma was made by comparison with a commercially available 18 db neon discharge noise generator with variable attenuation. Care was taken to maintain microwave matching of the radiometer to the discharge plasma, for ultimate electron densities in the range necessary to effect microwave "cutoff," so that full noise content of the plasma would be measured. A microwave load was placed on the discharge tube, opposite to that end with the radiometer attached, which established the temperature measured in the absence of the discharge at the load temperature, namely 300°K.

While the emphasis here is on electron collection by the metallic probe, a considerable early effort was expended[8] in an attempt to interpret the positive ion current collected by a strongly negative probe. Indications were obtained that a considerable and extended depression in charge density exists about the probe, which could not be meaningfully related to plasma charge density. Its usefulness in plotting rapid spatial variations in charge density is also questionable.

The positive column region was excluded from all discharges considered here and operation was always in the abnormal glow.

Helium gas supplied by Linde Rare Gases was used, and a charcoal trap at liquid nitrogen temperature isolated the discharge tube from the vacuum system. This procedure does not exclude the presence of trace neon impurities. At least two red neon lines are very faintly seen with a visual spectrograph, and from their intensity the impurity of neon is estimated at somewhat less than one part per million of helium.

RESULTS AND DISCUSSION

Probe potentials, V_p, positive with respect to space potential should lead from the Langmuir analysis to a dependence of probe electron current, $i_p \propto V_p^{0.5}$. This relationship was found to hold experimentally for helium gas pressures less than ~ 1 mm Hg and for neon gas pressures less than ~ 5 mm Hg. Gas pressures used were above these limits, preventing any simple interpretation of data for positive probe potentials. Ultimate electron density was therefore calculated from measured probe electron current collected at space potential, and electron temperature was found from the electron retarding potential probe characteristics. The expected shape of these curves and their interpretation was discussed by Davydov and Zmanovskaja.[9]

By the microwave method the maximum electron densities obtained for each of the discharge currents and gas pressures were measured and are presented on Fig. 1. The deviation at 3 mm Hg, also found by probe measurements, has not been explained.

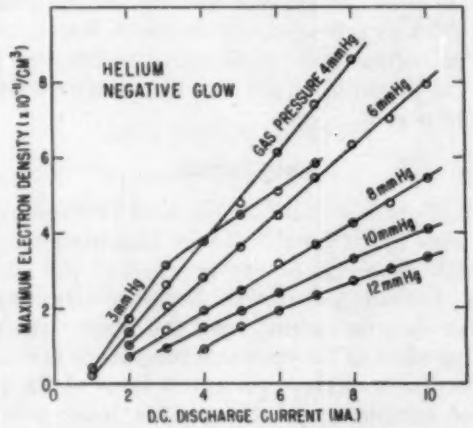

FIG. 1. Maximum electron density in the negative glow of a cold-cathode discharge established in helium (determined by the microwave propagation method).

[4] K. B. Persson, Phys. Rev. **106**, 191 (1957).
[5] Ll. G. Chambers, Brit. J. Appl. Phys. **3**, 19 (1952); J. A. Bradshaw, *ibid.* **3**, 332 (1952).
[6] R. H. Dicke, Rev. Sci. Instr. **17**, 268 (1946).
[7] L. D. Strom, IRE Wescon Conv. Record, Part 1 (August, 1957).
[8] J. M. Anderson, Report No. 58-RL-2010, G. E. Research Laboratory, Schenectady, New York (1958).
[9] B. Davydov and L. Zmanovskaja, J. Tech. Phys. U.S.S.R. **3**, 715 (1936).

Comparison of the probe and microwave methods is shown on Fig. 2 where the ratio of probe-to-microwave determined ultimate electron densities is plotted as a function of microwave determined density (presumed correct). Below an electron density of $\sim 4\times 10^{11}/cm^3$ all curves fall rapidly and the probe predicts much less electron density than the microwave. This effect may be due to a general depression of density in the probe vicinity, created by a condition of near ambipolar diffusion of charges to the glass sheath of the probe. At higher densities the extent of this depression may be limited and the probe may then pierce the undisturbed plasma. The effect may also be due to a falsified electron temperature indication, where for lower densities weak electric fields from the probe may sufficiently penetrate the plasma and heat the electrons diffusing to the probe. On the basis of observations described below, the latter process is most probably active.

Above densities $\sim 4\times 10^{11}/cm^3$ a pattern to the curves emerges. At these gas pressures a diffusion of electrons to the probe must be considered, and probe indicated density is still considerably lower than the microwave determination. Diffusion under a gradient of electron density only was considered, it being assumed that no strong dc probe fields penetrate the plasma at or near space potential. However, the influence of scattering of electrons by positive ions was included with the appropriate mean free path obtained from the conductivity reported by Spitzer and Harm.[10] The result of such an approximate calculation is shown as the dotted curves on Fig. 2. Some agreement with experiment is noted for electron densities above $\sim 4\times 10^{11}/cm^3$. For the calculation the probability of collision of electrons with atoms for momentum transfer was taken constant at 23 cm^2/cm^3 at 0°C and 1 mm Hg. In view of the assumptions necessary and the nature of the experiment, which involves correlation of two independent procedures, the agreement obtained may be fortuitous.

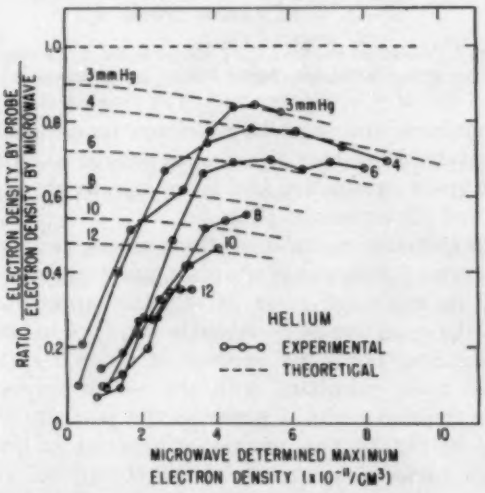

FIG. 2. Comparison of metallic probe-determined and microwave-determined maximum electron density in the helium negative glow.

[10] L. Spitzer and R. Harm, Phys. Rev. **89**, 977 (1953).

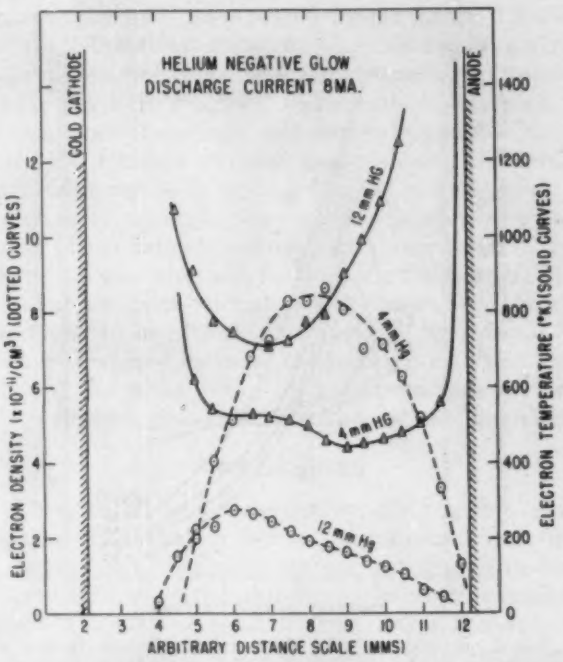

FIG. 3. Typical contours of ultimate electron density and temperature in the negative glow of a cold-cathode discharge in helium.

The above correlation permits a further approximate correction to the probe-measured electron density profile of the plasma. This has been attempted for two gas pressures, and representative results are presented on Fig. 3. At 4 mm Hg the density profile (dotted curves) may be closely approximated by a sinusoid, the form assumed for the microwave computation. At 12 mm Hg the somewhat "lop-sided" density profile would still not be expected to introduce a large error in the microwave calculations. Profiles of electron density normal to a line from cathode to anode, not reproduced here, are also reasonably sinusoidal at all gas pressures. Note that the electron temperature measured (solid curves) is quite low in this negative glow plasma, being $\cong$440°K, at the lowest gas pressure. It is imagined that electrons are cooled in their collisions with ions[11] as well as neutral atoms at these relatively high ion densities. It should be commented that the lowest temperature measured was $\cong$350°K at a discharge current of 25 ma and a helium gas pressure of 6 mm Hg. Such a low electron temperature is conducive to strong electron-positive ion recombination and "Quenching" of the negative glow by microwaves has been reported.[12] Estimates of the electron temperature based upon observation of the negative glow by photomultipliers gave $\sim$500°K for conditions similar to the above. This

[11] A. A. Dougal and L. Goldstein, Phys. Rev. **109**, 615 (1958).
[12] J. M. Anderson, Phys. Rev. **108**, 898 (1957).

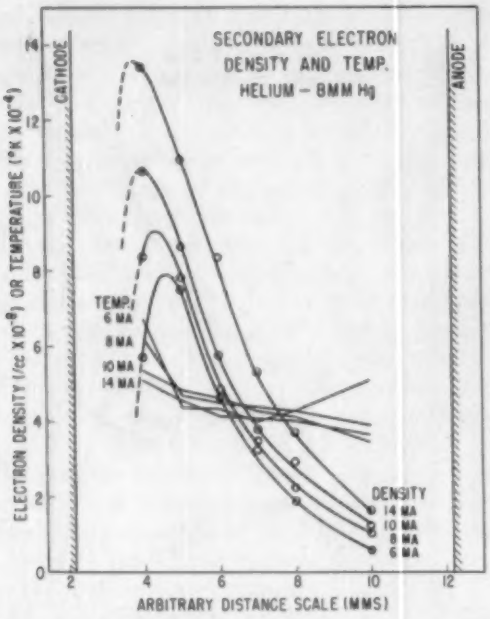

FIG. 4. Typical contours of secondary electron density and temperature in the negative glow of a cold-cathode discharge in helium.

latter experimental work will be reported when more complete.

Measurements of the density and temperature of the secondary electrons as a function of distance from cathode to anode were made at pressures of 4 and 8 mm Hg in the helium negative glow plasma. The representative results are presented on Fig. 4 for the case of 8 mm Hg. Note the peak density is considerably below that of the ultimate electrons but the temperature is two orders of magnitude greater. While the secondaries do not contribute to microwave propagation properties of the plasma they nevertheless have appreciable microwave noise content, as will be shortly discussed.

In a further attempt to establish the credulity of the metallic probe procedure, the noise power at microwave frequencies, radiated from the negative glow plasma, was measured with a Dicke-type microwave radiometer. It has been reported by Parzen and Goldstein[13] that this radiated noise may be theoretically correlated with the prevailing electron temperature of the portion of the discharge where microwave absorption occurs. For the negative glow the problem is somewhat complicated by the existence of at least three distinct electron groups. Only the contribution of the ultimate and secondary electrons will be considered here in the theoretical prediction of expected noise since they have approximately Maxwellian velocity distributions. Calculation of the expected noise contribution of the primary electrons would depend upon a determination of density and energy distribution of this group and this information was not obtained.

[13] P. Parzen and L. Goldstein, Phys. Rev. 82, 724 (1951).

It may be quickly derived from microwave absorption considerations that the noise power expected is

$$kT_{eff}df=e^{-2(\alpha_u+\alpha_s)z}kT_0df+\frac{\alpha_u}{\alpha_u+\alpha_s}(1-e^{-2(\alpha_u+\alpha_s)z})kT_udf$$
$$+\frac{\alpha_s}{\alpha_u+\alpha_s}(1-e^{-2(\alpha_u+\alpha_s)z})kT_sdf$$

where k is Boltzmann's constant, T_{eff} is the effective discharge temperature, df is the frequency interval, α_u is the absorption coefficient of the ultimate electrons, α_s is the absorption coefficient of the secondary electrons, T_0 is the load temperature=300°K, z is the discharge length along the wave guide, and T_u and T_s are

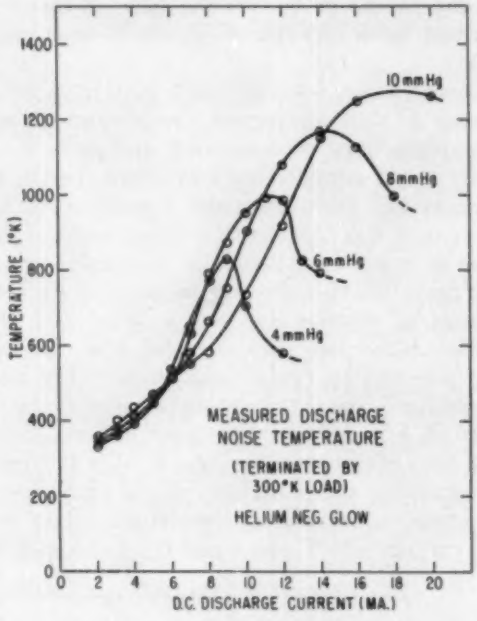

FIG. 5. Measured effective noise temperature of the negative glow plasma for various helium gas pressures.

the ultimate and secondary electron temperatures respectively. Note that if $\alpha_u+\alpha_s$ is a large number the wave guide terminating load is not seen by the radiometer and the expression simplifies.

The radiometer-measured effective noise temperature for several helium gas pressures is given on Fig. 5. The peak in measured noise corresponds approximately with the condition of wave-guide cutoff of microwave propagation. For a gas pressure of 8 mm Hg the expected noise calculated with the aid of appropriate probe measurements is given as the partially dotted curve of Fig. 6. The anomalous behavior at low discharge currents is a result of the abrupt rise of the ultimate electron temperature. If we argue that this indication by the probe is, in fact, erroneous and that the temperature is essentially constant at about 500°K for discharge currents below 10 ma, then the dotted

curve is calculated. This improved agreement with measurement of noise temperature (solid curve) lends support to the possibility of a false temperature indication by the probe mentioned earlier. It is hoped that experiments which will measure the extent of electron-ion recombination, planned for the near future, will clear up this point.

A considerable discrepancy between measured and calculated noise temperature remains, as is evident near wave-guide cutoff of Fig. 6. This is presumed due to a modified shot noise contribution by the primary electrons. At discharge currents beyond cutoff the radiometer is shielded from the primary electrons by the geometry of the discharge at the edge of the cathode. There is some agreement here in the projections of the calculated and measured noise temperatures. At a gas

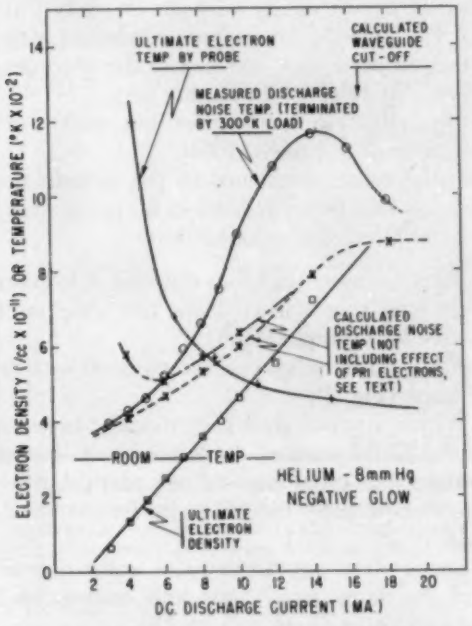

FIG. 6. Measured and predicted effective noise temperature of the negative glow plasma established in helium.

pressure of 4 mm Hg the same general agreement of projected temperatures beyond cutoff is more in evidence.

Before conclusion of these results it might be remarked that helium was the only rare gas where such low ultimate electron temperatures were measured. The neon negative glow plasma was examined by the above techniques and showed a temperature ~1000°K for the ultimate electrons. Presumably negative glow plasmas in other gases such as hydrogen and nitrogen, which also have relatively high-energy loss factors in the collisions of electrons with molecules and ions, may have low ultimate electron temperatures. The latter gases have not been examined as yet. In this work a comparison was made between the hollow cathode and single planar cathode with regards to the temperature of the ultimate electrons for discharges in helium. The ultimate electrons associated with the hollow cathode are found to be of higher temperature by a factor of 3 to 5 compared to those of the plane cathode. This may be due to an enhanced interaction with the primary electron group in the hollow cathode discharge.

CONCLUSIONS

Ultimate electron densities in the negative glow plasma established in helium, as measured with the Langmuir metallic probe, compare favorably with densities measured by the transmission microwave method above a density of $\sim 4\times 10^{11}/cm^3$. Below this density the probe indicates a lower density than the microwave, perhaps due to a depression of charge density in the probe vicinity by presence of the probe glass sheath, but more probably due to a falsification of electron temperature as indicated by the probe. It would be presumed that weak dc fields from the probe penetrate the plasma over sufficient number of mean free paths of the diffusing electrons to raise their mean random energy. The influence of electron-ion scattering in the reduction of the probe current at space potential is probably indicated, in that there is some agreement when this effect is included in calculations for the higher electron and ion densities.

For electron collection it was noted that plasma space potential varied positively in almost direct proportion to probe current. The correction of this effect resulted in measurement of a quite low ultimate electron temperature in the helium negative glow, ~400°K. The mean energy of the secondary electron group by contrast was found to correspond to an effective temperature of ~50 000°K. Further information, obtained with the Langmuir probe, concerning the spatial variations of electron density in the negative glow allows a calculation of the expected microwave noise power radiated from the plasma. This compares favorably with a direct measurement of noise power with the Dicke radiometer.

JOURNAL OF APPLIED PHYSICS VOLUME 31, NUMBER 3 MARCH, 1960

On The Behavior of Thermal Vacancies in Pure Aluminum

DORIS KUHLMANN-WILSDORF, *University of Pennsylvania, Philadelphia 4, Pennsylvania*

AND

H. G. F. WILSDORF, *The Franklin Institute Laboratories, Philadelphia 3, Pennsylvania*

(Received October 9, 1959)

The results are reported of an investigation of quenched-in prismatic dislocation loops in super-purity aluminum. Some new effects have been observed: in particular, that loops tend to be grouped in clusters containing a surplus of loops of one orientation; that more than four loop orientations are realized; and that often pairs of similarly oriented and similarly shaped loops are present in the quenched material. It is concluded that vacancies aggregate into three dimensional clusters, containing from a few to a few hundred or even thousand vacancies, before being converted into prismatic loops.

INTRODUCTION

THE quenched-in prismatic dislocation loops, previously called R loops or R-dislocations,[1] which are due to the condensation of thermal vacancies and have first been observed in quenched pure aluminum,[2] have been examined more closely, both experimentally and from the theoretical standpoint. Quenching pure aluminum specimens about 0.1 mm thick from about 630°C into iced brine easily produced the characteristic loops. Many of the R loops have a somewhat rounded shape, others are more or less well developed hexagons; a few are diamond shaped and others have irregular outlines. Often regions, in the order of one micron wide, border grain boundaries which are virtually free of R loops; and similar regions may be observed around dislocations, presumably because the vacancies diffuse towards these sinks of vacancies. Apparently, vacancies which reach dislocations in pure aluminum do not cause them to climb smoothly but instead form kinks, in agreement with a previous prediction.[3,4]

EXPERIMENTAL TECHNIQUES AND NEW RESULTS

All experiments were carried out with aluminum containing less than 0.001% impurities. The material was rolled and cut into strips 60 mm×3 mm×0.5 mm and recrystallized. Then, five indentations were put into each strip which was finally annealed at 600°C for 5 hr, producing a grain size of approximately 0.5 mm diam. As was to be expected, most grains showed the {110} orientation as well as {112}.

The strips were quenched from a vertical furnace into iced brine at a temperature of −10°C. In order to prevent the specimens from being bent during quenching, the strips were clamped to a small aluminum block and shielded by a U-shaped strip. After quenching, the actual specimens were cut from the strip with a razor blade taking great care not to deform them. The overall length of each specimen was 7 mm and each of them was polished individually with an electrolytical technique.[5] The thinning process was conducted with great care, and, in particular, washing of the specimens was done by slight agitation in alcohol only.

The investigation was carried out with a Philips electron microscope, model 100B.

The phenomena mentioned in the introduction are the same as had been reported in an earlier investigation.[2] In addition, it was found that:

(1) there are more than four different R loop orientations, proving that not all loops are lying on {111} planes (see for example Fig. 1).

(2) R loops arise in groups, interspersed with regions free of loops (Fig. 2).

(3) Within any one area, the prismatic loops are not necessarily distributed at random among the various orientations, but often loops of one particular orientation are unexpectedly frequent (see for instance Figs. 3 and 4).

(4) Loops often appear in pairs, consisting of two loops of the same size, shape and orientation lying close to each other (Figs. 4, 5, and 6).

POSSIBLE EXPLANATIONS FOR THE MULTITUDE OF LOOP ORIENTATIONS

The observation under point (1) above does not necessarily mean that dislocation loops are *formed* on other crystallographic planes besides the {111} planes. It might have the simple explanation that the R loops have rotated, after their formation on octahedral planes, since R loops as formed are not usually in equilibrium. Consider, for example, an R loop due to the condensation of a single close-packed layer of vacancies parallel to (111), collapsed with a tangential offset of $\frac{1}{6}[11\bar{2}]$, yielding a Burgers vector $b=\frac{1}{3}[111]+\frac{1}{6}[11\bar{2}]=\frac{1}{2}[110]$. This Burgers vector is inclined at an angle of 55° to the (111) plane. The slip surface of

[1] D. Kuhlmann-Wilsdorf, Phil. Mag. 3, 125 (1958).
[2] Hirsch, Silcox, Smallman, and Westmacott, Phil. Mag. 3, 897 (1958).
[3] Kimura, Maddin, and Kuhlmann-Wilsdorf, Acta Met. 7, 145, 154 (1959).
[4] Kuhlmann-Wilsdorf, Maddin, and Kimura, Z. Metallk. 49, 584 (1958).
[5] Wilsdorf, Cinquina, and Varker, Proc. 4th Intern. Congr. for Electr. Micr. (Springer-Verlag, Berlin, Germany, 1958) (to be published).

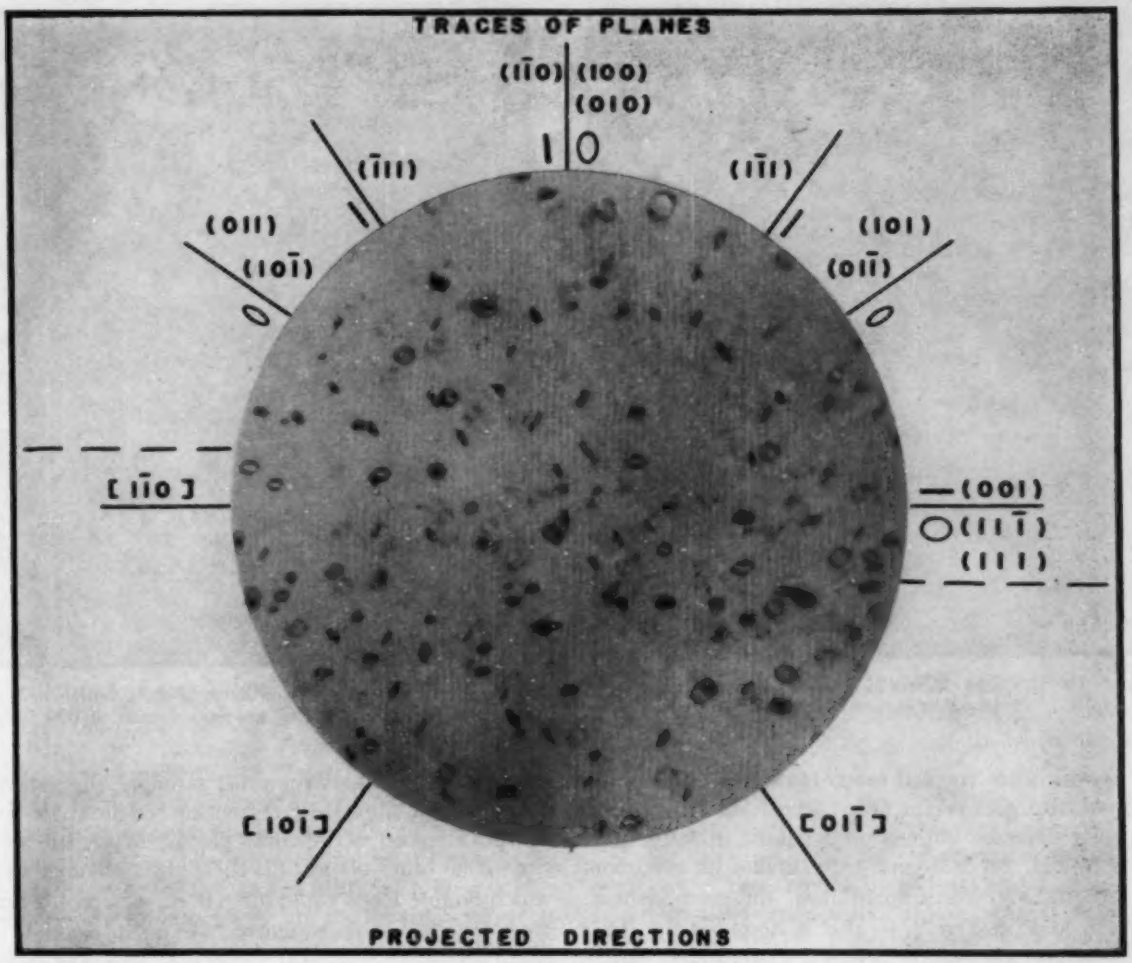

FIG. 1. Typical micrograph of quenched aluminum, showing more than four orientations of loops. Also note several loop pairs parallel to {111}. The crystallographic orientations of the dislocation loops are clarified on the margin, where projected directions, as well as the intersections between major planes and the specimen surface are given. The ellipses on the margin indicate in which shape circular loops, lying on the respective planes, would be seen. 32 000:1.

such a dislocation loop is the prismatic column which is generated by all vectors parallel to the Burgers vector which pass through the axis of the dislocation (Fig. 7). The loop is free to assume any shape on this slip surface; and, since its circumference will be at its lowest possible value when the loop plane is perpendicular to the prismatic slip surface, it will tend to rotate towards this orientation. The final position of the loop, however, will not ordinarily coincide with the position of smallest circumference because in that position, the loop has wholly edge character, while screw dislocations have a smaller energy per unit length than edge dislocations. Moreover, elastic anisotropy will influence the equilibrium shape of the *R* loops; random or applied stresses will deform them; lattice friction will hinder their motion; and, in very thin films, boundary conditions will influence the orientation of lowest loop energy.

The same arguments apply to any type of prismatic loop formed by the collapse of a vacancy disk accompanied by a tangential offset. For all the above reasons, a wide range of loop orientations, in specimens containing only loops originally generated on {111} planes, would not be impossible. Proof that rotation of loops, in the absence of obvious stresses, can actually take place may be found by comparing Fig. 8(a), which is an enlarged part of Fig. 1, with Fig. 8(b), showing the same area a short time later. One of the loops (see arrow) has clearly rotated during the time interval between the two micrographs.

The loop indicated by an arrow on Fig. 9 may represent another example of a rotated loop. It is clearly hexagonal but bounded by directions which are close to [$\bar{1}$12], [1$\bar{1}$2], and [1$\bar{1}$0] while its nearly equiaxial appearance suggests that it lies close to the plane of the specimen which, in this case, is very nearly parallel to (110). Thus, as nearly as can be determined, this loop is in that orientation and has that shape which would be expected from an *R* loop originally formed on a {111} plane in the shape of a hexagon (Fig. 7, posi-

FIG. 2. Large clusters of R loops separated by loop-free regions. 16 000:1.

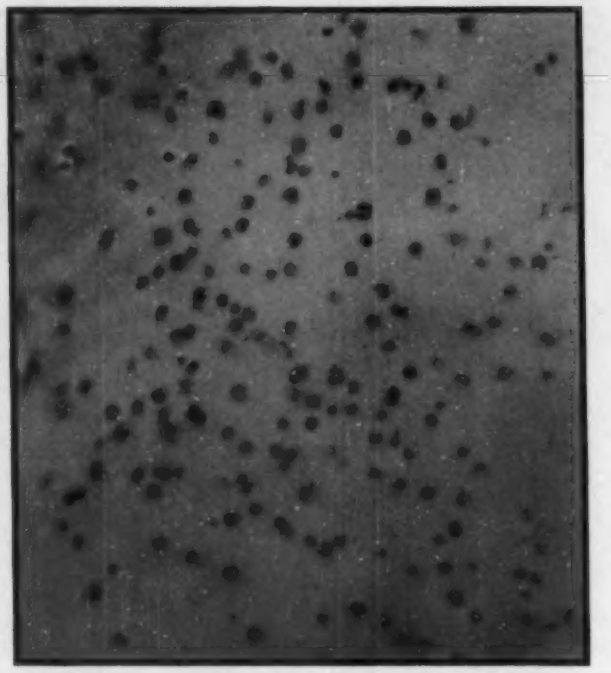

FIG. 3. Specimen area in which loops of one orientation (nearly parallel to plane of foil) are predominant. 40 000:1.

tion 1) which has rotated towards the position normal to its own Burgers vector (Fig. 7, position 2).

A quite different impression is gained from the loop shown in Fig. 10. It is markedly unlike its neighbors and presumably was formed in a different fashion. Like the loop in Fig. 9, it also is bounded by ⟨112⟩ directions and apparently lies in a {110} plane, but it is very sharply defined and is diamond shaped, not hexagonal. The assumption is reasonable that this special loop was formed on the {110} plane on which it still lies. Also observation (4) strongly suggests that condensation loops, while often formed as single layers of vacancies on octrahedral planes, may also be nucleated on other planes; for there is no obvious way in which double loops could arise if they were not nucleated together. Consequently, we must examine the possibility that the great variety of loop orientations is, after all, not due to loop rotations alone, but partly to precipitation of thermal vacancies on {110}, {100} and maybe still other planes besides {111}.

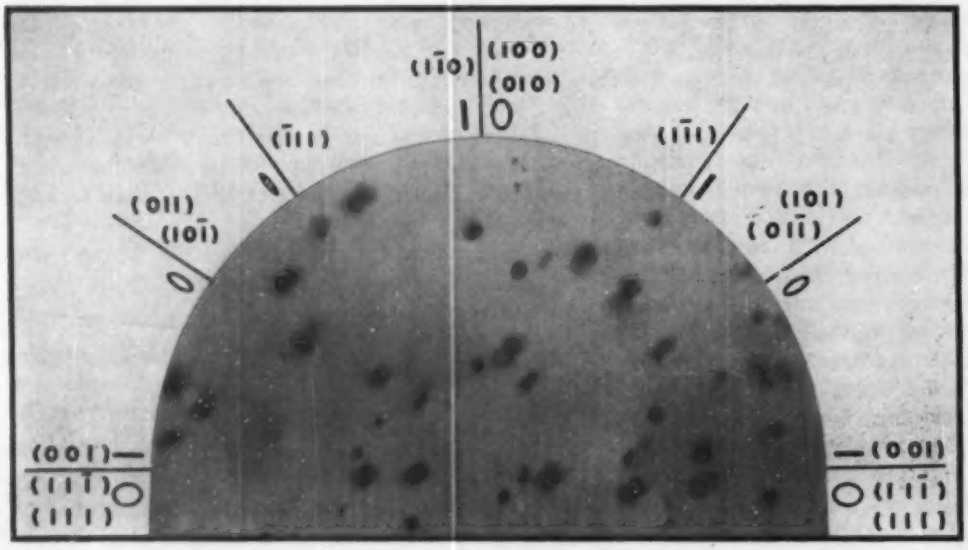

FIG. 4. Pairs of dislocation loops, most of them apparently parallel to {110} planes. Signs on margin have the same meaning as in Fig. 1. 52 000:1.

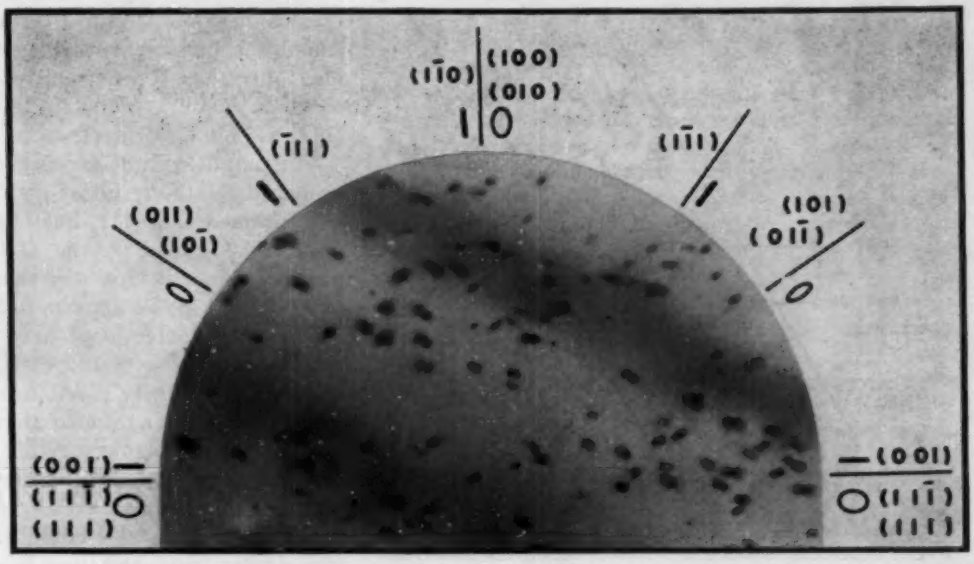

FIG. 5. Pairs of dislocation loops some with orientations near {100} and/or {010}. Signs on margin have the same meaning as in Fig. 1. 32 000:1.

QUANTITATIVE AND QUALITATIVE CONSIDERATIONS ON DIFFERENT MODES OF VACANCY CONDENSATION

Those types of loop might be expected to be formed preferentially which have the lowest relative energy, and, hence, an attempt was made to determine the energy of various types of R loop theoretically. The calculations necessarily have to remain semiquantitative, not only because it would be difficult to take into consideration the anisotropy of the elastic constants, but also because the theoretical formulae for the energy of small dislocation loops are not too firmly established. In the present paper, Franz and Kroener's[6] solution for this quantity has been used, believing that in it the nonlogarithmic term is somewhat overestimated, but that this is compensated by the contribution of the core energy which had not been taken into consideration. In Franz and Kroener's solution, E, the energy o, a dislocation loop of radius R, whose Burgers vector, b, is perpendicular to its own plane, is given as $E = \frac{1}{2}(\mu b^2/1-\nu)R(\ln R/b+5/3)$ where μ is the modulus of rigidity and ν is Poisson's ratio. Loop energies for nine simple modes in which vacancies could condense have been calculated, using the relationship that $R = (\alpha n/m\pi)^{\frac{1}{2}}$ if n vacancies condense in an m-fold layer, parallel to a crystallographic plane in which the atomistic cross section is α, i.e., neglecting the noncircular shape of the loops. The results of these calculations are presented in Table I and Fig. 11.

An R loop will be definitely unstable, at any temperature, if the value E/n exceeds the energy for an isolated single vacancy, E_V, taken to be 0.76 ev. This value lies within the limits of error of the determinations made by several authors[7–9] and has been entered in Fig. 11.

From the numerical results in Table I and Fig. 11 we see that, for a metal with low stacking fault energy, the formation of vacancy layers on {111} planes, symbol A, is the energetically most favorable mode of vacancy condensation. However, in aluminum this type

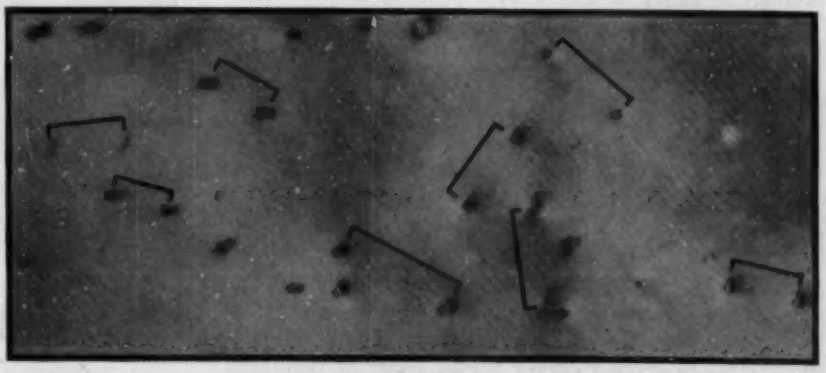

FIG. 6. Pairs of dislocation loops with large distances of separation. 40 000:1.

[6] H. Franz and E. Kroener, Z. Metallk. 46, 639 (1955).
[7] F. J. Bradshaw and S. Pearson, Phil. Mag. 2, 570 (1957).
[8] C. Panseri and T. Federighi, Phil. Mag. 3, 1223 (1958).
[9] W. de Sorbo and D. Turnbull, Acta Met. 7, 83 (1959).

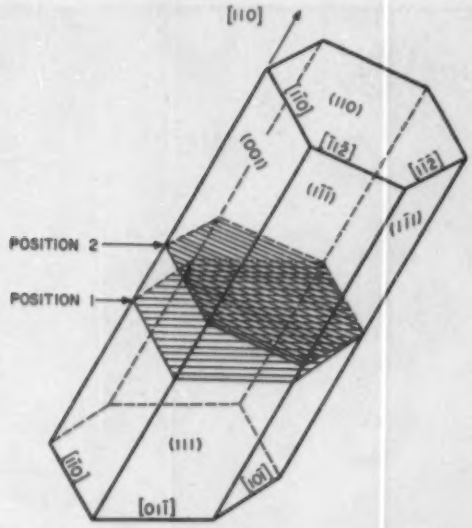

FIG. 7. Schematic drawing of prismatic, hexagonal dislocation loop, type B, and its slip surface. Loop lying in its plane of condensation, position 1, and after rotation into the (110) plane, normal to its Burgers vector, position 2.

of loop has a higher energy than loops condensed according to mode B; for in aluminum, stacking faults have such a high energy that they are eliminated spontaneously, i.e., a type A loop spontaneously converts into a type B loop. Now Fig. 1 and others show many well developed type B loops; and since loops due to double-layer condensation on {110} planes, symbol H, have a lower energy than type B loops we ought to conclude that also type H loops must be present among the multitude of quenched-in dislocation loops.

The equilibrium configuration of H-type loops, as well as of any other type loop, may be predicted with a reasonable degree of confidence. R loops grow by removing atoms from the edge of the missing atomic layer. Atoms in positions of high free energy are much more likely to be exchanged for a vacancy than those with a lower free energy. Atoms lying in a regular, atomistically smooth line, therefore, will not be removed as easily as atoms in a serrated front. Consequently, the missing layer, the outline of which coincides with the R loop, will tend to become atomistically smooth.

In Fig. 12 two successive atomic layers parallel to {110} have been drawn, where all atoms indicated as crosses belong to one layer, and those indicated as circles to the other. If over a certain continuous area all the crosses were removed, then, by the above principle, the edge of the remaining part of the layer would preferentially follow the only ⟨110⟩ direction in the {110} plane. Since no two-dimensional layer could be constructed with this one bounding direction alone, also ⟨100⟩ as second choice would serve as bounding direction, leading to a rectangular R loop. On the other hand, if a *double* layer of vacancies condenses parallel to {110}, symbol H, amounting to the removal of all crosses *and* dots within a certain area of Fig. 12, the smoothest possible bounding directions are the two ⟨112⟩ directions. Consequently, loops formed according to mode H are expected to be diamond shaped, with ⟨112⟩ as bounding directions.

The parallelogram-shaped loop in Fig. 10, thus, was probably not the result of the rotation of a loop originally formed on {111}, but has either been nucleated or at least grown on the (110) plane, according to mode H. Since in this way the occurrence of loops of two different modes appears to be established, the conclusion that double loops have been produced by nucleation according to modes C, F, and/or I appears valid. Of these three possibilities, F is the most likely to give two loops so similar that they would be clearly identified as belonging together: Two adjoining layers on {100} would collapse into a prismatic dislocation with a ⟨100⟩ Burgers vector (see Table I). This slip vector is in metastable equilibrium, and splitting into two similar, noninteracting loops would occur under the influence of stresses.[10] Both the condensed double

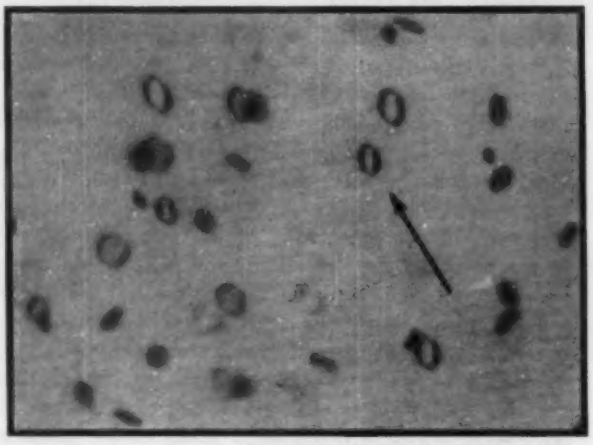

(a)

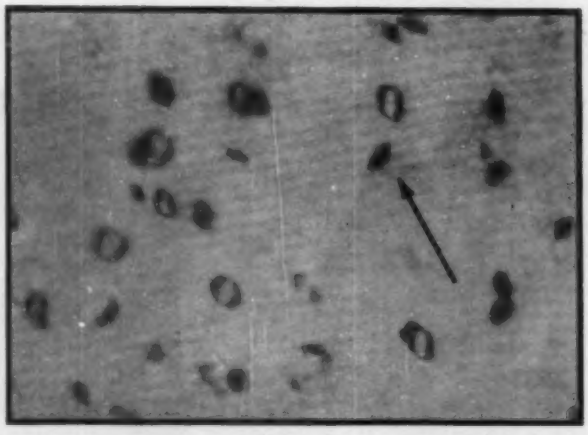

(b)

FIG. 8. (a), (b) Dislocation loop, indicated by arrow, changes its orientation as seen on successive micrographs. 62 000:1.

[10] F. C. Frank and J. F. Nicholas, Phil. Mag. 44, 502 (1953).

TABLE I. Data on the condensation of vacancy layers.

Symbol	Plane of condensation	m No. of consecutive vacancy layers condensing simultaneously	b Resulting Burgers vector	b may dissociate into	Expected bounding directions of R loop	Expected shape of R loop	No. of similar, parallel R loops, (after dissociation, if applicable)	Principal slip system(s) defined by R loop (after dissociation, if applicable)	α/a^2 Relative cross section of one atom in condensation plane	n No. of vacancies contributing to R loop	E Loop energy in ev	E/n in ev	N_{min} Minimum No. of vacancies which may form an R loop (from $E/n=0.76$ ev)	N_{min} Minimum No. of vacancies which may form an R loop (from $r=2b$)
A	{111}	1	$\frac{1}{2}$[111]	unstable in Al $\frac{1}{2}$[111] $+\frac{1}{2}$[11$\bar{2}$] $=\frac{1}{2}$[110]	⟨110⟩	Hexagonal	1	⟨110⟩, {111} and {100}	0.434	7 9 16 25 50 100	6.15 7.38 11.0 15.0 23.8 37.1	0.88 0.82 0.69 0.60 0.48 0.37	12	10
B	{111}	1	$\frac{1}{2}$[110]	stable	⟨110⟩	Hexagonal	1	⟨110⟩, {111} and {100}	0.434	16 36 50 100 140 500 1000	15.4 26.8 33.5 52.7 66.0 146.0 227.0	0.96$_3$ 0.74$_4$ 0.67$_4$ 0.53 0.47 0.29 0.23	34	14
C	{111}	2	$\frac{1}{2}$[112]	$\frac{1}{2}$[101] $+\frac{1}{2}$[011]	⟨110⟩	Hexagonal	2	⟨110⟩, {111} and {100}	0.434	30 50 100 120 130	33.8 50.4 81.5 92.4 98.5	1.12 1.01 0.82 0.77 0.75$_8$	127	87
D	{111}	3	[111]	$\frac{1}{3}$[011] + $\frac{1}{3}$[101] + $\frac{1}{3}$[110]	⟨112⟩[a]	Hexagonal	3	⟨110⟩, {110} and {113}	0.434	50 100 200 300	65.0 103.7 173.0 231.0	1.30 1.04 0.87 0.77	330	260
E	{100}	1	$\frac{1}{2}$[110]	stable	⟨110⟩, (⟨100⟩)	Rectangular (or octagonal)	1	⟨110⟩, {111}	0.500	20 46 50 100 110 140	20.5 35.0 37.0 58.1 61.9 72.5	1.02$_5$ 0.76 0.74 0.58$_2$ 0.56 0.52	46	13
F	{100}	2	[100]	indifferent [100] ↔ $\frac{1}{2}$[110] $+\frac{1}{2}$[1$\bar{1}$0]	⟨100⟩[b] (⟨110⟩)	Rectangular (or octagonal)	2	⟨110⟩, {100}	0.500	16 30 50 100 140	17.3 28.0 40.1 65.4 82.4	1.08$_2$ 0.93$_3$ 0.80 0.65 0.59	60	52
G	{110}	1	$\frac{1}{2}$[110]	stable	⟨110⟩ and ⟨100⟩	Rectangular	1	⟨110⟩, {111}, {100}	0.707	30 50 100 140	33.0 46.4 72.5 90.1	1.10 0.93 0.72 0.64$_3$	86	9
H	{110}	2	$\frac{1}{2}$[110]	stable	⟨112⟩[c] (⟨110⟩)	Diamond-shaped (or hexagonal)	1	⟨110⟩, {111}	0.707	10 20 30 50 100 140	9.45 15.5 20.6 29.2 46.1 58.0	0.94$_4$ 0.77 0.69 0.58 0.46 0.41$_2$	22	18
I	{110}	3	$\frac{1}{2}$[112]	$\frac{1}{2}$[011] $+\frac{1}{2}$[101]	⟨112⟩, (⟨110⟩)	Diamond-shaped (or hexagonal)	2	⟨110⟩, {111}	0.707	30 50 100 140	36.0 52.9 88.4 109.7	1.20 1.06 0.88 0.78	148	80

[a] For 3 consecutive atomic layers parallel to {111} in the fcc lattice the atomistically smoothest boundary is parallel to ⟨112⟩, not ⟨110⟩ as it would be for a single layer.
[b] For 2 consecutive atomic layers parallel to {100} in the fcc lattice the atomistically smoothest boundary is parallel to ⟨100⟩, not ⟨110⟩ as it would be for a single layer.
[c] For 2 or 3 consecutive atomic layers parallel to {110} in the fcc lattice the atomistically smoothest boundary is parallel to ⟨112⟩, not ⟨110⟩ as it would be for a single layer.

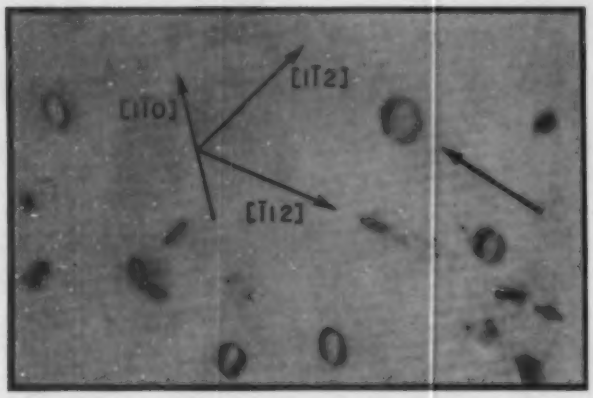

FIG. 9. Example of hexagonal loop which apparently has rotated from (111) to (110) according to Fig. 7. 62 000:1.

layer of vacancies on {111}, mode C, and the triple layer on {110}, mode I, would yield two mutually repelling loops, which would separate immediately after their formation and, hence, would continue to grow in somewhat different surroundings, presumably resulting in slightly different sizes and shapes. Moreover, loop condensation according to mode F is energetically more favorable than according to modes C and I, as seen on Fig. 11, so that we would expect loop pairs to be parallel to cube faces rather than parallel to {111} or {110} planes.

Experimental evidence is not in agreement with the latter conclusion. Most loop pairs of which the orientation could be determined with some confidence are parallel to {111}, as for instance on Fig. 1. Much less frequently loop pairs were found on {100} planes, Fig. 5, and some were discovered which appeared to be parallel to {110}, Fig. 4. This result seems to be significant in connection with the problem of how prismatic dislocation loops are nucleated, and it will be mentioned again later on.

ARGUMENTS FOR VOID FORMATION PRECEDING *R* LOOPS

While one may have confidence in the relative energy values for the various types of loops, which have been used in the argument above, the absolute values are rather more uncertain. As the results stand, according to Table I and Fig. 11, $n_{\min}$, the smallest number of vacancies which could form a dislocation loop, as derived from the consideration that the value of E/n cannot possibly be larger than $E_V=0.76$ ev, ranges from 22 for type H, to 127 for type C, and to 148 for type I. As we have shown, loops of types H, B and at least C have been observed, and it is impossible to see how 22, let alone many more vacancies could coalesce into an R loop without first forming a three-dimensional aggregate. Comparing, then, the energy of three-dimensional aggregates with that of dislocation loops shows that even the above values for $n_{\min}$ are grossly overestimated.

For a macroscopic spherical hole in an fcc lattice of lattice constant a, containing n vacancies, the surface energy, E_0, divided by the number of vacancies in the void is given by $E_0/n=n^{-\frac{1}{3}}\{4\pi\gamma(3a^3/16\pi)^{\frac{1}{3}}\}$, where γ is the surface energy. For aluminum, and assuming γ to be about 1000 ergs/cm², $E_0/n\cong 2/n^{\frac{1}{3}}$. The corresponding curve has been inserted in Fig. 11, marked with the symbol 0. For small n, this formula cannot hold since the specific surface energy depends on the surface curvature, being significantly lower for a small void than for a flat surface. Consequently, for small values of n, E_0/n has been estimated by drawing the tangent from $E_V=0.76$ ev, representing a void containing just one vacancy, onto the curve E_0/n (see Fig. 11). In all probability, the resulting curve, 0'0, lies still higher than actual values of E/n for small three-dimensional aggregates. The minimum number of vacancies, $n_{\min}$, for which it is energetically more favorable to form a

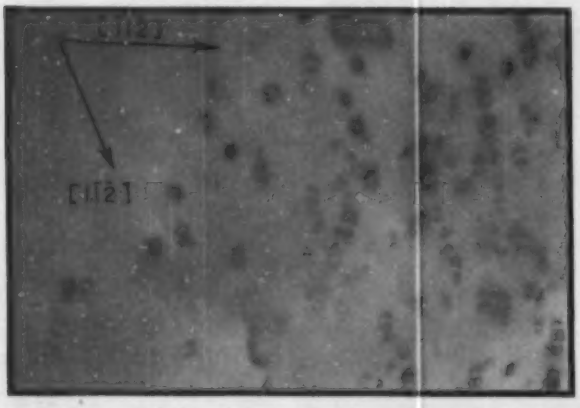

FIG. 10. Diamond-shaped dislocation loop of type H. 40 000:1.

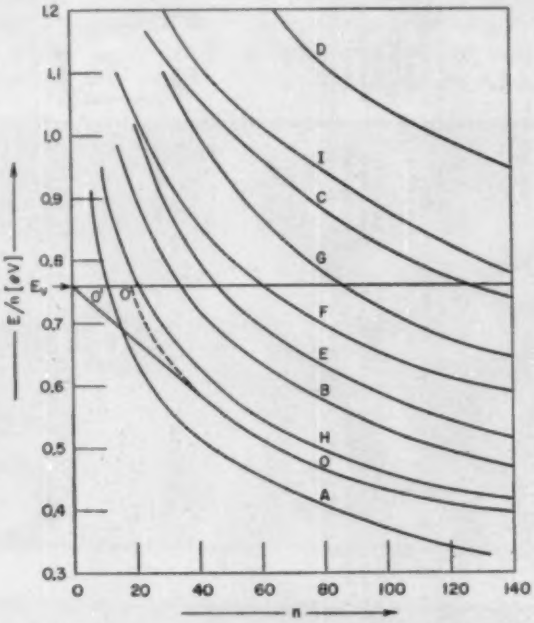

FIG. 11. Energy of different types of R loops and of voids.

dislocation loop instead of a void, is found as the point of intersection between each E/n curve for loops and curve 0'0 for the void, and this is seen to be quite large.

A third method of estimating $n_{\min}$ yields the same result. It is the most simple of all and purely geometrical: we cannot easily imagine an R dislocation the radius of which is smaller than double its Burgers vector. For still smaller diameters, the cores of opposite sides of the dislocation loop would start to overlap. The minimum number of vacancies necessary for a stable loop, as derived from this last concept, is listed in the last column of Table I. Those values are mostly in reasonable agreement with $n_{\min}$ as determined from $E/n \leqq 0.76$ ev, and, again, are generally much too large to allow the direct nucleation of R loops without three-dimensional aggregates as an intermediate stage. Therefore, it is submitted that the prismatic dislocation loops in quenched aluminum are not nucleated by chance collisions of single vacancies or di-vacancies, but have somehow been converted from three-dimensional aggregates, hardly containing fewer than 20 vacancies, and maybe up to thousands.

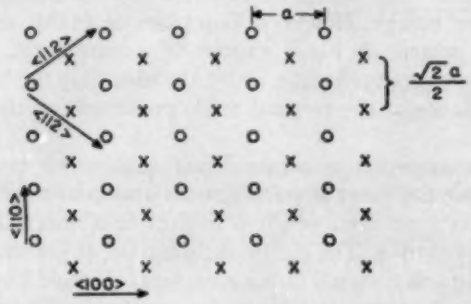

FIG. 12. Schematic representation of the atomic positions in two adjacent layers parallel to {110}.

PREVIOUS RESULTS AND THEIR INTERPRETATION

At this point, it seems advisable to consider the relation between our present results and conclusions, and those published in the literature on the behavior of vacancies in crystals. Panseri and Federighi,[8] after investigating the recovery of quenched-in resistivity in aluminum, concluded that vacancies might well form clusters before migrating to dislocations. In a later paper, Federighi[11] expresses the same idea again, believing that the dissolution of vacancy clusters would explain his results in stage II recovery of the resistivity of quenched aluminum. Tweet,[12] by direct observation of etched surfaces, found evidence of vacancy clusters in germanium slowly drawn from the melt. As reported,[2] Smallman and Westmacott studied the small angle scattering of x-rays in quenched aluminum. The effects found could be interpreted either by the presence of small voids, about 100 A diam, or by the mechanism of double Bragg scattering from dislocation loops, 100 to 500 A diam. It appears that the x-ray results were more in favor of the former explanation, but that it seemed more reasonable to accept the latter because R dislocations had just been discovered.

The evidence adduced so far indicates that voids may be present in quenched aluminum but does not prove their existence in any way. More favorable in this respect is the investigation of length changes during the recovery of quenched aluminum wire due to Takamura.[13] A curve representing the contraction of a wire on heating from 0°C to 400°C, and some slight, apparently unexplained expansion on cooling again to 0° is given. From this curve it may be seen that about 85% of the total irreversible contraction, amounting to $\Delta l/l = 1.4 \cdot 10^{-4}$, took place while heating from 0°C to 75°C, then the length stayed constant for roughly the next 30°C. From about 105°C on, a second stage of length contraction commenced accounting for the remaining 15% of the final permanent contraction, and extending to about 160°C. The latter limit is just about the temperature at which such prismatic dislocation loops as can be observed easily in the electron microscope begin to contract through climb at a noticeable rate.[14] It is also the temperature quoted by Panseri and Federighi[8] as typical for stage II recovery, which apparently takes place with the energy of self diffusion.

The elimination of R dislocations, as directly observed by Silcox and Whelan,[14] must certainly be accompanied by a reduction of electrical resistivity, but it will not cause noticeable length changes; by contrast, the dissolution of three-dimensional vacancy aggregates should have a small influence on electrical resistivity, but lead to length changes in wires directly proportional to the total volume of the voids affected. Moreover, the activation energy associated with the dissolution of R loops of typical size, say, more than 500 A diam, would indeed be the energy of self diffusion, so that almost certainly a great portion of stage II recovery in the experiments by Federighi and Panseri is due to the elimination of R loops.

Generally, the activation energy, U, with which any kind of vacancy aggregate is dissolved, will be given by $U = U_v - E/n + U_m$. Here, U_v and U_m are respectively the self-energy and the energy of motion for a vacancy, and E/n has the same meaning as before, being the share per vacancy of the aggregate's self energy. With U_D as the energy of self diffusion, this might also be written as $U = U_D - E/n$. For a normal sized R loop, say type B, 500 A diam, containing in the order of 3×10^4 vacancies, E/n amounts to only about $\frac{1}{16}$ ev, leaving U for this case practically indistinguishable from U_D, as was stated already.

The conditions are quite different, however, for voids. The average number of vacancies contributing to a

[11] T. Federighi, Phil. Mag. 4, 502 (1959).
[12] A. G. Tweet, J. Appl. Phys. 29, 1520 (1958).
[13] J. Takamura, Metal Phys. (Japan) 2, 112 (1956).
[14] J. Silcox and M. J. Whelan (private communication) (to be published, 1959).

void should be much smaller than that for an R loop because the latter has a considerable stress field associated with itself, attracting vacancies from larger distances, while, in first approximation, a void absorbs only those vacancies which directly meet it in random walk. If one takes, ρ, the radius around a dislocation axis within which all vacancies will be captured as, say 50 or 100 A,[15] then a void will start to absorb more vacancies per unit time than an R loop, containing the same number of vacancies, when its diameter becomes much larger than ρ. However, in the present case, this limit cannot nearly be reached because the average R loops of 500 A diam correspond to voids of only about 50 A diam. Values for E_0/n, as would apply to subcritical or small stable voids up to 17 A diam, may be taken from Fig. 11, and are found to be in excess of 0.4 ev. For clusters containing about 1000 vacancies, diam 32 A, $E_0/n=0.2$ ev; and even for clusters of 50 A diam, which, according to the above, are rather larger than expected to occur in quenched aluminum, $E_0/n=0.065$ ev.

From the results presented by Panseri and Federighi,[8] Federighi[11] and Takamura[12] it is estimated that values of E/n between 0.1 and 0.4 ev are consistent with the second stage of length contraction.[13] To sum up, the evidence available so far may be explained in the following way: On annealing quenched pure aluminum up to about 75°C, roughly 85% of all quenched-in vacancies condense at R loops with average diameters between 500 and 1000 A, and, to a lesser degree, at other possible vacancy sinks. At the same time, the remaining 15% of the vacancies aggregate into voids, containing several or up to several thousand vacancies. Between just over 100°C and 160°C, the redissolution of the voids takes place with activation energies from about 0.4 to 0.1 ev below that of the energy of self-diffusion, depending on the size of the voids. From about 160°C upwards, the R loops are eliminated by climb, as was directly observed by Silcox and Whelan.[14] This would not be detectable in dilatometric experiments, but become apparent through changes in the electrical resistivity, probably accounting for a major part of stage II in Panseri's and Federighi's experiments.[8,11] For theoretical reasons, as explained, the R dislocation climb should proceed with the activation energy of self-diffusion, which is in agreement with these results.[8,11]

ON THE CONVERSION OF VOIDS INTO LOOPS

In equilibrium, three dimensional aggregates in an fcc metal presumably are bounded by {111} planes. If such an aggregate collapses, so that opposite {111} faces fuse together, a series of concentric dislocation loops is formed which immediately will move apart due to their mutually repulsive forces. Under these conditions, it is likely that the smaller of those loops will "evaporate" rapidly, and that the vacancies from them will partly be attracted to the larger ones, condensing on them. While even the remaining one or two loops, now larger than the cross section of the original void, may still be too small to be stable as compared to a three-dimensional aggregate, it would require an activation energy of undetermined magnitude to reconvert such loops into voids. Therefore, the loops could continue to grow.

Faced with the strong evidence that voids are formed as an intermediate stage before prismatic loops, the foregoing mechanism is plausible because orientation determinations obtained in the present investigation indicate that most loops have in fact been formed on {111} planes, while if the loop plane was governed by dislocation energy, H loops on {110} should be frequent, rather than rare. Also, as has been discussed already, loop pairs frequently are parallel to {111} (in Fig. 1 for example), which corresponds to mode C, although their energy is much higher than that of loop pairs parallel to {100}, mode F. The latter seem to be present occasionally (see Fig. 5), but in much smaller numbers than would be expected from considerations of loop energy. However, loop pairs on {110}, as seem to be present on Fig. 4, cannot be accounted for, either by the energy principle, or by the idea that the bounding planes of the original voids predetermine the loop planes.

The question remains: What causes the voids to collapse and form loops? Consider an initially spherical void in a material which is subject to a uniaxial compressive stress. The elastic deformation of the material will deform the void into a rotational ellipsoid but with the ratio of the axes very close to unity. The region around the circumference of the ellipsoid will be subject to a stress concentration while the poles will be stress-free. As a consequence, surface diffusion will take place so as to transport vacancies from the poles towards the equator, thereby flattening the ellipsoid. A detailed calculation would be necessary to show whether at moderate random stresses this effect could convert approximately spherical voids of more than 20 vacancies into lens shaped voids with a thickness corresponding to, say, two or three atomic planes, which would then collapse to form prismatic loops. Such a process would account for the observation that prismatic loops tend to be arranged in clusters, often containing a high proportion of parallel loops, listed as observations 2 and 3.

The conversion of voids into loops might be simpler than would appear at first glance from the above discussion. It was stated in the foregoing that voids will tend to be bounded by {111} planes rather than being spherical. Quite possibly, then, voids at certain stages during their growth, up to and just beyond the critical size, could assume shapes which require only a small activation energy in order to collapse them into loops.

[15] C. W. Berghout, Acta Met. 6, 613 (1958).

SUMMARY

R loops in quenched aluminum were observed in a considerable variety of orientations. Partly, this was found to be due to the rotation of loops out of their original planes. However, the occurrence of loop pairs, as well as diamond shaped loops parallel to {110} and bounded by ⟨112⟩ directions, proves that the manifold loop orientations are not due to loop rotations alone, but also to the fact that vacancy condensation is not restricted to single layers of vacancies parallel to {111} planes. Calculations on the minimum number of vacancies for which various types of *R* loop are stable, as compared to single vacancies and to voids, show that void formation must precede the creation of *R* loops. Independent experimental results published in the literature give support to this latter conclusion. A mechanism is tentatively proposed, which could explain the conversion of voids into loops; and which, at the same time, would explain the observations that *R* loops as well as loop pairs mostly are parallel to {111} planes, and that they tend to arise in clusters, each containing a surplus of loops with one particular orientation, separated by regions virtually free of loops.

ACKNOWLEDGMENTS

This investigation was supported by the U. S. Atomic Energy Commission.

For the preparation of specimens, we wish to thank Mr. C. J. Varker and Mr. L. Cinquina, both at The Franklin Institute Laboratories, who also conducted the quenching experiments.

JOURNAL OF APPLIED PHYSICS VOLUME 31, NUMBER 3 MARCH, 1960

Numerical Calculation of Absolute Bremsstrahlung Intensity for a Fully Ionized Fully Dissociated Hydrogenic Gas*

G. Sargent Janes and H. Koritz
Avco-Everett Research Laboratory, Everett, Massachusetts
(Received September 29, 1959)

By using the approximate relationships of Kirkpatrick and Weidmann [Phys. Rev. 67, 321 (1945)] for bremsstrahlung intensities, numerical calculations have been made on the IBM 650 at the Avco-Everett Research Laboratory for a fully ionized, fully dissociated hydrogenic gas. The intensities are given in terms of a quantity having the units ergs/sec/unit frequency interval/steradian/cm³ as a function of $h\nu$, (from 0.5 to 4.0 ev) and kT (from 4 to 200 ev). A calibration method has been devised for measurement of absolute bremsstrahlung intensities which continually compensates for the errors present in most calibration procedures.

INTRODUCTION

ONE of the measurable properties of a highly ionized gas is the free-free continuous radiation spectrum resulting from the interaction of the free electrons with the atoms, ions, and molecules, which is called bremsstrahlung. From measurements of this radiation, one can obtain information concerning the electron density and temperature, providing thermal equilibrium can be assumed for the electrons.

For such experimental information to be meaningful, one must calculate the expected intensities at various wavelengths as a function of the gas state, specifically, the temperature and the electron energy distribution. Such calculations are difficult, since the expression for the differential cross section for such an interaction is complicated. An explicit expression has been developed by Sommerfeld[1] by using the dipole approximation and a "no screening" assumption, i.e., the assumption of a pure Coulomb field. Sommerfeld's expression, however, is not in a closed form.

Other expressions have been derived for bremsstrahlung intensities which are only useful under particular experimental conditions. The Born approximation (valid when $2Ze^2/h\nu \ll 1$) provides a simple radiant intensity formula. Unfortunately, this requires electrons near relativistic velocities for validity. In atomic hydrogen, for example, the electron thermal velocity must be large compared to 3×10^8 cm/sec, hence, $T \gg 200\,000°$K.

By assuming a Maxwellian distribution and the Born approximation, Spitzer[2] arrives at the total radiated energy

$$\epsilon = (2\pi kT/3m_e)^{\frac{1}{2}}(2^5\pi e^6/3hm_ec^3)Z^2N_eN_I. \quad (1)$$

where ϵ is the radiated energy in ergs/cc/sec.

To compute the intensity in most experimental situations where the velocities are small, one must use Sommerfeld's dipole approximation which neglects both relativity and the retardation term and assumes a pure

* This work was supported in part by the Directorate of Advanced Studies, Air Force of Scientific Research, ARDC, under contract 49(638)-61.

[1] Sommerfeld, Ann. Physik 11, 257 (1931).

[2] L. Spitzer, *Physics of Fully Ionized Gases* (Interscience Publishers, Inc., New York, 1956), p. 90–91.

coulomb field. This requires a numerical integration. Such integrations have been performed by Weinstock,[3] and by Kirkpatrick and Weidmann,[4] from whose data we calculated the absolute bremsstrahlung intensity curves on an IBM 650. Experimental data discussed in both papers[3,4] agree with their theoretical results when the Sommerfeld conditions are met.

INTENSITY EQUATIONS

When electron spin is ignored, the intensity of radiation of frequency ν in a direction θ is given by[4]

$$I_\nu(\theta)=I_x\sin^2\theta+I_y(1+\cos^2\theta), \tag{2}$$

where $I_\nu(\theta)$ is the intensity of radiation at frequency ν in the units of ergs/unit solid angle/unit frequency interval/bombarding electron/atom-per-cm^2 of target area and I_x, I_y is given by Eq. (3) in reference 4. Integration of Eq. (2) above over 4π steradians yields the following expression:

$$W=(8\pi/3)(I_x+I_y+I_z), \tag{3}$$

where W is the total energy of radiation in all directions in ergs/unit frequency interval/bombarding electron/atom-per-cm^2 of target area.

On page 328 of reference 4, approximate expressions are devised which fit their results with a mean error of 2% for the entire range of photon energies. Following are the equations from page 328 which were used in our numerical integration to obtain the Bremsstrahlung curves:

$$I_x'\times10^{50}V/Z^2=0.252+a(\nu/\nu_0-0.135)-b(\nu/\nu_0-0.135)^2 \tag{4}$$

where

$$a=1.47B-0.507A-0.833,$$
$$b=1.70B-1.09A-0.627,$$
$$A=\exp(-0.223V/Z^2)-\exp(-57V/Z^2),$$
$$B=\exp(-0.0828V/Z^2)-\exp(-84.9V/Z^2),$$

and

$$I_{y,z}'\times10^{50}V/Z^2=-j+[k/(\nu/\nu_0)+h], \tag{5}$$

where

$$h=-0.214y_1+1.21y_2-y_3/1.43y_1-2.43y_2+y_3,$$
$$j=(1+2h)y_2-2(1+h)y_3,$$
$$k=(1+h)(y_3+j),$$
$$y_1=0.220[1-0.390\exp(-26.9V/Z^2)],$$
$$y_2=0.067+0.023/[(V/Z^2)+(0.75)],$$
$$y_3=-0.00259+0.00776/[(V/Z^2)+0.116],$$

where V is the potential difference or energy of the electrons in ergs/esu, ν is the frequency of the emitted photon, ν_0 is the frequency associated with the initial energy of the electrons before collision ($h\nu_0=Ve$), and Z is the atomic number of the target.

[3] R. Weinstock, Phys. Rev. **61**, 584 (1942).
[4] P. Kirkpatrick and L. Weidmann, Phys. Rev. **67**, 321 (1945).

The results of these calculations were substituted in Eq. (3). From Eqs. (4) and (5), it is seen that W is a function of V/Z and ν/ν_0 only.

The following assumptions were made in developing the expression which was finally used on the IBM 650: (1) The gas is fully ionized and dissociated and is composed of atomic hydrogen or deuterium; (2) The ions are assumed fixed with respect to the electrons; (3) The electron motion is completely random, so that as many electrons are moving in one direction as are moving in any other direction and as a result the angular dependence of the emitted photons is isotropic; and (4) At least electron thermodynamic equilibrium exists in the gas, thus permitting the utilization of the Maxwell-Boltzmann distribution function.[5]

From assumptions (2) and (3) one can write a quantity R_ν' defined by

$$R_\nu'=N_e(E)v(E)N_I[W(\nu/\nu_0,V/Z^2)/4\pi]. \tag{6}$$

It is seen that $W/4\pi$ is a cross section term obtained in the unusual units of Eq. (2) by the normalization procedure of Weinstock.[3] In Eq. (6), $N_e(E)$ is the electron density in electrons/cm^3 having an energy E, N_I is the ion density in ions/cm^3, $v(E)$ is the velocity of electrons of energy E in cm/sec, and $W/4\pi$ is a cross section in the units ergs/unit solid angle/unit frequency interval/bombarding electron-per-cm^2 of target area. [Note: This division by 4π follows from assumption (3).] Thus R_ν' is in the units ergs/cm^3/sec/unit solid angle/unit frequency interval about $h\nu$ for electrons of velocity v or energy E where $E=Ve=1/2m_ev^2$ (ergs).

To obtain the total contributions to the frequency interval about $h\nu$, we must integrate Eq. (6) over all velocity or energy intervals $h\nu$. Thus in terms of energy we have a quantity $Y(\nu)$ given by

$$Y(\nu)=\int_{h\nu}^{\infty}N_e(E)v(E)N_I\frac{W(\nu/\nu_0,V/Z^2)}{4\pi}dE, \tag{7}$$

where $Y(\nu)$ has the units ergs/cm^3 of radiation $h\nu$ emitted per sec in unit solid angle.

Assumption (4) allows us to write the electron energy distribution as a Maxwell-Boltzmann distribution, i.e.,

$$N_e(E)dE=n2/\sqrt{\pi}(E^{\frac{1}{2}}/kT)e^{-E/kT}(dE/E), \tag{8}$$

where n is the total number of electrons/cm^3.

Upon substitution of Eq. (8) into Eq. (7), multiplication and division by 10^{50} [see Eqs. (4) and (5)] and conversion from esu to ev, the following equation results:

$$Y(\nu)=5.3\times10^{-44}\frac{n^2}{(kT)^{\frac{1}{2}}}\int_{h\nu}^{\infty}(W\times10^{50})e^{-E/kT}EdE, \tag{9}$$

[5] Should enough time have elapsed for ion-electron equilibration to take place, then these calculations apply to the ion temperature as well. The ion-electron equilibration time is on the order of 2000 times that of the electron-electron equilibration time.

where n^2, the electron density squared, results from assumption (1), and the units of E, kT, and $h\nu$ are ev.

NUMERICAL PROCEDURE

The procedure for calculating the bremsstrahlung intensities on the IBM 650 is roughly as follows: (1) assume kT, (2) assume the frequency of radiation $h\nu$, (3) assume the electron energy, (4) choose $Z=1$ from assumption one, (5) choose an energy interval equal to approximately 0.25 ev. Maintaining ν constant, the ratios ν/ν_0, and V/Z^2 are functions of electron energy. Thus any change in $N_e(E)$ results in new I_x, $I_{y,z}$ [Eqs. (4) and (5)] and a new W. Integrating over the Maxwell-Boltzmann distribution yields the total radiation of frequency ν.

RESULTS

The results of the calculations are shown in Fig. 1 where $Y(\nu)/n^2$ is plotted as a function of $h\nu$, the photon energy, and kT, the Boltzmann temperature. The Maxwell-Boltzmann distribution rises from zero towards a maximum number of particles having energy kT and then decreases somewhat exponentially toward zero. For small $kT/h\nu$ any change in $h\nu$ over kT is manifested by a rapid change in $Y(\nu)$ since the number of contributing electrons changes exponentially with energy. For $h\nu \ll kT$, the number of contributing electrons changes very slowly with $h\nu$. The primary energy dependence is then a general decrease in the intensity associated with the increased frequency range over which the radiant energy is spread.

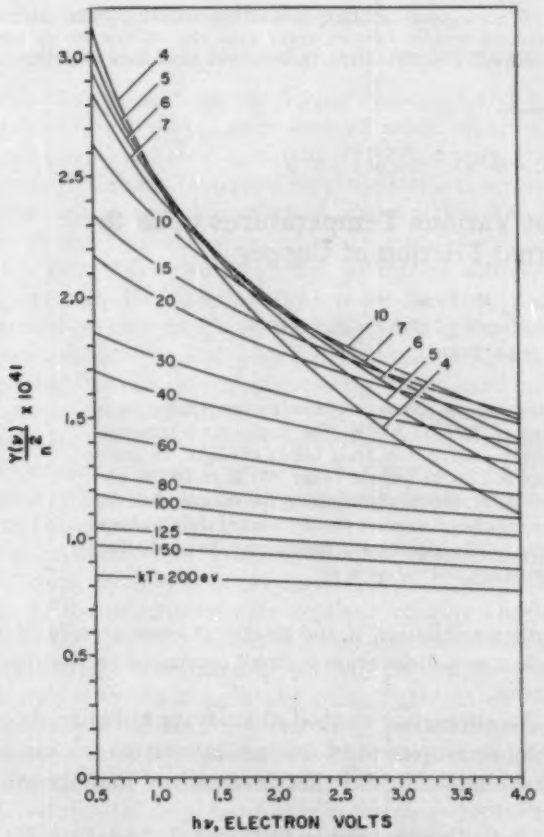

FIG. 1. Absolute bremsstrahlung intensity curves. Numerical integration of Eq. (9) results in the curves of the above figure. The ordinate is the ratio of the bremsstrahlung intensity to the square of the electron density, $Y(\nu)/n^2$, where $Y(\nu)$ has the units ergs/sec/unit frequency interval/cm³/unit solid angle. The abscissa is the energy of the emitted photons $h\nu$, in ev. Curves are shown for various kT.

Under this condition, measurement of the bremsstrahlung radiation intensity provides an excellent means of determining the plasma density, but relatively little information about the temperature.

APPENDIX

Method of Measurement

Absolute intensity measurement can be made by utilizing a photomultiplier with calibrated response in conjunction with a calibrated wavelength selective filter in an optical system which looks at a known portion of the plasma through a known solid angle. We have found it convenient to minimize the number of measured quantities by utilizing a substitution scheme whereby each measurement is a direct comparison of the plasma brightness, with the brightness of a tungsten filament whose temperature is known.

This is accomplished by the use of an optical train which contains a light chopper and a slit in front of the photomultiplier. This slit is automatically focused on a part of the filament and on a part of the plasma. This is accomplished either by direct substitution or with the aid of a single high quality mirror. By minimizing the number of measured quantities, we eliminate many sources of error, and the simplicity of the technique reduces the temptation to rely upon the consistency of a calibration over any extended period of time.

The result of radiation falling on a photomultiplier is to produce a voltage pulse of amplitude $V(\nu)$ where ν refers to the particular light frequency. Using the substitution technique, the intensity of the plasma, $[I(\nu)]_{\text{plasma}}$ can be related to the brightness of the tungsten lamp $[I'(\nu,T)]_{\text{lamp}}$, where T refers to the temperature of the tungsten lamp. Thus,

$$[I(\nu)]_{\text{plasma}} = \{[V(\nu)]_{\text{plasma}}/[V'(\nu,T)]_{\text{lamp}}\}[I'(\nu,T)]_{\text{lamp}} \quad (10)$$

or

$$[I(\nu)]_{\text{plasma}} = [V(\nu)]_{\text{plasma}}/K'(\nu) \quad (11)$$

where

$$K'(\nu) = [V'(\nu,T)]_{\text{lamp}}/[I'(\nu,T)]_{\text{lamp}}. \quad (12)$$

In Eqs. (10) to (12), $K'(\nu)$ has the unit of v/erg/cm²/sec/steradian/unit frequency interval and $[I(\nu)]_{\text{plasma}}$ and $[I'(\nu',T)]_{\text{lamp}}$ have the units of ergs/cm²/sec/steradian/unit frequency interval. Knowing the tem-

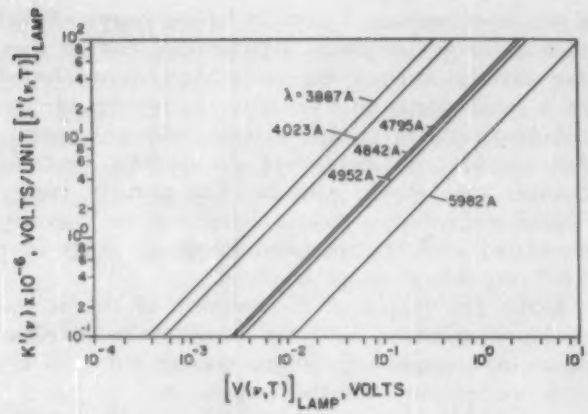

FIG. 2. Photomultiplier calibration curves for a tungsten lamp at 2738°K. The above curves are obtained from Eq. (12) and Table I of the Appendix. The ordinate is the photomultiplier sensitivity calibration, $K'(\nu)$. The abscissa is the oscilloscope signal, $[V'(\nu,T)]_{\text{lamp}}$ in v, for the lamp at 2738°K. *Note.*—The label at the bottom of the figure should read $[V'(\nu,T)]_{\text{lamp}}$, volts.

perature of the lamp (in our case it was 2738°K) we know $[I'(\nu,T)]_{\text{lamp}}$ from the Planck blackbody curve. Table I lists the pertinent information where $K'(\nu)$ is normalized to $[V'(\nu,T)]_{\text{lamp}}$ equal to 1 v. Figure 2 is a plot of $K'(\nu)$ *vs* $[V'(\nu,T)]_{\text{lamp}}$. By varying the photomultiplier voltage so as to obtain the desired $[V'(\nu,T)]_{\text{lamp}}$ conversion from one sensitivity to another is simple and rapid.[6]

TABLE I. Photomultiplier sensitivity calibration, $K'(\nu)$. The parameter is obtained from Eq. (12) with $K'(\nu)$ normalized to $[V'(\nu,T)]_{\text{lamp}}$ equals 1 v.

λ in Å	$h\nu$ in ev	$[I'(\nu,T)]_{\text{lamp}}\times10^{9}$ in ergs/cm²/sec/steradian/unit freq. interval	$K'(\nu)\times10^{-6}$ in v/unit $[I'(\nu,T)]_{\text{lamp}}$
3887	3.185	3.88	257.8
4023	3.08	5.30	188.7
4795	2.59	25.00	40.0
4842	2.56	27.2	36.8
4952	2.50	32.4	30.9
5982	2.07	107.0	9.3

Having decided upon $K'(\nu)$, one can easily obtain the intensity of radiation from the gas by utilizing Eq. (11), where one sees that $I(\nu)$ is merely $V(\nu)$ multiplied by the thickness of the gas sample.

ACKNOWLEDGMENT

The authors are indebted to Mr. Harry Kachedorian for the computational work done on the IBM 650.

[6] Transmission or absorption effects resulting from the use of windows and/or mirrors enter into the calibration as simple multiplying factors. Here, these factors have been assumed unity.

JOURNAL OF APPLIED PHYSICS VOLUME 31, NUMBER 3 MARCH, 1960

Effect of Fast Neutron Bombardment at Various Temperatures upon the Young's Modulus and Internal Friction of Copper

D. O. THOMPSON AND V. K. PARÉ
Solid State Division, Oak Ridge National Laboratory, Oak Ridge, Tennessee*

(Received September 14, 1959)

Studies have been made of the variations of internal friction and elastic modulus during irradiation of pure copper crystals at a number of temperatures in the range 90°K to 300°K. The results are interpreted in terms of pinning of dislocation lines by radiation defects migrating from their points of origin. In terms of the room temperature value the dislocation pinning rate is 2.5×10^{-2} in the range 100°K to 140°K and (from previous measurements) of the order of 2.5×10^{-5} at 20°K. On slowly warming the sample after the irradiation, it is found that at 260°K the modulus and decrement begin to move rapidly toward their "saturation" values. Presumably, defects "stored" in the sample due to a lack of thermal mobility at the irradiation temperature become mobile at this temperature and move to the dislocation lines.

I. INTRODUCTION

MANY measurements have been made in an effort to learn something of the effect of temperature on radiation damage processes in metals. In a large number of these experiments, the production and subsequent annealing of radiation defects have been observed by measuring the electrical resistivity of the material. While measurements of this property have yielded a great deal of information, they suffer from the drawback that processes such as migration of defects to dislocation lines may go undetected or be confused with annihilation if the electrical cross section of the defect in a dislocation is small compared to that in the lattice.

An alternative method of studying radiation defects is by measurement of changes in internal friction and elastic modulus.[1–5] It has been shown[1] that the varia-

* Oak Ridge National Laboratory is operated by Union Carbide Corporation for the U. S. Atomic Energy Commission.

[1] D. O. Thompson and D. K. Holmes, J. Appl. Phys. **27**, 713 (1956).
[2] H. Dieckamp and A. Sosin, J. Appl. Phys. **27**, 1416 (1956).
[3] Thompson, Blewitt, and Holmes, J. Appl. Phys. **28**, 742 (1957).
[4] R. S. Barnes and N. H. Hancock, Phil. Mag. **29**, 527 (1958).
[5] A. Sosin and L. L. Bienvenue, Bull. Am. Phys. Soc. Ser. II, **4**, 169 (1959).

tion of these quantities during irradiation at room temperature is well described by a simple theory of pinning of dislocation lines by the defects. Since measurements are made on samples having low dislocation densities, the defects must migrate an appreciable distance to reach the dislocations; in addition, the sensitivity of the experiment is very high, since a defect concentration of 10^{-9} atomic percent produces a readily measurable effect. Furthermore, the amplitude of vibration is kept very small, so that motion of the dislocations during the measurement is completely negligible. Thus, in this type of experiment the dislocations in the sample act as a stationary, highly sensitive detecting network for defects which migrate by diffusion or other processes.

With these considerations in mind, it was thought desirable to study the temperature dependence of the migration rates of radiation defects by measurements of the modulus and internal friction changes during irradiation at various constant temperatures. Although these experiments have not yet been completed, it appears worthwhile to report the results obtained to date in the temperature range 90°K to 300°K, leaving detailed interpretation to a later paper.

II. EXPERIMENTAL MATERIAL AND PROCEDURE

The measurements of the Young's modulus and internal friction reported here were all made upon one copper single crystal of nominally 99.999% purity at a frequency of about 11 kcps. This procedure has several obvious advantages, the principal one of which is that more or less the same dislocation structure is utilized as the defect detector from run to run at different temperatures. The effects of any one bombardment can be erased by an appropriate anneal. It is true that the dislocation density and loop length apparently vary somewhat from run to run, presumably due to handling, but these variations can be taken into account approximately by the simultaneous measurement of modulus and internal friction. A second advantage of using the same crystal is the absence of any effects due to varying crystal orientation.

The modulus and internal friction measurements were made by means of an apparatus previously described.[6] Bombardments were obtained utilizing a beam hole of the ORNL graphite reactor. In this facility a neutron beam was brought out of the reactor into incidence with the sample and then caught in an external shield. The flux and spectrum of the fast neutrons emanating from this hole have not yet been measured. On the basis of comparisons with other facilities it is believed that the total fast flux is in the range 1×10^6 to 3×10^6 neutrons/cm²/sec. The sample was held in a double-walled cryostat immersed in liquid nitrogen. Bombardment temperatures were maintained through a combination of helium exchange gas in the outer cryostat jacket and heat applied to the inner cryostat wall which surrounds the sample. With this system the maximum temperature variation during a 200-hour run was of the order of ±3°K. While closer regulation would have been preferred, it is felt that in the range 90°K to 300°K this variation is not sufficient to alter the results appreciably.

[6] D. O. Thompson and F. M. Glass, Rev. Sci. Instr. 29, 1034 (1958).

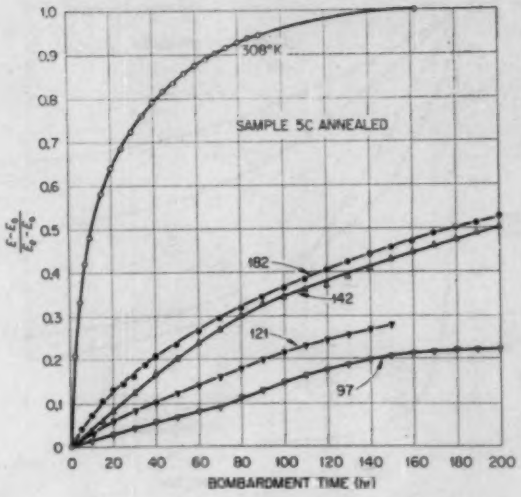

FIG. 1. Fractional completion of modulus change as a function of bombardment time. E is Young's modulus; E_0 is the initial value, and E_s is the final value after the irradiation effect is fully saturated.

The present study was made using constant-temperature bombardment in preference to pulse annealing because the delicately mounted, relatively massive internal friction sample is not amenable to rapid temperature changes. Only qualitative annealing data were obtained. This was done by measurement of the modulus and internal friction during the warmup to room temperature (at the rate of about 1°K per minute) immediately following each irradiation.

III. EXPERIMENTAL RESULTS

In Fig. 1 are shown the results of different constant temperature neutron bombardments upon the Young's modulus. The bombardment temperatures are noted in the figure. The symbol E in the ordinate is the measured modulus at time t, E_0 is the measured modulus at zero time, and E_s is the elastic or "saturated" modulus (with the dislocations completely pinned by defects). These are all measured at the bombardment temperature. Since it has been established that the dislocation contribution to the measured modulus is a function of temperature, at least at this measurement frequency, the ordinate in this figure has been chosen to represent a normalized fractional completion of the modulus change as a function of time (or integrated neutron flux) at several different temperatures. Consequently, each of the curves in the figure would approach unity if the bombardments at the various temperatures had been extended sufficiently long. Conversely, for a given

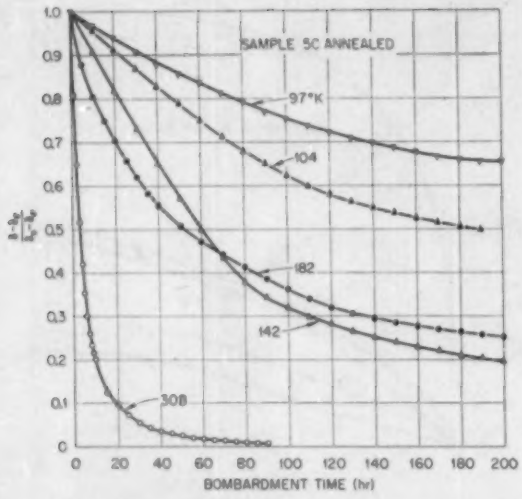

FIG. 2. Fractional completion of decrement change as a function of bombardment time. δ is the logarithmic decrement; the subscripts have the same meaning as in Fig. 1.

bombardment time, the fractional completion value gives a relative measure of the governing defect rate constant as a function of temperature.

Figure 2 shows the logarithmic decrement curves obtained in the same set of experiments given in Fig. 1. These data are normalized in a fashion similar to those given in Fig. 1, so that the relative completion is shown as a function of bombardment time at different bombarding temperatures. On the ordinate δ is the measured decrement at time t, δ_0 is the decrement at the beginning of the run, and δ_e is the final value of the decrement. These quantities are also measured at the bombardment temperature. It is to be noted that the decrement of the crystal used does not depend markedly upon the temperature in the range covered. As would be expected on the basis of previous work,[1] the decrement completion curves bear a marked relationship to the modulus completion curves.

Some other interesting results have been observed in the first sample warmups to room temperature following lower temperature bombardments. Figure 3 shows one of these warmups following a 90-hour bombardment at 168°K. In this plot the solid circles represent the measured resonant frequency during warmup, and the filled triangles represent the decrement values. The dashed line on the plot represents the "saturated" resonant frequency *vs* temperature values. The most striking feature in this plot is, of course, the rapid "annealing," in both the frequency and the decrement, which begins at about 260°K. This effect may apparently be identified with a similar one found at the same temperature in electron-irradiated copper by Sosin and Bienvenue,[5] who also observed an additional modulus increase in the range 200°K to 240°K.

It is to be noted that, while the term "annealing" is used for identification with the more familiar resistance annealing data, it actually involves in this case an increase, rather than a reduction, of the irradiation effect. Physically this can only mean that some radiation-produced defect produced and stored at lower temperatures becomes thermally mobile at about 260°K and migrates to the dislocation sinks. This "annealing" stage thus carries further toward saturation the dislocation pinning process which had been started by defects mobile at the temperature of irradiation. A similar "annealing" stage has been observed previously at 35°K.[3] True annealing in which the dislocations become unpinned occurs well above room temperature and is used in these experiments to restore the sample to its pre-irradiation state.

One other feature, frequently found in the warmup curves, is illustrated in Fig. 4. The circles and triangles in this figure have the same meaning as those in Fig. 3.

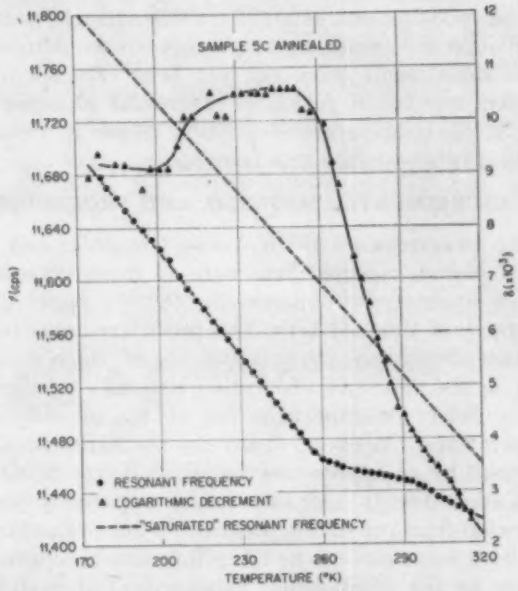

FIG. 3. Logarithmic decrement and resonant frequency during initial warmup after irradiation at 168°K.

In addition to the sharp maximum in the internal friction at about 220°K, there is an accompanying temporary rise in the resonant frequency at approximately the same temperature. While these peaks have been observed on a number of occasions, no concerted study of them has yet been made; thus, only meager information is available at present. They have occurred, with various magnitudes, between 210°K and 230°K, usually in the first warmups immediately following irradiations. They have appeared after bombardments made from 89°K to 142°K but not after bombardments at 168°K and 182°K. They seem to represent a transient phenomenon in that the decrement and modulus return, above the temperature of the peak, to curves which are good extrapolations of those existing below the peak temperature.

IV. DISCUSSION

Even though the data presented here are to be regarded as preliminary, and the conclusions drawn therefrom to be treated in a similar way, certain broad features of the data seem certain and justify further discussion. One of these features is the relative dislocation pinning rate as a function of bombardment temperature. It has been shown previously[1] that radiation-induced changes in the modulus and decrement can be described quite well by the equations

$$\frac{1}{E(l)}=\frac{1}{E_e}+\left(\frac{1}{E_0}-\frac{1}{E_e}\right)\cdot\frac{1}{(1+\gamma l)^2} \tag{1}$$

and

$$\delta(l)=\delta_e+\frac{\delta_0-\delta_e}{(1+\gamma l)^4} \tag{2}$$

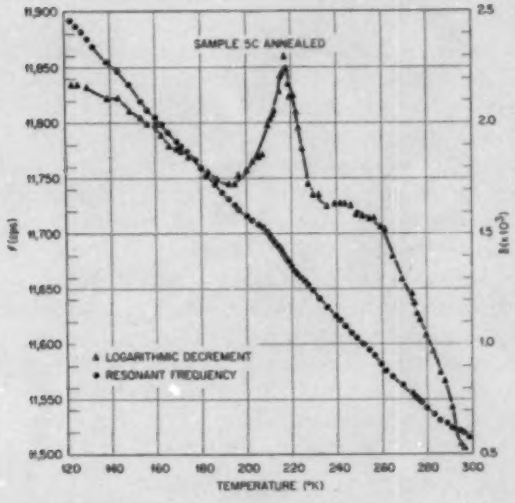

FIG. 4. Logarithmic decrement and resonant frequency during initial warmup after irradiation at 121°K.

in which $E(l)$ and $\delta(l)$ are the measured modulus and decrement values at time l, E_e and δ_e are the final or "saturated" values of the same quantities, and E_0 and δ_0 are the values at zero time. The terms containing $1+\gamma l$ are most simply interpreted in terms of a reduction by radiation defects of l, the average dislocation loop length between pinning points. That is, $l=l_0/(1+\gamma l)$, where l_0 is the average loop length at the beginning of the irradiation. Thus, the change in $1/E$ (due to dislocation motion) is proportional to l^2 and the change in δ to l^4 in agreement with the earlier theoretical work of Koehler[7] and of Granato and Lücke.[8] Using their results, one may write the proportionality constants in Eqs. (1) and (2) in the form

$$\frac{1}{E_0}-\frac{1}{E_e}=C_1L_0l_0^2$$

$$\delta_0-\delta_0=C_2BL_0l_0^4 \tag{3}$$

in which B is a dislocation damping constant, C_1 and C_2 contain an orientation factor as well as elastic and numerical constants, and C_2 also depends on the frequency of vibration.

The pinning rate constant, γ, is given by l_0 times the number of pinning points introduced per unit length of dislocation line per unit time; that is,

$$\gamma=n\sum_e\phi l_0/L_0 \tag{4}$$

where n is the number of pinning points per primary knock-on, $\sum_e$ is the average value of the macroscopic neutron scattering cross section of the target material, ϕ is the incident fast neutron flux, and L_0 is the dislocation density. Since n is the quantity of primary interest from the standpoint of radiation damage, the first requirement is to determine γ.

This may be done with the aid of Fig. 5, in which the data of Fig. 1 are plotted according to Eq. (1). It is assumed, of course, that Eq. (1) is valid over the whole temperature range covered, as well as at room temperature. The symbols used in this plot have the same meanings as those used previously. If Eq. (1) were obeyed exactly, the lines would be straight with slope γ. As can be seen from the plot, the lines actually show appreciable curvature in the early part of the bombardment and later become straight. This phenomenon is discussed more fully in the Appendix, where it is shown that the curvature can be accounted for very reasonably by assuming that two or more different types of dislocations are being pinned. Presumably,

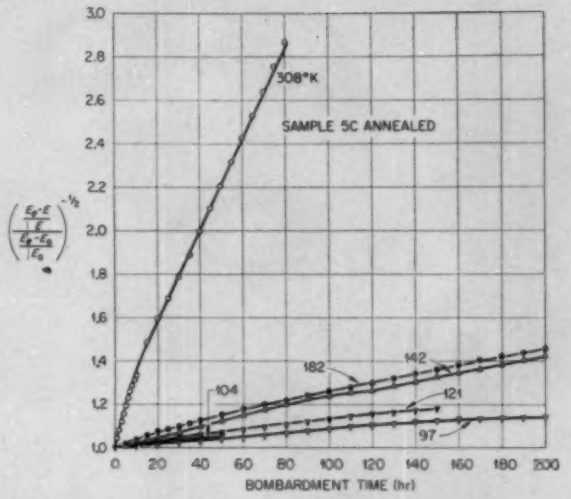

FIG. 5. $\{[(E_e-E)/E]/[(E_e-E_0)/E_0]\}^{-\frac{1}{2}}=\gamma^{-\frac{1}{2}}$ as a function of bombardment time at various temperatures. The symbols have the same meanings as in Fig. 1.

[7] J. S. Koehler, *Imperfections in Nearly Perfect Crystals*, edited by W. Shockley (John Wiley & Sons, Inc., New York, 1952), p. 197.

[8] A. Granato and K. Lücke, J. Appl. Phys. **27**, 583 (1956).

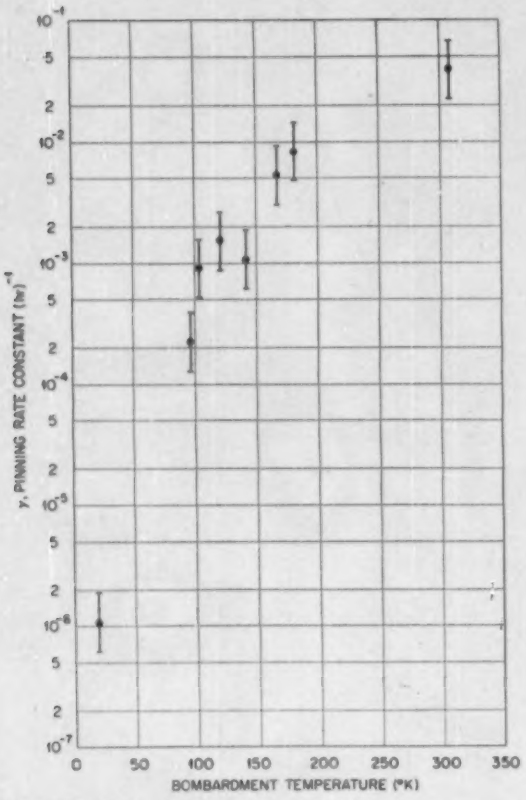

FIG. 6. Pinning rate constant γ as a function of temperature.

the types differ in the orientation of the Burger's vector with respect to the dislocation axis. It may also be shown that the initial slope on a plot, such as Fig. 5, is the average of the values of γ for the different types of dislocations, weighted according to their contributions to the modulus change. This weighted average value of γ was felt to be the most suitable one for representing the temperature dependence of n.

Since the sample had to be demounted for annealing between runs, some handling was involved. The result of the handling is that the quantities L_0 and l_0 differed somewhat from run to run. This effect is evidenced by differences in the measured parameters $(1/E_0)-(1/E_e)$ and $\delta_0-\delta_e$ in Eq. (3). As may be seen from Eq. (4), corrections must be made for these variations in order to obtain a true measure of the temperature dependence of n. Of course, the absolute values of L_0 and l_0 cannot be determined from Eq. (3) because the damping constant is not known; nevertheless, Eq. (3) does allow one to normalize the values of l_0 and L_0 for each run with respect to those values obtained in a specified run. For this work, the run at 308°K was chosen as the basis for normalization. Thus, the final result is not n but a set of values of γ, corrected to the loop length and dislocation density existing at the start of the 308°K run. The corrected value of γ should, of course, be proportional to n and thus have the same temperature dependence.

This correction involves two uncertainties. (a) It is necessary to make an assumption about the dependence of n on L_0. It was assumed in this work that n is independent of L_0; that is, that no other entities compete with the dislocations as sinks for migrating defects. (b) With the available data it is necessary to ignore the apparent existence of more than one kind of dislocation and treat the values of γ, l_0, and L_0 as averages. These assumptions worked well in the single case in which they were tested. For two runs made at 182°K the ratio of the uncorrected values of γ was 2.4, while the ratio of the corrected values was only 1.2.

The corrected, weighted average values of γ are plotted as a function of temperature in Fig. 6. There is included a point previously obtained in an in-pile cryostat at 20°K,[3] corrected to the flux estimated for the beam hole used in the present work. A logarithmic scale has been chosen so as to display the most significant feature of the plot—the extremely large variation of γ over the temperature range covered. This variation is by a factor of about 40 000 between bombardment temperatures of 20°K and 308°K. Even at 100°K the number of pinning defects is lower by a factor of about 40 than at 308°K.

Presumably, the most important factors determining the pinning rate constants displayed in Fig. 6 are the values of activation energy required for migration of the defects to the dislocations. At present, only a qualitative discussion can be given; however, before doing so it is desirable to make clear the expected relationship between the activation energy distribution and the values of γ measured at various temperatures.

The dislocation pinning rate is governed directly by the average delay time τ_i required for each type of defect to reach the dislocations; for purposes of qualitative discussion one may assume that

$$\tau_i=\tau_0{}^i \exp(E_i/kT) \qquad (5)$$

where E_i is the activation energy, $\tau_0{}^i$ is a jump time factor, and T is the absolute temperature. For a given defect the governing activation energy may be that for diffusion or that for escape from any of several kinds of traps. Since there may be more than one type of defect, many different activation energies may be involved. At a given bombardment temperature, those defects having τ_i values less than the minimum resolution time t_1 of the experiment (about one-half hour) will contribute fully to the pinning, while those for which τ_i is much greater than the duration t_2 of the bombardment (about 200 hours) will not contribute at all.

If there is a group of defects whose activation energies are in the narrow range such that $t_1<\tau_i<t_2$, there will be a contribution to the curve in Fig. 5 which will begin with zero slope and will not approach its full rate until several delay periods τ_i have passed; thus, the curve in Fig. 5 will be concave upward. In the measurements made to date, there is no clear evidence of such behavior, though it is possible that a small delayed contribution could be masked by the convex shape re-

sulting from the postulated existence of more than one type of dislocation. Thus, at the temperatures used in the present measurements, essentially all the defects are either "frozen in" or move to the dislocations in a short time (of the order of a few minutes or less).

Under these conditions each corrected value of γ, given in Fig. 6, is proportional to the number of defects which migrate rapidly at or below the temperature of measurement. If Eq. (5) held and all defects had the same value of τ_0^i, the graph of γ *versus* T would also represent the integral of the distribution function for activation energy up to approximately the value $kT\log(t_1/\tau_0^i)$.

Applying the above considerations to the data shown in Fig. 6, it appears that, in terms of the number which migrate at room temperature, only two to three per cent of the defects are mobile at 100°K. Apparently few, if any, additional ones appear as the temperature is increased to 140°K. At about 175°K more defects are mobile and, as may be seen in the warmup data of Fig. 3, a large release of defects begins at 260°K. The absence of time delay effects shows that there is no large group of defects which has a unique activation energy and also has a measurable migration delay time at any of the bombardment temperatures used in the present work. Thus, a continuous activation energy distribution would be consistent with the present data; however, it is quite possible that unique activation energy values will become apparent in the temperature ranges not yet covered.

In continuing these experiments, particular attention will be given to the ranges 30°K to 50°K and 260°K to 300°K. In the former range, a prominent and well-known resistivity annealing occurs, and there is also pinning of dislocations, though it is observable only after a much larger irradiation than used in the present work. In the latter range, resistivity annealing and pinning of dislocations both occur prominently. Thus, it is possible that dislocations are important as sinks for the defects which begin to migrate in this temperature range. To test this suggestion, it is planned to irradiate samples of different dislocation density, to see whether Eq. (4), with n constant, is obeyed, as it apparently is at 182°K.

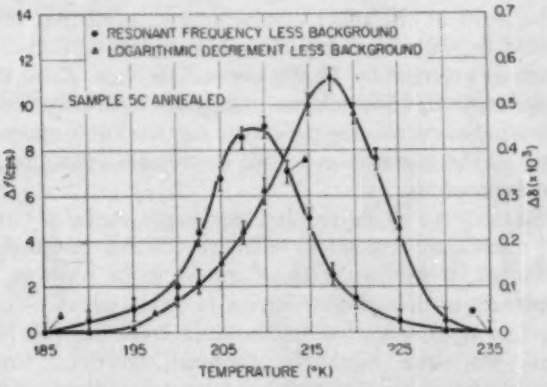

FIG. 7. Large scale plot of the sharp internal friction and frequency peaks shown in Fig. 4, after subtraction of a background, interpolated as a straight line.

The curves in Fig. 7 show the appearance of the peak structure of Fig. 4 after straight line interpolations from 185°K to 235°K have been subtracted from both the frequency and decrement curves. It can be seen that the modulus peak occurs at a slightly lower temperature than the decrement peak. While the present data do not provide a basis for interpreting these peaks, one can draw a negative conclusion: They are not due to a simple stress relaxation of a "polarized" defect, such as a divacancy. The most obvious reason is that the modulus behavior is completely inconsistent with such a model; furthermore, the concentration of radiation defects attained in these experiments—about 10^{-8} atomic percent—is far too low to produce a measurable effect. For instance, a concentration of about 3×10^{-3} atomic percent interstitial carbon atoms in iron is required to produce a stress relaxation peak of the same height.

V. SUMMARY

While these experiments are incomplete, certain tentative conclusions may be drawn. They are: (1) the number of defects which can migrate to dislocations falls off rapidly with decreasing temperature; in terms of the room temperature value, the dislocation pinning rate is about 2.5×10^{-2} in the range 100°K to 140°K and (from previous data)[3] about 2.5×10^{-5} at 20°K. (2) No evidence (in the form of delayed response of the internal friction and elastic modulus during fast neutron bombardment) has yet been found for the existence of any large group of defects with a well-defined activation energy; however, the experiments have not yet been done in the temperature range (around 260°K) where such effects are most likely to be found. (3) During warmup from a lower-temperature irradiation, a very pronounced movement of defects to the dislocation lines begins at 260°K. (4) The details of the variation of the internal friction and elastic modulus during bombardment can best be understood if it is assumed that there are two or more types of dislocation, which have different probabilities of capturing defects. One would expect such differences to occur among dislocations having different screw and edge components. In fact, analogous differences have been observed in the rates at which dislocations are "decorated" by diffusing impurities.[9,10]

VI. APPENDIX

The variations of elastic modulus and internal friction as a function of fast-particle irradiation were discussed theoretically by Thompson and Holmes.[1] It was tacitly assumed that the dislocations contributing to the anelastic effects all have the same line tension and also the same interaction with point defects. An additional assumption made was that both the pinning points

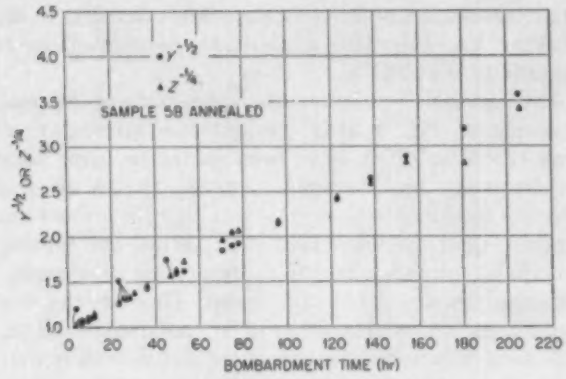

FIG. 8. $y^{-\frac{1}{2}}$ and $z^{-\frac{1}{2}}$ *vs* time, sample 5B, at room temperature, from reference 1.

produced by irradiation and those existing prior to irradiation were located randomly along the dislocation lines, so that the distribution of loop lengths retained the same (exponential) form throughout the experiment. Under these conditions, Eqs. (1) and (2) are obeyed, so that the quantities

$$\left.\begin{aligned} y^{-\frac{1}{2}} &\equiv \left[\left(\frac{E_e-E}{E}\right)\Big/\left(\frac{E_e-E_0}{E_0}\right)\right]^{-\frac{1}{2}} \\ \text{and} \qquad z^{-\frac{1}{2}} &\equiv \left[\frac{\delta-\delta_e}{\delta_0-\delta_e}\right]^{-\frac{1}{2}} \end{aligned}\right\} \tag{6}$$

are given by

$$y^{-\frac{1}{2}} = z^{-\frac{1}{2}} = 1+\gamma t. \tag{7}$$

Thompson and Holmes obtained good experimental agreement with these results in that the plots of $y^{-\frac{1}{2}}$ and $z^{-\frac{1}{2}}$ *versus* time were straight and coincided fairly well. These are shown in Fig. 8 for their sample 5B for a room-temperature bombardment. The measurements on 5B were made in the "west animal tunnel" of the Oak Ridge graphite reactor. The fast neutron flux in this facility is of the same order as that obtained from the beam hole used in the present work.

In the present work data were taken on sample 5C. This sample was grown in the same triple-mold crucible at the same time as 5B and has the same orientation; however, its subsequent handling and heat treatment have been different. Figure 9 shows data obtained on sample 5C for a comparable room-temperature bombardment. It may be seen that the curves of $y^{-\frac{1}{2}}$ and $z^{-\frac{1}{2}}$ *versus* time for this crystal do not coincide as they do for 5B, nor are they straight in the early portions. One might propose the following explanations for the behavior of sample 5C:

(a) There is a variation of the rate at which pinning defects reach the dislocations during bombardment.
(b) The fast neutron beam intensity is not uniform over the sample; therefore, the dislocations are pinned more rapidly in some regions of the sample than in others.
(c) The distribution of dislocation loop lengths changes its form as well as its mean value during the irradiation.
(d) Equations (1) and (2) are not correct.
(e) There exist two or more types of dislocations, presumably having different screw and edge components, of which some are pinned more rapidly than others.

One may dispose of explanation (a) by noting that, if it were true, samples 5B and 5C would show the same behavior and, in addition, the curves of $y^{-\frac{1}{2}}$ and $z^{-\frac{1}{2}}$ would coincide. Explanation (b) is rendered unlikely by the fact that the sample, which is less than five inches long, is suspended in front of a 4-in. square beam hole. This arrangement gives uniform intensity over all but the extreme ends of the sample where the vibrational stress is smallest. As will be shown later,

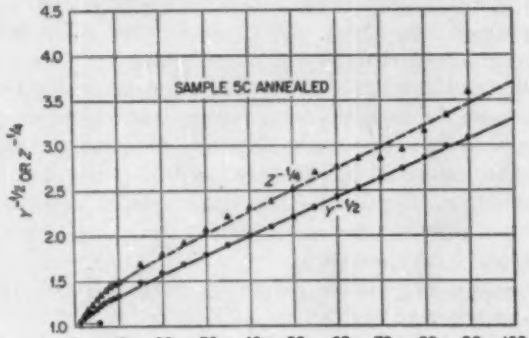

FIG. 9. $y^{-\frac{1}{2}}$(●) and $z^{-\frac{1}{2}}$(▲) *vs* time, sample 5C, at room temperature, from present measurements. The solid line is a plot of $y^{-\frac{1}{2}}$ from Eq. (8), and the dashed line is a plot of $z^{-\frac{1}{2}}$ from Eq. (9), using the parameters of Table I.

the data provide an additional reason for rejecting this explanation.

In investigating explanation (c) it was felt that interactions between the migrating defects would be so infrequent at the small bombardments used that they would become randomly spaced along the dislocation lines, as assumed by Thompson and Holmes. Thus, the loop length distribution can change its form only if the pre-irradiation pinning points are not randomly spaced; that is, the initial loop length distribution function is not exponential.

Since it can be shown that the shapes of the $y^{-\frac{1}{2}}$ and $z^{-\frac{1}{2}}$ curves are dependent upon the chosen initial distribution, it would therefore appear to be possible to construct an initial distribution function which would give an approximation to the data from sample 5C. This procedure would be artificial, however, since Fig. 8 shows that a simple exponential distribution describes the data from sample 5B very well. Consequently, acceptance of this hypothesis would require

that a distribution function be tailor-made for each and every sample. Since there is no other basis for the latter requirement, it appears that hypothesis (c) is highly improbable.

Data such as that given in Fig. 8 provide the best evidence for the applicability of Eqs. (1) and (2) and the rejection of hypothesis (d). Further, if a different law were postulated it would still be necessary to explain why the samples differ from one another.

One is led to explanation (e) by its plausibility as well as by the foregoing process of elimination. In general, a sample may be expected to contain dislocation lines having all orientations with respect to their Burger's vectors, from pure edge to pure screw. The study by Thompson and Holmes[11] of the structure of the Bordoni internal friction peak has indicated that at least four orientations contribute to internal friction effects. It is also to be expected that the various types of dislocations may differ markedly as to density, loop length, line tension, damping constant, and probability of being pinned by migrating defects. This last expectation is supported by the observations of Dash on silicon and of Amelinckx on sodium chloride and potassium chloride. Both found that screw dislocations were apparently decorated much less readily by diffusing impurities than edge or mixed edge/screw types.

In this picture there are many more parameters than can be determined from the present measurements. It is thus necessary to analyze the data by means of a simplified model which is represented by the following equation:

$$y=\frac{\alpha_1}{(1+\gamma_1 f)^2}+\frac{\alpha_2}{(1+\gamma_2 f)^2} \tag{8}$$

$$z=\frac{\beta_1}{(1+\gamma_1 f)^4}+\frac{\beta_2}{(1+\gamma_2 f)^4}. \tag{9}$$

Obviously, it is assumed that there are only two principal types of dislocations. The parameters α_1 and α_2 involve the density, loop length, and line tension of the two types, while β_1 and β_2 involve the same parameters in different combinations, together with the damping constants. Thus, one expects that in general $\alpha_1 \neq \beta_1$ and $\alpha_2 \neq \beta_2$. Table I summarizes the parameters obtained by fitting Eqs. (8) and (9) to the data obtained in bombardments at 142°K, 182°K, and 308°K.

TABLE I. Parameters in Eqs. (8) and (9).

Temp. of run, °K	Parameters obtained from modulus (y^{-1} vs f)			
	α_1	α_2	γ_1	γ_2
142	0.08	0.92	0.010	0.0018
182	0.10	0.90	0.020	0.0019
308	0.27	0.73	0.097	0.018
	Parameters obtained from decrement (z^{-1} vs f)			
	β_1	β_2	γ_1	γ_2
142	0.47	0.53	0.0056	0.0014
182	0.30	0.70	0.013	0.0018
308	0.68	0.32	0.078	0.018

It should be noted that the temperatures in Table I are given primarily to identify the runs. While it is true that γ_1 and γ_2 are strongly temperature-dependent, it is felt that the parameters α_1, α_2, β_1, β_2, and the ratio γ_1/γ_2 depend, in this temperature range, primarily on the dislocation structure induced in the sample by handling prior to each run. It may be seen that the rapidly saturating component (subscript 1) contributes relatively more to the decrement than it does to the modulus change. This behavior is inconsistent with explanation (b) above.

It should be noted that γ_2 (slowly-saturating component) can be determined with considerably more accuracy than γ_1 (rapidly saturating component), as evidenced by a comparison of the modulus and decrement data. This is particularly true if either α_1 or β_1 is small; further, it is quite possible that there are two or more rapidly saturating components which would lead to inconsistent values for γ_1. The existing data are not considered sensitive enough to decide this point. It is, however, clear from the data that only one slowly saturating component appears within the bombardment times used. Values of y^{-1} and z^{-1}, obtained from Eqs. (8) and (9) and Table I, are plotted as smooth curves on Fig. 9. It can be seen that the data are represented fairly well.

It would, of course, be desirable to test the above model by experiments in which the types of dislocation in the sample are controlled by the method of deformation. Such experiments would be somewhat difficult in both execution and interpretation, but the authors hope to perform them in the future.

ACKNOWLEDGMENT

The authors wish to acknowledge helpful discussions with D. K. Holmes, who suggested the explanation adopted above.

[9] W. C. Dash, J. Appl. Phys. **27**, 1193 (1956).
[10] S. Amelinckx, Acta Met. **6**, 34 (1958).
[11] D. O. Thompson and D. K. Holmes, J. Appl. Phys. **30**, 525 (1959).

Low Angle X-Ray Diffraction of Fibrous Polyethylene*†

A. S. Posner, L. Mandelkern, C. R. Worthington, and A. F. Diorio
National Bureau of Standards, Washington, D. C.

(Received August 17, 1959)

Highly axially oriented fibers of linear polyethylene are shown to display four orders of well defined, meridionally directed diffraction maxima corresponding to a fundamental spacing of 408 A. An interpretation of the low angle x-ray pattern is given in terms of the fiber morphology and the Hess-Kiessig postulate as to the origin of the periodic variation in electron density. The relative macroscopic length of the fibers was systematically altered both by thermal treatment and by crosslinking, melting, and recrystallization. The magnitude of the spacings observed does not bear any direct relation to the change in length incurred, but reflects the change in crystallite size that develops because of annealing, partial melting or the introduction of crosslinks. It is also shown that in a completely shrunken fiber, where wide-angle x-ray diffraction shows that the crystallites are randomly arranged relative to one another, discrete diffraction maxima are observed at about 255 A. These maxima are, however, circular in shape. Intermediate types of line shapes are also observed, which depend solely on the crystallite orientation and not on the method by which the orientation is developed.

INTRODUCTION

LOW angle x-ray diffraction techniques have been used in studying the structure and morphology of the highly crystalline, axially oriented fibrous proteins. Many orders of a well defined intensity maximum are usually observed with an axial period up to about 700 A occurring in certain cases. Important structural information has been deduced from these studies for collagen,[1,2] keratin,[3] and muscle fibers,[4] to cite but a few examples. In contrast, though diffraction maxima at low angles have been observed in a variety of oriented synthetic polymers,[5–11] the reflections have not been too well defined, the values of the long spacings have been relatively small and only one diffraction order has been reported. In addition, there has been no attempt to vary systematically the properties of the synthetic polymer fibers, particularly their macroscopic length, and to correlate these results with the low angle pattern.

A recent brief communication from this laboratory[12] reported on the examination of a highly axially oriented linear polyethylene fiber by means of x-ray low angle techniques. In this fiber, three well-defined diffraction maxima at angles corresponding to Bragg spacings of 408, 196, and 96 A were observed. Concurrently, it was reported by Statton[13] that for a variety of linear polyethylene fibers, two and, in one case, three orders of diffraction were present. It would thus appear that in highly ordered synthetic polymers it is possible to obtain well defined, multiordered diffraction maxima.

In the present paper, there is a more detailed discussion of the low angle pattern of the original polyethylene fiber. In addition, a report is presented on the changes incurred in the diffraction angle of the maxima, their relative intensities and shape as a result of various physical treatments. In particular, the effects of intermolecular crosslinking, controlled thermal shrinkage, and melting and recrystallization are presented.

EXPERIMENTAL

Equipment

The low angle camera that was used has already been described in detail.[14] It has a slit type collimating system and is capable of resolving spacings up to 800 A. Each specimen consisted of a bundle of fibers of optimum thickness for CuK_α radiation. The radiation was nickel-filtered and the specimen-to-film distance was 22.5 cm. The patterns were all taken with the x-ray beam normal to the fiber axis and typical exposure times ranged from 24 to 48 hrs. For the weaker reflections at the larger angles, exposure times of about 100 hrs were used. As a matter of convenience, the angles at which the intensity maxima occur have been reported in angstroms, the conversion being accomplished by means of Bragg's law.

Materials

The polymer used in this study was a linear polyethylene manufactured by the Phillips Petroleum Company under the name Marlex-50. It was rendered

* Presented in part at the June 1958 meeting of the American Crystallographic Association, Milwaukee, Wisconsin.

† This investigation was supported in part by Research Grant D-572 U. S. Public Health Service.

[1] R. S. Bear, J. Am. Chem. Soc. **66**, 1297 (1944).
[2] R. S. Bear, Advances in Protein Chem. **7**, 69 (1952).
[3] R. S. Bear and H. S. Rugo, Ann. N. Y. Acad. Sci. **53**, 627 (1951).
[4] R. S. Bear, J. Cellular Comp. Physiol. **49**, Supplement 1, 303 (1957).
[5] H. Kiessig, Kolloid Z. **152**, 62 (1957).
[6] Arnett, Meibohm, and Smith, J. Polymer Sci. **5**, 737 (1950).
[7] E. P. H. Meibohm and A. F. Smith, J. Polymer Sci. **7**, 57 (1951).
[8] L. G. Wallner, Monatsch. Chem. **79**, 279 (1948).
[9] W. O. Statton, J. Polymer Sci. **22**, 385 (1956).
[10] W. O. Statton and G. M. Godard, J. Appl. Phys. **28**, 1111 (1957).
[11] B. Belbeoch and A. Guinier, Compte rend. **247**, 310 (1958); B. Belbeoch and A. Guinier, Makromol. Chem. **31**, 1 (1959).
[12] Mandelkern, Worthington, and Posner, Science **127**, 1052 (1958).
[13] W. O. Statton, J. Polymer Sci. **28**, 423 (1958).
[14] C. R. Worthington, J. Sci. Instr. **33**, 66 (1956).

TABLE I. Description and summary of low angle diffraction data

A. Original fiber

Spacing in A	Line shape	Intensity[a]	Crystallite orientation[b]
{408 196 96}	Meridional	2nd most intense 1st weaker 3rd very weak	c axis

B. Thermally shrunk

Sample No.	Shrinkage ratio	Spacing in A	Line shape	Intensity[a]	Crystallite orientation[b]
168	1.42	447 231	Meridional	1st most intense	c axis
142	1.82	477 248	Meridional	1st most intense	c axis
169	2.50	510 257	Meridional	1st most intense	c axis
172	3.85	478 237	Meridional but indication of disorder	1st most intense	
158	8.33	277 125	"Unique shape"	1st most intense	Preferential orientation tilted
157	12.5	239	Unique shape starting to randomize		
152	21.5	255	Random		
151	28.0	255	Random		Slight orientation
147	60.0	255			Random

C. Crosslinked

Radiation dose in megarads	Spacing in A	Line shape	Intensity[a]	Orientation[b]
55.0	396 185	Meridional but smeared	Relative intensities equal	c axis
152.5	396 185	Meridional but smeared	1st more intense	c axis
295	396 185	Meridional but smeared	1st more intense	c axis
545	396 185	Meridional but smeared	1st more intense	c axis

D. Crosslinked; melted and recrystallized

Sample No.	Radiation dose in megarads	Shrinkage ratio	Spacing in A	Line shape	Intensity[a]	Orientation[b]
146	652	1.35	273 146	Meridional	(2nd most intense) (1st very weak)	c-axis
149	295	1.70	223 160	"Unique shape"	(2nd most intense) (1st very weak)	Preferential orientation tilted
155	55.0	3.18	198			Slight orientation
171	9.0	8.6	239	Random		Random
170	2.28	13.3	261	Random		Random

[a] Spacings are numbered according to their magnitude.
[b] Crystallite orientation as deduced from wide angle x-ray pattern.

fibrous by the Research Department of the American Viscose Company,[15] using melt spinning techniques. The wide angle x-ray pattern is similar to that of a single crystal with rotational symmetry about the fiber axis indicating a high axial orientation. When this fiber is completely melted and subsequently allowed to recrystallize at room temperature, the observed sixty-fold axial contraction is indicative of the high orientation of the crystallites in the original sample.

The thermal shrinkage of the fibers was accomplished by immersing them in a silicone oil bath at a predetermined temperature for an appropriate length of time. The dimensional changes that occur are expressed as the ratio of the original length to final length, and this quantity is called the shrinkage ratio. Smaller shrinkage ratios were obtained by very short immersions at temperatures just below the melting temperature while very high shrinkages were obtained at temperatures just above the melting temperature. (See Table I).

Intermolecular crosslinks were introduced into the fibers by subjecting the samples to the action of high energy radiation. Gamma radiation from a 2500-Curie Co^{60} source operating at a dose rate of 5.7×10^5 rad per hr was utilized and the radiations were performed *in vacuo* at 17°C.

RESULTS

Original Fiber

The original polyethylene fiber was subjected to three types of physical and thermal treatments and the low-angle x-ray patterns resulting from each of the treatments will be described. It has been previously reported[12] that the original fiber displays a well-defined

[15] We wish to thank the Research Department of the American Viscose Company, Marcus Hook, Pennsylvania, for supplying this material.

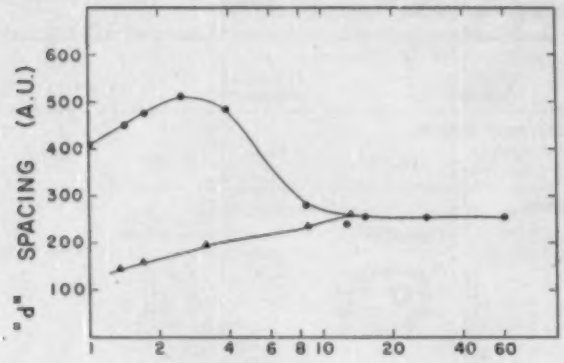

FIG. 1. Plot of first-order diffraction maxima (in Angstroms) against shrinkage ratio. Thermally shrunken fibers ●; crosslinked, melted, and recrystallized fibers ▲.

low-angle x-ray pattern, which is limited to meridional reflections and which correspond to Bragg spacings of 408 A, 196 A, and 96 A (±5%). These reflections are considered to be the first, second, and fourth order reflections of the long spacing. The relative intensities of the diffraction maxima, obtained from the original fiber are such that the second order reflection (196 A) is more intense than the first, and the maximum which occurs at 96 A is very weak (Table IA) and is developed only after very long exposure.

Thermally Shrunk Fibers

Table IB summarizes the data obtained after shortening the fiber by thermal treatment. In this table, each sample is characterized by its shrinkage ratio, the observed "*d*" spacings, their relative intensities, and a description of the shape of the diffraction maximum. A brief description of the crystal orientation of each specimen as observed in the wide angle pattern is also given. Characteristic of the low angle patterns of all thermally shrunken fibers is the fact that the most intense reflection corresponds to the largest observed spacing. The inversion of the relative intensities between the first and second orders that was observed in the original fiber has now disappeared.

In Fig. 1, the "*d*" values of the first-order reflections are plotted as a function of the shrinkage ratios of the fibers. During the initial shrinkage of the polyethylene fiber, there is an increase in the "*d*" spacings with a maximum value of 510 A observed at a shrinkage ratio of 2.5. When further decreases in the fiber length are affected, the magnitudes of the "*d*" spacings decrease progressively until a shrinkage ratio of about ten is reached at which point the spacings remain invariant with any further decrease in specimen length. Thus, no simple relationship exists between the "*d*" value of the long-range periodicities observed and the relative length of the fiber. Even the completely shrunken sample with a wide angle x-ray pattern typical of random crystallization displayed a well-defined maximum at 255 A.

The shape of the low angle reflections as seen on the film also changes as the fiber is shortened by heat treatment. Figure 2 shows some typical diffraction patterns of shrunken specimens and the pattern of the original fiber. In this figure, patterns (A), (B), and (C), which represent the original fiber, sample 168 and sample 169, respectively, show the well-defined meridional reflections of the highly ordered structures. The wide angle x-ray patterns indicate that *c* axis crystallite orientation is still maintained for these samples despite the fact that some shrinkage has occurred. The intense diffraction maximum at 277 A in pattern (D), sample 158, is unique in its circular shape. The wide angle pattern in this instance indicates that though a preferential orientation still persists at this shrinkage ratio, the *c* axes of the crystallites are now tilted relative to the macroscopic fiber axis. The occurrence of tilted crystallite orientation has been previously observed in

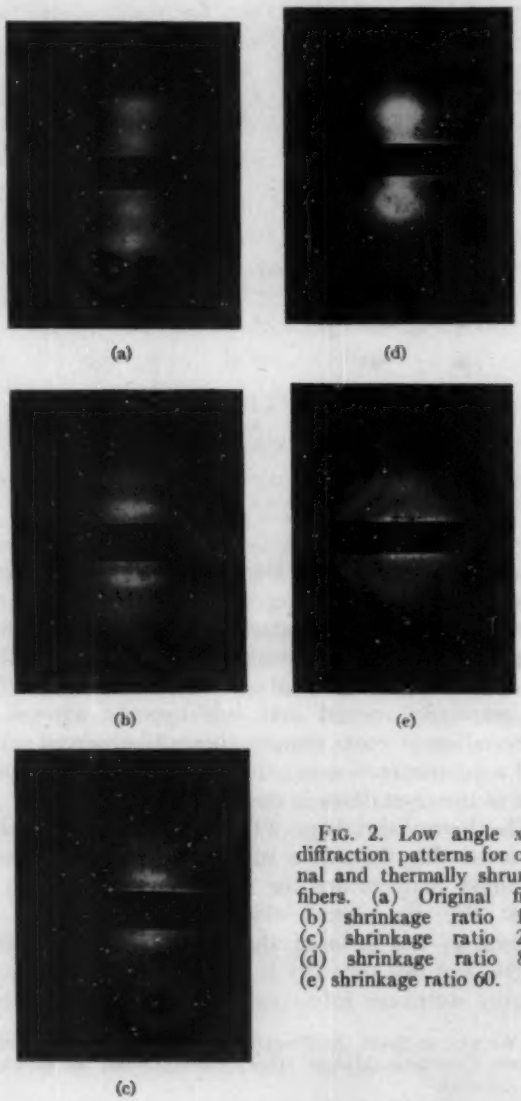

FIG. 2. Low angle x-ray diffraction patterns for original and thermally shrunken fibers. (a) Original fiber; (b) shrinkage ratio 1.42; (c) shrinkage ratio 2.50; (d) shrinkage ratio 8.33; (e) shrinkage ratio 60.

polyethylene.[16,17] Pattern (E) in this figure represents the completely shrunken fiber, and despite the fact that no preferential orientation of the crystallites exist, a well-defined circular low-angle maximum occurs. This is in contrast to the reflections from the more highly oriented specimens, which are straight lines parallel to the camera slit collimator. This circular shaped maximum is indicative of a random arrangement of the long range periodicity in the fully shrunken fiber.

Crosslinked Fibers

Certain alterations in the low angle pattern occur when the original fiber is crosslinked without any subsequent treatment. The values of the long spacings are slightly decreased, as is indicated in Table IC, but are independent of the radiation dose received by the sample. The relative intensities of the diffraction maxima also change with irradiation. For the smallest dosages, the first two orders are of about the same intensity but on additional radiation the largest spacing becomes the more intense. In addition, the reflections are no longer as sharply defined as in the original fiber, having become more diffuse with increasing irradiation. These results are in accord with the wide angle x-ray diffraction patterns previously reported[18] for polyethylene fibers receiving a similar treatment. No significant change occurs in the wide angle pattern for samples receiving radiation doses greater than that reported here.

After melting and subsequently recrystallizing the fibers which had been irradiated in the highly oriented state, a progressive increase occurs in the relative length with increased dosage. This is accompanied by the development of axial crystallite orientation despite the fact that no external force is maintained on the system. A detailed discussion and interpretation of this phenomenon has already been given.[18,19] The significant features of the low angle diffraction patterns of the recrystallized fibers are summarized in Table ID. It should be noted that with increased radiation dose (consequently increased cross linking), the relative length increased so that the shrinkage ratio decreased. At the lower shrinkage ratios, two low-angle diffraction maxima are again observed. As in the original fiber and in contrast to the thermally shrunken specimens (noncrosslinked), the smallest of the two spacings is the most intense. The first order of the spacings for this series of fibers are also plotted as a function of the shrinkage ratio in Fig. 1. With increasing relative length, there is a continuous decrease in the value of the observed spacing.

Some typical low angle diffraction patterns for this series of fibers are illustrated in Fig. 3. Pattern (A) in this figure, representative of the most elongated specimen, is very similar in respect to line shape to the patterns obtained for the original fiber and the partially shrunk, noncrosslinked fibers (see Fig. 2). Again for this specimen, the wide angle x-ray pattern is indicative of c axis crystallite orientation. Pattern (B) in Fig. 3 is very similar to pattern (D) of Fig. 2 with its unique line shape. In this instance also, the wide angle pattern indicates that chain direction within the crystallites are tilted relative to the macroscopic fiber axis. Figure 3, pattern (C) represents a specimen which has received a very small radiation dose and was consequently only lightly crosslinked. The single low-angle maximum seen on this pattern is characteristic of a randomly arranged long spacing. This corresponds to the random crystallite arrangement deduced from the wide angle pattern.

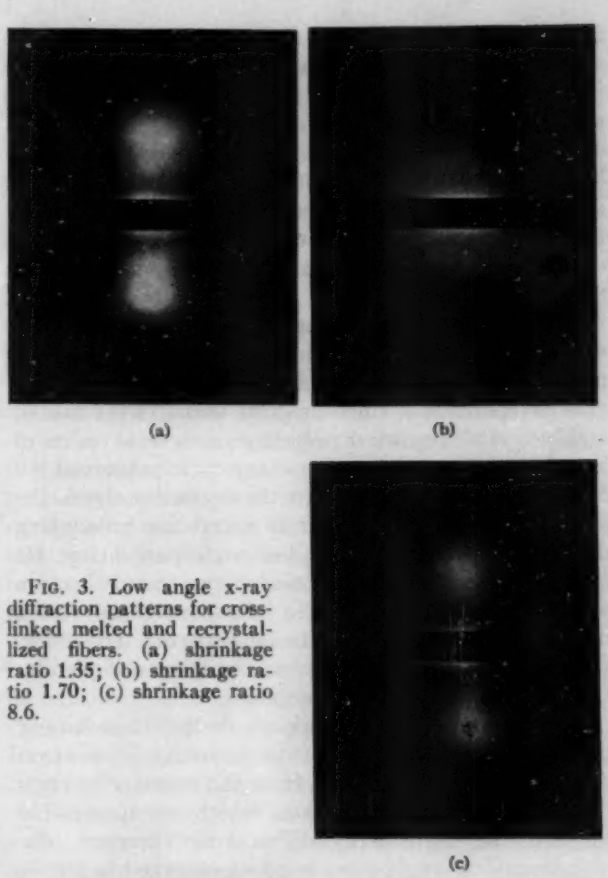

FIG. 3. Low angle x-ray diffraction patterns for crosslinked melted and recrystallized fibers. (a) shrinkage ratio 1.35; (b) shrinkage ratio 1.70; (c) shrinkage ratio 8.6.

DISCUSSION

Original Fiber

Hess and Kiessig[20–22] have suggested that the discrete x-ray low angle meridional diffraction maxima that are observed in oriented synthetic macromolecules find

[16] A. Brown, J. Appl. Phys. **20**, 552 (1949).
[17] H. A. Narcarrow and R. A. Horsley, Brit. J. Appl. Phys. **2**, 345 (1951).
[18] Mandelkern, Roberts, Diorio, and Posner, J. Am. Chem. Soc. **81**, 4148 (1958).
[19] Mandelkern, Roberts, and Diorio, J. Am. Chem. Soc. **80**, 500 (1958).
[20] K. Hess and H. Kiessig, Z. Physik Chem. (Leipzig), **193**, 196 (1944).
[21] K. Hess and H. Kiessig, Naturwissenchaften **31**, 171 (1955).
[22] K. Hess, Ricerca sci. Suppl. A, 594 (1954).

their origin in the unique crystalline and amorphous structure of polymeric systems. The periodicity which is observed at low angles is presumed to arise from the alternation of the ordered crystalline regions and the disordered amorphous regions which are constrained to be colinear with one another due to the imposed orientation. Thus, even in a system containing identical chain repeating units a periodic change in electron density can be obtained due to the density difference of the two states.

Until recently, only a single diffraction order at low angles has been reported for various synthetic polymers[6–11] indicating a lack of regularity and extensiveness of repetition of the diffracting units. In the case of highly crystalline, linear polyethylene several orders of low-angle, x-ray diffraction have been observed.[12,13] Statton[13] was able to correlate the crystallite size in the chain direction (obtained from x-ray line broadening data) with the meridional, low-angle periodicity. He showed that the crystallite size in the chain direction was always smaller than the long period and varied linearly in magnitude with the long spacing. The difference in length was attributed to the space occupied by the intervening amorphous regions.

Statton's results give support to the Hess-Kiessig postulate that the periodic discontinuity in electron density of the sample arises from the contrasting crystalline and amorphous regions which are responsible for the low angle x-ray diffraction. Therefore, the meridional low angle x-ray maxima observed in highly crystalline polyethylene fibers are a result of the morphology of the system. The amorphous regions occur as a consequence of the kinetic difficulties of completely crystallizing a flexible long chain molecule, even though it is composed of identical repeating units.[23] The observed spacings of the original fiber are relatively sharp and numerically consistent with the interpretation that they are the 1st, 2nd, and 4th order of a fundamental spacing of 410±20 A. The third order is either absent or too weak to be resolved. Preliminary experiments, involving the tilting of the fiber axis relative to the x-ray beam indicate that the highly oriented polyethylene fiber acts as a one dimensional diffractor.

In consideration of the above discussion and the observed wide angle pattern, the diffraction observed at low angles can be considered to result from a periodic arrangement of axially oriented crystallites of average size in the fiber direction of slightly less than 400 A and separated by amorphous regions so that the observed period is 410 A. The general appearance of the discrete diffraction maxima and in particular the sharpness of the diffraction in the meridional direction depends mainly on two factors. These are the regularity of the period and the number of crystallites in the repeating unit. Though the basic theory concerning the shape of diffraction maxima is well known,[24] considerations concerned with the sharpness of the reflections is more difficult due to the above factors as well as the possible variation in the number of crystallites in each repeating unit. If it is assumed, however, that the repeating units are composed of the same number of identical crystallites, then only four or five crystallites are necessary to produce the observed diffraction. This is supported by line broadening measurements on the low angle x-ray pattern of the untreated polyethylene fiber.

The effect of the variation in the crystallite size is similar to the influence of temperature on the diffraction of x-rays by crystals, with a rapid decrease in intensity occurring with increasing diffraction order. However, the intensity of the maxima depends primarily on the scattering factor of the crystallites. From the knowledge of the scattering factors of special shapes as cylinders and ellipsoids, a rapid decrease in intensity with diffraction order would also be expected. These considerations would indicate that the crystallites have a tendency to be of uniform size. A repeating unit containing a larger number of uniform crystallites should lead to sharper and more numerous diffraction maxima than is observed.

Studies by Norris and Stein[25,26] of the angular dependence of light scattered by stretched thin films of branched polyethylene suggest that crystallites and associated amorphous areas are arranged in regions of common crystal orientation which are comparable in size to the wavelength of light. The existence of such regions is consistent with the low angle x-ray results. A repetition of about five to ten 400 A, colinear, diffraction units would result in a size as determined by light scattering of about 2000 to 4000 A.

The classical example of low angle meridional diffraction in a macromolecular system is the case of the natural occurring polymer collagen.[1,2] This fibrous protein in its native state yields as many as thirty x-ray diffraction orders from a fundamental spacing which depending on conditions of preparation varies from 640 to 670 A. The changes that occur in this pattern with chemical or thermal treatment have also been studied. In this system, a characteristic alternation of the intensity of the orders is observed. The low angle diffraction pattern in this instance has been shown by tilting experiments[27] to be characteristic of a linear diffractor. It has been shown by structure analysis of the x-ray data that collagen may be represented by a cylindrical model with different levels of electron density varying periodically along the cylinder (fiber)

[23] L. Mandelkern, in *Growth and Perfection of Crystals*, edited by Doremus, Roberts, and Turnbull (John Wiley & Sons, Inc., New York, 1958), p. 467.

[24] R. W. James, *The Optical Principles of the Diffraction of X-Ray* (G. Bell and Sons, London, England).

[25] F. H. Norris and R. S. Stein, J. Polymer Sci. **27**, 87 (1958).

[26] R. S. Stein, *Growth and Perfection of Crystals*, edited by Doremus, Roberts, and Turnbull (John Wiley & Sons, Inc., New York, 1958), p. 549.

[27] O. E. A. Bolduan and R. S. Bear, J. Polymer Sci. **5**, 159 (1950).

axis.[28,29] In a formal fashion, a similar analysis could be performed on the fibrous polyethylene pattern. However, the amount of data presently available would not make this worthwhile. However, the striking similarity between the two patterns should be borne in mind since the differences appear to be those of degree rather than kind.

Thermally Shrunk Fibers

The melting or partial melting of a system of axially oriented crystallites must inevitably lead to an axial contraction.[30] For specimens which were slightly shrunken, the x-ray pattern reveals that the long period gradually increased with increasing shrinkage, as is illustrated in Fig. 1, reaching a maximum at 510 A for two and half fold shrinkage. The diffraction maxima displayed by these samples appear to be better resolved than those of the original fiber. The sharpened diffraction pattern and increased long spacing seen in the early stages of shrinkage probably results from the preferential melting of the smaller, less stable polymer crystallites and the concurrent growth of those remaining. A more uniform system of diffracting elements with a larger periodicity would thus result. The wide angle x-ray patterns indicate that the *c* axis crystallite orientation is still maintained during this early shrinkage accounting for the meridional character of the low angle pattern. In these experiments, no deliberate effort was made to attain the optimum conditions for partial melting and annealing, so that at present the largest spacing that can be obtained with synthetic polymers is not as yet known. Experiments designed to establish these conditions are currently underway in this laboratory. The present results, however, offer substantial evidence that the low angle diffraction is a consequence of the crystalline-amorphous morphology of the fiber and that dimensional changes and low angle x-ray spacings do not necessarily have a one to one correlation.

On further shrinkage, after the maximum "*d*" value is reached, the low angle spacing continuously decreases until it reaches a minimum at complete shrinkage. The wide angle pattern indicates that the preferred *c* axis orientation of the crystallites is no longer maintained, but until nearly complete shrinkage some preferred orientation is exhibited. The shrinkage again reflects the partial melting of the highly ordered structure and the subsequent disordered recrystallization. With the continuous decrease in the magnitude of the long period, there is an accompanying change in the shape of the diffraction maxima. For those specimens with wide angle patterns indicative of *c* axis orientation, the low angle patterns were sharp and meridionally oriented. When the crystallites were preferentially oriented, but not along the fiber axis, as in the case of the sample which had a shrinkage ratio of 8.33, the very unusual shape of the diffraction maximum as seen in pattern (D) of Fig. 2 was obtained. This line shape would appear to be a result of the fact that the crystallites are preferentially directed along an axis tilted 30° relative to the fiber axis.

Ultimately, as the shrinkage process progressed a completely random arrangement of the crystallites was obtained as evidenced by the wide angle x-ray patterns. Despite this disorientation, there was still a well defined low angle maximum corresponding to 255 A which was no longer confined to the meridion but was representative of a random arrangement of this long spacing. The nature of the long range order in this situation is not at present clearly defined. It is possible that individual aggregates containing from five to ten periods of crystallites arranged colinearly become randomly oriented during the complete shrinkage while the crystallites within the aggregates retain their orientation. It is alternately possible that all the crystallites have become randomly oriented and the low angle maxima is a reflection of an interparticle distance which is to be expected for a concentrated scattering system of reasonably uniform size.[31] The present low angle data cannot discriminate between the two possibilities. It can be demonstrated, however, that this random type of low angle diffraction is not a result of the fact that the specimen was originally in a highly fibrous state. Experiments have shown that similar random, low angle patterns can be observed merely by crystallizing from the melt linear polyethylene which had never been rendered fibrous.[32]

In contrast to the change that occurrs in the low-angle pattern of fibrous polyethylene with shrinkage, similar experiments with collagen yield different results.[33] For this highly organized collection of polypeptide chains, as shortening is induced by thermal treatment, the sample still exhibits its normal set of diffraction maxima but with a much reduced intensity. Thus, the melting process in this case does not involve any annealing or preferential melting, and the characteristic elements of axial order are maintained until the melting is complete.

Crosslinked Fibers

Subjecting linear polyethylene to the action of ionizing radiation in the absence of oxygen results primarily in the introduction of intermolecular crosslinks with other processes, such as chain scission, being severely restricted.[34,35] Though it is difficult to estimate the

[28] S. G. Tomlin and C. R. Worthington, Proc. Roy. Soc. (London) **A235**, 189 (1956).
[29] P. Kaesberg and M. M. Shurman, Biochim et Biophys. Acta **11**, 1 (1953).
[30] P. J. Flory, Science **124**, 53 (1953).
[31] A. Guinier and G. Fournet, *Small Angle Scattering of X-Rays* (John Wiley & Sons, Inc., New York, 1955.)
[32] Mandelkern, Posner, Diorio, and Roberts, in the paper presented before the 133rd Meeting of the Am. Chem. Soc. Boston, Massachusetts (April, 1958).
[33] B. A. Wright and N. M. Wiederhorn, J. Polymer Sci. **7**, 105 (1951).
[34] Lawton, Balwit, and Powell, J. Polymer Sci. **25**, 257 (1958).
[35] A. Charlesby, Proc. Royal Soc. London, **A215**, 187 (1952).

fraction of the units that are crosslinked an upper limit can be placed on this quantity by assuming proportionality between crosslinking and the radiation dose.[35] On this basis, the fraction of the units crosslinked in the fibers studied here range from 1×10^{-4} to 3.0×10^{-2}. The low angle x-ray patterns indicate that the major structural elements are not destroyed by irradiation crosslinking. The slight decrease in the value of the long spacing that is observed is indicative of a decrease in the size of the diffracting element. This decrease can be brought about by the introduction of imperfections into the crystalline regions, partial melting of those regions, or by slight shrinkage of the amorphous areas due to the crosslinking process. In any case, the changes that are incurred in the low angle pattern, though definitely perceptible by the present techniques, are relatively small. Bear[1] has reported a similar behavior of the collagen low angle pattern when this macromolecule was treated with a wide variety of crosslinking (tanning) agents. In these instances, the major characteristics of the patterns were maintained after crosslinking, but a four percent decrease in the magnitude of the periodicity was observed.

When the crosslinked polyethylene fibers were melted and then allowed to recrystallize merely by cooling, the previously described dimensional changes occur. As the crosslinking level in the recrystallized fibers was increased (decreasing shrinkage ratio), the "d" spacing corresponding to the most intense maximum that was observed decreased continuously in magnitude reaching a value of 146 A when about 3% of the chain units were crosslinked. Thus, the size of the diffracting element was severely decreased by crosslinking. In terms of the Hess-Kiessig theory it can be concluded that the introduction of intermolecular crosslinkages impose limitations on the longitudinal growth and the degree of perfection of the crystallites developed from the melt despite the fact that a pronounced axial orientation of the crystallites is concurrently being developed. Thus, a continued increase in the magnitude of the observed spacing with shrinkage ratio is observed in this instance in contrast to the results for the non-crosslinked thermally shrunk fibers. These results strongly emphasize the morphological origin of the diffraction maxima.

The low angle patterns also indicate the changes that occur in the crystallite orientation by virtue of the changes observed in the line shape. Thus, when the crystallites were randomly arranged, a corresponding randomness was exhibited in the low angle pattern. When the c axis of the crystallites were preferentially oriented along the fiber axis, a situation which is attained at the high levels of crosslinking, the maxima observed at low angles were confined to the meridion. Again, as in the case of the thermally shrunk fiber, when the crystallite orientation was tilted relative to the macroscopic fiber axis, an unusual low angle diffraction line shape was observed, as illustrated in Fig. 3B, which can be compared with the similar pattern of Fig. 2. The variations in line shape are therefore a result of the crystallite orientation and are not dependent on the particular method by which the orientation is obtained.

The crosslinking of collagen has been accomplished by treating the native material with formaldehyde. On melting, a large axial contraction is observed and specimens which have been crosslinked spontaneously regain about 85% of their initial length when allowed to recrystallize by cooling. Bear[1] has observed that after this melting-recrystallization cycle the number of reflections that are observed in the low angle pattern is severely reduced; only one very intense order is present along with two very faint ones. The magnitude of the first spacing has been reduced from the usual 640 A in the native fiber to 550 A. The effect of the intermolecular crosslinks on retarding the redevelopment of the crystallinty appears to manifest itself in the same way both for collagen and fibrous polyethylene.

SUMMARY

It can be seen from the above discussion that a wide variation in the nature of the low angle diffraction pattern can be obtained in fibrous polyethylene by various types of thermal treatment. The changes in the line shape that are observed at low angles can be correlated with the nature of the crystalline orientation as evidenced by the wide angle patterns. As has been pointed out by Bolduan and Bear,[37] a more detailed analysis of the line shape requires x-ray patterns obtained with a pin hole collimation system as opposed to the slit system employed herein. The change in the magnitude of the spacings of the thermally shrunk, crosslinked and crosslinked-recrystallized fibers can be given qualitative explanation by means of the Hess-Kiessig hypothesis, wherein the crystalline-amorphous morphology of polymers gives rise to a periodic variation in the electron density of the sample. Finally, some striking similarities have been pointed out between the low angle x-ray pattern of collagen and those of fibrous polyethylene. Particularly interesting is the similar variation of the two patterns with corresponding types of thermal and crosslinking treatment.

JOURNAL OF APPLIED PHYSICS VOLUME 31, NUMBER 3 MARCH, 1960

Reflection of Sound from Randomly Rough Surfaces*

J. M. Proud, Jr.,†‡ R. T. Beyer, and Paul Tamarkin§
Department of Physics, Brown University, Providence, Rhode Island

(Received September 23, 1959)

A study of the reflection of underwater sound from nonperiodic, pressure release surfaces is reported. The Eckart theory for wave reflection from rough surfaces has been adapted (with some modifications) to the experimental work. A portion of the investigation was directed toward a study of the dependence of the intensity reflected in the specular direction on angle of incidence, radiation wave number and the statistics of the reflecting surface. Secondly, a method is illustrated for determination of the rms amplitude and the correlation function of the reflecting surface from an analysis of the reflected intensity distribution. The radiation wavelength, in this case, must be much larger than the rms roughness amplitude.

I. INTRODUCTION

THE problem of wave reflection has been studied extensively in connection with diffraction grating phenomena in optics and acoustics. Current need for an understanding of the problem arises in the transmission of radar and radio waves over rough terrain, and in underwater sound propagation, where one must take account of reflections from the sea surface.

The study reported here is closely related to the latter situation, inasmuch as techniques of underwater sound were employed. Analogous results are to be expected, however, in the case of polarized electromagnetic radiation when the electric vector is parallel to the grooves of a perfectly reflecting rough surface. Two previous studies[1,2] have been reported which were similar experimentally to the investigation described here. Stationary periodic surfaces were used in both these cases to test the validity of several theories of rough surface reflection. This paper extends the investigation to the case in which the reflecting surfaces are time dependent and randomly rough. In the present experiment, a "randomly rough" surface is one whose nonperiodic profile is specified in terms of statistical quantities. The approach is such that one is able to form a description of the reflecting surface solely through an interpretation of the acoustic measurements. In particular, the description includes a specification of the correlation function and of the rms roughness amplitude about the average amplitude.

The investigation was concentrated on two aspects of the rough surface reflection problem. The first of these was a study of the dependence of the intensity reflected in the spectral direction upon such quantities as the angle of incidence, radiation wave number, and the statistics of the surface. In the second case, investigations were carried out which permitted a calculation of the rms amplitude and the correlation of a reflecting surface from an analysis of the reflected intensity pattern. It is shown that this can be done for a fixed radiation wavelength, which is much larger than the rms roughness amplitude.

II. THEORY

No existing theory of rough surface reflection solves the problem exactly. However, a large number of approximate theories have been developed.[3–11] The Eckart theory for sea surface reflection holds the advantage over most of the others in that it can be manipulated to apply to a variety of rough surface situations. It has been found to yield over-all agreement with experiments in the case of stationary sinusoidal surfaces.[1] Furthermore, it accounts explicitly for a directional incident beam shape, the type most often used experimentally. For these reasons, the Eckart theory has been adapted to the present problem.

The physical situation considered is illustrated in Fig. 1. An underwater sound source irradiates a perfectly reflecting (pressure release) surface whose displacement amplitude about the plane, $Z=0$, is specified by $\zeta=\zeta(x,t)$, where ζ is a slowly varying function of time. The incident pressure is given by

$$p=(P/r_0)\exp(ikr_0)$$

where P is a directional function for the source, r_0 is the distance from the source to any point on the surface, and k is the radiation wave number.

The solution of the problem consists in a determination of the acoustic pressure, p_1, at each point

* This work was supported in part by the Office of Naval Research.

† This paper is taken in part from a dissertation presented to Brown University Graduate School in partial fulfillment of the requirements for the degree of Doctor of Philosophy.

‡ Now at Allied Research Associates, 43 Leon Street, Boston, Massachusetts.

§ Now at RAND Corporation, Santa Monica, California.

[1] E. O. LaCasce, Jr., and P. Tamarkin, J. Appl. Phys. **27**, 138 (1956).

[2] Proud, Jr., Tamarkin, and Meecham, J. Appl. Phys. **28**, 1298 (1957).

[3] Lord Rayleigh, *Theory of Sound* (Dover Publications, New York, 1945), Vol. 2, pp. 89–96.

[4] H. S. Heaps, J. Acoust. Soc. Am. **27**, 698 (1955).

[5] J. G. Parker, J. Acoust. Soc. Am. **28**, 672 (1956).

[6] V. Twersky, J. Acoust. Soc. Am. **29**, 209 (1957).

[7] J. W. Miles, J. Acoust. Soc. Am. **26**, 191 (1954).

[8] W. C. Meecham, J. Appl. Phys. **27**, 361 (1956).

[9] L. M. Brekhovskikh, J. Exptl. Theoret. Phys. U.S.S.R. **23**, 275, 289 (1952).

[10] M. A. Isakovich, J. Exptl. Theoret. Phys. U.S.S.R. **23**, 305 (1952).

[11] C. Eckart, J. Acoust. Soc. Am. **25**, 566 (1953).

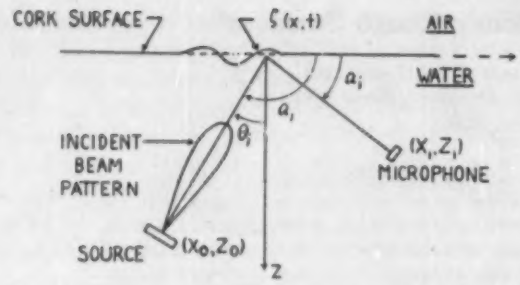

FIG. 1. Schematic diagram of the experimental configuration.

(x_1,z_1) in the half-plane $z\geq 0$. The Eckart solution makes use of the Helmholtz theorem and the approximation that the surface is nearly plane. The reflected pressure field is then given approximately by

$$p_1(x_1,z_1)=\frac{ikc}{r_{10}}\exp(ikcr_{10})\int D(x)\times\exp[-ik\{ax+c\zeta(x,t)\}]dx, \quad (1)$$

where

$$D(x)=1/(4\pi)\int \bar{p}(x,y)\exp(-ikby)dy,$$

and

$\bar{p}=(P/r_{00})\exp(ikr_{00})$

r_{00} = the distance to the source from the center of coordinates.

r_{10} = the distance to the point (x_1,z_1) from the center of coordinates.

a, b, c are the sums of the x, y, z direction cosines for r_{10} and r_{00}.

The reflected intensity is proportional to $p_1p_1^*$, where p_1^* is the complex conjugate of p_1. Thus,

$$p_1p_1^*=(k^2c^2/r_{10}^2)\int\int D(x')D^*(x'')\times\exp\{ikc[\zeta(x'',t)-\zeta(x',t)]\}\times\exp[ika(x''-x')]dx'dx''. \quad (2)$$

By using the transformation: $x''=x+\xi$, $x'=x$, and averaging over time, we get

$$p_1p_1^*=(k^2c^2/r_{10}^2)\int\int D(x)D^*(x+\xi)\times\langle\exp\{ikc[\zeta(x+\xi,t)-\zeta(x,t)]\}\rangle_t\cdot\exp(ik\xi)dxd\xi. \quad (3)$$

The surface is assumed to possess the following properties:

$$\text{(a)}\quad \langle\zeta(x,t)\rangle_t=\langle\zeta(x+\xi,t)\rangle_t=0$$
$$\text{(b)}\quad \langle\zeta^2(x,t)\rangle_t=\langle\zeta^2(x+\xi,t)\rangle_t=h^2 \quad (4)$$
$$\text{(c)}\quad \langle\zeta(x,t)\zeta(x+\xi,t)\rangle_t=h^2\Phi(\xi).$$

The rms surface amplitude is h, and $\Phi(\xi)$ is the correlation function. The time averages in Eq. (4) express the homogeneity of the surface roughness in that the results of the averages are independent of the orgin of coordinates.

Results for a Gaussian Surface

In order to determine the time average in the integrand of Eq. 3 without further approximation, it is necessary to know more about the statistics of the surface. We shall assume here that the surface is Gaussian, i.e., that all of the basic distributions are Gaussian. The desired time average can then be performed with the aid of the bivariate Gaussian distribution. Thus,

$$\langle\exp\{ikc[\zeta(x+\xi,t)-\zeta(x,t)]\}\rangle_t$$
$$=(2\pi h^2)^{-1}[1-\Phi(\xi)]\int\int\exp[ikc(\zeta_1-\zeta_2)]\times\exp\frac{-[\zeta_1^2+\zeta_2^2+2\Phi(\xi)\zeta_1\zeta_2]}{2h^2[1-\Phi(\xi)]}d\zeta_1d\zeta_2$$
$$=\exp\{-(chk)^2[1-\Phi(\xi)]\}. \quad (5)$$

By using this result, Eckart has obtained a geometric-optics approximate solution. In his calculation, the radiation wavelength is assumed to be much smaller than the surface roughness dimensions. We present here a solution valid for all wavelengths. By using Eq. (5), we can write Eq. (3) as

$$\langle p_1p_1^*\rangle_t=\frac{k^2c^2}{r_{10}^2}\Big\{\exp[-(chk)^2]\int\int D(x)D^*(x+\xi)\times\exp[(chk)^2\Phi(\xi)-1]\cdot\exp(ika\xi)d\xi dx+\exp[-(chk)^2]\int\int D(x)D^*(x+\xi)\times\exp(ika\xi)d\xi dx\Big\}. \quad (6)$$

Now $\Phi(\xi)$ is equal to unity at $\xi=0$, and usually vanishes rapidly with increasing ξ. We therefore employ a Fourier integral representation as follows:

$$\exp[(chk)^2\Phi(\xi)]-1=(2\pi)^{-1}\int G(q)\exp(iq\xi)d\xi. \quad (7)$$

We then set

$$K(ka)=\int\int D(x)D^*(x+\xi)\exp(ika\xi)d\xi dx. \quad (8)$$

Hence,

$$(r_{10}^2/k^2c^2)\langle p_1p_1^*\rangle_t=K(ka)\exp[-(chk)^2]+(2\pi)^{-1}\exp[-(chk)^2]\int G(q)K(q+ka)dq.$$

When the surface is plane ($h=0$) we obtain, in the specular direction ($a=0$, $c=c_s$),

$$(r_{10}^2/k^2c_s^2)\langle p_1p_1^*\rangle_t=K(0).$$

The reflected acoustic intensity relative to that reflected in the specular direction from a plane surface is then

$$I_1=(c/c_s)\exp[-(chk)^2]\cdot[K_n(ka)+F(ka)], \quad (9)$$

where

$$F(ka)=(2\pi)^{-1}\int G(q)K_n(q+ka)dq, \quad (10)$$

and

$$K_n(ka)=K(ka)/K(0) \quad (10a)$$

As a final result, a solution of the integral Eq. (10) yields an expression for the correlation function in terms of measurable acoustical quantities. The result is

$$\Phi(\xi)=(kch)^{-2}\ln\left[1+\frac{\bar{F}(\xi)}{\bar{K}_n(\xi)}\right], \quad (11)$$

where $\bar{F}(\xi)$ and $\bar{K}_n(\xi)$ are the inverse Fourier transforms of $F(ka)$ and $K_n(ka)$, respectively.

Thus, provided the rough surface is known to be Gaussian, one can (at least in principle) determine the correlation function by:

(1) knowing $K_n(ka)$; this is essentially equivalent to knowing the source beam pattern;
(2) determining $F(ka)$ by measurement of the reflected intensity distribution and applying Eq. (9).
(3) carrying out the operations indicated in Eq. (11).
(4) estimating the rms amplitude h by some auxiliary means since it cannot be determined from the acoustic data alone.

We have thus illustrated that it is possible to obtain the surface correlation function from acoustic measurements when the rms amplitude, h, and the surface statistics are known. Unfortunately, the difficulty in establishing these surface characteristics renders Eq. (11) of little use in practical situations. Indeed, it may not even be possible to obtain analytical solutions for $\Phi(\xi)$, when the surface statistics are other than Gaussian, and there is no evidence that the sea surface is ever describable by Gaussian statistics.[12] The statistical nature of the sea surface is discussed later.

Specular Results for Truncated $\Phi(\xi)$

When the surface is approximately purely random, that is, when there is little average correlation between neighboring points of the surface, the correlation function is nonvanishing only over a narrow region near the origin ($\xi=0$). It is not unreasonable, then, to expect $\Phi(\xi)$ to resemble

$$\Phi(\xi)=1, \quad -\epsilon_0\leq\xi\leq\epsilon_0$$
$$=0, \quad \text{otherwise.} \quad (12)$$

By using Eq. (11) we obtain

$$\bar{F}(\xi)=\bar{K}_n(\xi)[\exp(chk)^2-1], \quad -\epsilon_0\leq\xi\leq\epsilon_0$$
$$=0, \quad \text{otherwise.} \quad (13)$$

If the surface is "illuminated" uniformly over an area of half-width, ϵ,

$$K_n(ka)=\frac{\sin^2ka\epsilon}{(ka\epsilon)^2}, \quad (14)$$

then

$$\bar{K}_n(\xi)=(2\pi)^{\frac{1}{2}}\epsilon^{-1}(1-\xi/2\epsilon), \quad -2\epsilon\leq\xi\leq2\epsilon$$
$$=0, \quad \text{otherwise.} \quad (15)$$

Now, if $\epsilon_0\ll\epsilon$, $\bar{K}_n(\xi)$ can be replaced by its value at the origin. Equation 13 then becomes

$$\bar{F}(\xi)=(2\pi)^{\frac{1}{2}}\epsilon^{-1}[\exp(chk)^2-1]=\bar{F}(0). \quad (16)$$

On inverting Eq. 16 and substituting in Eq. (9), we get for the intensity in the specular direction (where $a=0$, $c=c_s$),

$$I^0=\exp[-(c_shk)^2]+(2\epsilon_0/\epsilon)\{1-\exp[-(c_shk)^2]\}. \quad (17)$$

Thus, if ϵ_0/ϵ is vanishingly small, the specular reflection decreases approximately as $\exp[-(c_shk)^2]$. For large hk, the specular intensity approaches $2\epsilon_0/\epsilon$. The dependence on c_shk is, of course, a consequence of the assumed Gaussian statistics. It will be shown later that in most cases, the specular intensity falls off as $1-(c_shk)^2+O(c_shk)^4$, independently of the surface statistics. Thus, by measurement of I^0 for small values of c_shk, one has the possibility of estimating the rms surface amplitude h. Somewhat more information can be obtained if the reflecting surface is highly random (small ϵ_0) in that it is reasonable to assume Gaussian statistics in such a case. Then, Eq. (17) may be used to determine ϵ_0 at short wavelengths.

Long Wave Theory

The above results demonstrate the difficulty in obtaining information about a reflecting surface from strictly wave reflection measurement. A technique is now given whereby the surface correlation function is determinable from long wave measurements for the case in which a knowledge of the complete surface statistics is lacking.

In the approximation that

$$kc\zeta_{max}\ll1, \quad (18)$$

[12] H. R. Seiwell and G. P. Wadsworth, Science **109**, 271 (1949).

Equation 2 can be written

$$p_1 p_1^* \doteq (k^2c^2/r_{10}^2)\int\int D(x')D(x'')\times\{1-ikc[\zeta(x',t)-\zeta(x'',t)]-(k^2c^2/2)[\zeta^2(x',t)+\zeta^2(x'',t)+\zeta(x',t)\zeta(x'',t)]\}\times\exp[-ika(x'-x'')]dx'dx'' \quad (19)$$

to second order in $kc\zeta$.

In the original Eckart theory, the scattering was described in terms of a scattered intensity proportional to the square of the magnitude of the difference in pressure reflected from the rough surface and that reflected from a plane surface replacing the rough one. This procedure dictates that one know both the amplitude and phase of these pressures in an experimental determination of the scattered intensity. The procedure we have adopted here leads to the experimentally simpler operation of forming the difference between plane and rough surface reflected *intensity*. No consideration of phase is then necessary. This, it is felt, is very important in that phase is usually a difficult experimental quantity. On employing Eq. (4), it is seen that

$$\langle p_1 p_1^* \rangle_t = \frac{k^2c^2}{r_{10}^2}\left\{[1-(kch)^2]\int\int D(x)D^*(x+\xi)\exp(ika\xi)d\xi dx + (kch)^2\int\int \Phi(\xi)D(x)D^*(x+\xi)\times\exp(ika\xi)d\xi dx\right\}. \quad (20)$$

On following the general techniques applied in the theory for all wavelengths, we set

$$\Phi(\xi) = (2\pi)^{-1}\int g(q)\exp(iq\xi)dq. \quad (21)$$

Then it can be readily shown that the reflected intensity relative to that reflected in the specular direction from a plane surface is given by

$$I_1 = (c/c_s)^2\{[1-(chk)^2]K_n(ka)+(chk)^2 f(ka)\}, \quad (22)$$

where

$$f(ka) = (2\pi)^{-1}\int g(q)K_n(q+ka)dq. \quad (23)$$

As before, a knowledge of the beam shape specifies $K_n(ka)$. The function $f(ka)$ is then a measure of the scattering and may be found empirically by determining I_1 for the rough surface. The same procedures which led to Eq. 11 now yield

$$\Phi(\xi) = \tilde{f}(\xi)/\tilde{K}_n(\xi), \quad (24)$$

where $\tilde{f}(\xi)$ and $\tilde{K}_n(\xi)$ are Fourier transforms of $f(ka)$ and $K_n(ka)$, respectively.

Some insight into the effect of various correlation functions on the scattering can be gained from the following qualitative considerations.

Let us define a half-width, Δ_ξ, for $\tilde{f}(\xi)$ and, similarly, Δ_{ka} for $f(ka)$. From the Fourier integral theorem it is known that $\Delta_\xi \cdot \Delta_{ka} \approx 1$. Now the half-width Δ_ξ is roughly determined by the half-width of the narrowest of $\Phi(\xi)$ or $\tilde{K}_n(\xi)$. Thus, for example, if $\Phi(\xi)$ is very narrow (as for a highly random surface), Δ_ξ must also be small. In that case, Δ_{ka} must be large and the scattering is highly diffuse. It is important to note, however, that although the reflected radiation is diffuse in this case, it is not described by Lambert's law. Diffuse reflection obeying Lambert's law arises when the incident wavelength is considerably less than the surface roughness dimensions.[13] The results here are applicable only to long-wave radiation.

Special Cases

The function $K_n(ka)$ for the source used in the experiments described below can be represented quite accurately by

$$K_n(ka) = \exp[-\sigma^2(ka)^2/2] \quad (25)$$

where σ is a constant. The correlation function for the surface used in the long wave experiments is, to a good approximation

$$\Phi(\xi) = \cos(q\xi)\exp(-\xi^2/2b^2). \quad (26)$$

Then, from Eq. (24),

$$\tilde{f}(\xi) = \sigma^{-1}\cos(q\xi)\exp(\xi^2/2\ell^2), \quad (27)$$

where

$$\ell^{-2} = b^{-2}+\sigma^{-2}. \quad (28)$$

By inverting Eq. (27), one obtains

$$f(ka) = (chk)^2(\ell/2\sigma)\{\exp[-\tfrac{1}{2}(q-ka)^2\ell^2] + \exp[-\tfrac{1}{2}(q+ka)^2\ell^2]\}. \quad (29)$$

With the known values of σ, b, and q, together with an estimate of h, one can predict the intensity distribution, I_1. Conversely, when the surface correlation function is unknown [except that it is of the type Eq. (26)], the values of b and q can be found empirically by using Eq. (29). Of particular interest is the problem of finding the correlation function of the sea surface from acoustic measurements. Usually, $\Phi(\xi)$ is not too unlike Eq. (26). In the general situation, $\Phi(\xi)$ must be determined directly from the ratio of the two empirical functions in Eq. (24). The transforms $\tilde{f}(\xi)$ and $\tilde{K}_n(\xi)$ must be found by numerical methods.

By way of illustration, let us consider the case of a purely sinusoidal surface. The correlation function is then given by Eq. (26) with $b=\infty$. Then, Eqs. (29)

[13] E. Skudrzyk, Akustische Z. 4, 189 (1939).

and (22) yield

$$I_1=(c/c_s)^2\{[1-(chk)^2]K_n(ka) +[(chk)^2/2][K_n(q-ka)+K_n(q+ka)]\}. \quad (30)$$

The first term on the right is that part of the reflected intensity which is just the plane surface specular reflection reduced by the factor $1-(kch)^2$. The second term represents the scattered intensity. The shape of these maxima is identical with that reflected in the specular direction, but they are located by the grating equation for first order.

$$q=\pm ka. \quad (31)$$

The effect of a damped harmonic correlation function (b finite) is to decrease the intensity at these maxima and to broaden them.

When the surface correlation is not oscillatory [e.g., $q=0$ in Eq. (26)] there are no first-order grating orders. Instead, the effect of scattering is merely to confuse the specular reflection.

A consideration of the grating equation together with the assumption of long wave radiation shows that the Eckart theory is applicable for wavelengths satisfying

$$h\ll\lambda<\Lambda, \quad (32)$$

where Λ is the wavelength of any periodic reflecting surface. It is interesting to note that this is essentially a statement of the conditions for which the Kirchhoff approximation is valid.

III. APPARATUS AND PROCEDURE

A. Apparatus

A pulsed underwater sound source irradiated the rough surfaces under study. The surfaces were made of cork (approximately pressure release) formed with the desired roughness profiles, and were floated on the surface of the water in a tank. The reflected pulses were observed by means of a scanning microphone. Details of the apparatus have been given previously.[1]

The basic construction of the surfaces used in the investigation was similar to that of periodic surfaces of previous studies.[1,2] A $\frac{3}{4}$-in. plywood backing is used to support sheet cork molded to give the desired roughness profile. The width of each surface is 18 in., whereas the lengths are more than twice this dimension. Since the beam typically irradiates an approximately circular region of 1 ft diam, one is assured that the entire main lobe of the beam makes contact with the rough surface. The surface lengths are such that the surfaces can be moved (along their lengths) with respect to the beam through wide limits. With reference to Fig. 1, the x and y directions run along the surface lengths and widths, respectively. The roughness variation is then a perturbation of the plane $z=0$. There is no y dependence of this variation so that the amplitude of variation can be specified by a function of x alone.

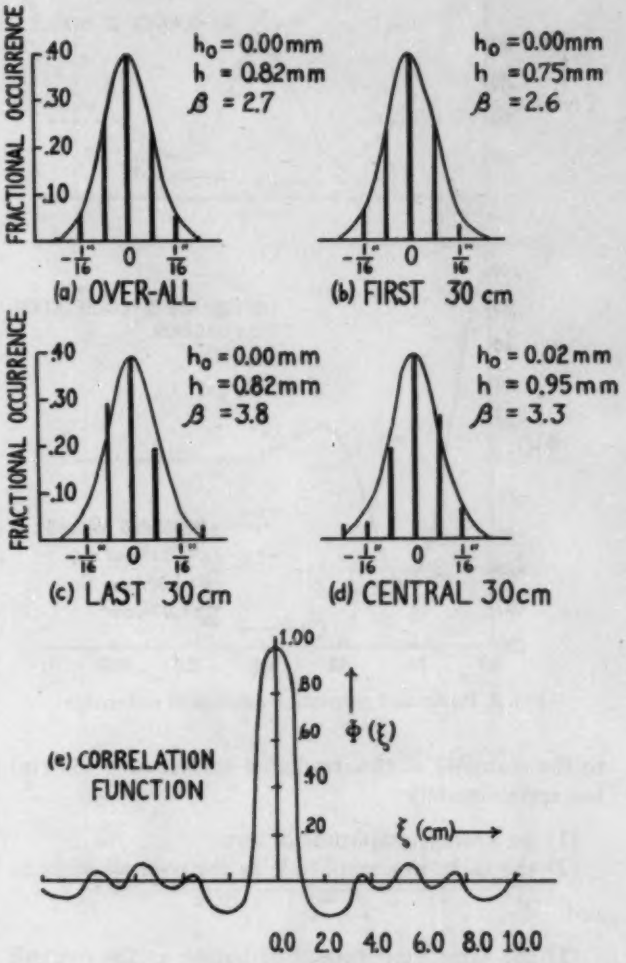

FIG. 2. Step-amplitude distributions and correlation function of surface I.

Surface I

Surface I was designed for use in investigating the dependence of the specular reflected intensity on the acoustic wave number, angle of incidence and surface roughness. The surface represents an attempt to establish a roughness whose constituent amplitudes are distributed according to a Gaussian law. In order to simplify construction, the roughness was composed of one hundred step-amplitude variations of equal width (1 cm). These consisted of flat cork strips cemented to the plywood base perpendicular to its length. The smallest step variation was limited to 1/32 in., the minimum thickness of available sheet cork.

The discontinuous distribution of amplitudes is shown in Fig. 2(a) and compared with a smooth Gaussian envelope. The ordinate represents the normalized frequency of occurrence of each amplitude shown along the abscissa. The hundred step amplitudes so distributed are arranged along the surface base in such a manner that any segment whose length is about equal

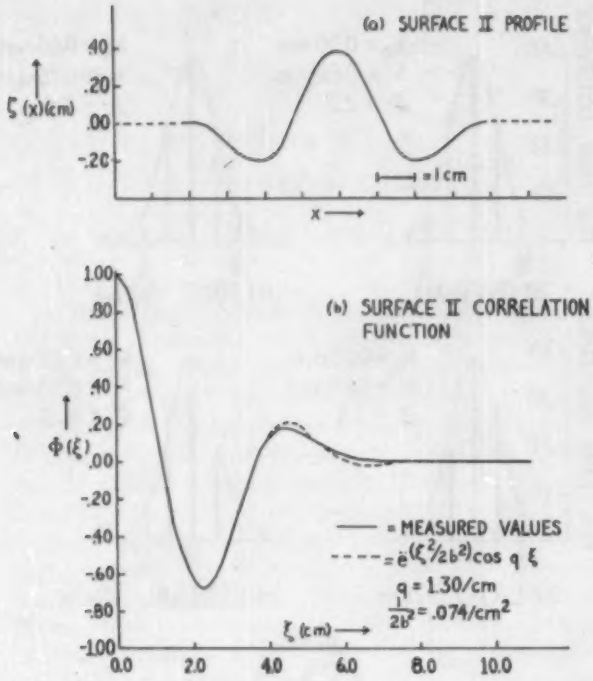

FIG. 3. Profile and correlation function of surface II.

to the diameter of the irradiated surface area (30 cm) has approximately:

(1) an average amplitude of zero;
(2) the same rms amplitude as the over-all surface;

and

(3) the same amplitude distribution as the over-all surface.

The degree to which these conditions were met is illustrated in Fig. 2(b,c,d). The distribution is shown for three 30 cm segments of surface; the first and last 30 cm of the roughness and a similar segment centered at the middle of the surface. Beside each figure is noted the average amplitude, h_0, the rms amplitude, h, and β, the ratio of the average fourth power of the amplitude to h^4. For a true Gaussian distribution, $\beta=3$.

The correlation function for Surface I is illustrated in Fig. 2(e). It demonstrates that there is little correlation on the average even between nearest neighbor step-amplitudes. The oscillations about zero indicate only slight irregular correlation for larger correlation distances. Note that while the surface profile is discontinuous, the correlation function is continuous.

Surface II

Surface II was constructed in order to investigate the dependence of the reflected intensity pattern on the surface correlation function. It was designed to yield an analytical correlation function that could be manipulated easily in the theoretical expressions.

To provide a smooth water-tight surface, a single $\frac{1}{16}$ in. cork sheet was bonded to a preformed cork mold attached to the plywood base. The surface is mostly planar with a brief spatial wave train impressed near the center. The profile of this surface "pulse" is shown in Fig. 3(a). The average amplitude is zero, while the rms amplitude h is 1.89 mm when the average is taken only over the rough portion of the surface. The plane portion of the surface is, of course, at $z=0$.

The correlation function (for positive argument) for Surface II is illustrated in Fig. 3(b) and is compared to the analytical function which approximates it. The adjustable parameters used in obtaining the fit are noted in the figure.

The correlation functions and other averages for Surfaces I and II have been computed as spatial averages over the lengths of the surfaces. Since the profiles themselves are fixed this method of averaging is completely equivalent to time averaging by a fixed observer observing the surface in uniform motion past a point in observer space. We note that the sea surface, for example, is not simple in this respect as the sea roughness profile itself changes in time.

B. Procedure

The portion of the investigation using Surface I was concerned with the dependence of the specular reflection on the quantity, $c_s hk$. The reflected intensity was observed for fixed angles of incidence (fixed c_s) as the acoustic frequency (and therefore, k) was varied over the available range. This was done for four angles of incidence: 0°, 30°, 45°, and 60°. The value of h was such that the available range of $c_s hk$ was then approximately: 0.25 to 2.00. A calibration procedure was followed whereby all data were taken relative to reflections from the still water surface.

The time average of the (relative) reflected intensity was determined at each frequency as the rough surface passed through the area insonified by the incident beam. In order to obviate the difficulties of an actual time average of the received pulse amplitudes, a sampling technique was employed. That is, the surface was moved in 5 cm steps along the x axis and held at rest while the reflected pulse amplitude was recorded. Usually, ten "snapshot" readings of this kind were made. The average square of the ten readings was then proportional to the average reflected intensity. A more detailed sampling technique was determined to be unnecessary. This result, indicated by experiment, is to be expected in view of the uniformity of the surface, together with the fact that the beam irradiates a surface area of about 30 cm.

A correction factor was applied to the observed values of the average reflected intensity to account for the lack of perfect reflectivity of cork at higher frequencies. This was done by noting the reflection from a plane cork surface when the latter replaced the rough one. All of

the observed average intensities were then adjusted by dividing them by the square of the reflection coefficient of the plane cork surface. This procedure is not strictly justifiable, since absence of perfect reflectivity indicates that the surface is not pressure release, as assumed in the theory. On the other hand, the discrepancy is only slight and occurs only at the highest frequencies used.

The long-wave theory was investigated experimentally by use of Surface II, with the intention of testing the theory and illustrating some of its limitations. Three angles of incidence were employed (24.5°, 30°, and 45°) while the frequency in each case was fixed at about 80 kc.

The function $K_n(ka)$ was defined in the theory by the intensity pattern observed when the sound beam is reflected from a plane, perfectly reflecting surface. $K_n(ka)$ was found experimentally by noting the form of the intensity distribution when the sound beam was reflected from the still water surface. All intensities observed in 1° to 2° steps throughout the angle describing the beam width were taken relative to: max $K_n(ka)=K_n(0)\equiv 1$.

The average reflected intensity I_1 was found by a technique similar to that just described for the determination of $K_n(ka)$. For each position of the receiving microphone, the average intensity was observed as Surface II moved through the incident sound beam in steps of 2 cm. About twenty readings were taken as the "rough" portion of the surface passed entirely through the incident beam. As in the case of Surface I, the average square of these readings was taken as the average intensity. In the neighborhood of the spectral direction, where the magnitude and slope of I_1 are large, observations were made at intervals of 2°. At angles well removed from the spectral direction, where I_1 varies slowly, sufficient detail was obtained by rotating the receiving microphone in steps of 5°. The reflected sound field was scanned in this way throughout the 180° in the water below the reflecting surface.

In specifying the rms amplitude, h, of Surface II we have given the value obtained by considering only the rough portion of the surface. Any value for h smaller than this is obtainable by including a part of the flat portion of the surface (amplitude=0) in the averaging procedure. This same flexibility arises in the acoustic measurements since the observed average intensity depends upon the number of reflection readings included which correspond to the reflection from the plane portion of the surface. Thus, the value of h to be used when applying the theory is somewhat elusive. The procedure used to obtain a value for h involved the use of the expression $I^0=1-(c_s hk)^2$, which is valid provided $f(ka)$ is very small near $ka=0$.

IV. RESULTS

A. Spectral Reflections

The results of the specular reflection from Surface I are summarized in Fig. 4. Here, the average intensity, I^0, observed in the specular direction is plotted *vs* $c_s hk$ for the four angles of incidence employed. Theoretical curves using Eq. (17) are shown for comparison with the data. The solid curve was calculated using the measured value of $\epsilon_0(=1$ cm) and the radius of the insonified area, estimated from the theoretical beam width for a piston source of the size we used as the value for ϵ. The dashed curve was calculated for the case where ϵ_0 is vanishingly small, as for a purely random surface.

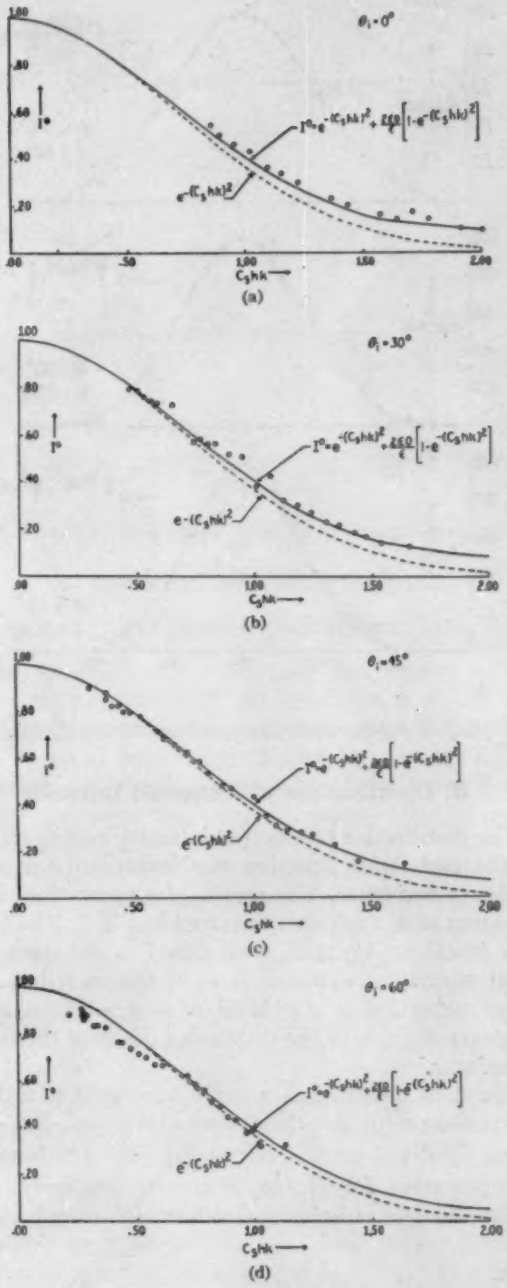

FIG. 4. Relative specular reflected intensity for surface I for various angles of incidence.

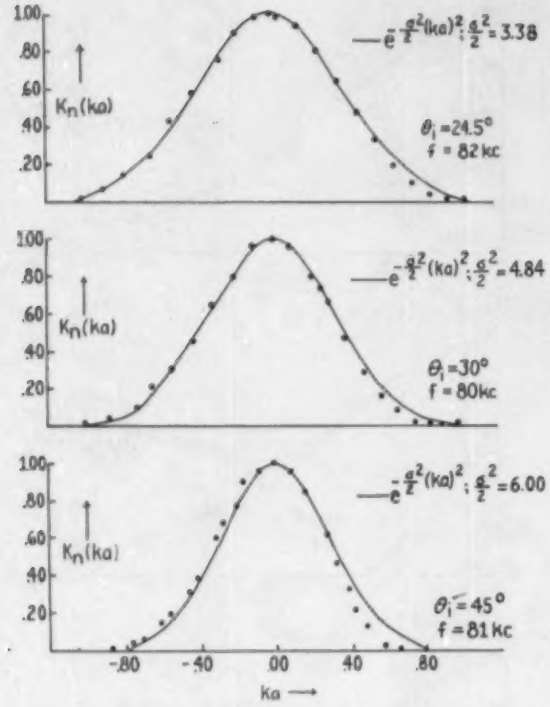

FIG. 5. Approximate Gaussian beam forms, $K_n(ka)$.

B. Distributions of Reflected Intensity

The distribution of reflected intensity and its relation to the correlation function was investigated at three angles of incidence. The results of an empirical determination of $K_n(ka)$ are illustrated in Fig. 5. The Gaussian function [Eq. (25)] was fitted to the data. The width parameter, σ, was then set by this procedure. The larger values of σ associated with greater angles of incidence are due to the decreasing depth of the source transducer.

The data obtained at $\theta_i=30°$ were used in a direct comparison with the theoretical expression, Eq. (22), where $f(ka)$ was calculated from Eq. (29). The Gaussian approximation for $K_n(ka)$ was also employed. The theoretical and experimental values of I_1 were matched

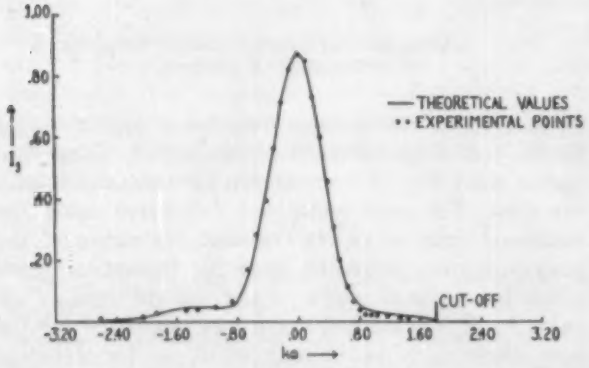

FIG. 6. Average reflected intensity distribution, $\theta_i=30°$.

at $ka=0$, so that the rms amplitude h is treated as a fitting parameter. The comparison is illustrated in Fig. 6 where theory is indicated by the solid curve. The cutoff value of ka, noted in the figure, is that value of ka for which the reflections are at the grazing angle, $\alpha_1=0$, in the forward direction.

An empirical evaluation of $f(ka)$ was determined from the same data using the back scattered reflections. The experimental points representing $f(ka)$ for negative ka are plotted in Fig. 7(a). The solid line again represents theoretical values determined from the directly measured surface correlation function. The parameters in the theoretical expression were then readjusted to determine $f(ka)$ empirically. The result is indicated by the dashed curve. In adjusting the parameters it is noted that the value of q is equal to the value of ka at which

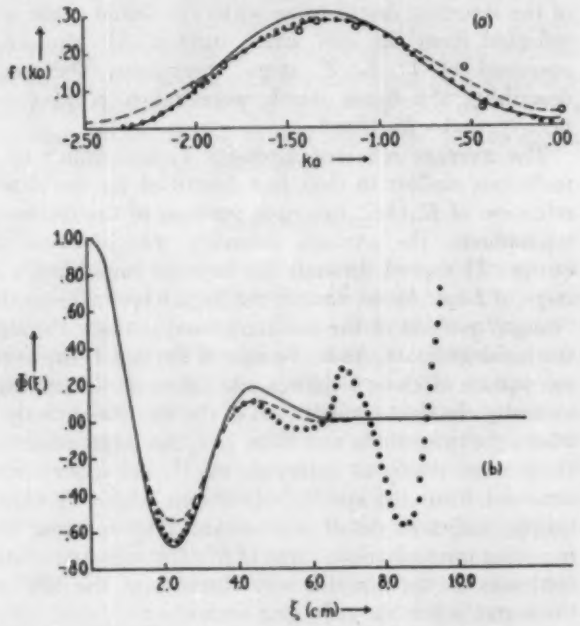

FIG. 7. Empirical determinations of correlation function, $\theta_i=30°$.

the maximum in $f(ka)$ occurs. The value of ℓ to be used in Eq. (28) can be found from the maximum value of $f(ka)$ or by the width as indicated by Eq. (29). The parameters b and q found in this manner were inserted into the assumed functional form of the correlation function. The results are indicated in Fig. 7(b) by the dashed curve. The solid curve represents the correlation function determined directly from measurements of the surface profile.

In the calculation just described, the choice of the analytical function used to fit the experimental data for $f(ka)$ was influenced by the expected theoretical form, Eq. (29). To the accuracy of the data, a number of other functional forms of $f(ka)$ could be assumed for obtaining an empirical evaluation. By way of illustration, the correlation function was calculated with the

assumption that $f(ka)$ could be fitted with the following form:

$$f(ka)=A\sin^2 pka, \quad -\pi/(p)<ka<\pi/(p)$$
$$=0, \text{ otherwise.}$$

A comparison with experiment is denoted by the dotted curve in Fig. 7(a). From Eq. (24), one then obtains

$$\Phi(\xi)=[A\sigma/(2\pi)^{\frac{1}{2}}][1/(\xi)+\xi/(4p^2-\xi^2)] \times\sin\pi\xi/(p)\exp(\xi^2/2\sigma^2).$$

The dotted curve in Fig. 7(b) was determined from this expression. Because of the positive exponential term, the function diverges rapidly beyond $\xi=6.5$, approximately.

The above measurements indicated a distortion of the forward scattering due to the proximity of the cutoff to the maximum of the function, $f(ka)$. In order to clarify this effect, a second set of data was taken with $\theta_i=45°$. For this angle of incidence, most of the forward scattering is absent due to cutoff.

The assumption is made in the analysis of the data that the functional form of $f(ka)$ is given by Eq. (29). In determining the correlation function, the problem is

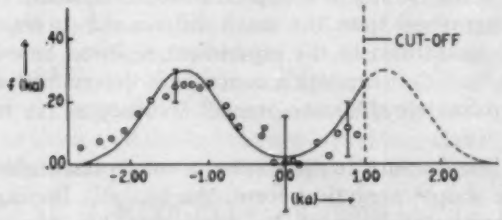

FIG. 8. $f(ka)$, experimental and theoretical, $\theta_i=45°$.

then one of evaluating the parameters b and q. The experimental values representing $f(ka)$ were calculated from smoothed values of $K_n(ka)$ and I_1. The results are shown in Fig. 8. The curve shown in the figure was calculated from the known values of b, q and σ. Estimates of the maximum possible experimental error are indicated. The large error near $ka=0$ is due to effect of determining experimentally a small difference between two large values.

The back scattering is illustrated again in Fig. 9(a). The experimental values are compared with the theoretical curve. The dashed curve represents the function $f(ka)$ when the parameters are adjusted to fit the data more closely. The resulting correlation function is illustrated in Fig. 9(b) where the dashed curve is the empirical result. The solid curve is the known function determined from the measured surface profile.

One further empirical determination of $\Phi(\xi)$ was carried out for the case where the forward scattering is nearly unaffected by the cutoff. The data and the fitted function, $f(ka)$, are shown in Fig. 10. By the methods outlined above, the correlation function was then determined and is illustrated in Fig. 11. Here, the dashed curve is the empirical result.

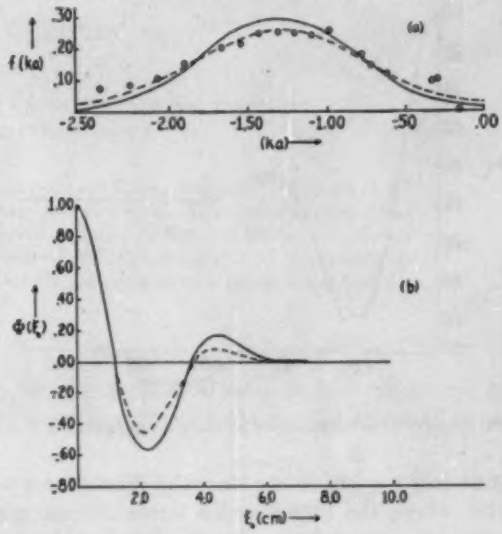

FIG. 9. Empirical determinations of correlation function, $\theta_i=45°$.

V. SUMMARY AND CONCLUSIONS

A. Specular Reflection

The results of the experiment and theory for the reflection from Surface I are illustrated in Fig. 4. The agreement is somewhat surprising since Surface I is only step-wise continuous. It thereby presents a clear violation of the basic condition required by the Eckart theory approximation that the surface slope is everywhere small.

The reason for the good agreement is probably due to the fact that the infinite slope portions of the surface reflect only a small portion of the incident sound, particularly at smaller angles of incidence. At the largest angle of incidence used (60°), there is definite disagreement with theory for the longer wavelengths. This may be related in some way to the fact that more reflection is occuring from the steep portions of the surface. The reason for the improving agreement with increasing $(c_s hk)$ may then be fortuitous.

The results of the spectral reflection study suggest that one might expect to determine the surface statistics by noting the dependence of I^0 on $(c_s hk)$. There is no available procedure to do this theoretically, however. Secondly, the spectral intensity is independent of the full surface statistics to second order in $(c_s hk)$. Furthermore, one can show that the fourth order term in $(c_s hk)$

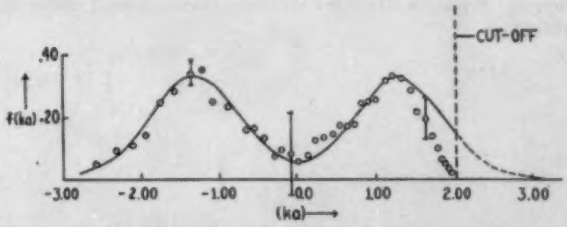

FIG. 10. $f(ka)$, experimental and theoretical, $\theta_i=24.5°$.

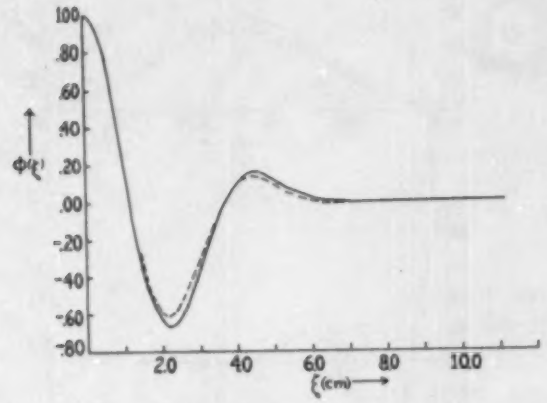

FIG. 11. Empirical determination of correlation function, $\theta_i = 24.5°$.

depends only weakly on the statistics. For shorter wavelengths, where the higher order terms assume greater importance, one violates the condition on radiation wavelength and minimum radius of curvature which must hold in order that the Kirchhoff approximation is valid.[14]

In the case of a high degree of randomness such as we have constructed in Surface I, it is reasonable to assume Gaussian statistics. Then, one has the possibility of estimating the range of the correlation function by observing the value of I^0 for large $(c_s hk)$. It may be seen that I^0 approaches $2\epsilon_0/\epsilon$ in this limit. The experiment shows this effect quite clearly in Fig. 4.

B. Determinations of Correlation Function

We have shown that in theory one can form an estimate of the reflecting surface correlation function from acoustic measurements alone. It was shown, furthermore, that all the information about the surface is contained in the back scattering. This fact is particularly important in situations where the forward scattering is cut off as illustrated by the experimental situation we have considered with $\theta_i = 45°$.

The correlation function provided by the profile of Surface II is quite general in that it is typical (though idealized) of many processes such as the sea surface roughness. The sea bottom is frequently characterized by a similar correlation function inasmuch as it is usually somewhat periodic. The acoustic measurements involve time averages which may be calculated by some sampling technique such as we have described. The procedure is apt to be difficult or even impossible when applied to the sea surface, however, in that the basic character of the sea roughness may change in time. That is, the sea surface roughness may not be a stationary random process. The reason is that the mechanisms generating the surface waves (local winds and large scale air mass motion) themselves change with time. For the type of acoustic measurements which need to be made, there appears to be only slight chance of obtaining the required data in a time that is short compared to the times characteristic of these changes.

When the radiation wavelength is very large compared to the dimensions of the surface irregularities, the reflected radiation is not greatly different from that reflected from a perfectly flat surface. That is, the scattered radiation which must be measured in order to determine the surface correlation function is not very evident. Great experimental accuracy is required, therefore, to obtain a representation of $f(ka)$. In fact, an uncertainty of more than one percent in the intensity measurements can lead to many times this uncertainty in the calculated values of $f(ka)$. This is particularly true in the vicinity of the spectral direction, where $f(ka)$ is determined from the small difference between two large quantities. In the experiment reported here it is seen that the correlation function is determined with approximately the same over-all accuracy as the function $f(ka)$.

When the surface correlation is not representable by some simple analytical form, the analysis leading to its computation must be performed by numerical methods. In particular, the Fourier transforms in Eq. (24) must be evaluated by numerical integration. This is not a real limitation inasmuch as the integration may be done readily by most electronic computers. In some instances it may suffice to assume that $f(ka)$ has some simple analytical form as we have done here. One then obtains an approximate correlation function which may be quite similar to the actual unknown function.

Further research into some of the basic problems of rough surface reflection is still necessary. All of the theories thus far developed are limited to surfaces which are nearly plane. A theory which is not so limited would have much greater applicability to real situations. Experimental studies of reflection from rough surfaces which have large slope and large amplitude compared to radiation wavelengths might provide considerable insight into the basic problem and might thus suggest theoretical techniques to be tried.

[14] B. B. Baker and E. T. Copson, *The Mathematical Theory of Huygens' Principle* (Oxford University Press, London, 1950) 2nd Edition.

Charged Sphere in Cylinder

W. R. SMYTHE
Norman Bridge Laboratory, California Institute of Technology, Pasadena, California
(Received November 4, 1959)

The method first used to solve the problem of a freely charged right circular cylinder in J. Appl. Phys. **27**, 917 (1956), is applied to the case of a charged conducting sphere enclosed by a coaxial circular conducting cylinder. The charge density on the sphere, the potential between it and the cylinder and the capacitance are given for sphere to cylinder radius ratios of 0.1, 0.2, 0.3, 0.4, 0.5, 0.6, 0.7, 0.8, 0.9, and 0.95. All results are accurate to one part in 10^7 or better. An approximate formula for the capacitance of a sphere in a cylindrical box is given.

1. INTRODUCTION

A COMMON configuration in high voltage machines is a spherical electrode inside a circular cylinder. No orthogonal system is known in which both the spherical and cylindrical surfaces are members so that none of the methods of classical potential theory apply. The method used here is essentially that used in the solution of the problem of a charged right circular cylinder,[1] but the details differ considerably. A charge distribution is found on the spherical surface such that it, together with the induced charge on the cylinder, put the latter at zero potential and such that the potential at the center of the sphere is V_0 and its $2p$ even z derivatives vanish there. It can be shown[1] that if p is sufficiently large the entire sphere will be at potential V_0. The units used throughout are mks. Most numerical calculation was done on a Burroughs Datatron 205.

2. METHOD OF SOLUTION

The charge distribution assumed on the sphere is

$$\sigma_s = V_0 \sum_{n=0}^{N} A_{2n} P_{2n}(\cos\theta). \tag{1}$$

The polar coordinates r, θ and cylindrical coordinates ρ, z are shown in Fig. 1. Only even harmonics are needed because of symmetry. Outside the sphere, the potential due to σ_s alone is

$$V_s = \frac{bV_0}{\epsilon} \sum_{n=0}^{\infty} \frac{A_{2n}}{4n+1} \left(\frac{b}{r}\right)^{2n+1} P_{2n}(\cos\theta). \tag{2}$$

The potential due to a multipole of strength M_{2n} is

$$\frac{M_{2n}}{4\pi\epsilon} \frac{\partial^{2n}(r^{-1})}{\partial z^{2n}} = \frac{M_{2n}(2n)!}{4\pi\epsilon r^{2n+1}} P_{2n}(\cos\theta). \tag{3}$$

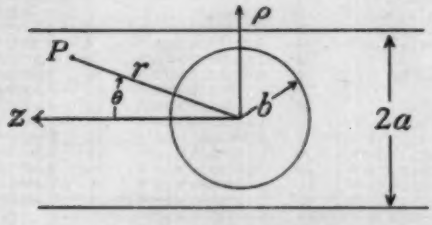

FIG. 1. Coordinate systems.

[1] W. R. Smythe, J. Appl. Phys. **27**, 917 (1956).

Thus, the potential due to σ_s is that produced by a collection of linear multipoles at the origin of strength

$$M_{2n} = \frac{4\pi b^{2n+2} V_0}{(4n+1)(2n)!} A_{2n}. \tag{4}$$

The potential of an isolated charge at the origin is[2]

$$q(2\pi^2\epsilon)^{-1} \int_0^{\infty} K_0(t\rho) \cos tz\, dt.$$

The solution of Laplace's equation which must be added to this to bring the cylinder to zero potential, and which is therefore the potential of the induced change is

$$V_q = -\frac{q}{2\pi^2\epsilon} \int_0^{\infty} \frac{I_0(t\rho) K_0(ta)}{I_0(ta)} \cos tz\, dt. \tag{5}$$

The potential V_{2n} of the induced charge produced by a linear multipole of order $2n$ and strength $q = M_{2n}$ is found by evaluation of $\partial^{2n} V_q / \partial z^{2n}$, so that with the aid of (4) there results

$$V_{2n}(\rho,z) = \frac{(-1)^{n+1} 2V_0 A_{2n} b^{2n+2}}{\pi\epsilon(4n+1)(2n)!} \times \int_0^{\infty} \frac{t^{2n} K_0(ta) I_0(t\rho) \cos tz}{I_0(ta)} dt \tag{6}$$

The $2p$th z derivative of the potential at the origin due to the charge induced by the $2n$th multipole is

$$\frac{\partial^{2p} V_{2n}}{\partial z^{2p}} = \frac{2(-1)^{p+n+1} b^{2n+2} A_{2n} V_0}{\pi\epsilon(4n+1)(2n)!} \int_0^{\infty} \frac{t^{2n+2p} K_0(ta)}{I_0(ta)} dt. \tag{7}$$

Integration by parts yields

$$(2n+2p+1) \int_0^{\infty} \frac{t^{2n+2p} K_0(ta)}{I_0(ta)} dt = \int_0^{\infty} \frac{t^{2n+2p} dt}{I_0^2(ta)} = I(2n+2p, a). \tag{8}$$

[2] W. R. Smythe, *Static and Dynamic Electricity* (McGraw-Hill Book Company, Inc., New York, 1950), Eq. (3), p. 194.

TABLE I. Values of $(n!)^{-2}I(2n,1)=(n!)^{-2}\int_0^\infty t^{2n}I_0(t)^{-2}dt$.

n	$(n!)^{-2}I(2n,1)$	n	$(n!)^{-2}I(2n,1)$	n	$(n!)^{-2}I(2n,1)$
0	1.3676768	14	6.6868809	28	9.4193736
1	1.9406676	15	6.9180978	29	9.5847327
2	2.5873235	16	7.1417841	30	9.7472835
3	3.1438519	17	7.3586400	31	9.9071649
4	3.6201479	18	7.5692613	32	10.064504
5	4.0381944	19	7.7741598	33	10.219419
6	4.4144149	20	7.9737798	34	10.372018
7	4.7595084	21	8.1685104	35	10.522403
8	5.0804586	22	8.3586954	36	10.670667
9	5.3819713	23	8.5446396	37	10.816897
10	5.6673135	24	8.7266154	38	10.961171
11	5.9388399	25	8.9048667	39	11.103567
12	6.1983516	26	9.0796137	40	11.244157
13	6.4472985	27	9.2510556	41	11.383003

At $\theta=0$ the potential of the spherical charge is

$$V_s=\frac{bV_0}{\epsilon}\sum_{n=0}^{\infty}\frac{A_{2n}}{4n+1}\left(\frac{z}{b}\right)^{2n}. \tag{9}$$

At the origin, its $2p$th derivative is

$$\frac{\partial^{2p}V_s}{\partial z^{2p}}=\frac{(2p)!}{\epsilon(4p+1)}\frac{A_{2p}}{b^{2p-1}}V_0. \tag{10}$$

The conditions that at the origin the potential be V_0 and its $2p$ z derivatives vanish may now be stated from (7) and (10) by the Eqs.

$$\frac{\epsilon\delta_{2p}{}^0}{b^2}=\frac{(2p)!A_{2p}}{(4p+1)b^{2p}}-\frac{2b}{\pi}\sum_{n=0}^{\infty}\frac{(-1)^{n+p}b^{2n}I(2n+2p,a)}{(4n+1)(2n+2p+1)(2n)!}A_{2n}. \tag{11}$$

Here, $\delta_{2p}{}^0$ is zero if $2p\neq 0$ and one if $2p=0$. The solution of these simultaneous equations yields the values of A_{2n}. Table I, which is needed for the calculations, was prepared by numerical integration using Weddle's rule. In many cases the last digit is not significant because of rounding off errors.

3. SOLUTION FOR CHARGE DISTRIBUTION

Equation (11) was solved for b/a values of 0.1, 0.2, 0.3, 0.4, 0.5, 0.6, 0.7, 0.8, 0.9 and 0.95. Values of A_{2n} of the order of $10^{-8}A_0$ or less were discarded. For b/a less than 0.6 the values given in the table are unchanged in the last place by inclusion of an additional equation. For 0.95 the use of nineteen equations instead of eighteen changes A_{36} in the fourth place but leaves A_0 to A_{14} unchanged in the eighth place. The available computer code, prepared by Dr. T. T. Taylor, was limited to nineteen equations. These coefficients are tabulated in Table II.

4. POTENTIAL CALCULATION

The potential at any point may be found by addition of the potential of the induced charge ΣV_{2n} given by (6) to that of the spherical charge given by (2). Expansion of $\cos tz$ and $I_0(t\rho)$ gives the integral in (6) the form,

$$\sum_{s=0}^{\infty}\sum_{q=0}^{\infty}\frac{(-1)^s z^{2s}(\tfrac{1}{2}\rho)^{2q}I(2n+2s+2q,1)}{(2s)!(q!)^2(2n+2q+2s+1)a^{2n+2q+2s+1}}. \tag{12}$$

This reduces to a single summation on the axis where ρ is zero and in the equatorial plane where z is zero. For small values of ρ and z very few terms are needed. Another expansion, useful for larger values of z or ρ is

$$\epsilon V=\sum_{s=1}^{\infty}C_s(b/a)e^{-k_s z/a}J_0(k_s\rho/a), \tag{13}$$

where k_s is chosen so that $J_0(k_s)=0$. The $C_s(b/a)$ is found from the Green's Function for a charge at the origin in a cylinder of radius a by differentiation $2n$ times to get the potential of a multipole of strength M_{2n}. When this is written in terms of A_{2n} by (4) and the contribution from all multipoles added, there results

$$C_s(b/a)=\frac{b^2V_0}{a[J_1(k_s)]^2}\sum_{n=0}^{N}\frac{b^{2n}A_{2n}k_s^{2n-1}}{a^{2n}(2n)!(4n+1)}. \tag{14}$$

Values of $C_s(b/a)$ for each b/a are given in Table III.

The equation for the boundary of a tube of electric flux ending on a spherical cap which carries a charge U is,

TABLE II. Charge distribution coefficient A_{2n}.

n	$b=0.1a$	n	$b=0.6a$	n	$b=0.9a$
0	1.0953731×10^{0}	0	3.5048255	0	6.0055044
1	-1.1277517×10^{-2}	1	-8.0040856×10^{-1}	1	−5.8572468
2	5.4127464×10^{-5}	2	1.4370096×10^{-1}	2	3.2315516
3	-2.0357573×10^{-7}	3	-2.0534841×10^{-2}	3	−1.5310745
		4	2.6519740×10^{-3}	4	6.8652632×10^{-1}
n	$b=0.2a$	5	-3.2542516×10^{-4}	5	-2.9962675×10^{-1}
		6	3.8846350×10^{-5}	6	1.2854822×10^{-1}
0	6.0543002	7	-4.5660040×10^{-6}	7	-5.4464381×10^{-2}
1	-4.9871192×10^{-2}	8	5.3198331×10^{-7}	8	2.2852573×10^{-2}
2	9.5758616×10^{-4}	9	-6.1669166×10^{-8}	9	-9.5147742×10^{-3}
3	-1.4409092×10^{-5}			10	3.9369597×10^{-3}
4	1.9291921×10^{-7}	n	$b=0.7a$	11	-1.6208121×10^{-3}
				12	6.6452129×10^{-4}
n	$b=0.3a$	0	3.7094049	13	-2.7151564×10^{-4}
		1	−1.3905359	14	1.1061820×10^{-4}
0	4.5120528	2	3.5615636×10^{-1}	15	-4.4956005×10^{-5}
1	-1.2552673×10^{-1}	3	-7.3862950×10^{-2}	16	1.8231499×10^{-5}
2	5.4285436×10^{-3}	4	1.4052950×10^{-2}	17	-7.3798032×10^{-6}
3	-1.8405275×10^{-4}	5	-2.5710192×10^{-3}	18	2.9822664×10^{-6}
4	5.5548090×10^{-6}	6	4.6156300×10^{-4}		
5	-1.5697738×10^{-7}	7	-8.2054175×10^{-5}	n	$b=0.95a$
		8	1.4504673×10^{-5}		
n	$b=0.4a$	9	-2.5541370×10^{-6}	0	8.6696202
		10	4.4837362×10^{-7}	1	-1.1399194×10^{1}
0	3.8370076	11	-7.8492102×10^{-8}	2	8.2413756
1	-2.5368613×10^{-1}			3	−5.2039367
2	1.9577083×10^{-2}	n	$b=0.8a$	4	3.1196181
3	-1.1862857×10^{-3}			5	−1.8185192
4	6.4091735×10^{-5}	0	4.3044479	6	1.0408318
5	-3.2476780×10^{-6}	1	−2.5717446	7	-5.8795965×10^{-1}
6	1.5815934×10^{-7}	2	9.4111371×10^{-1}	8	3.2888642×10^{-1}
		3	-2.8626273×10^{-1}	9	-1.8257829×10^{-1}
n	$b=0.5a$	4	8.1316378×10^{-2}	10	1.0075053×10^{-1}
		5	-2.2430614×10^{-2}	11	-5.5327418×10^{-2}
0	3.5462095	6	6.0944855×10^{-3}	12	3.0261902×10^{-2}
1	-4.6117806×10^{-1}	7	-1.6398804×10^{-3}	13	-1.6496413×10^{-2}
2	5.6179557×10^{-2}	8	4.3796403×10^{-4}	14	8.9665943×10^{-3}
3	-5.3966125×10^{-3}	9	-1.1622635×10^{-4}	15	-4.8614430×10^{-3}
4	4.6422544×10^{-4}	10	3.0671679×10^{-5}	16	2.6297421×10^{-3}
5	-3.7617855×10^{-5}	11	-8.0539884×10^{-6}	17	-1.4195133×10^{-3}
6	2.9422750×10^{-6}	12	2.1055980×10^{-6}	18	7.6465960×10^{-4}
7	-2.2505494×10^{-7}	13	-5.4835528×10^{-7}		
8	1.6965082×10^{-8}	14	1.4232500×10^{-7}		
		15	-3.6831700×10^{-8}		

by Gauss' theorem.

$$U=\epsilon\int_z^\infty 2\pi\rho(\partial V/\partial\rho)dz$$
$$=2\pi\rho\sum C_s J_1(k_s\rho/a)e^{-k_s z/a}. \quad (15)$$

5. ACCURACY

The numerical accuracy was checked by calculation of the potential at the pole of the sphere by (6) and (12) for $0.1\leq b/a\leq 0.8$. In all cases, the potential differed from V_0 by less than one part in 10^7. For b/a values 0.1, 0.2 and 0.3 it was also checked at the equator with slightly smaller errors than at the pole. The 0.8, 0.9, and 0.95 values were checked by (13) and (14) at the pole and gave 0.99999990 V_0, 0.99999991 V_0, and 0.99999970 V_0, respectively, and the number of terms in (13) that contributed were 7, 6, and 6. The large values of C_s shown in the table when s is large were completely suppressed by the z exponential. These calculations would indicate that many more coefficients are given in both Table II and Table III than are needed for seven place accuracy except for $b/a=0.95$. They may be needed in other regions of the field.

6. CAPACITANCE

The capacitance between sphere and cylinder is Q/V_0 or $4\pi b^2 A_0$. In the following table ϵ_0 is taken to be 8.85434×10^{-12} and C is in farads. The capacitance C in Table IV is the same as would be given by solving an infinite number of Eqs. (11) so the only errors are rounding off errors in the calculation. These, do not exceed one part in 10^7 and are usually much less. For purposes of interpolation, two approximate formulas are useful. The first, good for b/a between 0.1 and 0.7 is

$$C_1/a=-4.568\times10^{-12}C_0+1.68\times10^{-10}b(1-b)^{-0.6}. \quad (16)$$

The second, good for b/a between 0.7 and 0.95 is

$$C_2/a=-8.5712\times10^{-12}C_0$$
$$+2.093\times10^{-10}b(1-b)^{-0.53}. \quad (17)$$

7. CAPACITANCE FOR CYLINDER WITH CLOSED ENDS

It is possible, by use of Green's Reciprocation Theorem[3] to calculate the capacitance when the cylinder is closed at one or both ends with considerable accuracy provided the ends are not too close. The additional charge induced on the sphere at V_0 by a point charge $-q$ at P in the cylinder is qV_P/V_0. Substitution of the

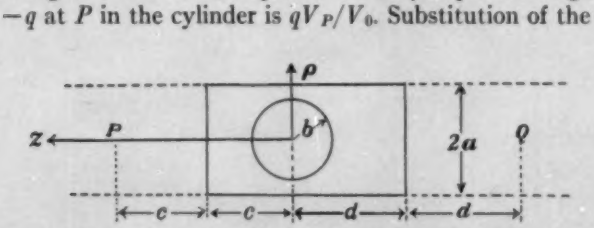

FIG. 2. Cylindrical box.

[3] Reference 2, p. 35.

TABLE III. Bessel function expansion coefficients $C_s(b/a)$.

s	$C_s(0.1)$	$C_s(0.2)$	$C_s(0.3)$	$C_s(0.4)$	$C_s(0.5)$	$C_s(0.6)$	$C_s(0.7)$	$C_s(0.8)$	$C_s(0.9)$	$C_s(0.95)$
1	0.33800597	0.74714706	1.2512754	1.8828742	2.6846856	3.7115062	5.0326816	6.7358716	8.9323950	1.0258594×10^{1}
2	0.34276712	0.75707495	1.2611290	1.8603039	2.5110749	3.0462330	3.0292038	1.4734044	−3.6974720	−8.8222370
3	0.34353287	0.75769353	1.2501072	1.7794209	2.1722060	2.0205762	0.7257038	−1.6514440	−0.4526880	7.2252920
4	0.34376666	0.75666466	1.2313466	1.6653872	1.7531445	1.0317902	−0.3236833	0.7891836	9.4955690	9.7861740
5	0.34385118	0.75484117	1.2066864	1.5281451	1.3267986	0.4286285	0.5587901	5.7199254	6.9500720	−0.1739860
6	0.34387498	0.75242748	1.1769901	1.3775211	0.9651262	0.4254727	2.7942595	7.5197601	0.2132570	5.4236430
7	0.34386715	0.74949869	1.1430041	1.2239246	0.7294101	1.0312531	4.9356806	4.4329106	0.7845470	−0.6143400
8	0.34383948	0.74609347	1.1055007	1.0779055	0.6605596	2.0452571	5.5963539	−0.0682231	0.5420950	1.6363899×10^{2}
9	0.34379751	0.74223862	1.0653024	0.9495192	0.7723656	3.1230572	4.3076950	−1.8524520	3.4472550	1.6483609×10^{4}
10	0.34374408	0.73795677	1.0232770	0.8476781	1.0490066	3.8899262	1.7329248	−0.7206147	3.5356561×10^{2}	9.6126244×10^{5}
11	0.34368084	0.73326967	0.9803209	0.7795627	1.4472866	4.0605215	−1.1474297	−4.5951810	1.3792626×10^{4}	3.7428758×10^{7}
12	0.34360872	0.72819920	0.9373362	0.7501420	1.9033082	3.5101121	−6.2691590	-1.0229474×10^{2}	3.8972798×10^{3}	1.0452057×10^{9}
13	0.34352838	0.72276820	0.8952025	0.7618408	2.3427157	2.2168038	-3.3284070×10^{1}	-1.3910295×10^{3}	8.3512682×10^{4}	2.2101355×10^{10}
14	0.34344017	0.71700041	0.8547409	0.8143836	2.6932350	−1.0666900	-1.9198168×10^{2}	-1.5152811×10^{4}	1.4133087×10^{5}	3.6910032×10^{11}
15	0.34334442	0.71092084	0.8166713	0.9048427	2.8986464	−5.1967333	-1.0069618×10^{3}	-1.3880803×10^{4}	1.9524872×10^{5}	5.0330696×10^{12}
16	0.34324131	0.70455560	0.7815561	1.0279118	2.9345093	-1.9650155×10^{1}	-4.7227891×10^{3}	-1.0955556×10^{4}	2.2614665×10^{6}	5.7558685×10^{13}
17	0.34313101	0.69793189	0.7497322	1.1764303	2.8291107	-6.4224178×10^{1}	-2.0057604×10^{4}	-7.5895578×10^{4}	2.2443585×10^{11}	5.6424235×10^{14}
18	0.34301363	0.69107797	0.7212196	1.3421989	2.6990545	-1.9785901×10^{2}	-7.8080476×10^{4}	-4.6853416×10^{5}	1.9431866×10^{12}	4.8277253×10^{15}
19	0.34288930	0.68402301	0.6956084	1.5171397	2.8207621	-5.7640695×10^{2}	-2.8135291×10^{5}	-2.6104097×10^{6}	1.4900291×10^{13}	3.6601473×10^{16}
20	0.34275808	0.67679705	0.6719099	1.6949097	3.7786670	-1.5888622×10^{3}	-9.4606930×10^{5}	-1.3266769×10^{6}	1.0248447×10^{14}	2.4904052×10^{17}

TABLE IV. Capacitances. Value for sphere of radius b on axis of cylinder of radius a is C. For isolated sphere of radius b it is $C_0=4\pi\epsilon_0 b$. Approximate C value from (16) is C_1 and from (17) is C_2.

b/a	$(C/a)\times10^{10}$	$C_0\times10^{10}$	$(C_1/a)\times10^{10}$	$(C_2/a)\times10^{10}$
0.10	0.12187741	0.11126566	0.1216	...
0.20	0.26945429	0.22253133	0.2694	...
0.30	0.45183289	0.33379699	0.4523	...
0.40	0.68308350	0.44506265	0.6837	...
0.50	0.98642839	0.55632832	0.9866	...
0.60	1.4038802	0.66759399	1.403	1.397
0.70	2.0223740	0.77885965	2.021	2.019
0.80	3.0651983	0.89012533	...	3.067
0.90	5.4124720	1.0013910	...	5.413
0.95	8.7057950	1.0570238	...	8.706

new value $q(1+V_P/V_0)$ gives as a second correction $q(1+V_P/V_0)V_P/V_0$, and so forth. Comparison of the result with that obtained by using the same method on free spheres shows that this charge is too small by an amount of the order of magnitude of $(V_P/V_0)^3$ so that, including both ends, the new capacitance is

$$C_2=C\left[1+\frac{V_P}{V_0}+\frac{V_Q}{V_0}+\left(\frac{V_P}{V_0}+\frac{V_Q}{V_0}\right)^2\right]. \qquad (18)$$

The quantities V_P and V_Q can be calculated from (13) and (14) by setting $\rho=0$ and substituting $2c$ and $2d$ for z. The result is too small by an amount whose order of magnitude is $C(V_P+V_Q)^3/V_0^3$.

JOURNAL OF APPLIED PHYSICS VOLUME 31, NUMBER 3 MARCH, 1960

Flow of Polyethylene into a Capillary

E. B. BAGLEY AND A. M. BIRKS
Canadian Industries Limited, Central Research Laboratory, McMasterville, Quebec, Canada
(Received September 10, 1959)

The flow of polyethylene from a reservoir into a capillary has been studied visually using a new technique for observing the flow patterns. Various patterns observed with different polyethylenes are shown, both below and above the critical shearing stress at which the extrudate becomes distorted. The technique is readily adaptable to observe directly the elastic energy stored in the melt above the capillary entrance and the rate at which this energy can be dissipated on the cessation of the steady flow into the capillary.

INTRODUCTION

WHEN a polymer melt is extruded from a reservoir through a capillary there may be observed a critical shear rate below which the extruded polymer filament is smooth but above which the filament is distorted.[1–5] Visual observations by Tordella, Clegg, and Schott and Kaghan have indicated that this extrudate roughness is associated with violently distorted flow behavior in the region immediately above the die entrance.

Both Tordella[2–4] and Clegg[5] used small tracer particles to follow the flow of the melt into the capillary. Schott and Kaghan, in later studies,[6] fed their reservoir and capillary from a screw extruder and traced the flow pattern by changing feed from natural to pigmented resin. The purpose of the present paper is to describe an alternative method for studying the flow patterns above the capillary entrance and to show certain typical patterns so far observed. The use of this method for marking the flow patterns has also given rise to some interesting observations on the behavior of the melt above the capillary when the driving force causing flow through the capillary is removed. These observations give a measure of the stored elastic energy in the melt above the capillary entrance and the rate at which this energy can be dissipated.

[1] R. S. Spencer and R. E. Dillon, J. Colloid Sci. 4, 241 (1949).
[2] J. P. Tordella, J. Appl. Phys. 27, 454 (1956).
[3] J. P. Tordella, Rheol. Acta 1, NR2/3, 216 (1958).
[4] J. P. Tordella, Trans. Soc. Rheology 1, 203 (1957).
[5] P. L. Clegg, "Elastic effects in the extrusion of polythene," in *The Rheology of Elastomers* (Pergamon Press, London, New York, 1958), p. 174.
[6] H. Schott and W. S. Kaghan, Ind. Eng. Chem. 51, 844 (1959).

EXPERIMENTAL

The viscometer used in these studies is shown schematically in Fig. 1. It consisted of two quartz blocks held together in an Invar steel frame. The larger quartz block (the barrel) was a 5 cm cube and had a central

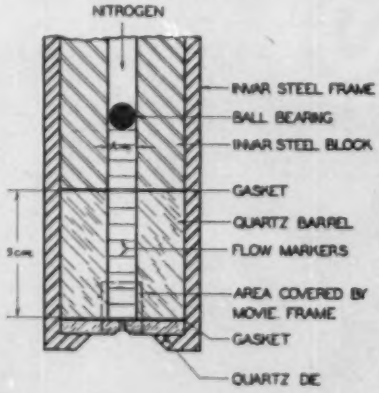

FIG. 1. Schematic diagram of the viscometer used to observe the flow of molten polyethylene into a capillary. The viscometer consists of a quartz barrel and die held together by an Invar steel frame.

cylindrical hole 1 cm in diam. This constituted the reservoir for the molten polymer. The second quartz block (the die) had a centrally located capillary of diam 0.05 cm and length 0.125 cm. One end of the capillary was a "flat entry" while the other end had a tapered entry region of included entry angle 120°. The edges of the quartz blocks were slightly rounded or "brushed" to prevent chipping. This brushed region along with the gasketing material between the quartz blocks resulted in an optically obscure region about 1 mm thick just at the die entry.

As can be seen from Fig. 1, the melt reservoir extended up into the Invar steel framework holding the two quartz blocks together and was connected by a "snap-tite" coupling arrangement to a pressure system as described previously.[7] The apparatus was suspended in an air bath thermostated to 190°C±2°C.

The polymer sample to be studied was premolded so that it would slide easily into the 1 cm barrel. A sample of the same polymer from which the mold had been made was milled with 3% carbon black and extruded from a 0.05-cm diam hole as a black filament. This black filament was then threaded through holes centrally drilled in the mold, perpendicular to the long axis of the cylinder, about half a cm apart.

The mold was dropped into the barrel of the viscometer. When melting of the resin was completed the usual water white polyethylene was seen to be spaced with a series of parallel black marker lines about half a cm apart, as indicated in Fig. 1.

Experiments were carried out as follows: The polyethylene with the markers was placed in the reservoir. Nitrogen was applied to the reservoir to force the polymer through the capillary, a loosely fitting brass plug having been placed on top of the polymer melt to prevent channeling of the nitrogen. The nitrogen pressure was measured on bourdon gauges. Sixteen mm cine film was taken of the flow (at approximately 16 frames/sec), the region appearing upon the frame being indicated on Fig. 1 by the dotted area in the region of the capillary. Timing markers were put on the film by means of a timed flashing light.

FIG. 2. Steady state flow pattern for polyethylene A at an applied pressure of 150 psi.

FIG. 3. Steady state flow pattern for polyethylene B at an applied pressure of 400 psi.

After a steady flow pattern was established the pressure could be reduced to zero by means of a quick opening on-off valve. A retraction of the flow lines from the capillary entrance occurred, as will be shown subsequently. Since the film speed is known from the timing blips it is possible to plot distance retracted from the die entry as a function of time.

RESULTS

The results of this study will be discussed under three headings: (a) the general character of the flow patterns observed at shear stresses below those required for extrudate distortion; (b) the behavior of the melt at stresses above those required for extrudate distortion; (c) the retarded elasticity exhibited by the melt on the sudden removal of the applied shear stress.

(a) Flow Patterns below the Critical Shearing Stress

Figure 2 shows the flow pattern observed for polyethylene A, a low density material of melt index[8] 2, at an applied pressure of 150 psi. This pressure is considerably

[7] E. B. Bagley, J. Appl. Phys. 28, 624 (1957).

[8] Am. Soc. Testing Materials, D-1238-57T.

FIG. 4. Flow pattern observed for polyethylene C just after applying a pressure of 400 psi.

less than that required to produce the phenomenon of extrudate distortion. It can readily be seen that the polymer has formed a natural funnel into the capillary. Material flows from the reservoir through this "wine glass stem" funnel and out through the capillary. The funnel is surrounded by a mass of polymer which forms a "dead space." The material in this dead space does not take part in the flow through the capillary at pressures below that at which extrudate distortion occurs, but does rotate slowly as is indicated in Fig. 2. This general type of behavior was pointed out also by Clegg[5] and Schott and Kaghan.[6] The size and shape of the "dead space" is not affected by pressure to any marked extent as long as the pressure is below that required to produce a distorted extrudate. However, the size and shape of the "dead space" varies in detail among polyethylenes.

Figure 3 shows the flow pattern set up by polyethylene B, a high density resin of melt index 0.7. The pattern is quite different in nature from that observed with the low density material. Any dead space which may exist must occupy a very small region in the corner. It should be noted that this particular resin is the same one which showed a discontinuity in its flow curve.[9] It is obvious that the flow behavior of this linear (high density) polyethylene is quite different from that shown by the low density polyethylene.

(b) Flow Behavior above the Critical Shearing Stress

Tordella,[2–4] Clegg,[5] and Schott and Kaghan[6] have shown that extrudate distortion is associated with violently discontinuous and oscillatory flow behavior in the region above the capillary entrance. The method of marking the flow patterns used in this work illustrates the nature of this "elastic turbulence"[10] particularly well. This is illustrated in Figs. 4, 5, 6, and 7.

In Fig. 4 is shown the flow pattern observed for polyethylene C, a low density resin of melt index 2, shortly after applying a pressure of 400 psi. This pressure is just slightly above the critical pressure. (It should be noted that although polyethylenes A and C are both low density resins of melt index 2, the sizes of the dead spaces are quite different.) Figure 5 is a cine frame showing the same polymer C taken just a second later than the frame in Fig. 4. It can be seen that a number of central flow lines which were actually extending into the capillary have "fractured" (in Tordella's nomenclature) and snapped back from the die entry

FIG. 5. The flow pattern observed for polyethylene C one second after the picture shown in Fig. 4 was taken. The applied pressure is 400 psi, which is just above that necessary for extrudate roughness. The central flow lines have "snapped back" and material in the dead space is surging through the capillary.

region. The central filament has snapped back 0.25 cm! This upward snap-back of central material has been compensated for by a rush of material from the dead space into the capillary. This effect has also been observed by Clegg[5] and Schott and Kaghan.[6] Since material from the dead space is now surging intermittently through the capillary, the dead space must decrease in size. That this actually occurs is shown in Fig. 6, which is the pattern observed for polyethylene C after flow for some minutes at 400 psi. It can be seen that the dead space has decreased both in width and height and the natural lead-in funnel has widened considerably. The pattern shown in Fig. 6 does not change

[9] Bagley, Cabott, and West, J. Appl. Phys. **29**, 109 (1958).

[10] E. B. Bagley, Ind. Eng. Chem. **51**, 714 (1959).

further with time. The wine glass stem is now apparently so wide that even when elastic snap-back occurs in one section of the stem material from the dead space no longer surges through the capillary, because the dead space is too far away from the capillary entrance.

This is also illustrated by the more extreme case shown in Fig. 7. Here polyethylene A, the same resin as in Fig. 2, is shown after flow at an applied pressure of 600 psi for some minutes. At this pressure the extrudate is violently distorted. In this figure the dead space has been reduced to about a third of its original size, and the lead-in funnel has become very wide. The situation shown in Fig. 7, as in Fig. 6, is, however, a steady state. Although the filament being extruded is violently distorted a snap-back of flow lines in one section of the

FIG. 6. Continued flow of polyethylene C at an applied pressure of 400 psi results in a steady pattern as in the above picture. The dead space has been reduced in size by intermittent loss of material through the capillary, but is now so far removed from the capillary that further loss by surging cannot occur.

lead-in stem is now compensated by increased flow from other sections of the stem. The dead space does not take part in this intermittent surging through the capillary. It has been reduced in size so far that it cannot surge over far enough to reach the capillary and hence the dead space size remains constant.

Discontinuous or oscillatory flow above the critical pressure for extrudate distortion was not observed for the high density polyethylene B using the gasketed apparatus of Fig. 3. However, experiments in which the region at the capillary entrance was not obscured by gasketing show that polyethylene B above the critical point does show oscillatory flow. The frequency of the oscillations is much higher than that observed in the other (low density) resins and the elastic "snap-back,"

FIG. 7. This figure shows the more extreme reduction in size of the dead space undergone by polyethylene A at an applied pressure of 600 psi, well above the critical point for extrudate roughness. Note the extremely wide lead-in channel.

if it exists, is much smaller than that for the low density resins.

(c) Elastic Retraction from the Die Entry

The elastic "snap-backs" observed when the shear stress is above the critical shear stress for extrudate distortion suggest that while the polymer melt is flowing into the capillary a good deal of elastic potential energy

FIG. 8. The retraction of flow lines from the capillary entrance observed for polyethylene A 23 sec after the applied pressure was reduced from 150 psi to zero.

FIG. 9. The equilibrium retraction from the capillary entrance observed for polyethylene A 13 min after the applied pressure was reduced from 150 psi to zero.

is stored in it. (The case for the existence of this stored elastic energy in stationary flow of a viscoelastic liquid has been discussed recently by Philippoff and Gaskins.[11]) The presence of the markers suggested the possibility of measuring this elastic energy, and the rate at which this energy could be dissipated, by measuring the marker movement after the applied stress was reduced to zero. The method used is illustrated in Figs. 2, 8, and 9.

Figure 2 shows the steady flow pattern observed for polyethylene A subject to an applied pressure of 150 psi. When this pressure was suddenly reduced to zero the flow ceased and the flow lines began to retract from the die entry. The extent of retraction after 23 sec is shown in Fig. 8. The camera was run for three minutes from the time at which the pressure was suddenly reduced to zero, and at 8, 13, and 18 min additional pictures were taken. Figure 9 shows the retraction observed at 13 min, after which time no subsequent movement took place, the picture at 18 min being unchanged from that taken at 13 min. Thus for polyethylene A it takes between 8 and 13 min for all the elastic energy stored during steady flow at 150 psi to be dissipated.

From Fig. 2 it is clear that some of the central marker lines have flowed into the capillary. When the pressure is reduced suddenly to zero the marker lines retract as shown in Fig. 8, and, in general, the lines which have reached and passed into the capillary will no longer be continuous during the retraction, but will appear as broken lines. In the particular case under consideration (Fig. 8) it is clear that three flow lines have passed into the capillary prior to the retraction. The distance retracted by each particular flow line from the capillary entrance is a function of the initial radial position of the line in the capillary, the lines closest to the central axis of the capillary retracting furthest.

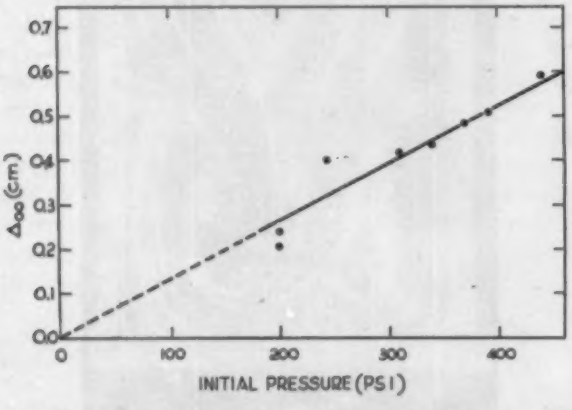

FIG. 10. A typical plot of the equilibrium retraction Δ_∞ *versus* initial applied pressure for polyethylene C.

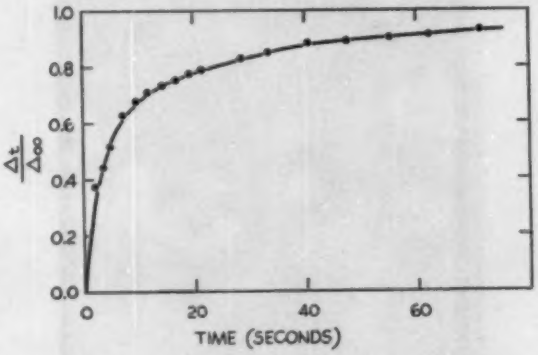

FIG. 11. A typical plot of (Δ_t/Δ_∞) *versus* time for the polyethylene C after steady flow at 293 psi.

Studies have been carried out on the kinetics of retraction including the equilibrium value, at a series of applied pressures for four different polyethylenes. In these experiments the pressure was reduced to zero just as a flow line entered the capillary, and a timed cine-film was made of the retraction. The measurement of interest is the distance retracted in time t, Δ_t, by the tip of this central flow line from the capillary entrance. Because of the gasketing arrangements and the brushed (rounded) edges of the quartz block, the capillary entrance is not visible. Therefore the measurement was arbitrarily made from the tip of the central flow line to the bottom of the optically obscure region. The equilibrium retraction is designated Δ_∞.

Typical equilibrium results are shown in Fig. 10, where Δ_∞ is plotted against the initial applied pressure for a low density polyethylene of melt index 2. This plot is linear and, within the experimental error induced by the uncertainty in the location of the capillary entrance,

[11] W. Philippoff and F. H. Gaskins, Trans. Soc. Rheol. 2, 263 (1958).

passes through the origin. In the four polyethylenes so far studied, the values of the slope of such plots varied from 2×10^{-4} cm/psi to 28×10^{-4} cm/psi.

Such plots as illustrated in Fig. 10 are in general linear only up to the critical point for extrudate distortion. Above this point the total observed retraction depends on the relative timing of the pressure reduction and the sudden elastic snap-backs in the flowing melt.

Kinetic data from these experiments take the form of a typical relaxation curve as shown in Fig. 11, where (Δ_t/Δ_∞) the relative retraction of the central flow line from the capillary at time t is plotted against time.

To analyze results such as these the method of Laplace pairs, as discussed by Macey,[12] has been used. A single expression was not found that would fit the whole of the data. A useful transform to use under these conditions is a sum of exponential terms in the square root of time. Such a function goes to unity at $t=0$ and to zero at very long times. Let ϕ be defined by

$$\phi=\frac{\Delta_\infty-\Delta_t}{\Delta_\infty}. \tag{1}$$

It has been found that two of the exponential $\sqrt{t}$ terms are adequate to fit the observations

$$\phi=A_1e^{-b_1\sqrt{t}}+A_2e^{-b_2\sqrt{t}}. \tag{2}$$

Now ϕ can be represented by a distribution function, $f(\lambda)$ given by

$$\phi=\int_0^\infty f(\lambda)e^{-\lambda t}d\lambda. \tag{3}$$

By using the constants in Eq. (2), $f(\lambda)$ can be calculated. For the relaxation curve shown in Fig. 11, the following Eqs. for ϕ and $f(\lambda)$ were found,

$$\phi=0.437e^{-1.069\sqrt{t}}+0.746e^{-0.279\sqrt{t}}, \tag{4}$$

$$f(\lambda)=\frac{0.1320}{\lambda^{\frac{1}{2}}}e^{-0.2857/\lambda}+\frac{0.0588}{\lambda^{\frac{1}{2}}}e^{-0.0195/\lambda}. \tag{5}$$

Note that the coefficient A_1 and A_2 of Eq. (2) should add up to unity while in Eq. (4) they add up to 1.183. This is due to the error in determining the zero time. A plot of $f(\lambda)$ *versus* $\log\lambda$ from Eq. (5) is shown in Fig. 12. The first (short-time) term has little effect on this curve. The peak occurs at 77 sec. The range in relaxation times so far observed for various polyethylenes is from about 30 sec to 600 sec.

CONCLUSIONS

This paper is intended primarily to present a new technique for studying the flow patterns formed by a polymer flowing into a capillary and, in a very general way, to describe a few empirical observations made using this tracing technique. No attempt will be made at this time to explain these observations in terms of molecular structure.

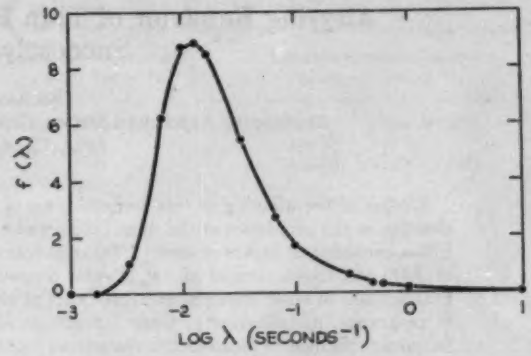

FIG. 12. The function $f(\lambda)$, calculated from the retraction curve of Fig. 11, plotted against $\log\lambda$.

At shear stresses below the critical shear stress at which extrudate distortion sets in all resins studied, except one, showed large dead spaces. The polymer from the viscometer reservoir funneled down a wine-glass shaped naturally formed lead-in into the capillary. The only polyethylene melt not showing this dead space and large lead-in section was the particular high density material which had previously been known to have an anomalous flow curve.

At critical shear stresses high enough to cause extrudate roughness the typical discontinuous flow and elastic "snap-back" observed by Tordella, Clegg, and Schott and Kaghan was found. It was also clearly shown that above the critical shear stress material from the dead space surged intermittently through the capillary. The dead space thus decreases with time and the natural funnel into the capillary widens. In the single case where a dead space was not observed, very rapid oscillations of the melt could be seen within one or two mm of the die entrance.

It was observed that when the applied pressure causing steady flow was suddenly reduced to zero, the flow lines broke at the capillary entrance and retracted back into the body of the melt. The measurement of this effect gives a measure of the elastic total potential energy stored in the melt in the region above the capillary entrance. The rate of disappearance or relaxation of this elastic energy can be determined. Relaxation times ranging from 30 to over 600 sec have been observed.

ACKNOWLEDGMENT

The authors wish to express their thanks to Canadian Industries Limited for permission to publish this paper.

[12] H. H. Macey, J. Sci. Instr. **25**, 251 (1948).

Alloying Behavior of Thin Bimetal Films, Simultaneously or Successively Deposited*

RICHARD B. BELSER
Engineering Experiment Station, Georgia Institute of Technology, Atlanta, Georgia
(Received September 10, 1958)

Studies of the alloying of thin bimetal films of 20 metal pairs have been conducted by measurement of changes in the properties of the films before and after heating to successively higher temperatures *in vacuo*. Films consisted of layers of about 1000 angstroms of each metal consecutively deposited or of a single layer of 2000 angstroms formed of two metals deposited simultaneously. Techniques of study included visual examination of color changes, measurements of changes in electrical resistivity and temperature coefficient of resistance, metallography, x-ray diffraction, electron microscopy and diffraction, and measurement of frequency changes of piezoelectric resonators coated with a metal pair. Regardless of the method of coating, i.e., evaporation, sputtering, or electroplating, films were found to interdiffuse or alloy at or below the temperature of recrystallization of the metal of higher melting point. The order of deposition of the films affected their subsequent behavior. Films of aluminum formed an oxide coating during a few minutes storage *in vacuo*; the oxide appreciably retarded diffusion between the layers until a temperature of about 400°C was reached. Simultaneous evaporation produced films which alloyed readily at relatively low temperatures or, in the absence of intrinsic alloying affinities of the metal pair, films of highly imperfect structure. The imperfection of the latter was exhibited by reductions of up to 90% in the electrical resistance of the films upon annealing. By the methods outlined valuable studies of the properties of metals can be conducted with microquantities of the metals at temperatures below $0.40°K_m$ (melting point °K); and alloys unavailable commercially can be prepared in the laboratory at minimum expense.

INTRODUCTION

STUDIES of thin films of single metals have been reported abundantly in the literature and film behaviors have been compiled in recent books[1–3] and summaries.[4] Studies of bimetal films have been less frequent but sufficient to outline methods of deposit and alloying effects occurring in the solid state at relatively low temperatures. Methods of alloy formation suggested have been evaporation of a metal alloy,[5,6] simultaneous evaporation of different metals from two filaments,[7] "flash" evaporation of a powder mix comprised of two metals,[8] deposition of two metals successively by one of several methods and alloying by heating[9,10] and, finally, by sputtering of an alloy.[1]

The author, having had considerable experience in the deposition of thin single metal films[11] and in studies of their structural changes during annealing by means of electrical resistance changes,[12–16] electron microscopy, electron and x-ray diffraction techniques, has applied these techniques and others to the study of films comprised of some 20 different metal pairs. These experiments outline the general behavior patterns of bimetal films over a considerable temperature range (25° to 600°C in many cases) and are described below.

PROCEDURES

Thin metal films of two metals have been deposited usually, on soft glass microscope slides, either successively or simultaneously by the common deposition methods of evaporation, sputtering, or electroplating. These methods have been described in detail in the papers and reports cited previously. Film thicknesses in general were approximately 1000 angstroms for each of the two metals although films as thin as 100 angstroms each were used in a few experiments.

Methods of study included:

1. Measurements of electrical resistance changes of the bimetal pair before and after aging by heating to successively higher temperatures *in vacuo* and cooling for each measurement.

2. Measurements of electrical resistance changes of the bimetal pair during several successive temperature cycles to 600°C *in vacuo* and establishment of a repeatable temperature coefficient of resistance of the pair.

3. Determination of the temperature at which color

* This work was supported in part by U. S. Army Signal Corps and the Wright Air Development Center, U. S. Army Air Force.

[1] L. Holland, *Vacuum Deposition of Thin Films* (John Wiley & Sons, Inc., New York, 1956).

[2] H. Mayer, *Physik Dunner Schichten* (Wissenschaftliche Verlagsgesellschaft M.B.H., Stuttgart, 1955), Vol. I and II.

[3] O. S. Heavens, *Optical Properties of Thin Solid Films* (Butterworths Scientific Publications, London, 1955).

[4] A. Blanc-Lapierre and M. Perrot, Mém. sci. phys. acad. sci. Paris, No. 57 (1954).

[5] H. W. Edwards, Phys. Rev. **43**, 205 (1933).

[6] H. W. Edwards and R. P. Petersen, J. Opt. Soc. Am. **27**, 87 (1937).

[7] S. Goldsztaup and P. Michel, Compt. rend. **232**, 1832 (1951).

[8] L. Harris and B. M. Siegel, J. Appl. Phys. **19**, 739 (1948).

[9] A. A. Burr, H. S. Coleman and W. P. Davey, Trans. Am. Soc. Metals **33**, 73 (1944).

[10] Konig, Reichsber. Physik **1**, 7 (1944).

[11] R. B. Belser and W. H. Hicklin, Rev. Sci. Instr. **27**, 293 (1956).

[12] R. B. Belser, J. Appl. Phys. **28**, 109 (1957).

[13] R. B. Belser, Rev. Sci. Instr. **25**, 180 (1954).

[14] R. B. Belser and W. H. Hicklin, J. Appl. Phys. **30**, 313 (1959).

[15] R. B. Belser, "Aging Study of Metal Plating on Quartz Crystals," Engineering Experiment Station, Georgia Institute of Technology, Interim Report No. 7, U. S. Army SCEL Contract No. DA-36-039 SC-42453 (May, 1952–April, 1954), ASTIA Document No. 48261.

[16] R. B. Belser and W. H. Hicklin, "Electrical Conductivity Studies of Metallic Films," WADC Technical Report 57-660 (December, 1957), ASTIA Document No. 155573.

TABLE I. Binary metal pairs examined by thin film techniques and minimum temperatures at which alloying occurred.

Evaporated + evaporated		Evaporated + electroplated		Sputtered + sputtered		Sputtered + electroplated	
Metals	Temp. °C	Metals	Temp. °C	Metals	Temp. °C	Metals	Temp. °C
Ag-Al	140	Ag-Ni	None to 600	Au-Fe	None to 450	Ag-Rh	None to 535
Ag-Au	75	Au-Ni	190	Au-Pt	200	Au-Ni	200
Ag-Cr	None to 500	Cu-Ni	400	Ir-Pt	600	Au-Rh	None to 550
Ag-Ni	None to 600			Ni-Pt	450		
Al-Au	90[a]						
Al-Cu	190						
Al-In	60						
Al-Pd	225						
Al-Zr	350						
Al-Zn	...[b]						
Au-In	85						
Au-Ni	190						
Cu-Ni	400						
Fe-In	None to 525						

[a] X-ray diffraction data indicated that alloying of gold and aluminum occurred in samples not exposed to heat treatment. Some alloying may have occurred during the deposition process, at which time the surface temperature of the film may have exceeded the temperature of 90°C indicated above. This value is probably too high.
[b] The zinc proved too volatile when heated *in vacuo* to give interpretable results.

changes of metal films paired with films of gold or copper occurred when subjected to experiment No. 1.

4. Metallographic examination of the upper and lower surfaces of metal films subjected to experiment No. 1.

5. Examination by x-ray diffraction techniques of the specimens subjected to experiment No. 1.

6. Examination by the electron microscope and electron diffraction of a thin specially prepared film of gold+aluminum before and after heating *in vacuo*.

7. Examination of thickness changes of a bimetal pair before and after heating *in vacuo* by use of an interferometer technique.

8. Measurement of the long term stabilities of piezoelectric resonators coated with bimetal layers in comparison with similarly fabricated resonators coated with a single metal only.

Twenty different metal pairs were examined by one or more methods. The pairs and the method of deposition are shown in Table I. Observed behaviors were dependent on the order of deposition; therefore, ten pairs of metals were prepared in the order A+B, B+A, and A, B simultaneously.

Films consisting of evaporated plus evaporated metals were prepared by evaporation from two filaments sited approximately equidistant (about 5–7 cm) from the substrate. Successive evaporation followed each other as rapidly as practicable; however in a few cases ten or more minutes of pumping were allowed to intervene between deposition of the two films.

Films formed by simultaneous evaporation of two metals were deposited with the same apparatus; the filament supplies were controlled by separate Variacs. No shutter was employed. By filament current control evaporation of the two metals was begun and completed as nearly simultaneously as possible. If this is not accomplished a thin layer of either metal may be deposited first or last.

For the other combinations of deposition techniques used: evaporation plus electroplating, sputtering plus electroplating, and sputtering plus sputtering, the vacuum system was opened between successive depositions.

MEASUREMENTS OF ELECTRICAL RESISTANCE BEFORE AND AFTER HEATING *IN VACUO*

1. Procedures

The general procedure used was that described in a paper[12] by the author. Glass slides, 25 mm×37 mm, were cleaned by the common procedure of a detergent, a suitable rinsing, and an immersion in a chromic acid solution plus final rinsing and drying. Leads consisting of copper foil were attached to the film with indium:[13] resistances were measured with a Wheatstone bridge. The samples were placed in an infrared vacuum oven *in vacuo*, heated to the specified temperature[17] for five

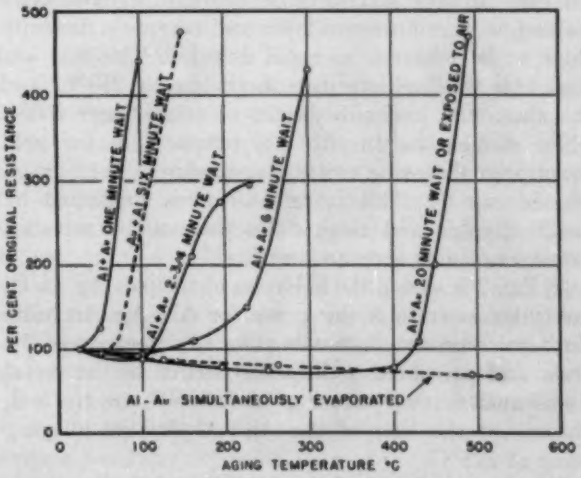

FIG. 1. Changes in electrical resistance of evaporated bimetal films of aluminum and gold subjected to successive heat treatments *in vacuo*.

[17] R. B. Belser and J. W. Johnson, Ceram. Age **66**, 28 (1955).

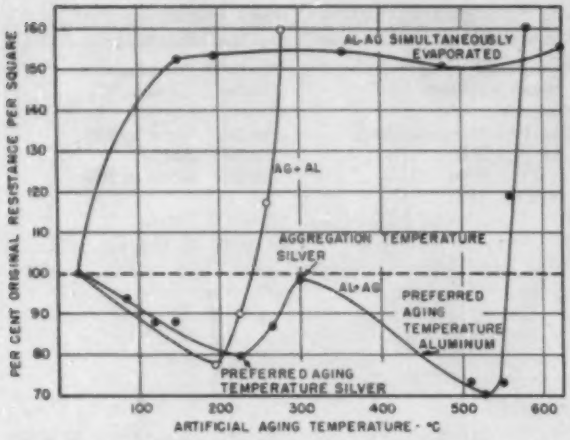

FIG. 2. Changes in electrical resistance of evaporated bimetal films of aluminum and silver subjected to successive heat treatments *in vacuo*.

minutes, and cooled. Electrical connections were remade and the resistance redetermined. Measurements were made at successive temperatures in 100°C steps until 600°C was reached or until the films exhibited damage. Time of annealing at the higher temperature was extended to 20 to 30 minutes where doubt existed that maximum alloying had been attained. Measurements were generally made for five specimens.

2. Resistance Behavior of Deposits in the Orders A+B and B+A

In Fig. 1 may be seen a typical series of plots for the metal pair aluminum and gold deposited in the orders outlined previously. For Au+Al, the gold film annealed slightly first; then a rapid increase in resistance per square occurred because of the alloying of the gold and aluminum. This action began below 100°C.

For Al+Au, alloying was delayed in accordance with the time between successive depositions. An oxide layer formed on the aluminum layer and became sufficiently thick to be a barrier to rapid diffusion. The gold was thus able to complete its annealing near 250°C, and the aluminum had only begun to anneal near 400°C when alloying began. At this temperature the gold penetrated the oxide and the resistance of the film increased rapidly. This interpretation is supported by metallographic and x-ray diffraction studies reported under succeeding sections (see Fig. 7).

In Fig. 2 is shown the behavior of the pair Ag-Al. Of particular interest is the curve for Al+Ag. An oxide film formed on the aluminum prior to deposition of the silver and presented a diffusion barrier to the metal atoms until a temperature of about 550° was reached, whereas in the case of the Ag+Al definite alloying began at 225°C.

The silver film annealed at 225°C and then agglomerated at about 300°C [see Figs. 5(a) and 5(b)]. The aluminum film then annealed. The partial or full agglomeration of the silver minimized the volume of silver diffused into the aluminum until the relatively high temperature of 550°C was reached. Note that the silver atoms saw the aluminum oxide layer of only a few atomic layers in thickness as a nonmetallic substrate and agglomerated at the same temperature (300°C) at which silver agglomerates on an SiO electron microscope grid or on glass.

The metal pair Ag-Ni are reported to be nearly immiscible in the solid state.[18] The resistances of the metal pairs, in the order A+B and B+A as shown in Fig. 3, decreased upon annealing and did not exhibit the rapid increase at relatively low temperatures characteristic of an alloying pair. In fact, the films behave as two films in electrical parallel. The slight increase in resistance in the range 600°C to 625°C may be caused by oxidation or physical damage to the film.

3. Simultaneously Deposited Bimetal Films

Simultaneous deposition of two materials at the same rate is difficult and data obtained by this method are subject to more dispersion than that for successively deposited films. Nevertheless, interesting information is obtainable by this technique. Re-examination of Figs. 1, 2, and 3 discloses different behaviors for the simultaneously deposited pairs. If one examines the Ni-Ag pair first (Fig. 3), one observes the typical pattern of behavior of a bimetal pair which does not alloy. The resistance is decreased greatly by annealing, in this case to approximately 25% of the original value. It is

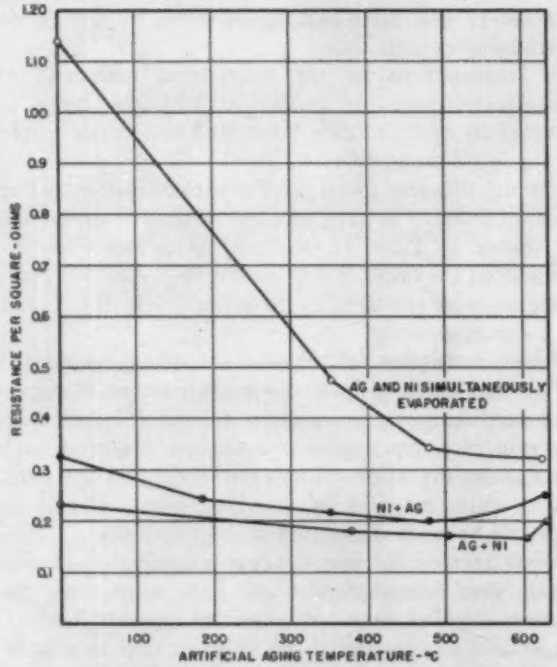

FIG. 3. Changes in electrical resistance of evaporated bimetal films of nickel and silver subjected to successive heat treatments *in vacuo*.

[18] *Metals Handbook* (American Society for Metals, Cleveland, Ohio, 1948), p. 1151.

TABLE II. Comparison of resistance changes undergone by simultaneously evaporated bimetal films after aging by heating.

Metal pairs	Aging temperature (°C)	Percent original resistance	Initial R/Sq	Final R/Sq	ρ/ρ_b using ρ_b for metal of lowest resistivity	ρ/ρ_b using ρ_b for metal of highest resistivity	ρ/ρ_b using average ρ_b of two metals
Gold-indium	355	625	0.512	4.27	35.1[a]	10.4[a]	15[a]
Silver-aluminum	410	350	0.512	1.75	21.6	12.3	16.4
Silver-gold	450	160	0.388	0.620	7.65	5.08	6.11
Gold-aluminum	535	72	1.07	0.78	6.38	5.88	6.11
Copper-aluminum	575	49	1.80	0.95	11.2	7.2	8.75
Silver-nickel	625	28	1.14	0.320	3.95	0.94	1.52
Indium-iron	480	12	6.77	0.8	1.78	1.65	1.71

[a] There are three choices of ρ/ρ_b values for dual-layer films. The ρ_b may be selected as being that of the metal with the lowest resistivity, the highest resistivity or an average value of the two. Admittedly, none of these appears to be an excellent choice. All three have been included in this table as a means for temporary interpretation.

evident that a high degree of imperfection was incorporated into the film during its growth. This annealed out near the recrystallization temperature of nickel, about 400°C, giving a resistivity approximately 1.5 times the bulk resistivity, ρ_b.

For Au-Al (Fig. 1) a smaller drop in resistance was registered and the final resistivity was higher, about 6 ρ_b. For Ag-Al a drop in resistance was not registered but an increase occurred instead; the resistivity was high, 16 ρ_b. Similar patterns of behavior are exhibited by other metals as shown in Fig. 4. Positive slopes of these data plots are characteristic of metals of high alloying affinities and high final resistivities. The more negative ones are characteristic of immiscible alloys of low resistivity. The intermediary ones have moderate alloying affinities and intermediary resistivities. Typical resistance and resistivity data are shown in Table II.

The films described thus far were deposited by evaporation but behaviors of films deposited by electroplating or sputtering were essentially the same except that temperatures at which appreciable alloying was noted were sometimes elevated. This was true in part because of exposure of the first deposited film to air before deposition of the second film and in part to the intrinsic properties of the sputtered and electroplated films.

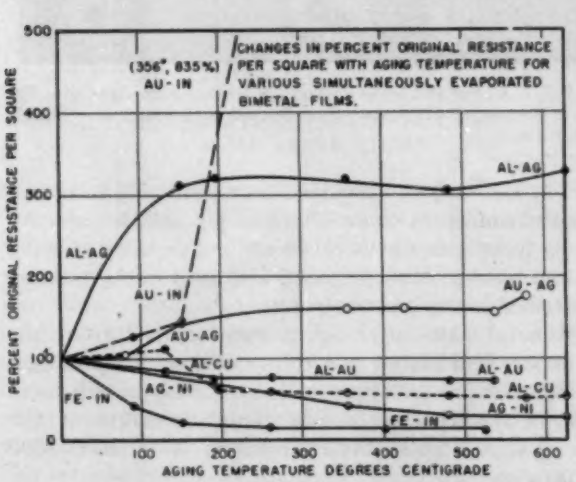

FIG. 4. Changes in electrical resistance of simultaneously evaporated bimetal films subjected to successive heat treatments *in vacuo*.

Sputtered films as usually deposited contain oxides and occluded gas and have been observed to anneal less readily[12] than evaporated metal films.

In Table I are given the temperatures at which appreciable alloying commenced for the metal pairs studied. The temperatures listed are the lowest observed, and, in general, are for pairs deposited in a manner to avoid an oxide barrier at the interface, i.e., in the order A+B where B is the active metal. This same procedure is desirable for any metal forming a highly protective and refractory oxide.

Since further evidence may be desired as to the interpretation of the resistance data on the film orders Al+Au and Al+Ag, the metallographic studies will be presented next.

METALLOGRAPHIC STUDIES

Bimetal films on glass slides are suitable for direct metallographic examination. Since the substrate was transparent, both the upper and lower surfaces of the metal film were examined with a Leitz Neophot metallograph. The position of the silver of the Ag-Al pair was revealed by exposure to H_2S gas from $(NH_4)_2S$.

The agglomeration of the silver at 300°C is demonstrated in Figs. 5(a) and 5(b). Typical films are shown before and after heating to 350°C and after etching with H_2S. The large crater in Fig. 5(a) was caused by the eruption of an adsorbed gas bubble throwing the aluminum particles about its periphery.

The behavior of the Ag+Al specimens is shown in Fig. 6. Definite evidence of a melt at less than 625° was obtained. These areas differ from bubbles by the lack of interference fringes when observed from beneath. The phase diagram of Ag-Al denotes an eutectic composition melting at 558°C in agreement with Fig. 6; and the melted areas appear to have changed in thickness. This is in agreement with data obtained subsequently by interferometry and by stability studies of quartz resonators plated with bimetal layers. Calculation of the density of the alloy γ Ag-Al revealed that a thickness decrease would be expected.

A final bit of evidence with regard to the penetration of the oxide of an aluminum film, this time by gold, is demonstrated in Fig. 7 for an Al+Au film heated to 500°C. The penetration of the oxide at scattered points

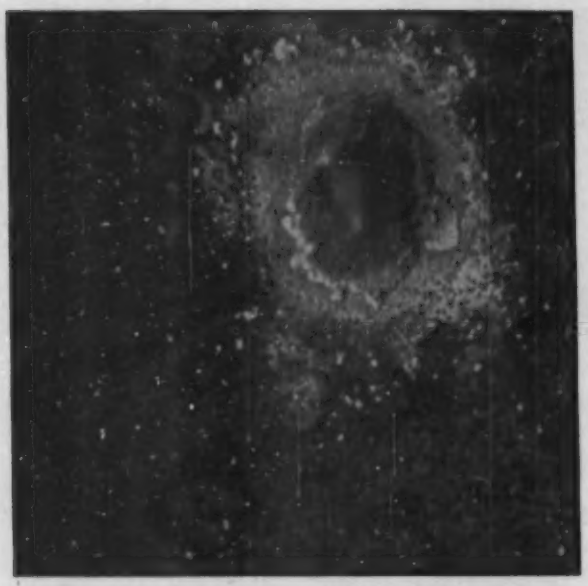

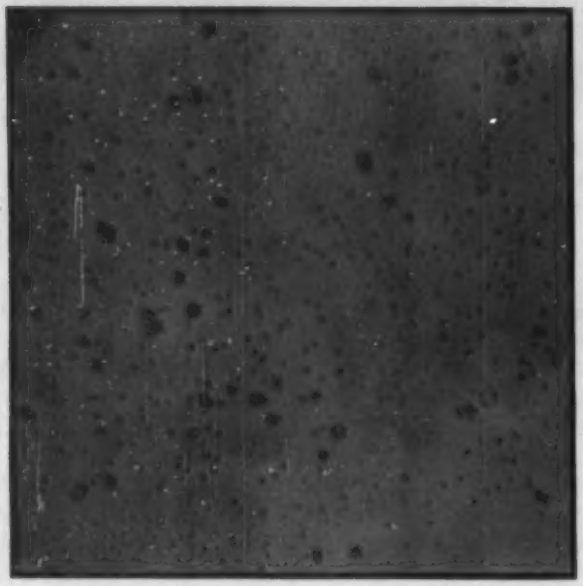

FIG. 5. Surfaces of an aluminum plus silver film before and after heating to 350°C *in vacuo*. Etched with fumes of $(NH_4)_2S$.

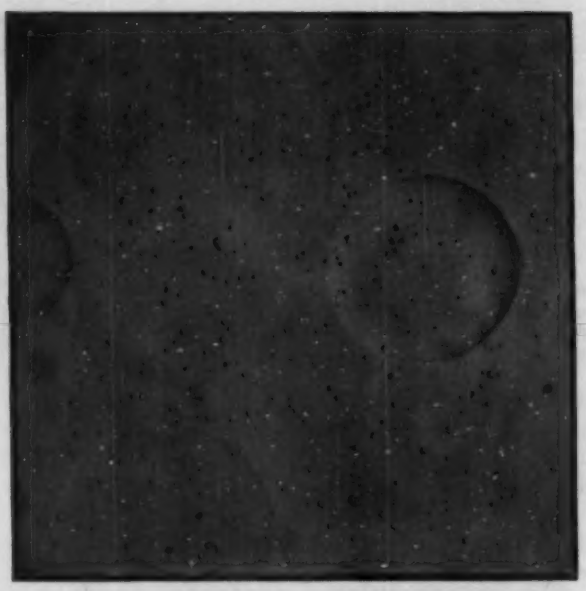

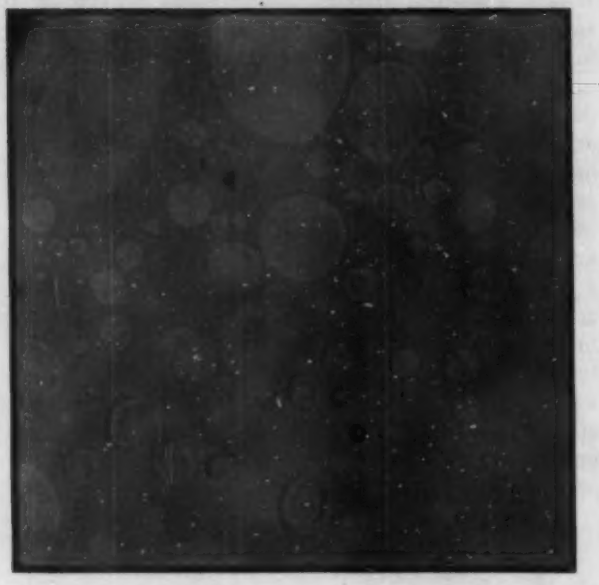

FIG. 6. Upper and lower surfaces of a silver plus aluminum film after heating to 625°C *in vacuo*. Etched with fumes of $(NH_4)_2S$, 15 minutes.

is observed. Through these random orifices the gold has diffused into the aluminum film increasing its resistance in accordance with the data of Fig. 1.

The metallographic studies furnished the additional information necessary for proper interpretation of the electrical resistance data. Studies were made of the bulk of the metal pairs examined and have been exhibited more extensively in a report cited.[15] Palladium and aluminum formed a pink alloy PdAl resembling the purple one of gold-aluminum ($AuAl_2$).

X-RAY DIFFRACTION STUDIES

X-ray diffraction studies of bimetal films of zinc and copper were made by A. A. Burr, H. S. Coleman, and W. P. Davey,[9] who reported they were able to obtain results similar to those obtained for bulk metals. An x-ray technique was therefore utilized to study alloying of the bimetal films prepared and aged in the manner described in the preceding sections.

Bimetal films after aging were scraped from the substrate and placed in a thin-walled capillary holder. Diffraction patterns were made by normal procedures in the Debye-Scherrer camera. Total thickness of the metal-film samples before removal were 2000–3000 angstroms.

In general, the x-ray diffraction data, exhibited in Table III, corroborated alloying predicted from resist-

TABLE III. Summary of x-ray diffraction studies of bimetal films after aging by heating.

Type of film	Metals deposited	Major components	Minor components
Dual layer	Aluminum+copper	γ (Cu-Al)	Unidentified
Dual layer	Copper+aluminum	γ (Cu-Al)	Unidentified
Simultaneously evaporated	Copper−aluminum	γ (Cu-Al)	Unidentified
Dual layer	Gold+aluminum	$AuAl_2$, Au	Unidentified
Dual layer	Aluminum+gold	Au, Al	Unidentified
Simultaneously evaporated	Aluminum−gold	$AuAl_2$	Unidentified
Dual layer	Aluminum+silver	Al, Ag	
Dual layer	Silver+aluminum	γ (Ag-Al)	
Dual layer	Palladium+aluminum	PdAl	Pd_2Al_3; Al
Dual layer	Aluminum+palladium	PdAl; Pd	Al
Dual layer	Indium+aluminum	In	Unidentified
Dual layer	Aluminum+indium	In_2O_3; Al	
Dual layer	Aluminum+zinc	Al[b]	
Dual layer	Zinc+aluminum	Al[b]	
Dual layer	Indium+gold	$AuIn_2$	Unidentified
Simultaneously evaporated	Indium−gold	$AuIn_2$	Unidentified
Dual layer	Gold+nickel[a]	Au; Ni	
Dual layer	Iron+indium	Fe; In	
Dual layer	Silver+gold	Solid solution (AuAg)	
Dual layer	Gold+silver	Solid solution (AuAg)	
Simultaneously evaporated	Gold−silver	Solid solution (AuAg)	

[a] This metal was deposited by electroplating. All others were deposited by evaporation.
[b] Zinc sublimated from the films at aging temperatures used in the infrared vacuum oven.

ance studies of bimetal films and gave additional information. The Al+Ag heated to 600°C exhibited no evidence of alloying, whereas the Ag+Al showed alloying after heating to 260°C. The presence of the oxide-film barrier on aluminum was again suggested; the agglomeration of the silver on the surface of the aluminum oxide reduced the contact area between the metals and apparently prevented alloying in sufficient quantity to be detected by the x-ray technique utilized.

The x-ray diffraction data gave definite proof of the alloying of bimetal films. Data obtained correlated well with those obtained for the same metal pairs examined by resistance and metallographic means. The possibility of studying unknown binary alloys of metals by x-ray diffraction methods and thin bimetal film techniques appears worthy of further investigation.

VISUAL OBSERVATION OF COLOR CHANGES OF DUAL LAYER FILMS

Metal films successively deposited and heat treated *in vacuo* underwent color changes with artificial aging as diffusion between the two metal layers progressed. The metals copper and gold, because of their intrinsic color, were found to be especially useful when paired with the usual silver colored metals. The temperature of disappearance of one metal into the other correlates to a reasonable degree with the temperatures at which resistance rises were observed. For copper or gold paired with an aluminum film in the order Al+Au or Al+Cu, the retardation of diffusion by the oxide layer was readily observed. Even with metals as similar in appearance as silver and aluminum, surface reflection changes were observed as diffusion progressed.

A list of temperatures at which visual observation indicated that diffusion between metal pairs was virtually completed is given in Table IV.

EXAMINATION BY THE ELECTRON MICROSCOPE AND BY ELECTRON DIFFRACTION

Since the electron microscope had proved useful in studies of the structure and behavior of single metal films it was also employed in studies of bimetal films.

A silicon monoxide coated electron microscope grid

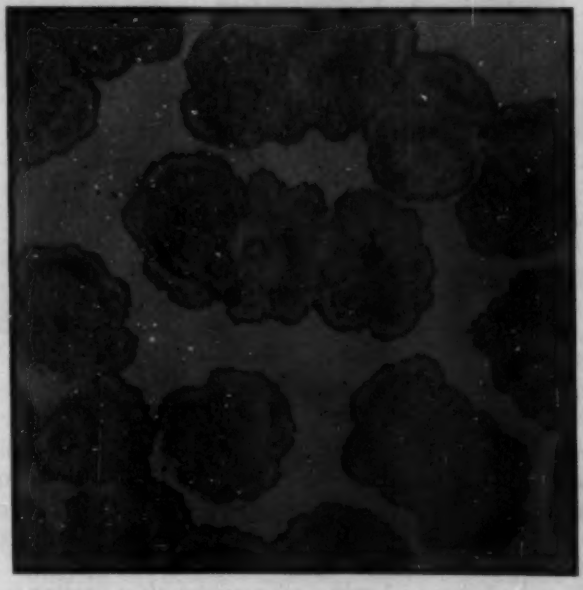

FIG. 7. Upper surface of aluminum plus gold film after heating to 505°C.

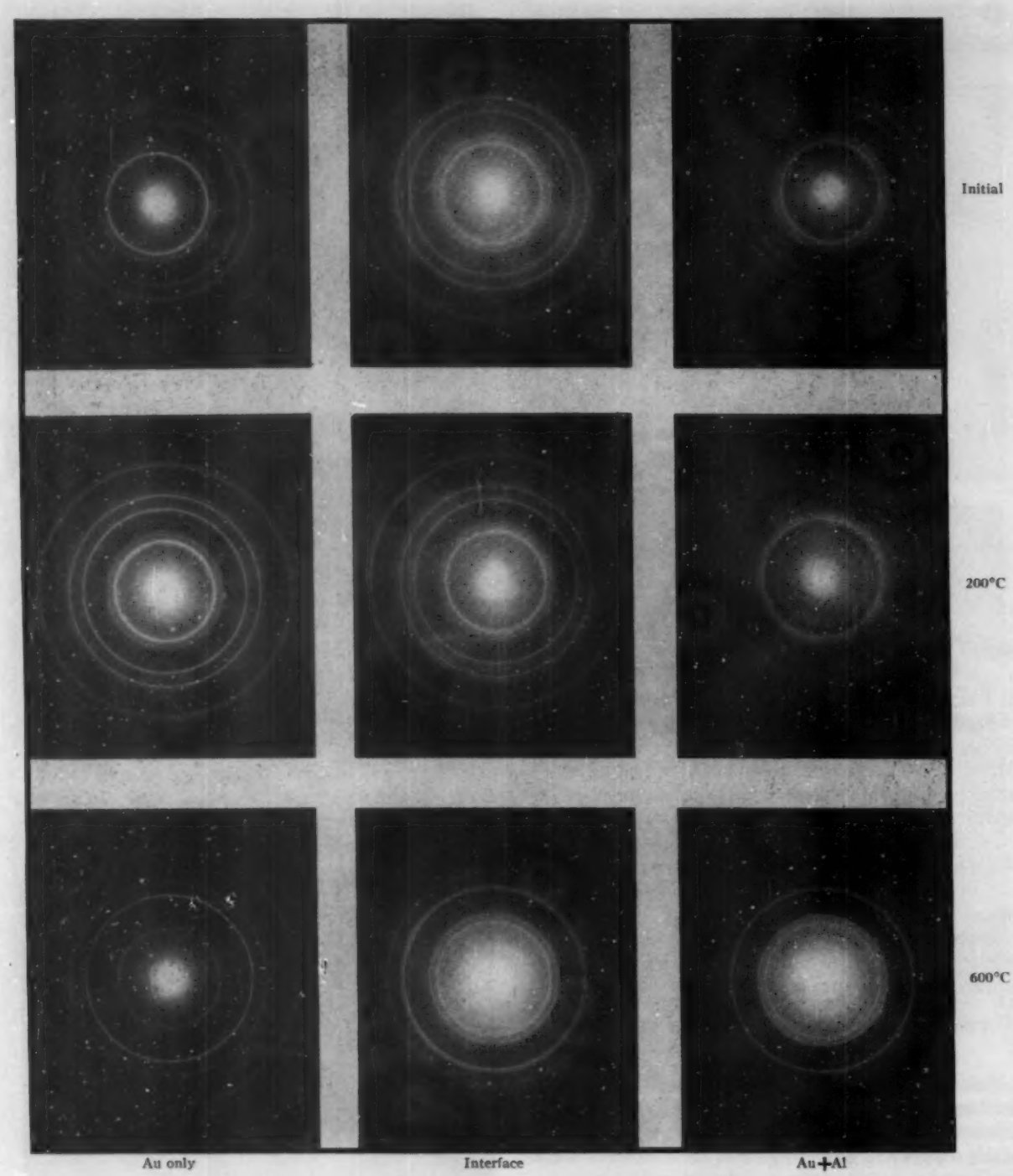

FIG. 8. Electron diffraction patterns of films of gold plus aluminum heated to 200°C and to 600°C.

was coated with gold by evaporation to a thickness of about 150 angstroms. Over one half the surface, an aluminum film of similar thickness was evaporated. The sample was examined in the electron microscope before and after it was successively aged to 200°C and 600°C. The single layer of gold agglomerated after heating to 600°C whereas the bimetal film did not.

An electron diffraction holder was adapted so that the entire sample could traverse a plane perpendicular to the electron beam. Diffraction photographs were made in the position gold-only, at the border of the single and double layers and for the gold-plus-aluminum film. Typical patterns obtained before and after aging are shown in Fig. 8. The annealing of the single gold

film is clearly seen in the sharpening of the diffraction lines after heating and the alloying of the bimetal pair is indicated by the complete change of the respective patterns. Three gold-aluminum intermetallic phases were observed but only one, the B' phase (Au_4Al), was identified. There are five phases reported in the literature but x-ray data on only two phases are available.

STUDIES OF TEMPERATURE COEFFICIENTS OF RESISTANCE OF ALLOY FILMS

Studies of the temperature coefficients of resistance of bimetal films utilizing refined techniques were made subsequent to the other studies reported. Complete details of the experiments have been previously reported[14,16] by the author.

Films of dimensions approximately $\frac{1}{2}$ in.$\times\frac{1}{32}$ in. over the area under test were deposited successively in thickness of less than 1000 angstroms by sputtering onto fused quartz or Vycor tubing. Onto the end of the specimens silver wires were attached with fired silver paste to a previously fired platinum-bright end-coat. The films under examination had expanded end areas overlapping the platinum-bright end-coat sufficiently to make good electrical contact.

The successively deposited pairs Pt-Au, Pt-Ir, and Pt-Ni were studied over the temperature range 25°C to 600°C. In Fig. 9 may be seen the data for the pair Pt-Au. During the first temperature cycle the portion of the curve from 25°C to 200°C is a region in which the gold is annealing and some alloying may be occurring. In addition, the normal temperature coefficient of resistance of the metal was impressed on the measurements. At 200°C a definite increase in slope indicative of alloying occurred. Three additional tests followed the slope of curve No. 2 with little change except for a total ten percent increase in resistance, apparently due to more complete alloying. Other influences such as agglomeration may have been active and cannot be entirely discounted.

The temperature coefficient of resistance of the pair was about 0.0007/C° over the temperature range of 25°C to 600°C. This may be compared with values of

TABLE IV. Temperatures at which dual-layer metal films intermingled with their companion metal as determined by film color changes.

Position A (Next to substrate)	Position B (Top film)	Temperature (°C)
Indium	Gold	Substrate temperature
Silver	Gold	120
Gold	Silver	175
Gold	Aluminum	190
Aluminum	Gold	480–505
Copper	Aluminum	260–355
Aluminum	Copper	495 (complete)
Copper	Nickel	520–555
Copper	Electroplated nickel	475 (begins)
Gold	Electroplated nickel	510 (complete)
Palladium	Aluminum	260

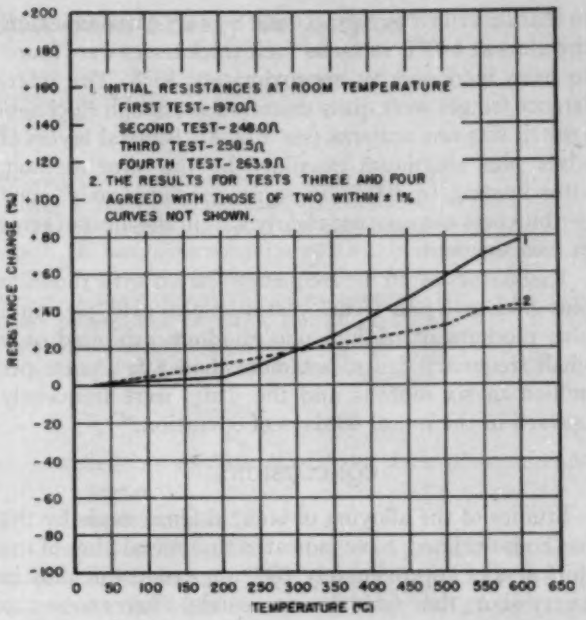

FIG. 9. Resistance *versus* temperature characteristics of a sputtered bimetal film of platinum plus gold. Alloying increased the resistivity and decreased the temperature coefficient of resistance as expected; alloying became vigorous at 200°C.

about 0.0028/C° and 0.0024/C°, respectively for films of gold and of platinum measured by a similar method. The measurements indicated that films of sputtered platinum and gold begin to alloy in the solid state at a temperature of less than 200°C. Alloying of nickel plus platinum was indicated at 450°C and of iridium and platinum near 600°C.

OTHER EXPERIMENTS

In order to determine the possible effect of bimetal electrodes on the stabilities of plated quartz resonators the stabilities of resonators plated with aluminum and gold, aluminum and silver, rhodium and gold, and nickel and silver were measured. These were compared with resonators plated with a single layer of gold, rhodium, or silver. AT-cut resonators of 16.25 mc plated with a single metal have been shown consistently capable of maintaining their original frequency within less than one part per million in six months when held in a test oven at 85°C. AT-cut resonators of 6 mc frequency plated with films of gold and aluminum or silver and aluminum were shown to undergo frequency shifts of as much as 100 parts per million in 60 days. These shifts could only be accounted for by moment of inertia changes of the vibrating system. A change in the center of mass of the film and the moment of inertia of the system occurs if the coating thickness changes or if atoms of different atomic weights diffuse from one layer of metal to a second layer of a different metal.

Bimetal layers of gold plus aluminum were examined by means of an interferometer technique closely allied

to that described by Sennett and Scott.[19] After annealing the films at 140°C *in vacuo* their thicknesses were found to have increased by approximately 30%. The interference fringes were quite distorted as though thickness growth was not uniform (see Fig. 8). Bimetal layers of silver plus aluminum examined by the same method, after heating to 300°C *in vacuo*, exhibited only small ± thickness changes not clearly within the limit of error in measurement.

Resonators of 16 mc frequency coated with rhodium plus gold, gold plus nickel, platinum plus gold, platinum plus rhodium or iridium plus rhodium exhibited only small frequency drifts, not more than a few parts per million in six months and the drifts were frequently upward in the initial 60 days of operation.[20]

CONCLUSIONS

Studies of the alloying of bimetal films, made by the methods outlined, have indicated that metal films of the thickness of approximately 1000 angstroms will alloy in a very short time (minutes or seconds) when exposed to temperatures near the recrystallization temperature of the metal of higher melting point or at a lower temperature. Evidences of alloying may be detected by the eight methods outlined.

The behavior of the metal films under study is different according to the order of deposition and may differ whether the method of deposition is evaporation, sputtering, electroplating or another. If the orders A+B and B+A are deposited in rapid sequence without opening the vacuum chamber little difference will be noted in the behavior of the resultant films. If, on the other hand, the sequence is interrupted by a pumping interval of several minutes or by opening the chamber, an oxide will be formed on the surface of chemically active metals. This oxide will act as a barrier to diffusion and alloying will be prevented until a temperature higher than that normally required is reached. Penetration of the aluminum oxide on aluminum films occurs at a temperature of 400 to 450°C.

If the sequence is A, B simultaneously, the metals behave differently in accordance with their alloying affinities for each other. Metals of high affinity will alloy during the deposition or at very low temperatures. Metals with no alloying affinity are deposited in a film of highly imperfect structure and will subsequently anneal to a structure with an electrical resistivity markedly lower than the original value. Metals of intermediate alloying affinities fall between these two extremes. For studies of alloying by the electrical resistance method the order A+B (where B is the more chemically active metal) is preferred.

Differences in alloying temperatures of the same metal pair deposited by different methods are not large. The necessity for opening the vacuum chamber for successive deposition and the time interval between depositions are of greater importance. The temperature of the substrate during deposit of the first and second metals will influence the subsequent alloying of the films and alloying may commence during an operation accompanied by a high temperature of the substrate, i.e., sputtering and sometimes evaporation.

In conclusion, methods for studying the alloying of bimetal films have been outlined. These films alloy at temperatures below 40% of the melting temperatures of the respective metals in degrees Kelvin and a rapid means of studying the binary alloys of some 1000 metal pairs yet unreported in the literature is suggested. This method avoids the necessity for any major financial outlay for expensive metals or for high temperature equipment. The temperatures required for study of the refractory metals are reduced from the range 2500°C to 3500°C to the range 600°C to 1200°C; and alloys unobtainable from any commercial source may be formed from films of the metals concerned. Exploratory studies of the behavior of tertiary, quaternary, or higher order alloys can be undertaken and studies of diffusion through oxide layers which are sandwiched between metal layers appear feasible.

Experiments of the nature discussed can add significantly to our knowledge of metal behavior; and materials presently unavailable to industry through normal sources can be prepared and employed in the rapidly advancing fields of electronics and instrumentation.

ACKNOWLEDGMENTS

Acknowledgement is made to Mrs. Margaret C. Chester and Miss Dorothy A. Brine for assistance in the preparation and examination of film specimens; to Mr. James W. Johnson and Mr. John L. Brown for the electron microscope and diffraction studies; to Mr. W. E. Woolf for the x-ray diffraction examinations; and to Miss Dorothy A. Brine, Miss Virginia A. Rouse, and Mrs. Carol Luciani for their assistance in preparing this paper in final form.

[19] G. D. Scott and R. S. Sennett, J. Opt. Soc. Am. **40**, 203 (1950).
[20] R. B. Belser, "Study of the Effect of Processing Techniques and Materials on Aging of Quartz Crystal Units," Final Report, U. S. Army SEL Contract No. DA-36-039 SC-64613 (July, 1957).

Effect of Temperature on Photovoltaic Solar Energy Conversion*

JOSEPH J. WYSOCKI AND PAUL RAPPAPORT
RCA Laboratories, Princeton, New Jersey

(Received August 3, 1959)

Photovoltaic solar energy conversion is investigated theoretically over a temperature range of 0–400°C using semiconductor materials with band gaps varying from 0.7 to 2.4 ev. Three cases are considered. In Case *I*, the junction current is the ideal current. In Case *II*, the junction current is the ideal plus a recombination current; and in Case *III*, a recombination current. The best conversion performance is obtained for the ideal current; the worst, for the recombination current. The maximum conversion efficiency occurs in materials with higher band gap as the temperature is increased. GaAs is close to the optimum material for temperatures below 200°C. Experimental measurements are presented on Si, GaAs, and CdS cells. The measurements on Si and GaAs agree with theoretical expectations as far as the gross behavior is concerned. The CdS cell behaves anomalously as if it were made from a material with band gap of 1.1 ev.

TABLE OF SYMBOLS

a	concentration gradient in a diffused junction
α	absorption coefficient in a semiconductor
D_n	diffusion constant for electrons
D_p	diffusion constant for holes
D	$D_n[1+(D_p/D_n)^{\frac{1}{2}}]^2$, effective diffusion constant
E_g	energy gap of a semiconductor
E_f	Fermi energy level
E_T	energy level of traps
E_i	intrinsic energy level
ϵ	permittivity of semiconductor
g	generation rate of electron-hole pairs per cm³ per sec
I_s	short-circuit current density
I_j	junction current density
I_L	load current density
I_{mp}	load current density at maximum power
I_0	reverse saturation current of a p-n junction
k	Boltzmann's constant
κ	dielectric constant of semiconductor
L_n	diffusion length of electrons
L_p	diffusion length of holes
l	thickness of absorbing semiconductor
m_p^+	hole effective mass for density of states
m_n^+	electron effective mass for density of states
$n_{ph}(E_G)$	number of photons with energy greater than the band gap E_G
η	solar conversion efficiency
N_A	number of net acceptor impurities per unit volume
N_D	number of net donor impurities per unit volume
N_s	geometrical mean of the number of states in the conduction and valence bands
n_i	intrinsic carrier density
ϕ	barrier height in a p-n junction
P_{mp}	maximum power output of a solar converter
Q	collection efficiency of p-n junction
R_{mp}	load resistance at maximum power
r	reflection coefficient of front face of solar converter
T	temperature in °K
τ_n	electron lifetime
τ_p	hole lifetime
τ_{no}	electron lifetime in material in which all the traps are empty
τ_{po}	hole lifetime in material in which all the traps are full
V_{mp}	voltage at maximum power
W	width of the depletion region
λ	q/kT

INTRODUCTION

A SEMICONDUCTOR photovoltaic cell converts solar energy directly into electrical energy by means of a p-n junction. Incident photons with energies greater than the band gap of the semiconductor create electrons and holes which are separated by the junction. A potential is thus created across the junction, and energy can be delivered to a resistive load.[1–12] The factors which make the conversion process temperature dependent are introduced by the properties of the semiconductor and the behavior of p-n junctions. This temperature dependence is the subject of the present paper. The discussion will be concerned with solar energy conversion. However, the conclusions are equally applicable to the conversion of other forms of ionizing radiation.

* This work was supported by the U. S. Army Signal Research and Development Laboratory, Fort Monmouth, New Jersey.

[1] Early history: V. K. Zworykin and E. G. Ramberg, *Photoelectricity and Its Applications* (John Wiley & Sons, Inc., New York, 1949).
[2] K. Lehovec, Phys. Rev. **74**, 463 (1948).
[3] R. Cummerow, Phys. Rev. **95**, 16 (1954).
[4] R. Cummerow, Phys. Rev. **95**, 561 (1954).
[5] Reynolds, Leies, Antes, and Marburger, Phys. Rev. **96**, 533 (1954).
[6] E. Rittner, Phys. Rev. **96**, 1708 (1954).
[7] Chapin, Fuller, and Pearson, J. Appl. Phys. **25**, 676 (1954).
[8] W. Pfann and W. van Roosbroeck, J. Appl. Phys. **25**, 1422 (1954).
[9] M. Prince, J. Appl. Phys. **26**, 534 (1955).
[10] Jenny, Loferski, and Rappaport, Phys. Rev. **101**, 1208 (1956).
[11] J. J. Loferski, J. Appl. Phys. **27**, 777 (1956).
[12] Rappaport, Loferski, and Linder, RCA Rev. **17**, 100 (1956).

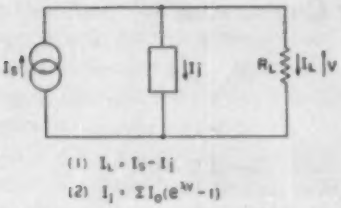

FIG. 1. Equivalent circuit of photovoltaic solar converter.

THEORY

1. General

The equivalent circuit of a photovoltaic cell[11,12] is shown in Fig. 1. Series resistances and shunt conductances are assumed negligible.

The junction current I_j is related to the junction voltage V by an equation of the form,

$$I_j = \sum I_0(e^{\lambda V} - 1) \tag{1}$$

where the summation sign is used to indicate that more than one mechanism may determine the junction behavior; i.e., the total current may be the sum of the ideal junction current,[13] a recombination current,[14] and a leakage current,[15] all of which can have a voltage dependence of the type shown under certain conditions. The short-circuit current I_s is related to the input radiation by the following equation[11]

$$I_s = Q(1-r)(1-e^{-\alpha l})qn_{ph}(Eg). \tag{2}$$

When the p-n junction is suitably located and the lifetimes are sufficiently great, I_s can be express as[16]

$$I_s = qg[L_n + L_p]. \tag{3}$$

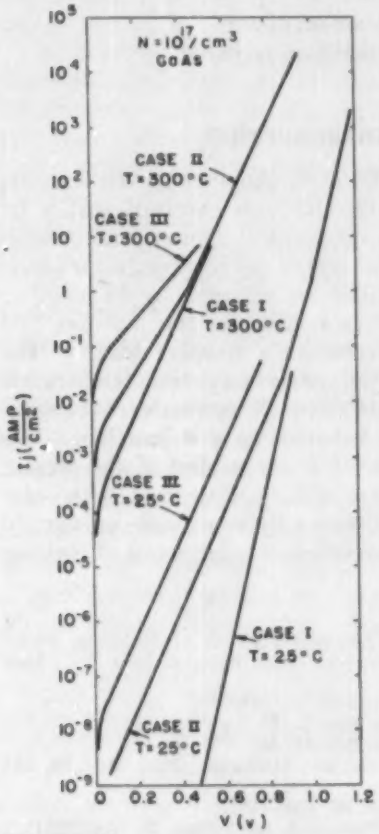

FIG. 2. Junction current *vs* voltage.

2. Effect of Temperature on I_s

The temperature dependence of the short-circuit current arises primarily with the diffusion lengths, which can be expressed as

$$L = (D\tau)^{\frac{1}{2}}. \tag{4}$$

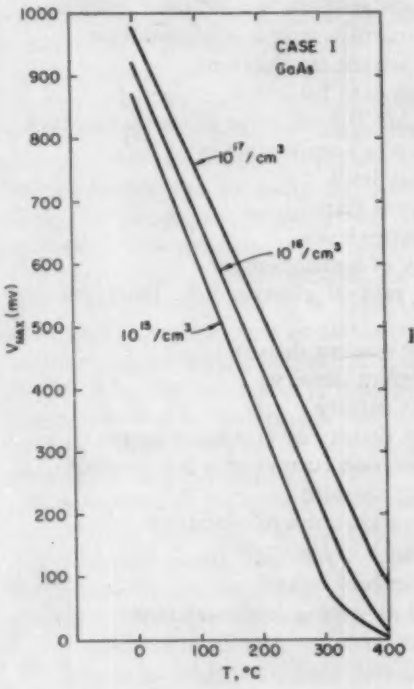

FIG. 3. V_{max} *vs* T, N as parameter.

Since the temperature dependence of the diffusion constant is $T^{-\frac{1}{2}}$, the net effect on L is small. It was assumed that the temperature dependence of the lifetime is determined by the single-level recombination statistics of Hall, Shockley, and Read[17,18] who show the lifetime in the n-type region to be

$$\tau = \tau_{po}\left[1 + \exp\left(\frac{E_T - E_F}{kT}\right)\right], \tag{5}$$

and

$$\tau = \tau_{no} + \tau_{po}\exp\left(\frac{E_T + E_F - 2E_i}{kT}\right) \tag{6}$$

[13] W. Shockley, *Electrons and Holes in Semiconductors* (D. Van Nostrand Company, Inc., Princeton, New Jersey, 1950), p. 314.
[14] Sah, Noyce, and Shockley, Proc. Inst. Radio Engrs. **45**, 1228 (1957).
[15] M. Cutler and H. Bath, Proc. Inst. Radio Engrs. **45**, 39 (1957).
[16] R. Gremmelmaier, Proc. Inst. Radio Engrs. **46**, 1045 (1958).
[17] W. Shockley and W. T. Read, Phys. Rev. **87**, 835 (1952).
[18] R. Hall, Phys. Rev. **87**, 387 (1952).

in the p-type region. The temperature dependence of the lifetime arises from the exponential terms in the foregoing equations. If the difference between E_F and E_T is large compared to kT, the exponential terms in Eq. (5) and (6) are negligible, and they remain negligible as the temperature is increased until E_F is within a few kT of E_T. The temperature at which the lifetime increases depends upon the doping and the trap level. For convenience in performing the calculations, the trap level will be located at the intrinsic Fermi level. The lifetime will thus be approximately constant in the temperature range in which solar energy conversion will be considered for material with a doping level of 10^{17} per cm^3.

Another factor in I_s to consider is the generation rate g. The generation rate increases slightly with temperature. This increase is due to the decrease in band gap, and consequent increase in the number of photons which are effective in creating electron-hole pairs. The effect is small in the temperature range considered, however, and will be neglected.

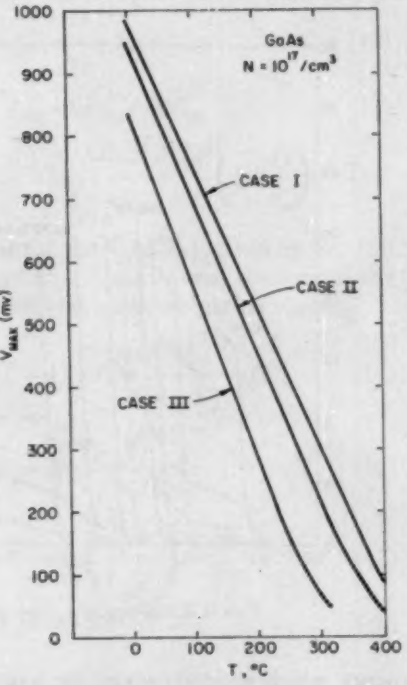

FIG. 4. V_{max} vs T, case as parameter.

It is concluded that I_s is not a rapidly varying function of T for heavily doped material, and its temperature dependence will be neglected hereafter.

3. Effect of Temperature on I_j

The junction current, as has been indicated, can be determined by several mechanisms. The leakage mechanism will not be considered in what follows because leakage through surface channels gives rise to equations similar in form to those obtained with the recombination model. Its effect can be inferred, therefore, from the results obtained with the recombination model. The following two mechanisms will be considered in detail.

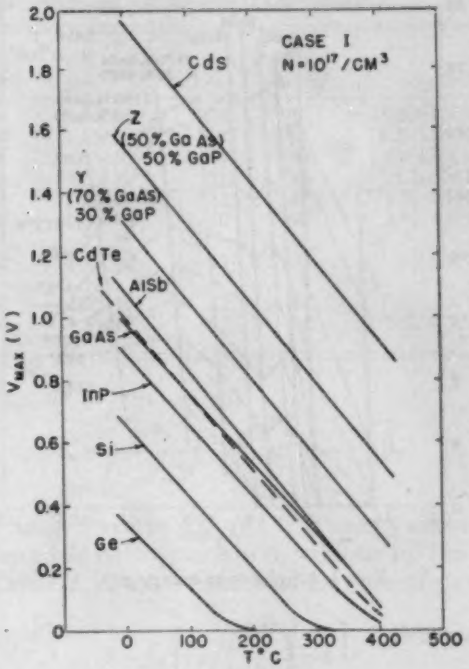

FIG. 5. V_{max} vs temperature.

a. Ideal Junction Current

This current arises from carriers which flow over the junction barrier; it depends upon voltage in the follow-

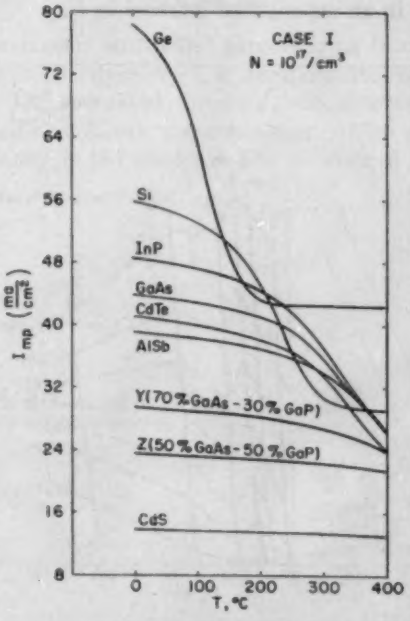

FIG. 6. I_{mp} vs temperature.

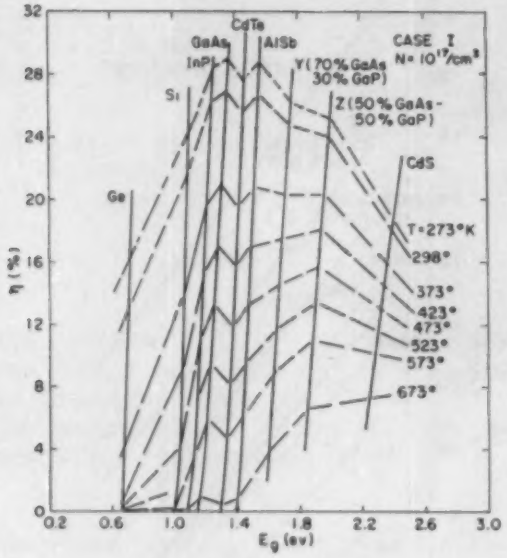

FIG. 7. Efficiency *vs* energy gap.

ing manner[13]:

$$I_j = I_0\left[\exp\left(\frac{qV}{kT}\right)-1\right], \tag{7}$$

$$I_0 = qn_i^2\left[\frac{1}{N_A}\left(\frac{D_n}{\tau_n}\right)^{\frac{1}{2}}+\frac{1}{N_D}\left(\frac{D_p}{\tau_p}\right)^{\frac{1}{2}}\right]. \tag{8}$$

The behavior predicted by Eqs. (7) and (8) is well known. The magnitude of I_0 and I_j is determined primarily by the band gap of the semiconductor through its effect on the square of the intrinsic density n_i^2. The coefficient I_0 increases exponentially with temperature resulting in an exponential increase in I_j.

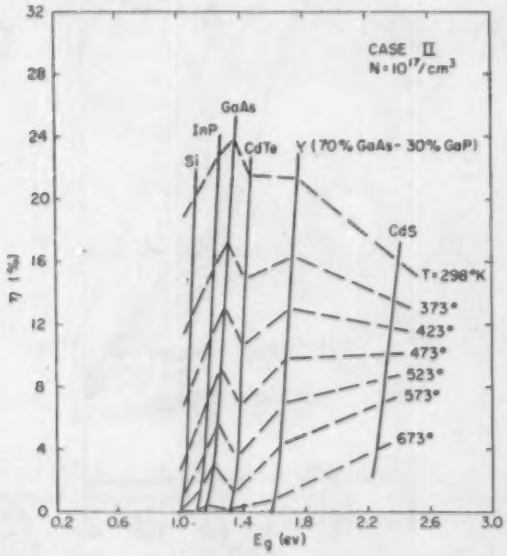

FIG. 8. Efficiency *vs* energy gap.

b. Recombination current

The recombination current arises from carriers which recombine in the depletion region from centers existing in the forbidden gap.[14] For single-level centers, the current is determined by integrating the Shockley-Read expression for the recombination rate[17] over the depletion region, leading to the following equation[14]:

$$I_j = \frac{qn_i}{(\tau_{p0}\tau_{n0})^{\frac{1}{2}}} W \frac{2\sinh(qV/2kT) f(b)}{(\phi - V)(q/kT)}. \tag{9}$$

$f(b)$ is a slowly varying function of the voltage, trap level, lifetimes, and barrier height. The magnitude of the current varies as n_i, instead of n_i^2 consequently, it is determined by half the band gap. The current increases exponentially with temperature with an activation

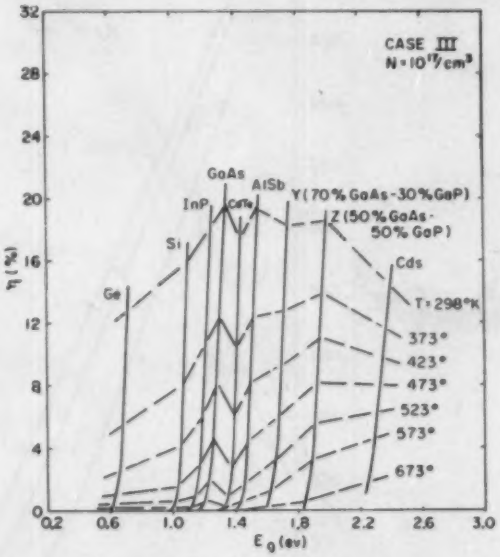

FIG. 9. Efficiency *vs* energy gap.

energy which depends upon the location of the trap level.

4. Effect of Temperature on Solar Energy Conversion

The temperature effects already considered were incorporated into the equations governing photovoltaic energy conversion, and conversion performance was calculated as a function of temperature. The calculations were performed on an IBM 650 Digital Computer. Three cases were considered.

In Case *I*, I_j was the ideal junction current. Consequently the equations for photovoltaic energy conversion could be put into the following closed form:

$$V_{max} = \ln\left(\frac{I_s}{I_0}+1\right), \tag{10}$$

TABLE I. Semiconductor parameters used in calculations. (Note: estimated and state-of-the-art values.)

Semiconductor	μ_n cm²/v-sec	μ_p cm²/v-sec	$\tau_p=\tau_n$ (sec)	m_n^+	m_p^+	n_i No./cm³ (300°K)	κ	I_s (ma/cm²)	E_g (ev)
Ge	3000	1350	10^{-6}	0.55	0.36	8.3×10^{12}	16	85	$0.83-4\times10^{-4}\,T$
Si	710	360	10^{-7}	1.08	0.60	1.1×10^{10}	12	58	$1.2-3.5\times10^{-4}\,T$
InP	4000	100	10^{-8}	0.08	0.60	8×10^{7}	11	50	$1.39-4.6\times10^{-4}\,T$
GaAs	5000	400	10^{-8}	0.06	0.50	9.2×10^{6}	11	45	$1.5-5\times10^{-4}\,T$
CdTe	300	30	10^{-8}	1.08	0.60	1.2×10^{7}	12	42	$1.57-4\times10^{-4}\,T$
AlSb	710	360	10^{-8}	1.08	0.60	1.7×10^{6}	10	40	$1.67-4\times10^{-4}\,T$
Y (70% GaAs–30% GaP)	200	20	10^{-8}	1.08	0.60	3.7×10^{4}	12	30	$1.9-4\times10^{-4}\,T$
Z (50% GaAs–50% GaP)	200	20	10^{-8}	1.08	0.60	3.1×10^{3}	12	24	$2.1-4\times10^{-4}\,T$
CdS	200	20	10^{-6}	1.08	0.60	1.2×10^{-1}	12	14	$2.52-4\times10^{-4}\,T$

$$R_{mp}=\frac{1}{\lambda I_0 e^{\lambda V_{mp}}}, \tag{11}$$

$$e^{\lambda V_{mp}}(1+\lambda V_{mp})=\frac{I_S}{I_0}+1, \tag{12}$$

$$I_{mp}=\lambda V_{mp} e^{\lambda V_{mp}} I_0, \tag{13}$$

$$\eta=\frac{\lambda V_{mp}^2}{1+\lambda V_{mp}}\frac{I_s}{1.35}\left(1+\frac{I_0}{I_s}\right), \tag{14}$$

for a power input of 135 mw/cm². I_0 is given by Eq. (8).

The junction current in Case *II* was the sum of the ideal junction current and a recombination current.

$$I_j=I_0(e^{\lambda V}-1)+I_n\frac{\sinh(\lambda V/2)}{\lambda(\phi-V)}f(b), \tag{15}$$

where

$$f(b)=\int_{z_1}^{z_2}\frac{dz}{Z^2+2bZ+1}; \tag{16}$$

$$b=\exp\left(-\frac{\lambda V}{2}\right); \tag{17}$$

$$Z_{1,2}=e^{\mp\lambda/2(\phi-V)}; \tag{18}$$

and

$$I_n=\frac{2qn_i}{(\tau_{p0}\tau_{n0})^{\frac{1}{2}}}[(12\epsilon/qa)(\phi-V)]^{\frac{1}{2}}. \tag{19}$$

I_0 is again given by Eq. (8). The energy conversion equation could not be put into closed form for this case.

In Case *III*, I_j was a recombination current given by

$$I=I_n'\left[\exp\left(\frac{\lambda V}{2}\right)-1\right], \tag{20}$$

with

$$I_n'=\frac{qn_i}{(\tau_{p0}\tau_{n0})^{\frac{1}{2}}}[(12\epsilon/qa)\phi]^{\frac{1}{2}}. \tag{21}$$

The energy conversion equations could again be put into closed form yielding equations similar to Eqs. (10)–(14) with the exceptions that I_0 is replaced by I_n' and λ is divided by 2.

5. Assumptions and Values Used in Calculations

Semiconductors with band gaps ranging from 0.7 to 2.4 ev were studied over a temperature range of 0–400°C. The generated current I_s was determined by solar conditions outside the atmosphere where the solar power density is 135 mw/cm². The number of photons

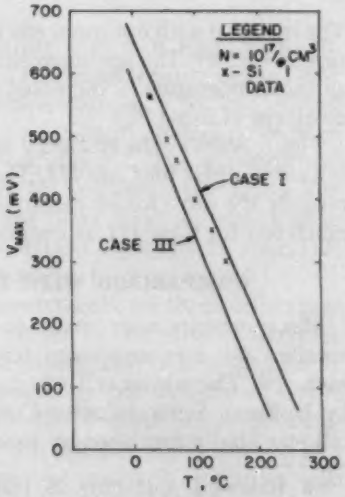

FIG. 10. V_{max} vs temperature—silicon solar cell.

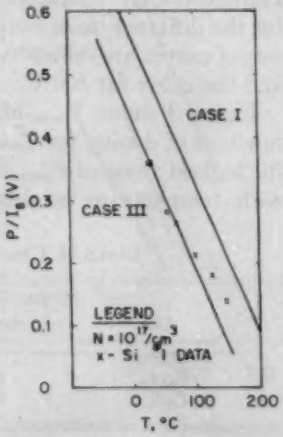

FIG. 11. P/I_s vs temperature for silicon solar cell.

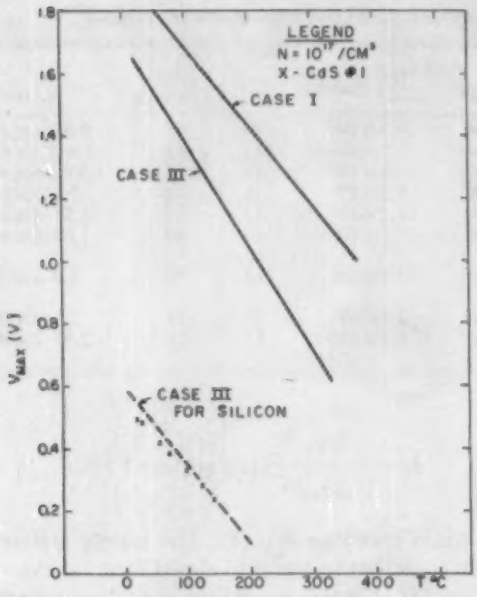

FIG. 12. V_{max} *vs* temperature for cadmium sulfide.

effective in creating hole-electron pairs was taken from published curves.

The following assumptions were made to simplify and to facilitate the calculations. The collection efficiency was taken as unity. Losses due to reflection, leakage conductance, and series resistance were assumed negligible. The electron and hole lifetimes, and impurity concentrations in the *n* and *p* regions were assumed equal. Traps were located at the intrinsic energy level and a concentration gradient of 4×10^{19} per cm^4 was assumed for diffused junctions.

Table I lists the values used in the calculations for the various semiconductor parameters. These values are state-of-the-art values in some cases, and in others estimates of the actual values.

RESULTS

The results of the calculations are summarized in Figs. 2 through 10. Figure 2 illustrates the forward current-voltage characteristic of a GaAs *p-n* junction for the different cases assumed in the calculations. Two sets of curves are shown—one for a temperature of 25°C and the other for 300°C.

Figure 3 shows V_{max} of a GaAs solar converter as a function of doping for Case *I*. The curves indicate that the highest value of V_{max} and the lowest rate of decrease with temperature is obtained at the higher doping levels. The effect of the different I_j on V_{max} of a GaAs junction doped to 10^{17} per cm^3 is depicted in Fig. 4. It is obvious that best performance is obtained with Case *I* operation. Figure 5 is a plot of V_{max} *vs* T for the semiconductors investigated for Case *I* and a doping level of 10^{17} per cm^3. The slopes of the lines are all roughly the same—approximately 2 mv/°C. The maximum voltage is greater, of course, for higher band gap values.

A composite curve of I_{mp} *vs* T for Case *I* and a doping level of 10^{17} per cm^3 is shown in Fig. 6. I_{mp} approaches $\frac{1}{2}I_s$ as the temperature is increased. This asymptotic behavior is a consequence of the fact that junction resistance approaches zero as the temperature is increased. It is therefore not apparent in the higher band gap materials over the temperature range studied.

Composite curves of efficiency and power *vs* bandgap are shown in Figs. 7 to 9. Case *I* is considered in Fig. 7.

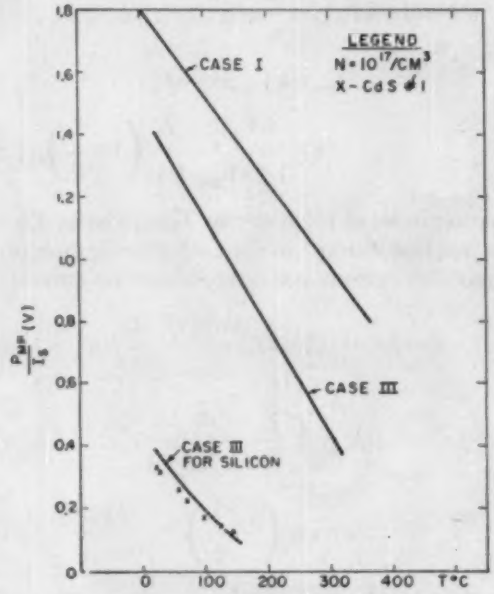

FIG. 13. P_{mp}/I_s *vs* temperature for cadmium sulfide.

The material with optimum efficiency at room temperature is GaAs.[11] The optimum shifts to higher bandgaps as the temperature is increased in agreement with the results of Halsted.[19]

Figure 8 shows the efficiency for Case *II*, while Fig. 9 is a similar plot for Case *III*. The optimum band gap is roughly the same for all cases, however the efficiency is much less for Case *III* as compared to Case *I*.

TABLE II. Characteristics of Cells.

Cell	Area (cm^2)	Room temperature efficiency
Silicon	1.7	10%
GaAs	0.2	3.8
CdS	0.385	3.6

COMPARISON WITH EXPERIMENT

Measurements were made on three cells. Table II specifies the area and room temperature efficiency of each cell. The silicon cell was a commercial unit made by Hoffman Semiconductor Corporation and the CdS cell was kindly furnished by Reynolds of WADC.

[19] R. Halsted, J. Appl. Phys. **28**, 1131 (1957).

During measurement, the cells were mounted in a small furnace with a glass window to allow the cells to be irradiated. A Chromel-Alumel thermocouple was attached to the cells to measure the temperature, and dry helium was pumped through the system to maintain a standard atmosphere. A light source supplied an input power density of 100 mw/cm² to the cells.

The results of the measurements are plotted in Figs. 10 to 16 together with theoretical curves for Case *I* and Case *III* at a doping level of 10^{17} per cm³. Figure 10 is a plot of V_{max} *vs* T for silicon. The experimental points fall between the theoretical curves, and the rate of decrease agrees well with the theoretical value. Similar agreement is found in Fig. 11 where (P_{mp}/I_s) is plotted *vs* T.

The CdS curves are shown in Figs. 12 and 13. The experimental points fall below the theoretical curves; in fact, they lie roughly on the theoretical curves for Si, Case *III*.

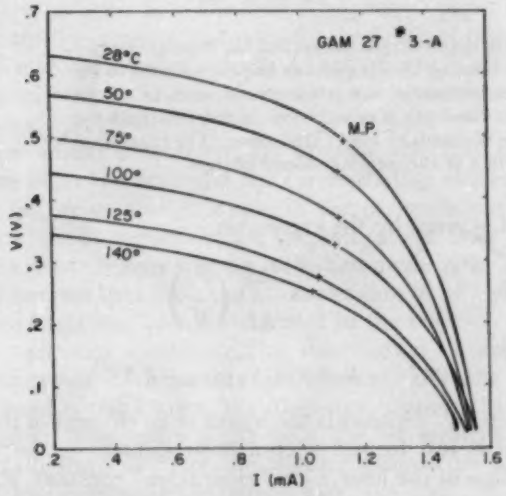

FIG. 14. Current-voltage characteristics of gallium arsenide cell *vs* temperature.

The curves for GaAs are shown in Figs. 14 to 16. Figure 14 is a plot of the *i–v* characteristics of the GaAs cell in the light with temperature as a parameter. The figure illustrates that I_s is substantially independent of T as assumed in the calculations. The experimental curves in Figs. 15 and 16 are somewhat below the theoretical curves but not to as great an extent as in the case of CdS. The theoretical curves for Si, Case *III*, are also shown for comparison.

The temperature measurements on these cells agree quite well with theory as far as the rates of decrease with temperature is concerned. The lack of agreement in absolute values in some cases can be ascribed to the use of nonoptimum cells. One feature of the measurements is the behavior of the CdS cell which corroborates the results found in spectral analyses of similar cells where appreciable absorption is found at wavelengths

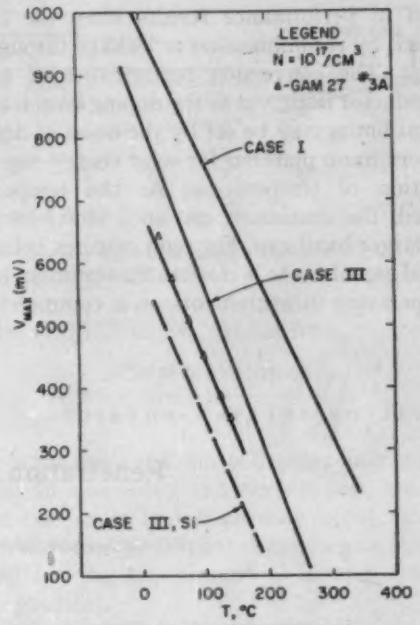

FIG. 15. Maximum voltage *vs* temperature for gallium arsenide solar cell.

greater than that corresponding to the band edge.[20] The spectral response and the temperature behavior of the solar cell indicate that the CdS cell is behaving as if it were made from a material whose band gap is closer to that of Si than that of CdS.

CONCLUSIONS

The optimum conversion performance is obtained when the junction current is the ideal current. A deg-

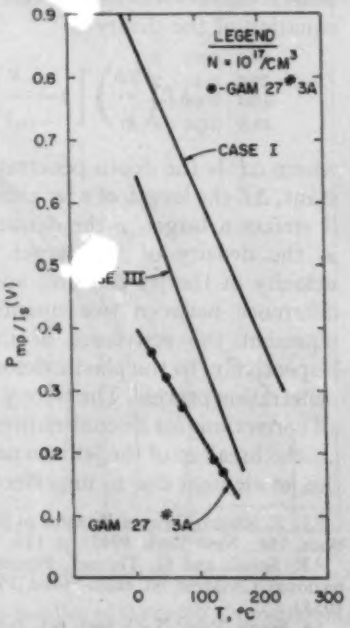

FIG. 16. P_{mp}/I_s *vs* temperature for GaAs solar cell.

[20] D. C. Reynolds, "The photovoltaic effect in CdS crystals," Trans. Conf. Use of Solar Energy (Tucson, Arizona, 1955).

radation in performance results when the current is influenced by recombination or leakage through surface channels. The conversion performance of any given semiconductor improves as the doping level is increased. Practical limits may be set by the onset of degeneracy.

The optimum material for solar energy conversion is a function of temperature. As the temperature is increased, the maximum efficiency shifts to materials with a larger band gap. For temperatures below 200°C, the band gap of GaAs is close to the optimum band gap.

Temperature measurements on a commercial Si cell agree well with theory. Measurements on experimental GaAs and CdS cells indicate the following. The GaAs cell was not optimum. Losses which were not considered in the analysis led to lower values of V_{max} and P_{mp}/I_s than expected. The CdS cell, on the other hand, behaved as if it were made from a material with lower band gap.

ACKNOWLEDGMENTS

The authors wish to acknowledge the suggestions and discussions of Joseph J. Loferski. The calculations were performed by Paul Rygg and Sherwood Skillman.

JOURNAL OF APPLIED PHYSICS VOLUME 31, NUMBER 3 MARCH, 1960

Penetration of Rotating Shaped Charges

SAMPOORAN SINGH
Defence Science Laboratory, Ministry of Defence, New Delhi, India
(Received September 10, 1959)

This paper presents an attempt to correlate theoretically the depth of penetration and the angular velocity of the liner in a rotating shaped charge. Each element of the rotating liner imparts an angular velocity to the corresponding jet element, and this results in a continuous increase of the cross-sectional area of the jet element as it travels in space and a corresponding decrease in the depth of penetration. In order to check the theory, numerical evaluations have been carried out in case of standard M9A1 steel cones. The theoretical results seem to explain the scanty published experimental data of the rotating shaped charges.

IT is well established that when a shaped charge rotates about its axis, there is loss of penetration. Kerr cell photographs[1] and x-ray flash photographs[2] of rotating shaped charges about their axes show that rotation brings about an increase of the cross-sectional area of the jet. The theory of penetration by rotating shaped charges was developed by Singh[3–5] and the basic equation of the theory is

$$\Delta P=\epsilon\Delta L\left(\frac{\gamma\rho}{\rho_t}\right)^{\frac{1}{2}}\left[1-\frac{\sigma}{\rho_t V^2}\left\{\left(\frac{\rho_t}{\gamma\rho}\right)^{\frac{1}{2}}+1\right\}^2\right], \quad (1)$$

where ΔP is the depth penetration, ϵ an empirical constant, ΔL the length of a jet element at the instant when it strikes a target, ρ the density of the liner material, ρ_t the density of the target material, V the mean velocity of the jet element, and the quantity σ is the difference between two quantities, σ_t and σ_j, which represent the resistance of the target and the jet, respectively, to the plastic deformation required by the penetration process. The term γ takes into consideration all corrections for discontinuities within the jet element, i.e. the breakup of the jet into particles and the waver of the jet element due to imperfections in charge or liner; and is given by the expression

$$\gamma=\frac{C\Delta L'}{\Delta L}\left(\frac{R_j}{R_t}\right)^2 \quad (2)$$

and

$$R_t=R_j+S_d\tan\phi+R_r, \quad (3)$$

where $\Delta L'$ represents the length of an element of the jet that is just formed from a finite element in the slant surface of the liner, C an "elongation" constant, R_j the

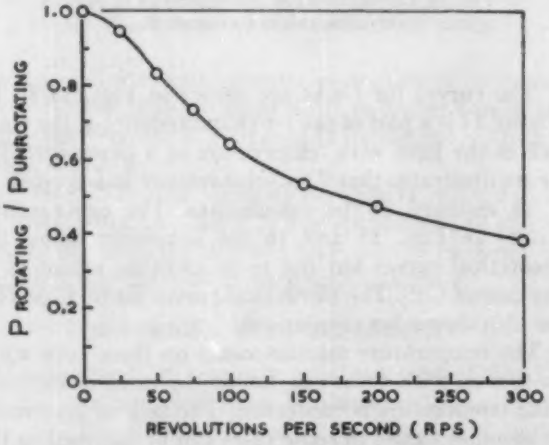

FIG. 1. Ratio of the depth of penetration by rotating charges/depth of penetration by unrotating charges at 7.62 cm standoff distance in mild steel targets as a function of the speed of rotation of the standard M9A1 steel linear in the standard C.I.T. laboratory charge.

[1] L. E. Simon, *German Research in World War II* (John Wiley & Sons, Inc., New York, 1947), p. 119.
[2] R. Schall and G. Thomer, Proceedings of the Second International Congress on High-Speed Photography (Dunod, Paris, 1954).
[3] S. Singh, Proc. Natl. Inst. Sci. India **19**, 665 (1953).
[4] S. Singh, J. Sci. Ind. Research (India) **14B**, 669 (1955).
[5] S. Singh, Proc. Phys. Soc. (London) **71**, 508 (1958).

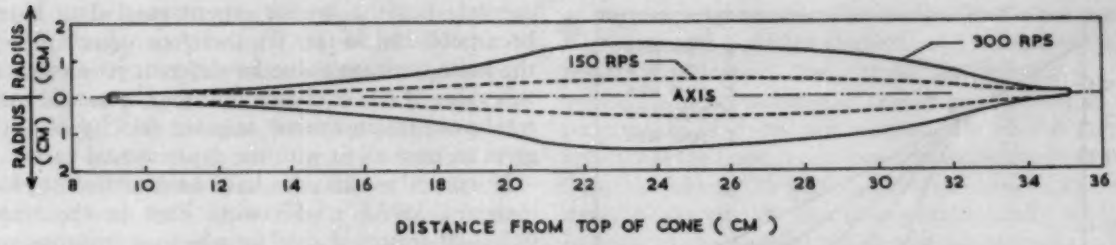

FIG. 2. Calculated profiles of the jet at 50 μsec after the detonation wave had passed the base of the liner and the equipment was rotating at 150 and 300 rps.

initial radius of a jet element before the element starts breaking into particles, and R_t the radius of the jet element when its length is ΔL. S_d is the axial distance from the point of normal breakup of an element of the jet to the point of its impingement on the target, ϕ the angle of spread which the particles subtend with the axis, and R_τ the increase in radius at any time τ due to the angular velocity of the jet element. As pointed out by Schall,[6] the penetration must be independent of the sign of the spin, ω, of the liner. The present paper is an attempt to correlate theoretically the depth of penetration and the angular velocity of the liner in a rotating shaped charge, and is basically an extension of the author's previous work.[5]

Let ω and Ω represent the angular velocities of an element in the liner and the corresponding element in the jet, respectively; $x\tan\alpha$ is the perpendicular distance of the element in the original conical liner from the axis of the liner where α is the half-angle of the liner. We assume that the angular momentum of an element of the rotating liner is conserved in the corresponding jet and slug elements. The distribution of angular momentum between the jet element and the slug element is not known. We, therefore, assume that the angular momentum going into the jet element is a certain fraction F, of the angular momentum of the original element in the parent liner

$$F\Delta m\omega x^2\tan^2\alpha=\tfrac{1}{2}\Delta m_j\Omega R_j^2, \tag{4}$$

where Δm is the mass of the liner element included between two planes perpendicular to the axis at x and $(x+\Delta x)$, and Δm_j the mass of the corresponding jet element. Each jet element is rotating with a certain angular velocity and in consequence is subject to centrifugal forces. The effect of these forces on the *particles* forming the jet element is to cause a continuous spreading (increase of cross-sectional area) as the jet element advances. During the very small time τ this spreading takes place, the radial acceleration of the jet element may be treated as practically constant and equal to Ω^2R_j. The resulting increase in radius R_τ at any time τ is given by the expression

$$R_\tau=\tfrac{1}{2}\Omega^2R_j\tau^2. \tag{5}$$

By substituting the value of Ω from Eq. (4) and putting $\Delta m_j=\Delta m\sin^2(\beta/2)$ in Eq. (5), we have

$$R_\tau=\frac{2F^2\omega^2x^4\tan^4\alpha\,\mathrm{cosec}^4(\beta/2)\tau^2}{R_j^2}, \tag{6}$$

where β is the angle that the collapsing liner makes with the axis. In discussing the penetration, we have to consider two cases and both may occur at different stages in the same jet element depending on the distance available for the jet element to stretch due to the velocity gradient.

Case 1. ($\Delta L\leqslant C\Delta L'$)

We assume that the spreading of a jet element due to its angular momentum is negligible as long as ductile drawing continues and the value of C for a given jet element is the same for a nonrotating and a rotating shaped charge. For a continuous jet element γ is unity, and ΔP is given by Eq. (1).

Case 2. ($\Delta L>C\Delta L'$)

The time interval τ is identified as the time taken for the jet element to stretch from $C\Delta L'$ to ΔL and is given

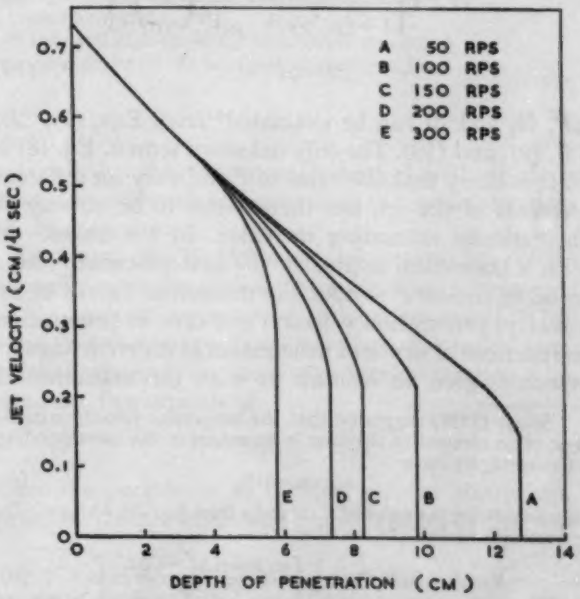

FIG. 3. Jet velocity as a function of the depth of penetration at 7.62 cm standoff distance in mild steel for several representative speeds of rotation of the liner.

[6] R. Schall, Tek. Tidskr. 88, 393 (1958).

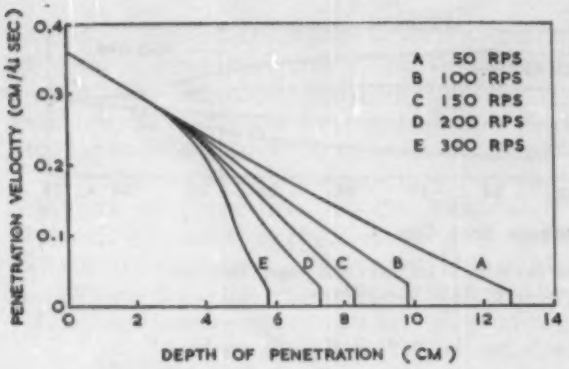

FIG. 4. Velocity of penetration as a function of the depth of penetration at 7.62 standoff distance in mild steel for several representative speeds of rotation of the liner.

by the expression,

$$\tau=\frac{\Delta L-C\Delta L'}{V_j-V_j'}. \tag{7}$$

By substituting the value of R_τ and τ from Eqs. (6) and (7) respectively in Eq. (3), we have

$$R_t=R_j+S_d\tan\phi+\frac{2}{R_j}\left[\frac{F\omega x^2\tan^2\alpha\,\mathrm{cosec}^2(\beta/2)(\Delta L-C\Delta L')}{R_j(V_j-V_j')}\right]^2. \tag{8}$$

Let U be the time rate of change of the depth of the hole by the given jet element and Δt the time taken for it to penetrate to a depth ΔP; U and Δt are given by the expressions,

$$U=V\left[\frac{1}{1+(\rho_t/\gamma\rho)^{\frac{1}{2}}}-\frac{\sigma}{\rho_t V^2}\left(\frac{\rho_t}{\gamma\rho}\right)^{\frac{1}{2}}\right] \tag{9}$$

$$\Delta t=\Delta P/U. \tag{10}$$

ΔP, U, and Δt can be evaluated* from Eqs. (1), (2), (8), (9), and (10). The only unknown term in Eq. (8) is F. It is likely that the value of F will vary for different elements of the jet, but there seems to be no way of theoretically estimating its value. In the absence of such a theoretical approach, the best procedure seems to be to choose F so that the theoretical curves of jet velocity, penetration velocity, and time of penetration as functions of depth of penetration at different angular velocities give an over-all fit with the experimental curves†; but the precise experimental data have not been published so far. We therefore assume F to have the same constant value for different jet elements and this value of F is so chosen that the theoretical curve of total penetration against angular velocity of the cone gives an over-all fit with the experimental curve.

Numerical evaluations have been carried out for the standard M9A1 steel conical liner in the standard C.I.T. laboratory charge[7] for which experimental results are available[8]. A comparison of the experimental and theoretically calculated depth of penetration (taking $C=4.5$, $\sigma=12\times10^9$ d cm^{-2}) at a standoff of 7.62 cm in mild steel targets against angular velocity suggests that the value of F is about 0.075. F is assumed to be constant for different jet elements. It is rather surprising that the angular momentum in the jet is such a small fraction of the original angular momentum in the liner. Figure 1 shows the theoretical curve of the ratio of the penetration with rotation to the penetration without rotation as a function of the speed of rotation. Penetration at first decreases slowly with increase in speed of rotation, then more rapidly as speed is further increased, and again more slowly at very high rotational speeds. The curve has a horizontal tangent at $\omega=0$. At small angular velocities, the loss of penetration is slight and angular velocities up to 50 revolutions per sec can be permitted with these charges.

Figure 2 shows the calculated profile of the jet traveling in space at 50 μsec after the detonation wave

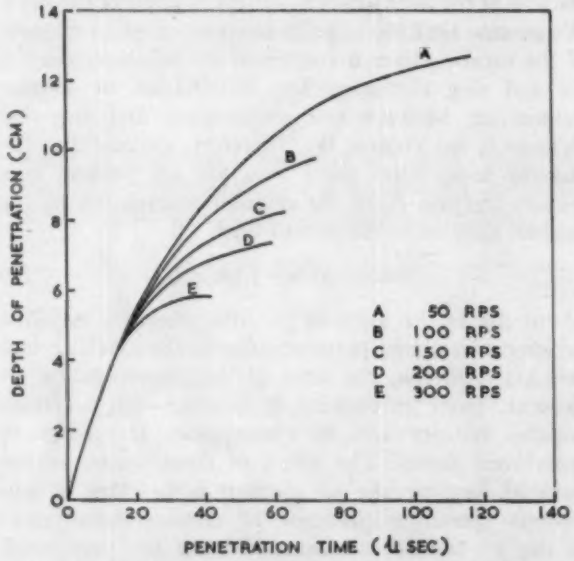

FIG. 5. Depth of penetration at 7.62 cm standoff distance in mild steel as a function of the time for several representative speeds of rotation of the liner. The instant of impact of the front of the jet on the face of the target is referred to as zero time.

* Schall (1958) suggested that the tangential velocity component of an element of the liner is conserved in the corresponding jet element, we have

$$\omega x\tan\alpha=\Omega R_j. \tag{A}$$

On substituting the value of R_τ, Ω and τ from Eq. (5), (A), and (7), respectively, in Eq. (3), we have

$$R_t=R_j+S_d\tan\phi+\frac{1}{2R_j}\left[\frac{\omega x\tan\alpha(\Delta L-C\Delta L')}{(V_j-V_j')}\right]^2. \tag{B}$$

On substituting the value of R_t from Eq. (B) in Eq. (2), ΔP can be evaluated by Eqs. (1) and (2). The values of the total penetration so obtained do not agree with the experimental values.

† By means of the observations of jet parameters for the charges, estimates can be made of the elongation of the various parts of the jet.

[7] R. J. Eichelberger and E. M. Pugh, J. Appl. Phys. **23**, 537 (1952).

[8] R. J. Eichelberger, J. Appl. Phys. **26**, 398 (1955).

had passed the base of the liner and the rotational speed of the equipment being 150 rps and 300 rps. It seems that the jet diameter has a maximum somewhere in the middle and tapers off towards the two ends. The head of the jet, which comes from the summit of the liner, seems to be uneffected by the rotation. The spreading is not uniform along the axis of the jet, nor is it constant with time. These results can be compared with some flash radiographs of Schall and Thomer[2] (Fig. 13 of reference 2) although their charges were of different design than the C.I.T. laboratory charge. It is of interest, however, to note that the flash radiographs also show a maximum jet diameter near the middle of the jet, which tapers off to the front and rear of the jet.

Theoretical curves of the velocity of the impinging jet element, velocity of penetration and time of penetration as functions of the instantaneous depth of penetration at varying angular velocities of the liner are shown in Figs. 3, 4, and 5. As the elements at the head of the jet remain continuous, the curves for velocity of jet, velocity of penetration, and time of penetration up to a penetration of 3 cm are independent of the angular velocity of the liner. As the penetration increases beyond 3 cm, the jet velocity and the penetration velocity (slope dp/dt of the curves) decrease systematically with the increase of the angular velocity of the shaped charges.

ACKNOWLEDGMENTS

The author is grateful to Professor D. S. Kothari, Scientific Adviser to the Minister of Defence, for suggesting this work and for encouragement and interest throughout the course of this investigation. Thanks are also due Dr. V. R. Thiruvenkatachar and Dr. S. N. Baura for valuable suggestions.

JOURNAL OF APPLIED PHYSICS VOLUME 31, NUMBER 3 MARCH, 1960

Grain Boundaries in Germanium*

RICHARD S. WAGNER AND BRUCE CHALMERS†
Division of Engineering and Applied Physics, Harvard University, Cambridge 38, Massachusetts
(Received July 22, 1959)

The relative energies and the boundary orientations of simple tilt boundaries in germanium crystals have been measured. The measurements were made on columnar tricrystals prepared by the modified Czochralski method. The orientations of the columnar tricrystals were either ⟨100⟩ and ⟨111⟩ isoxial or (100) isoplanar. The relative grain boundary energies were measured as a function of the angular misorientation θ between two grains. The crystallographic orientations of the grain boundary plane were also determined.

It was found that the relative energy of ⟨100⟩ and ⟨111⟩ tilt boundaries up to about 15° of misorientation changes with misorientation as predicted by Read and Shockley's theory. For larger angles of misorientation, the grain boundary energy is essentially independent of the angle of misorientation. This indicates a significant but continuous change in boundary structure at the transition region.

Additional evidence for the difference in the structure of low- and high-angle tilt boundaries was found in the apparent strong dependence of the energy of low-angle boundaries on the boundary orientation. Low-angle (100) twist boundaries were not observed.

INTRODUCTION

J. M. BURGERS[1] and W. L. Bragg[2] were the first to point out that a low-angle grain boundary can be described as an array of dislocations. Such an array corresponds geometrically to the orientation difference between the crystals on the two sides of the interface. Read and Shockley[3] applied the dislocation model to describe the grain boundary structure in f.c.c. and b.c.c. materials. Frank[4] made a mathematical analysis of the dislocation structure corresponding to a grain boundary for the general case.

Read and Shockley[5,6] made predictions of certain physical properties, such as the grain boundary energy, on the basis of an assumed dislocation model. They found that the energy E of a low-angle dislocation grain boundary depends on the angle of misorientation θ between the two crystals as

$$E=E_0\theta(A_0-\ln\theta), \qquad (1)$$

where the parameter E_0 depends on the elastic constants of the material, and A_0 is related to the core

* Contribution from the Division of Engineering and Applied Physics, Harvard University, Cambridge 38, Massachusetts. This paper is based on a thesis submitted by Richard S. Wagner in partial fulfillment of the requirements for the degree of doctor of philosophy. This work was supported in part by the U. S. Atomic Energy Commission and the National Science Foundation.

† Now at Bell Telephone Laboratories, Inc., Metallurgical Research Department, Murray Hill, New Jersey.

[1] J. M. Burgers, Proc. Phys. Soc. (London) 52, 23 (1940).

[2] W. L. Bragg, Proc. Phys. Soc. (London) 52, 54 (1940).

[3] W. T. Read and W. Shockley, *Imperfections in Nearly Perfect Crystals* (John Wiley & Sons, Inc., New York, 1952), p. 352.

[4] C. F. Frank, Carnegie Institute of Technology, Symposium on the plastic deformation of crystalline solids, Office of Naval Research (NAVEXOS, p. 834).

[5] W. Shockley and W. T. Read, Phys. Rev. 75, 692 (1949).

[6] W. T. Read and W. Shockley, Phys. Rev. 78, 275 (1950).

energy of a dislocation. The energy of such a grain boundary in the general case depends on five parameters.[7] By a suitable choice of the orientation relationship between the adjoining crystals and the direction of crystal growth, it is possible to form simple tilt and simple twist boundaries. The energy of such a boundary depends on two parameters only, the misorientation angle θ, and the boundary inclination angle φ, where φ is the angle of inclination with respect to the symmetrical grain boundary orientation.[7]

Relative grain boundary energies can be determined by the "tricrystal method."[8] These experimental results can then be compared with the predicted theoretical values[5,6] of the energy and orientation dependence of a grain boundary having two degrees of freedom. By this comparison, it is possible to assess the validity of the dislocation model of a grain boundary assumed in the calculation.

Measurement of the Grain Boundary Energy

It has been shown[9] that in solids under the conditions of high annealing temperature, the grain boundary free energy is numerically equal to the grain boundary tension.

C.S. Smith[10] pointed out that in a well-annealed polycrystalline sample, the grain boundaries intersect at grain boundary junctions in such a way as to establish a local equilibrium configuration. If there is equilibrium at the junction, then the three interfacial tensions σ_i are balanced vectorially and the equilibrium condition can be written as

$$\sum_i \sigma_i t_i = 0. \tag{2}$$

The t_i are the unit vectors in the direction tangential to each grain boundary, perpendicular to the line of intersection. This formula expressed in explicit form is the well-known Neuman triangle relationship,

$$\sigma_1/(\sin\alpha) = \sigma_2/(\sin\beta) = \sigma_3/(\sin\gamma), \tag{3}$$

where α, β, and γ are the dihedral angles between the boundaries measured on a plane perpendicular to the line of intersection of three boundaries. In such an investigation, one of the energies, say σ_1, is kept constant, and the two unknown relative energies $\sigma_2/(\sigma_1)$ and $\sigma_3/(\sigma_1)$ can be evaluated as a function of the angular misorientation θ between the crystals.

Theory predicts, however, that the energy of a grain boundary can also depend on the boundary inclination, represented by the angle φ. C. Herring[9] has taken account of this effect and derived the equilibrium condition of grain boundary junctions for the general case

$$\sum_i \sigma_i t_i + \frac{\partial \sigma_i}{\partial t_i} = 0 \tag{4}$$

The first term is identical with formula (2). The second term, however, corresponds to a torque acting on the grain boundary, tending to pull the boundary into a position of lowest energy. For the calculation of relative grain boundary energies, it is more convenient to express Herring's formula as

$$\frac{\sigma_1}{(1+\epsilon_2\epsilon_3)\sin\alpha + (\epsilon_3-\epsilon_2)\cos\alpha} = \frac{\sigma_2}{(1+\epsilon_1\epsilon_3)\sin\beta + (\epsilon_1-\epsilon_3)\cos\beta} = \frac{\sigma_3}{(1+\epsilon_1\epsilon_2)\sin\gamma + (\epsilon_2-\epsilon_1)\cos\gamma}, \tag{5}$$

where

$$\epsilon_i = \partial\sigma_i/(\sigma_i \partial\varphi_i).$$

EXPERIMENTAL

Columnar tricrystals of high purity (10–30 ohm cm) germanium have been grown by the "vertical crystal pulling" method.[11] This method,[12] adapted to the requirement of the present problem, is most convenient for the preparation of germanium multicrystals. A tricrystal of controlled orientation relationship can be grown by a gradual withdrawal of three seed crystals from the molten material. It was to be expected that an unwanted macrostructure and microstructure inside the crystal would strongly influence the experimental results on the grain boundary experiments. Twinning, random nucleation of stray crystals, and the generation of an excessive number of dislocations have to be avoided during and after growth.[13–16]

To produce tricrystals containing three tilt, or three twist boundaries, whose energies depend on two parameters only, special precautions must be taken.

First, a rather high degree of accuracy is required for the common orientation of the three grains in the columnar tricrystals. This orientation was kept within ± 10 min of the desired crystallographic orientation. In order to obtain the high degree of accuracy, the seed crystals were oriented by means of an x-ray Laue back

[7] W. T. Read, *Dislocations in Crystals* (McGraw-Hill Book Company, Inc., New York, 1953).
[8] C. Herring, *Physics of Powder Metallurgy* (McGraw-Hill Book Company, Inc., New York, 1951), p. 157.
[9] C. Herring, *Structure and Properties of Solid Surfaces* (Chicago Press, 1953), p. 5.
[10] C. S. Smith, Trans. Am. Inst. Mining Met. Engrs. **175**, 15 (1948).
[11] K. A. McCarthy and B. Chalmers, Can. J. Phys. **36**, 1645 (1958).
[12] J. Czochralski, Z. physik. Chem. **92**, 219 (1917).
[13] I. G. Cressell and J. A. Powell, *Progress in Semiconductors* (John Wiley & Sons, Inc., New York, 1957), Vol. 2.
[14] D. C. Bennett and B. Sawyer, Bell System Tech. J. **32**, 637 (1956).
[15] W. C. Dash, *Growth and Perfections of Crystals*, Proc. of an International Conference on Crystal Growth, Cooperstown, N. Y. (John Wiley & Sons, Inc., New York, 1958), p. 361.
[16] R. S. Wagner, J. Appl. Phys. **28**, 1679 (1958).

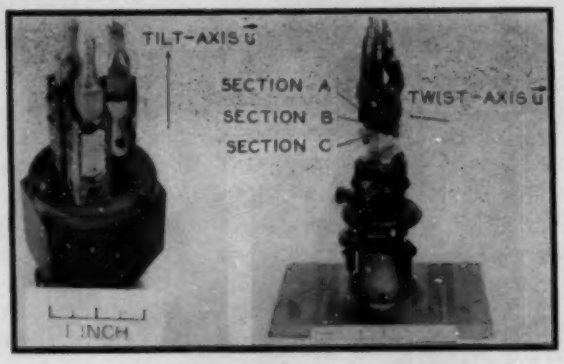

FIG. 1. (a) Seedholder for the tilt experiment. (b) Seedholder for the twist experiment.

reflection method with a specimen to film distance of 12 cm.

Secondly, the tilt axis around which the misorientation θ between the crystals is produced, is also kept within ± 10 min of the common crystallographic direction.

Thirdly, during crystal growth, the growth direction must coincide with the tilt axis. If this condition is not satisfied, an additional degree of freedom of the grain boundary can be introduced. Lastly, the misorientation angle θ between the seed crystals, the most important parameter with respect to the energy of the grain boundary, must also be determined with a high degree of accuracy. The misorientation angle θ was determined within ± 2 min by an optical method.

Figure 1 shows the seed holder arrangement for tilt and twist experiments.[17]

After crystal growth, the tricrystal was separated from its three seed crystals by means of a chemical cutting method. The tricrystal specimen was then reoriented and ground on a plane perpendicular to the direction of growth.

The germanium tricrystals were annealed at 900°C in a helium atmosphere up to 200 hrs. It was found that both the contact angles at the grain boundary junction and the position of the junction itself change with annealing time and temperature until local equilibrium is established.

For the observation of grain boundaries and dislocations, the tricrystals were subsequently chemically etched. For (111) faces a silver etch, and for (100) faces a copper etch was used.[18]

RESULTS AND DISCUSSION

⟨100⟩ Tilt Boundaries

It was observed that the energy of high-angle boundaries over a large range of misorientations is independent of the angle of misorientation. It was also observed that the energy of these boundaries does not depend on the boundary inclination. For the low-angle experiment, an orientation relationship between the three grains was chosen, such that the tricrystals contained two high-angle and one low-angle boundary.

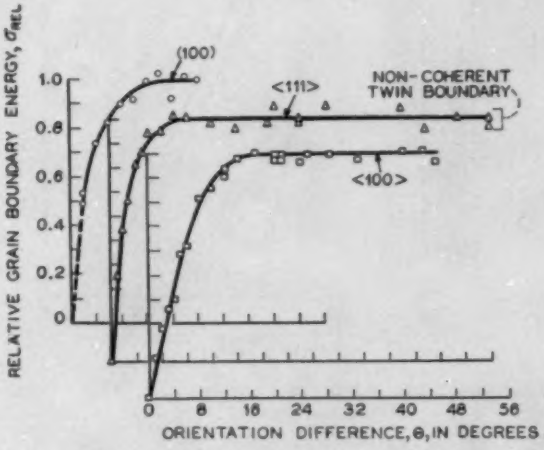

FIG. 3. Relative grain boundary energy as a function of orientation difference for ⟨100⟩ and ⟨111⟩ isoaxial and (100) isoplanar tricrystals.

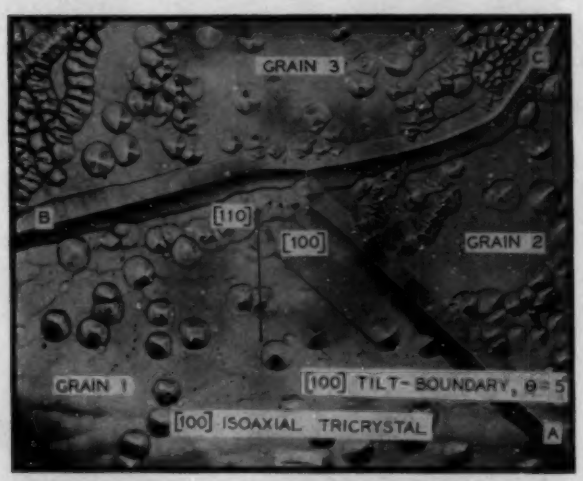

FIG. 2. Intersection of three ⟨100⟩ tilt boundaries. The chemically etched surface is perpendicular to the ⟨100⟩ tilt axis. The five degree boundary is either oriented symmetrically between the nearest (110) or the (100) planes of the adjacent crystals. Magnification 500×.

Figure 2 shows a photograph of the junction of three ⟨100⟩ tilt boundaries as observed on the (100) plane perpendicular to the ⟨100⟩ tilt axis. Boundary A is a low-angle boundary corresponding to a tilt angle of 5°. The misorientation θ across boundary B is 28.5° and across boundary C is 33.5°. The crystallographic etch pits, showing 4-fold symmetry, occur at the termination of dislocations in the (100) plane of observation. The two high-angle boundaries B and C are rather curved and do not exhibit any particular orientation relationship with regard to the adjoining grains. The low-angle

[17] R. S. Wagner, Ph.D. Thesis, Harvard University (1959).

[18] S. G. Ellis, RCA, LB 948.

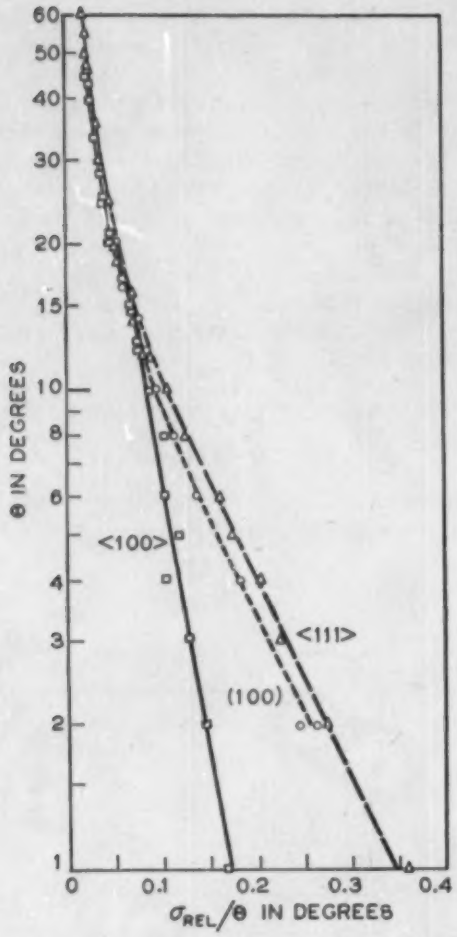

FIG. 4. σ_{rel}/θ as a function of θ for ⟨100⟩ and ⟨111⟩ isoaxial and (100) isoplanar tricrystals.

boundary, however, consists essentially of two segments. Furthermore, it can be seen with reference to crystallographic etch pits that these boundary segments are symmetrical with respect to the two nearest (110) or (100) planes, respectively. Within the range of misorientation from $\theta=1°$ to approximately 15°, the low-angle tilt boundaries always join the other two high-angle boundaries in such a way that the boundary can be described as a symmetrical tilt boundary with $\varphi=0°$. This indicates a marked dependence of the energy of a low-angle ⟨100⟩ tilt boundary on its boundary orientation. This orientation dependence requires the application of Eq. (5) for the evaluation of the unknown relative grain boundary energy of low-angle boundaries. Figure 3 shows the variation of the measured relative grain boundary energy as a function of the misorientation angle θ. The E *vs* θ curve consists of three different regions. In the first, from 0 to about 7° of misorientation, the slope of the curve remains essentially constant. This part is followed by a region of decreasing slope. Finally, from 15° up to 45° the energy of the high-angle boundaries remains constant within the accuracy of the experiment. No low-energy cusps in the large-angle region were observed.

From the equation derived by Read and Shockley, it follows that σ_{rel}/θ should be a linear junction of $\ln\theta$. Figure 4 shows this relationship for the ⟨100⟩ tilt experiment in germanium. From about 15° to 20° there is a definite deviation from linearity. The linear relationship from 20° to 45° is simply due to the fact that over this region of misorientation the energy of the grain boundary remains essentially constant.

Figure 5 shows an etched cross section of a ⟨100⟩ isoaxial tricrystal. The growth direction of the crystal and the ⟨100⟩ tilt axis are normal to the plane of the photograph. The misorientation across the grain boundary separating grains 1 and 2 is 3°. The misorientation between 1 and 3 is 28.5, and 2 and 3 is 31.5 deg, respectively. This tricrystal, grown under the condition of low temperature gradient in the liquid, exhibits fourfold symmetry in each grain. The straight contours of the tricrystal correspond to ⟨110⟩ directions of the individual grains.

The two high-angle boundaries are straight close to the intersection of the three grain boundaries; further out, they are rather curved.

The low-angle boundary, however, exhibits characteristic orientation changes. From the outside towards the grain boundary junction of the tricrystal, this boundary alternates between the orientations $\varphi=45°$, $\varphi=0°$ and $\varphi=45°$ and terminates again in a $\varphi=0°$ inclination.

The experimental results on the orientation effect of low-angle ⟨100⟩ tilt boundaries indicate that: (A) low-

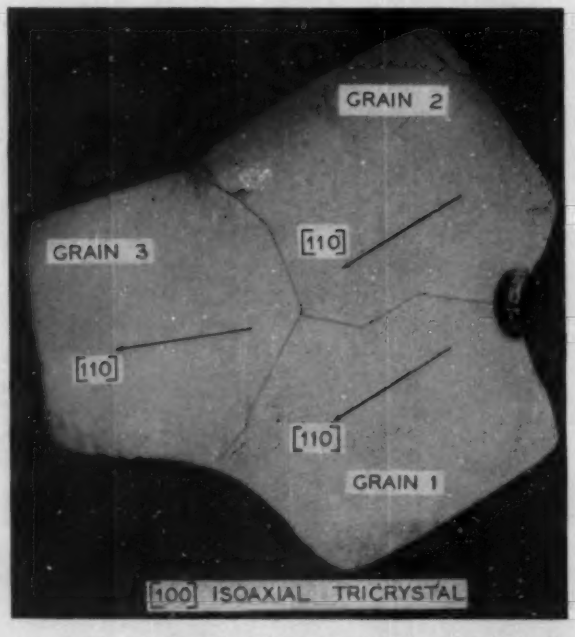

FIG. 5. Chemically etched ⟨100⟩ isoaxial tricrystal. The plane of the figure is perpendicular to the common ⟨100⟩ direction. Magnification 10×.

angle ⟨100⟩ tilt boundaries in the misorientation range from 1 to 15° show a marked preference for either of two orientations. (B) The first corresponds to an inclination of $\varphi=0°$ which is symmetrical with respect to the nearest (110) planes of the two adjoining grains. (C) The other corresponds to an inclination of $\varphi=45°$ which is symmetrical with respect to the nearest (100) planes in the adjoining grains. (D) The low-angle grain boundary assumes a finite radius of curvature where its inclination changes from $\varphi=0$ to $\varphi=45°$.

The experimental results on the orientation effect of ⟨100⟩ tilt boundaries in germanium can be explained by considering the variation of energy with boundary orientation for a grain boundary with two degrees of freedom.

Previous experiments on germanium[19] have verified that a dislocation in the ⟨100⟩ direction is possible. The Burgers vector in this material is a $\frac{1}{2}\langle 110\rangle$ displacement. The Read and Shockley equation for the energy of a two degrees freedom grain boundary is

$$E=E_0(\cos\varphi+\sin\varphi)\theta\left[A_0-\frac{\sin 2\varphi}{2}-\frac{\sin\varphi\ln\sin\varphi+\cos\varphi\ln\cos\varphi}{\cos\varphi+\sin\varphi}-\ln\theta\right], \quad (6)$$

where E_0 depends on the elastic constants of the material, θ and φ are the angles of misorientation and boundary inclination. A_0 depends on the unknown core energy of the dislocation.

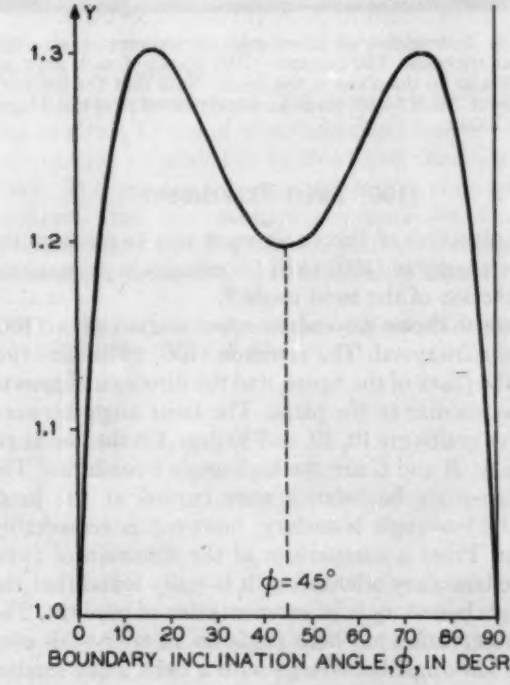

FIG. 6. Y vs φ.

[19] W. G. Pfann and F. L. Vogel, Acta Met. 7, 377 (1957).

For $\varphi=0$, as in the case of a symmetrical boundary, the equation simplifies to $E=E_0\theta(A_0-\ln\theta)$. A grain boundary in such an orientation would consist of an array of edge type dislocations with the same Burgers vector.

In order to account for the other orientation, one must consider the energy dependence on the inclination angle φ more rigorously.

Figure 6 shows the function

$$Y(\varphi)=(\cos\varphi+\sin\varphi)\times\left[A_0-\frac{\sin 2\varphi}{2}-\frac{\sin\varphi\ln\sin\varphi+\cos\varphi\ln\cos\varphi}{\cos\varphi+\sin\varphi}\right]$$

for $A_0=1$

$\varphi=0°$ corresponds to a principal minimum in the Y vs φ relationship. At $\varphi=45°$, however, there is a subsidiary minimum in the Y vs φ curve and therefore, a minimum in the energy vs φ function. For $\varphi=45°$, the grain boundary consists of an array of X and Y dislocations with a total density of $\sqrt{2}$ times the density of a $\varphi=0°$ boundary.

This dependence of the boundary energy on the inclination accounts for the two observed (110) and (100) orientations. The orientation of lowest energy corresponds to a symmetrical grain boundary with $\varphi=0$. If, however, directional changes are necessary for the boundary to conform to those constraints on it, the boundary will also assume a $\varphi=45°$ inclination instead of any random orientation.

⟨111⟩ Tilt Boundaries

The general properties of the ⟨111⟩ tilt boundaries were very similar to those of the ⟨100⟩ tilt boundaries. Firstly, the low-angle ⟨111⟩ tilt boundaries again exhibit a strong preference for certain boundary orientations. Secondly, the energy of high-angle ⟨111⟩ tilt boundaries remains almost constant over a wide range of misorientations. Thirdly, it was noticed that certain high-angle ⟨111⟩ tilt boundaries have a strong tendency to dissociate into three boundaries.[20]

Figure 3 displays the variations of the measured relative energies as a function of misorientation θ. The transition angle between low- and high-angle boundaries is at about 12 deg. Although there is some experimental scatter in the high-angle region, it is concluded that the energy remains essentially constant from about 12 up to 60 deg. No pronounced energy cusps were observed anywhere in the high-angle region. A cusp in the E vs θ curve might be expected for a tilt angle of 60 deg, where the two grains assume a twin relation with each other.

The plot of the function $\sigma_{\text{rel}}/\theta$ vs $\ln\theta$ is shown in Fig. 4. The relationship is linear for values of θ between 1 and approximately 15 deg. For larger angles, however, a distinct deviation from linearity is found.

[20] R. S. Wagner and B. Chalmers (to be published).

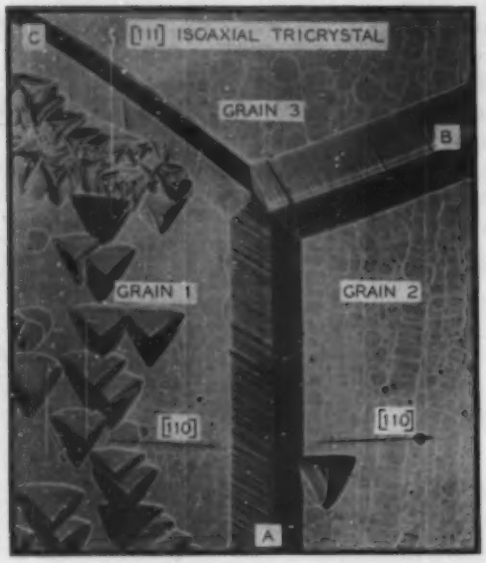

FIG. 7. Intersection of three ⟨111⟩ tilt boundaries. The chemically etched surface is perpendicular to the ⟨111⟩ tilt axis. The low-angle boundary A ($\theta=4°$) is oriented symmetrically between the nearest (110) planes of the adjacent crystals. Magnification 1000×.

Figure 7 shows the grain boundary function of three ⟨111⟩ tilt boundaries. It can be seen that the orientation of boundary A, the low-angle boundary ($\theta=4°$), is symmetrical with respect to the geometry of the etch pits in both grains. In this orientation, one of the three available Burgers vectors is perpendicular to the boundary trace. It is convenient to classify this boundary orientation as a $\varphi=0°$ inclination. Generally, it was observed that all low-angle ⟨111⟩ tilt boundaries terminate at the grain boundary junction in the $\varphi=0°$ inclination. This is presumably an orientation of minimum energy. If orientation changes are imposed, the low-angle ⟨111⟩ tilt boundaries assume another low-energy orientation, corresponding to an inclination angle $\varphi=30°$. In some cases, even a third orientation was observed with about $\varphi=10°$.

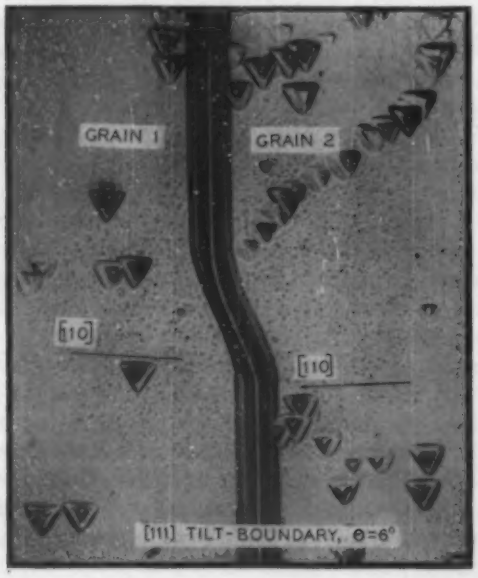

FIG. 8. Orientation change of a low-angle ⟨111⟩ tilt boundary.

The simplest dislocation model for a ⟨111⟩ tilt boundary could consist of an array of edge-type dislocation having a ⟨111⟩ dislocation direction. A boundary in the $\varphi=0°$ orientation would consist of dislocations of one type only with $b=\frac{1}{2}\langle\bar{1}10\rangle$. For $\varphi=30°$, two sets of dislocations are required with $b=\frac{1}{2}\langle 011\rangle$ and $b=\frac{1}{2}\langle\bar{1}01\rangle$. For any other intermediate boundary orientation all three kinds of dislocations would be required. A typical observed orientation change of a low-angle ⟨111⟩ tilt boundary is shown in Fig. 8.

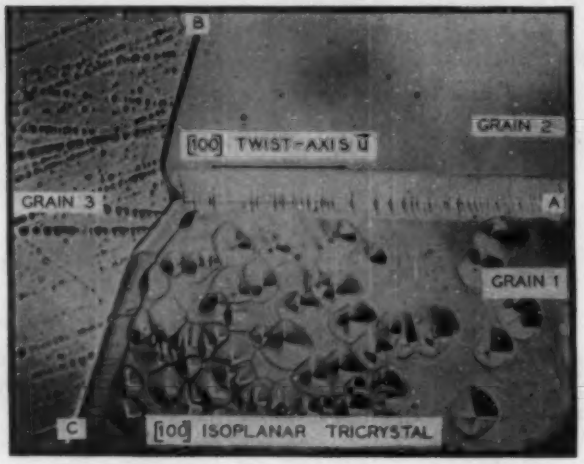

FIG. 9. Intersection of three grain boundaries in an (100) isoplanar tricrystal. The common (100) planes of each grain are perpendicular to the plane of the figure. Note that the low-angle boundary A (with $\theta=10°$) is in an orientation of pure tilt. Magnification 1000×.

(100) Twist Experiment

The objective of this experiment was to measure the relative energy of (100) twist boundaries in germanium, as a function of the twist angle θ.

Figure 9 shows an etched cross section of a (100) isoplanar tricrystal. The common ⟨100⟩ twist direction lies in the plane of the figure, and the direction of growth is perpendicular to the plane. The twist angle between the three grains are 10, 20, and 30 deg. A is the low-angle boundary, B and C are the high-angle boundaries. The two high-angle boundaries were curved at the junction; the low-angle boundary, however, is remarkably straight. From a comparison of the direction of twist and the boundary orientation, it is easily found that the low-angle boundary is in an orientation of pure tilt. The same observation has been made on all tricrystals containing low-angle boundaries with a twist angle smaller than approximately 18°. If orientation changes are necessary, the low-angle boundaries assume another

orientation which can be classified as one half $\sqrt{2}\theta\langle 110\rangle$ tilt combined with one half $\sqrt{2}\theta(110)$ twist.

The measured relative energy values are shown in Fig. 3. The experiment cannot be considered to be very accurate since the low-angle boundary in the pure tilt orientation is inclined by an angle $\theta/2$ to the direction of growth. The two high-angle boundaries, however, still contain the growth axis except in the immediate vicinity of the line of intersection.

Figure 4 displays the variation of $\sigma_{\text{rel}}/\theta$ *vs* $\ln\theta$. This relationship is again linear for values of θ up to approximately 10 deg. Owing to experimental difficulties, it was not possible to investigate more rigorously the high-angle region for values of θ larger than 20 deg.

The total energy of a twist boundary[21] in an isotropic material is

$$E=Gb/(2\pi)\theta(A-\ln\theta).$$

The energy of a corresponding tilt boundary is

$$E=Gb/[4\pi(1-V)]\theta(A-\ln\theta).$$

On assuming Poisson's ratio to be $\frac{1}{3}$, we find that in the isotropic case the energy of a twist boundary should be about 1.3 times the energy of a tilt boundary. Although these experiments do not permit the determination of the numerical value of this ratio, they clearly indicate that the energy of a (100) twist boundary is larger than the energy of an equivalent $\langle 100\rangle$ boundary.

CONCLUSIONS

It was observed that grain boundaries in germanium consist of a definite array of dislocations, when the misorientation angle between the crystals was not more than a few minutes of arc.

The relative energy of $\langle 100\rangle$ and $\langle 111\rangle$ tilt boundaries up to about 15 deg of misorientation changes with misorientation as predicted by Read and Shockley's equation. The present experimental results thus appear to indicate that the assumptions made by Read and Shockley are satisfied for dislocation spacings larger than approximately four interatomic distances.

For a misorientation θ corresponding to a $\langle 100\rangle$ tilt of about 15° and a $\langle 111\rangle$ tilt of about 12°, a transition was found to occur in the relative boundary energy *versus* θ relation. For misorientations larger than the transition angles, the grain boundary energy is essentially independent of the amount of misorientation. This indicates a significant but continuous change in boundary structure at the transition region. Additional evidence for the difference in the structure of low- and high-angle boundaries was found in the apparent dependence of the energy of low angle boundaries on the boundary orientation.

It was found that low-angle $\langle 100\rangle$ tilt boundaries are either in an orientation classified as $\varphi=0$ or $\varphi=45°$. In the first case, the orientation of lowest energy, the boundary plane is symmetrical with respect to the nearest (110) planes of the adjacent crystals. In the second case, the boundary is symmetrical with respect to the (100) planes.

Similar observations on the boundary orientation dependence were made for $\langle 111\rangle$ tilt boundaries. In this case, the low-angle boundary prefers mostly a symmetrical (110) orientation, and the less favorable symmetrical (211) orientation.

Low-angle (100) twist boundaries were not observed. Even under the most favorable conditions for the formation of such a boundary, it was observed that the boundary takes up an orientation of pure $\langle 100\rangle$ tilt, or an orientation which can be conveniently resolved into $\langle 110\rangle$ tilt and (110) twist.

Although the reported experimental investigation supports the assumed dislocation structure of low-angle grain boundaries in germanium, it does not give any detailed information on the structure of high-angle grain boundaries.

ACKNOWLEDGMENTS

Our colleagues at the Gordon McKay Laboratory, particularly K. McCarthy, K. A. Jackson, and C. Elbaum, assisted in this investigation with stimulating and fruitful discussions. We would like to express our gratitude to the Raytheon Manufacturing Company for their generosity in supporting this research through the loan of high-purity germanium.

[21] D. McLean, *Grain Boundaries in Metals* (Clarendon Press, Oxford, England, 1957), p. 28.

Production of Very High Magnetic Fields by Implosion*†

C. M. Fowler, W. B. Garn, and R. S. Caird
Los Alamos Scientific Laboratory, Los Alamos, New Mexico
(Received September 17, 1959)

Magnetic fields are produced in the 10–15 megagauss range by use of high explosives which compress the flux obtained from initial fields of approximately a hundred thousand gauss. The fields described here occupy a cylindrical volume and are essentially axial. A typical field might have these general characteristics: Peak field 14 megagauss; 2 μsec duration from 10–14 megagauss; field volume around peak, 6 mm diameter, 50 mm estimated length.

1. INTRODUCTION

THE principle upon which the production of the large magnetic fields described here depends is that of the conservation of flux enclosed within the boundaries of a perfect conductor.

The rate of change of the flux of a vector **A** included within the boundary of a moving surface of velocity **V** is given by the following expression‡:

$$\frac{d\varphi}{dt}=\int_S\left[\frac{\partial \mathbf{A}}{\partial t}+(\nabla\cdot\mathbf{A})\mathbf{V}+\nabla\times(\mathbf{A}\times\mathbf{V})\right]\cdot d\mathbf{S}. \quad (1.1)$$

For use here and later the following electromagnetic equations are cited:

$$\nabla\times\mathbf{E}=-\partial\mathbf{B}/\partial t \text{ (in vacuum)}, \quad (1.2)$$

$$\nabla\times\mathbf{B}=(1/c^2)(\partial\mathbf{E}/\partial t) \text{ (in vacuum)}, \quad (1.3)$$

$$\mathbf{E}+\mathbf{V}\times\mathbf{B}=0 \text{ (in a perfect conductor)}. \quad (1.4)$$

The flux of the magnetic vector **B** in a vacuum enclosed by a perfectly conducting moving boundary is seen to be constant from the foregoing equations, with the help of the equation $\nabla\cdot\mathbf{B}=0$.

Referring now to Fig. 1, suppose an initial axial field B_0 is enclosed by a perfectly conducting cylindrical liner of radius r_0. If the liner is somehow contracted to a smaller radius r_1, by explosives for example, the field must increase to a new value B, such as to conserve the flux. Thus

$$B=B_0(r_0^2/r_1^2). \quad (1.5)$$

The field B defined by this equation is actually a space average field over the liner interior. The fields determined by the Maxwell equations exhibit a space-time structure, some comments about which will be given in Sec. 5.

Explosives offer two unique advantages in compressing the flux. First, the compression times (of the order of a few μsec) are short enough that the cylindrical metal liners, which trap the flux, behave essentially as perfect conductors. Secondly, the magnitude of the magnetic fields which can be obtained by flux compression are determined by the pressures which the driver-liner system is capable of sustaining. Magnetic pressures of the order of millions of atmospheres are developed with the fields described here, and it is clear that explosives of some type are necessary to contain them, even momentarily.

A fairly extensive, but perhaps not complete, literature search indicates that the first use of explosives in flux trapping occurred at the Los Alamos Scientific Laboratory. A report summarizing this work was written by Joseph L. Fowler[1] in 1944. This work, dealing partly with classified matters, employed field measurements to measure liner motion. Typically, initial field values of a few gauss were compressed to values of a few hundred gauss.

About ten years later, I. Terletskii[2] proposed the use of explosively collapsed fields to accelerate particles. This short mathematical paper employed Eq. (1.5), and suggested use of explosives for compressing the flux. It appears to be the first suggestion of explosive flux compression in the open literature. It also gives a formula for the relaxation time of copper conductors.

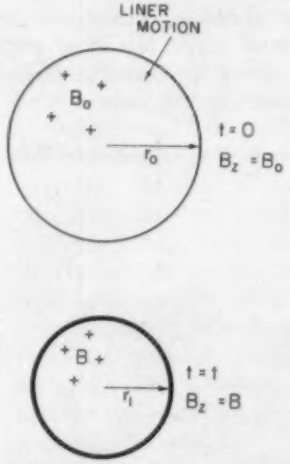

FIG. 1. Cylindrical implosion geometry.

* Work done under the auspices of the U. S. Atomic Energy Commission.

† A preliminary version of this paper was presented at the Southwestern Meeting of the American Physical Society at Austin, Texas on March 7, 1959.

‡ Here, and elsewhere in the text, no effort is made to preserve relativistically correct forms. Also, unless stated otherwise, mks electromagnetic units are employed.

[1] J. L. Fowler (private communication).

[2] Ia. P. Terletskii, "Production of very strong magnetic fields by rapid compression of a conducting shell," J. Exptl. Theoret. Phys. Transl. (U.S.S.R.) **32**, 301 (1957) (from a 1952 article).

About the time of the Terletskii paper, Frank J. Willig, now with the Emerson Radio Corporation, and Edward Teller suggested that experiments of this nature be undertaken with the direct aim of achieving high magnetic fields. Work was carried out intermittently for two or three years along these lines. A report was written sometime later by W. B. Garn.[3] Magnetic fields up to 200 000 gauss, and possibly somewhat higher, were achieved. Many of the techniques described in this report are refinements of those developed by Garn, and earlier by J. Fowler's group.

2. EXPERIMENTAL ARRANGEMENTS

A schematic for the complete experiment is presented in Fig. 2. Initial fields are produced within the conducting liners by discharging a condenser bank through a coil system at the liner. At a predetermined time a cylindrical ring of explosive surrounding the liner is detonated. The subsequent implosion of the liner compresses the magnetic flux, with a corresponding increase in the magnetic field.

Field measurements during the implosion are effected with one or more calibrated pickup probes. Occasionally two probes are used, one of which might be located outside the liner. The condenser discharge current preceding the flux compression is also usually measured to establish the initial flux within the liner. A toroidally wound pickup coil surrounding a main current lead has proved adequate for this measurement.

Upon occasion, a framing camera is employed for the purpose of observing the liner motion during the implosion.

The schematic in Fig. 2 shows some of the components enclosed within a dotted rectangle. These components are on the firing table and are destroyed with each shot. These include the coil-liner assembly, pickup probes, and lead cables. All other equipment is housed in bunkers, or otherwise protected.

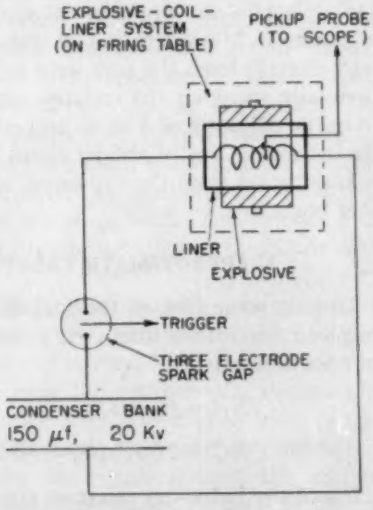

FIG. 2. Schematic diagram of a cylindrical implosion system.

[3] W. B. Garn (private communication).

Timing is achieved by a versatile delay unit in which trigger pulses are available from three variable delay channels. The delay unit can be triggered by an external pulse or, when a camera is used, by a pulse from the camera.

Following the general discussion in the foregoing, some of the components used will now be described.

Condenser bank.—The bank consists of twenty 7.5-μf, 20-kv condensers connected in parallel. The bank is triggered by pulsing the middle electrode of a three-element spark gap.[4] The discharge current is carried by twelve RG-8/U cables in parallel. These cables can be protected from blast up to within 5 or 6 ft of the explosive. The lead connection at the coil end is effected by separate 8-ft lengths of cable. These lengths are so made as to couple easily to the main condenser leads as well as to the load coil. Only this length is destroyed with the shot.

Coils.—Several coil types have been used. For higher initial fluxes, coils are sometimes wound with No. 10 solid copper wire, with nominal 600-v insulation, spaced approximately three turns per inch. Other coils have been machined from brass tubing and wrapped with insulating tape. The high flux coils are placed inside the conducting liners as shown in Fig. 2. To prevent breakdown between the coils and the liner, twenty to thirty mils of polyethylene sheet are wrapped between the coil and liner. To minimize the opposing return flux outside the coils, the spacing between the coil and liner is kept as small as possible. Average initial fields up to 100 000 gauss over volumes of 3-in. diam by 3-in. length may be produced with the internal coils. Occasionally, a pair of external coils is employed, one coil on each side of the explosive ring. These coils are generally wound with No. 6 magnet wire on a grooved Micarta base. An outer Micarta cylindrical sleeve protects the coils. These and other coil constructions have been used for various applications, with inductances ranging from 2–15 μh.

Liners.—The conducting liners are cut from commercially available brass or copper tubing, usually of $\frac{1}{8}$-in. wall thickness, and for the experiments described here, of 3-in. i.d. The preparation of the liner has proved to be one of the most critical procedures of the experiments. The magnetic fields produced by the coils are transient. With the initial field buildup periods used, closed brass or copper liners behave as nearly perfect conductors, so that very little flux can be induced within them. To permit induction of the initial fields the liners have an axial slot milled in them. The liners thus act as open one turn secondaries during the initial field buildup. However, during this period the liner slot must be able to hold off voltages up to 2 kv. The requirement that the liner be an open circuit during initial field buildup is accompanied by another—that the liner be a conductor during flux compression. A rather critical compromise has been effected, in which

[4] Schofield, Lier, Tuck, and Dike: Spark Gap patent applied for, Drawing Numbers 45Y-23149 and 45Y-23151.

FIG. 3. Body of half-turn probe used in high field measurements.

the liner slot is insulated with a 0.007-in. thick strip of Scotch electrical tape. When sufficient care has been exercised in placement, the tape is usually able to withstand the potential difference induced across the slot during field buildup. When the explosive detonation reaches the liner, the slot is closed.

Most of the experimental failures that occur result from either a breakdown across the slot during field buildup, or a rupture of the field coil before the liner is closed.

The slot is milled nearly tangential to the liner circumference. This design has two advantages. First, the slot is more easily closed by explosive action. Secondly, the metallic jets, which are almost invariably produced by explosive action on such configurations, are greatly reduced in radial intensity. A thin-walled glass tube covering serves as sufficient protection for axial probes.

For applications involving very small flux it is sometimes possible to use direct current fields. In these cases, the liners are unslotted and the difficulties cited in the foregoing are eliminated.

Probes and calibrations.—Depending upon the particular application, effective probe areas have ranged from 0.05 to 10 cm^2. The probes are built integrally with the coaxial cables which carry the signals from the shot assemblies to the detection equipment in the firing bunkers. Figure 3 shows the brass probe body with the "half-turn" coil usually employed for high field measurement probes.

The coaxial cable core lead, with insulation, is run through the brass body and soldered to the tip (a). The cable ground shield is attached to the tube at (b). The slotted portion of the combination ground and shield cylinder is packed with silicone insulation grease. The entire assembly is then inserted in 1-mm wall glass tubing, the coil pickup loop being thoroughly embedded in silicone grease. A layer of copper foil is wrapped around the glass assembly, with Scotch electrical tape insulation, to prevent the foil from closing upon itself. The foil is also grounded to the coaxial cable shield at one point. Finally, the entire assembly is doubly wrapped with Scotch electrical tape, or enclosed in a thin-walled glass cylinder. The over-all probe diameters can be held to 7.5 mm, or to 10 mm when a second outer glass sleeve is used.

Each probe used in an experiment is calibrated by comparing its pickup voltage in a standardized coil with that of a calibrated standard probe. The same condenser bank used in the implosion experiments serves as the source for probe calibrations.

Periodically, a number of interrelated checks are made on the various electronic components employed. These include comparison of calculated currents with measured currents, calculated fields with measured fields, calculated integration of emf signals with direct electrical integration of the signals, and calculated with measured area of the standard probe. In addition to these tests, a continual check on the accuracy of oscilloscope calibrations and condenser voltage readings is maintained.

A general assessment of these various tests and an analysis of the probe circuits suggests that the final field measurements obtained are accurate to within $\pm 15\%$.

Explosives.—All explosive charges are of Composition B(64/35/1:RDX/TNT/*wax*) and are machined to within two or three mils in all critical dimensions. Most of the cylindrical charges used here are of $3\frac{1}{4}$ in. i.d. and either 8 or $9\frac{1}{4}$ in. o.d. Axial thicknesses vary from $1\frac{1}{2}$ to 4 in.

Cylindrical detonation is approximated by firing simultaneously one or more rings of high quality detonators closely spaced around the outer diameter of the explosive.

Framing camera.—A fast framing camera was used for some experiments to observe the liner collapse during implosion. Framing intervals varied from 0.3 to 0.6 μsec. Measurements of the liner diameter are read directly from the film strip as a function of time. Generally speaking the collapse can be followed from an initial diameter of 3 in. to around $\frac{1}{2}$ in. At this point the increasing size of the jet cloud from the liner slot, or blast gases from the explosive, usually obscures the liner boundary.

3. APPROXIMATE CALCULATIONS

To gain some idea of the magnitude of the electromagnetic quantities involved, consider Eq. (1.5) and its time derivative:

$$B(t)=B_0 r_0^2/r_l^2, \tag{1.5}$$

$$\dot{B}(t)=2B_0 r_0^2 v_l/r_l^3=2B(t)v_l/r_l. \tag{3.1}$$

Use of the induction equation gives as the tangential electric field strength, and the emf around a circle of

radius r,

$$E_\theta = B_t v_l r / r_l, \tag{3.2}$$

$$\text{emf} = 2\pi r^2 B(t) v_l / r_l. \tag{3.3}$$

In these equations B is an axial magnetic field with initial value B_0. The liner radius is designated by r_l with initial value r_0, while r is the radius of an arbitrary point such that $r \leq r_l$. The liner velocity is v_l.

A typical example might start with an initial field $B_0 = 12$ webers/m^2 and an initial liner radius $r_0 = 0.038$ m. At a later time we assume that $r_l = 0.005$ m and $v_l = 1.5 \times 10^3$ m/sec. Then, from Eq. (1.5), $B = 690$ webers/m^2 or 6.9 megagauss. At a radius r of 0.004 m the tangential field is 8.3×10^5 v/m, and the emf is 21 000 v. The emf over a half turn pickup probe with a 0.002-m radius would be 5200 v.

The complete description of the electric and magnetic fields obtained during an implosion can be calculated from Eqs. (1.5) and (3.2) only when the liner radius and velocity are known as functions of time. A solution to this problem was obtained by H. C. Hoyt and P. Kazek of the Los Alamos Scientific Laboratory. These men coded for IBM 704 calculation the complete one-dimensional radial implosion problem with the following arbitrary parameters: explosive inside and outside diameters; liner inside and outside diameters; initial magnetic field within the liner. The hydrodynamic and thermodynamic equations of state for several different explosives as well as several liner materials are available. The internal liner boundary was subject to the pressure defined by the following equations:

$$p = B^2(r_l)/2\mu_0; \quad B(r_l) = B_0 r_0^2 / r_l^2. \tag{3.4}$$

Some of the simplifying assumptions in their formulation are the following. First, edge effects are ignored. Since the implosion times are only a few microseconds, sufficient time is not available for edge influence to disturb the motion greatly at the axial center. Internal probe measurements are normally made at this point. Secondly, only normal magnetic pressures are considered. The magnetic shear stresses are of the same order of magnitude as the pressures. The omission of these stresses may be serious. At the present time, however, hydrodynamic flow calculations of this type involving more than one space variable are not feasible. In common with other calculations presented here, no resistive losses are considered. This implies a perfectly conducting liner and no losses to the air within the liner.

Figures 4 and 8 in the following section show the results of some of these calculations. The following general remarks are of interest.

1. Around maximum flux compression, the inner liner radius exhibits oscillations. These arise from competition between the magnetic pressure (very strongly dependent upon the liner radius) and the explosive pressure. Maximum compression occurs at the first turnaround radius, designated by r_t in Fig. 4, since the explosive pressures are gradually diminished as the detonation products are blown outward radially.

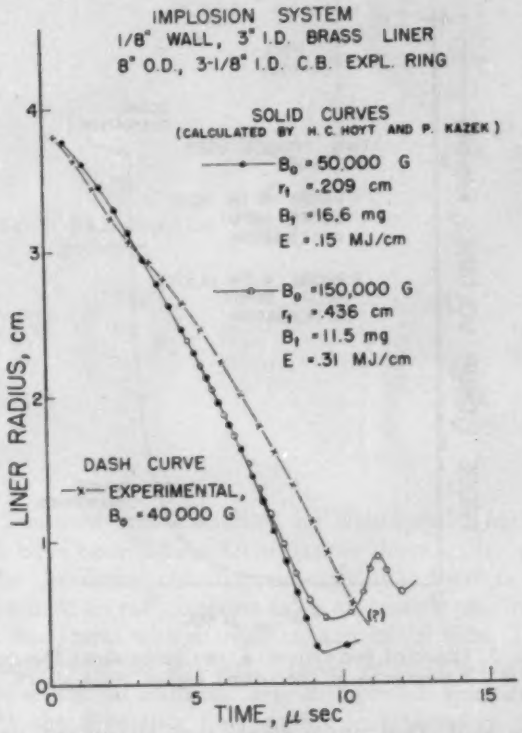

FIG. 4. Calculated and observed liner motion. Quantities shown for the calculated curves are the initial field in gauss, the turnaround radius in centimeters, the field at turnaround radius in megagauss, and the energy at turnaround in megajoules per centimeter of axial length.

2. For initial fields and geometries described here, the liner radius motion is largely independent of the initial field except near the turnaround radius.

3. As far as pressure dependence is concerned, the magnetic field behaves mathematically as an ideal gas with $\gamma = 2$. It is not surprising therefore that as the initial field strength is increased the maximum fields attained decrease and the turnaround radii increase.

4. A calculation of magnetic field energy shows that for lower initial fields there may be as much as a thousand times the energy per centimeter of axial length at r_t over that in the initial field. Up to 15–20% of the energy available in the explosives may be converted to electromagnetic field energy.

4. EXPERIMENTAL RESULTS

Figure 4 shows calculated liner radius variations with time together with an experimental measurement of the same variation obtained from a framing camera record. The agreement is good considering the various approximations involved in the calculations. The liner collapse time appears to be about 2 μsec longer than that predicted by theory.

Reproduced as Fig. 5 are simultaneous records obtained from two identical axial probes employed in the

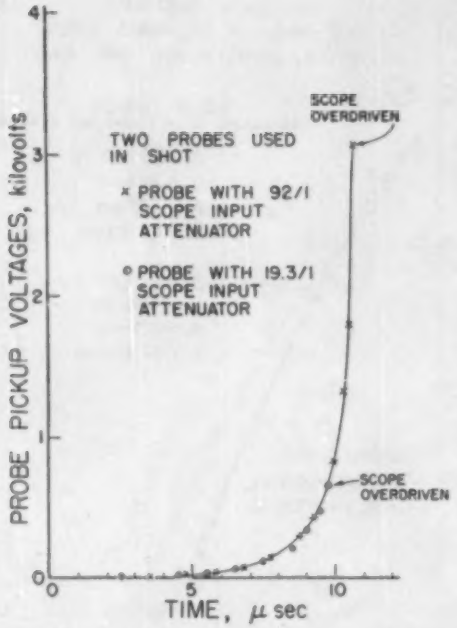

FIG. 5. Observed emf's from a two probe shot. The field is 1.2 megagauss at the second highest point shown.

same shot. One probe signal was attenuated much more than the other so that the field could be measured more accurately over a wider range. Integration of the signal record, with the probe area of 0.14 cm², gives a field of 1.2 megagauss at the second highest voltage point shown. More recently, electrical integrators consisting of simple resistance-capacitance networks have been employed with the probes.

Figure 6 shows a magnetic field record obtained with a probe placed on the axis, but outside of the liner. The probe was located about 10 in. from the liner center, and the peak field obtained was several hundred gauss. Rough calculations show that as long as the initial flux is trapped by the liner the field in this probe should be essentially constant. The vertical scale

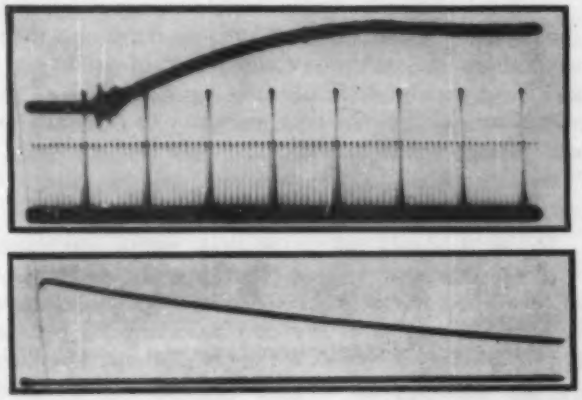

FIG. 6. Magnetic field record obtained from an external probe. The probe record (upper trace) indicates a field increase of several hundred gauss. A timing base shows 1 and 10 μsec markers. The lower pulse is an amplitude calibration signal.

shown on this trace is proportional to the axial field at the probe. Time is measured on the horizontal scale, the large markers indicating 10-μsec intervals. The scope sweep, started at time zero, preceded the condenser discharge by 10 μsec. It will be noted that a couple of microseconds elapsed before the gap triggered, a delay which arises primarily in the triggering circuit employed. The explosive was fired at 42 μsec. For this explosive system, 13 μsec were required for the detonation front to reach the liner. The liner slot closed at 55 μsec, a time previously established to achieve peak initial field for this coil system. The implosion trapped the flux and held it nearly constant well beyond the time when the first turnaround radius occurred. This is not surprising since the central flux most likely is well surrounded with metal for many more microseconds. This test is not as definitive as it might seem since essentially the same results would be obtained so long as the flux is confined to within a three- or four-centimeter diameter circle.

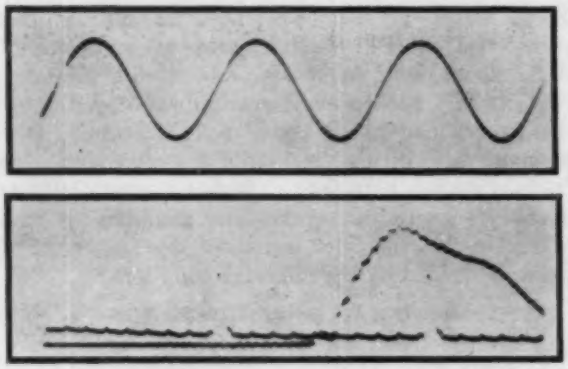

FIG. 7. High magnetic field record obtained from internal probe. Liner collapse begins at 6 μsec, peak field of 14.3 megagauss occurs at 17 μsec. A time base trace with 1 μsec and 10 μsec marks is superimposed on the record. The sinusoidal trace is a calibration signal.

Figure 7 is the record of a typical high field test shot. As before, the horizontal time scale has large 10 μsec markers while the vertical scale is proportional to B. The initial field was 90 000 gauss and the peak field was 14.3 megagauss. Figure 8 shows the values of B calculated from this record using the probe area and the time constant RC of the integrator. A comparison is made with theoretical curves. The time to build up to maximum field was somewhat longer than theoretically predicted. This result is consistent with the liner collapse measurement shown in Fig. 4.

The situation prevailing at the turnaround radius is probably a complicated one, especially with the probes filling the center of the cylinder. For this shot the calculated turnaround radius is only 20% greater than the pickup probe radius. The presence of the glass tubing shields could give rise to spurious effects by transmitting shocks to the pickup probe and imparting motion to it not necessarily the same as that of the liner proper.

For this reason the fields measured after the time of the maximum field cannot be relied upon even though the turnaround feature seems to be in evidence.

A summary of typical results obtained with the more or less standardized geometry employed here follows.

Initial flux is controlled by varying the condenser discharge voltage and by the use of different coil designs. The spread of initial fields used was from about 25 000 gauss to somewhat over 100 000 gauss. Theoretical calculations plotted in Fig. 4 show that for lower initial fields, the turnaround radii are smaller but the turnaround fields are higher.

The probes used for field measurements had a 2.3 mm radius. According to the calculated curves in Fig. 4, all

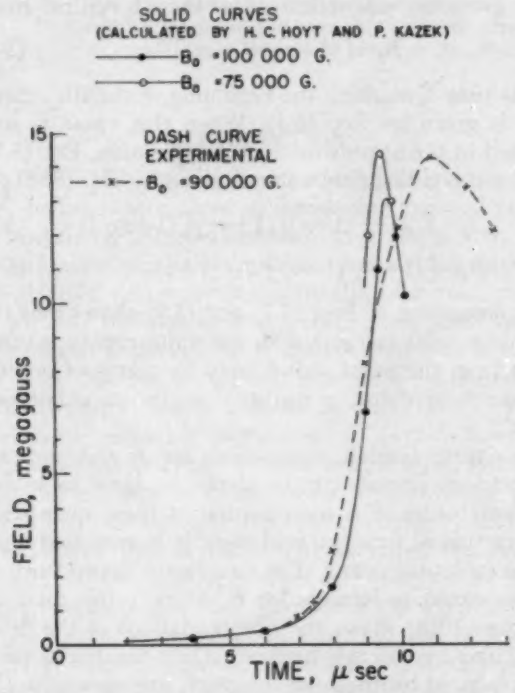

FIG. 8. Calculated and observed magnetic fields for shot giving record of Fig. 7.

initial fields lower than 50 000 gauss have turnaround radii less than the probe radius. This means that for low initial field shots the probe is destroyed before maximum field is reached. Experimentally, 25 000 gauss initial field shots gave measured final fields of around 2 to 3 megagauss which were still increasing rapidly at the time of probe destruction. Other experiments starting with initial fields greater than 50 000 gauss have produced maximum recorded fields up to about 15 megagauss. The record reproduced as Fig. 7 and the experimental curve plotted in Fig. 8 show an example of a high initial field (90 000 gauss) experiment. All of these results are in rough quantitative agreement with the Hoyt-Kazek calculations.

Both copper and brass liners have been used. Within

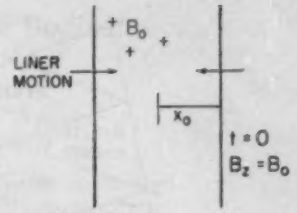

FIG. 9. Plane implosion geometry.

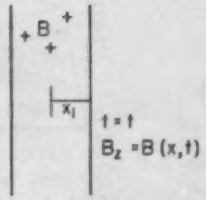

the limits of reproducibility no significantly higher fields have been obtained with copper liners.

The theoretical calculations imply that there is no upper limit on the magnetic fields obtainable provided that one starts with a small enough initial field. The turnaround radius, however, quickly becomes too small to be useful. In addition, lack of implosion symmetry limits the minimum liner radius and therefore the maximum attainable field for a given geometry.

A method of obtaining higher peak fields of useful dimensions is to scale up the radial dimensions of the explosive, liner and coil. The energy available in the condenser bank must be increased correspondingly in order to fill the larger volume with the initial field. A condenser bank of about twice the capacitance of the present bank is now under construction. With this bank, and with suitable scaling, it is anticipated that fields in excess of 20 megagauss can be produced for a microsecond or more over a radius of 4 mm.

5. DETAILS OF THE FIELD STRUCTURE

It has been mentioned earlier that a space-time field structure actually exists which is not displayed in the approximate formulas developed in Sec. 3.

Exact solutions to the cylindrical problem have not been obtained. It is possible, however, to write down simple analytic expressions for the field variables for the idealized plane implosion. The analysis which follows compares various electromagnetic quantities obtained in the approximate manner with precise solutions to the same idealized problem. The agreement is shown to be good to one part in a hundred thousand. The agreement for the plane case is taken to imply similar agreement for the cylindrical case, even though it is possible that instantaneous field singularities exist at the center in the ideal cylindrical problem.

Figure 9 gives the initial geometry as well as the geometry at a later time for the plane implosion. The liners are taken as perfect conductors, and the region between is assumed evacuated. For symmetric liner

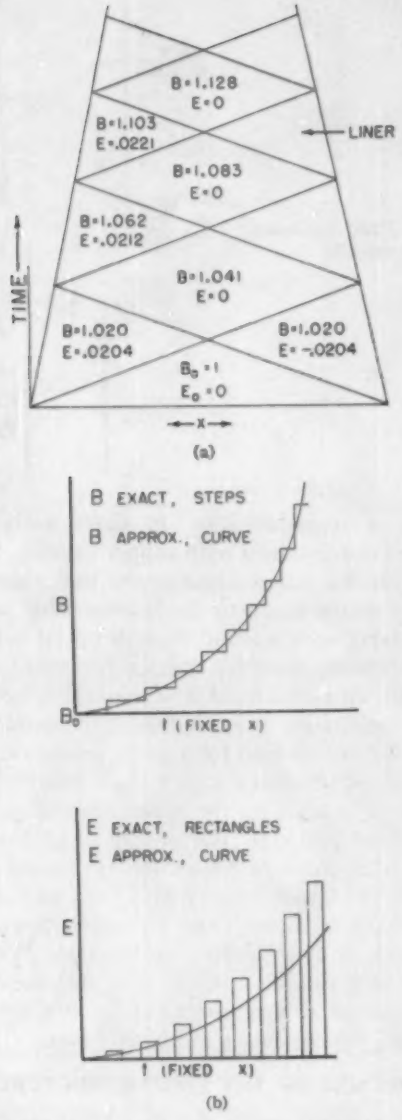

FIG. 10. (a) Field zone structure for symmetric plane implosion; (b) comparisons of exact and approximate values of B and E fields.

motions v along the X axis and field B along the Z axis, the field E is parallel to the Y axis. Equations (5.1) and (5.2) are obtained in the same approximate manner as sketched in Sec. 3 for the cylinder:

$$B=B_0x_0/(x_0-vt), \tag{5.1}$$

$$E=-xB. \tag{5.2}$$

For the precise analysis Eqs. (1.2) through (1.4) reduce to the following:

$$(\partial E/\partial x)+(\partial B/\partial t)=0;$$

$$(\partial B/\partial x)+(1/C^2)(\partial E/\partial t)=0; \tag{5.3}$$

interior fields

$$E+vB=0 \quad \text{at} \quad x=-x_1;$$

$$E-vB=0 \quad \text{at} \quad x=x_1. \tag{5.4}$$

By the method of characteristics, Eqs. (5.3) yield the relations

$$E+BC=\text{constant along lines of slope}+C, \tag{5.5}$$

$$E-BC=\text{constant along lines of slope}-C. \tag{5.6}$$

The lines of slope $\pm C$ divide the space-time region into zones, as shown in Fig. 10(a). In order to show details of the fields, the unrealistic situation is pictured in which $v_l=0.02\ C$. The initial magnetic field B_0 is taken as unity, while the initial electric field is zero. In the results given in the following the velocity of light is taken as unity, as is the initial plate separation, $x_0=1$.

Without going into details it may be shown that Eq. (5.7) gives the magnetic field in the ith central zone:

$$B_i=[(1+v)/(1-v)^i]B_0. \tag{5.7}$$

The time t_i marking the beginning of the ith central zone is given by Eq. (5.8). When this value is substituted in the approximate field expression, Eq. (5.1), the corresponding field value is given by Eq. (5.9):

$$t_i=1/2v-[(1-v)/(1+v)]^i[(1+v)/2v], \tag{5.8}$$

$$B_i=[(1+v)/(1-v)]^iB_0/(1+v). \tag{5.9}$$

A comparison of Eqs. (5.7) and (5.9) shows that the magnetic fields calculated in the approximate manner differ from the exact values only by terms of order v compared to unity, a quantity in the neighborhood of 10^{-5}.

In similar fashion, expressions for E and the emf around loop circuits can be shown to agree to within the same order. For computation of these quantities, the fraction of time the field point is in zero field must be taken into account. The coordinate dependence of the approximate formula for E enters in this manner.

Figure 10(b) shows the time variations of the fields calculated by the two methods. Only the fine details, characterized by the zone structure, are missing in the approximate solutions developed in earlier sections.

Some additional calculations for the plane implosion case have been carried out by J. N. Fritz. A detailed treatment of these results will be published later, but Fritz has kindly permitted us to cite one of his results here. By allowing an appropriate reflection coefficient, the characteristic treatment is extended to take into account the finite liner conductivity. It is found that the high frequency components, with wavelengths of the order of liner dimensions, are damped out severely. The total flux loss, however, is only a few percent for systems paralleling those employed here. Although little appears to be known about metal conductivities under the extreme pressures to which the liners are subjected here, it would require at least a tenfold decrease in conductivity to limit the flux trapping capacity seriously.

JOURNAL OF APPLIED PHYSICS VOLUME 31, NUMBER 3 MARCH, 1960

Grain Boundary and Lattice Diffusion in Polycrystalline Bodies*

H. S. LEVINE AND C. J. MACCALLUM
Sandia Corporation, Albuquerque, New Mexico
(Received October 12, 1959)

Diffusion in a polycrystalline body is discussed under the assumption that two interrelated mechanisms consisting of diffusion through the grains and in the boundaries around the grains are dominant in different penetration regions. The general behavior of the average concentration-distribution of diffusant is described for the separate action of each mechanism, and the effects of their combined action are inferred. A realistic diffusion model for a polycrystalline body and a suitable empirical function to describe the loss of diffusant from the boundaries to the grains form the basis for these computations.

Results are specifically applied to the analysis of the usual sectioning technique for measuring the ratio of grain boundary to lattice diffusion constants in a polycrystalline body. It is shown that, in the penetration range most commonly covered in polycrystalline diffusion experiments, the log of the average concentration varies as the 6/5 power of penetration depth contrary to the linear law reported previously. Comparison is made between the present and previous methods for establishing the grain boundary diffusivity of silver. The results are found to differ by a factor of 3 or 4. Criteria for validity of the method associated with the relative magnitudes of reduced time, grain size, and the ratio of grain boundary to lattice diffusion constants are established. Some of the results reported for Zn and Cd do not satisfy these criteria.

INTRODUCTION

DIFFUSION in the boundaries of polycrystalline bodies is recognized as influencing many physical and metallurgical processes such as grain growth, recrystallization, plastic deformation, and whisker growth. Quantitative values for boundary diffusion coefficients are not only of value in interpreting these phenomena, but are also important in boundary structure studies.

A large fraction of the available data on boundary diffusion coefficients is a direct result of one type of experiment involving deposition of a thin layer of radioactive material on the surface of a polycrystalline body and subsequent measurement of its average concentration distribution throughout the body by analysis of successive thin sections. The accepted theory for this method, originally described and analyzed by J. C. Fisher,[1] predicts that the logarithm of the average concentration varies linearly with penetration depth, in contrast with the penetration squared behavior of single crystals. Fisher's analytical result, however, was established for a simplified diffusion model, representing the polycrystalline body, only by making many restrictive assumptions in the theory. The end result is some lack of confidence even though many experiments appear to confirm the predictions.

The theory has been the subject of several additional publications. R. T. P. Whipple[2] examined the same problem with fewer assumptions and found asymptotically a $\frac{4}{5}$ power dependence of the logarithm of the concentration on penetration. This conclusion, however, was clearly valid only at relatively great penetration depths.

Turnbull and Hoffman[3] attempted subsequently to reconcile the two theories by showing that Whipple's $\frac{4}{5}$ power relationship resulted in a nearly linear graph in the experimental range with a slope equivalent to that derived by Fisher. Their conclusions may be questioned, however, because of the use of Whipple's theory outside its range of validity, as well as because of certain computational inaccuracies.

Other aspects of this problem have also been considered. Turnbull[4] attempted to clarify the limitations imposed by grain size. Roe[5] considered various modifications of the Fisher model. LeClaire[6] pointed out a modification that would permit the use of concentration contours.

In summary, the effects of grain size, bulk diffusion from the specimen surface, and exposure time have not been fully clarified, nor have the limitations of the method or its range of validity been fully explored. Our objective is to provide additional information on these matters and to further clarify the theory.

We consider two major interrelated diffusion mechanisms to be involved in polycrystalline diffusion; namely, diffusion from the specimen surface through the grains, and diffusion around the grains through the boundaries. These two processes are, of course, not strictly separable as each one affects the other. We believe, nevertheless, that the very small volume fraction and the very high diffusivity of the grain boundaries do, in fact, allow the two mechanisms to be considered separately in certain regions. In a very thin region near the exposed surface, ordinary bulk diffusion is completely dominant, the boundaries play little or no role, and the solution to the diffusion problem is known. At larger penetrations, the boundaries play the crucial role; this is the region of experimental interest, and the major effort in the next

* This work was performed under the auspices of the U. S. Atomic Energy Commission.
[1] J. C. Fisher, J. Appl. Phys. **22**, 74 (1951).
[2] R. T. P. Whipple, Phil. Mag. **45**, 1225 (1954).
[3] D. Turnbull and R. E. Hoffman, Acta Met. **2**, 419 (1954).
[4] D. Turnbull, "Grain Boundary and Surface Diffusion," *Atom Movements* (American Society for Metals, Cleveland, Ohio, 1951), p. 129.
[5] G. M. Roe (private communication); see also, Phys. Rev. **83**, 871 (1951).
[6] A. D. LeClaire, Phil. Mag. **42**, 468 (1951).

several sections will be devoted to obtaining a solution of the diffusion problem in this region. There is an intermediate region where these two mechanisms are of comparable size, and here no quantitative conclusions can be drawn.

In the region of experimental interest, our basic assumption is that diffusion through the boundaries is so much more rapid than diffusion into the lattice that the grains can be considered simply as passive "sinks" in the diffusion process. This is based on the experimental fact that the boundaries fill very rapidly with diffusant,[7] and diffusion then takes place into any given grain from all sides. Furthermore, it is believed that in a boundary only a few atoms thick it is meaningless to consider concentration gradients across the thickness of the boundary. We depart from the simplified model used by previous workers,[1] and establish instead a more realistic diffusion model. After selecting an empirical function for loss of diffusant from the boundaries to the grains, the problem is reduced to quadrature by the use of Laplace transforms.

DIFFUSION MODEL

Consider a polycrystalline material that is macroscopically homogeneous. According to Smith,[8,9] the randomly oriented grains in such a body are polyhedra and no one shape can be regarded as typical. On the average, there would be 24 corners and 14 faces with 5 1/7 edges per face on a grain. The mean linear dimension, $\langle l\rangle$, of a grain can be established by a simple linear grain boundary intercept counting on a random two-dimensional section of the body. If λ is the total length of grain boundary trace exposed per unit area of a random section through the body and σ is the total grain boundary surface area of the separated grains per unit volume of the body then, without any assumption regarding the actual shape of the grains or disposition of the boundaries, one can show that

$$\sigma=4/\langle l\rangle \tag{1}$$

$$\lambda=\pi/2\langle l\rangle. \tag{2}$$

These theorems were established by Smith.[8,9]

The grain boundaries are not all perpendicular to an arbitrary section through the body. We define a "tortuosity" coefficient, θ, as the mean secant of the tilt angle between the grain boundary and the normal to the exposed plane. Then θ is also the ratio of the mean width of the grain boundary trace measured in the exposed plane to their true average thickness, δ. If ϵ is the volume fraction of grain boundaries in the body, then by definition

$$\epsilon=\delta\sigma/2=2\delta/\langle l\rangle. \tag{3}$$

Since $\delta\lambda\theta$ is the fractional exposed grain boundary area in a random section, then it follows that

$$\epsilon=\delta\lambda\theta. \tag{4}$$

From Eqs. (2), (3), and (4), we conclude that

$$\theta=4/\pi. \tag{5}$$

Let the subscripts 1 and 2 refer to grain boundaries and to the grains, respectively. Assume that concentration gradients are in the grain boundary direction. Then the flux of diffusant across a unit area of the body is

$$F_1(y)=\sum_i f_i(y)=-\sum_i \delta_i\lambda_i D_i(\cos\xi_i)(\partial C_i/\partial y)$$

where the subscript i refers to the ith grain boundary, ξ_i is the tilt angle, y is the perpendicular penetration distance, and the summation is taken over the n boundaries that are exposed by the unit section in the body. Since the distribution of D_i is unknown, we assume an average value $D_1=\langle D_i\rangle$. To the same degree of approximation, we assume that λ_i is independent of ξ_i and that $\lambda=n\langle\lambda_i\rangle$, $\delta=\langle\delta_i\rangle$, $C_1(y)=\langle C_i(y)\rangle$. Within the accuracy of these approximations,

$$F_1(y)=-(\epsilon D_1/\theta)(\partial C_1(y)/\partial y)\langle\cos\xi_i\rangle. \tag{6}$$

Although the value of $\theta=\langle\sec\xi_i\rangle$ was readily established, it was not possible to evaluate $\langle\cos\xi_i\rangle$. It is believed that $\langle\cos\xi_i\rangle$ is within a factor of 2 of θ and, indeed, if a reasonable distribution function for ξ_i is chosen, then $\langle\cos\xi_i\rangle\approx 8/3\pi$. We take this value as being approximately correct. Then

$$\epsilon\frac{\partial C_1}{\partial t}(y,t)=\frac{2\epsilon D_1}{3}\frac{\partial^2 C_1}{\partial y^2}(y,t)-\sigma F_2(y,t) \tag{7}$$

where F_2 is the flux of diffusant passing out of the boundary into the grains for which the surface concentration is $C_1(y,t)$. This result is readily shown to be the same as that used by Fisher[1] with appropriate choice of function for $F_2(y,t)$. For a semi-infinite polycrystalline body, Eq. (7) must be solved with the concentration satisfying the following conditions:

$$\begin{aligned} C_1(0,t)&=1\\ C_1(\infty,t)&=0\\ C_1(y,0)&=0. \end{aligned} \tag{8}$$

From Duhamel's theorem,[10] it can be shown that

$$F_2(y,t)=\int_0^t \frac{\partial C_1}{\partial t}(y,\nu)G(t-\nu)\,d\nu \tag{9}$$

where $G(t)$ is the flux into a grain with diffusivity D_2 and with zero initial diffusant concentration due to a unit concentration maintained at the surface from time $t=0$. The exact nature of $G(t)$ depends on the shape assumed for the grain, and since no single grain shape can

[7] R. Smoluchowski, "Movement and Diffusion Phenomena in Grain Boundaries," *Imperfections in Nearly Perfect Crystals* (John Wiley & Sons, Inc., New York, 1952), pp. 451-475.

[8] C. S. Smith, "Grain Shapes and Other Metallurgical Applications of Topology," *Metal Interfaces* (American Society for Metals, Cleveland, Ohio, 1952), p. 65.

[9] C. S. Smith and L. Guttman, J. Metals **5**, 81 (1953).

[10] H. S. Carslaw and J. C. Jaeger, *Conduction of Heat in Solids* (Oxford University Press, New York, 1947), pp. 19-21.

be considered typical, a reasonable empirical function will be introduced.

It is convenient to introduce a reduced time τ and a reduced penetration depth η, defined by

$$\tau=[4D_2/\delta^2]t$$

$$\eta=\left[\frac{\sqrt{6}}{\delta\Delta^{\frac{1}{2}}}\right]y \tag{10}$$

where $\Delta=D_1/D_2$, the ratio of diffusivity in the boundary to that in the grain.

Denoting the Laplace transform with respect to τ by a bar, Eq. (7) then becomes

$$\frac{d^2\bar{C}_1}{dy^2}(\eta,p)-p[1+(\delta/2D_2)\bar{G}(p)]\bar{C}_1(y,p)=0 \tag{11}$$

with

$$\bar{C}_1(0,p)=1/p$$
$$\bar{C}_1(\infty,p)=0 \tag{12}$$

resulting in

$$\bar{C}_1(\eta,p)=\frac{1}{p}\exp[-\eta p^{\frac{1}{2}}\alpha(p)] \tag{13}$$

where

$$\alpha^2(p)=[1+(\delta/2D_2)\bar{G}(p)]. \tag{14}$$

Equation (13) is the Laplace transform of the concentration distribution in the grain boundaries which cannot be established experimentally, except perhaps by special techniques. The average concentration measured over a thin section of the body can be determined and it will include the material that has diffused into the grains. Therefore, if $\phi(y,t)$ is the average concentration, then:

$$\phi(y,t)=\epsilon C_1(y,t)+\sigma\int_0^t C_1(y,\nu)G(t-\nu)d\nu \tag{15}$$

from which

$$\bar{\phi}(\eta,p)=\epsilon\bar{C}_1(\eta,p)\alpha^2(p), \tag{16}$$

that is,

$$\bar{\phi}(\eta,p)=\frac{\epsilon}{p}\alpha^2(p)\exp[-\eta p^{\frac{1}{2}}\alpha(p)]. \tag{17}$$

In principle, Eq. (17) is the desired general solution for the average distribution of diffusant through a polycrystalline body subject only to the validity of our initial basic assumption. We must now construct a sink function $G(t)$ appropriate to a real polycrystalline solid.

GRAIN MODEL

We define an "effective exposure" $\epsilon^2\tau=16Dt/\langle l\rangle^2$. Experimental values for $\epsilon^2\tau$ have been on the order of about 10^{-4} to 10^{1} with values of the reduced time τ varying from 10^{6} to about 10^{11}. In this range, consider next the rate of diffusion into grains from the boundaries in order to establish a reasonable function for $\alpha(p)$.

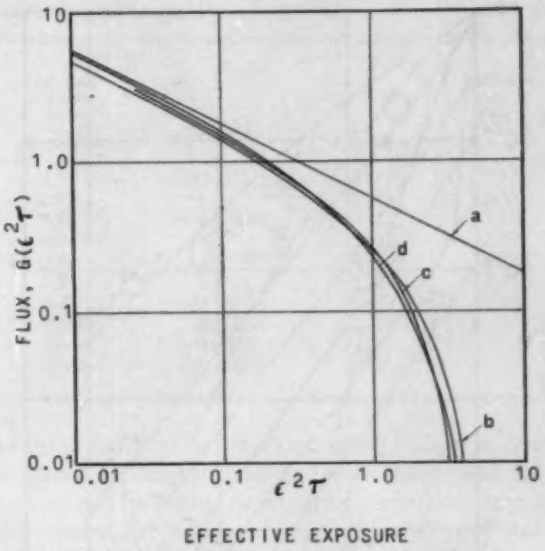

FIG. 1. Flux of diffusant per unit time per unit area into various bodies *versus* the effective exposure $\epsilon^2\tau$. Curve a, semi-infinite body; b, sphere; c, infinite circular cylinder; d, empirical model.

The flux of diffusant into a semi-infinite body theoretically decreases in proportion to $t^{-\frac{1}{2}}$. In finite bodies this time dependence lasts for a finite interval only and ultimately changes to a decreasing exponential relationship. This behavior is illustrated in Fig. 1 in which logarithmic graphs of the flux, G, into a semi-infinite body, sphere, and infinite circular cylinder are presented as a function of effective exposure. Without question, in the limited region with $\epsilon^2\tau$ less than 10^{-1}, the semi-infinite body represents a valid grain model. It is clear, however, that for larger $\epsilon^2\tau$, a semi-infinite body grossly overestimates the flux. Since the grains are finite in size, it is reasonable to expect a behavior consistent with the other simple finite bodies. For simplicity the following empirical function is chosen, to approximate the flux into the grain, that exhibits the proper functional behavior in the entire experimental exposure range.

$$G(t)=(D_2/\pi t)^{\frac{1}{2}}\exp[-\epsilon^2 4D_2t/\delta^2]. \tag{18}$$

Therefore

$$\frac{\delta}{2D_2}G(\tau)=\frac{1}{(\pi\tau)^{\frac{1}{2}}}\exp[-\epsilon^2\tau]. \tag{19}$$

A logarithmic plot of this function is also presented in Fig. 1, curve *d*, for comparison. Since grain shape cannot be precisely defined, it is believed that the function is as good as that for any of the simpler shapes and is, in fact, better than the assumption of a spherical shape which it was originally designed to approximate. It will be referred to as an empirical grain model.

From Eq. (19) $\alpha^2(p)$ becomes

$$\alpha^2(p)=[1+(p+\epsilon^2)^{-1}] \tag{20}$$

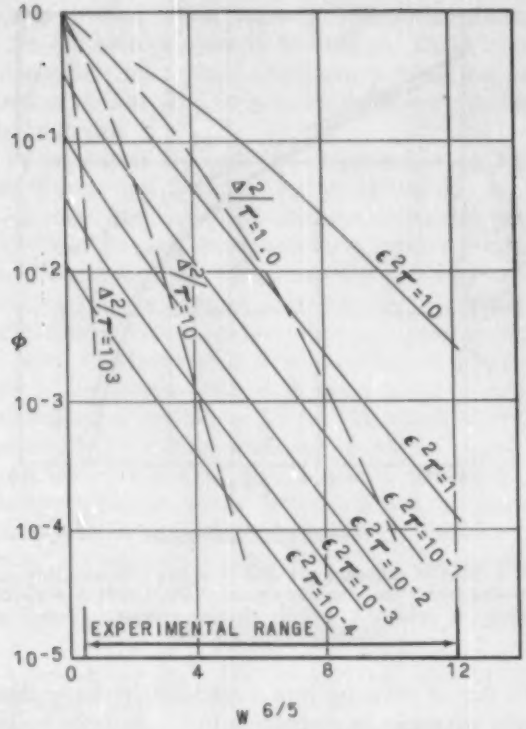

FIG. 2. Average concentration of diffusant in polycrystalline body *versus* $w^{6/5}$. Dashed curves indicate concentration due to bulk diffusion alone. Solid curves indicate concentration due to grain boundary diffusion alone. See text for definition of τ(reduced time), w(effective penetration), $\epsilon^2\tau$(effective exposure), Δ(ratio of diffusion constants).

and the problem is reduced to evaluation of the integral

$$\phi(\eta,\tau,\epsilon)=\frac{\epsilon}{2\pi i}\int_{\gamma-i\infty}^{\gamma+i\infty} e^{p\tau}\bar{\phi}(\eta,p,\epsilon)dp \qquad (21)$$

where the path of integration is to the right of all singularities in the integrand.

INVERSION OF THE LAPLACE TRANSFORM

Three methods were used to establish the behavior of Eq. (21). The method of steepest descents was found to be valid only at relatively great penetration depths. A series expansion established the initial behavior of ϕ. Finally, a numerical evaluation was used to cover the usual experimental penetration depth range. In each case the significant parameter defining the "effective penetration" was found to be the quantity

$$w=\eta/\tau^{\frac{1}{2}}=\frac{\sqrt{3}y}{(\Delta\delta)^{\frac{1}{2}}(D_2 t)^{\frac{1}{2}}}. \qquad (22)$$

The method of steepest descents was found to be applicable to Eq. (21) only if w exceeds the larger of 15 or $8(\epsilon^2\tau)^{\frac{1}{2}}$, speaking roughly, so that it is valid only beyond a certain depth of penetration. Unfortunately, at such depths the concentration is too small to measure accurately unless the effective exposure is very large. If one uses the asymptotic formula so obtained, however, and considers the case of very small ϵ (semi-infinite grain model), then, providing $w\ll\tau^{\frac{1}{2}}$, the average concentration will vary as

$$\phi\sim\left(\frac{w}{\sqrt{2}}\right)^{-1}\exp\left[-\tfrac{3}{4}\left(\frac{w}{\sqrt{2}}\right)^{4}\right]. \qquad (23)$$

One can, instead, proceed by expanding the integrand of Eq. (21) in a double Taylor series about $\eta=0$ and $\epsilon^2=0$ and invert the series termwise. Neglecting terms of order $\tau^{-\frac{1}{2}}$, the result of these operations is as follows:

$$\phi=[\epsilon+\operatorname{erf}\epsilon\sqrt{\tau}]+[\epsilon\sqrt{\tau}\exp(-\epsilon^2\tau)]\left[\sum_{n=1}^{\infty}\beta_n(\epsilon,\tau)\frac{w^n}{n!}\right] \qquad (24)$$

where the first few β_n are

$$\begin{aligned}\beta_1&=-[4/\Gamma(\tfrac{1}{4})]\left[1+\frac{2}{5}\epsilon^2\tau+\frac{2}{15}(\epsilon^2\tau)^2+\frac{4}{117}(\epsilon^2\tau)^3+\cdots\right]\\ \beta_2&=1\\ \beta_3&=-\frac{1}{\Gamma(\frac{3}{4})}\left[1-\frac{2}{3}\epsilon^2\tau-\frac{2}{21}(\epsilon^2\tau)^2-\frac{4}{231}(\epsilon^2\tau)^3-\cdots\right].\end{aligned} \qquad (25)$$

Using this power series and considering the case of very small ϵ (semi-infinite grain model), then the initial slope of the $\ln\phi$ *versus* depth of penetration will be

$$\left.\frac{\partial\ln\phi}{\partial y}\right|_{y=0}=-\left[\frac{\pi^{\frac{1}{2}}(3\pi/8)^{\frac{1}{2}}}{\Gamma(5/4)}\right]\left[\frac{2^{\frac{1}{2}}}{(\Delta\delta)^{\frac{1}{2}}(\pi D_2 t)^{\frac{1}{2}}}\right] \qquad (26)$$

which differs from Fisher's result by the numerical factor 1.57.

In the range of penetration depths of experimental interest, extending roughly from $w=0.5$ to 8.0, neither of the above methods is satisfactory, and a numerical evaluation of the complex integral (21) is required. Since the concentration is initially zero, one can write

$$\phi(\eta,\tau,\epsilon)=\frac{\epsilon}{2\pi i}\int_{\gamma-i\infty}^{\gamma+i\infty}(e^{p\tau}-1)\bar{\phi}(\eta,p,\epsilon)dp \qquad (27)$$

and in this form the path of integration can be taken along the imaginary axis ($\gamma=0$). One then has a definite integral to evaluate; this was done using Sandia Corporation's IBM-704 computer.

RESULTS

The results of the numerical evaluation are illustrated in Fig. 2 in which semilogarithmic graphs are presented of the average concentration as a function of $w^{6/5}$, with $\epsilon^2\tau$ as a parameter (solid curves). After a slight initial curvature, the graphs are all linear with $w^{6/5}$ for $\epsilon^2\tau\leq 1$ with a slope, $S=-(d\log\phi/dw^{6/5})$, of 0.335 for $\epsilon^2\tau\leq 10^{-2}$, and 0.329 and 0.316 for $\epsilon^2\tau=0.1$ and 1.0, respectively.

TABLE I. Summary of published experimental results.

Substance	Temp. T°C	Reduced time $\tau\times10^{-4}$	Grain boundary volume fraction $\epsilon\times10^{6}$ (Estimated)	Effective exposure $\epsilon^3\tau\times10^{2}$	Diffusion constant ratio $\Delta\times10^{-6}$ (Reported)	$\frac{\Delta^2}{\tau}\times10^{-3}$	Reference	Diffusion constant ratio $\Delta\times10^{-6}$ (Revised)
Ag	427	0.093	1	0.09	2.84	280	(11)	9.72
Ag	450	2.35	1	2.4	1.03	4.3	(14)	3.38
Ag	456	0.22	1	0.2	0.90	22	(11)	3.58
Ag	478	0.21	1	0.2	0.94	43	(1)	2.82
Ag	479	0.41	1	0.4	0.94	12	(11)	2.98
Ag	502	28.0	1	28.0	0.35	2.9	(14)	1.21
Zn	90	0.046	0.5	0.012	0.44	42	(12)	1.68
Zn	157	4.86	0.5	1.22	0.068	0.0095	(12)	...
Cd	85	13.7	1.7	39.6	0.066	0.0032	(13)	...
Cd	105	41.4	1.7	120.0	0.031	0.00023	(13)	...

The experimental region is roughly indicated by the two heavy bars on the abscissa. As expected, the logarithm of the concentration is proportional to a power of the penetration depth intermediate between the initial value of one and the asymptotic value of four-thirds.

If there were no grain boundaries at all, diffusion from the surface would still take place through the grains, producing a concentration distribution

$$\phi=\operatorname{erfc}\left[\frac{y}{2(D_2t)^{\frac{1}{2}}}\right]=\operatorname{erfc}\left[\left(\frac{\Delta^2}{\tau}\right)^{\frac{1}{2}}\frac{w}{\sqrt{6}}\right]. \qquad (28)$$

This function is also illustrated in Fig. 2, with Δ^2/τ as a parameter (dashed curves).

A graph of the true concentration distribution in a polycrystalline body must lie above both of the corresponding dashed and solid curves. It should be asymptotic to the dashed curve wherever it is much the larger, and run parallel to the solid curve at large penetrations where bulk diffusion is insignificant.

One might argue qualitatively that bulk diffusion in a layer near the surface would merely shift the origin of the grain boundary diffusion curves at large penetrations; this would have no practical effect since only the slope is used in the analysis of experiment.

The graphs in Fig. 2 make it clear, however, that information about grain boundaries can be obtained unambiguously only if the parameter, Δ^2/τ, is sufficiently large, say $>10^3$. Many of the experimental data in the literature do not satisfy this criterion.

DISCUSSION

Table I summarizes published experimental results for which complete experimental data are available. In Table I, ϵ was estimated and τ computed from known values of D_2 assuming $\delta=5\times10^{-8}$ cm.

In the case of silver, the values of Δ obtained by use of the present analyses are higher by a factor of 3 or 4 than those reported by others using the Fisher[1] analysis. The activation energy computed from the revised data, assuming no effects due to impurity variations, appears to be somewhat lower than that reported previously, i.e., $\Delta H_1=18.2$ kcal as compared with 21.5 kcal.[11]

On the basis of the low Δ^2/τ ratios for Zn and Cd,[12,13] three of the results are rejected as being erroneous which suggests the remaining experimental data for these materials be re-examined.

Experimentally, concentration measurements cover approximately three or four orders of magnitude. Referring again to Fig. 2, it appears that insufficient experimental data would be available for establishing slopes if $\epsilon^3\tau<10^{-4}$. Furthermore, the curves are not linear for $\epsilon^3\tau>1$. This, then, represents an additional limitation on the method.

Experiments with silver were carried out between 425° and 500°C, approximately. Attempts to measure Δ at higher temperatures[14] resulted in curves that were not interpretable, mainly because of significant contributions from bulk diffusion. This temperature range could be extended, however, by a more suitable choice of experimental conditions. For example, a simple computation shows that an experiment conducted with $\langle l\rangle=9.1\times10^{-2}$, $\tau=8.2\times10^{7}$, $T=590$°C would be consistent with the limitations $\epsilon^3\tau\geq10^{-4}$, $\Delta^2/\tau\geq10^3$, and concentration measurements could be made at experimental penetrations of $0<y\leq5\times10^{-3}$ cm.

ACKNOWLEDGMENTS

The authors wish to express their appreciation to C. M. Williams for carrying out the numerical computations. We also wish to thank Professor Henri Sack of Cornell University for valuable discussions and criticism.

[11] R. E. Hoffman and D. Turnbull, J. Appl. Phys. 22, 634 (1951).
[12] E. S. Wajda, Acta Met. 2, 184 (1954).
[13] Wajda, Shirn, and Huntington, Acta Met. 3, 39 (1955).
[14] Slifkin, Lazarus, and Tomizuka, J. Appl. Phys. 23, 1032 (1952).

JOURNAL OF APPLIED PHYSICS VOLUME 31, NUMBER 3 MARCH, 1960

Growth of Gallium Arsenide by Horizontal Zone Melting

J. L. RICHARDS
Research Division, Philco Corporation, Philadelphia, Pennsylvania
(Received August 19, 1959)

The growth of single crystals of GaAs is discussed with reference to the horizontal zone melt technique. The crystalline perfection and polarity of grown crystals can be determined from a study of edge dislocations revealed on {111} by an HF, H_2O_2 etchant. Evidence of good thermal control during crystal growth is found from a correlation between the incidence of dislocations and the shape of the freezing interface. Dislocation densities can be reduced to a very low order by careful control of growth conditions.

INTRODUCTION

THE current interest in gallium arsenide, stimulated largely by its potential as a material suitable for diode and transistor fabrication, has emphasized the need for the growth of crystals of high perfection. Crystal growth of gallium arsenide is complicated, since melts of this material tend to become nonstoichiometric by arsenic evaporation. In order to prevent evaporation, it is necessary to use a closed system, the minimum temperature of which corresponds to the vapor pressure of arsenic over gallium arsenide at the temperature of the melt.

These principles have been incorporated into a number of systems designed to grow this material by the vertical pulling technique.[1–3] The floating zone method has also been applied successfully.[4]

This paper describes the growth of gallium arsenide by the horizontal zone melt method. The principles of zone melting and zone refining have been described in detail.[5] The method has been applied to the growth of high quality germanium crystals and the thermal conditions necessary for the production of crystals of low dislocation density have been defined.[6,7] As applied to the growth of thermally decomposing compounds, this method offers a number of advantages over the vertical pulling technique:

(1) The need for a pulling mechanism operating inside a sealed system is eliminated.

(2) The human element can be eliminated after the initial setting-up. (Crystals were usually grown overnight.)

(3) Reaction of the elements, zone refining and crystal growth can be carried out *in situ*.

The method has certain inherent difficulties largely associated with the use of a crucible:

(1) Differences in thermal conductivity and emissivity between ingot and crucible may make radial thermal symmetry about the crystal growth axis difficult to achieve.

(2) Constraint may be placed on the ingot during growth because of the large area of contact with the crucible. There is a consequent increased risk of crystal imperfection and contamination.

The following section presents a furnace design for the growth of this material; an etching technique is then described which will reveal edge dislocations and the correlation between growth conditions and crystalline perfection is discussed in a final section. Emphasis is placed solely on the imperfections incurred during crystal growth. No discussion of the electrical properties of the grown crystals is included in this paper.

CRYSTAL GROWING FURNACE

A final design of the zone melt furnace is sketched diagramatically in Fig. 1.

The furnace consists essentially of a winding of $\frac{1}{8}$ in. diam kanthal Al wire, supported inside a $2\frac{1}{2}$ in. bore alundum tube 20 in. long, using alundum spacers. A firebrick, 6×12×12 in., with a 4 in. diam hole machined along its minor axis, surrounds the furnace. The insulation of this firebrick is capable of creating a liquid zone (1240°C) on the ingot when the background temperature in the furnace is set at about 800°C. This zone can be made to traverse the ingot by pulling the firebrick along the track.

Provision is made for viewing the freezing interface during crystal growth. The alundum furnace tube is split along its length and is laid in the supports in such a manner as to leave a 1 inch gap along the top of the furnace. A vertical hole in the firebrick together with an angled mirror then enables the top of the liquid zone to be viewed. Regulation of the zone width to form either a concave, near planar, or convex interface is made by changing the current input to the furnace. The ratio of top-to-bottom heat can be changed by adjusting the separation between the alundum tubes at the base of the furnace.

The manner in which the charge is set up in the furnace is shown in the figure. The quartz boats, 23 mm diam, are carefully coated with carbon, and baked in an argon atmosphere for 2 hrs at a temperature of 1100°C.

[1] R. Gremmelmaier, Z. Naturforsch. **11a**, 511 (1956).
[2] J. L. Richards, J. Sci. Instr. **34**, 289 (1957).
[3] P. L. Moody and C. Kolm, Rev. Sci. Instr. **29**, 1144 (1958).
[4] J. L. Whelan and G. H. Wheatley, Bull. Am. Phys. Soc. Ser. II, **2**, 120 (1957).
[5] W. G. Pfam, Trans. Am. Inst. Mining Met. Engrs. **194**, 747 (1952).
[6] D. C. Bennett and B. Sawyer, Bell System Tech. J. **35**, 637 (1956).
[7] I. G. Cressell and J. A. Powell, *Progress in Semiconductors* (John Wiley & Sons, Inc., New York), Vol. 2, p. 139.

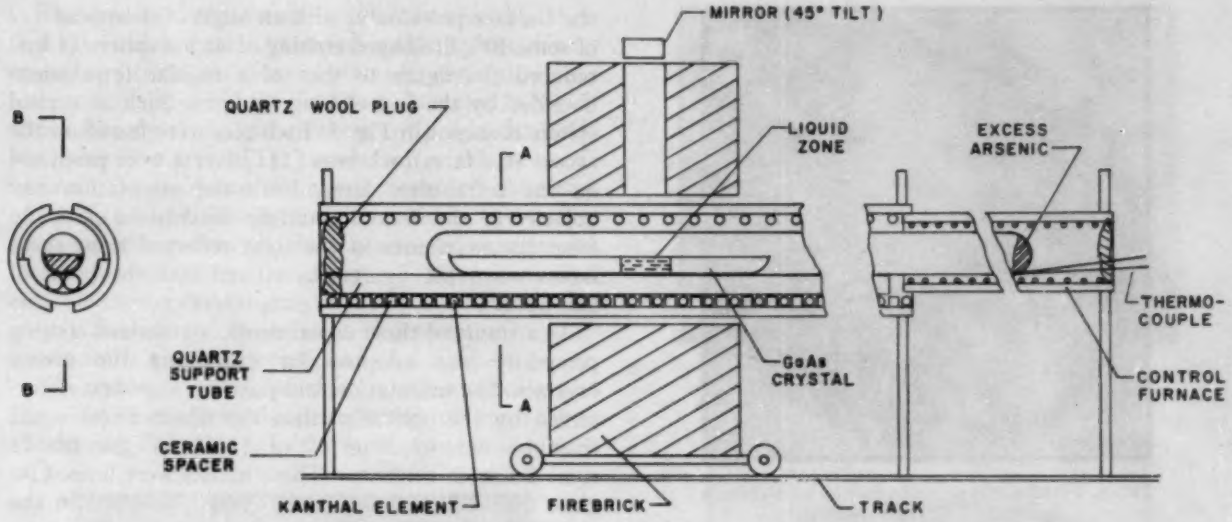

FIG. 1. Diagram of the zone melt furnace.

The charge, together with a small quantity of excess arsenic, is sealed inside a 24 mm diam quartz tube some 50 cm in length, which is laid on the quartz tube supports so that the ingot is axially symmetrical with respect to the furnace. The vapor pressure of the arsenic inside the sealed tube can be regulated by adjusting the temperature of the control furnace. Power input through a line voltage regulator in series with variable autotransformers was found to give sufficient protection against thermal fluctuations due to instabilities in line voltage. The furnace described is designed to grow crystals 1.5 cm^2 in cross section and 23 cm in length. The zone-pass rate was constant for a given crystal and usually in the range 1.25 to 5 cm per hr. Of some 40 crystals grown in this manner, half of them were doped by the deliberate addition of foreign impurities. The rest were grown from zone refined material.

ETCHING TECHNIQUES

The crystalline perfection of the grown crystals was determined from a study of the dislocations revealed by etch pits on {111} faces. Because the gallium arsenide (zincblende) lattice does not possess a centre of inversion, it is necessary to distinguish between the ⟨111⟩ direction and the reverse or ⟨$\bar{1}\bar{1}\bar{1}$⟩ direction. The polar nature of the crystal can be seen by considering a view of the lattice in a direction parallel to a {111} face. When viewed in this direction, the lattice is characterized by a series of alternate double layers of gallium and arsenic atoms. The two ⟨111⟩ directions perpendicular to these layers will then be physically different. In one of these ⟨111⟩ directions, the gallium atoms preceed the arsenic atoms, whereas they succeed them in the reverse or ⟨$\bar{1}\bar{1}\bar{1}$⟩ direction.

By correlating x-ray diffraction experiments with the action of a specific etchant on two opposite {111} faces of a wafer of GaAs, it has been shown[8] that etch pits are revealed by this etchant only on that {111} face in which the Ga atoms preceed the As atoms. The direction associated with this face is designated as ⟨111⟩. The

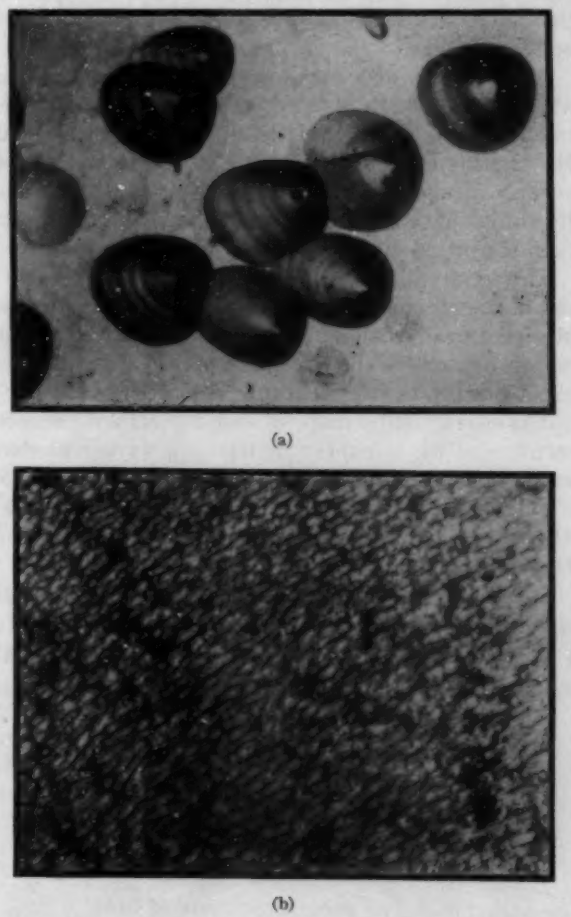

(a)

(b)

FIG. 2. The two opposite faces of a GaAs wafer after etching in HF, H_2O_2 solution for 45 min; (a) Ga face, (b) As face.

[8] J. C. White and W. C. Roth, J. Appl. Phys. **30**, 946 (1959).

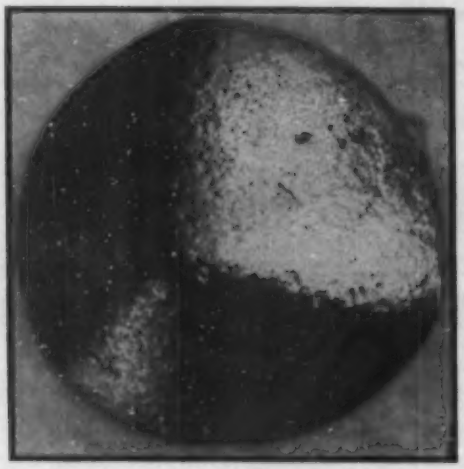

FIG. 3. Tetrahedron of GaAs formed by etching a sphere in HF, H_2O_2 solution.

solution used had the composition 2 parts HCl, 1 part HNO_3, 2 parts H_2O, and the etch pits revealed were embryonic in nature. (For the sake of brevity and clarity in the following text, the face associated with the $\langle 111 \rangle$ direction will be called the "Ga face," whereas that associated with the reverse or $\langle \bar{1}\bar{1}\bar{1} \rangle$ direction will be the "As face".)

An etchant, developed in this laboratory, which would reveal clearly defined etch pits on one face of a wafer of GaAs cut on {111} had the compositions 1 part HF, 2 parts H_2O_2(30%), 5 parts H_2O. The reverse side of this wafer revealed a terraced pattern in the etchant. By subjecting the same wafer to the HCl, HNO_3 solution, the pitted face was shown to be a Ga face.

The nature of the pits developed by the HF, H_2O_2 solution is of some interest. After 10 min of etching, the pits were small, shallow, and conical. Prolonged etching not only increased the size of the pits considerably, but also tended to develop features within the pits.

The characteristic features were a central depression, surrounded by a number of terraces, similar to some which have been observed on germanium using an alkaline etch.[9] Typical etch pits are shown in Fig. 2(a). The etched As face of the same wafer is shown in Fig. 2(b) for comparison.

Spheres about 0.8 cm diam were ground from single crystals. These were chemically polished in a mixture of 1 part HF: 3 parts HNO_3 and etched in the HF, H_2O_2 solution. Etch pits were found to be clustered around the Ga face poles only, with an angle of disappearance of some 10°. Prolonged etching of such a sphere (4 hrs) reduced the figure to that of a regular tetrahedron bounded by the fast etching As faces. Such an etched sphere is shown in Fig. 3. Etch pits were found on the apices (Ga faces), whereas [111] facets were produced on the tetrahedral faces. Both the orientation and polarity of the crystal could be determined optically from the maximum in the light reflected from these facets when the figure was viewed into the point of any apex.

FIG. 4. Zone grown single crystal of GaAs.

As a result of these experiments, a standard etching procedure was adopted for examining the grown crystals. The orientation and polarity were first determined by the optical method described. Faces could then be cut to 2 or 3° of {111} to give blanks some 2 mm in thickness. These blanks were lapped on glass with 600 carborundum, washed, polished in the HF, HNO_3 solution, and immersed immediately in the peroxide etchant. The etching was carried on for 45 min in order to develop the pits fairly fully prior to microscopic examination.

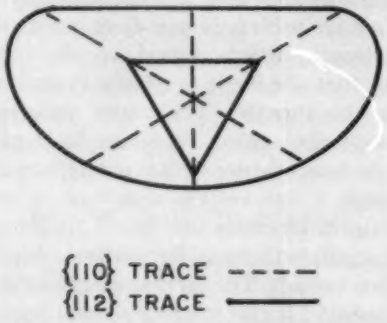

FIG. 5. Schematic diagram of a {111} face, showing orientation adopted. Solid lines show {112} traces indicative of slip. Dashed lines show intersection of {110} planes normal to the $\langle 111 \rangle$ growth direction where lineage is most frequently encountered.

CRYSTAL GROWTH AND CRYSTALLINE PERFECTION

Several of the crystals produced by the horizontal zone melt method were self seeded in order to avoid contamination introduced with the seed. These crystals generally oriented themselves within some 10° of a $\langle 111 \rangle$ direction of either polarity. The remainder were seeded to grow in either $\langle 111 \rangle$ or $\langle \bar{1}\bar{1}\bar{1} \rangle$. A typical crystal is shown in Fig. 4.

It has been suggested[10] that crystal growth might be affected by seed polarity, and that crystals of this material prefer to orient themselves in such a manner as to present an As face to the melt. In the case of the crystals described here, no correlation has been found between either ease of growth or crystalline perfection and a preference for crystal growth in a particular $\langle 111 \rangle$ direction.

[9] S. G. Ellis, J. Appl. Phys. **26**, 1140 (1955).

[10] S. G. Ellis, J. Appl. Phys. **30**, 947 (1959).

The seed axis was chosen so that the vertical, longitudinal section of the crystal was a {110} plane. Under these conditions, the lines of etch pits associated with lineage and slip are in the directions indicated in Fig. 5. From a study of the etched slices cut perpendicular to the growth direction, a correlation could be made between the incidence of imperfections and the shape of the liquid-solid interface, which could be checked by decantation experiments. Such a series of experiments clearly demonstrates the degree of thermal control possible during crystal growth. The results follow very closely those found in the case of germanium crystals grown using a similar technique.[7]

The use of a freezing interface, which is concave into the solid, resulted in the introduction of lineage into the crystal. This may take the form of fine lineage with

FIG. 6. Fine lineage on the etched Ga face obtained with a slightly concave interface.

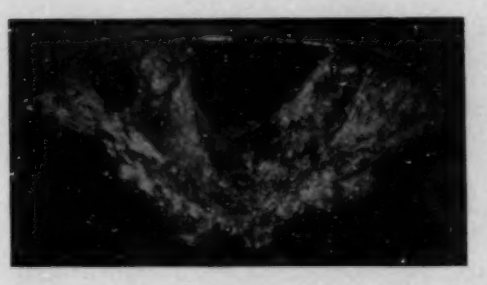

FIG. 7. Etched Ga face revealing gross lineage introduced into the crystal by the use of a concave interface.

the formation of one or a series of near parallel tilt boundaries as illustrated in Fig. 6.

When the interface is made more concave, over-riding slip is introduced into the crystal. If this condition is permitted to persist, dense arrays of dislocations are produced as a result of differential thermal contraction on cooling, to give a condition bordering on polycrystallinity. This condition is illustrated in the etched section shown in Fig. 7.

It was found that lineage could be completely avoided by the use of a convex freezing interface during growth. However, if this interface is curved beyond some small threshold value, slip will occur to effect stress relief. Figure 8 shows the etch pit distribution typical of slip on {111} planes in a ⟨110⟩ direction. The pit density of

FIG. 8. Symmetrical slip, typical of the use of a convex interface, revealed on the Ga face of a crystal.

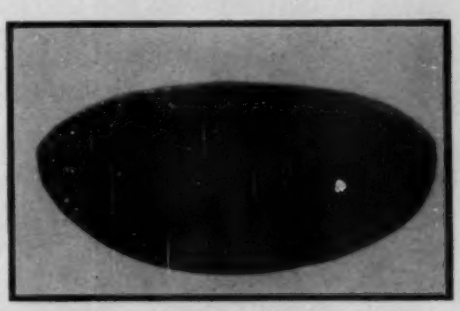

FIG. 9. Etched Ga face of a crystal grown with a near planar interface.

the slipped region is of the order of $10^5/cm^2$, whereas the low density area contains between 10 and 10^2 dislocations/cm^2.

By adjustment of furnace conditions to give an interface which is essentially planar, the dislocation density may be reduced as illustrated in Fig. 9. Here, the interface remained planar except at the sides of the cross section.

Because the adjustment of furnace conditions is very critical for the establishment of a convex interface of very close to planar, it has not been possible to grow crystals with an average dislocation density of less than $10^3/cm^2$, although some regions of the cross section of certain ingots may show a dislocation count as low as $10-10^2/cm^2$.

SUMMARY AND CONCLUSIONS

Large single crystals of GaAs can be grown readily by the horizontal zone melt technique.

The crystalline perfection and polarity of the grown crystals can be determined from a study of etch pits revealed on Ga faces by an HF, H_2O_2 etchant. By rigid control of the shape of freezing interfaces, dislocation densities can be reduced to a very low order, comparable with those achieved in germanium crystals.

ACKNOWLEDGMENT

The author wishes to thank J. Maciel for valuable assistance in growing the crystals.

Evidence for Dislocation Reactions in Copper

F. W. YOUNG, JR., AND T. S. NOGGLE
Solid State Division, Oak Ridge National Laboratory, Oak Ridge, Tennessee*
(Received November 13, 1959)

Observations of slip lines and etch pits at dislocations on a copper crystal hardened by irradiation and deformed by bending are interpreted in terms of dislocation reactions.

RELATIONS between dislocations have been demonstrated in ionic crystals by Amelinckx and Dekeyser.[1] By internal decoration of the dislocations in these crystals and analysis of the networks thus made visible, they showed that dislocation reactions were necessary to account for the detailed configurations of the dislocations in the network. Recently, Whelan[2] has studied the dislocation networks in thin foils of stainless steel, and he has shown that dislocation reactions occurred in this material. This paper presents evidence for dislocation reactions in copper crystals hardened by neutron irradiation as obtained from observations of slip lines and of etch pits formed at dislocations.

The technique used for forming etch pits was similar to that described by Lovell and Wernick.[3] This technique produces pits at dislocations on the {111} face of 99.999% copper and pits are formed at clean dislocations. It has not been established that there is a one-to-one correspondence between these pits and dislocations, but it is at least approximately so.

EXPERIMENTAL

A 99.999% copper crystal, of the dimension 3.6×1 ×0.1 cm, and of the orientation shown in Fig. 1 was grown by seeding and was irradiated in the Oak Ridge Graphite Reactor at ambient temperature with 10^{18} nvt. It was subjected to a bending deformation, and the development of slip lines was observed. The crystal was then etched so as to reveal the dislocations as etch pits. The particular appearance of the slip lines after the deformation and the location of the dislocations observed on subsequent etching can be accounted for on the basis of the geometry of slip systems in the f.c.c. system and the interactions of dislocations.

The crystal was bent using a "4-point" bending jig about the $[10\bar{1}]$ axis to a radius of curvature of approximately 10 cm. Very faint slip lines corresponding to $(\bar{1}11)$ and $(11\bar{1})$ planes were seen in the central portion of the convex (111) surface. No evidence of interaction between these lines was observed. That is, no jogging of the lines on intersection and no increase in the height of the slip lines near intersection points was observed (see Fig. 2). Toward the ends of the crystal, on the surface of the specimen directly opposite the line contact of the loading points of the bending jig, another set of slip lines was observed. These lines corresponded to the $(1\bar{1}1)$ plane, and the step height of these lines was very large. The faint lines from the $(\bar{1}11)$ and $(11\bar{1})$ planes crossed these big slip lines, and were more easily observed in the vicinity of the intersections. Electron micrographs of a carbon replica of such intersections are shown in Fig. 3.

On etching the crystal with the dislocation etch, some new dislocations were seen in the central part of the crystal. Figure 4 shows the etch pits in the same area as the slip lines shown in Fig. 2. It can be seen that there are new dislocations corresponding to a few of the slip lines and particularly at some intersections of the lines.

Rows of pits were found corresponding to the $(1\bar{1}1)$ slip lines. Thus, many dislocations were left in the crystal after slip on this plane. Where the $(11\bar{1})$ and $(\bar{1}11)$ lines had crossed the $(1\bar{1}1)$ lines, many pits were seen in rows corresponding to the former lines for a short distance away from the intersection points (Fig. 5).

DISCUSSION

The foregoing facts can be accounted for on the basis of the geometry of the f.c.c. slip systems and the interaction of the dislocations. The slip planes and slip directions with the relative resolved shear stress for each

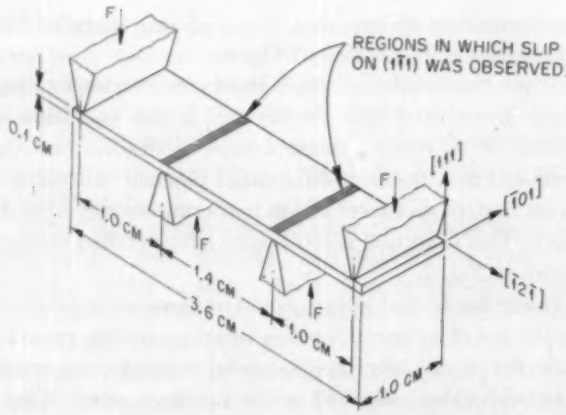

FIG. 1. Orientation of the crystal before bending and schematic representation of the arrangement in the bending jig.

* Oak Ridge National Laboratory is operated by Union Carbide Corporation for the U. S. Atomic Energy Commission.

[1] S. Amelinckx and W. Dekeyser, *Solid State Physics* edited by F. Seitz and S. Turnbull (Academic Press, Inc., New York, 1959), Vol. 8, p. 325.

[2] M. J. Whelan, Proc. Roy. Soc. (London) **A249**, 114 (1959).

[3] L. C. Lovell and J. H. Wernick, J. Appl. Phys. **30**, 590 (1959).

system for bending a crystal with this orientation are given in Table I. This table is applicable only for the constant bending stress region between the two inside loading points on the specimen.

The faint slip lines correspond to the $(\bar{1}11)$–$[0\bar{1}1]$ and $(11\bar{1})$–$[\bar{1}10]$ systems, which are the favored systems for slip. The Burgers vectors for these systems lie in the (111) plane. Therefore, for a crystal truly oriented as in Fig. 1 and atomically smooth, no slip lines corresponding to these two systems could be seen on the (111) surface. From the electron micrograph of the cutting of a $(1\bar{1}1)$ line by a $(11\bar{1})$ line (Fig. 3), it can be seen that the length of the jog in the $(1\bar{1}1)$ line is approximately equal to the height of the $(1\bar{1}1)$ line. Therefore, the amount of slip in the $(\bar{1}11)$ and $(11\bar{1})$ planes was actually $\sim$1000 A, the lines being faint because the slip vectors lie nearly in the surface being examined. The $(1\bar{1}1)$ planes slipped only near the ends of the crystal in the vicinity of the

FIG. 2. Slip lines on central portion of (111). The crystal was etched to show original dislocation structure prior to bending. The lines of intersection of $(\bar{1}11)$ and $(11\bar{1})$ with (111) are indicated. ×300.

points of contact with the bending jig. The direction and magnitude of the stress on the various planes is not known in these regions, but it is probable that both the $(1\bar{1}1)$–$[110]$ and $(1\bar{1}1)$–$[0\bar{1}1]$ systems were operative. Dislocations with Burgers vectors $\frac{1}{2}a[110]$ and $\frac{1}{2}a[011]$ would repel each other [this reaction is of the same type as that given in Eq. (2)]. Therefore, if the two systems operated on $(1\bar{1}1)$, it would be expected that the slip band resulting would differ from a band formed by slip of a single system and that many dislocations would be left along the line of the band. This hypothesis is in agreement with the experimental observations.

The observations of the increased visibility of $(\bar{1}11)$ and $(11\bar{1})$ slip lines on intersection with $(1\bar{1}1)$ lines, and the subsequent finding of dislocations in the $(\bar{1}11)$ and $(11\bar{1})$ lines near these intersections indicate an interaction between these slip systems. The equations

(a) (b)

FIG. 3. Electron micrographs of preshadowed carbon replicas of intersections of $(1\bar{1}1)$ and $(11\bar{1})$ slip lines. (a) ×6000 (b) ×3000.

for the possible dislocation reactions on the $(\bar{1}11)$ and $(1\bar{1}1)$ planes are given below:

$$\tfrac{1}{2}a[0\bar{1}1]+\tfrac{1}{2}a[110]=\tfrac{1}{2}a[101], \quad (1)$$

$$\tfrac{1}{2}a[0\bar{1}1]+\tfrac{1}{2}a[\bar{1}\bar{1}0]=\tfrac{1}{2}a[\bar{1}\bar{2}1], \quad (2)$$

$$\tfrac{1}{2}a[0\bar{1}1]+\tfrac{1}{2}a[011]=\tfrac{1}{2}a[002], \quad (3)$$

$$\tfrac{1}{2}a[0\bar{1}1]+\tfrac{1}{2}a[0\bar{1}\bar{1}]=\tfrac{1}{2}a[0\bar{2}0]. \quad (4)$$

Reaction (1) will occur because the energy is decreased, while reaction (2) indicates a repulsion between the dislocations.† For reactions (3) and (4) no change in energy is involved, but $\frac{1}{2}a[002]$ is not a slip vector. The dislocation of Burgers vector $\frac{1}{2}a[101]$ which is formed by reaction (1) lies in the $(\bar{1}11)$ plane and, thus it can move in that plane. Since $\frac{1}{2}a[101]$ has a screw component on intersection with (111) (the surface examined here), when it moves on $(\bar{1}11)$ it leaves a large step, increasing visibility of the line locally. This accounts for the increase in step height of the slip lines corresponding to $(\bar{1}11)$ near the intersection with $(1\bar{1}1)$.

FIG. 4. Etch pits at dislocations after bending. Same area as Fig. 2. ×300.

† For the reaction $\mathbf{b}_1+\mathbf{b}_2=\mathbf{b}_3$, $\mathbf{b}_1$, and $\mathbf{b}_2$ will attract if $b_3^2<(b_1^2+b_2^2)$ and will repel if $b_3^2>(b_1^2+b_2^2)$ as suggested by Frank.[4]

[4] F. C. Frank, Physica **15**, 131 (1949).

FIG. 5. Etch pits at dislocations showing interaction of $(\bar{1}11)$ and (111) with $(1\bar{1}1)$. ×300.

Since the $\frac{1}{2}a[101]$ dislocations are held at one end, they can move a relatively short distance along $(\bar{1}11)$. Thus, pits corresponding to these dislocations are seen close by the intersection points of the two slip planes (see Fig. 5). These dislocations are not pile-ups in the usual sense of this term. According to the symmetry of the f.c.c. system the intersection of $(11\bar{1})$ with $(1\bar{1}1)$ should act in a similar way. From the dislocation reactions for these planes, it is found that the $\frac{1}{2}a[011]$ on $(1\bar{1}1)$ dislocations react with $\frac{1}{2}a[1\bar{1}0]$ on $(11\bar{1})$ to form $\frac{1}{2}a[101]$ dislocations which can glide on $(11\bar{1})$ in the same way as already described.

The fact that few dislocations are found along the $(\bar{1}11)$ and $(11\bar{1})$ slip lines indicates that the dislocations moved large distances. From a comparison of Fig. 2 with Fig. 4, it is obvious that sub-boundaries in the crystal rarely stopped these dislocations.

From the observation of the intersections of $(\bar{1}11)$ and $(11\bar{1})$ slip lines, and from the positions of dislocations after slip as revealed by etch pits, it is clear that these slip systems do not interact in the same way as that described in the foregoing. The dislocation reactions for these systems are

$$\frac{1}{2}a[0\bar{1}1]+\frac{1}{2}a[1\bar{1}0]=\frac{1}{2}a[1\bar{2}1], \quad (5)$$

$$\frac{1}{2}a[01\bar{1}]+\frac{1}{2}a[1\bar{1}0]=\frac{1}{2}a[10\bar{1}]. \quad (6)$$

Reaction (5) describes a repulsive interaction. Reaction (6) is the Lomer[5] reaction. The dislocation $\frac{1}{2}a[10\bar{1}]$ formed by this reaction is sessile because the line of the dislocation does not lie in either the (111) or the $(1\bar{1}1)$ planes for which $[10\bar{1}]$ is a proper slip vector. (As pointed out by Cottrell,[5] for metals in which the dislocations are extended, this reaction would result in a truly sessile dislocation.) The difference between Eqs. (5) and (6) is merely the sign of one or the other Burgers vectors. Thus, whether or not interaction occurred would be a statistical question. If reactions occurred [reaction (6)] further slip on these planes would be inhibited, and dislocations would form a pile-up at the intersection points. Since these slip lines are faint, changes in the amount of slip near these intersection points cannot be detected. If, on the other hand, no reaction occurred [reaction (5)], there would be no observable effect of the intersecting of the slip lines nor any dislocations left near the intersections.

[5] A. H. Cottrell, *Dislocations and Plastic Flow in Crystals* (Oxford University Press, New York, 1953), p. 170.

TABLE I. Slip plane, slip direction, and resolved shear stress.

Slip plane	Slip direction	Relative resolved shear stress
	$\bar{1}10$	0
111	$10\bar{1}$	0
	$0\bar{1}1$	0
	$0\bar{1}1$	3
$\bar{1}11$	110	1
	$\bar{1}0\bar{1}$	2
	110	2
$1\bar{1}1$	$10\bar{1}$	0
	$0\bar{1}\bar{1}$	2
	$0\bar{1}\bar{1}$	1
$11\bar{1}$	101	2
	$\bar{1}10$	3

This explanation is in qualitative agreement with the experimental observations as can be seen in Figs. 2 and 4.

Thus, the appearance of the slip lines and the subsequent location of the dislocations is accounted for by dislocation interactions. It should be noted that the effects observed here would only be seen on hardened crystals. For annealed crystals, if dislocation interaction occurred on one plane, the slip process would simply shift to an adjacent plane before an observable number of dislocations had piled up in one plane.

ACKNOWLEDGMENT

The authors wish to thank D. K. Holmes of this Laboratory for many helpful discussions.

Letters to the Editor

Comments on Article by Cook

M. H. MILLER
The University of Michigan, Ann Arbor, Michigan
(Received September 22, 1959)

COOK has recently described a classification of long, dense electron beams with a uniform velocity profile.[1] His description is based on a consideration of magnetic flux linkages through the cathode and is, in essence, a special case of the well-known classification of beams as irrotational or nonirrotational. This latter more general classification has the advantage of emphasizing the congeneric nature of the different beam models considered as well as more clearly indicating the physical effect of various parameters.

The beam classification referred to is based on a theorem of classical mechanics known variously as Poincare's invariant, Lagrange's invariant, or Busch's theorem. For the present purpose this theorem may be stated as follows: In a hydrodynamical, laminar flow of electrons the circulation of the canonical momentum around any closed contour is a constant. In the special case of axially symmetric beams this statement is equivalent to that made by Cook to the effect that the canonical angular momentum is a constant of motion. The somewhat unfamiliar statement above of Newton's law as applied to electron beams is particularly convenient because it is relatively easy to derive from it the fact that the curl of the canonical momentum is zero if there is no magnetic field normal to the cathode on which the beam originates.[2] It is shown below that, among other things, the Class I and II beams of Cook are special cases of the general axially symmetric irrotational beam and that his Class III and IV beams are derived from the axially symmetric irrotational beam.

Consider a beam which is both axially symmetric ($\partial/\partial\theta=0$) and axially uniform ($\partial/\partial z=0$). This is a somewhat more general case than considered by Cook in that the axial velocity need not be radially invariant. The two symmetry conditions make it mandatory to further assume zero radial velocities in order to keep the beam together. By definition an irrotational beam is one for which

$$\nabla\times\mathbf{v}-\eta\mathbf{B}=0, \tag{1}$$

where $\mathbf{v}$ is the electron velocity, η is the magnitude of the charge-to-mass ratio, and $\mathbf{B}$ is the magnetic field. Maxwell's equations, subject to the symmetry constraints, require the magnetic field components to be

$$\mathbf{B}=(B_\theta/r)\boldsymbol{\theta}+B_z\mathbf{Z}, \tag{2}$$

where B_θ and B_z are both constants, and $\boldsymbol{\theta}$ and $\mathbf{Z}$ are unit vectors in a cylindrical coordinate system.

Expansion of Eq. (1) in cylindrical coordinates and integration of the results leads to the following expressions:

$$\dot{\theta}=(\omega_c/2)+(\Omega_0/r^2), \tag{3}$$

$$v_z=v_0-\eta B_\theta \ln r, \tag{4}$$

where ω_c is the cyclotron frequency ηB_z, and v_0 and Ω_0 are as yet unspecified constants of integration. Substitution of the above expressions into Poisson's equation (using the energy conservation relation to relate velocity and potential) results in the following expression for the space-charge density:

$$2\omega_p^2-\omega_c^2-2\left(\eta\frac{B_\theta}{r}\right)^2-\frac{4\Omega_0^2}{r^4}=0, \tag{5}$$

where ω_p is the plasma frequency. Expressions for other beam parameters can be derived easily from the last three equations. For example, the potential variation can be found by appropriately combining the squares of Eqs. (3) and (4), and the beam current density can be obtained through multiplication of Eqs. (4) and (5).

The above equations describe all irrotational beams which satisfy the prescribed conditions. From Eq. (4) it is seen that a θ-directed magnetic field and a uniform axial velocity profile are incompatible. This is the physical interpretation of Cook's parameter α being zero for Class I and II beams. It is further seen that an irrotational beam in the presence of a θ-directed magnetic field must necessarily be hollow under the prescribed conditions.

We now restrict consideration to beams with a uniform axial velocity profile since these are the more familiar ones and are each indicative of a general type of beam. In this case, with B_θ zero, the constant v_0 is simply the constant axial velocity. Its magnitude may be arbitrarily adjusted by a suitable choice of electrode potentials. The single constant Ω_0 then serves to differentiate various types of beams.

For Ω_0 equal to zero the beam is either a solid axial Brillouin flow or a hollow modification of this flow. The axial velocity may be zero in which case the flow is a circumferential counterpart of rectilinear Brillouin flow. Note that Ω_0 must be zero for any flow which includes the axis.

A variety of flows are possible with nonzero values of Ω_0. One familiar flow occurs if $\dot{\theta}$ vanishes on some cylindrical surface (cathode, for example). This boundary condition can be used to evaluate Ω_0; the result is a description of single stream magnetron flow.

It is, of course, necessary to assume that the cathode for the above flows is so oriented or shielded with respect to the magnetic field as to make the beam irrotational. One way to insure an irrotational beam is to make the magnetic field zero. In this case Ω_0 is necessarily nonzero. If the axial velocity is not zero, the result is Harris flow. If the axial velocity is zero the result is sometimes called E flow. These flows must exclude the axis; they are necessarily hollow beams.

Straightforward substitution shows that Cook's parameter Ω_0, the canonical angular momentum divided by mass is identical with Ω_0 as used here. We prefer, however, to consider Ω_0 primarily as a measure of the radial electric field (or potential).

We now consider whether it is possible to meet the prescribed flow conditions with a nonirrotational stream. In this case we must turn back to the general theorem which, in its differential form, can be stated as

$$\mathbf{v}\times\nabla\times\mathbf{p}=0, \tag{6}$$

where $\mathbf{p}$ is the canonical momentum. Expanding this equation we have

$$\dot{\theta}(\partial/\partial r)(r^2\dot{\theta})=\omega_c r\dot{\theta}-(\alpha/r), \tag{7}$$

where $\alpha=\eta B_\theta v_0$. We have assumed the axial velocity v_0 is constant for simplicity. When α is zero (no θ-directed magnetic field), it is found that $\nabla\times\mathbf{p}$ is also zero. The stream is hence irrotational, and the previous discussion exhausts all possible beams meeting the prescribed conditions with a purely axial magnetic field. The other limiting case, for which ω_c is zero (Class III beam) leads to the equations

$$\dot{\theta}^2=(\Omega_0/r^4)-(\alpha/r^3), \tag{8}$$

$$\omega_p^2=(2\Omega_0/r^4). \tag{9}$$

Cook's parameter Ω is then

$$\Omega^2=\Omega_0-\alpha r^2. \tag{10}$$

It is clear that these nonirrotational streams are necessarily hollow streams. By integrating Eq. (7) with neither α nor ω_c zero (Class IV beams) it can be seen that this is true in general for nonirrotational beams of the type considered.

From the classification used above a number of general observations may be made. It is seen that, with purely axial magnetic field, beams meeting the prescribed conditions must necessarily be irrotational. Hence there can be no magnetic field normal to the cathode of such beams. It is also seen that Cook's parameter Ω must be a constant for all these beams and, except for an axial Brillouin flow, cannot be zero. The relationship of Ω to such beam parameters as space-charge density, potential, angular velocity,

etc., follows directly from the analysis. The gun problem in these cases is one of launching an irrotational beam for which ω_e is not zero and matching this with another irrotational beam for which ω_e may or may not be zero. Consideration of the general expressions for the velocity and space-charge density of these beams suggests that a gun based on an appropriate modification of magnetron flow holds some promise.

It is further seen that the Class III beam is the only beam which meets the prescribed conditions with a purely θ-directed magnetic field. Such a beam degenerates into Harris flow if the magnetic field is removed. Since this beam is not irrotational there must be a magnetic field normal to the cathode surface. This is a necessary condition for the general Class IV nonirrotational beam.

[1] E. J. Cook, J. Appl. Phys. **30**, 860–865 (1959).
[2] D. Gabor, Proc. Inst. Radio Engrs. **33**, 792–805 (1945).

Diffusion of Copper into AlSb

R. H. Wieber,* H. C. Gorton, and C. S. Peet
Battelle Memorial Institute, Columbus, Ohio
(Received October 30, 1959)

THE diffusion of copper into AlSb was studied in the temperature range from 150°C to 500°C by radio tracer techniques. AlSb samples were prepared by lapping on 600 grit SiC paper, polishing to a mirror finish with dry Linde *A* on photographic blotter paper, and etching for 1 min in 4:4:1 $HCl:HNO_3:H$ tartaric, then for 2–3 sec in 1:1 $HCl:HNO_3$, and drying in alcohol. Cu^{64} was plated onto one surface of single-crystal samples of AlSb from a solution of potassium acid tartrate, using a Cu^{64} anode. In order for plating to initiate, Cu ions must be present in the solution. Part of the radioactive Cu electrode therefore was dissolved in HNO_3 and added to the electrolyte. The electrolyte was then made slightly basic by the addition of K_2CO_3. Plating was carried out at about 15 ma/cm² for 30 min.

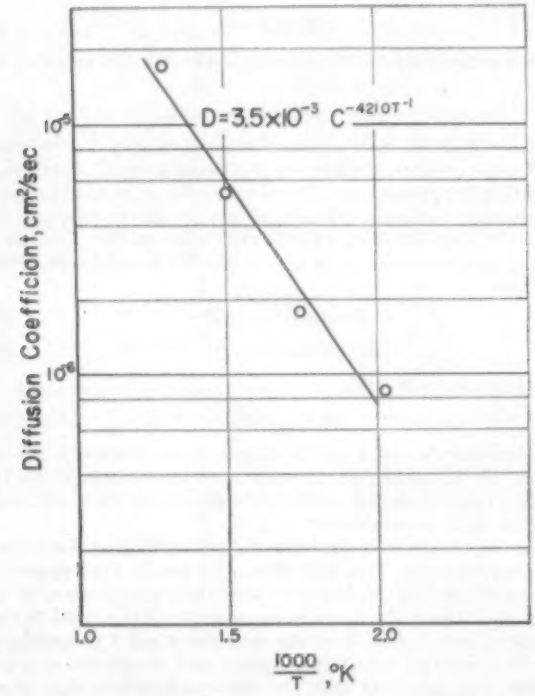

FIG. 1. Temperature dependence of the diffusion coefficient for copper in AlSb.

The plated samples were placed in quartz containers and heated in an argon atmosphere. After the heating cycle, excess Cu was removed from the AlSb surface, and the activity of successive layers of the diffused crystal was counted with a sodium iodide-thallium activated crystal in conjunction with a 100 channel analyzer.

Although appreciable scatter was observed in the data on concentration as a function of depth, tentative values for D_0 of 3.5×10^{-3} cm²/sec and an activation energy of 0.36 ev are obtained from the plot of D *vs* T^{-1}, Fig. 1. The complementary error function solution to Fick's law of diffusion is assumed. The first two points on the curve in Fig. 1 are averages of D obtained from two diffusion runs at each temperature for different times. The value of D at 150°C is substantiated by observations of the depth of p-n junctions produced by diffusing copper into n-type AlSb at that temperature. The extremely rapid diffusion rate of copper into AlSb not only precludes the use of copper as a dopant in the formation of p-n junctions for high temperature operation, but also points up the extreme care that must be taken to avoid copper contamination during the processing of AlSb crystals for device application.

Gratitude is expressed to the Compound Semiconductor Research Group for supplying the AlSb used in these studies.

* Michigan College of Mining and Technology, Battelle Summer Training Program.

Operation of a Chromium Doped Titania Maser*

H. J. Gerritsen and H. R. Lewis
RCA Laboratories, Princeton, New Jersey
(Received October 28, 1959)

A MASER using Cr^{3+} paramagnetic ions in titania has been operated at several frequencies between 8.2 and 10.6 kMc using a pump frequency of 35 kMc (Fig. 1). It has also been operated at 22.3 kMc with a pump frequency of 49.9 kMc (Fig. 2).

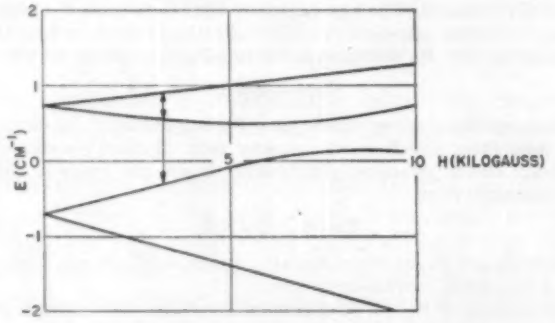

FIG. 1. Energy levels for *X* band maser. $H=3300$ g. $\theta=80$, $\phi=90$ Coordinates as in reference 1.

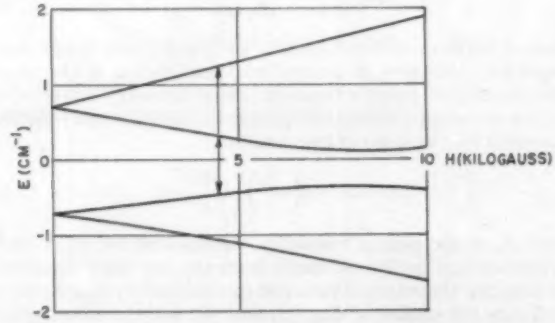

FIG. 2. Energy levels for *K* band maser. $H=4500$ g. $\theta=30$, $\phi=90$. Coordinates as in reference 1.

A description of the paramagnetic spectrum of chromium in titania has previously been published.[1] The doping used in the material reported here is such that 0.12% of the titanium ions were replaced by chromium.

The high dielectric constant of titania lends itself to a novel and useful mode of operation in which the maser crystal itself acts as a dielectric cavity operating in a very high mode. This produces a dense spectrum of possible operating frequencies; moving from one of these to another requires only a small change of the magnetic field. Moreover, at some orientations, two or more of these modes can be made to amplify simultaneously. For example at X band, amplification at two modes centered 12 Mc apart has been observed. In a single mode, the voltage gain-bandwidth product was 25 Mc at 4.2°K. Since performance was limited by oscillation, it is expected that this figure can be considerably increased by properly coupling the cavity to the input wave guide. The gain-bandwidth product at 22.3 kMc was limited by low pump power.

Because of its high zero field splitting (43 kMc) chromium-doped titania is a suitable material for cw operation of a maser at least as high as 40 kMc using magnetic fields smaller than 10 kilogauss. Moreover, at and below X band, the relatively high pump frequencies which can be used with this material may result in lower magnetic Q's than can be obtained in ruby, and thus, in improved amplifier characteristics.

* This work was supported by the U. S. Army (Signal Corps).

[1] Gerritsen, Harrison, Lewis, and Wittke, Phys. Rev. Letters 2, 153 (1959).

Manipulation of Cesium

P. Leliak
The Martin Company, Baltimore, Maryland
(Received November 9 ,1959)

THE use of cesium for obtaining high ion currents, such as in the field of ionic propulsion, has led to the necessity of transferring large amounts of this metal into glass or metal boilers. Usually, pure cesium for laboratory usage is available in small glass ampoules weighing from 1 g to 5 g.

Because cesium reacts vigorously with air, the ampoule should be opened without exposing the metal to air. In the past, the special procedures developed for this purpose (see, for example, *Procedures in Experimental Physics*, by J. Strong) have been quite cumbersome and have required qualified operators.

We have found experimentally that ampoules with cesium, after being cooled in liquid nitrogen, can be opened and exposed to air without an explosion. Such an opened ampoule containing cesium will not explode even if allowed to return to room temperature.

It is very probable that cesium does not react with air at liquid nitrogen temperatures. With the rise in temperature, oxidation of cesium starts on the surface of the metal and creates a film of cesium oxides and hydroxide which considerably decrease the rate of penetration of air to the metallic surface of cesium. The reaction heat created during the oxidation of the upper layer of cesium is dissipated in the metal, but because of its low temperature it cannot produce vaporization of the metal, which would destroy the surface film of cesium oxides.

With the rise in temperature, the thickness of the layer of cesium oxides increases and can last a few hours. Thus, the opened ampoule can easily be put into a boiler.

The cesium boiler we used consists of a stainless cylinder with a welded top and bottom and two steel tubes welded in at the top. One tube has a packless stainless steel valve with copper gaskets and stainless bellows and is joined to the vacuum pump. The other tube bears a flange and has a sharpened edge on its open end.

This opening can be closed by a cap with a copper gasket which is tightened by means of bolts. The frozen ampoules are put into the boiler through this tube. This boiler can be heated up to 400°C without corrosive effects. The whole procedure, which is not dangerous at any stage, can be accomplished in a few minutes.

Print-Out Process in Photographic Emulsion Grains*

J. F. Hamilton and L. E. Brady
Research Laboratories, Eastman Kodak Company, Rochester, New York
(Received October 9, 1959)

THE print-out process[1] in silver halides consists of the alternate migration, to a growing silver speck, of photoelectrons and positively charged ionic defects. Since interstitial ions (Frenkel disorder) are found to predominate by far over halide-ion vacancies (Schottky disorder),[2] they are presumably the positively charged ionic defects involved. This mechanism, however, requires a means for providing space within the lattice for a growing silver speck, since it constitutes a net transport of material to that site. The spatial limitation would not exist if the ionic step came about by approximately equal numbers of interstitial silver ions and halide-ion vacancies, since spacewise they roughly cancel one another. However, equilibrium concentrations of halide-ion vacancies are generally thought to be too low to support this latter type of mechanism at rates which are frequently observed.

Mitchell and co-workers[3–5] found that stresses set up by the inclusion of foreign particles in silver halide crystals could relax by causing plastic deformation of the crystal. Prismatic dislocations[6,7] form at the interface between the crystal and the inclusion, and glide away from the particle along [110] directions with negligible climb. The result is that a set of 12 prisms, radiating out from the particle, are deformed in compression. This mechanism applies not only for small glass beads immersed in the melt from which the crystals are grown,[3] but also, in crystals of silver chloride containing copper, for particles of silver formed by photolysis.[4]

Electron-microscopic examination of replicas of heavily photolyzed silver halide grains from a photographic emulsion has provided a direct confirmation of this mechanism and evidence that it applies also for the formation of print-out silver in photographic grains.

In a tabular photographic grain, the twelve [110] prisms centered on an internal particle of print-out silver (except particles very near the side faces) are oriented in the following way: Six lie in a plane parallel to the large faces and intersect the sides; three intersect the top face in a triangular configuration; and three, the bottom face in a similar way. Grain thicknesses are generally only a fraction of a micron, so that most of the prismatic dislocations which glide along the six [110] directions toward the large faces actually reach the grain surface.

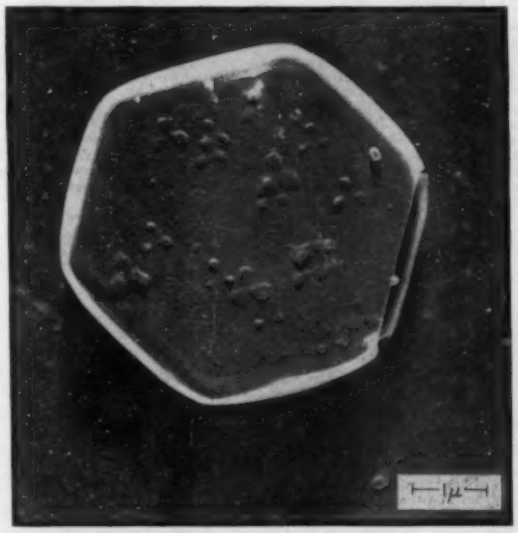

FIG. 1. Electron micrograph of a replica of a heavily exposed grain from a photographic emulsion, showing triangular patterns of protrusions caused by internal silver particles.

The result of this mechanism has been directly observed on electron micrographs of the silver bromide grains of a suitable emulsion: Each internal silver particle causes on each of the large faces a triangular group of three protrusions, which represent the intersection of the dislocation loops with the grain surface. The length of the side of the triangle formed by the three is determined by the distance of the particle from the surface.

On the grain[8] shown in Fig. 1[9] may be seen a number of these protrusions. They appear in triangular groups of three, the triangles having the orientation which would result from the intersection of [110] lines with the [111] face. Although the sizes of the protrusions vary from group to group, that of the three within any one group is the same, representing apparently the size and shape of the silver particle. It is also apparent that the sides of the triangles formed by the groups are all the same length. It is generally true that, on a single grain, the triangles have no more than two distinct sizes, and usually only one. The constant size of the triangular pattern over a grain indicates that all of the internal silver particles form on a single plane (or sometimes two) parallel to the large faces. The distance of this plane from the top face may be computed from the dimensions of the triangles and the crystallographic geometry, and may be compared with the grain thickness as measured by shadow length. In 95% of the grains examined, the plane of the silver particles was found to lie in the central half of the grain.

These conditions suggest the possibility that the twin plane which exists in such tabular grains[10,11] provides a favorable site for the formation of silver particles, either by virtue of its own electrical properties or possibly as a result of preferential impurity segregation near the twin plane. Although twin planes in themselves introduce no marked electrical effects in metals, zinc sulfide crystals do exhibit anisotropic photoconduction, which has been attributed to the interaction of photoelectrons with twin planes.[12] Nontabular photographic grains, which presumably are not twinned, also print out internally. The twin plane is certainly not the only type of defect on which silver can separate. However, it appears possible that, when present, a twin plane serves as a highly preferential location for the formation of silver particles.

* Communication No. 2057 from the Kodak Research Laboratories.
[1] C. E. K. Mees, *The Theory of the Photographic Process* (The Macmillan Company, New York, 1954), 2nd edition Chap. 4, p. 101.
[2] C. R. Berry, Phys. Rev. **82**, 433 (1951).
[3] D. A. Jones and J. W. Mitchell, Phil. Mag. **3**, 1 (1958).
[4] A. S. Parasnis and J. W. Mitchell, Phil. Mag. **4**, 171 (1959).
[5] J. W. Mitchell, Faraday Society Discussion on Crystal Imperfections and the Chemical Reactivity of Solids, Kingston, Ontario, September 2–4, 1959.
[6] J. F. Nye, Proc. Roy. Soc. (London) **A198**, 191 (1949).
[7] F. Seitz, Phys. Rev. **79**, 723 (1950).
[8] This is a grain from an unsensitized silver bromide emulsion, such as has been used in previous studies: Hamilton, Hamm, and Brady, J. Appl. Phys. **27**, 874 (1956); Hamilton, Brady, and Hamm, *ibid.* **29**, 800 (1958); J. F. Hamilton and L. E. Brady, *ibid.* **29**, 944 (1958).
[9] Figure 1 is an electron micrograph of a carbon replica, preshadowed with platinum-palladium (80%–20%) at an angle of 3:1. The grain was heavily exposed to ultraviolet radiation after removal of the gelatin. Most of the print-out silver formed is not on the surface of the grain, and so is not retained quantitatively by the replica. Those silver particles which do adhere to the replica are merely those which make a chance contact with the replica during fixation and washing. Therefore, no significance can be attached to their locations in the micrograph.
[10] R. W. Berriman and R. H. Herz, Nature **180**, 239 (1952).
[11] J. F. Hamilton and L. E. Brady, J. Appl. Phys. **29**, 944 (1958).
[12] Lempicki, Frankl, and Brophy, Phys. Rev. **107**, 1238 (1957).

Solution-Precipitation Deformation under an Applied Stress

W. D. Kingery and M. P. Lepie
Massachusetts Institute of Technology, Cambridge, Massachusetts
(Received December 21, 1959)

It has previously been shown[1] that the densification which takes place during the sintering of a solid-liquid mixture results from solubility differences caused by applied compressive stresses at the contact point between solid particles. This pressure causes an increase in chemical potential or activity of the solid phase at the contact point according to the relation,

$$\mu-\mu_0=RT\ln(a/a_0)=\Delta PV_0. \quad (1)$$

This change in solubility with applied pressure can lead to other effects which are similar to those observed in ice where an applied pressure lowers the melting point and causes local melting.

Perhaps, the best example of the pressure effect in ice is the experiment of Bottomley[2] in which a wire with weights hung on either end was observed to cut through a block of ice. The ice melts under the compressive stress side of the wire and refreezes above the wire, so that the wire passed through the entire block without doing permanent damage. This same sort of result has been observed in sodium chloride by comparing the rate of penetration of a spherical indenter on a dry sample and one in contact with a saturated solution.

Plates of single crystal sodium chloride were prepared by cleavage and fresh surfaces were inserted under a $\frac{1}{4}$ in. diam spherical indenter on a modified micro-hardness tester. The tester was arranged such that the contact area could be observed from below, focusing on the interface with a micrometer telescope through a prism. One set of measurements was made with freshly cleaved dry surfaces. A plastic indentation was observed; the size of the indentation did not change with time under the indenter. Other measurements were carried out with a drop of saturated sodium chloride solution affixed to the indenter. Under these conditions, the initial size of the indentation was similar to that observed with the dry sample, but the indentation diameter increased with time as shown in Fig. 1. Evaporation tended to

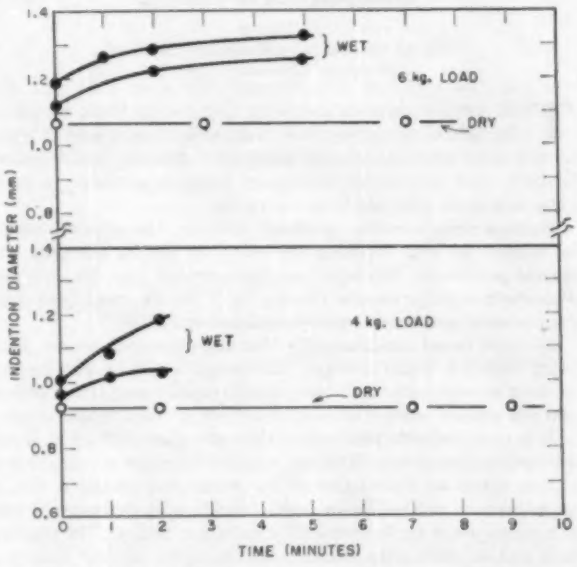

FIG. 1. Indentation of sodium chloride crystal with $\frac{1}{4}$ in. indenter under two loads using (a) dry indenter and (b) indenter wetted with saturated solution of sodium chloride.

dry the sample, so that observations were restricted to a time period of several minutes.

When in contact with a solvent under conditions of applied compressive stress, the solubility increases in the zone of high pressure as indicated in Eq. (1). There is a resultant transfer of material by solution, diffusion through the liquid, and precipitation at the sides of the indentation. This result is interpreted as being similar to the experiment of Bottomley and another example of the mechanism proposed for liquid phase sintering.

[1] W. D. Kingery, J. Appl. Phys. **30**, 301 (1959).
[2] J. T. Bottomley, Nature **5**, 185 (1872).

Etch Pits in Gallium Arsenide

J. L. RICHARDS AND A. J. CROCKER
Research Division, Philco Corporation, Philadelphia, Pennsylvania
(Received October 15, 1959)

THE etching characteristics of single crystal GaAs have been studied with a view to revealing edge dislocations on different crystal faces. Since the zinc blende lattice is polar, opposite ⟨111⟩ directions are not equivalent[1]; thus, the etching characteristics of opposite {111} faces will be different. In general, the acidic oxidizing etchants normally used will reveal etch pits only on the *A* face of the crystal, i.e., the (111) face. Such etchants will attack the *B* [or $(\bar{1}\bar{1}\bar{1})$] face to polish, oxidize, or to give specular reflections. The experiments outlined here describe the development of etchants, which will reveal dislocations on the *A* face, the *B* face, or both.

The crystals used were boat grown[2] and had a dislocation density between 10^3 and 10^4 cm^{-2}. They were oriented by observing the maximum in the intensity of specular reflections produced by etchant 2 (Table I) and (111) slices were cut. This etchant can, with practice, be used to orient the crystals to ±2–5° of ⟨111⟩ (as determined by x-rays). The slices were ground with 600 carborundum, then chemically polished with etchant 3.

TABLE I.

Etchant	Face	Action of etchant	Final form of etched sphere	Nature of pits shown in figure
1. 1 HNO_3:3 H_2O (Schell)[3]	*A*	Pits	Tetrahedron bounded by terraced *B* faces.	1a
	B	Terrace	Pits on apices.	
2. 1 HF:1–2 H_2O_2: 4–6 H_2O	*A*	Pits	Tetrahedron bounded by terraced *B* faces.	1b
	B	Terrace	Pits on apices.	
3. 1 HF:3 HNO_3:2 H_2O	*A*	Polish	Tetrahedron bounded by polished *B* faces.	
	B	Polish		
4. 1 HNO_3:3 H_2O (approx 1% $AgNO_3$ added)	*A*	Pits	...	
	B	Pits	...	
5. 1 HF:5–7 HNO_3: 8–12 H_2O (approx 1% $AgNO_3$ added)	*A*	Pits	Rhombic dodecahedron bounded by 110 faces (conc.) or cube bounded by 100 faces (dilute). Pits on *A* and *B* apices.	1c (*A* face)
	B	Pits		1d (*B* face)
6. 1 HF:3 HNO_3:0–4 H_2O (approx 1% $AgNO_3$ added)	*A*	Polish	Rhombic dodecahedron bounded by 110 faces.	
	B	Pits	Pits on *B* apices.	1e

The Table lists a number of etchants developed for GaAs. The nature of the etch pits developed on {111} is shown in the figures. The acidic oxidizing etchants reveal etch pits on *A* faces only.

The addition of metallic Ag ions to an HF/HNO_3 etchant slows down the rate of attack and enables etch pits to be revealed on the *B* faces or on both *A* and *B* faces depending on the composition of the etch. Figure 1 shows the nature of the etch pits revealed by

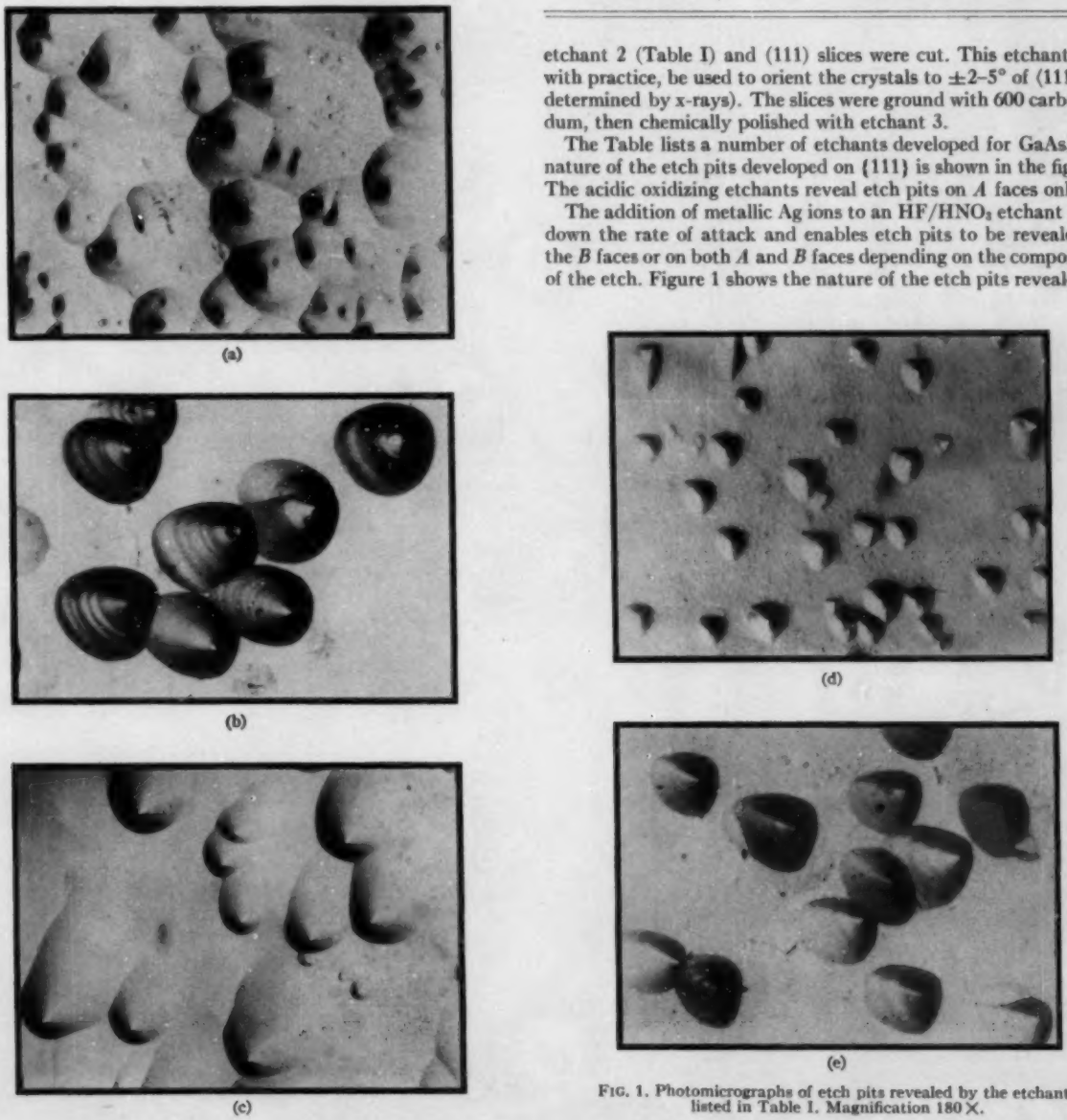

FIG. 1. Photomicrographs of etch pits revealed by the etchants listed in Table I. Magnification 180×.

the various etchants listed in Table I. Metallic ions other than Ag do not affect the etchant in this way. From a study of the etching of 6 mm diam spheres prepared by ultrasonic cutting, relative rates of attack on different crystal planes were observed. The fast oxidizing etchants attack the B faces preferentially to produce tetrahedra bounded by these faces. Due to its noncentro-symmetric structure a tetrahedron in GaAs is equivalent to an octahedron in Ge. Addition of Ag slows down the over-all attack and enables a sequence of polyhedra to be observed. This sequence is consistent with the atomic density of different planes as has been observed in Ge.[4]

[1] J. C. White and W. C. Roth, J. Appl. Phys. **30**, 946 (1959).
[2] J. L. Richards, J. Appl. Phys. (to be published).
[3] M. A. Schell, Z. Metallk. **48**, 158 (1957).
[4] R. C. Ellis, J. Appl. Phys. **25**, 1497 (1954).

Several New Methods to Measure the Thermal Diffusivity of Semiconductors*

J. H. Becker
National Bureau of Standards, Washington D. C.
(Received October 2, 1959)

THE techniques suggested in this note are well suited for measurements of thermal diffusivity on small semiconducting samples.[1] The thermal diffusivity is derived from changes in the steady-state temperatures when the front surface of the specimen is heated at a sinusoidally time-varying rate (ac) and in some cases with a nontime-varying component (dc). The temperature changes are usually deduced from thermalelectric effects produced in the samples. These effects include the *bolometric, Nernst,* and *Seebeck* effects. The bolometric effect depends upon the variation of the electrical conductivity with temperature ($d\sigma/dT$), while the Nernst and Seebeck effects depend upon the Nernst coefficient Q_n, and thermoelectric power θ, respectively.

The experimental arrangement of *method 1* is illustrated in Fig. 1(a). The front surface ($x=0$) of a rectangular parallelepiped sample is heated uniformly with flux $P=P^{dc}+P^{ac}\cos\omega t$, and the back surface ($x=a$) is *maintained at its prehealed temperature.* For the measurement of the bolometric effect, the sample is biased with an electric field E from a constant current supply, while for the Nernst effect, E is removed and a transverse magnetic field B is applied.

The dc temperature throughout the sample varies linearly with x, while the ac temperature is given approximately by[2]

$$T^{ac}(x,t)=|T^{ac}(x=0)|(\exp-\gamma x)\cos(\omega t-\phi), \tag{1}$$

where $|T^{ac}(x=0)|=(\kappa/\omega)^{\frac{1}{2}}\cdot p^{ac}/K$ and $\phi\approx\pi/4+\gamma x$. The net dc and ac heat fluxes into the surface are represented by p^{dc} and p^{ac}, respectively. The thermal diffusivity κ is related to the thermal conductivity K, heat capacity per gram c, and density d, by $K=\kappa cd$. The thermal diffusion length γ^{-1} equals $(2\kappa/\omega)^{\frac{1}{2}}$. It was assumed that the sample thickness a was small compared with its length l and width W and that the heating frequency was sufficiently high that $\gamma a\gg 1$. The resulting open-circuit bolometric and Nernst effect voltages are[1,2]

$$\Delta V_{bol}^{dc}=(Ela/2\sigma K)(d\sigma/dT)p^{ac} \tag{2}$$

$$V_{bol}^{ac}=(El\kappa/\sigma aK\omega)(d\sigma/dT)p^{ac}\cos(\omega t-\pi/2) \tag{3}$$

$$V_n^{dc}=(Bl/K)Q_n p^{dc} \tag{4}$$

$$V_n^{ac}=(Bl/aK)(\kappa/\omega)^{\frac{1}{2}}Q_n p^{ac}\cos(\omega t-\pi/4). \tag{5}$$

The thermal diffusivity can be evaluated from appropriate combinations of these voltages; four such combinations will be discussed. One can, for instance, measure the ac bolometric and Nernst effects and evaluate κ in a manner which is analogous to the determination of carrier lifetimes from the ratio of the photoconductive and photoelectromagnetic effects.[1] It follows from Eqs. (3) and (5) that

$$|V_{bol}^{ac}|/|V_n^{ac}|=(E/B\sigma Q_n)(d\sigma/dT)(\kappa/\omega)^{\frac{1}{2}} \tag{6}$$

from which κ can be evaluated if the electrical properties of the sample are known; the voltage calibration, heating flux, and surface loss terms cancel, as long as these remain constant during the course of the measurements.

One can also measure the magnitude of the ac *and* dc bolometric and Nernst effects; from Eqs. (2) to (5) it follows that

$$|V_{bol}^{ac}|/(\Delta V_{bol}^{dc})V_n^{dc}/|V_n^{ac}|=(2/a)(\kappa/\omega)^{\frac{1}{2}}. \tag{7}$$

The thermal diffusivity is thus obtained in terms of the voltage ratios, sample thickness, and heating frequency, and knowledge of the electrical properties is not required.

It is clear from examination of Eqs. (2) to (5) that other combinations of the measured voltages are useful, for instance, the ratio of the ac and dc bolometric or the ac and dc Nernst effects.

While in the above experiments the back surface of the specimen was maintained at constant temperature,[3] in *method 2* this temperature is *allowed to vary* slightly, and the thermal diffusivity is deduced from Seebeck voltages. The experimental arrangement illustrated in Fig. 1(b) uses three electrical contacts. Small probes are located at position 1 on the back ($x=a$) and position 3 on the front ($x=0$) faces of the specimen. These faces are parallel and their area is large compared with the area of the sides. Contact 2 can be massive and is located several times the thickness of the sample away from the heated region. It acts as an ac=0 reference point with respect to the ac temperatures and voltages at 1 and 3. The heating flux incident on the front surface is again represented by $P=P^{dc}+P^{ac}\cos\omega t$. The Seebeck voltages V_{21}^{ac} and V_{23}^{ac} are proportional to the ac temperatures at 1 and 3, respectively, while the Seebeck voltage V_{13}^{dc} is proportional to the dc temperature difference.

The small but finite ac temperature at the back surface is now essential in the analysis and is given by Eq. (1) with $x=a$. Again, several combinations of the ac and dc voltages can be used to evaluate the diffusivity. One can measure the ac Seebeck voltages at the front and back surfaces at a single frequency ω and determine κ from either a ratio of the amplitudes of these temperatures ($V_{23}^{ac}/V_{21}^{ac}=T_3^{ac}/T_1^{ac}$) or their phase difference [see Eq. (1) with $x=a$]. Another possibility is to perform the experiment at several heating frequencies, in which case a plot of $\ln(T_3^{ac}/T_1^{ac})$ or the phase difference vs $(\omega)^{\frac{1}{2}}$ should yield a straight line with slope $a/(2\kappa)^{\frac{1}{2}}$.

Still another way to determine κ is to make use of the dc temperature difference between the front and back surfaces. It can be shown that $T_3^{ac}/(T_3^{dc}-T_1^{dc})=a^{-1}(\kappa/\omega)^{\frac{1}{2}}p^{ac}/p^{dc}$.

In order to illustrate *method 2* with the simplest analysis, the effects of losses at the back surface were not included. Also, for most semiconducting materials, they will generally be unimportant

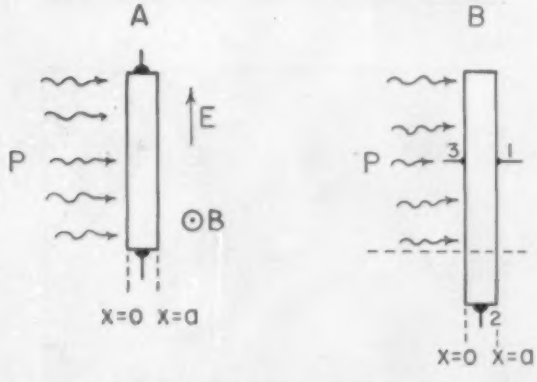

FIG. 1. Sample geometries and electrode positions. In Fig. 1(a), a rectangular parallelepiped sample is heated with flux $P=P^{dc}+P^{ac}\cos\omega t$. The directions of the electrical bias field E or magnetic field B used in the measurements of the bolometric or Nernst effects are indicated. In Fig. 1(b), a slab with parallel faces is heated (except at one end) with the ac and dc flux P, and no external fields are applied.

except for radiation losses at very high temperatures. This is due to the fact that departures of the phase difference and $\ln T_2^{ac}/T_1^{ac}$ from γa are of order $H/K\gamma$, where H is the heat transfer coefficient[3] and large values of $\gamma(\gg 1\ \text{cm}^{-1})$ are used.[1] Thus, a convenient test for large losses is that the thermal diffusivity calculated from the uncorrected relations of *method 2* will not be equal; moreover, the sample geometry lends itself to cancellation of these losses experimentally, e.g., by a modification in which two samples are positioned back to back.

In both *methods 1 and 2* the method of heating the samples is rather arbitrary. The use of strongly absorbed light has many desirable features; however, one should insure that the photoeffects (photoconductive, photoelectromagnetic, or Dember effects) are negligible compared with the corresponding thermalelectric effect.[1] Fortunately, even with samples a few tenths of a mm thick, the heating frequencies required to realize $\gamma a \gg 1$ are generally larger than a few cps. Narrow-band-pass ac amplifiers sensitive at these frequencies can be used. When tuned to the fundamental frequency, the effects of higher harmonics will not be measured. Thus a purely sinusoidal waveform is not required for the ac heating; e.g., in our experiments, square-wave chopping of the light has been used successfully.[1]

By considering other techniques for the measurement of thermal diffusivity,[4] the advantages of the proposed methods for small semiconducting samples can be evaluated.

* This research was supported in part by the U. S. Air Force through the Air Force Office of Scientific Research of the Air Research and Development Command.

[1] Preliminary accounts of some of these techniques have been described by I. I. Sochard and J. H. Becker, Bull. Am. Phys. Soc. Ser. II, **3**, 114 (1958); **4**, 134 (1959). A paper which includes the derivation of some of these equations and the interrelation between the thermalelectric and photoelectric effects has been prepared for publication.

[2] H. S. Carslaw and J. C. Jaeger, *Conduction of Heat in Solids* (Oxford University Press, New York, 1947), p. 57. See also pp. 88, 89, 104, and 259.

[3] An increase in the dc temperature at the back surface will not alter the equations for the Nernst effects or the ac bolometric effect.

[4] P. H. Sidles and G. C. Danielson, J. Appl. Phys. **25**, 58 (1954).

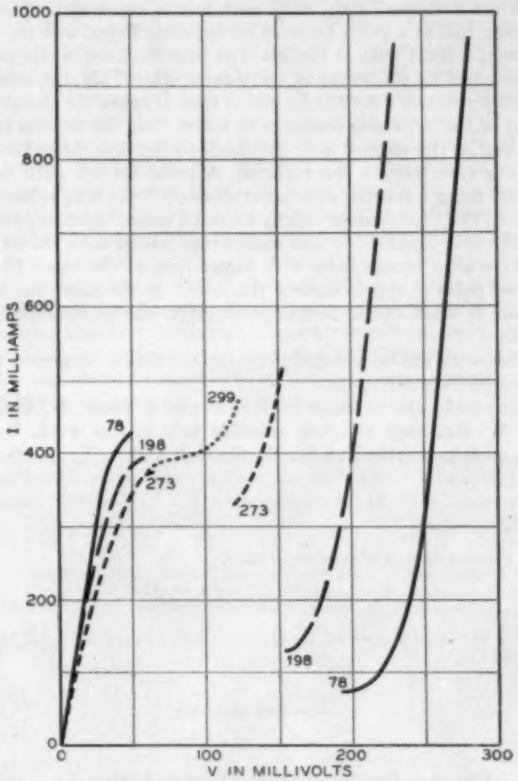

FIG. 1. V–I characteristics for InSb Esaki diode for various temperatures. Negative resistance region not shown.

Esaki Diode in InSb

R. L. BATDORF, G. C. DACEY, R. L. WALLACE, AND D. J. WALSH
Bell Telephone Laboratories, Incorporated, Murray Hill, New Jersey
(Received October 30, 1959)

A SEARCH for a simple microwave amplifier and power source has led to the investigation of devices exhibiting the Esaki effect.[1,2] Because of the low effective mass of the carriers in InSb, devices made of this semiconductor should show the Esaki effect at lower dopings or with wider transition regions than is possible in germanium or any other known semiconductor; therefore, they should be capable of smaller RC products than those reported in germanium.[2]

Negative resistance diodes have been fabricated by forming cadmium alloy p^+ junctions on n^+ single crystal InSb.[4] The crystals were doped with tellurium in the range from 10^{16} to 7×10^{17} cm^{-3}. The alloying was done in a hydrogen atmosphere on a resistive strip heater. Temperatures from 425 to 500°C were used with time cycles of 30 sec to several minutes. After masking and mesa etching, the diodes were mounted in a header of very low inductance.

Figure 1 shows the V–I characteristics of one such InSb diode with temperature as a parameter. Only the stable portions of the curves are shown because it is difficult with these extremely low impedance diodes to prevent relaxation oscillations in the negative resistance region. Data from other diodes when stabilization was accomplished indicated that the value of R in the negative resistance region is approximately 0.5 times the slope of the line passing through the maximum and minimum current. At 78°K, the value of R obtained in this way is approximately -0.2 ohm and the capacity is of the order of 25 mmfd leading to an RC product of 5×10^{-12} sec. The measurements described below were all performed at 78°K.

Relatively poor InSb diodes ($RC=10^{-9}$) have been used as rf oscillators by placing them in a suitable coaxial line cavity where the diode and mount become part of the center conductor. A stabilizing resistance was incorporated in the cavity to make it always appear as a positive impedance to the driving dc power supply. Fundamental rf oscillations up to 2.3 kMc were obtained with this cavity oscillator. It is believed that this operation was circuit limited and does not constitute an upper bound for the frequency cutoff of the negative resistance.

The diodes may be switched from one stable state to the other in an exceedingly short time. The diode is placed in the center conductor of a 50 ohm coax line as near as possible to a short-circuited end of the line. Direct current bias and a 160 Mc sine wave are applied to the diode through a circuit, which has almost no coupling to the coax line except through the diode under observation. The signal is observed with a stroboscopic oscilloscope[5] at the other end of the coax. This sampling oscilloscope can display rise times of the order of 0.1 mμsec on pulses which are periodic.

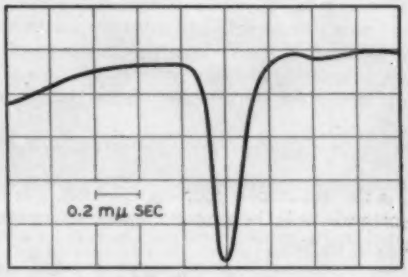

FIG. 2. Pulse formed with InSb Esaki diode and 7 cm shorted stub. Repetition rate 160 Mc.

When a shorted stub of 25 ohm line is connected across the 50 ohm line at a point between an isolating T-pad and the oscilloscope, a short pulse is formed. The time duration of the pulse is determined by the length of the shorted stub. This stub acts as a 25 ohm resistance for the length of time it takes the sharp wave front of the switching transient to travel from the 50 ohm line to the end of the shorted stub and back to the line. After this, the stub is essentially a short circuit. A pulse formed with such a circuit using a shorted stub approximately 7 cm long is shown in Fig. 2. The time base on this figure is 0.2 mμsec between lines. An ideally fast Esaki diode and oscilloscope would have shown with this circuit a square pulse 0.46 mμsec long at the base. The observed pulse is approximately this width at the base, but is not square in shape due to limitations of either the oscilloscope or the diode.

This work will be reported in greater detail in a paper now being prepared for publication.

We should like to thank D. E. Thomas, J. Klein, W. Wolfritz, and W. Kallensee for their valuable help in this work. We are also greatly indebted to W. M. Goodall and A. F. Dietrich for their help as well as for the use of their stroboscope. Many helpful discussions with D. Kleinman and C. A. Lee are gratefully acknowledged.

[1] L. Esaki, Phys. Rev. **109**, 603 (1958).
[2] T. Yajima and L. Esaki, J. Phys. Soc. Japan **13**, 1281 (1958).
[3] H. S. Sommers, Proc. Inst. Radio Engrs. **47**, 1201 (1959).
[4] C. A. Lee and G. Kaminsky (submitted as Letter to Editor of J. Appl. Phys.).
[5] W. M. Goodall and A. F. Dietrich, Bell System Tech. J. (to be published).

On the Possibility of Maser Action in Nuclear Quadrupole Systems

R. E. Donovan and A. A. Vuylsteke
Research Laboratories, General Motors Corporation, Warren, Michigan
(Received September 23, 1959)

IDEALLY, it should be possible to achieve a gain by stimulated emission in any assembly whose microscopic constituents each have three energy levels disposed in the manner described by Bloembergen.[1] More often than not, however, such a gain cannot be achieved in practice because losses in the circuitry required to couple radiation into a material are greater than the gain in the material, resulting in a net loss. We have recently analyzed certain nuclear systems which at first glance appeared to hold promise for achieving net gains. One system in particular involves a Zeeman-perturbed nuclear quadrupole spectrum and exhibits properties which are very nearly the best available for a three-level nuclear system. It is found, however, that here also the material gain is not quite sufficient to overcome circuit losses. Since it has been proposed elsewhere[2] that a similar system might be feasible, we present our calculations.

While there is a sufficient variety of systems to make complete generalization difficult, it is possible to establish reasonable limiting conditions on available gains. One might, for example, impress a Zeeman field, H_0, normal to an axially symmetric electric field gradient on a nucleus with half-integral spin which also has a quadrupole moment. If the Zeeman splitting is small relative to the quadrupole splitting the energy levels of the system can be calculated by first-order perturbation theory and are given by[3]

$$E_{I,\pm|m|}=\frac{e^2qQ}{4I(2I-1)}[3m^2-I(I+1)]\mp|m|\delta_{|m|\frac{1}{2}}\hbar\gamma H_0(I+\tfrac{1}{2}), \quad (1)$$

where e^2qQ is the quadrupole coupling constant, I is the nuclear spin (half-integral), m is the magnetic quantum number, γ is the gyromagnetic ratio, and

$$\delta_{|m|\frac{1}{2}}=\begin{matrix}0, & |m|\neq\frac{1}{2}\\ 1, & |m|=\frac{1}{2}\end{matrix}\Big\}.$$

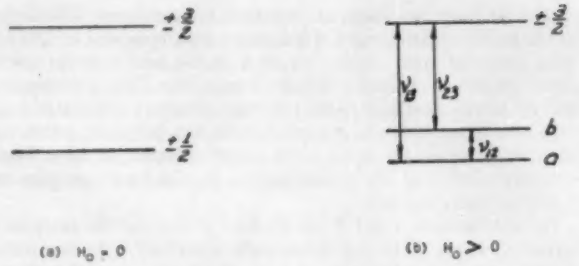

FIG. 1. Energy level scheme for a nucleus with $I=\frac{3}{2}$ and a nonzero quadrupole moment in an axially symmetric electric field. (a) Without Zeeman field; (b) with Zeeman field, H_0, normal to symmetry axis of the electric field.

With the selected Zeeman field orientation, then, the levels with $|m|>\frac{1}{2}$ are not affected by the magnetic field while the unperturbed level, $|m|=\frac{1}{2}$, is split into two perturbed levels, (a,b), each representing a mixture of equal parts of the $\pm\frac{1}{2}$ unperturbed eigenfunctions. The three lower levels of the perturbed system may then be displayed as in Fig. 1. Selection rules allow first-order transitions between all three levels shown in the figure.

In thermal equilibrium, the population densities of the levels, a, b, and $\pm\frac{3}{2}$ are

$$\left.\begin{aligned} n_a&\cong N_0/(2I+1)\\ n_b&\cong N_0(1-h\nu_{12}/kT)/(2I+1)\\ n_{\pm\frac{3}{2}}&\cong 2N_0(1-h\nu_{12}/kT)/(2I+1)\end{aligned}\right\}, \quad (2)$$

where N_0 is the total number of spins per unit volume and where the frequencies ν_{ij} are defined in Fig. 1(b). In the presence of a saturating field with frequency ν_{12}, on the other hand, the populations of levels a and $\pm\frac{3}{2}$ become

$$n_a^*=\tfrac{1}{2}n_{\pm\frac{3}{2}}^*=N_0(1-2h\nu_{12}/3kT)/(2I+1). \quad (3)$$

Thus, the population excess in level b relative to level a becomes

$$n_b-n_a^*=N_0h(2\nu_{12}/3-\nu_{12})/(2I+1)kT,$$

or

$$n_b-n_a^*=N_0h(2\nu_{23}-\nu_{12})/3(2I+1)kT. \quad (4)$$

This result is exactly equivalent to Bloembergen's[1] for $I=\frac{3}{2}$, and $w_{32}\cong w_{21}$ much greater than the transition rate induced by the signal field, if one accounts for the twofold degeneracy of the $\pm\frac{3}{2}$ level. It can also be shown that when $I>\frac{3}{2}$, Eq. (4) is still a good first-order approximation. With $I=\frac{5}{2}$, for example, the permitted transition $(\pm\frac{3}{2},\pm\frac{5}{2})$ will result in a small adjustment in the population distribution which is equivalent to an effective, small reduction in N_0.

The magnetic Q of the material described in Eq. (4) may be expressed as[1]

$$-(1/Q_{max})=4\eta h(n_b-n_a^*)W_{ab}/H_s^2, \quad (5)$$

where η is the filling factor, H_s is the maximum value of the magnetic vector of the signal field in the active material, and W_{ab} is the induced transition probability between levels a and b. Since[4]

$$W_{ab}=\tfrac{1}{4}\gamma^2H_s^2(I+\tfrac{3}{2})(I-\tfrac{1}{2})g(\nu), \quad (6)$$

with $g(\nu)$ the shape factor,

$$-(1/Q_{max})=\eta\gamma^2h(I+\tfrac{3}{2})(I-\tfrac{1}{2})(n_b-n_a^*)g(\nu). \quad (7)$$

It can also be shown[1] that the gain in such a system exceeds unity when

$$-(1/Q_{max})>1/Q_0,$$

where Q_0 is the unloaded Q of the circuit or cavity employed to couple the signal power into the active material.

As an example of what may be expected with a good material, consider the iodine nucleus $(I=\frac{5}{2})$ in CH_3I. Here, N_0 is of the order of 10^{22} cm^{-3}, $\gamma\cong 5300$, while for $H_0=10^4$ gauss, $\nu_{23}\cong 250$ Mc, and $\nu_{12}\cong 26$ Mc. The shape factor, $g(\nu)$, in this case would very probably be limited by spin-spin relaxation[5] to about 10^{-8} sec,

which would yield a $|Q_{mag}|$ for a 1 cm³ sample of the order of 10^5 at 4°K. At these frequencies, however, $Q_e \cong 250$ is likely and $Q_0 = 10^3$ represents a very optimistic upper limit. By using the optimistic estimate $\eta \cong 0.1$, one finds

$$-(1/Q_{mag}) \cong 10^{-2}(1/Q_0),$$

and no net gain.

Some adjustment of parameters might possibly be made by the selection of some other material. For example, a spin-spin relaxation time of 10^{-4} sec is conceivable. The likelihood of a system of this general type with a net gain is quite small, however.

[1] N. Bloembergen, Phys. Rev. **104**, 324 (1956).
[2] A. Javan, Phys. Rev. **107**, 1579 (1957).
[3] T. Das and E. Hahn, "Nuclear Quadrupole Spectroscopy" in *Solid State Physics*, edited by F. Seitz and D. Turnbull (Academic Press, Inc., New York, 1959), Suppl. 1, 8.
[4] Bloembergen, Purcell, and Pound, Phys. Rev. **73**, 679 (1948).
[5] H. G. Dehmelt, Naturwissenschaften **37**, 398 (1950).

Dislocation Etch Pits on P-Type Lead Telluride

B. B. Houston and Marriner K. Norr
U. S. Naval Ordnance Laboratory, White Oak, Silver Spring, Maryland
(Received November 23, 1959)

THE literature[1] contains descriptions of pit-producing etches for a number of materials and considerable evidence that the pits occur at the points where dislocations intersect the etched surface. This paper describes two etches for PbTe and some experiments, which indicate that the pits produced by these etches mark points where dislocations intersect the surface.

The first etch (which will be referred to as the iodine etch) was prepared from 10 ml of distilled water +5 g of NaOH+0.2 g of I_2. After the NaOH had dissolved, and while the solution was still hot, the I_2 was added. The final solution was colorless. Fresh cleavage-surfaces of p-type PbTe were etched by treating them with the solution for 5 min at 94–98°C. They were then rinsed with distilled water and carefully dried on filter paper. The pits thus obtained were approximately 5 μ across.

The second etch (which will be referred to as the iodate etch) was prepared from 10 ml of 0.5% $NaIO_3$ solution +5 g of NaOH. The etching process was the same as with the iodine etch. The pits were approximately 7 μ across. Reagent grade chemicals were used in the preparation of both etches.

The chemical species producing the pits are believed to be the same in both etches, namely IO_3^- and OH^-. Although in the iodine etch NaIO is formed initially, more than 90% of it disproportionates to $NaIO_3$ in one minute at 94–98°C (from a calculation based on the rate law given by Li and White).[2]

Both etches produced results qualitatively very similar to the results obtained on LiF by Gilman and Johnston[3] using their "*A*" etch. Pits were observed along small-angle grain boundaries, along the traces of active slip planes, and at isolated points on the surface. The pit densities found on pulled crystals as grown were between 10^4 and 10^5/cm². There were also preferential attack at cleavage steps. Etching before and after plastic deformation at room temperature showed that dislocations introduced by the deformation were attacked at about the same rate as those already present. In lightly deformed material, the new pits were found along the traces of active slip planes. In more heavily deformed material, the pits were almost uniformly distributed with densities ranging from 10^7 to 10^8/cm².

In a number of as-grown crystals the comparison of the pit patterns on the two surfaces, which were formed by the same cleavage, showed that the two surfaces were almost perfect mirror images of one another (see Fig. 1). If areas which showed traces of active slip planes were avoided, the numbers of pits in corresponding areas showed only two to three discrepancies per hundred pits. In areas where there was an indication of plastic deformation, the correspondence was not as good, probably because some of the deformation had occurred during the cleaving and after the surfaces had separated. Even in areas such as the one shown in Fig. 1 there was some indication of unequal motion of the dislocations on opposite sides of the cleavage plane; however, at this pit density (8×10^4/cm² not including the grain boundary) the resulting displacements were not large enough to obscure an almost perfect one-to-one correspondence between the pits on the two surfaces. There appeared to be little or no relation between the sizes of corresponding pits. Qualitatively, the skewness of corresponding pits appeared consistent with the hypothesis that the skewness was the result of the apex of the pit following the dislocation line into the crystal. Cleavage steps were moved in the direction of the higher surface and rounded slightly by the etch.

The chief disadvantage of the etching techniques described was that they must be used on fresh cleavage-surfaces. "Fresh" means

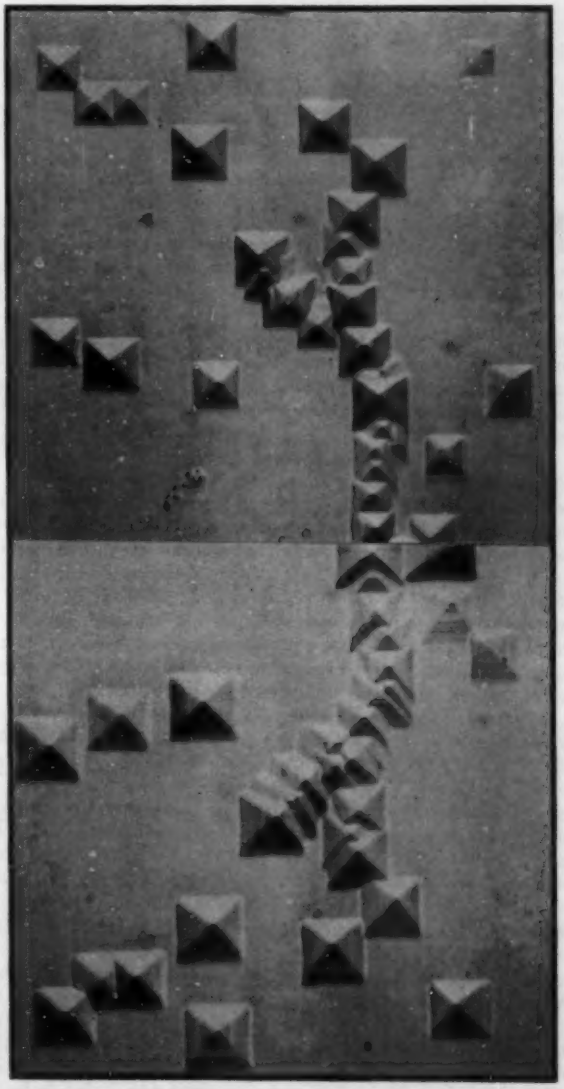

FIG. 1. These photographs show the pit patterns on the two opposite faces of the same cleavage. The upper pattern was formed by the iodine etch; the lower, by the iodate etch. In the area shown a well-defined small-angle boundary becomes diffuse. The cleave face is (001), and the [100] and [010] directions are parallel to the edges of the photographs. Magnification 870×.

that the surfaces must be unspoiled by mechanical damage or chemical contamination. There was no evidence that a lapse of time of hours between cleaving and etching was detrimental. Cleavage of PbTe is difficult because PbTe is slightly plastic at room temperature and because it frequently fractures conchoidally. Attempts to cleave PbTe at liquid nitrogen temperature indicate that it is less plastic at that temperature, but that the tendency toward conchoidal fracture may be even more pronounced. A polishing etch would be very helpful. Even with this restriction the etching techniques described in this letter should be very useful in studies of the effects of dislocations in PbTe.

We wish to acknowledge the advice of Dr. Robert F. Brebrick whose suggestion initiated this work.

[1] A bibliography is given by W. G. Pfann in *Solid State Physics*, edited by F. Seitz and D. Turnbull (Academic Press, Inc., New York, 1957), Vol. 4, p. 513.
[2] C. H. Li and C. F. White, J. Am. Chem. Soc. **65**, 335–339 (1943).
[3] J. J. Gilman and W. G. Johnston in *Dislocations and Mechanical Properties of Crystals* (John Wiley & Sons, Inc., New York, 1957), p. 117.

Ductility of NaCl Crystals

ROBERT G. GREENLER AND WILLIAM S. ROTHWELL
Research Laboratories, Allis-Chalmers Manufacturing Company, Milwaukee 1, Wisconsin
(Received June 8, 1959)

RECENTLY, a growing interest in the brittle-ductile behavior of ionic crystals has been evidenced by a number of papers reporting a variety of factors which influence the ductility of single crystal samples.[1–6] The interpretation of the effects of the various treatments on the ductile behavior of a sample lies in the comparison of the tests of samples which have received special treatment with those which have not. It is our opinion that uncontrolled random variations in stress history produce effects, which are of a much greater magnitude than those attributed to various other reasons.

Our initial work on NaCl[6] was concentrated on an attempt to obtain reproducible stress-strain curves for some constant set of reference conditions. The samples were tested in a three-point-loaded bending device under a constant loading rate. The supports used are $\frac{3}{16}$ in. steel rods mounted in ball bearings, rather than the usual knife edge supports. These rods are observed to rotate during the test, initially in one direction and, as bending proceeds, to reverse and rotate in the opposite direction through angles of 45 deg or more. If knife edge supports were used, over which the sample could not slide, the test results would be complicated by a set of stresses other than those resulting from bending.

As expected from many reports, starting with Joffe,[7,8] samples which had been dissolved for a time in water were much more likely to undergo large deformations than were those crystals tested as-cleaved. However, despite careful control of source of crystal samples (including a record of position in the original block), time after cleaving (from a few seconds to several months), length of time soaked (a few seconds to 10 minutes), time after soaking (a few seconds to several months), type of solvent (H_2O, various concentrations of NaCl solution, and ethylene glycol), environment of sample (air and oil), we were unable to find any combinations which consistently gave the same type stress-strain curve. A large sampling invariably gave a distribution such as that shown in Fig. 1, with a gross statistical separation into soaked and unsoaked samples. For example, in investigating the reported embrittling effect of exposure to air[8,5] we record a sample of NaCl which was soaked in water for three minutes, then stored in air (relative humidity about 30%) for over seven months before being tested. At rupture, this sample shows a strain of 12%. We have also tested several cleaved samples, which were not soaked in water, which undergo strains of 10% or more several days after being cleaved.

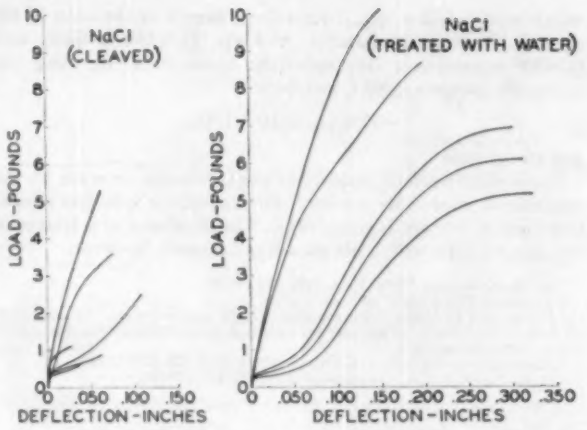

FIG. 1. Force-deflection curves of a group of cleaved crystals, $\frac{1}{4}$ in. by $\frac{1}{4}$ in. cross section, and a group of crystals cleaved to $\frac{1}{4}$ in. by $\frac{1}{4}$ in., then dissolved to the approximate dimensions $\frac{1}{8}$ in. by $\frac{1}{8}$ in. Distance between support rods is one inch.

We have concluded that the variations we have observed can be accounted for by the unavoidable different amounts of strain introduced by cleaving the samples plus the effect of surface damage in handling. It is found that the act of measuring the sample with a micrometer, or very lightly scratching or abrading the surface by other means before bending, drastically reduces the observed ductility. (Maximum strain introduced by simple bending is considered to be a measure of ductility.) In a controlled test of this factor, ductility was greater on the average by an order of magnitude for samples which were not measured with a micrometer prior to bending than for the samples which were measured prior to bending.

To investigate the effect of controlled strains on the stress-strain behavior of single crystal samples, a batch of crystals were prepared by cleaving samples with $\frac{1}{4}$ in. square cross sections and dissolving them in water to about $\frac{1}{8}$ in. square cross sections. These standard prepared samples loaded to twice their yield stress and then quickly unloaded. Only those samples which deformed to greater than 1.8% strain in the tension side of the crystal were accepted for further tests. These initially bent samples were then divided into three groups. The samples of the first

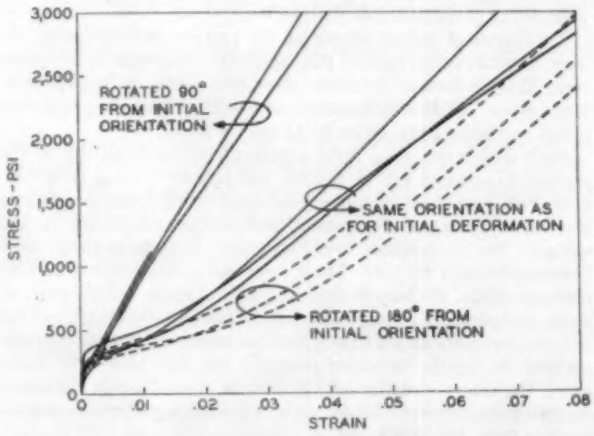

FIG. 2. Stress-strain curves for a group of water soaked NaCl crystals which were strained, then tested in three different orientations. Stress, $\sigma = (3FL/2bh^2)[1+(8y^2/L^2)]$ and strain, $\epsilon = 4hy/L^2$, are calculated from simple bending theory with a geometrical correction term, which follows from an assumption that the tension side of the bent crystal approximates a parabola. h is the width of the sample; b is the height; L, the distance between supports; and y, the deflection.

group were loaded again in the same test orientation as before. Their stress-strain curves are a continuation of the initial curves, as would be expected. The samples of the second group were rotated 90 deg about their long axis in the test apparatus before further testing. The samples of the third group were turned over (i.e. rotated 180 deg about their long axis) before testing. Figure 2 shows that the second group of prestrained crystals (turned on their sides) show quite different stress-strain curves from either of the other groups. These crystals are much stiffer than the others, particularly in the low stress portion of the curves which are shown here. This behavior is consistent with the view that dislocations generated in the crystal by the initial test deformation intersect those dislocations whose motions attend the deformation in the second test orientation, and are therefore effective in inhibiting their motion.

The method of selecting these crystals insures that the work hardening effects were the result of the experimental deformations rather than some previous stresses. The crystals, which have received a controlled deformation, essentially reproduce the different shapes of the curves shown in Fig. 1 and it has been shown that the presence of minor surface damage can introduce the early rupture which characterizes the cleaved crystal curves shown in Fig. 1.

[6] Obtained from Harshaw Chemical Company.
[1] Lad, Stearns, and Del Duca, Acta Met. 6, 610 (1958).
[2] E. Aerts and W. Dekeyser, Acta Met. 4, 557 (1956).
[3] Gorum, Parker, and Pask, J. Am. Ceram. Soc. 41, 161 (1958).
[4] T. Suzuki, *Dislocations and Mechanical Properties of Crystals* (John Wiley & Sons, Inc., New York, 1957), pp. 215–228.
[5] E. S. Machlin, J. Appl. Phys. 30, 1109 (1959).
[6] Stearns, Pack, and Lad, NASA Technical Note D-75 (1959).
[7] A. Joffe, *The Physics of Crystals* (McGraw-Hill Book Company, Inc., New York, 1928).
[8] R. Houwink, *Elasticity, Plasticity, and Structure of Matter* (Harren Press, Washington, D. C., 1953), pp. 101–108.

Radiation Limited Dislocation Motion in Crystals*

ROBB THOMSON
Department of Mining and Metallurgy, University of Illinois, Urbana, Illinois
(Received November 18, 1959)

LOTHE and Hirth[1] have discussed the thermal activation of dislocations across the Peierls energy barriers in crystals. On the other hand, Mott and Nabarro and Seitz[2] have suggested that a large Peierls energy does not necessarily inhibit the dynamic motion of a dislocation (as contrasted to motion which is assisted by thermal fluctuations) if it lies slightly skew to a symmetric crystallographic direction. Consider an actual dislocation source in the crystal. Initially, the dislocation may lie skew to the Peierls ridges and move easily under an applied stress, however as the dislocation loop expands, the advancing nose of the loop must eventually be activated across successive lattice hills as it moves into new regions of the crystal. The question arises whether in this case the dislocation can be mobile in a dynamic sense.

The possibility exists that during the initial skew motion of the expanding source, the dislocation builds up enough kinetic energy to overcome the Peierls hill structure by the time the advancing nose has to be activated across the first new hill. However, the dislocation in traversing the Peierls hill and valley structure must be expected to radiate as it moves in a roller coaster fashion through the crystal. The condition that sustained motion be possible is therefore that the radiation during the traversal of one Peierls hill and valley be less than the energy gained by the dislocation line in moving through the external stress field. E. Hart[3] has previously calculated this radiation for stresses larger than the Peierls stress and for dislocation velocities near that of sound and found that the radiation is negligible. We are instead interested here in the case of nearly zero average velocity and assume that the external stress is smaller than the Peierls stress. We shall assume that the dislocation starts from rest at the top of a Peierls hill and accelerates to the bottom due to the gain in self energy. The radiation loss[4] per atom length of line in moving to the bottom of one hill and up to the top of the next (a distance of one Burgers vector) is

$$W_R=\tfrac{1}{2}\pi^3 b^3\rho c^3(E_p/E_0), \tag{1}$$

where ρ is the mass density of the material, c is the velocity of sound, E_0 is the rest energy of the dislocation, E_p is the Peierls energy, and b is the Burgers vector. In (1), the radiation is independent of the average velocity of the dislocation and represents the low velocity limit of Hart's results. (1) is valid when the average dislocation velocity is less than the velocity of the core of the dislocation at the bottom of the Peierls valley. This result is to be compared with the energy gained per atom length of line as it moves one atomic distance through the stress field, $W_\tau=\tau b^3$, where τ is the external stress and is approximately the critical shear stress. The ratio of these two quantities is

$$W_R/W_\tau=\tfrac{1}{2}(\pi\rho c^3/\tau)\left(\frac{E_p}{E_0}\right)$$
$$\simeq 10^9/\tau \text{ cgs}, \tag{2}$$

where E_p/E_0 is assumed to be 10^{-3}. The energy radiated is much larger than the energy gained for any crystal with a critical shear stress of the usual magnitude. In fact, the ratio W_R/W_τ only becomes of the order of one when the stress becomes approximately the Peierls stress. The result is therefore that in crystals with large Peierls energy, the observed critical shear stress where the dislocations become mobile cannot be due to a dynamic motion of the dislocation, but the dislocations must be thermally activated through the lattice hill-valley structure in some manner similar to that of Lothe and Hirth.

* Supported by the U. S. Air Force through the Office of Scientific Research of the Air Research and Development Command.
[1] J. Lothe and J. P. Hirth, Phys. Rev. 115, 543 (1959).
[2] N. F. Mott and F. R. N. Nabarro, *Report on Strength of Solids* (Physica Society, London, 1948); F. Seitz, *Report of Pittsburgh Symposium on Plastic Deformation* (Carnegie Institute of Technology, Pittsburgh, 1950).
[3] E. Hart, Phys. Rev. 98, 1775 (1955).
[4] J. Eshelby, Proc. Roy. Soc. (London), A197, 396 (1949).

Formation of Cavities on Dislocations in Crystals of NaCl and KCl

L. W. BARR* AND J. A. MORRISON
Division of Pure Chemistry, National Research Council, Ottawa, Canada
(Received October 23, 1959)

MICROSCOPIC examination of a single crystal specimen of NaCl, which had been heated at high temperatures in an atmosphere of chlorine ($p\sim500$ mm), showed the structure illustrated in Fig. 1. There is a marked resemblance between this structure and that delineated by etching crystals of the alkali halides.[1] In the present instance, however, the subgrain boundaries and dislocations are demarked not by the normal pyramidal etch-pits, but by small cubic cavities lying in a band typically 80 μ thick, parallel to the free surface of the crystal and about 20 μ beneath it.

The observation was made in connection with measurements of the anion diffusion in NaCl and KCl by using a solid-gas isotopic exchange method.[2] Because the diffusion rates in the crystals seemed to depend upon their dislocation content,[3] a microscopic study of the crystals was undertaken. In addition to crystals used in the diffusion experiments (prepared from Johnson and Matthey Specpure materials by the Kyropoulos technique), some crystals from other sources were examined. Treatment with Cl_2 for 48 hr at about 700°C formed cavities in all but one of the NaCl crystals, but in only one of the KCl crystals. These conditions were not critical; the only requirement seemed to be that the

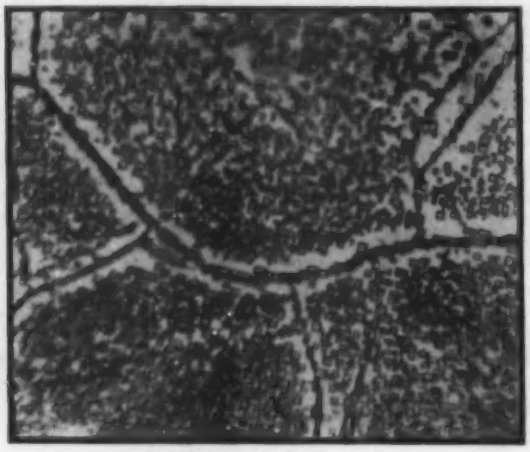

(a)

(b)

FIG. 1. Cavities in an NaCl single crystal (×185).

time and temperature be sufficient for appreciable diffusion to occur.

Cavities of a similar type to those described here have been observed in KCl annealed in H_2[4] and Cl_2.[5] In both cases, their occurrence was traced to the presence in the crystal of small quantities of an impurity. Subsidiary experiments have shown that the same explanation may be applied here although the impurity has not been identified specifically in each case. The single KCl crystal in which cavities formed had been doped with K_2CO_3 (0.001%). Figure 2 shows the transmission spectra of two plates cleaved from this crystal and given identical annealing treatments (a) in pure argon and (b) in Cl_2. The significant feature is that the carbonate absorption band at about 205 mμ has been completely removed by the Cl_2. Presumably, the relevant chemical reaction is of the type $CO_3^{=}+Cl_2 \rightarrow 2Cl^{-}+CO_2+\frac{1}{2}O_2$, and the cavities are formed by the gaseous reaction products. It should also be noted that the spectrum (b) in Fig. 2 shows no trace of the very strong Cl_2 absorption band in the region of 330 mμ. Hence, it may be concluded that the cavities contain no free Cl_2. Similar results were obtained with NaCl crystals, but since the band maxima lay below 200 mμ the impurity could not be identified positively. It is likely, however, that the impurity was the hydroxide which has been shown to occur commonly in laboratory grown crystals.[6] That the cavities in NaCl crystals contained permanent gas at greater than atmospheric pressure was verified by observing the release of gas bubbles when the crystals were dissolved in water.

Etching of crystals of NaCl containing cavities showed that the cavities occurred on dislocations. The etching was done by immersing the crystals for 1 min in a solution of $Fe(NO_3)_3$ in absolute ethyl alcohol (3 g/liter) and rinsing in CCl_4.[7] Figure 3 indicates the result obtained by repeated etching and polishing (in 95%

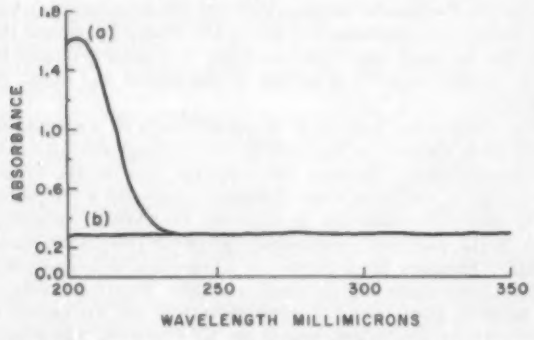

FIG. 2. Absorption spectra of KCl crystals (a) heated in argon and (b) heated in chlorine.

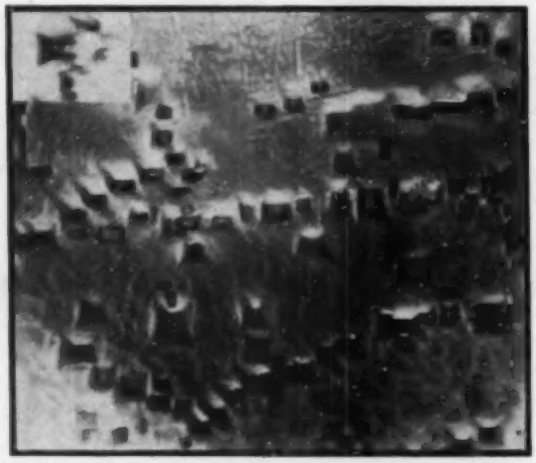

(a)

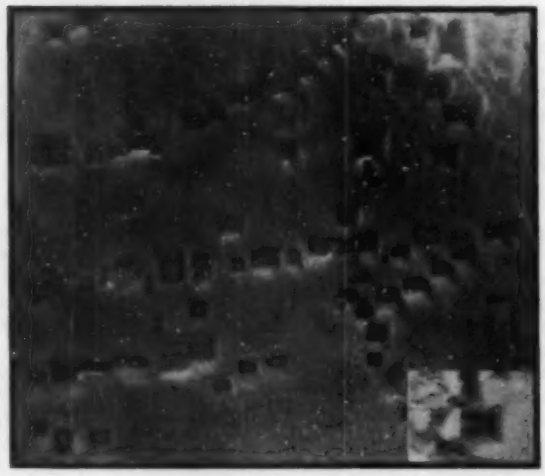

(b)

FIG. 3. Polished and etched NaCl crystal containing cavities. Inset. Cavity with associated etchpit in NaCl (×265).

ethyl alcohol) of the crystal shown in Fig. 1. The shallower cavities have been removed and the deeper cavities along the subgrain boundaries are clearly seen. Associated with most of the cavities is the typical pyramidal etchpit indicative of a dislocation. A small number of cavities had no associated etch pits showing that the pyramid is not a consequence of the cavity itself. In these cases, it seemed that the dislocation had become detached from the cavity. When this happens, the etching action does not occur.[1] The inset in Fig. 3 shows a cavity exposed by cleaving a crystal and examining the edge of the new plane nearest the free surface. In this case, the cleavage plane has cut through the cavity and the resulting pit in the surface is sufficiently shallow to show not only the etched region round the cavity, but also the point of the pyramid in the cavity floor.

While chlorine treatment of crystals containing impurities such as $CO_3^{=}$, OH^-, etc., may thus be used for decorating the dislocations, perhaps the method will have wider applications. A striking feature apparent in Fig. 1 is the cavity free region round the subgrain boundaries, about $20\,\mu$ in width. The agreement between the width of the zone and the depth of the cavity layer below the free surface suggests that this distance represents the migration length of the gaseous reaction products under the conditions of the experiment. We cannot, of course, from any one experiment reach definite conclusions about the initial distribution of the impurity, the mode of penetration of the chlorine, nor about the nature of the necessary vacancy sources. But it seems probable that information on these points may be obtained from a systematic study in which the time and temperature of treatment are varied. If the width of the cavity free zone is interpreted as a migration length for the gaseous products, the order of magnitude of the diffusion coefficient is $\sim 10^{-10}$ cm²/sec. As far as we know, no direct measurements of the diffusion of permanent gases in single crystals of alkali halides have been made. In a similar way, if the maximum depth of cavity formation is interpreted as a measurement of the chlorine penetration, the appropriate diffusion coefficient is $\sim 10^{-9}$ cm²/sec, which compares with the value of 6×10^{-10} cm²/sec for the diffusion of the chloride ion in the same specimen at 728°C measured by an isotropic exchange experiment.

We should like to thank Dr. J. Rolfe for helpful discussions, for providing some of the specimens and the facilities for the spectroscopic measurements.

* National Research Council Post-doctorate Research Fellow.

[1] J. J. Gilman and W. G. Johnson, *Dislocations and Mechanical Properties of Crystals* (John Wiley & Sons, Inc., New York, 1957).
[2] Patterson, Rose, and Morrison, Phil. Mag. Ser. 8, 1, 393 (1956).
[3] Barr, Hoodless, Morrison, and Rudham (to be published).
[4] Amelinckx, Maenhout-Van Der Vorst, and Dekeyser, Acta Met. 7, 8 (1959).
[5] E. Mollwo and R. W. Pohl, Ann. Physik 39, 321 (1941).
[6] J. Rolfe, Phys. Rev. Letters 1, 56 (1958).
[7] W. G. Johnson (private communication).

Depth of Indentation on an Impacting Projectile

R. A. GRAHAM
Department of Physical Research, Sandia Corporation, Albuquerque, New Mexico
(Received November 9, 1959)

A SERIES of experiments is being conducted in which a 1018 steel projectile is fired at high velocity and impacted upon a barium titanate ceramic. The objective of the experiments is to study the ferroelectric charge release from the barium titanate due to the passage of the stress wave produced by the impact. Aside from the electrical observations, it was noted that the flat-faced steel projectile was indented by the flat face of the barium titanate target and that the depth of indentation was a function of impact velocity in the manner noted by Backman.[1]

Figure 1 shows the relation between depth of indentation and mpact velocity for 1018 steel impacting on barium titanate. It

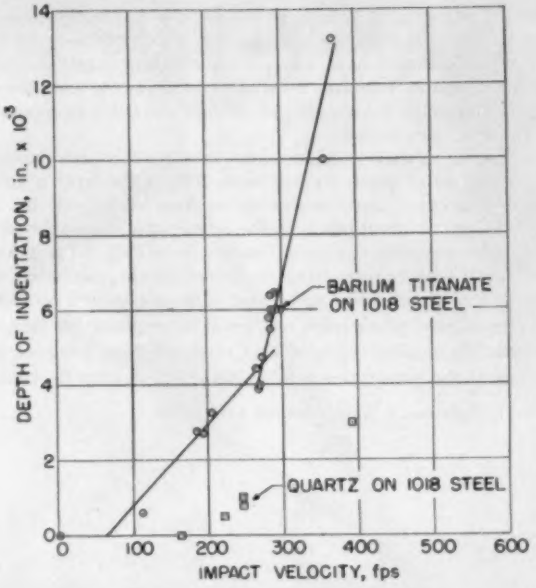

FIG. 1. Depth of identation.

should be noted that the knee in the curve as observed by Backman is present in this case also. The knee evidently corresponds to a change in the mechanism of indentation since inspection of the indented projectile shows a basic difference in the appearance of the indented surface for velocities below 270 ft per sec and the indented surfaces for velocities greater than 270 ft per sec. For the lower velocities, the indentation is essentially a clean punch. For velocities greater than 270 ft per sec, the bottom of the indentation is marked by ridges of material that have undergone plastic flow. The ridges of material are thicker toward the edges of the indentation and decrease in thickness toward the center of the indentation.

An attempt was made to correlate the observed depth of indentation with predictions based on Backman's theoretical development. The observed depths did not correlate well with those calculated by Backman's method. These experiments were designed to study electrical rather than indentation phenomenon; as a consequence, the geometry involved makes a theoretical prediction of the absolute indentation depth difficult. The geometry of the test arrangement is shown in Fig. 2.

The particle velocity imparted to the target and projectile are given by Backman's Eq. (8). It is shown that the particle velocity is given by KU_0, where U_0=impact velocity. According to Backman's analysis, the depth of penetration is essentially a direct

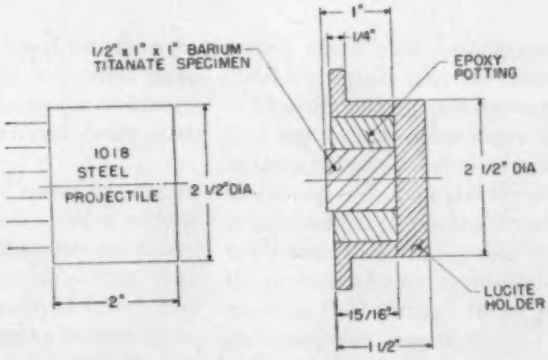

FIG. 2. Geometry of test.

function of the particle velocity produced in the projectile material and the time to reduce this particle velocity to zero.

Some experiments have been performed using quartz instead of barium titanate. The data from these experiments are shown in Fig. 1. The factor K for quartz on 1018 steel is 0.236 as opposed to 0.359 for barium titanate.

According to these considerations, one would expect the depth of indentation of quartz on steel to be 70% of the depth of indentation of barium titanate on steel at the same impact velocity. The experimental observations with the quartz specimens showed the depth of indentation at a given velocity to be 25% of the indentation depth with barium titanate instead of the predicted 70%. This lack of quantitative agreement is to be expected because of the complicated geometrical configuration required for electrical reasons. The qualitative agreement observed does, however, give support to the indentation mechanism postulated by Backman.

[1] M. E. Backman, J. Appl. Phys. **30**, 1397 (1959).

Announcements

Symposium on Superconductive Techniques for Computing Systems

A Symposium on Superconductive Techniques for Computing Systems will be held on May 17 and 18, 1960, sponsored by the Information Systems Branch, Office of Naval Research. The Symposium will be held in the Department of Interior Auditorium on C Street, between 18th and 19th Streets, N.W., Washington, D. C.

Individuals may receive further information and a preliminary Symposium program when available by contacting: Miss Josephine Leno, Code 430 A, Office of Naval Research, Washington 25, D. C. (Phone OXford 6-6213.)

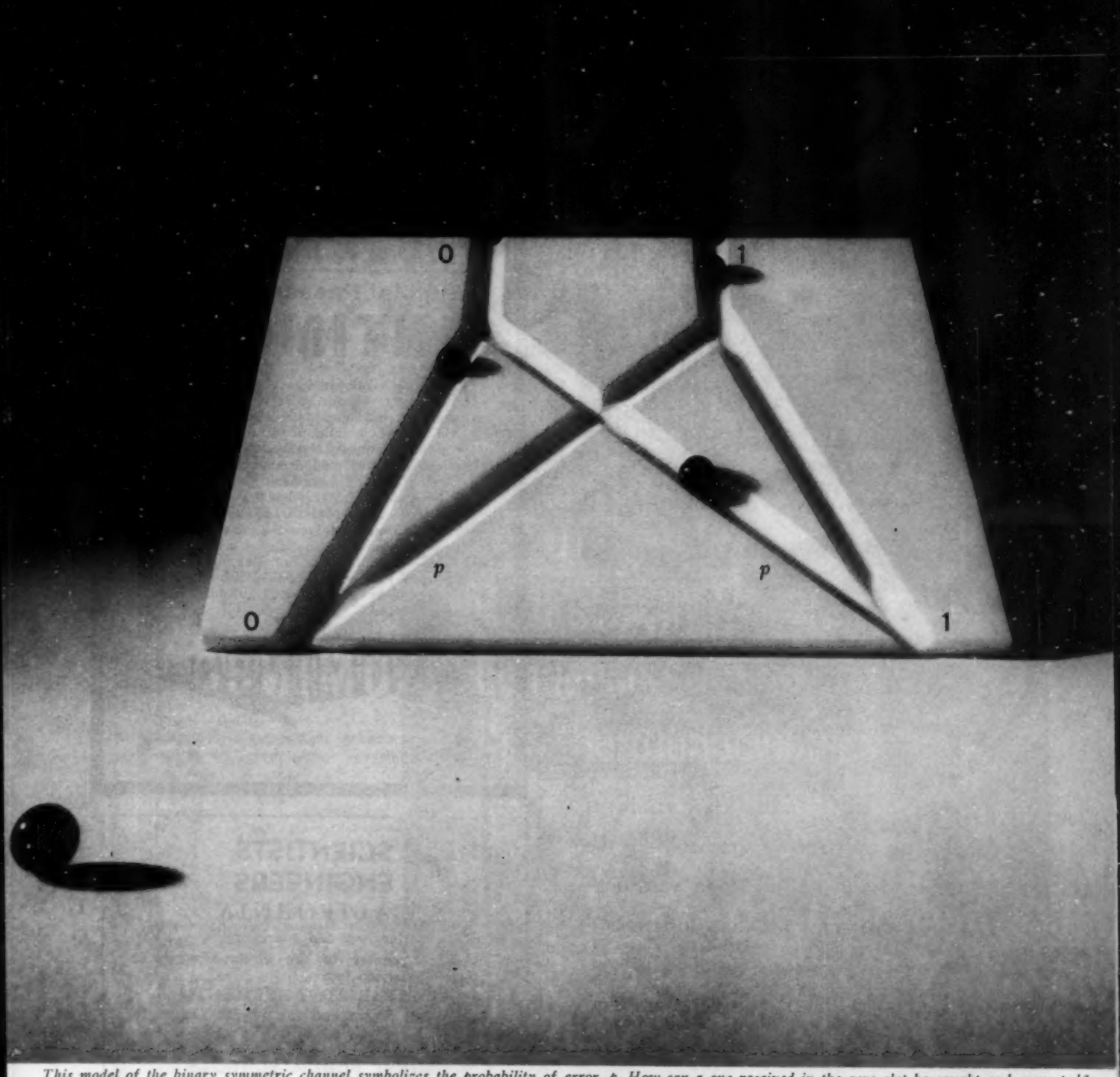

This model of the binary symmetric channel symbolizes the probability of error, p. How can a one received in the zero slot be caught and corrected?

Group codes for prescribed error patterns

Information signals, representing zeros and ones, are transmitted through a binary symmetric channel at such high speeds that they are subject to channel noise. Through group codes it is possible to detect and correct automatically large classes of errors that may arise from such disturbances.

Usually, in optimizing these codes all possibilities are classified and samples of each are evaluated. But this task can become enormously complex. For large information blocks, such as a 70-place code, there may be billions of possibilities to evaluate. To reduce the need for these exhaustive methods, IBM scientists have evolved a preliminary theory for constructing group codes through a correlation analysis of error patterns.

Correlated patterns of errors are organized into equivalent classes and a code is formulated to overcome the error-producing characteristics of the communications channel. A code for one pattern of errors may be transformed mathematically into codes for other patterns of the same class. By prescribing which error patterns can be corrected, codes with a minimum number of checking signals may be formulated.

This optimizing process can have practical significance since every checking signal for a given number of information signals in a group code increases the cost and delay in information processing. In addition to the work described here, other approaches to the problem of code simplification are being made at IBM through linear programming and computer simulation.

IBM® RESEARCH

Investigate the many career opportunities available in exciting new fields at IBM.
International Business Machines Corporation, Dept. 579O, 590 Madison Avenue, New York 22, New York

YOUR POTENTIOMETRIC INSTRUMENTS

NO matter how perfect otherwise, the human organism isn't much good without a dependable heart. The same is true of your automatic temperature and pH control instruments. The "heart" of most such instruments for the past forty years has been the Eplab Standard Cell. It is a "yardstick" for translation of voltage to temperature or pH. The first American commercial cell of its type, constantly improved by research, it is "as standard as sterling". Get ACCURATE temperature or pH control with potentiometers and make sure the standard cells are EPLAB.

The Eppley Laboratory, Inc. 6 SHEFFIELD AVE. NEWPORT, R. I.

EPLAB *Standard* CELLS
FOR POTENTIOMETRIC INSTRUMENTS
"As Standard as Sterling"

483-9

TADANAC BRAND
Special Research Grade
ANTIMONY

TADANAC Brand Special Research Grade antimony is primarily developed for production of intermetallic compounds such as indium and aluminum antimonides. No individual impurity exceeds 0.1 ppm. and shipments can be made from sections of zone refined bars. These bars contain large crystals and have a very low oxygen content.

Other TADANAC Brand high purity metals or compounds include Special Research Grade indium and tin, High Purity Grade bismuth, cadmium, indium, lead, silver, tin, zinc, and indium antimonide. Send for our brochure on TADANAC Brand High Purity Metals.

COMINCO

THE CONSOLIDATED MINING AND SMELTING COMPANY OF CANADA LIMITED
215 ST. JAMES ST. W., MONTREAL 1, QUEBEC, CANADA · PHONE AVenue 8-3103

0161

SCIENTISTS
ENGINEERS
CALIFORNIA
offers you and your family

- **A world center of the electronics-missile-space industries for CAREER ADVANCEMENT**
- **The High Sierra and the Pacific Ocean for RECREATION**
- **And for your children some of the nation's FINEST PUBLIC SCHOOLS**
- **World Famous Universities for ADVANCED STUDY**
- **MAJOR CULTURAL CENTERS**

while living in such places as
Exciting San Francisco
Fabulous Southern California
Cultural Palo Alto

Companies pay interview, relocation and agency expenses

Submit resume in confidence to:
PROFESSIONAL and TECHNICAL RECRUITING ASSOCIATES
(a Division of the Permanent Employment Agency)
Suite A
825 San Antonio Road
Palo Alto, Calif.

senior applications engineers

experienced in
SEMICONDUCTOR R&D
for staff level assignments

GROUP HEAD

Senior applications engineer with experience in semiconductors, transistors, diodes, rectifiers, circuit applications and sales engineering. Must be oriented for a responsible managerial position. Ph.D. degree preferred.

STAFF ENGINEERS

Applications engineers with at least five years' experience for senior staff level assignment in semiconductor circuit research and development. Our research project is directed toward development of new uses for existing devices, and creation of circuitry using new devices which will become the building blocks of tomorrow's systems.

These positions were created as a result of the sustained growth of advanced research and development activity at the Semiconductor Division of Hughes Aircraft Company. The recently completed facilities of the Semiconductor Division are located in Newport Beach, California—just south of Los Angeles.

If you meet the requirements for the above positions, or if you are a senior engineer or physicist with experience in the field of semiconductors, we invite your confidential inquiry.

Please contact:

Mr. C. L. M. Blocher
Scientific Staff Representative
HUGHES SEMICONDUCTOR DIVISION
500 Superior Avenue
Newport Beach 4, California

Creating a new world with ELECTRONICS

HUGHES

SEMICONDUCTOR DIVISION

Scylla

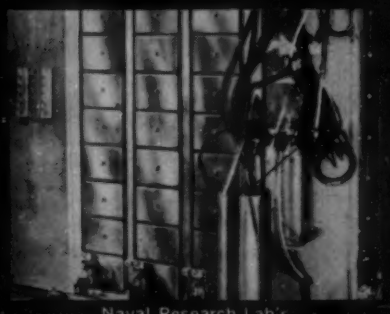

Naval Research Lab's Condenser Battery

Tobe... first with condensers for thermonucleonics

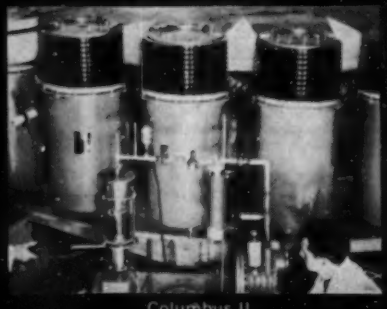

Columbus II

Of particular interest to the thousands of international visitors to the historic Geneva Atoms-For-Peace Conference, was the display of thermonuclear fusion research equipment which the U.S. Government set up. Significantly, several of these devices use Tobe low-inductance condensers. Three of the machines are shown here.

Even now — long after the conference — inquiries and orders are being received from every corner of the globe. The postmarks read like a roll call at the United Nations: Great Britain, Japan, Italy, U.S.S.R., France, Brazil, The Netherlands, Sweden and many others.

Scientists and engineers of these countries are in perfect accord in their recognition of Tobe thermonuclear condensers.

We invite inquiries for a single energy storage capacitor or a complete energy storage system including capacitors, racks, interconnecting lines, protective devices and charging power supply. For further technical information or engineering aid, write to Cornell-Dubilier Electric Corp., Marketing Office, Norwood, Massachusetts.

CDE **CORNELL-DUBILIER ELECTRIC CORPORATION**
Affiliated with **Federal Pacific Electric Company**

expansion

IS A CONSTANT AT **RHEEM**

***Scientists & Engineers**—Physicists, Metallurgists, Physical Chemists, Electronic Engineers, Process Engineers, Application Engineers, District Sales Managers, Sales Engineers, Jr. Sales Engineers*

A growth curve that sparks the imagination of any progressive individual. Right now, the scope and diversity of activities at Rheem Semiconductor Corporation are assuming impressive proportions. Some of the country's best scientists and engineers are in charge of our spacious new facilities where the research, development and manufacture of semiconductor devices are constantly being expanded. Everything at Rheem points to a future filled with material success and professional satisfaction. It may be possible for you to share this future. We suggest that you inquire, now, into the specific openings available.

We look forward to seeing you at the **IRE** Convention in New York, March 21 thru 24th. We will be at the Barbizon-Plaza Hotel, 106 Central Park South, New York City, and our telephone number will be **PLaza 7-9572.** If you do not plan to attend, your resume will receive our most serious and confidential consideration.

RHEEM SEMICONDUCTOR CORPORATION
327 Moffett Boulevard, Mountain View, California

NEW HIGH POWER PULSE OSCILLATOR PG-650-C

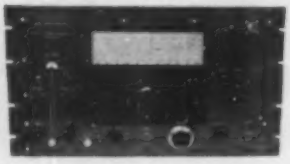

The successful introduction of the PG-650 Pulsed oscillator to many test applications has led to an improved model of interest to workers in ultrasonics, r.f. transient analysis, nuclear magnetic resonance, etc. The following characteristics and features are available only with the PG-650-C.

Frequency Coverage	5–90 MC in 7 ranges*
R.F. output Voltage (Min.) into 93 ohms	0–300 p. to p.
Pulse length continuously variable	1½–15 usec
Rise and Fall times (Max.)	0.5 usec
Pulse Droop	5% Max.
Noise Output between Pulses	Thermal Noise from Termination
Harmonic Content (Max.)	mostly 3rd 10%
R. F. Leakage	Negligible
Trigger to Pulse Jitter	.005 usec

SPECIAL FEATURES

Pulse lengths available from ½ to 50 usec
Internal Delay Ranges available from calibrated Helipot 200, 1100, 11,000 usec
Gate Pulse output available for intensifying and blanking purposes.
External modulation of r.f. oscillator using varying pulse lengths and p.r.f.'s for Carr Purcell Method.
Fine controls of P.R.F., Pulse length, and delay times.
Usable as C.W. source or Pulsed Amplifier.

* *Special coils will extend coverage from 0.5 to 150 MC.*

Please write for our bulletins on other test equipment: Wide Band Amplifiers, Preamplifiers, and Precision Attenuators.

ARENBERG ULTRASONIC LABORATORY, Inc.
94 Green Street, Jamaica Plain 30, Mass.

From Cenco—developed by MIT and the AC Spark Plug Div. of General Motors. For visual demonstration of gyroscopic principles—inertia, precession, nutation, single and two degrees of freedom gyro, automatic pilot or inertial guidance, gyro compass, laws of motion. Motor driven. Complete with built-in turn table and handbook of experiments and theory. **No. 74730 Deluxe Research Model $254.00**

cenco

CENTRAL SCIENTIFIC CO.
A Subsidiary of Cenco Instruments Corporation
1718-A Irving Park Road • Chicago 13, Illinois
Branches and Warehouses—Mountainside, N. J. Boston • Birmingham • Santa Clara • Los Angeles • Tulsa Houston • Toronto • Montreal • Vancouver • Ottawa

HIGH SPEED CUTTER

Patent No. 2461621

Blade Velocity = or ≥ Velocity of Sound

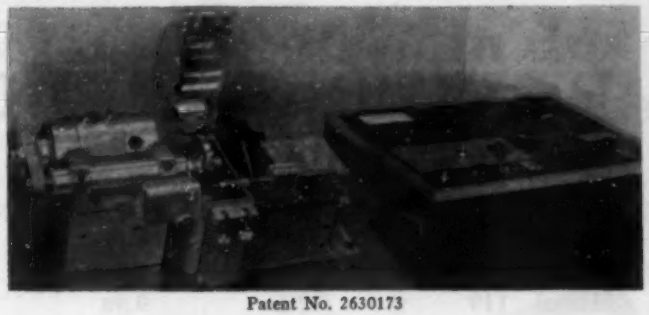

Patent No. 2630173

The figure in the upper left shows the blade engaging the sample as the disk rotates at 60,000 rpm. In the upper right is our Ultramicrotome. Either this unit or other versions tailored to the customer's requirements have cut samples in vacuum, inert gas and at atmospheric conditions. The samples cut from various materials have ranged in length (0.1 microns to 3.0 inches), width (0.001 to 12.0 inches) and thickness (0.0005 to 0.125 inches).

Write for information and brochure.

CUSTOM SCIENTIFIC INSTRUMENTS, INC.

541 Devon St. **Kearny, N. J.**

Tel. WYman 1-6403

NOW!

Easy Demonstration of basic Gas Laws

CENCO Kinetic Theory Apparatus

Permits quantitative determination of the most fundamental principles of gas mechanics. Adapted from a design by H.F Meiners of Rensselaer Polytechnic Institute. Plot p-V and p-T curves· measure molecular diameters, verify the fundamental gas laws and Van der Waals Corrections.

No. 77722 without stroboscope, $295.00

cenco®

CENTRAL SCIENTIFIC CO.

A Subsidiary of Cenco Instruments Corporation

1718-A Irving Park Road • Chicago 13, Illinois

Branches and Warehouses—Mountainside, N. J
Boston • Birmingham • Santa Clara • Los Angeles • Tulsa
Houston • Toronto • Montreal • Vancouver • Ottawa

ELECTRON MICROSCOPIST

Raytheon's Research Division has an unusually provocative opening for a physicist or metallurgist with experience in electron microscopy. Your initial studies will be of problems connected with the surface textures of thin films. Other research areas will include electron diffraction and transmission microscopy.

This position will be in the suburban Boston area, where educational, cultural and family-living advantages are abundant. Relocation assistance and full modern benefits.

Please send your detailed resume to Mr. G. Wermert, Raytheon Company, Gore Building, Stanley Avenue, Watertown, Massachusetts.

RAYTHEON

Excellence in Electronics

LOW VOLTAGE DC POWER SUPPLIES

6, 12, and 28 volt

	Voltage	Current	Price
Model 125B	6.3	1.5a	$47.00
Model 119	12.6	0.9a	$43.50
Model 227	28.0	1.2a	$59.00

These small "Uniplugs" operate on 115 volts AC to furnish a DC output with low ripple voltage. Useful at many jobs in the lab. The octal plugin feature makes them very economical as they can be removed from equipment which is no longer in use,

C. J. APPLEGATE & CO.

1840 24th Street *Phone Hillcrest 2-8750* Boulder, Colorado

NOW!

a pulsed neutron generator for less than $5,000.00

OMNITRON

shown mounted in use.

Greatly increases research capabilities of sub-critical assemblies and training reactors. Allows demonstration of fusion reactions and neutron counting techniques, makes radio isotopes and studies transient behavior of neutrons. Is simply constructed, compact, portable. Requires no special installation or power facilities. Five different models available.

Prices start at $4,950.

cenco®

CENTRAL SCIENTIFIC CO.

A Subsidiary of Cenco Instruments Corporation

1718-A Irving Park Road • Chicago 13, Illinois

Branches and Warehouses—Mountainside, N. J. Boston • Birmingham • Santa Clara • Los Angeles • Tulsa Houston • Toronto • Montreal • Vancouver • Ottawa

---

NOISE CONTROL

One of the leading manufacturers of home appliances wishes to add to its Research Laboratories staff a scientist who has theoretical training in acoustics and vibration theory to work on practical problems of noise reduction in household appliances. At least M.S. level, in Physics, Mechanical Engineering, or Electrical Engineering, is required. Experience in solution of such problems would be helpful but is not mandatory.

Excellent Mid-Western location; salary and compensation plan second to none. Qualified applicants should send resumes to the Company through this journal, Box 360, 335 East 45th Street, New York 17, New York.

MASSACHUSETTS INSTITUTE OF TECHNOLOGY
OPERATIONS EVALUATION GROUP

The M.I.T. OPERATIONS EVALUATION GROUP enjoys an enviable position within the Naval Establismment, with which they have been associated since early 1942. This position of mutual respect and confidence is a prime factor underlying OEG's continued growth and success as a scientific advisory group.

The problems dealt with are operational in nature and range from the evaluation of newly developed weapons systems or operational strategy to the formulation of new requirements and the correlation of research and development with Fleet needs.

To the graduate mathematician or physical scientist possessing the ability to envision and solve complex operational problems outside conventional fields of specialization, we offer a stimulating and professional atmosphere and the opportunity to participate at the highest level in the solution of problems directly concerned with the national defense.

In addition, we are currently extending our activities into the area of technological research that lies midway between the research conducted in the nation's laboratories and that traditionally conducted by groups such as OEG in the purely operational field.

OPERATIONS EVALUATION GROUP

Office of the Chief of Naval Operations
Navy Department
Washington 25, D.C.

U. S. Citizenship Required

Kinney®

UH-9 ULTRA HIGH VACUUM SYSTEM
for Work in the 10^{-9} mm Hg Range

A most significant advance in High Vacuum Technology, which brings yesterday's theoretical pressures to you in a practical working tool! The KINNEY UH-9, employing differential Pumping, gives you 1 x 10^{-9} mm Hg or better, enabling you to arrive at determinations that were, heretofore, unattainable. Write for full information today.

KINNEY VACUUM DIVISION
THE NEW YORK AIR BRAKE COMPANY
3556C WASHINGTON STREET • BOSTON 30 • MASS.

Please send me full information on KINNEY UH-9 Ultra High Vacuum System.

Name_____
Company_____
Address_____
City_____ Zone____ State_____

known around the world
for unequalled dependability.

ELECTRONS, INCORPORATED
127 SUSSEX AVENUE
NEWARK 3, N. J.

Reliable Thyratrons

MICROWAVE TUBE RESEARCH SECTION HEAD

An expanding program at PHILIPS LABORATORIES affords an excellent opportunity for a well qualified senior Microwave Tube Research Scientist (Ph.D. preferred) who will assume complete charge of a small, but well equipped research section.

His ability and personality will play a key role in the continued success of this program. He must be capable of providing top technical leadership for this Section, plan, initiate, and supervise research programs, and assist in the selection of additional scientific personnel required.

He will work in a pleasant academic-like atmosphere, associate with very high calibre scientists, and will be free from many general administrative duties.

PHILIPS LABORATORIES is located on a beautiful estate in Irvington-on-Hudson, New York, Westchester County, offering the advantage of suburban living, yet near a metropolitan area. The salary for this position is open.

We welcome and will treat as confidential all inquiries concerning this position. Send your resume including salary requirements to:

MARTIN G. WOLFERT, 100 E. 42 St.,
Rm. 802, New York 17

NORTH AMERICAN PHILIPS CO., INC.

NORELCO

new - - from Columbia

QUANTUM ELECTRONICS

A comprehensive review of the most recent developments in the fast-moving field of quantum electronics. Based on a symposium on quantum electronics held in September, 1959, the book contains many examples of the latest investigations in physics and electronics. Topics include: beam-type masers, solid-state masers, optical and infrared masers, and radio-frequency masers. Contributors to this volume are leading researchers and scientists from the United States, Western Europe, and the Soviet Union.

Edited by Charles H. Townes

600 pp. *Price: $15.00*

Columbia University Press
New York 27

Senior Research Scientist

Exceptional opportunity for a Senior Research Scientist for applied research in magnetic materials. Must have Ph.D. in solid state, physical metallurgy or physical chemistry. Ferrite and magnetic material research experience essential.

Will establish and administer program for research in soft ferrites including square loop materials and soft magnetic materials which are not spinels.

Salary is open. Relocation expenses and/or agency fee paid by company. Location 32 miles from Pittsburgh.

Write or call collect,
K. W. Stanat, Personnel

Magnetics, Inc.

Butler, Pennsylvania. **Butler 7-1745**

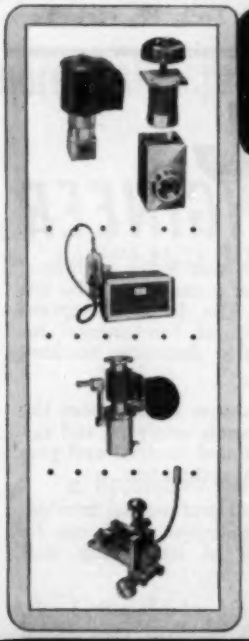

trouble-free
HIGH VACUUM COMPONENTS

VALVES...GAUGES...CONTROLS
PUMPS...ACCESSORIES

VALVES: Bellow sealed, brass & stainless steel • Manual • Solenoid • Pneumatic

GAUGES & CONTROLS: Non-burnout Ionization gauges, Bayard-Alpert type • Ultra-stable ionization gauge controls • Cold cathode discharge gauges and controls • Thermocouple gauges and controls

PUMPS: Diffusion pumps, air-cooled & water-cooled • Mechanical pumps, complete stock

ACCESSORIES: Standard and variable leaks • Quick couplings • Cold traps, Baffles • Electric degassing gun • "O"-ring sealed flanges • *Many others.*

FREE TECHNICAL BULLETINS
or complete CATALOG.
Write Department A-1437.

Veeco **VEECO VACUUM CORP.**
86 J Denton Avenue, New Hyde Park
Long Island, New York
HIGH VACUUM & LEAK DETECTION EQUIPMENT

Visit our Booths #3001-#3002 **I.R.E. Show, N.Y.C.**

Gaertner Ellipsometer uses polarized light to study ultra-thin films

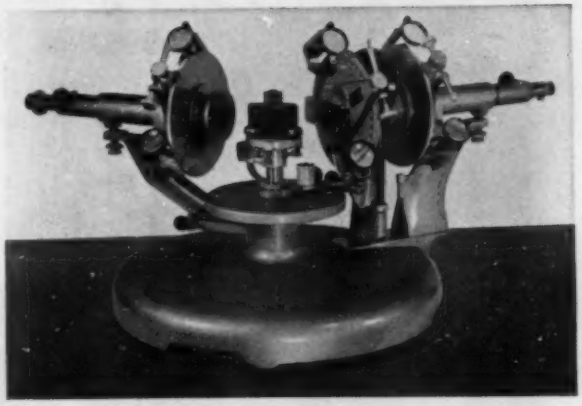

L119 Ellipsometer with L118TN Tronstad and Nakamura Biplate Assembly

This Ellipsometer, or polarizing spectrometer, is one of many fine optical and measuring instruments designed and manufactured by Gaertner Scientific Corporation. The instrument is a basic research tool for investigating and measuring ultra-thin films, and is of particular interest to those working in the field of solid state physics. Using the methods of Drude, Rothen, Tronstad and others, it permits precise determination of film thickness from a few angstroms to 200 angstroms, or approximately to one-tenth of a microinch. It is also adaptable to the study of birefringence, index of refraction, and other characteristics and phenomena associated with thin films and surfaces.

Gaertner Ellipsometers are, in effect, dual-purpose tools. They can be readily converted to a spectrometer by adding an entrance slit to the collimator, and Gauss eyepiece and adapter to the telescope.

Gaertner offers a wide range of precision optical and measuring instruments to scientists in all fields. Our services include modifications of these instruments to meet unusual needs, complete design and manufacture of special instruments and optical systems, and manufacture of assemblies and instruments from customer sketches and drawings. **Write for information on optical or measuring instruments used in your field. Bulletin 203-58 describes Gaertner Ellipsometers.**

Gaertner
SCIENTIFIC CORPORATION
1246 Wrightwood Avenue • Chicago 14, Illinois

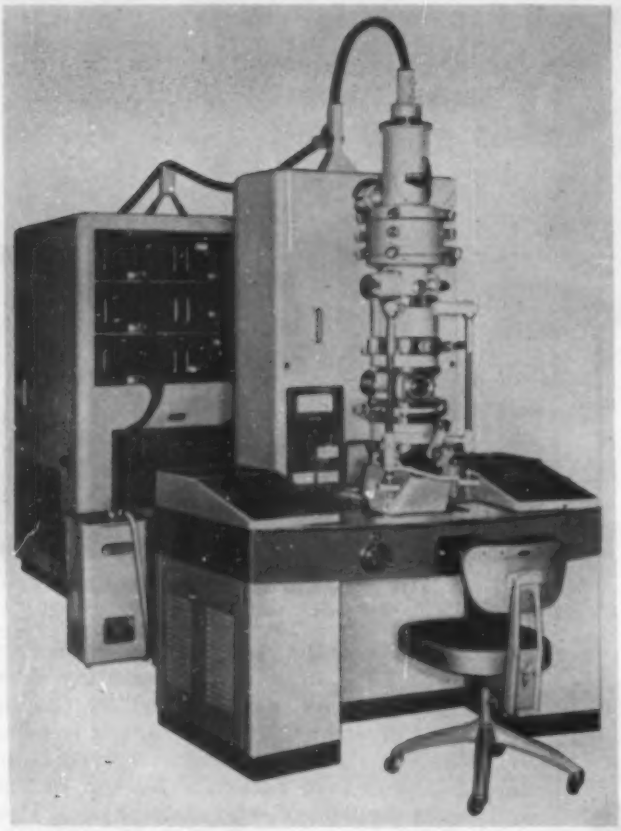

the new HITACHI HU-11 ELECTRON MICROSCOPE

The HU-11 offers a guaranteed 8 Angstrom Unit resolution, 200 to 250,000 × magnification range, selected area diffraction, reflected electron diffraction, double condensers and 50, 75 and 100 KV operation. Standard accessories permit reflected electron microscopy, work at high and low temperatures, X-Ray shadow camera techniques and charge neutralization. Your inquiries are invited at either our West Coast or East Coast offices, where competent sales personnel will answer your questions, and arrange a demonstration.

ERB & GRAY SCIENTIFIC, Inc.

Exclusive Hitachi distributor for the United States

854 S. FIGUEROA ST., LOS ANGELES 17, California

New York Address:

ERB & GRAY SCIENTIFIC, Inc.
501 Fifth Avenue, New York 17, New York

OPPORTUNITY

to be a part of a growing company

FACILITIES

and equipment to carry out the job

RECOGNITION

for your accomplishments

COMPENSATION

for your achievements

SECURITY

with a progressive well established company.

PHOTO SURFACE PHYSICIST

Well grounded in development, formation and measurement of photosensitive surfaces. Background should include high vacuum technique, tube design, electron optics and associated skills.

Please send resume to:

General Manager, Electronics Div.
Diamond Power Specialty Corp.
Box 415, Lancaster, Ohio

IR SYSTEM ENGINEER

Our Radiation Systems Division has a high-level creative position now open for a candidate who has substantial formal training. The position requires experience in the application of fundamental infrared theory and technique to detection, tracking and guidance systems.

System engineering at Emerson encompasses the full spectrum of applied research, analysis, and development from initial operational analysis and preliminary system design to final system test.

This position affords unusual professional freedom and a wide degree of diversification which can be exercised in an environment of stimulating staff associates.

Emerson is located in beautiful suburban St. Louis, wonderfully convenient, with excellent educational facilities. Our fringe benefits are quite liberal.

Write in complete confidence to A. L. Depke.

YOUR FUTURE IS OUR BUSINESS!

EMERSON ELECTRIC

ELECTRONICS & AVIONICS DIVISION

8100 West Florissant • St. Louis 36, Mo.

unequalled for

SENSITIVITY

The most precise instrument for **all** fluorometric methods of analysis . . . for research and routine procedures. Provides precise, reliable measurements over a wide range of sensitivities. Ideal for extremely low concentrations in micro or macro volumes.

Farrand Photo-Electric

FLUOROMETER

Technical data available on request
Specify Bulletin No. 803AP

FARRAND OPTICAL CO., INC.
BRONX BLVD. AND EAST 238th STREET • NEW YORK 70, N. Y.
Engineering, Research, Development, Design and Manufacture of Precision Optics, Electronic and Scientific Instruments

---

Theoretical Aerodynamicists ▪ Applied Physicists ▪ Applied Mathematicians

(PhD or equivalent)

An Invitation to Join in

APPLIED RESEARCH INVESTIGATIONS WITH REPUBLIC AVIATION

Immediate openings are available for senior scientists and engineers in the Applied Research and Development Division of Republic Aviation.

By joining Republic's continuing research and development expansion program — a major area of which is aimed at advancing all aspects of the field of aeronautics — you may carry on or initiate new studies in:

▪ Hypersonic aerodynamics ▪ Low density aerodynamics ▪ Real gas effects ▪ Magnetoaerodynamics

Republic's new $14,000,000 Research & Development Center at Farmingdale, Long Island is scheduled to open late this Spring. To existing facilities supporting current comprehensive research and development programs, it will add a highly sophisticated environment making possible wider technical investigations, as well as stimulating entirely new avenues of scientific experiment.

Forward resume in confidence to:
Mr. George R. Hickman, Technical Employment Manager, Dept. 17C

REPUBLIC AVIATION

Farmingdale, Long Island, New York

INDEX TO ADVERTISERS

Name	*Page*
APPLEGATE & CO., C. J.	xxviii
ARENBERG ULTRASONIC LAB.	xxvi
ARNOLD ENGINEERING CO.	iii
BELL TELEPHONE LABS.	v
C.B.S. ELECTRONICS	xix
CENTRAL SCIENTIFIC CO.	xxvi, xxvii, xxviii
COLUMBIA UNIVERSITY PRESS	xxx
CONSOLIDATED MINING & SMELTING CO.	xxiv
CORNELL-DUBILIER ELECTRIC CORP.	xxv
CUSTOM SCIENTIFIC INSTRUMENTS INC.	xxvii
DATA DISPLAY INC.	xvii
DIAMOND POWER SPECIALTY CORP.	xxxii
EASTMAN KODAK CO.	vii
ELECTRONS, INC.	xxx
EMERSON ELECTRIC MFG. CO.	xxxii
EPPLEY LAB., INC.	xxiv
ERB & GREY	xxxii
FARRAND OPTICAL CO.	xxxiii
GAERTNER SCIENTIFIC CORP.	xxxi
GENERAL ELECTRIC, ELECTRONICS LAB.	xvi
GENERAL RADIO CO.	Cover 4
HARSHAW CHEMICAL CO.	ix
HUGHES AIRCRAFT CO.	xviii, xxv
I.B.M. CORP.	xxiii
INSTROM ENG. CORP.	xv
JARRELL-ASH CO.	xxi
KEITHLEY INSTRUMENTS, INC.	xi
KINNEY VACUUM DIVISION, N. Y. AIR BRAKE CO.	xxix
LOS ALAMOS SCIENTIFIC LAB.	viii
McGRAW-HILL BOOK COMPANY, INC.	x
MAGNETICS, INC.	xxxi
NORTH AMERICAN PHILIPS CO., INC.	xxx
OPERATIONS EVALUATION GROUP	xxix
PERMANENT EMPLOYMENT AGENCY	xxiv
PHILIPS ELECTRONICS	Cover 2
RAYTHEON CO.	xxvii
REPUBLIC AVIATION	xxxiii
RHEEM SEMICONDUCTOR CORP.	xxvi
SPACE TECHNOLOGY LABS.	Cover 3
STOKES CORP., F. J.	xxxiv
SYLVANIA ELECTRONIC SYSTEMS	iv, xx
UNITED AIRCRAFT CORP.	vi
VARIAN ASSOCIATES	xiii
VEECO VACUUM CORP.	xxxi
WELCH SCIENTIFIC CO., W. M.	xxii
WESTINGHOUSE BETTIS ATOMIC POWER LAB.	xiv
WILEY & SONS, INC., JOHN	xii

Now!

a new concept in

Compound High Vacuum Pumps

- **PRECISION**
- **RUGGEDNESS**
- **QUIET OPERATION**
- **VIBRATION-FREE**
- **SMOKELESS EXHAUST**

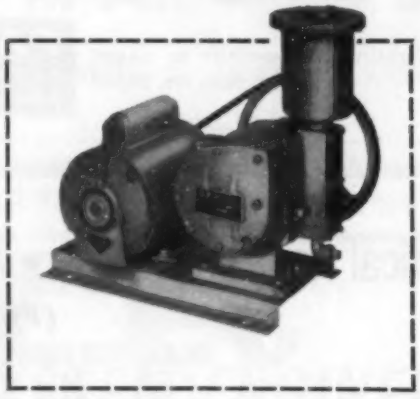

New Stokes Compound High Vacuum Pumps combine the sturdy, reliable construction demanded in an industrial pump with the precision performance of a laboratory unit. Lightweight, compact design. Fast pumping. Exceptionally low vacuums. Vapor-free discharge. Quiet, smooth operation. No vibration! Displacement: 2.3 and 3.7 cfm. Prices: $230 and $245.

Write for full information

High Vacuum Division
F. J. STOKES CORP.
5565 Tabor Road
Phila. 20, Pa.

STOKES

SUPERCONDUCTIVITY

A NEW ERA IN ELECTRONIC COMPUTING

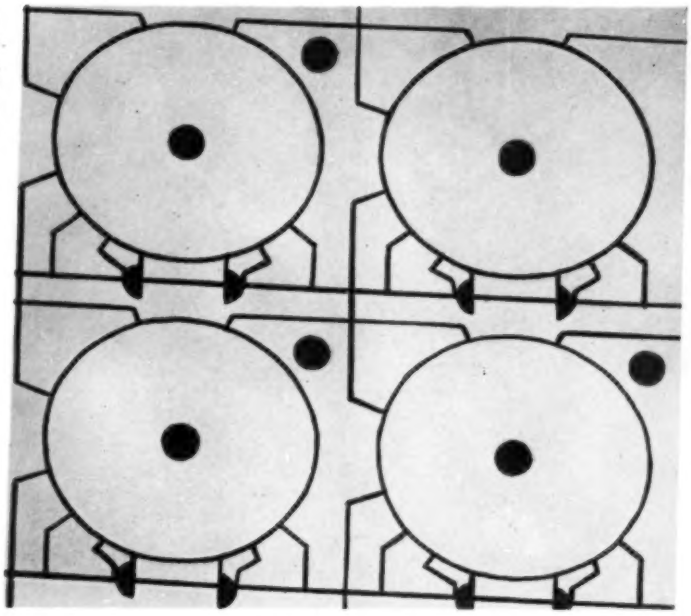

An array of Persistors

Experimental research demonstrates that superconducting memory elements are feasible as computer components and offer speeds 10 to 100 times the speed of existing computers using conventional components.

The Physical Research Laboratory of Space Technology Laboratories, Inc., has for some time devoted intensive research to the study of superconductivity and its possible application to electronic computing.

A major breakthrough in this field was realized when STL's Dr. Eugene Crittenden developed the Persistor, a superconducting memory device. This unique development, using thin film techniques, allows a current to be trapped indefinitely in a circuit. The memory unit or current direction, can then be interrogated by the use of fast pulse techniques.

STL's explorative applications of these techniques in computer technology studies will be continued toward the solution of problems arising in the high vacuum deposition of thin films.

In addition, basic research on the switching properties of single films and magnetically interacting films will be continued.

Openings are now available for engineers and scientists with experience in:

Computer Logic	**Low Temperature Physics**
Computer Design	**High Vacuum Deposition**
Computer Circuitry	**of Thin Films**

Resumes and inquiries are welcome. Please apply to:
Mr. T. W. Griesinger
Physical Research Laboratory
Space Technology Laboratories, Inc.
P. O. Box 95004, Los Angeles 45, California

SPACE TECHNOLOGY LABORATORIES, INC.

P.O. BOX 95004, LOS ANGELES 45, CALIFORNIA

NEW 20c to 12-Mc Beat-Frequency Generator

for Sine/Square Wave and Sweep Applications

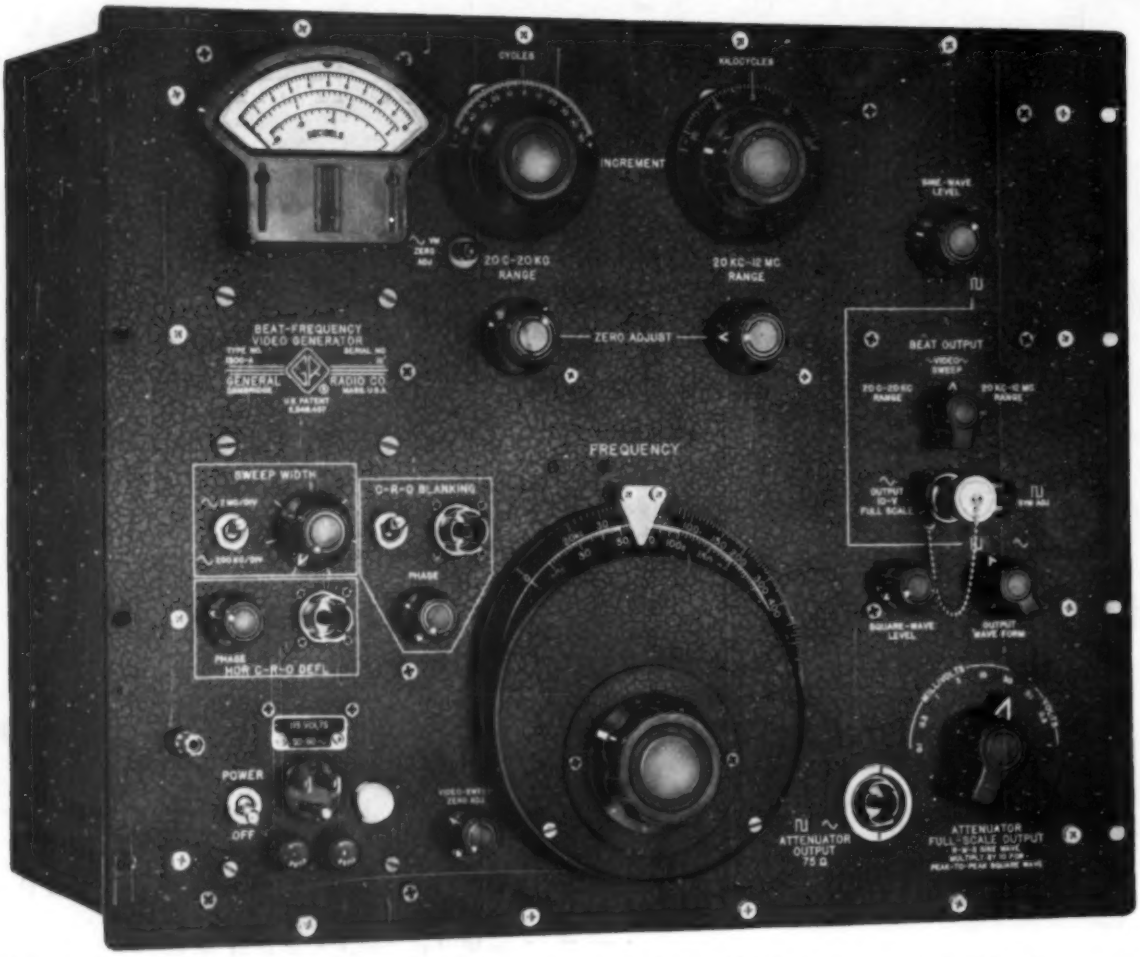

The features of beat-frequency generators, so well liked for audio-frequency testing, are now available for ultrasonic and video-frequency work. Features include: complete audio- or video-band coverage in one sweep of the dial without annoying range switching . . . high resolution provided by incremental frequency dials for accurate point-by-point studies of amplitude peaks and dips . . . continuously adjustable electronic sweep for video measurements at center frequencies to 12 Mc . . . automatic graphic-level and x-y recording with accessory G-R Dial Drives . . . square-wave output for frequency-response testing by transient techniques (e.g., rise-time and ramp-off measurements) . . . adjustable ± 6-Mc sweep at center frequencies from 36 to 42 Mc (obtained directly from internal oscillators) for television i-f testing.

This instrument's many outputs and different modes of operation, coupled with excellent frequency stability and high output (10v) over the entire frequency range, make it the most versatile audio-video test instrument commercially available.

Type 1300-A Beat-Frequency Video Generator . . . $1950.

As Manually-Tuned Generator:
Sine Wave: 20c to 12 Mc
Square Wave: 20c to 2 Mc

As Sweep Generator (60c sweep rate):
Sine Wave: 20 kc to 12 Mc
Sweep width is continuously adjustable from 0 to ±6 Mc at any center frequency from 0 to 12 Mc.
Horizontal deflection voltage and blanking pulse provided for scopes.

Calibration Accuracy:
20c to 20 kc, ±(1% + 1c)
20 kc to 500 kc, ±(2% + 1 kc)
500 kc to 12 Mc, ±(1% + 1 kc)

In addition to the main frequency dial, two increment dials calibrated from −50c to +50c, and −20 kc to +20 kc, are provided. Calibration accuracies are ±1c and ±0.5 kc, respectively.

Sine Wave — harmonic distortion
20c to 20 kc: < 1.5% of output
20 kc to 12 Mc: < 4% of output

Square Wave
Rise time less than 0.075 μsec above 300 kc
Top flat to 2% of peak-to-peak at 60c, 5% at 20c.

Hum: less than 0.1% of output

	Voltage Range: Sine-Wave (rms)	Voltage Range: Square-Wave (peak-to-peak)	Accuracy	Frequency Characteristic	Output Impedance
Attenuator output	0.1, 0.3, 1, 3, 10, and 30 mv; 0.1, 0.3, and 1v full scale, open circuit	1, 3, 10, 30, 100, and 300 mv; 1, 3, and 10v	±3% of full scale; attenuator db increments ±1%	flat within ±0.25 db from 40c to 20 kc (±0.75 db at 20c); ±1 db from 20 kc to 12 Mc	75Ω ± 2%
High output	0 to 10v	0 to 10v	±3% of full scale	flat within ±0.25 db from 20c to 20 kc; ±1 db from 20 kc to 12 Mc (open circuit)	820Ω ± 2%

Write for complete information

AT THE IRE SHOW

Booth Nos. 3201 to 3208

See a Typical Standards and Measurements Laboratory in Operation . . . Impedance Measurements from D-C to Microwave Frequencies

The New Beat-Frequency Generator Will Be on Display as well as many other instruments

GENERAL RADIO COMPANY

Since 1915 — Manufacturers of Electronic Apparatus for Science and Industry

WEST CONCORD, MASSACHUSETTS

NEW YORK AREA: Tel. N. Y. WOrth 4-2722, N. J. WHitney 3-3140 **CHICAGO:** Tel. VIllage 8-9400
PHILADELPHIA: Tel. HAncock 4-7419 **WASHINGTON, D. C.:** Tel. JUniper 5-1088
SAN FRANCISCO: Tel. WHitecliff 8-8233 **LOS ANGELES 38:** Tel. HOllywood 9-6201
In CANADA, TORONTO: Tel. CHerry 6-2171